Novus Scientia 2025

22. Medzinárodná vedecká konferencia doktorandov strojníckych fakúlt technických univerzít a vysokých škôl

Novus Scientia 2025

Zborník príspevkov z XXII. Medzinárodnej vedeckej konferencie doktorandov strojníckych fakúlt technických univerzít a vysokých škôl

30.01.2025

Strojnícka fakulta

Technická univerzita v Košiciach

Zameranie konferencie:

- Automatizácia, mechatronika a robotika
- Technologické a materiálové inžinierstvo
- Manažment, priemyselné a digitálne inžinierstvo
- Konštrukčné a procesné inžinierstvo
- Špeciálne inžinierske procesológie

Vedecký a organizačný výbor konferencie

Patronát konferencie

Dr.h.c. mult. prof. Ing. Jozef Živčák, DrSc., MPH, akademik UčSS
Technická univerzita v Košiciach, Slovensko

Garant konferencie

prof. Ing. Ján Slota, PhD.
Technická univerzita v Košiciach, Slovensko

Vedecký výbor konferencie

prof. Ing. Jozef Bocko, CSc., Technická univerzita v Košiciach, Slovensko

prof. Ing. Radovan Hudák, PhD., Technická univerzita v Košiciach, Slovensko

prof. Ing. Michal Kelemen, PhD., Technická univerzita v Košiciach, Slovensko

prof. Ing. Peter Trebuňa, PhD., Technická univerzita v Košiciach, Slovensko

prof. Ing. Emil Spišák, CSc., Technická univerzita v Košiciach, Slovensko

prof. Ing. Tomáš Brestovič, PhD., Technická univerzita v Košiciach, Slovensko

doc. Ing. Ján Kráľ, PhD., Technická univerzita v Košiciach, Slovensko

prof. Ing. Peter Frankovský, PhD., Technická univerzita v Košiciach, Slovensko

doc. RNDr. Tibor Krenický, PhD., Technická univerzita v Košiciach, Slovensko

doc. Ing. Michal Holubčík, PhD., Žilinská univerzita v Žiline, Slovensko

prof. Ing. Stanislav Ďuriš, PhD., Slovenská technická univerzita v Bratislave, Slovensko

prof. Ing. Peter Šugár, CSc., Slovenská technická univerzita v Bratislave, Slovensko

doc. Ing. Jaroslav Katolický, Ph.D., Vysoké učení technické Brno, Česká republika

doc. Ing. Miroslav Mahdal, Ph.D., VŠB Technická univerzita Ostrava, Česká republika

prof. Ing. Tomáš Jirout, Ph.D., ČVUT Praha, Česká republika

doc. Ing. Petr Lepšík, Ph.D., Technická univerzita v Liberci, Česká republika

doc. Ing. Václav Vaněk, Ph.D., Západočeská univerzita v Plzni, Česká republika

prof. dr hab. inż. Jarosław Sęp, Politechnika Rzeszowska, Poľsko

Dr inż. Tomasz Jachowicz, Politechnika Lubelska, Poľsko

Dr inż. Jacek Rysiński, Uniwersytet Bielsko – Bialski, Poľsko

Organizačný výbor konferencie

prof. Ing. Ján Slota, PhD.

Ing. Erika Dubňanská

Ing. Martina Hančinová

Ing. Barbara Schürger

Ing. Jaroslav Melko

Ing. Lucia Žuľová

Recenzovaný zborník z vedeckej konferencie

Príspevky v zborníku z vedeckej konferencie boli recenzované recenzentmi prostredníctvom anonymného recenzného konania.

Novus Scientia 2025

Zborník príspevkov z XXII. Medzinárodnej vedeckej konferencie doktorandov strojníckych fakúlt technických univerzít a vysokých škôl

Názov:	Novus Scientia 2025
Editor:	© prof. Ing. Ján Slota, PhD.
	© Ing. Erika Dubňanská
	© Ing. Martina Hančinová
	© Ing. Barbara Schürger
Vydavateľ:	Technická univerzita v Košiciach,
	Strojnícka fakulta,
	Letná 1/9, 042 00 Košice-Sever
Rok:	2025
Náklad:	75 výtlačkov
Rozsah:	360 strán
Miesto konania:	Strojnícka fakulta, Technická univerzita v Košiciach
Dátum konania:	30.01.2025

ISBN 978-80-553-4828-5

OBSAH

Autorský kolektív a názov príspevku	Strany
ALI T., ŽIVČÁK J., ŠIŠKOVÁ S.: Design of Wilkie syndrome biomechanical algorithms in vascular surgery	8 – 12
BADIDOVÁ M., SOBOTOVÁ L.: Research on ultrafine particles emitted from road traffic	13 – 20
BENDA M. M., SPIŠÁK E.: Experimental analysis of blanking technology for electrical steel in double layer configuration	21 – 26
BRADA L., MIKOVÁ Ľ., PRADA E.: Gamification of learning in the industry	27 – 34
BRINDZA J., DEMKO M., KUŠNÍR J., VRABEĽ M., IŽOL P.: Development of Textured Turning Cutting Inserts	35 – 40
BUBER M., TOMÁŠ M., EVIN E.: Use of modern techniques in evaluating the dimensions of pressing made from dual-phase steel	41 – 46
ČAJKOVÁ J., TREBUŇOVÁ M., BAČENKOVÁ D.: Differentiation potential of mesenchymal stem cells in vitro	47 – 53
ČURMA P., LÁZÁR M.: Research into potential application of EHD propulsion in the conditions of gravitational interaction	54 – 59
DOMINIK F., SLOTA J., VRABEĽ M., IVANČÁK P.: Design of an experimental system for detecting permeability values of felt electrodes in redox batteries	60 – 64
DOWBYSZ A., KUKFISZ B., SAMSONOWICZ M.: Safety in archives - archival box fire with emphasis on their flammability and smoke density	65 – 69
DUBŇANSKÁ E., HANČINOVÁ M., SCHÜRGER B., HUŇADY R.: 3D Printing of Silicate Materials and their Advanced Application: A Review	70 – 76
DUDOVÁ K., BEDNARČÍKOVÁ L., ŽIVČÁK J.: Evaluation of 3D Scans Generated by Artec Eva and Revopoint Miraco Scanners for Healthcare Applications	77 – 81
DZURŇÁK P., MANTIČ M., BERKO L.: Increasing of data processing security of container terminal model	82 – 88
EIBEN V., KRÁLIKOVÁ R., LUMNITZER E.: Thermal imaging systems: new possibilities for detection and analysis of thermal radiation	89 – 94
GREGA M., BREZINOVÁ J.: Locating the failure of forged bearing rings	95 – 103
GRYKO A., PROCHOR P.: Numerical analysis of the influence of scaffold implantation on load distribution in long bones	104 – 108
HANČINOVÁ M., DUBŇANSKÁ E., SCHÜRGER B., HUŇADY R.: Trends in the Development of Non-Pneumatic Tyres: A Review	109 – 114
HUDÁK Š., LÁZÁR M.: Optimization of a Heat Exchanger for Hydrogen Storage Using AI-Driven Generative Design and Additive Manufacturing	115 – 121
JÁNOŠÍK R., GAZDA T.: Influence of microbiological aspects and dust environment on quality in the automotive industry	122 – 127
KAČÍR M., ŽUĽOVÁ L., GREGA R., URBANSKÝ M.: Design and construction of the pneumatic torsional vibration tuner	128 – 132
KAPRAĽ V., GAJDOŠ I., SLOTA J.: Advanced Designs in Single-Screw Extruders: Enhancing Efficiency and Material Flow Control	133 – 139
KOKARDA V.: Quality control of products, manufactured by additive technologies	140 – 148

KOLEMBUSOVÁ P., FERENČÍK N., HUDÁK R.: Sustainable Dyeing of Polyamide 12: Research and Prospects	149 – 153
KOPEC J., PEKARČÍKOVÁ M.: Using IOA and educational robots to create a digital twin	154 – 159
KRAJNÝ P., JANEKOVÁ J.: EHS Data Digitization and Integration into Production Monitoring Tools to Prevent Occupational Diseases	160 – 165
KULYA J. M., TOMÁŠ M.: Prediction of the limit strain curve by numerical simulation and its verification by experiment	166 – 172
KUŠNÍR J., BRINDZA J., DEMKO M., VRABEĽ M.: Design of a modular fixture for cyclic testing and climate exposure	173 – 178
MAJERČÁK O., VAGAŠ M.: Node-RED as a tool for industrial data visualization	179 – 185
MÁLIK M., JÁNOŠ R.: Laser welding using a collaborative robot	186 – 191
MAŚLANKA M., JANUSZ J., KUROWSKA A., JABŁOŃSKI A., RAJZER I.: The Potential of 4D Printing in Designing Adaptive Medical Implants	192 – 196
MAŚLANKA M., JANCARCZYK D., PYTKA D.: Impact of Lighting Conditions on Vision Inspection Systems: Analysis, Cost Estimation, and Operational Overview of Cognex Cameras	197 – 202
MERVA T., VIRGALA I.: Exploring Operational Space Controllers for Robotic Manipulators	203 – 207
MIHÁLIK I., TÓTH L., LÁZÁR M.: Analysis of heat transfer in a delivery bag to assess the possibility of drug transportation	208 – 213
MIKITA S., VIŇÁŠ J.: Overview of the situation and trends of additive manufacturing using a laser beam	214 – 218
MILENOVSKÝ P., JASMINSKÁ N., LÁZÁR M.: Design of a hydrogen storage system for a four-cylinder internal combustion engine	219 – 223
ONDERČO P., RYBÁŘ J., ZARGHOON S., LEJA J.: Tortuosity Decoder as a Tool for Measuring Parameters of Overhead Contact Lines in Tram Systems	224 – 229
ONDREJOVÁ B., BEDNARČÍKOVÁ L., FERENČÍK N., ŽIVČÁK J.: Innovative Approach to Somatotype Determination	230 – 235
PILÁT P., VARGA J., SEMJON J.: Comparison of sensing technologies for mobile robot intended for environments with increased radiation	236 – 241
PORUBČANOVÁ D., BALÁŽIKOVÁ M.: Risk factors for psychological stress in the workplace	242 – 247
PYTKA D., JANCARCZYK D., MAŚLANKA M.: A Case Study on Improvements for Sumo Robotics Competitions	248 – 252
ROMANČÍK J., VAGAŠ M.: Real-time monitoring of the response of the SMA actuator	253 – 258
RUDA F., SPIŠÁK E.: The influence of the galvanizing method on the surface properties of thin steel sheets	259 – 266
SAVKOVÁ N., ŠTEFANOVIČ B., SCHNITZER M., BÁNOVČIN J., ŽIVČÁK J.: Reverse engineering of palate cleft impression trays	267 – 272
SEDLÁKOVÁ V., DRSTVENŠEK I., HLUBEŇOVÁ J., KNEPPO P., HUDÁK R.: Overview of the Effects of Light on Mesenchymal Stem Cells	273 – 277

SCHÜRGER B., FRANKOVSKÝ P., HANČINOVÁ M., DUBŇANSKÁ E.: Comparative analysis of honeycomb and re-entrant auxetic structures: Poisson´s ratio and mechanical properties using finite element method	278 – 283
SMETÁNKA A., RYBÁŘ J., ĎURIŠ S., ZARGHOON S., GERNESCHOVÁ J., SEDLÁK V.: Contribution to Blood Pressure Metrology	284 – 288
SUKOPOVÁ D., FIĽO M., VYROSTKOVÁ L.: Advanced Analytics and Digitalization as Tools for Modern Business Management	289 – 294
ŠIŠKOVÁ S., ŽIVČÁK J., ALI T., POTOČKOVÁ V., DOBRODENKOVÁ S.: Assessment tools and study design for evaluation of Autonomic Dysfunction in patients with Abdomino-pelvic Vascular Compression Syndromes	295 – 301
ŠTEFČÁK P., GAJDOŠ I., SLOTA J.: Bypassing CAD modelling through Parametric G-Code Generation for 3D Printing	302 – 307
TARBAJOVSKÝ P., PUŠKÁR M., VIROSTKO M.: Preparation for hydrogen combustion	308 – 313
TOMASZEWSKA A., ŽIVČÁK J.: Current Trends and Future Perspectives in Personalized Anatomical Implants: A Review of Dental Implant Design	314 – 320
VARJÚ E., KOVÁČ J.: Development of an AR Training Simulation Using Unity and AR Foundation	321 – 327
VELIGOTSKYI N., GUZANOVÁ A.: Change in hardness of lightweight alloys when thermal drilling	328 – 334
VIĽCHA J., ŽIVČÁK J.: Planning the reconstruction of mandible with patient specific implant	335 – 339
VIROSTKO M., MANTIČ M., TARBAJOVSKÝ P.: Genetic algorithms in Generative design	340 – 345
VÝBOCH J., ČOMAJ M., VIŇÁŠ J.: Methods of investigating the wear of cylinders intended for the continuous casting of steel into plates and of solving their service life.	346 – 351
ŽUĽOVÁ L., GREGA R., KAČÍR M.: A targeted energy transfer in mechanical drive achieved by varying torsional stiffness	352 - 357

TECHNICAL UNIVERSITY OF KOŠICE
Faculty of Mechanical Engineering

Design of Wilkie syndrome biomechanical algorithms in vascular surgery

Talal Ali [1,2,*], Jozef Živčák[1], and Silvia Šišková[1,3]

[1] Technical University of Košice, Faculty of Mechanical Engineering, Department of Biomedical Engineering, Letná 1/9 | 042 00 Košice-Sever
[2] National Institute of Cardiovascular Diseases, Pod Krásnou hôrkou 1/7185, 833 48 Bratislava; dr.talal.ali8@gmail.com
[3] Dr Asociácia Vaskulárnych Kompresívnych Syndrómov a Ehlers-Danlos, o.z., Balkánska 110/108, 851 10, Bratislava, Slovakia, silvia.siskova.phd@gmail.com
* Correspondence: talal.ali@student.tuke.sk

Abstract: The objective of this paper is to define the pathology of Wilkie syndrome and design biomechanical algorithms for its diagnostic process as well as treatment options in vascular surgery. The diagnostic process is complex, consisting of a set of different radiologic imaging methods as well as detailed analysis of the patient's medical history and clinical symptoms. Radiography, upper GI fluoroscopy, computed tomography angiography or magnetic resonance angiography and ultrasound with aortomesenteric angle and distance measurements are all considered essential diagnostic modalities. Treatment strategies are similarly as complex, including first-line therapy of non-invasive options such as enteral and parenteral feeding with the goal to decompress gastroduodenal dilation, correct nutritional deficiencies, and promote increase of the aortomesenteric fat pad. In case of failure, surgical options should be considered, including duodenojejunostomy, Strong's procedure or vascular decompression by infrarenal transposition of the superior mesenteric artery. Both, diagnostics and treatment of Wilkie syndrome require a high degree of expert knowledge and care.

Keywords: Wilkie syndrome; Superior mesenteric artery syndrome; SMAS; biomechanical algorithms; radiography; upper GI fluoroscopy; computed tomography angiography; magnetic resonance angiography; ultrasound; duodenojejunostomy; Strong's procedure; infrarenal transposition of the superior mesenteric artery

1. Introduction and pathology

Superior mesenteric artery syndrome (SMAS), also called mesenteric duodenal compression syndrome, Wilkie syndrome, chronic duodenal ileus or cast syndrome, is a rare clinical condition defined as a compression of the third portion of the duodenum in between the SMA and abdominal aorta (AA), due to narrowing of the space between them. SMAS is primarily attributed to loss of the intervening mesenteric fat pad, leading to partial or complete duodenal obstruction. Its manifestations are complex and non-specific, including postprandial epigastric pain, nausea, vomiting, early satiety, weight loss and anorexia. SMAS may present as an acute syndrome, or it may have an insidious onset with chronic symptoms. SMAS mainly affects patients, males and females between 10 and 60 years of age. This study aims to discuss the best design of biomedical - mechanical algorithms to set the most accurate diagnostic parameters as well as to decide the most optimal management of this medical problem [1,2].

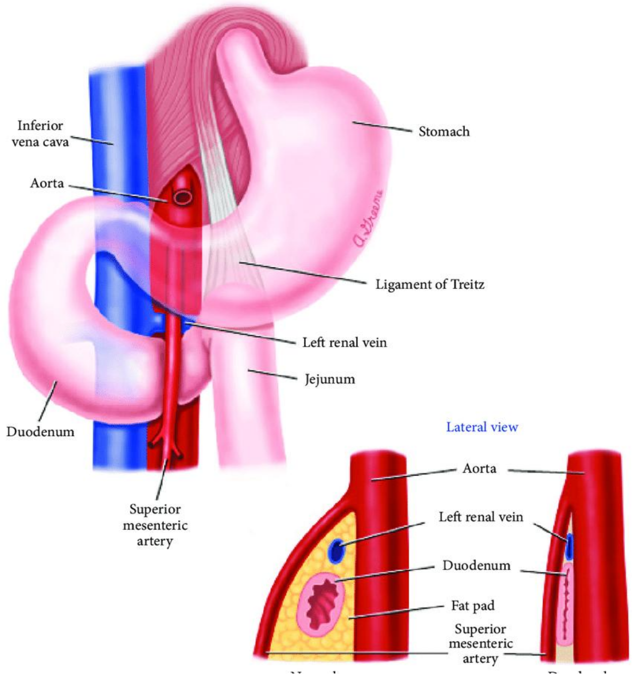

Figure 1. Abdominal Aorta – AMS Angulation; normal angle 38-65 degrees on the left, reduced angle below 25 degrees on the right, 3rd part of duodenum compression-obstruction [3].

2. Diagnostic Methods

The diagnosis of Superior mesenteric artery syndrome is based on clinical symptoms of the patient and radiologic evidence of duodenal obstruction. The following imaging methods aid in the diagnostic process in order to obtain a more accurate diagnosis:

1. Radiograph
   A plain radiograph allows to visualize a dilated stomach and proximal duodenum, which are filled with fluid and/or gas [4].
2. Upper GI fluoroscopy
   Fluoroscopy is a superior diagnostic technique. While a plain radiograph displays only a static image, upper GI fluoroscopy allows for visualization of moving pictures. It lets the examiner to visualize dilation of stomach and duodenum, a collapsed small bowel distal to the crossing on the superior mesenteric artery, while at the same time look for the typical to and fro motion of the contrast in the gastroduodenal part. It is considered a gold standard technique and important part of the diagnostic process of Superior mesenteric artery syndrome [4,5]
3. CTA/MRA
   Computed tomography angiography and magnetic resonance angiography enable visualization of the vascular structures, compression of the duodenum in the aortomesenteric space and measurement of the aortomesenteric angle and distance. Although there are different opinions in the literature on the exact range of a normal aortomesenteric angle, measurements in between 20-70 degrees are generally considered as normal. Angle measurements below 16 degrees are considered as reduced and indicative of Superior mesenteric artery syndrome. Similarly, aortomesenteric distance of 10-28mm is considered a normal finding, while distance less than 8mm is indicative of Superior mesenteric artery syndrome [4-6]

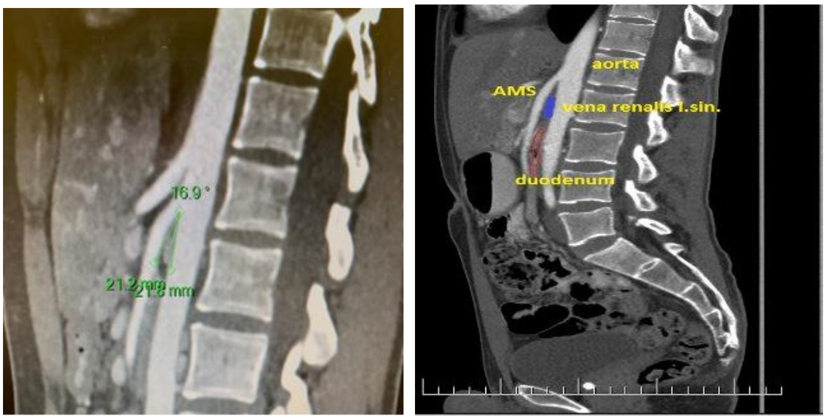

Figure 2. CTA with visualization of aortomesenteric angle and measurements.

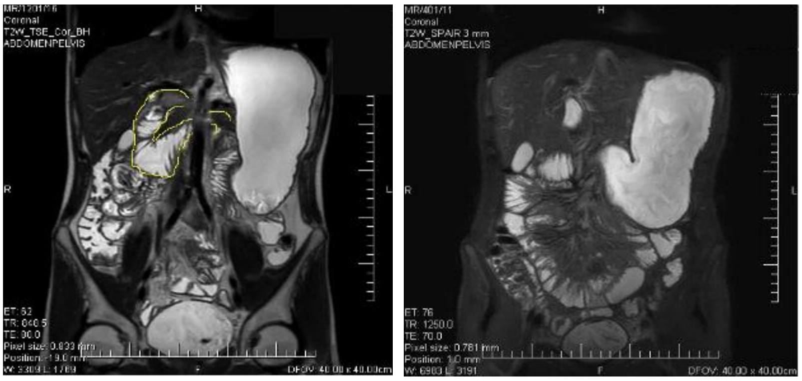

Figure 3. MRA with visible stomach dilation.

4. Ultrasound

   Doppler ultrasound with velocity measurements, generally used for diagnosing also other vascular compression syndromes from the same pathology family, or also a normal ultrasound is an accessible and minimally invasive diagnostic method, which serves as an additional modularity in the diagnostic process of Wilkie syndrome. Similarly as CTA or MRA, it allows for aortomesenteric angle and distance measurements. The advantage is that as opposed to CTA and MRA, ultrasound allows for examination in both supine and standing positions. This provides valuable insights into angle and distance differences while standing up versus lying down. The reductions are normally seen in supine position. However, it must be taken into account that not all patients with aortomesenteric angle and distance reduction will have Superior mesenteric artery syndrome. Therefore, the imaging findings must always be correlated with the patient's clinical symptoms [4-6].

3. Treatment strategies

Traditionally, treatment has consisted of conservative measures such as:

- start with medical management, including decompression of the stomach and duodenum with a nasogastric tube, correction of nutritional and electrolytes deficiencies, through total parenteral nutrition, or preferably, if possible, enteral feeding with a nasojejunal tube past the point of compression, which fulfils nutritional requirements while avoiding the complications of total parenteral nutrition. When tolerated, oral feeding may be resumed. This helps build up the fat cushion between the superior mesenteric artery and aorta and, hence, may help in reversing the situation.

- posturing manoeuvres during meals and motility agents may be helpful in some patients
- lying in right decubitus position may relieve compression of duodenum

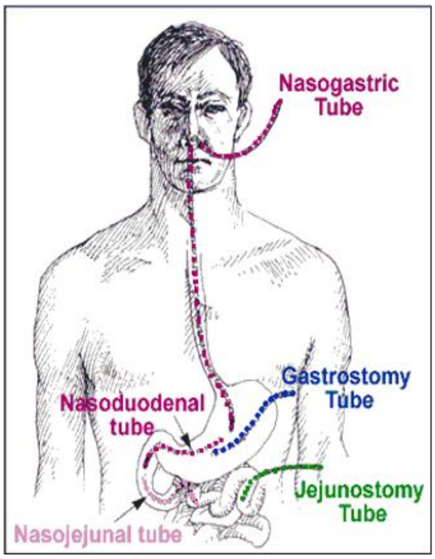

Figure 4. Gastrointestinal tubes [7].

Surgery may be considered if conservative treatment fails:

- duodenojejunostomy is effective in the majority of patients
- laparoscopic duodenojejunostomy offers a new minimally invasive therapeutic approach to superior mesenteric artery syndrome
- Strong's procedure, laparoscopic surgery involving lysis of the ligament of Treitz with the mobilisation of the duodenum is another minimally invasive approach
- vascular decompression by transposition of SMA to the infrarenal part of the aorta [8-10]

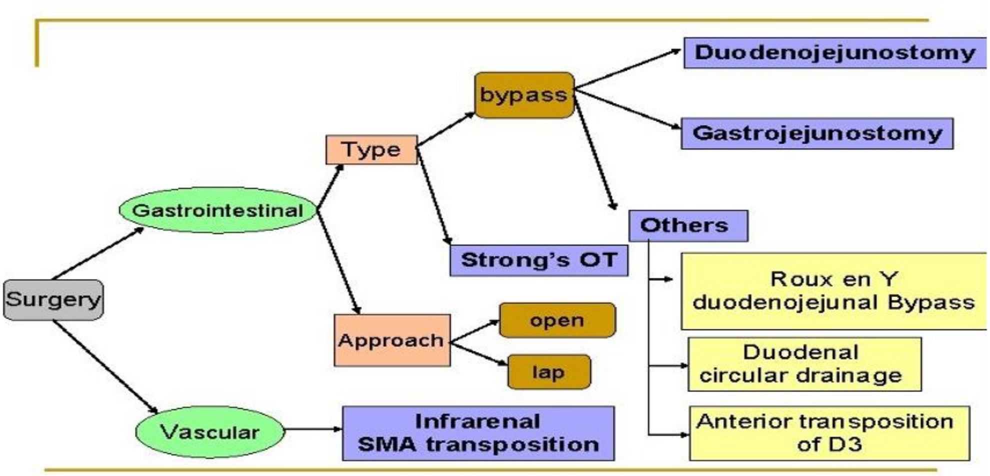

Figure 5. Surgical treatment options of Superior mesenteric artery syndrome [10].

4. Conclusion

Due to its rarity and nonspecific symptoms, Wilkie's syndrome poses a really challenging diagnosis. High index suspicion in cases of severe weight loss and upper gastrointestinal symptoms is of utmost importance. Enhanced CT and upper GI fluoroscopy are the gold standard diagnostic modalities and should be employed whenever the patient presents with suggestive symptoms. Early detection can not only avoid the syndrome-associated complications but also improve the prognosis, making conservative measures more likely to be effective. Surgery should be considered in more severe, chronic cases or whenever medical treatment fails [8,10].

Acknowledgements: This paper was written with the financial support from the KEGA granting agency within the project solutions No. 050TUKE-4/2022 and No. 021TUKE-4/2022, and with financial support from the APVV granting agency within the project solutions No. APVV-20-0068 and No. SK-CZ-RD-21-0056.

References

1. Strong, E. K. (1958). Mechanics of arteriomesenteric duodenal obstruction and direct surgical attack upon etiology. Annals of Surgery, 148(5), 725–730. https://doi.org/10.1097/00000658-195811000-00001
2. Sapkas, G., & O'Brien, J. P. (1981). Vascular compression of the duodenum (cast syndrome) associated with the treatment of spinal deformities. A report of six cases. Archives of Orthopaedic and Traumatic Surgery, 98(1), 7–11. https://doi.org/10.1007/bf00389703
3. Pillay, Y. (2016). Superior mesenteric artery syndrome: A case report of two surgical options, duodenal derotation and duodenojejunostomy. Case Reports in Vascular Medicine, 2016, 8301025. https://doi.org/10.1155/2016/8301025
4. Knipe, H., & Ranschaert, E. (2010). Superior mesenteric artery syndrome. In Radiopaedia.org. Radiopaedia.org.
5. D'Oria, M., Zlatanovic, P., Anthony, A., Dua, A., Flores, A. M., Tanious, A., Rodríguez Morata, A., Scerrati, A., Baccellieri, D., Biscetti, F., Baldazzi, G., Mantovani, G., Sen, I., Peinado Cebrian, J., Rocha-Neves, J., Sousa, J., Davidovic, L., Juszynski, M., Markovic, M., … Komlos, P. P. (2023). International Union of Angiology consensus document on vascular compression syndromes. International Angiology: A Journal of the International Union of Angiology, 42(4), 282–309. https://doi.org/10.23736/S0392-9590.23.05100-3
6. Lukáš Vincze, Silvia Šišková, Jozef Živčák, Talal Ali. (2024, November 15). Abdomino-Pelvic Vascular Compression Syndromes in the Abdominal Cavity. 13. Slovenská Konferencia o Zriedkavých Chorobách.
7. Surgery 6th year, Tutorial (Dr. AbdulWahid). (n.d.). SlideShare. Retrieved November 21, 2024, from https://www.slideshare.net/slideshow/surgery-6th-year-tutorial-dr-abdulwahid/10349417
8. Rehman, A., Saeed, A., Shaukat, T., Jamil, K., Zaidi, A. H., & Abdullah, K. (2011). Wilkie's syndrome. Journal of the College of Physicians and Surgeons--Pakistan: JCPSP, 21(1), 43–45. https://doi.org/01.2011/JCPSP.4345
9. Von Rokitansky, C. (n.d.). Lehrbuch der pathologischen Anatomie (Vol. 3). Braumüller und Seidel.
10. Ali, T., Tomka, J., Bakirli, I., & Bakirov, I. (2022). Surgical treatment of Wilkie's syndrome by vascular transposition. Cureus, 14(4), e24251. https://doi.org/10.7759/cureus.24251

TECHNICAL UNIVERSITY OF KOŠICE
Faculty of Mechanical Engineering

Research on ultrafine particles emitted from road traffic

Miroslava Badidová [1,*] and Lýdia Sobotová [1]

[1] Technical University of Kosice, Faculty of Mechanical Engineering, Letna 9, 042 00 Kosice; miroslava.badidova@estudent.tuke.sk
[*] Correspondence: miroslava.badidova@student.tuke.sk, lydia.sobotova@tuke,sk , Tel.: +421 55 602 2793

Abstract: The emissions of tyre wear particles (TWPs) into the environment are increasing from last years and have negative impacts on the human health. The environmental fate of tyre and road wear particles (TRWPs) receives increasing attention due to the per capita emission volumes of 0.2 – 5.5 kg/ (cap year) and recent reports on the environmental hazard of TRWP constituents. It is also expected that aging impacts TRWPs fate in the environment, but detailed knowledge is quite limited, yet. Making use of information on tyre aging, the available knowledge on environmental aging processes such as thermooxidation, photooxidation, ozonolysis, shear stress, biodegradation and leaching is very important in future studies. There is a complex interplay between aging processes in the environment that needs to be considered in future aging studies. In addition to existing basic qualitative understanding of the aging processes, quantitative understanding of TRWP aging is largely lacking.

Keywords: Ultrafine Particles, Aerosols, Environmental Engineering, Road Traffic

1. Introduction

The following parts give a brief overview of the generation, characteristics, and pathways of TRWP related to the atmosphere, road runoff, and soil to clarify the complex, interrelated, and dynamic systems in which TRWP are generated, transported, transformed, and interact with the environment. These complex interrelationships must be thoroughly understood to derive suitable mitigation strategies for TRWP.

Tyre wear and abrasion are inevitable outcomes of friction between the tyres of vehicles and the road. The rate at which tyre tread is abraded depends on several parameters [1, 2, 3]:

- tyre characteristics (e.g., size, tread depth, construction, composition, age, mileage, and tire pressure),
- road surface characteristics (e.g., material, macro and micro texture, binder, wet/dry, porosity, temperature),
- road topography and design (e.g., steepness, curvature),
- vehicle operation (e.g., velocity, linear, and radial acceleration rate),
- vehicle characteristics (e.g., type of vehicle, vehicle weight, suspension, steering alignment.

After initial emission and deposition, particles that are not cleaned from the road will remain in place or be transported in natural or engineered environmental systems. The interconnected environmental and engineered compartments into and through which the particles flow is road surface, atmosphere, adjacent surfaces, storm water or combined sewers, surface water and groundwater, and sediments. The Fig. 1 shows the distribution of tyre wear particles in environment media.

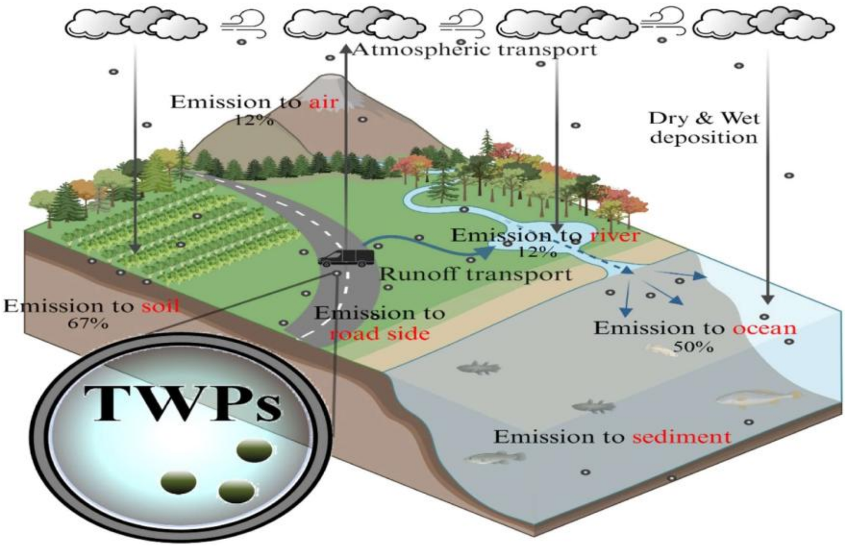

Figure 1. Characteristics of tyre wear particles in the environmental media [3].

Aerosols from **combustion of vehicle engines** originate from five sources: fuel, fuel additives, inlet air, lubrication oil and the mechanical breakdown of pre-existing materials. The latter can also form from other sources in the vehicle (e.g., brake dust). Of those formed in the engine, there are four main types of aerosols: carbonaceous, organic, sulphate and ash. These usually appear in combination. Fuel and oil contribute to all four fractions; fuel additives, air and mechanical breakdown contribute to the ash fraction. A typical aerosol from a heavy-duty diesel engine is 41 % carbon, 13 % ash, 14 % sulphate/water, 25 % unburnt oil and 7 % unburnt fuel [21].

Sources from **non-combustion particle sources** of course - mode particles include dust from brake linings, tyre wear, road - surface wear, engine wear and rust, dust and scale from the exhaust and catalyst system.

This article will deal with part of non-combustion particle sources in next chapters.

2. Materials and Methods

The review on mitigation measures for TRWP is based on very comprehensive research on literature from all over the world including scientific literature, proceedings, and policy papers, using SciFinder, ScienceDirect, Google Scholar, and SpringerLink. Furthermore, the authors of this study assessed information from European and US expert panel organizations and networks [1,2,3].

The study assigns the identified measures to the following TRWP mitigation classes:

- mitigation measures to prevent the generation of TRWP,
- mitigation measures at the vehicle and the road surface to prevent TRWP from being spread in air, water, and soil,
- mitigation measures on road runoff and atmosphere to prevent TRWP from accumulation and fate in natural environmental.

In the Fig. 2 is shown that after bad maintenance of tyres the life-service s are dramatically shortens.

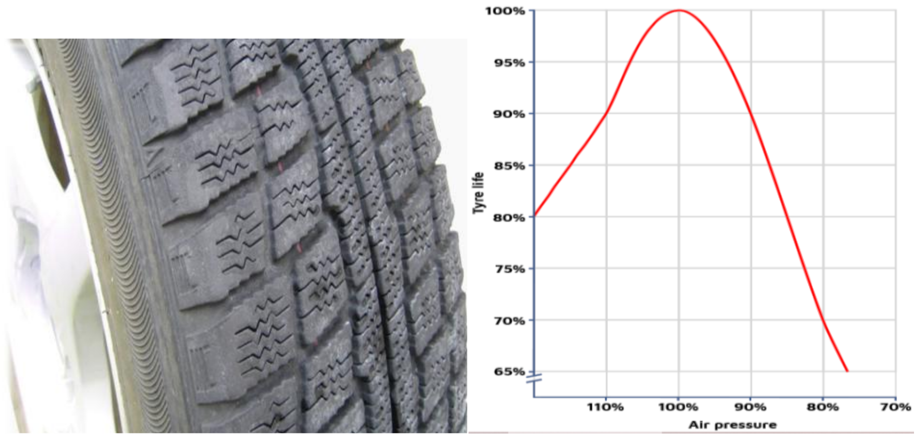

Figure 2. Incorrect air pressure dramatically shortens tyre service life [2].

As TRWPs are generated at the road surface, light exposure and temperature are likely to control the aging during the initial stage after release. TRWP aging occurs in various environmental compartments, Fig. 3. as TRWPs are generated at the road surface, light exposure and temperature are likely to control the aging during the initial stage after release. Sooner or later, TRWPs are transported by atmospheric redispersion or rain water road runoff to the road side, where photooxidation, leaching and microbial degradation may occur. Further transport of TRWPs to sewer systems eventually to terrestrial and aquatic environments is taking place, Fig. 3. During transport, TRWPs experience mechanical shear stress which can cause break-up of particles, but also aggregation may occur. As soon as TRWPs are dispersed in water, inorganic or organic constituents may leach. TRWPs in the PM_{10} fraction may be transported via the atmosphere and volatile compounds may evaporate from these particles as well, Fig.3. All these processes, oxidation, mechanical aging, biodegradation and leaching will affect TRWP properties. [8]

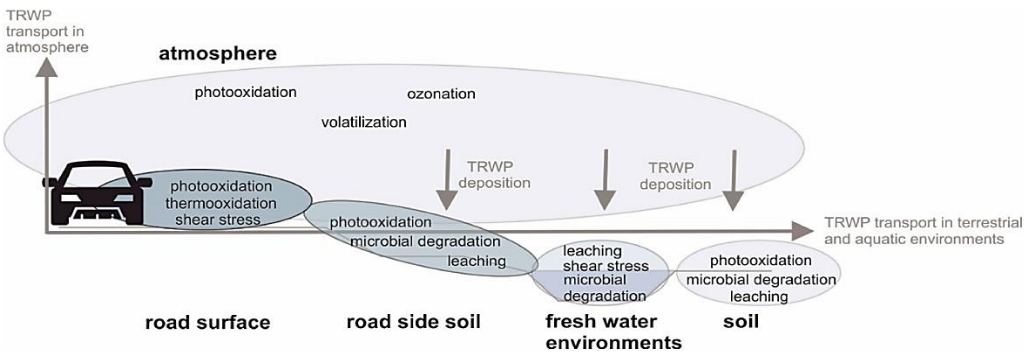

Figure 3. TRWP aging processes on road surface, in atmosphere, road side soil, freshwater environments and soil; grey arrows indicate transport pathways of TRWPs, and shading from dark to light represents expected concentrations of TRWPs from high to low in environmental compartments [1].

It is estimated that non-exhaust traffic emissions of medium sized cars consist of approximately 45 % road wear, 32 % tyre wear and 23 % brake wear [9].

A literature review [10] shows that the share of TWPs of non-exhaust emissions from traffic is 5 – 30 %. Other studies on aerosols or deposited dust show that the size of TWPs was found to be between 10 nm and several 100 µm (from $PM_{0.1}$ to PM_{10}) [13], [16], [20]:

- **PM_{10-80}:** Analysis of PM_{10-80} collected samples next to German motorways and highways revealed that many collected aerosol particles (Apr. 54 % by volume) could be traced back to tyre wear [11]. The rubber from tyre wear was roundish or kidney shaped and contained traces of C, Si, Zn which are typical elements in fillers and vulcanization agents for tyres (i.e., C, silica, or zinc oxide) [10]. Contribution of tyre wear to PM_{10} accounts for up to approx. 11 mass-% [14].

- **$PM_{2.5-10}$:** [15] summarized that TWPs are predominantly coarse particles ($PM_{2.5-10}$), which are generated by shear forces and in turn are influenced by the road-surfaces, tyre types and driving conditions. -
- **$PM_{1-2.5}$**: Aerosol measurements at the road-tyre interface showed that nanoscale emissions between 5 and 700 nm are generated, which depend on speed and tyre type [12], [16], [17].
- Other measurements in an urban street area showed that over 99 % of the particle concentrations were found in the size range of 10 – 300 nm, whereas the particle mass concentration was almost equally distributed between **PM_1 and $PM_{2.5}$. - $PM_{0.1}$**: [17] highlighted that ultrafine particulate matter ($PM_{0.1}$) must not be neglected.

Schematic diagram of ultra-fine particles and transmission, process is shown in the Fig.4.

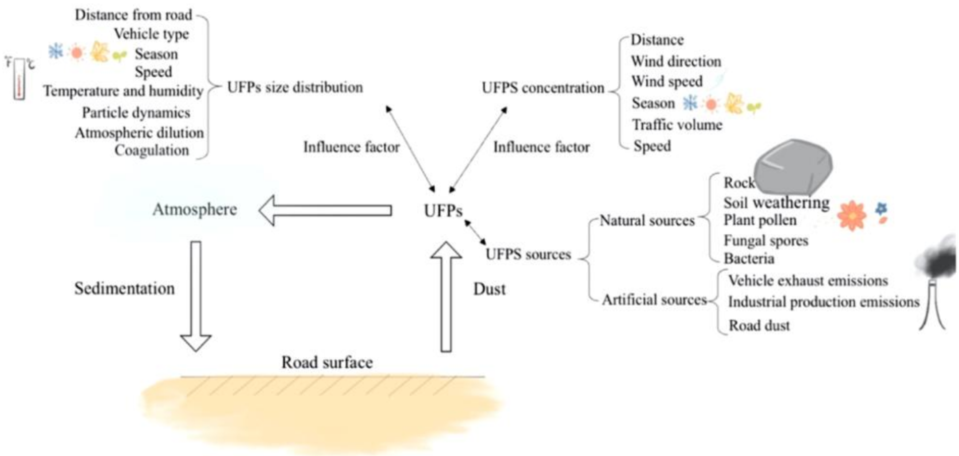

Figure 4. Schematic diagram of ultra-fine particles and transmission process [5].

3. Results

The physicochemical characteristics of micro- and nano-sized brake particles emitted from non-asbestos organic (NAO) and low-metallic (LM) brake pads were investigated under normal and harsh braking conditions using a brake dynamometer. Silication oil is another source of non-combustion aerosol, as well as of combustion aerosol

Under normal braking conditions, 28 % and 12 % of the total wear mass of brake pad and disc was emitted as PM_{10} and $PM_{2.5}$, respectively. [5, 6, 7,8].

In the Fig.5. and Fig.6 are shown the micro particles and nano particles measured from roads wear.

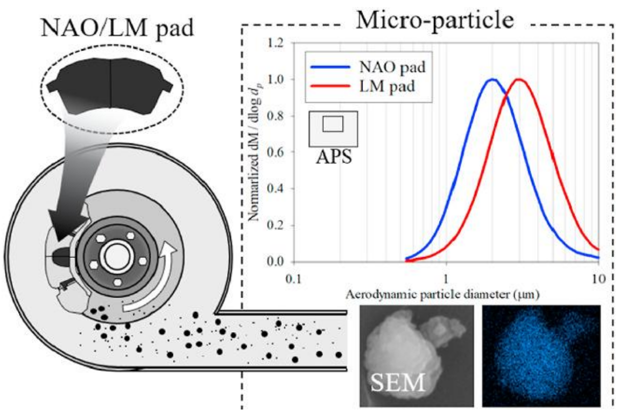

Figure 5. Structure, morphology and particle size of the brake-wear - micro- particles [5].

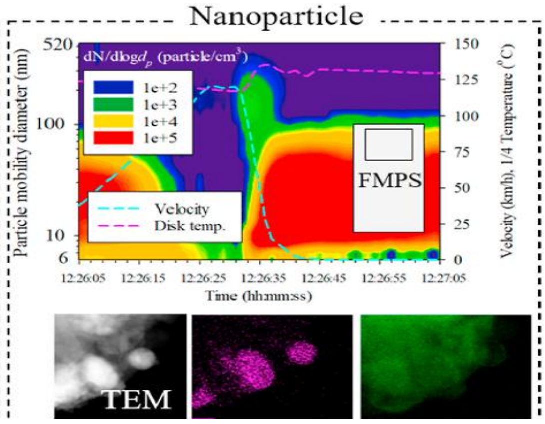

Figure 6. Structure, morphology and particle size of the brake-wear - nano- particles [5].

The scanning (SEM) and transmission (TEM) electron microscopy were used to obtain independent information on the composition, structure, morphology and particle size of the brake-wear particles. Overview of prevalent size of brake-wear particles shows SEM image on Fig 7 and Fig. 8. The main fraction of wear particles was around 1 μm in size. The larger, sharp-edged particles were also observed in both samples. Agglomerates composed of different sizes particles were noted. [5]

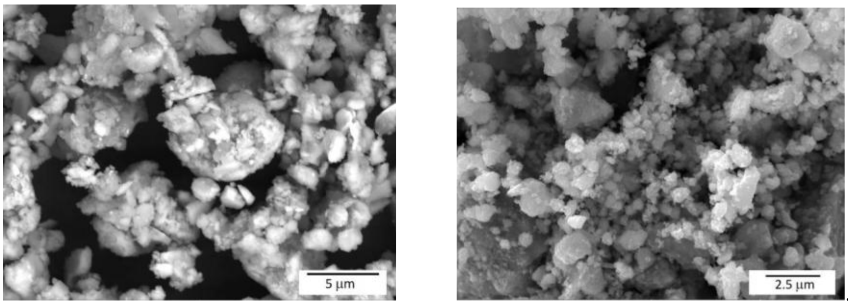

Figure 7. SEM images of brake wear particles obtained from samples(L -left) and (R-right) [6].

Compared to that only agglomerates of nanoparticles without any carbon matrix were observed on sample (Fig.8, right). High concentration of carbon in the form carbon matrix (Fig. 8 – left) can be probably connected with type of resin used for production of this brake pads.

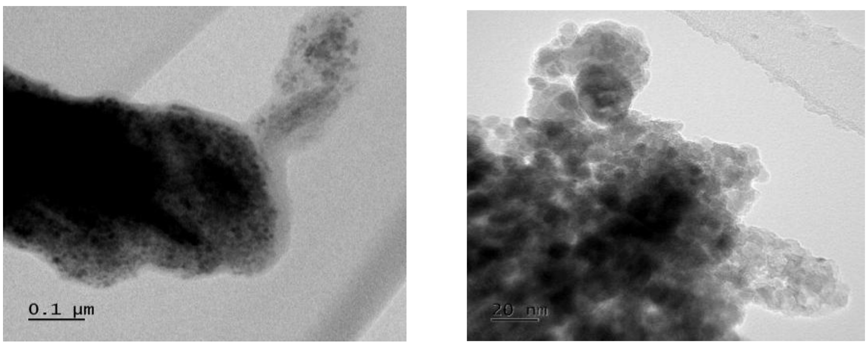

Figure 8. TEM images of brake wear particles. Matrix with trapped nanoparticles in sample (left) and detail of agglomerate found in sample (right) [6].

All particles, agglomerates but also larger grains, have similar elemental composition typical of brake emissions. The dominant elements are Fe, C and O, and Cu, Al, Si, S, Mg, Mn, Zn, and Ca are present to a lesser extent. According to EDX analysis is possible to say that the wear particles predominantly contain iron.

Representative spectra of microplastics from soil and road dust samples are shown in Fig.9 and Fig. 10. The spectra were compared with those of synthetic rubbers to support the hypothesis that the black debris originated from the tyre.

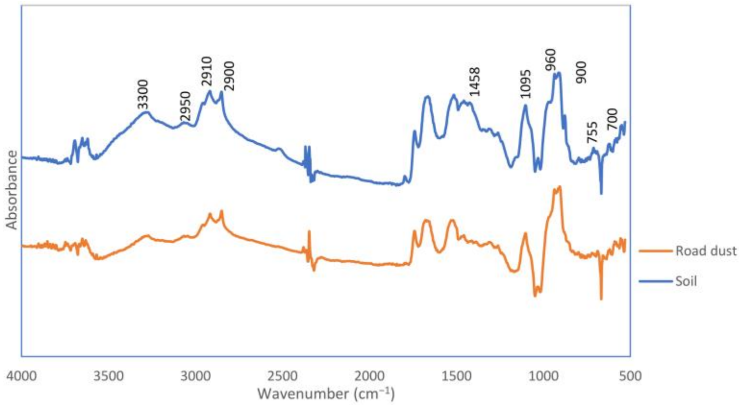

Figure 9. FTIR spectra of black fragments detected in soil and road dust samples [8].

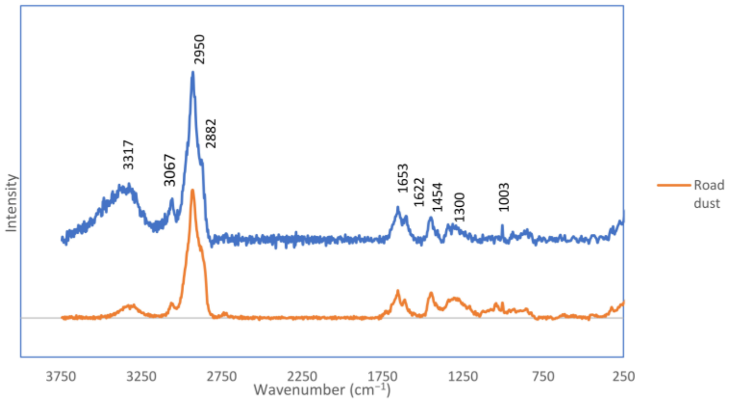

Figure 10. Typical Raman spectra of black fragments from soil and road dust samples [8].

4. Discussion

In all samples, a huge amount of black debris (91% from soil and road dust) was found, which were defined as synthetic materials originating from vehicle tires. In road dust samples, a higher amount of microplastics is found than in soil. This may be due to the direct effect of braking, which causes a greater accumulation of samples at the emission source than over a short distance in soil. Schematic representation of the formation of tyre wear nanoparticles and factors influencing it is shown in the Fig. 11. In the case of soils, the majority of cases represent the fraction below 50 μm. When analyzing road dust samples, it can be observed that most fractions are between 50 and 200 μm. This may be due to the possibility of smaller emission particles over longer distances and the greater degradation process that occurs in soil. Given the presence of run-off and street washing, it can be assumed that emissions of tire debris in road dust pose a very high risk, which are emitted directly into the wastewater treatment plant and subsequently into reservoirs. Degradation processes of microplastics occur downstream into the aquatic ecosystem. It should be emphasized that in both soil samples and road dust samples over 90 % of the microplastics present in the soil are a source of high pollution by releasing toxins into the soil and thus into groundwater and surface runoff. Degradation processes of microplastics occur downstream into the aquatic ecosystem. should discuss the results and how they can be interpreted from the perspective of previous studies and of the working hypotheses. The findings and their implications should be discussed in the broadest context possible. Future research directions may also be highlighted.

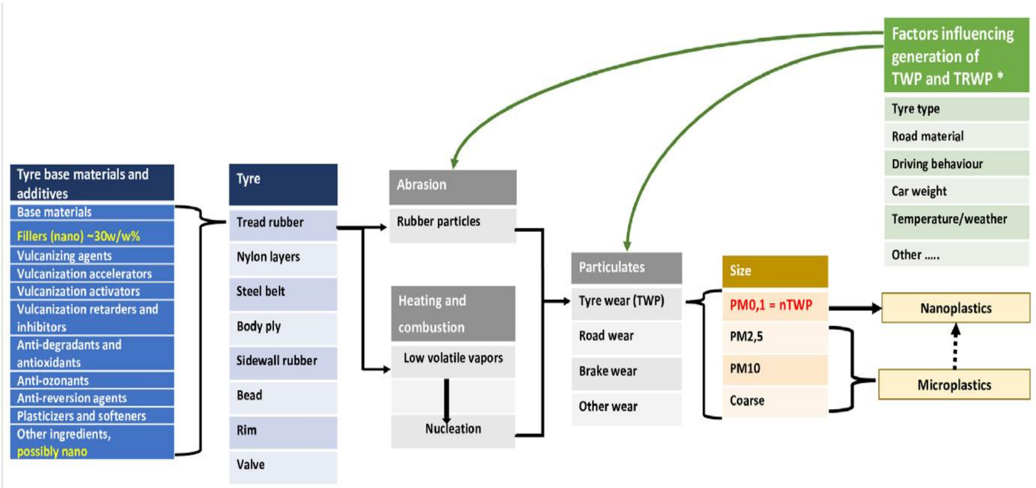

Figure 11. Schematic representation of the formation of tyre wear nanoparticles and factors influencing it. * TWP, Tyre Wear Particles; TRWP, Tyre and Road Wear Particles; PM, Particulate Matter [7].

5. Conclusions

The study analyzed environmental samples for the presence of microplastic fractions. Research confirms that an important source of microplastic emissions into the environment are communication roads. It was difficult to analyze the smallest particles below 10 μm, which are the most harmful to health. The main problems with microplastic analysis include the lack of standardization and a reference unit for the results obtained, which would allow comparisons between researchers.

Standardised analytical methods are needed to determine both particle size distributions and mass concentrations, particularly for nanoscale emissions such as airborne particulate matter ($PM_{0.1}$) or nanoparticles (< 100 nm) dispersed in agricultural soil or surface water. In addition, the development of innovative vehicle tyres and eco-friendly rubber formulations is needed to reduce tyre wear and facilitate recyclability. Nanotechnology-based fabrication methods (e.g. shown by [18] or the use of engineered nanomaterials (e.g. summarized in [19] could allow the reduction of the amount of tyre wear compared to conventional vehicle tyres.

Electrification is positive in terms of emissions, but it does not solve the problem of worn particles. Emissions of these particles need to be reduced for both health and environmental reasons.

You can do a lot by adapting the way you drive and care for your car. Tyre wear can be reduced by driving smoothly with slow acceleration and braking and the correct tyre pressure and wheel geometry. Brakes also wear less when driving in this way and thanks to the increased engine braking. The road surface is worn a hundred times more by studded tyres than by non-studded winter tyres. However, public transport and even more by cycling and walking are the most effective ways to contribute to reducing emissions.

Acknowledgments: This contribution was created based on the solution of the project UNIVNET 2024 and KEGA No. 032TUKE-4/2025,

Conflicts of Interest: The authors declare no conflict of interest. "The funders had no role in the design of the study; in the collection, analyses, or interpretation of data; in the writing of the manuscript, or in the decision to publish the results".

References

1. Wagner, S., Klockner, P., Reemtsma, T.: Aging of tire and road wear particles in terrestrial and freshwater environments – A review on processes, testing, analysis and impact, 2022, Chemosphere, Volume 288, Part 2, Available on: https://doi.org/10.1016/j.chemosphere.2021.132467
2. Yu Wang, Xinao Li, Hao Yang, Yang Wu, Quikn Pu, Wei He : A view of tire particles: Occurrences, adverse effects and control strategies, 2024, Ecotoxicology and Environmental Safety , 283 2024, Available on: doi.org/10.1016/j.ecoenv.2024.116782
3. Tyrewatch – life service of tyres, 2024, Available on: https://tyrewatch.com/knowledge/fuel-economy-tyre-wear/
4. Van Broekhuizen, P. Airbone release of tyre wear particles Technical Report 2022 NanoRigo 2022, Amsterdam
5. Sang-Hee Woo, Hyungjoon Jang, Min Young Na, Hye Jung Chang , Seokhwan Lee: Characterization of brake particles emitted from non-asbestos organic and low-metallic brake pads under normal and harsh braking conditions,2022, Atmospheric Environment, Vol. 278, Available on: https//doi.org/10.1016/j.atmosenv.2022.119089
6. Švábenská, E., Roupcová, P., Friák, M., Schneeweiss, O.: Nanoparticles from brake pads wear, In: NANOCON 2022, October 19 - 21, 2022 Brno, Available on: https://www.researchgate.net/publication/370534388
7. Pieter van Broekhuizen, Arto Säämänen, Daan Schuurbiers, Panagiotis Isigonis4, Keld A. Jensen, Dana Kühnel , Kees Le Blansch: Tyre wear nanoparticles as test for a nano risk governance framework,,2022 Frontiers in Environmental Science, Available on: DOI 10.3389/fenvs.2022.1045246
8. Jagoda Worek, Xymena Badura, Anna Białas , Joanna Chwiej, Kamil Kawo´n , Katarzyna Styszko: Pollution from Transport: Detection of Tyre Particles in Environmental Samples, Energies 2022, 15, 2816. Available on: https://doi.org/10.3390/en15082816
9. Ntziachristos, L., Boulter, P., 2019. EMEP/EEAAir Pollutant Emission Inventory Guidebook 2019 - Road Transport: Automobile Tyreand Brake Wear
10. Wagner, S., Hüffer, T., Klöckner, P.,Wehrhahn,M., Hofmann, T., Reemtsma, T., 2018. Tire wear particles in the aquatic environment - a review on generation, analysis, occurrence, fate and effects. Water Res. 139, 83–100. Available on: https://doi.org/10.1016/j.watres.2018.03.051.
11. Sommer, F., Dietze, V., Baum, A., Sauer, J., Gilge, S., Maschowski, C., Gieré, R., 2018. Tire abrasion as a major source of microplastics in the environment. Aerosol Air Qual. Res. 18, 2014–2028. Available on: https://doi.org/10.4209/aaqr.2018.03.0099.
12. Mathissen, M., Scheer, V., Vogt, R., Benter, T., 2011. Investigation on the potential generation of ultrafine particles from the tire–road interface. Atmos. Environ. 45 (34), 6172–6179.
13. Aatmeeyata, Kaul, D.S., Sharma, M., 2009. Traffic generated non-exhaust particulate emissions from concrete pavement: a mass and particle size study for two-wheelers and small cars. Atmos. Environ. 43, 5691–5697.
14. Beate Baensch-Baltruschat , Birgit Kocher , Friederike Stock, Georg Reifferscheid: Tyre and road wear particles (TRWP) - A review of generation, properties, emissions, human health risk, ecotoxicity, and fate in the environment, Science of the Total Environment 733(2020)137823, pp 1-19, Available on: https://doi.org/10.1016/j.scitotenv.2020.137823
15. Pallavi Pant, Roy M. Harrison: Estimation of the contribution of road traffic emissions to particulate matter concentrations from field measurements: A review. Atmospheric Environment 77 (2013) 78-97, Available on: http://dx.doi.org/10.1016/j.atmosenv.2013.04.028
16. Andreas Dahl et al: Traffic-related emissions of ultrafine particles from pavement-tire interface, Atmospheric Environment 40(7):1314-1323, Available on: https://doi.org/ 10.1016/j.atmosenv.2005.10.029.
17. Foitzik et al.: Investigation of ultra fine particulate matter emission of rubber tires , Wear (394- 395) 2018, Available on: https://doi.org/10.1016/j.wear.2017.09.023.
18. Togo, R., Saito, N., Ogawa, T., Haseyama, M., 2019. Estimating regions of deterioration in electron microscope images of rubber materials via a transfer learning-based anomaly detection model. IEEE Access 7, 162395–162404, Available on: https://doi.org/10.1109/ACCESS.2019.2950972.
19. OECD (2014), Nanotechnology and Tyres: Greening Industry and Transport, OECD Publishing. Available on: http://dx.doi.org/10.1787/9789264209152-en.
20. Kreider, M. L., Panko, J. M., McAtee, B. L., Sweet, L. I., & Finley, B. L. (2010). Physical and chemical characterization of tire-related particles: Comparison of particles generated using different methodologies. Science of the Total Environment, 408(3), 652e659.
21. David Kittelson et al: Particle emissions from mobile sources: Discussion of ultrafine particle emissions and definition, Journal of Aerosol Science, Vol. 159, 2022, 105881, Available on: https://doi.org/10.1016/j.jaerosci.2021.105881.

TECHNICAL UNIVERSITY OF KOŠICE
Faculty of Mechanical Engineering

Experimental analysis of blanking technology for electrical steel in double layer configuration

Martin Matej Benda [1,*], Emil Spišák [1]

[1] Technical University of Košice, Faculty of Mechanical Engineering, Košice, Slovakia
* Correspondence: - martin.matej.benda@tuke.sk, Department of Mechanical Engineering Technologies and Materials, Technical University of Košice, Letná 9, 042 00 Košice, Slovakia

Abstract: Increased interest in electric automobiles, coupled with the vision of a greener future, is leading the producers of the electric motors into implementation of the new technologies and optimization of the current technologies to increase productivity and improve product quality. One of the current technologies for production of rotor and stator laminations is stamping. The productivity of this technology can be improved by cutting an additional layer of electrical steel in a single stroke. Research into this change in technology is relevant, as its potential implementation after addressing of its flaws may provide us with cheaper production alternative for electric motors. This paper investigates results of change in this technology by analyzing the interaction between tool and material in single layer stamping and predicting the interaction in double layer stamping. The study continues with a comparison of the samples which were produced by experimental stamping of the electrical steel produced by POSCO, confirming the negative predictions gained by theoretical analysis. The discusion contains a brief summary on these results and potential directions of the research on the problems produced by this change in technology.

Keywords: stamping; blanking; double-layer stamping; laminations; electrical motor

1. Introduction

Conventional technology of blanking in stamping is a shearing process in which the sheared material is in contact with the die on which it is positioned, the blankholder which holds the material in place and the punch which separates the blank from the material [1].

During the blanking process the material goes through these phases which are shown in simulation of Figure 1.:

1. Elastic deformation phase - Starts when punch comes into contact with the material. Punch acts upon the material with increasing force, compressing and bending it over the edge of the die. No permanent changes to the material occur until the end of this phase [1,2,3].
2. Plastic deformation phase - As soon as the stress in the area of material is in contact with the die and the punch exceeds the yield strength, the material will start to plastically deform and the punch will start to penetrate into the material, forcing it to flow around the edge of the die. Roll-over and the burnished zone are produced in this phase [1,2,3].
3. Fracture initiation and fracture propagation phase - When the stress exceeds the ultimate tensile strength of the material, cracks will start to appear in the area in contact with the edges of the punch and die. These cracks continue to propagate along the line between the edges of the punch and the die until they connect and separate the blank from the material. Fracture zone and the burr are the result of this phase [1,2,3].

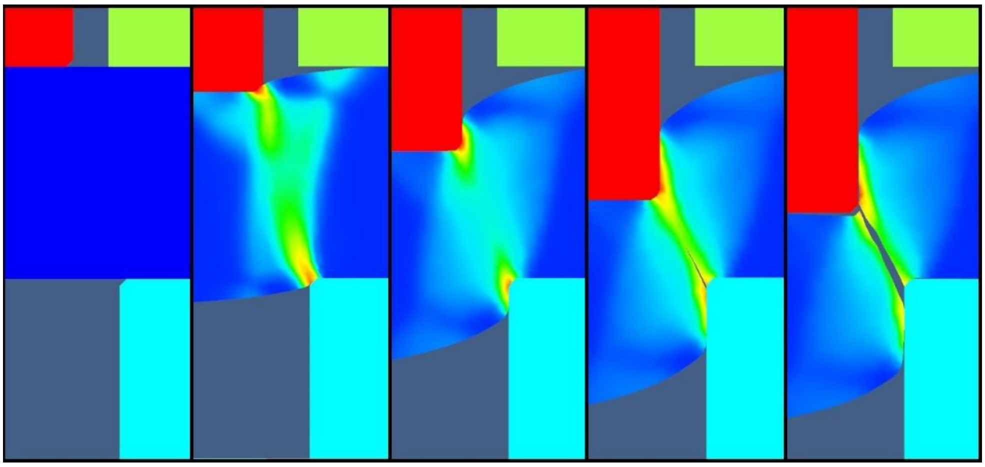

Figure 1. Single layer blanking process - illustrational picture from simulation in SIMUFACT Forming software (contact with punch/elastic phase/plastic phase/fracture initiation/break).

2. Theoretical analysis of double layer blanking

The technology of double layer blanking is trying to double production efficiency of the process by modifying the conventional blanking process. This is achieved with the addition of the second layer of the sheet on top of the first sheet. These sheets form a pair which is blanked simultaneously in a single stroke and during the blanking process they are not bonded or mechanically joined in any way. Both sheets are made from the same material, and their dimensions are the same.

This change in the process modifies the interaction between the material and the tool, as the influence of the tool is partly replaced by one of the sheets dividing the process into two parts:

- Top layer – Top sheet is in direct contact with the punch and blankholder, but not with the die. The geometry of the die is replaced by the bottom sheet.
- Bottom layer – Bottom sheet is in contact with the die, but not directly with the blankholder or the punch. In this case their geometry is replaced by the top sheet.

The challenge of this arrangement is in the fact that material is not able to fully replace the precision and stability of the tool geometry. Shape and position of each layer is fluidly changing because of the deformation during the blanking process, which results in a problem with the stress distribution, deformation patterns and the fracture behavior as can be seen in simulation shown in figure 2.

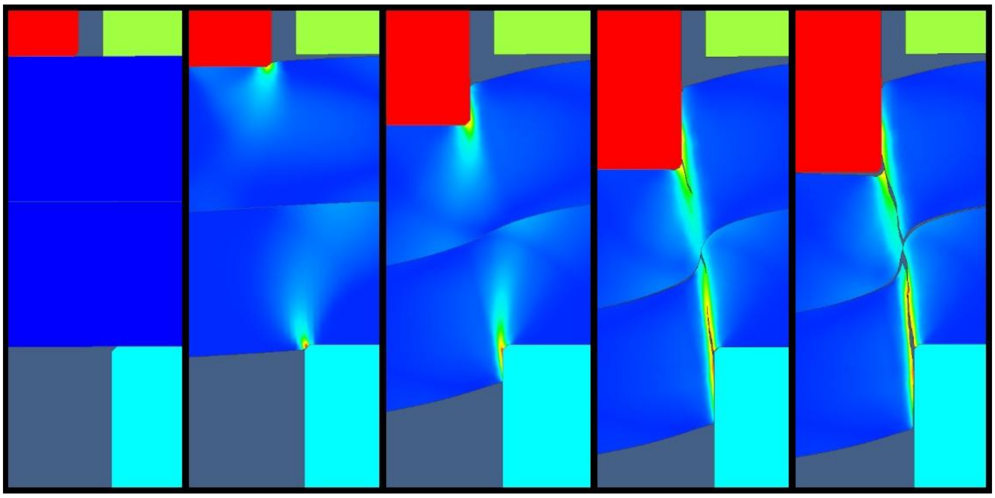

Figure 2. Double layer blanking process - illustrational picture from simulation in SIMUFACT Forming software (contact with punch/elastic phase/plastic phase/fracture initiation/break).

Potential predicted complications produced by this modification based on the theoretical analysis are:

- Higher necessary cutting force – Addition of the second layer of the material is practically doubling the thickness of the material blanked which results in an increase of the necessary cutting force. This negatively impacts tool life and can have an impact on the quality of the sheared edge.
- Different course of the plastic deformation – Since the top layer is affected by the compressive force of the punch first, the bottom layer is exposed to uneven forces of the transmitted force. This can potentially lead to local thinning of the sheet and different deformation in the area of the edge, especially a difference in the rollover area and overall dishing of the blank. Bottom blank will also have bigger burr than top because of higher concentration of stress in the area of contact with the die.
- Different shape of the burnished zone – While the bottom layer is bent around the smaller radius of the die, the top layer is bent over the radius created on the bottom layer. As a result, both of the layers end in a different orientations relative to the punch during the blanking process. This may result in worse quality of the burnished area on the top layer.
- Different diameters of each blank in the pair – While the outer diameter of the bottom layer is influenced by the precise geometry of the die, the outer diameter of the top layer is influenced by the geometry of the bottom layer which is fluidly changing due to the deformation process. This is expected to result in difference in the outer diameters, with the bottom blank having slightly larger diameter than the top blank. This will also be highly influenced by the cutting clearance.

3. Experimental double layer blanking

3.1. Materials

Experiment was conducted on the thin electrical steel sheet produced by POSCO, designated as 30PNX1500FY. This type of electrical steel is characterized by its high strength and is commonly used in electric motors. Its mechanical properties are provided in Table 1. [4]

Table 1. Mechanical properties of POSCO 30PNX1500FY [4].

Grade	Tensile strength (MPa)		Yield Point (MPa)		Elongation (%)		Hardness HV1	Lamination factor (%)
	L	C	L	C	L	C		
30PNX1500FY	573	579	450	457	20	19	230	97.5

Note: L : specimen is parallel to the rolling direction / C: Specimen is transverse to the rolling direction.

3.2. Experimental setup and equipment

The blanking experiment was conducted on a hydraulic press with a nominal force of 250 kN. The tool used in the experiment was a progressive shearing tool with a die clearance of 0.005 millimeters. The diameters of the dies were: Ø25.013 mm and Ø15.049 mm. The diameters of the punches were Ø25.003 mm and Ø15.039 mm.

Nominal thickness of the material is 0.3 mm, and material was set in two configurations:

- Single layer configuration of a 0.3 mm sheet.
- Double layer configuration of two 0.3 mm sheets (total nominal thickness of 0.6 mm).

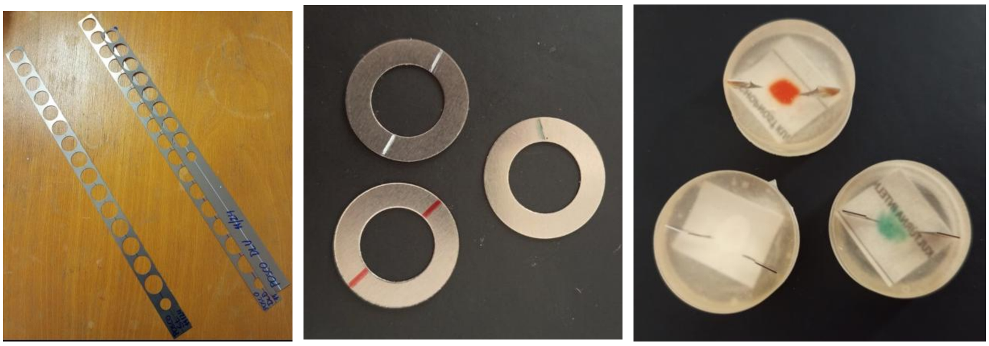

a.) **b.)** **c.)**

Figure 3. a.) Leftover material from experiment; b.) blanking specimens; c.) samples prepared for study under the microscope.

The shape of the sheared surfaces on the outer diameter of the specimens was observed separately for each layer of the configurations on a ring shape blanks using a Keyence microscope. Small magnification of the observed samples can be seen on figure 4.

Figure 4. Blank samples under microscope, with outer diameter on left side and inner diameter on right side of picture.

Thickness of the samples was measured in proximity to the sheared edge at at least four points. The top blank in the double layer configuration experienced much higher thinning compared to the bottom blank which had minimal thinning similar to the thinning of blank in the single layer configuration.

A difference in the burr between the sheets was observed. No burr was produced on single layer blank or on the top blank of the double layer configuration, however, the bottom blank had a burr proportionate to 9% of the shear area.

A change in radius of the rollover was observed. The radius of the bottom layer blank is similar to the radius of the blank of single layer configuration, but the radius of the rollover on the top layer blank is doubled in comparison.

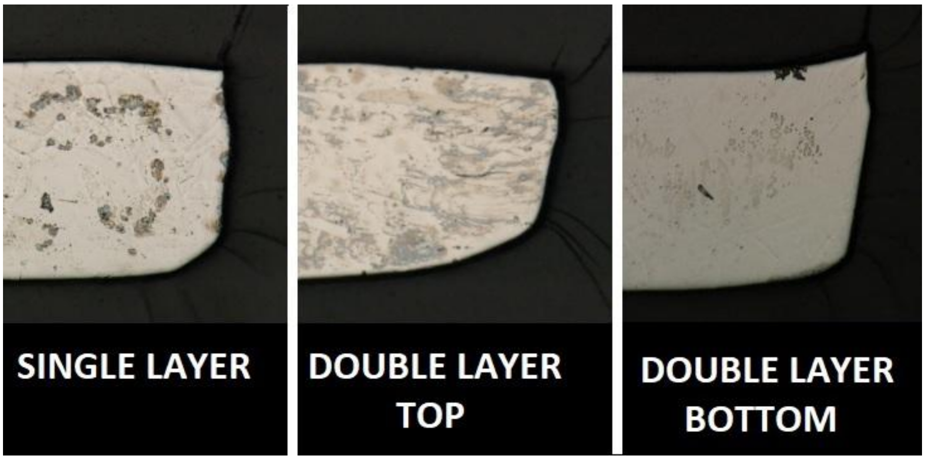

Figure 5. Blank samples under microscope with detail on the shearing edge.

A difference in the shape of burnished area between layers in double blanking was observed and can be seen on figure 5. The shearing edge of the top blank in the double layer configuration is drastically deformed, as the radius of the rollover is doubled in comparison to the single layer blanking. Burnished area is smaller and the fracture area is rounded, which may indicate deformation causing the blank part of the material to change orientation during this part of the shearing process. Bottom blank of the configuration is more similar to the conventional single layer blanking configuration, with main difference located at the area of burr, where the material is not compacted but instead forms a negative shape of the rollover area of the top layer, producing a burr, comparison of these two layers is shown in figure 6.

Figure 6. Comparison of the rollover of the top layer blank and radius in the area of the burr on the lower layer blank in two layer blanking configuration.

Increased dishing deformation on the double layer samples was observed with a naked eye and orientationally measured with a caliper. While the single layer configuration had an overall thickness of 0.3 mm, the double layer configuration had overall thickness of 0.57 mm and 0.55 mm. Although dishing should be different for each layer of the pair, as observed in simulation shown on figure 7, it is somewhat uniform due to a balancing effect. This effect occurs in the die, as blanks are compressed and pushed through narrower section of the die by the blanks produced before and after them.

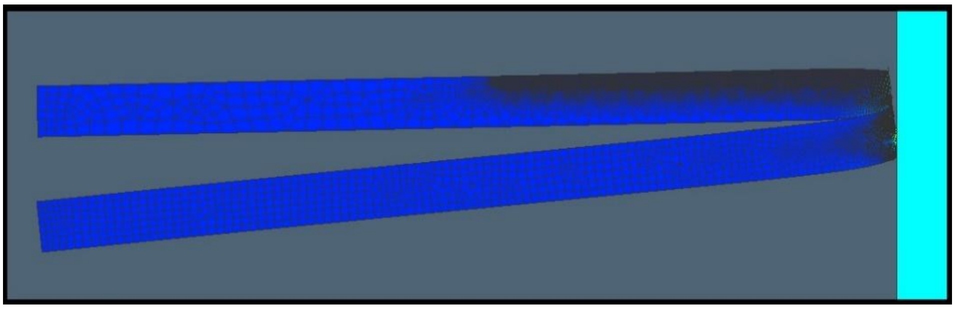

Figure 7. Dishing immediately after blanking in double layer blanking process, illustrational picture from simulation in SIMUFACT Forming software.

4. Discussion

The experiment provided us with an insight into the complications which are produced during the double layer blanking of thin electrical steel sheets, which are not joined together in any way.

These results confirmed theoretical predictions, such as:

- Localized thinning – The top blank experienced increased thinning in comparison with the lower blank.
- Burr difference – There is no burr produced on the top blank but the lower blank had a burr creating 9% of its sheared edge.
- Quality of the sheared edge – The bottom blank had better quality of the sheared edge compared to the top blank.
- Dishing – Dishing was present on both blanks produced by the double layer blanking configuration. This dishing may vary between the layers immediately after the cut but it is balanced in the die by other blanks compressing them together. This may be a problem as blanks can damage surface of each other, which may result in increase of eddy currents in the iron cores of electric motors, whose production can benefit mostly from this improvement.

More research needs to be conducted on this topic and some of the options are:

- Simulations to improve our understanding of the interaction between the tool and each layer.
- Simulations of the interaction of blanks in the die after the cutting.
- Experiments with different parameters as die clearance, different materials, different geometry of the tool and others.

The technology of the double layer blanking may be significant improvement in productivity which may increase the viability of the electrical motors, but the complications produced by it must be addressed before this technology can be considered in production.

Acknowledgments: This work was supported by the project APVV-21-0418 and project KEGA 018TUKE-4/2024.

Conflicts of Interest: "The authors declare no conflict of interest."

References

1. Dheeraj Dilip Kulkarni, Rakesh AdhikraoShinde, Jaai Prakash Badgujar. "Clearance optimization of blanking process." International Journal of Scientific & Engineering Research, Volume 6, Issue 12, December-2015: 178-191.
2. Ľudmila Dulebová, Branislav Duleba, Emil Spišák. "Analysis of some aspects of fine blanking process." Scientific letters of Rzeszow University of Technology – Mechanics 30(85(2/2013)): 119-127.
3. S.K Maiti, A.A Ambekar, U.P Singh, P.P Date, K Narasimhan. "Assessment of influence of some process parameters on sheet metal blanking." Journal of Materials Processing Technology – Volume 102, Issues 1-3, 15 May 2000, Pages: 249-256.
4. Non-oriented electrical steel catalogue - Posco [on-line] 2024 [cit. 20234-13-12]. Available on internet: https://www.posco.co.kr/homepage/product/eng/jsp/support/s91c5000200b.jsp

TECHNICAL UNIVERSITY OF KOŠICE
Faculty of Mechanical Engineering

Gamification of learning in the industry

Leo Brada [1,*], Ľubica Miková [1] and Erik Prada [1]

[1] Technical University of Košice, Faculty of Mechanical Engineering, Department of Industrial Automation and Mechatronics, Park Komenského 8, 042 00 Košice; leo.brada@tuke.sk; lubica.mikova@tuke.sk; erik.prada@tuke.sk
* Correspondence: leo.brada@tuke.sk

Abstract: This paper focuses on the concepts of gamification and its implementation in industrial settings. Gamification offers many benefits such as motivation, engagement, a safe virtual environment, and much more with only a few limitations, making it interesting for industry applications. As industries continue to evolve with automation and digital transformation, gamified learning offers an effective and scalable solution for workforce training. Techniques, benefits, limitations, and current use are discussed. Furthermore, 2 experimental applications are proposed utilizing virtual reality for immersive and interactive experiences. Plans for future improvements of simulations are discussed along with a proposal for new simulations. A survey of a test group is present along with their feedback.

Keywords: gamification, simulation, industry

1. Introduction

Gamification is a term with many definitions based on its use. While no standard exists yet, most sources agree that gamification is generally defined as using game elements and mechanics in non-game contexts [1]. Gamification as a concept was first observed in the marketing sector in the form of memberships with variable rewards based on the given criteria but it soon became much more. The core of gamification is an incentive for workers and students to learn new concepts and subjects playfully and interestingly. Engagement, motivation, and productivity boosts are the main factors for investing time and money to gamify [2]. Motivated users are willing to spend more time and effort on the given task. Also, they are encouraged to think about the problem and potential solutions. Hamari et al. conducted a literature review of gamification articles. The review shows the positive outcomes in motivation, engagement, and enjoyment of gamified applications. However, results are case-dependent because not every application can be easily gamified. Gamification must be applied correctly according to the options available for the experience to be coherent and engaging [3].

The second key factor is interactivity. Giving users the ability to interact freely with the virtual world and to engage with it has proven to be a great way of learning new skills. Since there are no standards as to how gamification of an application should be achieved there are recognized mechanics and game types used for gamification. Mechanics used include achievements, levels, progression, challenges, status bars, collaboration, and leaderboards. Achievements are used as a reward for the successful completion of a given task. They are considered the main motivation for the user to use the application. Based on the design of achievements they can appear as milestones on progress bars, badges, currency, or in the form of bonuses. Achievements and subsequent rewards must be considered thoroughly to keep the user engaged in the activity. Levels can be described as stages of the game. Level design and level objectives are 2 criteria that every level has and that distinguish each level from the others. A level design is considered the look, atmosphere, and layout of the level. The design of a level can stay the same for all levels depending on the application, but the level objectives need to be different on every level. The only exception is increasing the difficulty of the objective or adding new obstacles and situations that complicate the completion of the objective. In education, every level is considered either as a lecture or a part of a lecture. In mechanical engineering, every level can be a different mechanism or system. Progression is the progress of a level and is measured by the number of objectives the user completed in the level. Challenges are a means of motivation for the user to complete the level in a certain amount of time, in a different way, or complete a specific bonus task. In engineering training, challenges can be considered difficult situations that are not very likely to occur but are potentially possible to occur. Status represents the rank or the experience of the user. It changes when the user completes a set number of levels or challenges. Collaboration is a specific mechanism used for complex applications where multiple users work on the same problem. The tutor and tutee system can also be applied to teach multiple users simultaneously about the topic. The last mechanism used for gamification is the use of leaderboards. This mechanism is used to compare users and encourage them to work harder on the topic and to improve their scores. Leader boards can display the achievements, number of levels completed, points from the challenges, etc. [4].

Implementing the game elements in the industrial application without changing the form and purpose of the original application is the most used way of gamifying. The second option for gamification is giving the application form of a game which essentially changes the application in a way resembling a video game. The 5 game types used are puzzle games, adventure games, simulation games, strategy games, and edutainment. Puzzle games require logical thinking to overcome the problem either by finding the correct solution or coming up with a new one. Users are required to solve puzzles, use different tools, and manipulate objects. The purpose of this game is to teach the users how to use the new tools and think about the most optimal ways of solving the problem. The advantage of puzzle games is that they do not require complex graphics and programming. Adventure games are basically puzzle games with a simple story and the ability to carry tools, weapons, and such across levels. A simple story is in the form of a narrative of a real-life situation that might occur or has occurred before. This style of games is favored in engineering education and for the reeducation of workers. Simulation games simulate the controlling of real-life vehicles or machines such as CNC milling machines, drones, cars, or heavy machinery. Simulations are complex and expensive to create due to the need for realistic digitalization of the simulated mechanism and environment. Vehicle or machine simulations can be used for autonomous vehicle testing or machine learning as a visualization layer. Strategy and real-time strategy games can be compared to a city-building game or a war game where users command troops. The strategic aspect is in the management of the city and creating the layout of the buildings. Users must make strategic decisions in the building and equipment placement, plan future expansion and changes, command people, and manage the equipment. This type of game is beneficial mostly for civil engineering and simulations of a city's infrastructure. The last type of game is edutainment. Edutainment is as the name suggests the combination of education and entertainment. The goal of this application is to teach in an entertaining form of gameplay. Edutainment is aimed at young children to teach them in a fun way with the use of licensed games and TV show characters [4].

Gamification offers many advantages such as previously stated motivation and user engagement. Motivation and engagement come from the sense of achievement due to the use of leaderboards, point systems, progression, and optional challenges. Users are encouraged to invest more time to improve their score and come up with new more optimal solutions. Learning is faster and easier because the concepts are explained in a visual and in some cases more realistic way. Applications offer simplified visual instructions for users to follow. Visual learning is very beneficial, and gamification can enhance the whole experience even further. Be it high-fidelity applications or simplified ones, visual learning is beneficial either way. In the case of collaborative experiences, the clear benefit is improving team building and strengthening the collaboration of workers on the same problem.

The disadvantage or rather limitation of gamification is that users might be driven into following certain patterns to finish the objective and not try other ways that might be more appropriate. This can be prevented by creating a more robust system that encourages users to try new things and optimize their performance. Users might come up with new ways of finishing the object and give feedback on further improvement of the application. Another big limitation is incorporating gamification mechanics into the existing application. This limitation occurs when the applications' internal components are not directly available thus making the complex integration problematic. Application Programming Interface (API) and Software Development Kit (SDK) availability are problems and, in some cases, even if available they offer only tools for automating tasks and not for visual elements and systems. This leaves developers with only the User Interface (UI) for implementing game elements. In this case, the developers must decompose the UI into widgets and send commands through these UI components [5].

2. Use in the industry

Despite the youth of the topic, there have already been plenty of studies and examples on how to incorporate gamification into the industry. For example, Markopoulos et al. provided a case study on the use of gamification in manufacturing. In manufacturing, gamification is used for learning CAD programs and 3D modeling [5].

Bennett & Vijaygopal conducted a study about electric car simulators in order to allow people to learn about electric vehicles. They developed an integrated model of determinants of consumer attitude towards electric vehicles which is in many cases negative due to the stereotypic view of the topic [6].

Müller et al. present a training concept for industrial assembly by creating a tutorial and training game. The tutorial game was created for mobile and computer and allows users to understand the assembly steps necessary to assemble a bicycle hub. Training games consist of a physical assembly workplace and a camera with tracking and monitoring with immediate feedback on workers' actions [7].

Donatiello et al. presented the virtual dressing room for the fashion industry. They utilized virtual reality (VR) technology to create a peaceful environment, an island to be precise, and user avatars to try different outfits. The feasibility of such a system was questioned and results were gathered. Testers were questioned if they would use this application if they would use it to buy clothes online, and if they would use the application for fun. The answers were mostly positive [8].

Keepers et al. present a review of gamification used in manufacturing and industrial settings. They also discussed the different technologies utilized such as augmented reality (AR), VR, facial recognition, and more [9].

Roh et al. presented a gamification interface for bolt-tightening work in the automotive industry, on the assembly line to be precise. Experimental settings were created to test the potential of making a repetitive task of bolt-tightening into a game with short-, medium-, and long-term goals, progress, score, and audio-visual feedback. The conducted study was limited due to the low number of participants [10].

Korn et al. proposed three designs for an application in the automotive industry. Different colors were assigned to the work processes based on the speed of task completion and if any errors occurred. Green-colored processes were completed faster than usual, and slowly finished processes were yellow, orange, or red based on the amount of time. Errors were assigned to red color and may lead to the removal of visual items. Out of three tested visual designs, namely Tetris, circles, and pyramid, the pyramid one was most preferred by the testers [11].

Morêda Neto et al. created a visual management system for construction sites. The system offers visual management, employee and team ranking, and displays the information needed by each employee, such as which activities they will perform, on which site, and with which team [12].

3. Created scenarios

This paper presents 2 scenarios implementing gamification elements and design proposals to further improve gamification and the experience as a whole. Simulations were created for VR using Unreal Engine 5. Because the existing equipment such as robots and PLCs don't offer any way of implementing gamification elements, it was chosen to create custom scenarios which will be shown in this chapter. Simulation games are the simplest and most effective ways of teaching users new skills or concepts. Emergency scenarios are hard to mentally visualize because nothing can replace real experience. Because emergency scenarios may occur it is important to teach how to react in these situations. Teaching new concepts and technologies is also important and beneficial not only in the university environment but also in professional work environments. 3D printing technology is used everywhere in industry and because of this, it was proposed to create the simulation of 3D printer assembly.

3.1. Virtual warehouse

The first example is a VR simulation of an emergency inside the virtual warehouse. The simulation was created as a safety simulation for new employees to teach them how to behave in emergencies. The simulation starts in the warehouse where users will familiarize themselves with the environment and the controls. As shown in Figure 1 the environment looks very detailed with high-quality models and textures. The first objective of the simulation is to put on safety equipment such as a safety vest, helmet, and safety gloves. After putting on the equipment the playful sound plays, and the scene fades to black. After a second the user will see clearly again. This transition ensures the proper load of the next event which is fire. Fire will start in the warehouse and the user needs to find it and put it out. Fire extinguishers need to be picked up and used to put out fires. To simply find the fire extinguisher its texture is gently blinking yellow. After picking up the texture returns to normal. If the user is unable to put out fire in the set amount of time it gets bigger, and the user needs to run into the exit and escape. The last scenario of the simulation is the electrocution emergency. In this scenario, the male character walks near the water dispenser with loose cables next to it. He gets electrocuted and the user needs to shut down the power via the main power switch. The main power switch is also gently blinking for better visibility.

In terms of gamification, this simulation offers a basic adventure with 3 quests to complete. In Figure 2 all stages of simulation are displayed. Because this example was mainly used as a simulation it doesn't offer a scoring or achievement system. However, it has hints to lead the user like blinking textures of the fire extinguisher and the main power switch. Another important gamification element is a narrator that guides the user between the different stages of the simulation. This simulation can be improved by implementing a more robust quest system and timer for measuring the reaction speed of the user. The system for fire to spread was also proposed but was not finished in time. More scenarios are proposed for the future such as identifying the electrical short circuits and fixing them, water leaks, and earthquakes.

Figure 1. Virtual warehouse environment.

Figure 2. Activities in the warehouse environment.

3.2. 3D printer assembly

The second simulation is the simulation of 3D printer assembly. The 3D printer of choice was Ender 3. The simulation consists of a table with the printer parts and the stand on which the user will place the assembled parts of the printer as displayed in Figure 3. The assembly system consists of a set of trigger volumes that are triggered when the part enters it. The system will check if the part that enters the volume is the one that should be connected to the first part and if it's true then the part will be connected. Another trigger volume is added to check for the correct orientation of the part for added realism. Every time 2 parts are connected the number above the stand counts up. Figure 4 depicts the process of assembly and the number above the stand. When the number reaches 20 the assembled printer switches for the complete model that the user can pick up and check it from different angles. For added immersion, the assembly manual was added for the users who are assembling the printer for the first time.

Gamification elements utilized are the counter and the gradual process of assembly with interactable instructions included. The users can choose if they want to assemble the printer by themselves or by following the assembly manual step by step. The simulation is simple but has a lot of potential for improvement. In the future, it is planned to further extend the capabilities of the simulation to simulate the control of the virtual printer, 3D printing simulation with the ability to import custom Gcode, and control of the real printer via the simulation. In terms of gamification, it is planned to add multiple levels of simulation and more options of approach. Also, the timers, achievements, and ranking system are planned to improve user engagement.

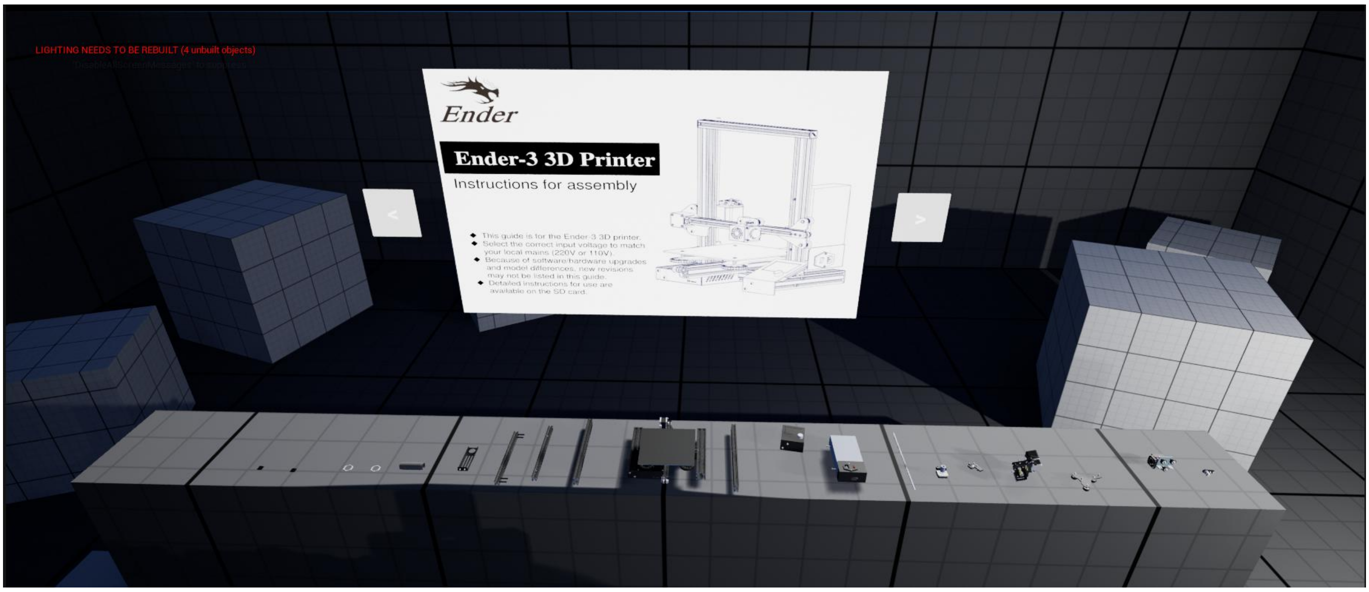

Figure 3. 3D printer in a virtual environment.

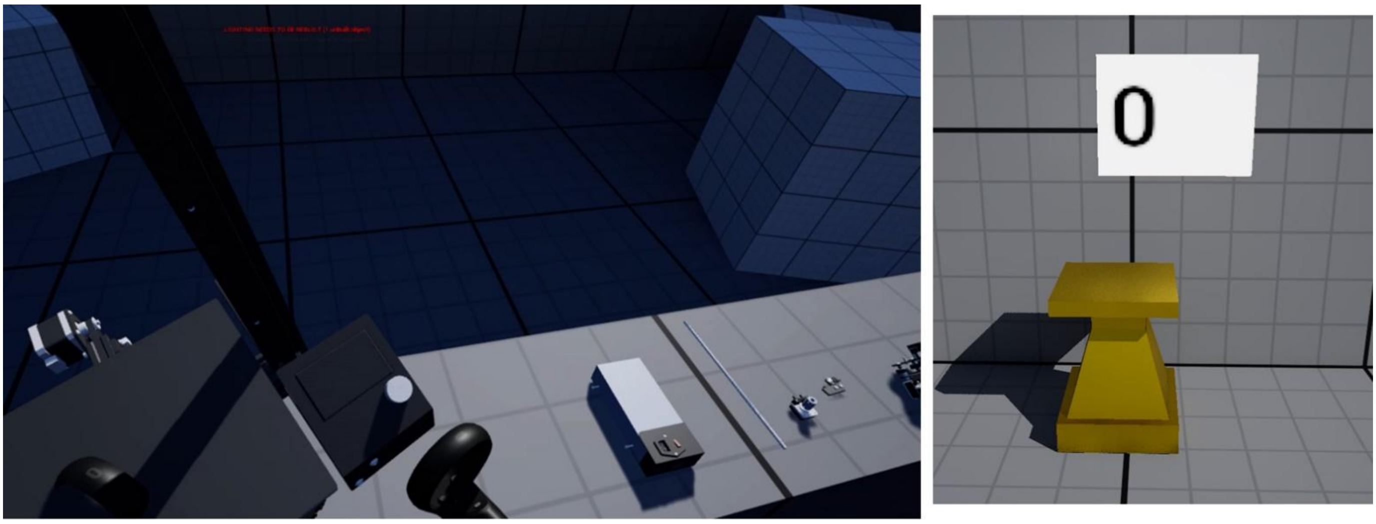

Figure 4. 3D printer assembly and the stand.

The possibilities for simulations and gamification are endless. Mechanical engineering offers many possible implementations of gamification elements. From robotic arms, PLCs, autonomous vehicles, safety management, and many more. Apart from implementing new elements to existing simulations, the future simulations planned for testing are gamified robotic arm programming with many different objectives and challenges.

The plan is for the simulation to be in VR and to be robust enough to offer many possible solutions to the problems or quests. The narrator won't be present, but the instructions will be available in the environment in the form of texts and pictures. Integration with the Robot Operating System (ROS) is planned to further improve the usability of the simulation.

A group of students were asked to try the simulations and give feedback on their experience. Feedback was given verbally, and the conclusion of their experience was very positive. They pointed at the immersion of the simulations because of the VR experience. Engagement was also very high because of the technology used and the high fidelity of the environment. The contents of the simulations were interesting, but a small level of discomfort was noticed because of the VR controls. They also recommended continued development and requested more gamification elements to be implemented. Students gained new information about the 3D printing technology and concluded that because of the simulation they understand the technology better. Emergencies were also interesting and useful in case of the emergence occurring.

4. Conclusions

Gamification is an interesting topic with many advantages and disadvantages. The main advantages are interactive and realistic experiences in a safe virtual environment. Many possible scenarios with different outcomes can be created for the user to try. The points, progression, and achievement systems allow for competition and motivation for the user to try different approaches to solve the problem and acquire new skills. The disadvantages mentioned are the complexity, high price of such programs, and the susceptibility to following one pattern all the time without thinking about the steps required thus making the simulation ineffective as a learning tool. Gamification itself is still an early concept that needs to be studied further and could greatly help in many kinds of industries. Two gamified applications were proposed to show the potential use of gamification and the future changes that might be added to further improve the applications. A survey of the student group was conducted, and the response was very positive. Gamified simulations proved to be a useful and viable solution for learning and professional cases. Proposed simulation cases contribute to a better understanding of gamification and simulation technology.

Acknowledgments: This article was created thanks to the project support: VEGA 1/0436/22 Research and development of modeling methods and control algorithms for kinematically redundant mechanisms, KEGA 008TUKE-4/2024 Implementation of machine learning methods in the teaching of industrial automation and robotics.

References

1. Seaborn, Katie, and Deborah I. Fels. "Gamification in theory and action: A survey." International Journal of human-computer studies 74 (2015): 14-31.
2. Kapp, Karl M. "What is gamification." The gamification of learning and instruction: game-based methods and strategies for training and education (2012): 1-23.
3. Hamari, Juho, Jonna Koivisto, and Harri Sarsa. "Does gamification work?--a literature review of empirical studies on gamification." 2014 47th Hawaii international conference on system sciences. IEEE, 2014.
4. Markopoulos, Angelos P., et al. "Gamification in engineering education and professional training." International Journal of Mechanical Engineering Education 43.2 (2015): 118-131.
5. Baalsrud Hauge, Jannicke M., et al. "Integrating gamification in mechanical engineering systems to support knowledge processes." International Design Engineering Technical Conferences and Computers and Information in Engineering Conference. Vol. 57052. American Society of Mechanical Engineers, 2015.
6. Bennett, Roger, and Rohini Vijaygopal. "Consumer attitudes towards electric vehicles: Effects of product user stereotypes and self-image congruence." European Journal of Marketing 52.3/4 (2018): 499-527.

7. Müller, Bastian C., et al. "Simulation-games for learning conducive workplaces: a case study for manual assembly." Procedia CIRP 40 (2016): 353-358.
8. Donatiello, Lorenzo, et al. "Exploiting immersive virtual reality for fashion gamification." 2018 IEEE 29th Annual International Symposium on Personal, Indoor and Mobile Radio Communications (PIMRC). IEEE, 2018.
9. Keepers, Makenzie, et al. "Current state of research & outlook of gamification for manufacturing." Journal of Manufacturing Systems 64 (2022): 303-315.
10. Roh, Seunghwan, et al. "Goal-based manufacturing gamification: bolt tightening work redesign in the automotive assembly line." Advances in Ergonomics of Manufacturing: Managing the Enterprise of the Future: Proceedings of the AHFE 2016 International Conference on Human Aspects of Advanced Manufacturing, July 27-31, 2016, Walt Disney World®, Florida, USA. Springer International Publishing, 2016.
11. Korn, Oliver, Peter Muschick, and Albrecht Schmidt. "Gamification of production? A study on the acceptance of gamified work processes in the automotive industry." Advances in Affective and Pleasurable Design: Proceedings of the AHFE 2016 International Conference on Affective and Pleasurable Design, July 27-31, 2016, Walt Disney World®, Florida, USA. Springer International Publishing, 2017.
12. Neto, Hugo Morêda, et al. "Visual communication panels for production control using gamification techniques." 22nd Annu. Conf. Int. Gr. Lean Constr. Underst. Improv. Proj. Based Prod. IGLC. 2014.

TECHNICAL UNIVERSITY OF KOŠICE
Faculty of Mechanical Engineering

Development of Textured Turning Cutting Inserts

Jozef Brindza [1,*], Michal Demko [1], Ján Kušnír [1], Marek Vrabeľ [1] and Peter Ižol [1]

1 Prototyping and Innovation Centre, Faculty of Mechanical Engineering, Technical University of Kosice, Slovak republic
* Correspondence: jozef.brindza@tuke.sk; Tel.: 0556023364

Abstract: Surface texturing of cutting tools has emerged as a sustainable approach to enhance machining performance, particularly in challenging applications such as turning heat-resistant superalloys. This study investigates the texturing of the CNMG 12 04 08-SMR 1105 cutting insert, a carbide tool widely used for roughing Inconel 718 in aerospace machining. The research focuses on improving tool life, reducing friction, and enhancing the machined surface finish by creating micro-scale patterns on the tool's rake and flank surfaces. Using advanced CAD modelling and laser processing, three texture variants were designed: shallow holes, inclined grooves, and perpendicular grooves. Key parameters, including coating thickness and texturing depth, were optimized based on confocal microscopy and coating analysis. The textured patterns were carefully positioned to avoid compromising the cutting-edge coating, which could reduce tool longevity. Prior studies highlight the potential of solid lubricant retention in textured features to further enhance lubrication and thermal management. The findings suggest that these textures can significantly improve tool durability and machining efficiency while addressing sustainability goals. This work provides a foundation for future experimental validation and the development of tailored texturing strategies for high-performance machining applications.

Keywords: texturing, cutting insert, lubricating

1. Introduction

Turning is a widely utilized machining process that employs a single point cutting tool on lathe machines to create circular geometries. Carbides, valued for their exceptional toughness and thermo-chemical stability, are commonly used as cutting inserts in turning, particularly at high speeds and feed rates.

Modern cutting tools often incorporate advanced materials with low thermal conductivity and high melting points to enhance performance. However, elevated temperatures and stresses in the turning zone can weaken the cutting edge, accelerating tool wear and leading to poor surface finishes, especially in aerospace and automotive applications [1].

The machining of sticky materials introduces additional challenges due to their poor thermal conductivity, which results in excessive heat generation at the cutting zone. This heat transfer to the cutting tool accelerates wear on both the crater and flank edges, further compromising tool life and machining quality [2].

In recent years, surface texturing of cutting tools has emerged as a sustainable alternative to mitigate the negative impacts of conventional machining, as highlighted by numerous researchers. This innovative technique, a cornerstone of modern green manufacturing, involves modifying the structure of cutting tools—particularly the rake surface—to improve their tribological performance [3].

Surface texturing reduces the friction coefficient at the tool-chip interface by minimizing the contact area between the tool and chip during turning. This leads to reduced material adhesion on the rake face and a decrease in cutting forces. The primary purpose of these engraved patterns is to ensure a continuous supply of fluid to the contact area, enhancing performance and efficiency during the turning process [4].

To extend the lifespan of cutting tools, solid lubricants such as graphite, carbon nanotubes (CNTs), multi-walled carbon nanotubes (MWCNTs), tungsten disulfide (WS_2), molybdenum disulfide (MoS_2), hexagonal boron nitride (hBN), and calcium fluoride (CaF_2) are integrated into the recesses of textured tools. These lubricant-filled textured tools have demonstrated significant improvements in turning performance [5,6].

Ze et al. [7] fabricated textured grooves filled with MoS_2, observing a reduction in primary cutting force (tangential) by 6–34% and an increase in wear resistance by 10–15% compared to conventional tools. These findings highlight the potential of textured tools with solid lubricants to enhance cutting efficiency and durability.

Turning with patterned tools offers several advantages, including reduced friction, lower cutting temperatures in the cutting zone, a smaller tool-chip contact area, decreased tool wear, and enhanced surface finish of the machined material [8].

In a study conducted by Arulkirubakaran et al. [9], textured tools were employed for turning Ti–6Al–4V alloy, resulting in a significant improvement in the machined surface finish. This enhancement was primarily attributed to the thermal softening of the work material at high cutting speeds, which facilitated smoother machining.

2. Analysis of cutting insert

The CNMG 12 04 08-SMR 1105 cutting insert from Sandvik Coromant was selected for texturing the face and flank. This insert has a corner radius of 0.8 mm and is designed for machining stainless steels and heat-resistant superalloys. It was chosen after consultation with a partner company we collaborate with, which has extensive experience in machining for the aerospace industry and uses this insert for roughing Inconel 718.

The STEP format model of the insert, downloaded from the manufacturer's website, was used as a basis for the texturing design. However, the model was simplified and featured a completely flat face surface. To accurately design the textured face, it was necessary to approximate and remodel the face surface to match the actual insert.

To scan the face surface of the cutting insert, the ZEISS Smartproof 5 confocal microscope was employed. Dimensions essential for modeling were subsequently obtained from this scan, as shown in Figure 1, using the accompanying ZenCore software.

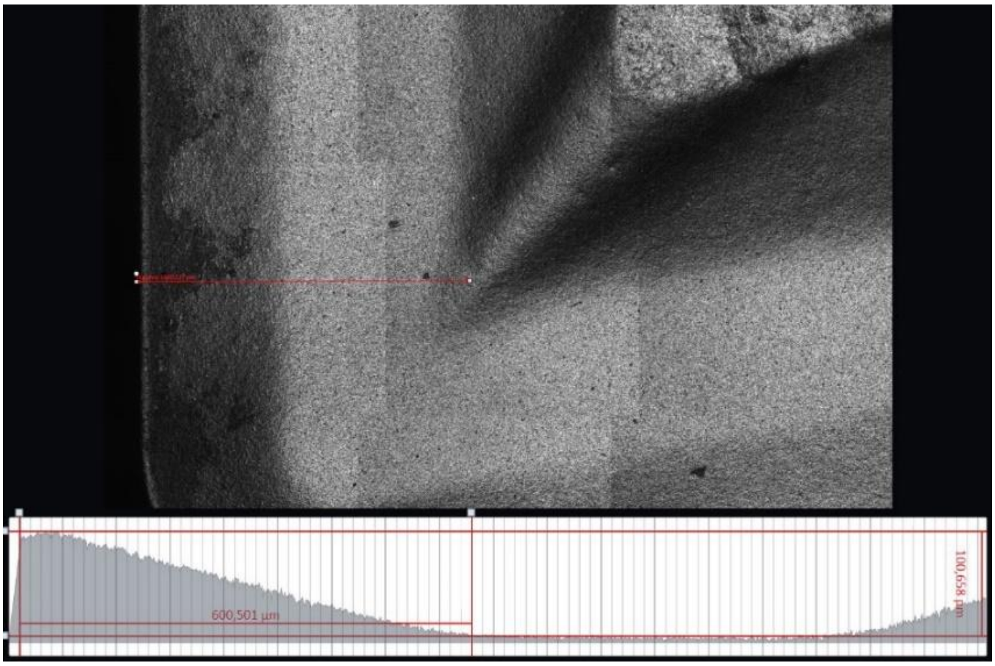

Figure 1. Analysis of the dimensions of the cutting insert's face.

One of the main purposes of texturing in the planned application is to ensure that the structures created on the surface of the cutting insert improve the retention of an additive containing tungsten disulfide nanoparticles (IF-WS_2). This additive is mixed with an emulsion fluid at approximately 1% concentration. The nanoparticles then form a lubricating film on the surface of the cutting insert, which is expected to reduce friction, enhance the machined surface quality, and extend the tool's edge life.

The depth of the textured structures does not need to be excessively deep but must penetrate the carbide substrate to ensure that the structures remain functional on the surface even after the coating is worn.

It was therefore necessary to determine the coating thickness to appropriately select the depth of the texturing. The cutting insert has a TiAlN coating applied via PVD technology. A laser calotest was performed, and an image was captured using Alicona InfiniteFoxus. The distance between the red and green markers (Figure 2), indicating the beginning and end of the coated layer, was measured.

The coating thickness was approximately 0.8 μm on the insert's face and ranged between 1.6–2 μm on the flank. Based on these measurements and articles related to texturing, the texturing depth was set to 5 μm.

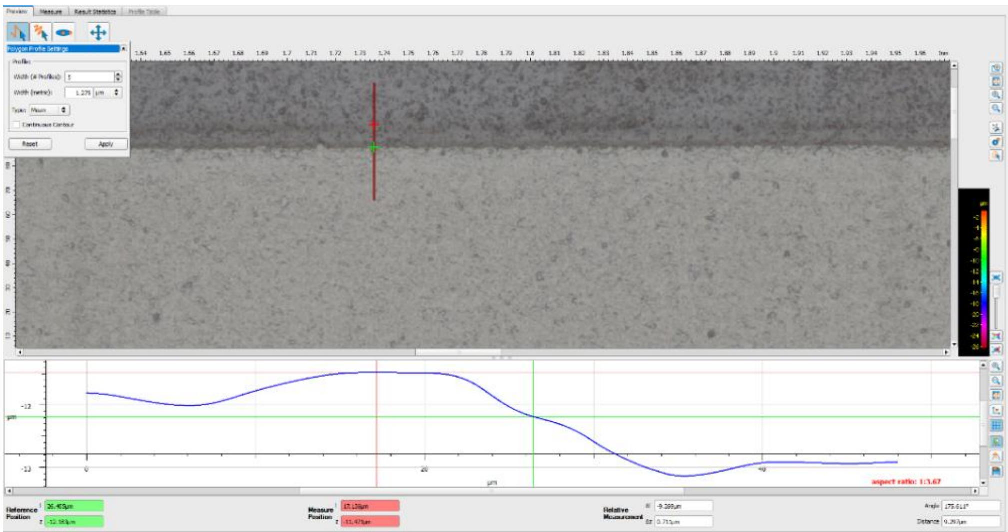

Figure 2. Measurement of coating thickness on the face.

3. Design of textured cutting insert

After studying articles on the texturing of cutting inserts, three different texture variants for the face and back of the cutting insert were designed using the CAD system SolidWorks 2024.

The first variant, shown in Figure 3, consists of shallow holes with a diameter of 50 μm and a spacing of 100 μm. According to the study by Sugihara et al. [10], shape of holes provides a sufficient lubricating layer on the tool surface, while dimple textures with a small diameter exhibited greater friction reduction compared to larger dimples. Additionally, it features easy manufacturing and excellent oil retention capability. In all variants, the textured area is offset by 0.2 mm from the cutting edge to prevent the coating near the edge from being compromised, which could adversely affect the tool's lifespan.

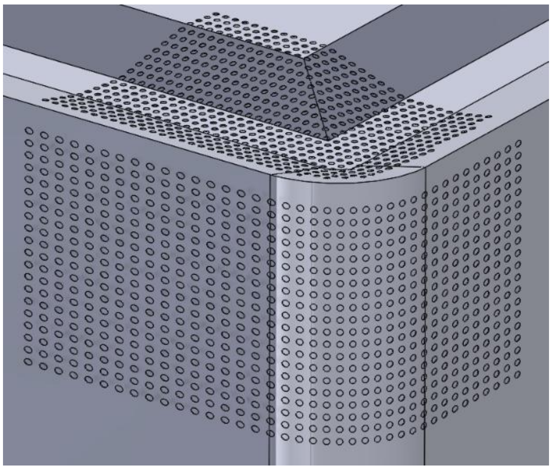

Figure 3. Variant holes.

The next variant, shown on the left in Figure 4, features inclined grooves oriented at a 40° angle on the face and a 45° angle on the flank relative to the main cutting edge. The grooves have a width of 50 μm and a spacing of 100 μm. Texturing in the form of inclined grooves creates a lower coefficient of friction compared to linear grooves and non-textured tools. Lower cutting forces, increased tool life, and reduced cutting temperature were observed in these samples compared to non-textured tools [11].

The final variant, displayed on the right in Figure 4, consists of grooves perpendicular to the cutting edge, with a width of 15 μm and a spacing of 50 μm. The 15 μm width was chosen based on the minimum material removal diameter achievable with a laser, approximately 10–12 μm.

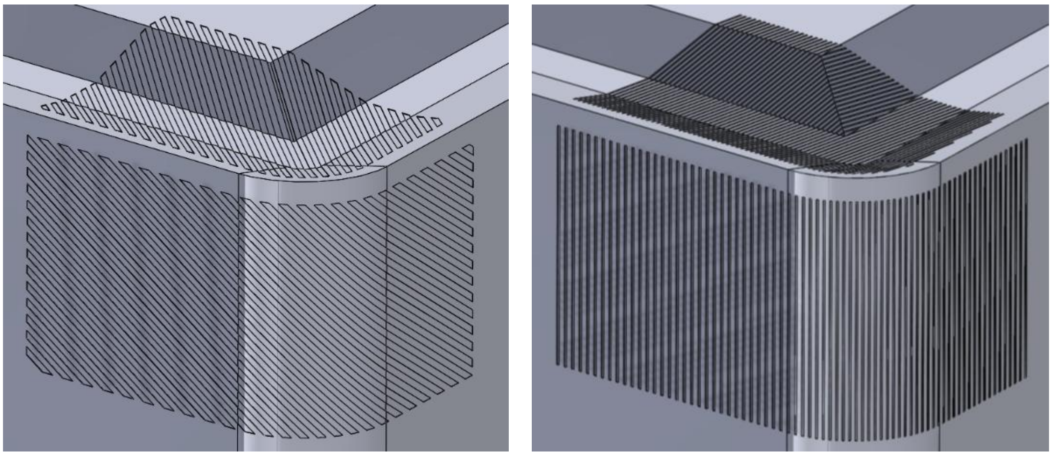

Figure 4. Variant inclined and perpendicular grooves.

The initial design was intended as a grid pattern. However, according to research by Tatsuya Sugihara and colleagues [12], grooves parallel to the cutting edge can serve as initiation points for crack formation. This is because the friction force between the tool's rake surface and the machined surface acts perpendicular to the groove direction, leading to chipping.

All the parameters for the face and flank texturing of the cutting insert for each variant are summarized in Table 1.

Table 1. Texturing parameters.

Variant	Width	Spacing	Depth	Offset from cutting edge	Size of textured area
Holes	50 μm	100 μm	5 μm	200 μm	3x2 mm
Perpendicular grooves	15 μm	50 μm	5 μm	200 μm	3x2 mm
Inclined grooves	50 μm	100 μm	5 μm	200 μm	3x2 mm

For laser programming, each variant for the face and flank was exported separately in the neutral DXF format. During the preparation process, all unnecessary lines were removed, leaving only the shapes for texturing and the cutting-edge curve, which serves as a reference. Figure 5 shows the texture design for the face and flank of the cutting insert in DXF format.

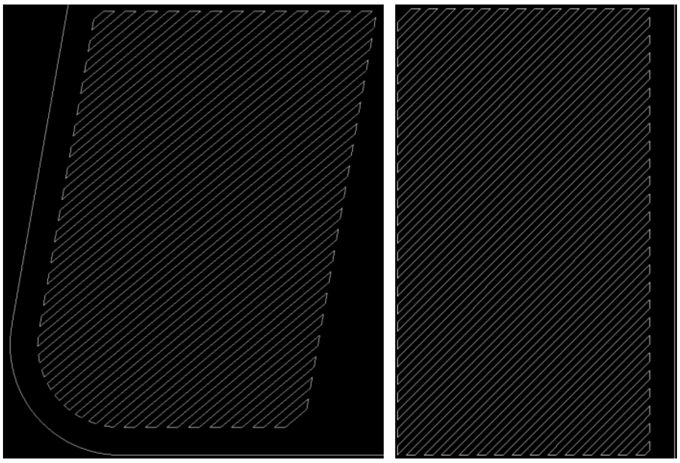

Figure 5. Texture design for the face and flank of the cutting insert in DXF format.

4. Conclusions

This study highlights the promising potential of surface texturing to enhance the performance of cutting tools in turning operations, particularly for challenging materials like Inconel 718. By incorporating textured patterns on the CNMG 12 04 08-SMR 1105 cutting insert, several advantages can be achieved, including reduced friction, better retention of solid lubricants, and improved thermal management. These improvements are expected to contribute to extended tool life, enhanced surface quality of the machined material, and greater overall machining efficiency.

The analysis and design of three distinct texture variants demonstrate a methodical approach to optimizing the tribological performance of cutting inserts. The careful consideration of coating thickness, pattern geometry, and alignment relative to the cutting edge ensures the effectiveness and durability of the texturing under real machining conditions.

Future work will explore the experimental validation of these designs to quantify their impact on cutting forces, wear resistance, and surface finish. Additionally, the integration of solid lubricants into textured patterns represents a valuable direction for further enhancing machining sustainability and reducing the environmental impact of cutting operations.

Acknowledgments: The paper was created within the solution of the project VEGA 1/0457/21 Efficiency improvement in machining nickel based super alloys by texturing cutting tools and utilization of solid lubricants.

This research has been supported by the grant of KEGA Nr. 026TUKE-4/2023 Development Knowledge Support in the field of the quality management system requirements implementation in Aviation, Space and Defense Industry.

Conflicts of Interest: The authors declare no conflict of interest.

References

1. Pramanik, A., Littlefair, G.: Machining of titanium alloy (Ti–6Al–4V)—theory to application. Mach. Sci. Technol. 2014.
2. Singh, T., Singh, P., Dureja, J.S., Dogra, M., Singh, H., Bhatti, M.S.: A review of near dry machining/minimum quantity lubrication machining of difficult to machine alloys. Int. J. Mach. Mach. Mater. 18. 201; pp. 213–251.
3. Journal, A.I., Chen, Y., Wang, J., Chen, M.: Enhancing the machining performance by cutting tool surface modifications: a focused review. Mach. Sci. Technol; 2019.
4. Arslan, A., Masjuki, H.H., Kalam, M.A., Varman, M., Mufti, R.A., Mosarof, M.H., et al.: Surface texture manufacturing techniques and tribological effect of surface texturing on cutting tool performance: a review. Crit. Rev. Solid State Mater. Sci. 8436. 2016; pp- 1–35.
5. Wenlong, S., Jianxin, D., Ze, W., Hui, Z., Pei, Y., Jun, Z., et al.: Cutting performance of cemented-carbides-based self-lubricated tool embedded with different solid lubricants. Int. J. Adv. Manuf. Technol. 52; 2011; pp. 477–485.
6. Sun, J., Zhou, Y., Deng, J., Zhao, J.: Effect of hybrid texture combining micro-pits and micro-grooves on cutting performance of WC/Co-based tools. Int. J. Adv. Manuf. Technol. 86, 2016; pp. 3383–3394.
7. Ze, W., Jianxin, D., Yang, C., Youqiang, X., Jun, Z.: Performance of the self-lubricating textured tools in dry cutting of Ti–6Al–4V. Int. J. Adv. Manuf. Technol. 62, 2012; pp. 943–951.
8. Gachot, C., Rosenkranz, A., Hsu, S.M., Costa, H.L.: A critical assessment of surface texturing for friction and wear improvement. Wear 372–373, 2017; pp. 21–41.
9. Arulkirubakaran, D., Senthilkumar, V., Kumawat, V.: Effect of micro-textured tools on machining of Ti–6Al–4V alloy: an experimental and numerical approach. Int. J. Refract. Met. Hard Mater. 54, 2016; pp. 165–177.
10. Sugihara T., Nishimoto Y., Enomoto T.: Development of a novel cubic boron nitride cutting tool with a textured flank face for high-speed machining of Inconel 718. Precis Eng, vol. 48, 2017; pp. 75–82.
11. Jianxin D., Ze W., Yunsong L., Ting Q., Jie C.: Performance of carbide tools with textured rake-face filled with solid lubricants in dry cutting processes. Int J Refract Metals Hard Mater, vol. 30, no. 1, 2012; pp. 164–172,
12. Sugihara T, Nishimoto Y, Enomoto T.: Development of a novel cubic boron nitride cutting tool with a textured flank face for high-speed machining of Inconel 718. Precision Engineering, 2017; pp. 75–82.

TECHNICAL UNIVERSITY OF KOŠICE
Faculty of Mechanical Engineering

Use of modern techniques in evaluating the dimensions of pressing made from dual-phase steel

Marek Buber [1,*], Miroslav Tomáš [1] and Emil Evin [1]

[1] Department of Automotive Production, Faculty of Mechanical Engineering, Technical University of Košice, Mäsiarska 74, 040 01 Košice; emil.evin@tuke.sk, miroslav.tomas@tuke.sk
* Correspondence: marek.buber@tuke.sk, Tel. +421 55 602 3519

Abstract: Industry using new procedures based on contactless techniques of evaluating the pressings' shape as part of the Industry 4.0 concept. Springback evaluation is essential for checking final shape of car body. Although the industry has been using photogrammetric techniques based on 2D images for over ten years, 3D optical techniques based on surface scanning are used because of their increased precision. The paper assessed cylindrical pressings with flat and hemispherical bottoms constructed of dual-phase steel DP800 that had a thickness of 1.6 mm. The photogrammetric system GOM Scan 1 was used to determine the thickness of the pressing part (cylinders). The thickness of the scanned cylinder in relation to thickness obtained from simulation. The scanned object was compared with surface from simulation of pressing with using constitution law—Vegter Lite yield law, and Krupkowski hardening law as the results of numerical simulation in the PamStamp software. The real pressed cups with a 50 mm diameter were pulled from a 90 mm blank using the Erichsen 145-60 testing machine and lubricated with plastic foil. Comparison of thickness from simulation with thickness from scanned data.

Keywords: flat and hemispherical bottomed cup, photogrammetry, 3D scanning, numerical simulation, thickness comparison

1. Introduction

Sheet metal forming is used in the automobile industry to create many of the body car parts. Stamping, also known as deep drawing, is one of the primary processes that determines the pressings' final shape. The shape of pressings is therefore determined by the formability of the material and process parameters, such as die geometry, friction, blankholder force, brawbead force and location, etc. [1,2], which are the primary determinants in deep drawing.

Industry 4.0 concept employs a range of measurement instruments and techniques for product quality assurance. It is based on collecting digital data from the production to ensure the quality of all processes. By using specialized equipment as scanners and software for postprocessing digital data we know to convert physical models into CAD forms [3,4]. When compared with typical contact coordinate measurements, intelligent automated contactless inspection equipment reduces inspection time while maintaining ongoing process quality monitoring [5,6]. By using triangulation to convert 2D digital photos into spatial data, photogrammetric algorithms are able to reconstruct an object's surface into a 3D object that closely matches the original in terms of dimensions [7,8]. Helle et al. investigated the applicability of 3D scanners for quality control and reverse engineering. They found that it is possible to control the quality of parts based on the obtained scan, but in reverse engineering, the usability of the scanner is limited by the time required to reconstruct the part. Helle et al. said that with simple parts, it is easier and less time-consuming to measure the part manually and construct it in a CAD system than to reconstruct an old part based on a scan [9]. Mendricky [10] concentrated on a thorough examination of the precision of object digitization using several scanners. He conducted the analysis using the ATOS II MV400 and RevScan laser scanners, examining the devices' performance on complexly shaped parts outside of a lab setting. He discovered that the aforementioned scanners may be used to verify the shape, size accuracy. The aim of the paper is to evaluate the thicknesses of dual-phase steel extrusions by comparing surfaces obtained from simulation and surfaces obtained using an optical scanner. Then, the surface obtained by optical scanning is used to evaluate the results of numerical simulation for constitutive models of dual-phase steel.

2. Materials and methodology of experiment

2.1 Material and its properties

The article examined cylindrical pressings with flat and hemispherical bottoms produced of dual-phase steel DP800, with a thickness of 1.6 mm. Using the optical scanning with GOM Scan 1 scanner, the thickness of the pressing was ascertained. These were contrasted with numerical simulation outcomes of PamStamp software when the material was modeled using the Krupkowski hardening rule and the Vegter Lite yield law. On the Erichen 145-60 testing machine, actual cups (pressings) with a diameter of 50 mm were deep pressed from a 90 mm blank and lubricated with plastic foil. The obtained data allowed determining the thickness of the press made, the effect of stamping on the change in thickness, and the deviations between the numerical simulation and the actual thickness of the cup. Dual-phase steel DP800 was tested in experiments with thickness of 1.6 mm. The chemical composition of the steel is shown in Table 1. Mechanical properties, shown in Table 2, were measured by standards ISO 6892-1 [11], plastic strain ratios according to standard ISO 10113 [12] and strain-hardening exponent and strength constant according to standard ISO 10250 [13] within the range yield strength elongation-uniform elongation.

Table 1. Chemical composition of dual phase steel DP800 [wt.%].

C max	Si max	Mn max	P max	S max	Al total	Cr+Mo max	Nb+Ti max
0.170	0.3	2.000	0.050	0.010	0.015-0.08	1.000	0.050

Table 2. Mechanical properties of dual phase steel DP800. (rolling dir.).

Property	$R_{p0.2}$ [MPa]	Rm [MPa]	A_g [%]	A_{80} [%]	n [-]	K [MPa]	r_0 [-]	r_{45} [-]	r_{90} [-]
Value	527	828	12.5	19.9	0.125	1219	0.873	0.907	0.979
Std. Dev.	3	2	0.5	0.5	0.001	3.4	0.028	0.022	0.030

Figure 1. Flat bottomed cup.

Figure 2. Hemispherical bottomed cup.

Cups of 50 mm in diameter were deep drawn on Erichsen 145-60 testing machine. Two types of cups – flat bottomed and hemispherical (Fig. 1 and Fig. 2) – were deep drawn with blankholder force of 25 kN applied and lubricated by microten foil. Drawing die diameter D_d was 54.8 mm, die radius rd 3 mm, punch diameter dp 50 mm, punch radius rp 7 mm. Blank diameter D_0 was 90 mm, thus the drawing ratio D_0/dp = 1.8.

2.2 Optical scanner GOM Scan 1

The method for evaluate the thickness of the cups was contactless scanning. The GOM Scan 1 scanner (Fig. 3) was used to scan the cups with a measuring volume of MV 400. 3D models were then produced using the Zeiss Inspect Pro program (Fig. 4). With an accuracy of 0.02 mm (acc. to VDI 2634 part 3.) [14], the device can scan 6 million points on a 400x250 mm area. Cups were positioned on a rotating table at the proper distance from the scanner before the scanning. Reference points were sticked to the sample to assure the correct overlap of the scans and precise placement of the scanned layers. Eight scans were performed on each side (inside and outside) as the rotary table moved by 45 degrees.

Figure 3. Photogrammetric system GOM Scan 1 MV400.

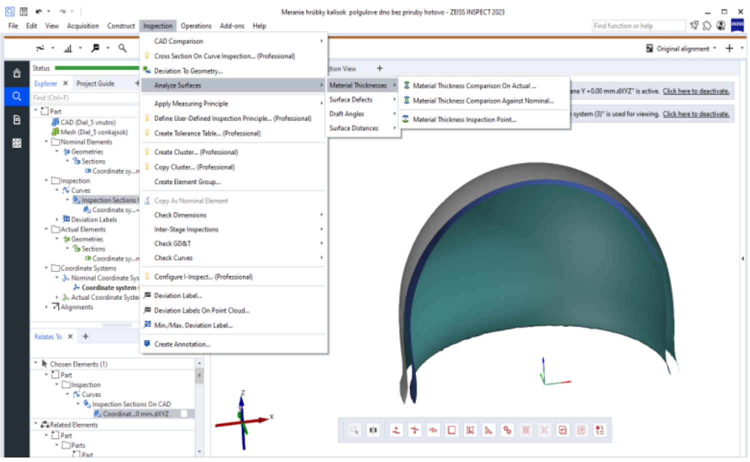

Figure 4. Data processing in ZEISS INSPECT Pro software.

2.3 Numerical simulation

Vegter Lite yielding condition is described as follows:

$$\begin{pmatrix}\sigma_1\\ \sigma_2\end{pmatrix}=\frac{\left(1+\lambda^2\right)\begin{pmatrix}\sigma_1\\ \sigma_2\end{pmatrix}_i^r+w.2.\lambda.(1-\lambda).\begin{pmatrix}\sigma_1\\ \sigma_2\end{pmatrix}_i^h+\lambda^2.\begin{pmatrix}\sigma_1\\ \sigma_2\end{pmatrix}_{i+1}^r}{(1-\lambda)^2+w.2.\lambda.(1-\lambda)+\lambda^2} \tag{1}$$

and Kupkowski (Swift) hardening law:

$$\sigma_{true}=K.\left(\varphi_0+\varphi^n\right) \tag{2}$$

where σ_1, σ_2 [MPa] are major and minor true stress; λ [-] is Bezier interpolation factor; w [-] is weight factor depending on material (steel or aluminum) and defining shear weight and plane strain weight; σtrue [MPa] is true stress; φ [-] is true strain; φ_0 [-] is offset strain; K [MPa] is strength constant and n [-] is strain hardening exponent. It should be noted that K and n are not the same for both hardening models.

Parameters of models were calculated using a MatWizard function on the base of measured material properties as specified in Table 2. In the simulation, springback was calculated after deep drawing process. Then, resulted surface was exported as a mesh surface in STL file format. The stiffness constant c can be determined from the record of the bending force Fmax depending on the path of the bender x_{max}. With the assumed linear course of the dependence, the stiffness constant c will represent the direction of the straight line indicated in the dependence.

Surfaces from simulation were compared with scanned surface in software ZEISS Inspect PRO. Both of cups were cut in half and measured manually by point micrometer with accuracy 0.01mm.

3. Reached results and their evaluation

To verify the differences in the thickness of a cup-shaped cup of DP 800 sheet metal with a flat and hemispherical bottom, a comparison of the surfaces obtained from simulations in PamStamp software and surfaces created using the GomScan 1 scanner. It was assumed that the scanned surface almost exactly matches the real cup. Thickness measurements were evaluated in the rolling direction 45°. The results can be seen in Fig. 5 - 7 for the stamping with a flat bottom and in Fig. 8 - 10 for the cup with a hemispherical bottom. Evaluated maximal and minimal deviation is shown in Table 4. The cup with a flat bottom showed the smallest thickness in the middle area of the walls, namely in the side walls 1.38mm for the scanned part (real cup) and 1.406mm for the simulation. In the lower part of the cup, the walls were thickened to 1.94 mm for the scan (real cup) and 2.128 mm for the simulation of the influence of tangential stress in the flange during the drawing of the blank. In both cases, the thickness change occurred in the same area. Cup with a hemispherical bottom were thinned in the area of the top of the hemisphere. In the scanned part (real cup), the smallest thickness was in the area of the top of the hemisphere with a value of 0.9 mm and in the simulation 1.249 mm. In this case, the results were not identical. The thickness values did not match either at the top of the cup or at the lower part of the cup. The only place where the thickness change values match is the area where the hemisphere transits into the cylindrical part of the cup. This thickness match can be seen in the graph (Fig. 10).

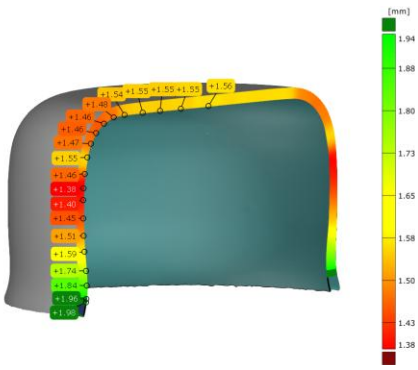

Figure 5. Thickness profile of flat-bottomed cup – Scan.

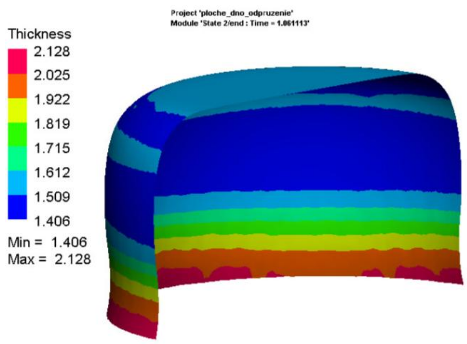

Figure 6. Thickness profile of flat-bottomed cup – Simulation.

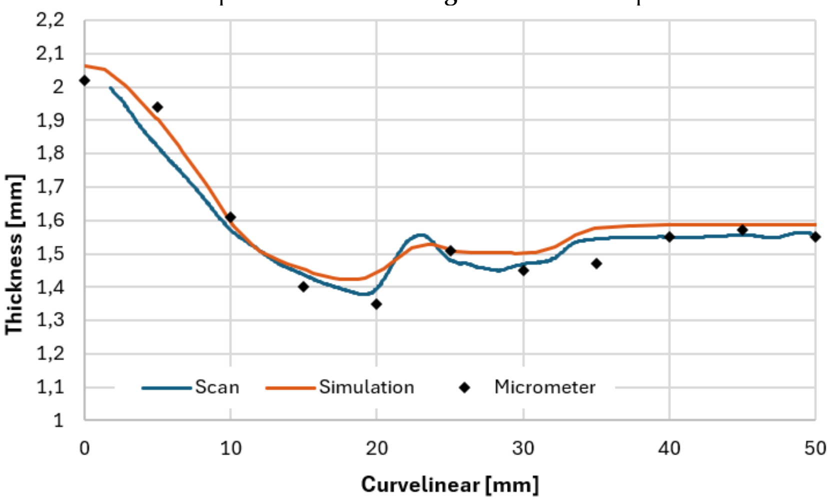

Figure 7. Thickness profile curvilinear (rolling angle 45°).

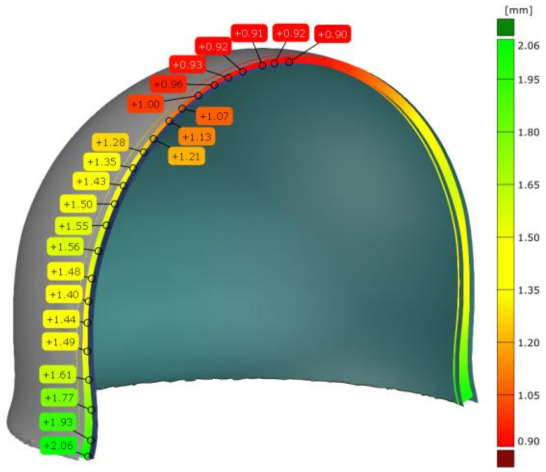

Figure 8. Thickness profile of hemispherical cup – Scan.

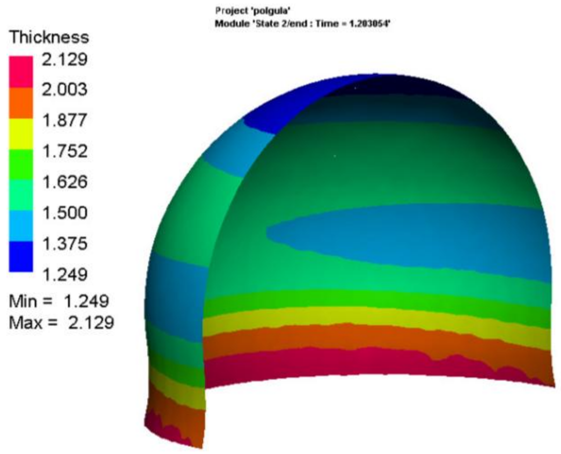

Figure 9. Thickness profile of hemispherical cup – Simulation.

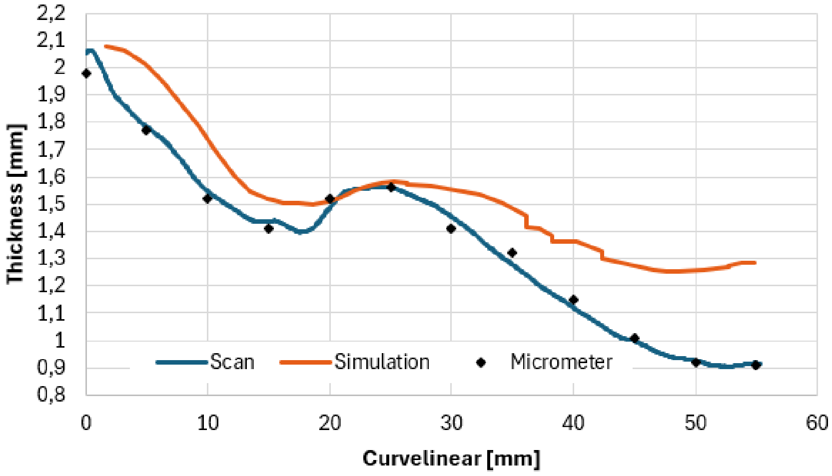

Figure 10. Thickness profile curvilinear (rolling angle 45°).

Table 3. Thickness comparison.

	Scan (real pressed cup)		Simulation - Vegter Lite/Krupkowski	
	Spherical cup	Flat-bottomed cup	Spherical cup	Flat-bottomed cup
Max. thickness	2.06	1.94	2.129	2.128
Min. thickness	0.9	1.38	1.249	1.406
Max-Min	1.16	0.56	0.88	0.722

When comparing manually measured values to scanned and simulated ones. Simulation reached a very good correlation of manually measured and scanned values of the thickness of both cups. A higher difference was found for hemispherical bottomed cups between manually measured and numerically simulated results. Thus further research would be focused on the influence of yield surface on the thickness change of the cups due to stress-strain state during the deep drawing process.

4. Conclusions

As part of the Industry 4.0 idea, 3D scanning is being used more and more in stamping factories to monitor the quality of the pressings due to its good automation potential and quick data processing. In this study, the thickness of dual-phase steel pressings is compared to the surface of pressings computed using numerical simulation of the deep drawing process when cups with flat and hemispherical bottoms were drawn. The actual surface was reached by using 3D scanner GOM Scan 1. Vegter-lite constitutive equation with Krupkowski hardening law was used in simulation to describe the behavior of materials. The data examination could lead to the following conclusions:

• When comparing the thicknesses of the flat-bottomed cup obtained using the GOM Scan 1 scanner and the results of the simulation based on the Krupkowski mathematical model, the results were demonstrably consistent in all parts. The thickness reached values of 1.98 mm in the lower part of the cup and 1.38 mm in the flat top part of the cup. The minimum thickness was in the area of the transition of the arcuate part to the cylindrical surface and reached a value of 1.38 mm.

• When comparing the thicknesses of the hemispherical cup, the simulation with the applied Krupkowski mathematical model did not match the real thickness of the cup obtained by scanning. The thickness values during the scan were 2.06 mm in the lower part of the cup and 0.9 mm at the top, while the simulation assumed thickness values of 2.129 in the lower part and 1.124 at the top.

A good correlation was found between manually measured dimensions of thicknesses and thicknesses reached by the scanner.

For better correlation of results, it is necessary to perform simulation calculations on multiple mathematical models and evaluate which of the models is most ideal for predicting thickness changes during the forming of spherical surfaces.

Future research will focus on applying different combinations of hardening models and yield conditions.

Acknowledgments: This work was supported by the Scientific Grant Agency of the Slovak Republic within the project VEGA 1-0238-23 “Implementation of CAx systems and virtual engineering techniques in the redesign of car-body parts for deformation zones” and project VEGA 1/0609/25 “Research and development of methodologies for the assessment of strains of sheet metal and manufacturability of the car components in a virtual environment”.

References

1. 1A. Hrivňák, E. Evin: Formability of steel sheets.1st ed., Košice-Elfa, 2004.
2. T. Trzepieciński: Acta Metallurgica Slovaca, 26(2), 2020, p.42-44. https://doi.org/10.36547/ams.26.2.553.
3. Pilar Valerga Puerta, R. Aletheia Jimenez-Rodriguez, S. Fernandez-Vidal, S. Raul Fernandez-Vidal: Photogrammetry as an Engineering Design Tool, Product Design. IntechOpen, 2020. doi: 10.5772/intechopen.92998
4. G. Morteza: Industry 4.0, digitization, and opportunities for sustainability, Journal of Cleaner Production,Vol. 252, 2020, https://doi.org/10.1016/j.jclepro.2019.119869.
5. M. Javaid, A. Haleem, R.P. Singh, R. Suman: Sensors International, 2, 2021, 100114, https://doi.org/10.1016/j.sintl.2021.100114
6. M. Bilušić, L. Olivari: Journal of Industrial Information Integration, 41, 2024, 100654, https://doi.org/10.1016/j.jii.2024.100654
7. T. Schenk: Introduction to Photogrammetry, Department of Civil and Environmental Engineering and Geodetic Science, The Ohio State University: Columbus, OH USA, 2005.
8. J. Valença, E.N.B.S. Júlio, H.J. Araújo: Experimental Techniques, 36(5), 2012, pp. 71-81, https://doi.org/10.1111/j.1747-1567.2011.00731.x
9. R. H. Helle, H. G. Lemu: A case study on use of 3D scanning for reverse engineering and quality control, Materials Today: Proceedings, Vol. 45, Part 6, 2021, p. 5255-5262, https://doi.org/10.1016/j.matpr.2021.01.828.
10. R. Mendricky: Analysis of measurement accuracy of contactless 3D optical scanners. MM Science Journal, 10, 2015, p.711-716, DOI: https://doi.org/10.17973/MMSJ.2015_10_201541
11. ISO 6892-1:2019; Metallic Materials—Tensile Testing—Part 1: Method of Test at Room Temperature. International Organization for Standardization: Geneva, Switzerland, 2019.
12. ISO 10113:2020; Metallic Materials—Sheet and Strip—Determination of Plastic Strain Ratio. International Organization for Standardization: Geneva, Switzerland, 2020.
13. ISO 10275:2020; Metallic Materials—Sheet and Strip—Determination of Tensile Strain Hardening Exponent. International Organization for Standardization: Geneva, Switzerland, 2020.
14. VDI/VDE 2634 Part 3:2008-12; Optical 3D-measuring systems - Multiple view systems based on area scanning: Verein Deutscher Ingenieure e.V., Düsseldorf 2008.

Differentiation potential of mesenchymal stem cells in vitro

Jana Čajková [1,*], Marianna Trebuňová[1] and Darina Bačenková [1]

[1] Technical University of Košice, Košice, Slovakia; ; jana.cajkova@tuke.sk
* Correspondence: jana.cajkova@tuke.sk

Abstract: Mesenchymal stem cells (MSCs) represent a promising cell source for regenerative medicine and tissue engineering due to their ability to differentiate into various lineages. In this study, we successfully isolated chorionic mesenchymal stem cells (CMSCs) from human placental tissue and evaluated their differentiation potential under in vitro conditions. The CMSCs were cultured and induced to differentiate into adipogenic, osteogenic, and chondrogenic lineages to confirm their multipotency in our laboratory settings. Morphological analysis revealed the characteristic spindle-shaped appearance of CMSCs post-seeding, along with the presence of elongated filopodia and granular endoplasmic reticulum arranged in parallel rows within the cytoplasm, with the nucleus eccentrically located. These observations confirmed the identity of the isolated cells as MSCs. The differentiation assays demonstrated the capability of CMSCs to form adipocytes, osteoblasts, and chondrocytes under appropriate induction conditions. Our findings validate the differentiation potential of CMSCs and their suitability for use in regenerative medicine and biomedical engineering applications.

Keywords: stem cells, biocompatibility, differentiation

1. Introduction

Mesenchymal stem cells (MSCs) are multipotent progenitor cells with the potential to differentiate into a variety of cell types, including adipocytes, chondrocytes, and osteocytes [1] [2]. In 2006, MSCs were precisely characterized according to the International Society for Cell Therapy (ISCT), which established minimum criteria for defining human mesenchymal stem cells, namely: adherence to plastic cultivation dishes, necessity of expression of markers CD73, CD90, CD105; they must not express CD45, CD34, CD14 or CD11b, CD79a or CD19 and HLA-DR, and the necessity of differentiation under in vitro conditions into adipocytes, chondrocytes and osteoblasts [3][4]. While mesenchymal stem cells can be derived from various tissues such as bone marrow, adipose tissue, and umbilical cord, chorionic mesenchymal stem cells (CMSCs) isolated from fetal membranes are emerging as a compelling alternative due to their unique properties [5]. Unlike MSCs sourced from invasive procedures, CMSCs are obtained from placental tissue, which is typically discarded postpartum, thereby circumventing significant ethical controversies associated with other stem cell sources. CMSCs exhibit a high proliferative capacity, immunomodulatory effects, and robust multipotency, enabling differentiation into adipogenic, chondrogenic, and osteogenic lineages [6] [7].

Adipocytes, chondrocytes, and osteocytes represent critical cellular phenotypes in regenerative medicine and tissue engineering [8]. Adipocytes, derived through adipogenic differentiation, are essential for studying metabolic disorders, such as obesity and diabetes, and for developing cell-based therapies for soft tissue reconstruction [9]. Chondrocytes, generated via chondrogenic differentiation, form the cellular basis of cartilage, making them invaluable in cartilage repair and regenerative strategies for conditions such as osteoarthritis [10]. Osteocytes, arising from osteogenic differentiation, are fundamental to bone tissue engineering and fracture repair, offering potential solutions for osteoporosis and other bone-related diseases. Understanding the differentiation of MSCs into these cell types not only sheds light on their biological plasticity but also underscores their therapeutic potential in developing targeted regenerative treatments [11] [12] [13].

This study evaluates the differentiation potential of CMSCs under in vitro conditions to confirm their adaptability in laboratory settings. Given their ability to differentiate into multiple lineages and their non-invasive origin, CMSCs present significant promise in biomedical engineering, particularly in developing cell-based therapies, tissue scaffolds, and regenerative constructs for repairing damaged or diseased tissues [14] [15].

2. Materials and Methods

2.1. Isolation of CMSCs

Chorionic mesenchymal stem cells were isolated from the fetal chorion following a planned pregnancy termination via caesarean section at Gynecology and obstetrics clinic, Hospital AGEL Kosice-Saca. The tissue was collected aseptically and transferred to chilled DMEM with antibiotics (penicillin, streptomycin, and amphotericin B). The chorion was separated from the amnion and fragmented into small pieces (0.5-1 cm). Cells were isolated enzymatically using dispase II (2.4 U/ml) for 10-15 minutes, followed by collagenase II (1 mg/ml) for 90 minutes to digest the mesenchymal layer. After enzyme removal and filtration, a single-cell suspension was obtained. The suspension was seeded in culture flasks at 4000 cells/cm^2, cultured in DMEM with 10% FBS, and incubated at 37 °C in a 5% CO_2 atmosphere. Medium was changed 2-3 times a week, and once an 80% monolayer was formed, cells were trypsinized.

2.2. Adipogenic differentiation

Adipogenic differentiation was tested after the second passage of chorionic stem cells. The cells were seeded at a density of 2.0×10^4 cells/cm^2 on Nunc Lab-Tec polystyrene plates. A commercial "MSC Functional Identification Kit" (R&D Systems, USA) was used for adipogenic stimulation, containing hydrocortisone, indomethacin, and isobutylmethylxanthine. The differentiation medium was changed 2-3 times per week. After two weeks, morphological changes were observed, with the formation of lipid vacuoles. Oil Red O staining was used to detect lipids. Samples were fixed in 10% formaldehyde, washed, and stained with 0.5% Oil Red O. After washing, samples were incubated in 75% glycerol.

2.3. Osteogenic differentiation

Osteogenic differentiation was tested after the second passage of chorionic stem cells. CMSCs were seeded at a density of 4.0×10^3 cells/cm^2, and osteogenic differentiation medium containing dexamethasone, ascorbic acid, and beta-glycerophosphate was added, using the same "MSC Functional Identification Kit" as in the previous step. Cells were cultured in osteogenic medium for 14 days, with medium changes 2-3 times per week. After 14 days, calcium deposits were observed, and samples were stained using the Von Kossa method. Samples were first fixed in 10% buffered formalin, followed by washing and staining with a 5% silver nitrate solution for 30 minutes, then washed with distilled water.

2.4. Chondrogenic differentiation

Chondrogenic differentiation was tested after the second passage of chorionic stem cells. CMSCs were seeded at an optimal density of 2.5×10^5 cells/cm^2, and chondrogenic induction medium containing dexamethasone, ascorbate phosphate, proline, and insulin-transferrin were added using the "Human MSC Functional Identification Kit" (R&D Systems, USA). After three weeks of incubation, the differentiated CMSCs were histochemically stained. The culture medium was aspirated, and samples were washed with PBS. Cells were fixed in 4% paraformaldehyde for 5 minutes and then washed with distilled water. The samples were stained for 30 minutes with a 1% Alcian Blue solution (Sigma, USA), followed by washing with 0.1N hydrochloric acid.

3. Results

3.1. Cultivation of in vitro CMSCs

The suspension of nucleated cells was enzymatically isolated from the fetal envelope of the chorion. Cells were cultured in simulated physiological conditions in an incubator environment. Cells that did not adhere to the culture surface even after three to four days were aspirated. Adhered cells were characterized by high clonogenicity potential. Passage of cells was performed after 70-80% monolayer formation. Figure 1 shows the observed CMSCs on individual days of cultivation.

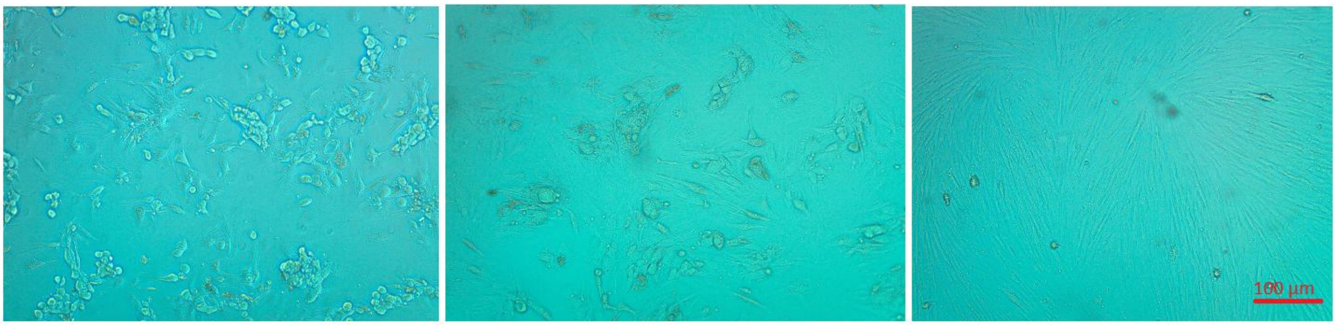

Figure 1. 4th Day (Left Image): Cells are more rounded with visible filopodia, showing early attachment and spreading. Some are beginning to adhere to the surface. 6th Day (Middle Image): By day six, cells are more spread out, with increased confluence. Elongated shapes typical of mesenchymal stem cells start to appear, and some cells take on a spindle shape. 10th Day (Right Image): By day ten, cells show organized, elongated morphology with more spindle-shaped cells. Growth is uniform, and cells are densely packed, indicating active proliferation.

3.2. Adipogenic differentiation

In suitable stimulating culture conditions of adipogenic medium, which contained hydrocortisone, indomethacin and isobutylmethylxanthine, after the first passage, CMSCs differentiated for two weeks into cells forming lipid vacuoles, which are characteristic of adipocytes. After differentiation, CMSCs were stained with Oil red, which stained lipid inclusions in the cytoplasm of cells orange. Lipid vacuoles typical for adipocytes were detected in the preparation. Morphological changes in the cytoplasm of differentiated cells and the formation of vacuoles of neutral lipids, as well as the number of smaller lipid granules, were observed. During adipogenic differentiation, there was a change in phenotype and the expression of specific markers of adipogenesis, such as lipoprotein lipase, adiponectin, adipocyte protein-2 (AP2) and peroxisome proliferator-activated receptor (PPAR). Adipogenic differentiation of CMSCs cells is shown in Figure 2. Stained with Oil Red and hematoxylin after the first passage, shows red-stained lipid droplets, indicating adipocyte differentiation. The dark blue or purple areas represent cell nuclei, stained with hematoxylin. The contrast between the red droplets and purple nuclei highlights the differentiation process.

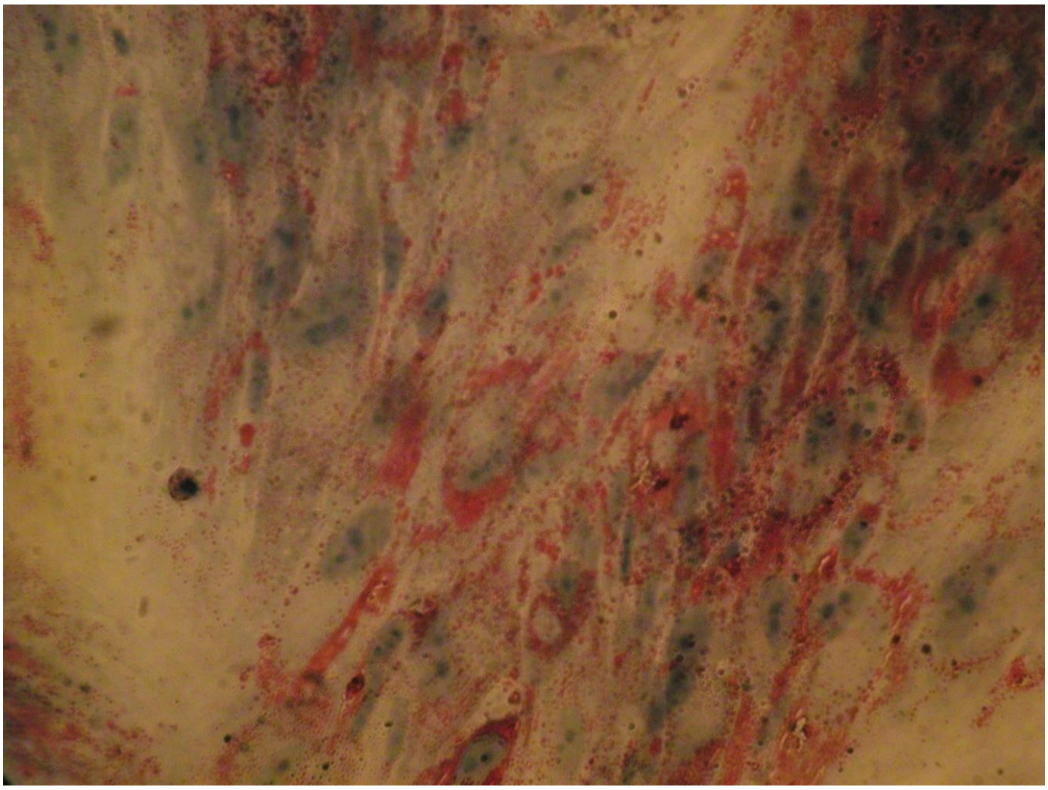

Figure 2. Adipogenic differentiation.

3.3. Osteogenic differentiation

The essence of osteogenic differentiation is a change in the extracellular environment (ECM) and the formation of ECM mineralization. CMSCs that were cultured in an osteogenic induction solution containing dexamethazole, ascorbic acid, and beta-glycerol phosphate showed the formation of calcium and phosphate-containing calcifications, which are characteristic of differentiated osteoblasts. CMSCs that are osteogenically stimulated produce alkaline phosphatase (ALP). The phenotype of osteogenically induced CMSCs changes and they express osteogenic markers, ALP, osteocalcin, osteopontin (OSP), bone sialoprotein and also bone morphological protein 2 (BMP2). Differentiated cells are in ECM containing type I collagen, which further responds stimulatingly to calcium deposition. CMSCs are characterized by a significant ability to differentiate into osteoblasts. The observed osteogenic differentiation of CMSCs cells is shown in Figure 3. The black or dark brown areas in the image indicate mineralized bone matrix, which is a hallmark of osteogenic differentiation. Von Kossa staining is used to detect the presence of calcium phosphate deposits, typically seen in osteocytes or osteoblasts during the differentiation process. These dark areas represent the areas where the cells have deposited mineralized extracellular matrix, a key feature of osteogenesis. The cells appear to be clustered around the mineralized regions, suggesting that these CMSCs have begun differentiating into osteoblast-like cells capable of producing mineralized matrix.

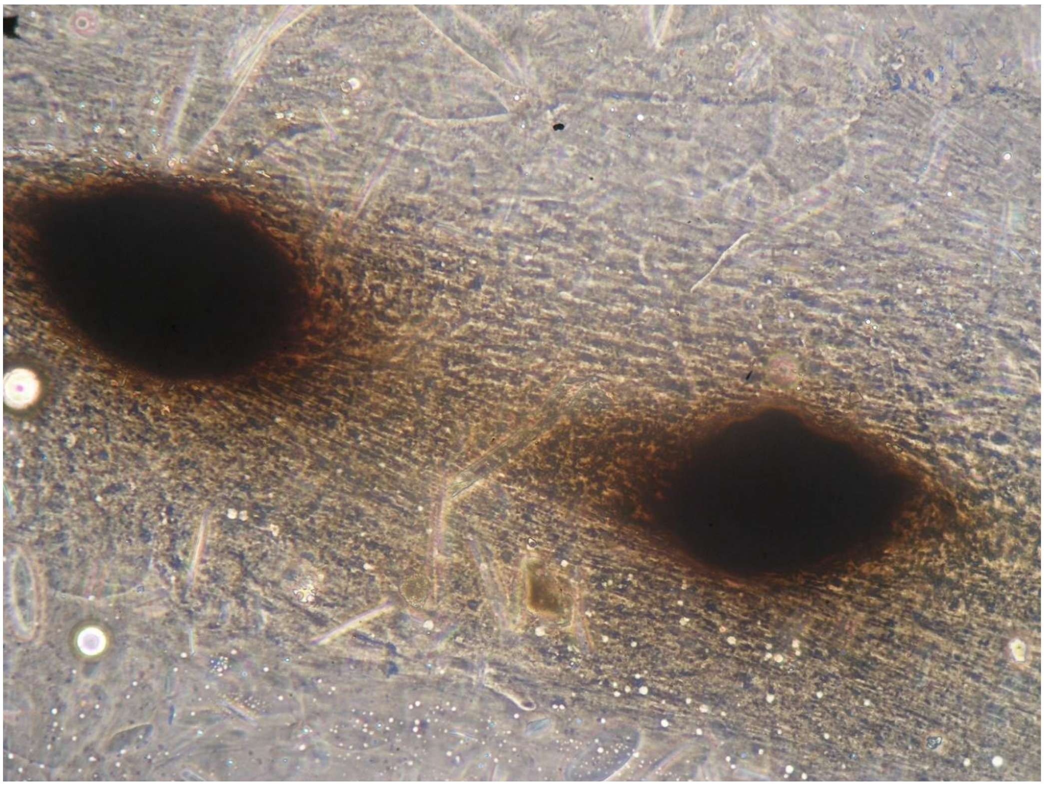

Figure 3. Osteogenic differentiation.

3.4. Chondrogenic differentiation

CMSCs were cultured in chondrogenic stimulation medium containing dexamethasone, ascorbate phosphate, proline and insulin-transferrin. After two weeks, the formation of a proteoglycan matrix was observed in the culture, which was also confirmed by histological staining with alcian blue. After the first week of differentiation, CMSCs were elongated in shape with a prominent nucleus and endoplasmic reticulum in the cytoplasm. During differentiation, genes encoding the proteoglycan aggrecan, collagen I, collagen X, collagen XI, as well as elastin, are activated. CMSCs observed during chondrogenic differentiation had the ability to differentiate into the chondro-lineage, through proven extracellular matrix formation. In Figure 4 shows chondrogenic differentiation after the first passage. Alcian blue stains the GAGs in the extracellular matrix of differentiated chondrocytes. The regions where the cells have accumulated these GAGs appear blue. The cells undergoing chondrogenic differentiation are organized in clusters, with a cartilaginous-like matrix around the cells. This matrix is rich in sulfated proteoglycans, such as aggrecan, which are stained by Alcian blue. The presence of intense blue staining indicates successful chondrogenic differentiation, as the accumulation of GAGs is essential for the development of cartilage tissue. If some areas are less stained or lighter, it may indicate earlier stages of differentiation, with less cartilage matrix formed.

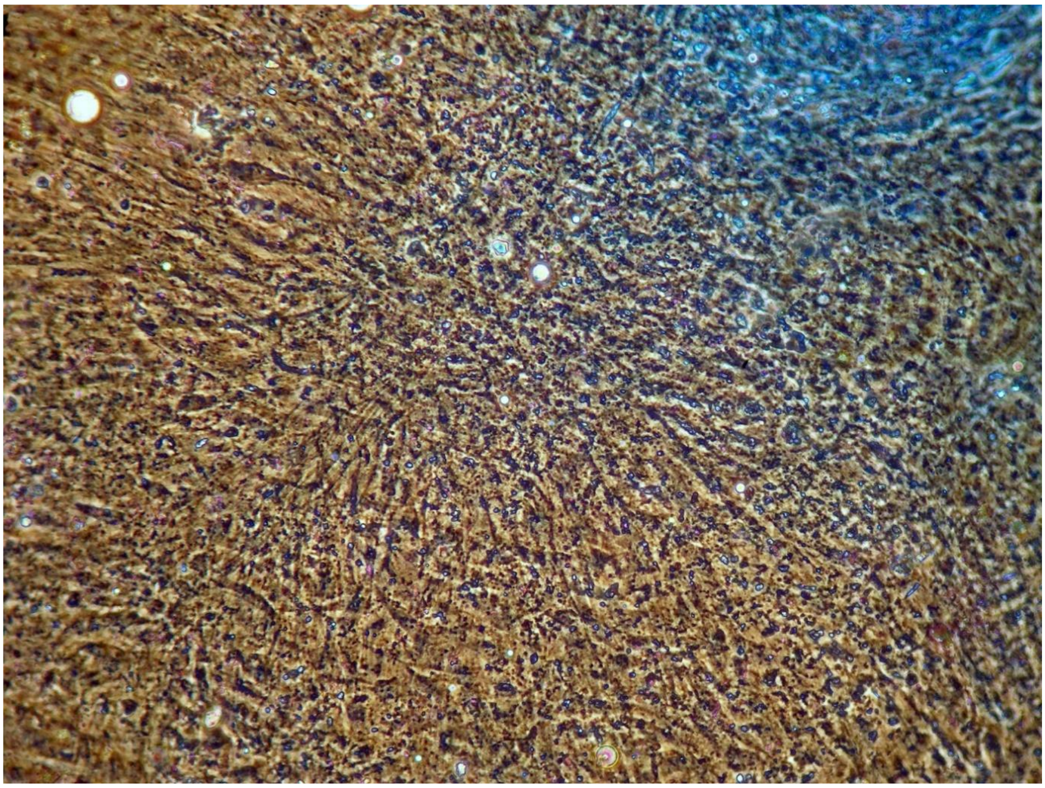

Figure 4. Chondrogenic differentiation.

4. Discussion

In this study, we successfully demonstrated the differentiation potential of chorionic mesenchymal stem cells (CMSCs) derived from donated placental tissue, an ethically unburdened and discarded source. By isolating CMSCs from placental tissue, which would otherwise be discarded, we have found a sustainable and ethical method to obtain stem cells with multilineage differentiation potential. Using our in-house protocols, we induced adipogenic, osteogenic, and chondrogenic differentiation. Oil Red O staining revealed the formation of lipid droplets, confirming adipogenic differentiation, while Von Kossa staining highlighted calcium phosphate deposits, marking successful osteogenesis. These results underscore the ability to differentiate CMSCs into adipocytes, osteoblasts, and chondrocytes using placental tissue as an accessible and ethical source of stem cells. Moreover, CMSCs can serve as a valuable tool for biocompatibility testing of various biomaterial scaffolds [5] [16], offering promising applications in tissue regeneration within the field of biomedical engineering. By utilizing placental tissue in this way, we contribute to advancing both ethical stem cell research and tissue engineering applications, fostering sustainable practices for the development of regenerative therapies.

Acknowledgments: This work was funded by KEGA 018TUKE-4/2023 and VEGA 1/0403/25.

Conflicts of Interest: The authors declare no conflict of interest.

References

1. Maumus, M.; Pers, Y.-M.; Ruiz, M.; Jorgensen, C.; Noël, D. Mesenchymal Stem Cells and Regenerative Medicine. *médecine/sciences* **2018**, *34* (12), 1092–1099.
2. Berebichez-Fridman, R.; Montero-Olvera, P. R. Sources and Clinical Applications of Mesenchymal Stem Cells: State-of-the-Art Review. *Sultan Qaboos University Medical Journal* **2018**, *18* (3), e264.
3. Han, Y.; Li, X.; Zhang, Y.; Han, Y.; Chang, F.; Ding, J. Mesenchymal Stem Cells for Regenerative Medicine. *Cells* **2019**, *8* (8), 886.
4. Caplan, A. I. Mesenchymal Stem Cells in Regenerative Medicine. In *Principles of regenerative medicine*; Elsevier, 2019; pp 219–227.

5. Trebuňová, M.; Demeterová, J.; Bačenková, D.; Rajťuková, V.; Živčák, J. Surface Biocompatibility of Porous Titanium Structures with Stem Cells. **2023**, *53* (1). https://doi.org/10.14311/CTJ.2023.1.03.
6. Yang, G.; Fan, X.; Liu, Y.; Jie, P.; Mazhar, M.; Liu, Y.; Dechsupa, N.; Wang, L. Immunomodulatory Mechanisms and Therapeutic Potential of Mesenchymal Stem Cells. *Stem Cell Reviews and Reports* **2023**, *19* (5), 1214–1231.
7. Seo, Y.; Yoon, H.; Park, Y.; Song, K.; Lee, W.; Park, J. Correlation between Scaffold in Vivo Biocompatibility and in Vitro Cell Compatibility Using Mesenchymal and Mononuclear Cell Cultures. *Cell biology and toxicology* **2009**, *25* (5), 513–522.
8. Zhang, X.; Zhang, S.; Wang, T. How the Mechanical Microenvironment of Stem Cell Growth Affects Their Differentiation: A Review. *Stem cell research & therapy* **2022**, *13* (1), 415.
9. Trohatou, O.; Roubelakis, M. G. Mesenchymal Stem/Stromal Cells in Regenerative Medicine: Past, Present, and Future. *Cellular reprogramming* **2017**, *19* (4), 217–224.
10. Bačenková, D.; Trebuňová, M.; Demeterová, J.; Živčák, J. Human Chondrocytes, Metabolism of Articular Cartilage, and Strategies for Application to Tissue Engineering. *International Journal of Molecular Sciences* **2023**, *24* (23), 17096.
11. Park, J. S.; Suryaprakash, S.; Lao, Y.-H.; Leong, K. W. Engineering Mesenchymal Stem Cells for Regenerative Medicine and Drug Delivery. *Methods* **2015**, *84*, 3–16.
12. Zhao, W.; Li, K.; Li, L.; Wang, R.; Lei, Y.; Yang, H.; Sun, L. Mesenchymal Stem Cell-Derived Exosomes as Drug Delivery Vehicles in Disease Therapy. *International Journal of Molecular Sciences* **2024**, *25* (14), 7715.
13. Garg, A.; Khan, S.; Luu, N.; Nicholas, D. J.; Day, V.; King, A. L.; Fear, J.; Lalor, P. F.; Newsome, P. N. TGFβ1 Priming Enhances CXCR3-mediated Mesenchymal Stromal Cell Engraftment to the Liver and Enhances Anti-inflammatory Efficacy. *Journal of Cellular and Molecular Medicine* **2023**, *27* (6), 864–878.
14. Bačenková, D.; Trebuňová, M.; Morochovič, R.; Dosedla, E.; Findrik Balogová, A.; Gašparová, P.; Živčák, J. Interaction between Mesenchymal Stem Cells and the Immune System in Rheumatoid Arthritis. *Pharmaceuticals* **2022**, *15* (8), 941.
15. Bačenková, D.; Demeterová, J.; Dosedla, E.; Gašparová, P.; Trebuňová, M. The Use of Alginate in the Cultivation of Mesenchymal Cells in Biomedical Engineering. *Acta Technologia* **2024**, *10* (2). https://doi.org/10.22306/atec.v10i2.198.
16. Trebuňová, M.; Gromošová, S.; Bačenková, D.; Rosocha, J.; Živčák, J. Biocompatibility of the Human Mesenchymal Stem Cells with Bovine Bone Tissue at the Cellular Level in Vitro. **2018**, No. 2.

TECHNICAL UNIVERSITY OF KOŠICE
Faculty of Mechanical Engineering

Research into potential application of EHD propulsion in the conditions of gravitational interaction

Peter Čurma [1,*], Marián Lázár [1]

[1] Department of Energy Engineering, Faculty of Mechanical Engineering, Technical University of Košice, 04200 Košice, Slovakia; peter.curma@tuke.sk; marian.lazar@tuke.sk
* Correspondence: peter.curma@tuke.sk; Tel.: +421 911 078 466

Abstract: Ion engines represent a progressive type of propulsion that is currently widely applied in the space industry. In the conditions of gravitational interaction, the use of similar effectors is only rarely present. An ion engine that uses the Biefeld-Brown effect facilitates the formation of electrically charged particles which transfer their own mobility to the surrounding electroneutral particles while the asymmetric electrodes are exposed to high direct-current voltage. The purpose of the present article is to analyse the issues related to the application of ion engines in the conditions of gravitational interaction, including their designs and mechanism of action. In the experimental section, the verification of the device functionality is presented and the efficiency of this type of propulsion is quantified.

Keywords: electrohydrodynamic propulsion; ionic wind; corona discharge

1. Introduction

Progress in the field of energy systems and energy storage methods, as well as efforts aimed at increasing the energy utilisation efficiency, entails the progress in all of the related fields, i.e. energy production, storage and utilisation. Development of methods for better energy utilisation has caused that the systems which were not expected to be applicable in terrestrial conditions a few decades ago are now being gradually brought into use. Such technologies now also include those that are based on the use of the Biefeld-Brown effect, observed for the first time in 1920 [1].

The principle of the Biefeld-Brown effect is based on the formation of electrically charged particles that subsequently move from the emitter to the collector with the opposite charge. Such a movement of ionised particles produces a thrust.

In the early stage of the development of that technology, the generated thrust produced only a negligible amount of kinetic energy relative to the weight of the whole equipment [2]. Therefore, the engines based on the use of a stream of ionised particles for the production of kinetic energy were only used in the exploration of the cosmic space.

Their main advantage, compared to conventional propulsion units, was their ability to produce a thrust for a much longer period of time, albeit of a small magnitude. Spacecrafts may thus achieve higher speeds in the long run. The key advantage is the temporal effect of the acting force, expressed through a force impulse, which is a few orders higher than the one achieved with the use of conventional propulsion.

The use of those propulsion technologies is also appropriate for the cosmic space since they primarily use the electric energy that is easy to produce and only small quantities of propulsion media, i.e. inert gases or mixture thereof, which is not the case in the conventional chemical propulsion. They thus contribute to a significant reduction of take-off weights, which brings a notable cost reduction.

Progress in material sciences, development of novel alloys, ultra-light materials, energy storage systems and related software and hardware facilitated achieving a significant reduction of the weights of propulsion units, which are currently so low that the thrust produced in ion engines generates kinetic energy in the quantity that is sufficient for the equipment to move in the conditions of gravitational interaction. Low noise emissions of EHD propellers represent an advantage especially in the field of unmanned aircraft propulsion.

2. Physical description of EHD propulsion processes

A corona discharge typically occurs at voltages lower than the breakdown voltage. A corona discharge occurs at pressures above 1,000 Pa, and its occurrence significantly depends on the shapes of the electrodes – a small curvature radius of an electrode is a precondition for the formation of an inhomogeneous electric field [3].

The value of the electric field around a coronating electrode must be higher than its critical value. While multiple empirical equations have been developed for the approximation of that critical value, the best-known one is Peek's law with multiple modifications:

$$E_{\mathrm{C}} = 3{,}15 \cdot 10^4 \cdot m_{\mathrm{a}} \cdot \delta \cdot \left(1 + \frac{0{,}305}{\sqrt{\delta \cdot \frac{D_{\mathrm{E}}}{2}}}\right) \ (\mathrm{kV} \cdot \mathrm{cm}^{-1}) \quad (1)$$

wherein m_a is the factor determined by the quality and cleanness of the coronating electrode surface (1); δ is the correction factor determined by the ambient pressure and temperature (1); and D_E is the diameter of the emitter conductor (cm) [23].

With regard to a continuous power supply during the operation, a constant value of the electric charge between the plates of the asymmetrical capacitor was applied. The law of conservation of charge indicates the following:

$$\nabla \bar{J} = -\frac{\partial \rho_q}{\partial t_{\mathrm{t}}} \ (\mathrm{A} \cdot \mathrm{m}^{-2}) \quad (2)$$

wherein ∇ is the divergence (1); $\bar{J}$ is the current density per square meter ($A \cdot m^{-2}$); ρ_q is the electric charge density per square meter ($C \cdot m^{-2}$); and t_t is time (s).

In the case that direct current is applied to the clips of the asymmetrical capacitor, the time gradient of the current density is zero:

$$\frac{\partial \rho_q}{\partial t_{\mathrm{t}}} = 0 \quad (3)$$

As a result, the following equation applies:

$$\nabla \bar{J} = 0 \quad (4)$$

The current density per square meter changes due to the effects of the drift velocity $\mu \cdot \bar{E}$ of the charged particles, the effects of the velocity of the medium flowing through the asymmetrical capacitor $\rho_Q \cdot w_0$, as well as the effects of the diffusion velocity $D \cdot \nabla \rho_Q$ of the charged particles. Provided that cations are expelled from the ionisation zone to the ion drift zone by the coronating electrode, a current density per square meter that is present in any of the cross-sections of that zone, perpendicular to the $\bar{E}$ vector, is as follows:

$$\bar{J} = \mu_{\mathrm{m}} \cdot \rho_Q \cdot \bar{E} + \rho_Q \cdot \bar{w}_0 - D \cdot \nabla \rho_Q \ \ (\mathrm{A} \cdot \mathrm{m}^{-2}) \quad (5)$$

wherein μ_m is the electrical mobility ($m^2 \cdot V^{-1} \cdot s^{-1}$); ρ_Q is the volume charge density ($C \cdot m^{-3}$); $\bar{E}$ is the electric field ($V \cdot m^{-1}$); $\bar{w}_0$ is the medium flow velocity ($m \cdot s^{-1}$); and D is the diffusion rate of the charged particles ($m \cdot s^{-1}$).

The drift velocity of the charged particles in a homogeneous electric field is as follows:

$$\bar{v}_d = \mu_{\mathrm{m}} \cdot \bar{E} \ \ (\mathrm{m} \cdot \mathrm{s}^{-1}) \quad (6)$$

If, for simplification purposes, a homogeneous electric field is taken into consideration, the following equation applies:

$$\bar{E} = \frac{U}{d} \ (\mathrm{V} \cdot \mathrm{m}^{-1}) \quad (7)$$

wherein U is the difference in electrode potentials (V) and d is the inter-electrode distance (m).

Subsequently, the volume charge density may be expressed as follows:

$$\rho_Q = \frac{I}{\mu_{\mathrm{m}} \cdot \bar{E} \cdot A} = \frac{I \cdot d}{\mu_{\mathrm{m}} \cdot U \cdot A} \quad (\mathrm{C} \cdot \mathrm{m}^{-3}) \tag{8}$$

The magnitude of the Lorentz force acting on a charged particle in an electromagnetic field, consisting of the contributions of the electric $q \cdot \bar{E}$ and magnetic $q \cdot (\bar{v} \times \bar{B})$ fields, is as follows:

$$\bar{F} = q \cdot \bar{E} + q \cdot (\bar{v} \times \bar{B}) \ (\mathrm{N}) \tag{9}$$

wherein q is the electric charge of the particle in the electromagnetic field (C); $\bar{v}$ is the instantaneous velocity of the particle ($\mathrm{m \cdot s^{-1}}$); and $\bar{B}$ is the magnetic field (T).

While neglecting the contribution of the magnetic field, and after dividing both sides of the equation by the volume value, the resulting equation for calculating a magnitude of the force per one volume unit is as follows:

$$\bar{f} = \rho_Q \cdot \bar{E} \quad (\mathrm{N} \cdot \mathrm{m}^{-3}) \tag{10}$$

The resulting electrohydrodynamic force is then calculated using the following equation:

$$\bar{F}_{\mathrm{EHD}} = \int_V \bar{f} \, dV = \int_0^d \rho_Q \cdot \bar{E} \cdot A \, dx = \int_0^d \frac{I \cdot d \cdot U \cdot A}{\mu_{\mathrm{m}} \cdot U \cdot A \cdot d} \, dx = \frac{I \cdot d}{\mu_{\mathrm{m}}} \quad (\mathrm{N}) \tag{11}$$

The Towsend's empirical equation indicates that the electric current flowing through the inter-electrode space is a function of the difference between electrode potentials:

$$I = \mathrm{C} \cdot U \cdot (U - U_0) \quad (\mathrm{A}) \tag{12}$$

wherein C is a constant determined by the electrode shape ($\mathrm{A \cdot V^{-1}}$); U is the voltage at a current I (V); and U_0 is the corona-starting voltage (V).

After substituting the relevant variables in the equation, the resulting equation for calculating the magnitude of the electrohydrodynamic force is as follows:

$$\bar{F}_{\mathrm{EHD}} = \frac{\mathrm{C} \cdot U \cdot (U - U_0) \cdot d}{\mu_{\mathrm{m}}} \quad (\mathrm{N}) \tag{13}$$

For each electrode set geometry (at a given inter-electrode distance), the C constant is typically determined through experiments. With an identical voltage above the critical voltage, an identical inter-electrode distance, and an identical diameter of the coronating electrodes, the value of electrical current flowing between them is proportional to their lengths.

As mentioned above, those charge carriers exhibit a drift and diffusion in the formed electrical field.

Mobility of electrons in the air is $\mu_{\mathrm{m(e^-)}} = 620 \cdot 10^{-4}\ \mathrm{m^2 \cdot V^{-1} \cdot s^{-1}}$, while mobility of $\mathrm{N_2^+}$ ions in the air is $\mu_{\mathrm{m(N_2^+)}} = 2.5 \cdot 10^{-4}\ \mathrm{m^2 \cdot V^{-1} \cdot s^{-1}}$.

The values of electrical mobility indicate that heavier nitrogen ions exhibit lower mobility than that of electrons; however, with a positive corona, they remain in the plasma zone surrounding the coronating electrode. When the corona is negative, and with an assumption that the electron drift is the key mechanism of propulsion, the resulting magnitude of the electrohydrodynamic force is as follows, provided that the electric current flowing between the electrodes is 1.5 mA:

$$\bar{F}_{\mathrm{EHD}(e^-)} = \frac{I \cdot d}{\mu_{\mathrm{m}}} = \frac{1.5 \cdot 10^{-3} \cdot 30 \cdot 10^{-3}}{620 \cdot 10^{-4}} = 7.258 \cdot 10^{-4}\ \mathrm{N} \tag{14}$$

Therefore, the force observed on the asymmetrical capacitor cannot be explained by the electron drift, not even with a negative corona.

Nevertheless, an ion mobility value is directly proportional to the magnitude of the electrohydrodynamic force, and thus the following equation applies when the $\mathrm{N_2^+}$ ion drift is taken into account:

$$\bar{F}_{\mathrm{EHD(N_2^+)}} = \frac{I \cdot d}{\mu_{\mathrm{m}}} = \frac{1.5 \cdot 10^{-3} \cdot 30 \cdot 10^{-3}}{2.5 \cdot 10^{-4}} = 0.180\ \mathrm{N} \tag{15}$$

The aforesaid statements clearly indicate that the notable propulsion effect in electrohydrodynamic propellers is attributable to an ion drift [4–8].

3. Test equipment design

The practical application of the Biefeld-Brown effect requires the use of a complex set of devices. It was necessary to design and construct a Greinacher voltage doubler, a two-stage Cockcroft-Walton voltage multiplier, as well as propulsors in multiple versions.

The high voltage power supply (HVPS) topologically represents a half-bridge circuit. The PWM TL494CN gate driver was used as an exciter; its fixed exciter frequency was 22 kHz and the duty cycles were changed within an interval of 2–15%. The output voltage pf the HVPS was regulated using a regulating autotransformer. comparators. The maximum output voltage of the HVPS was 15 kV_P.

However, the voltage required was much higher so the simplest solution was to engage voltage multipliers – a Greinacher voltage doubler and a two-stage Cockroft-Walton multiplier, both of which are intended to be immersed in electrical insulating oil. The maximum output voltage of the Greinacher voltage doubler, as indicated by its name, was 30 kV. The maximum output voltage of the Cockroft-Walton voltage multiplier was 60 kV. Since the formation of a corona discharge was the desired outcome, the electric current used amounted to fractions or units of mA. Consequently, the formation of waves and a decrease in the output voltage in both multipliers was neglected.

The value of breakdown electric current was modified using a net of resistors with a total resistance of 1MΩ.

The designed and constructed equipment for measuring the quantitative parameters of propulsion included a high-voltage DC voltmeter based on a voltage divider and a preparation facilitating the measurement of high-frequency HV and a DC milliampere meter. The measurement equipment is shown in Figure 1.

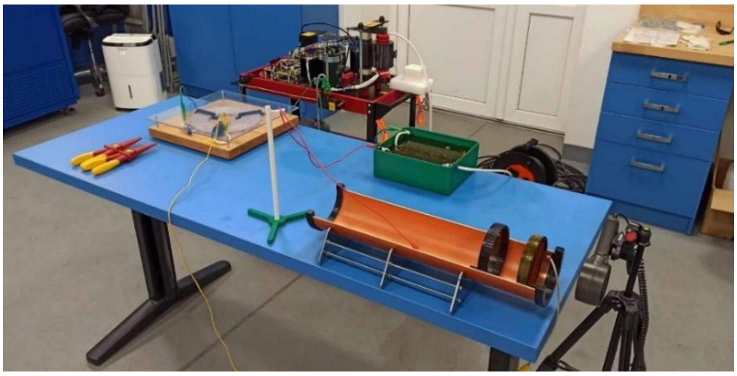

Figure 1. Measurement equipment with an EHD propeller.

Testing of the functionality of the prototypes was facilitated thanks to the designs of the devices – the effectors, which were constructed in two different designs variants (Figure 2). The variants were represented by the propellers that were fixedly attached and accelerated the flow of the medium.

The functionality of the individual versions of the medium accelerators, as well as their individual variants, was verified by gradually increasing the distance between the electrodes and simultaneously by proportionally increasing the inter-electrode potentials until the breakdown voltage was reached. The output velocity of the accelerated medium was identified using the UT363S propeller anemometer.

The first system tested was an emitter-collector system of the first Type with a corona electrode conductor diameter of 0.08 mm (w_{real1}, P_{real1}). Subsequently, the same system was tested with a corona electrode conductor diameter of 0.15 mm (w_{real2}, P_{real2}). Last, the Type 2 emitter-collector system was tested (w_{real3}, P_{real3}). The output velocities of the accelerated medium as well as their corresponding performances are shown in Figure 3.

Figure 2. Individual versions of the one-stage medium accelerators, wherein: (a) System of the emitter and the Type 1 collector; (b) System of the emitter and the Type 2 collector.

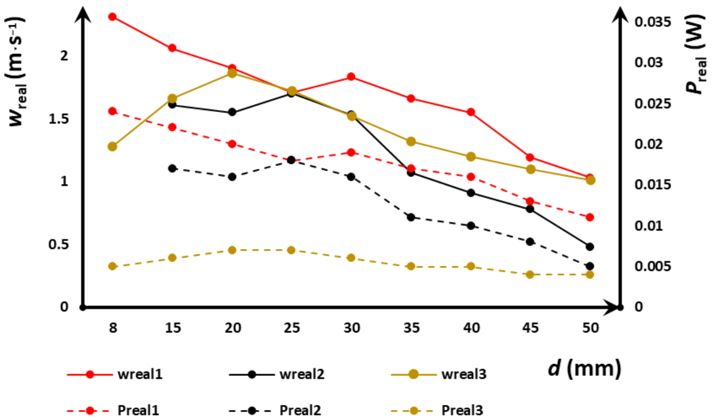

Figure 3. Graphical representation of the effect of the inter-electrode distance on the output velocity of the accelerated medium and the real performance values.

The dependence of the output medium velocity on the inter-electrode potential at a constant inter-electrode distance of 30 mm was investigated for emitter and Type 1 collector with a corona conductor diameter of 0.08 mm. The effect of the magnitude of the electric current flowing between the electrodes as a function of the inter-electrode potential was then investigated at an identical inter-electrode distance. The data are shown in Figure 4.

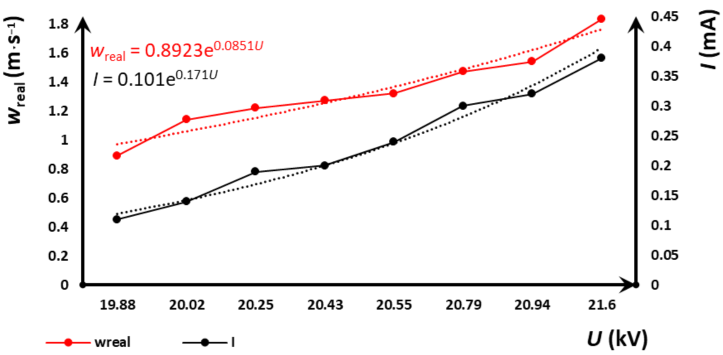

Figure 4. Graphical representation of the effect of the inter-electrode potential on the output velocity of the accelerated medium and the electric current.

4. Conclusions

The conducted experiments revealed a significant effect of the diameter of the emitter conductor in the asymmetric capacitor. As the diameter increased, the inter-electrode potential required for achieving a critical intensity of the surrounding electric field also increased. As a result, the corona discharge initiation voltage was shifted towards higher potentials.

The effective length of the electrodes proved to be a factor affecting the current flow between the emitter and the collector. As the effective length of the electrodes increased, the current density between the electrodes also increased.

The distance between the electrodes had two opposite effects on the output velocity of the accelerated medium. As the distance from the emitter increased, the gradient of the electric potential decreased. A decreasing intensity of the electric field represented a decrement in the magnitude of the force acting on the nearby located ions. An increase in the inter-electrode distance also caused that the volume of the polarisable air to increase, and that resulted in a higher velocity of the accelerated medium.

The experiment confirmed that an increase in the inter-electrode potential contributes to the intensification of the ionisation process. As a result, the number of electric charge carriers increased, which was manifested in an elevated current density between the plates of the asymmetric capacitor, and thus the output velocity of the accelerated medium exhibited an exponential increase.

The experimental measurements, performed with various arrangements of the electrodes, revealed that the most beneficial arrangement was the one with the emitter and the Type 1 collector with the 0.08 mm diameter of the emitter conductor. With this arrangement, in the case of a one-stage configuration and an inter-electrode distance of 8 mm, the maximum achieved velocity of the accelerated medium was 2.310 m·s-1. With the use of a coronating electrode conductor of the same diameter at an inter-electrode distance of 50 mm, the highest efficiency of 1.710% was achieved out of all the tested arrangements.

Acknowledgments: This paper was written with the financial support from the VEGA granting agency within the Project No. 1/0224/23 and with the financial support from the APVV granting agency within the Projects No. APVV-23-0266 and APVV-21-0274.

Conflicts of Interest: The authors declare no conflict of interest.

References

1. LEE, Bong Han. *Theoretical and Experimental Study of the Biefeld Brown Effect*. Online. Richmond: Eastern Kentucky University, 2015. Available at: https://encompass.eku.edu/cgi/viewcontent.cgi?article=1269&context=honors_theses. [cit. 2024-04-12].
2. BAHDER, Thomas and Christian FAZI. *Force on an Asymmetric Capacitor: by Thomas B. Bahder and Chris Fazi*. Adelphi: ARMY RESEARCH LABORATORY, 2003.
3. *ZÁKLADY FYZIKY PLAZMY*. In: MARTIŠOVITŠ, Viktor. Bratislava: COMENIUS UNIVERSITY, 2004.
4. Čurma, P., Lázár, M., Jasminská, N., Brestovič, T., Duda, F., & Milenovský, P. (2024). Electrohydrodynamic Propeller as One of the Alternatives to Replace Conventional Propulsion Systems. *Applied Sciences*, *14*(23), 10885. https://doi.org/10.3390/app142310885
5. TIRUMALA, Rakshit. *CORONA DISCHARGES IN ASYMMETRIC ELECTRIC FIELDS AND ITS IMPACT ON IONIC WIND GENERATION*. Online, Dissertation, Supervisor: Dr. David B. Go. Notre Dame: University of Notre Dame, 2013. Available at: https://curate.nd.edu/articles/thesis/Corona_Discharges_in_Asymmetric_Electric_Fields_and_its_Impact_on_Ionic_Wind_Generation/24831165. (cit. 2024-04-12).
6. SALIKIS, Dimitrios G.; MAVRANTZAS, Vlasis G. and PRATSINIS, Sotiris E. Dynamics of molecular collisions in air and its mean free path. Online. *Physics of Fluids*. 2023, Volume 35, Issue 9. ISSN 1070-6631. Available at: https://doi.org/10.1063/5.0166283. (cit. 2024-04-12).
7. SEGĽA, Štefan and HUŇADY, Róbert. *Dynamics*. V1. Košice: Technical University (Košice), 2022. ISBN 978-80-553-4312-9.
8. MONROLIN, Nicolas; PRAUD, Olivier and PLOURABOUÉ, Franck. Electrohydrodynamic ionic wind, force field, and ionic mobility in a positive dc wire-to-cylinders corona discharge in air. Online. *Physical Review Fluids*. 2018, Volume 3, Issue 6. ISSN 2469-990X. Available at: https://doi.org/10.1103/PhysRevFluids.3.063701. (cit. 2024-04-12).

Design of an experimental system for detecting permeability values of felt electrodes in redox batteries

Filip Dominik [1,*], Ján Slota [2], Marek Vrabeľ [1], Peter Ivančák [1]

[1] Prototyping and Inovation centre, Faculty of Mechanical Engineering Technical University of Kosice, Slovak republic; filip.dominik@tuke.sk; marek.vrabel@tuke.sk; peter.ivancak@tuke.sk
[2] Department of Technology, Materials and Computer Supported Production, Faculty of Mechanical Engineering, Technical University of Kosice, Slovak republic; jan.slota@tuke.sk
* Correspondence: filip.dominik@tuke.com

Abstract: The promising future of redox batteries comes with many hurdles to answer. One of them is the optimization of the redox flow battery system hydromechanically, where the first step is to experimentally determine the permeability values of the carbon felt electrodes. To obtain sufficient experimental values, the design a reliable device is necessary. In this paper, the process to obtain empirical permeability values of felt electrodes is reported.

Keywords: Felt electrode, vanadium redox flow battery, permeability, electrolyte,

1. Introduction

With the increasing emphasis on the generation of electricity from renewable sources, there is a growing need to store and use this energy efficiently and in a timely manner, ideally with the least environmental impact. In this context, redox flow batteries are coming to the fore as a more environmentally friendly alternative to the prevailing lithium batteries. Due to their nature, redox batteries are particularly suitable for static solutions such as electrification systems, large capacity backup power sources and similar applications [2].

Redox flow batteries represent a promising technology for energy storage, especially in renewable energy applications. One of the key elements of this technology is the carbon-felt electrodes through which the electrolyte flows and which also create the environment for electrochemical reactions. The permeability of the felt electrodes is an essential parameter affecting the efficiency and performance of the battery.

Permeability determines the flow rate at which electrolyte can flow through the felt electrode structure. This directly affects electrolyte distribution, electrochemical efficiency and operating losses. Too much permeability of the electrolyte through the felt means an inefficient electrochemical reaction, too little permeability means inefficient circulation of the electrolyte. Thus, in both cases, unoptimized parameters lead to reduced efficiency of the whole system.

Technical University of Košice, Pavol Jozef Šafárik University and Ino-Hub Energy are collaborating on the development of a redox battery. The battery has already successfully undergone primary development and a functional battery stack has been created. Due to the need to optimize the system, a test rig has been developed to measure the permeability of the felt electrodes and experimental measurements are currently being prepared. So far, an initial experiment has been performed with demineralized water at ambient temperature and a liquid medium temperature of 22.5°C.

Experimental detection of permeability is essential to accurately understand the interaction between the electrolyte and the structure of the felt electrodes. The results of the upcoming measurements will allow quantification of the Darcy permeability of the felts.

Subsequently, using flow analysis to simulate the pressure gradient under controlled fluid flow through the system, it will be possible to optimize the system parameters, predict the behavior of the system at different compression levels, different temperature conditions, and optimize both the compression and material of the electrodes.

The present paper deals with the description of the proposed test rig for compression measurement and the description of the planned experiments.

2. Planning the experiment

The device for measuring the permeability of nonwoven fabrics (felt electrodes) shall be resistant to acidic environments, including the electrolyte which are vanadium and sulfuric acid ($V + H_2SO_4$) used in the VRFB (Vanadium Redox Flow battery). The device allows accurate permeability values to be obtained directly from the media with which the felt electrodes will be in contact. Permeability values for felts can also be obtained using demineralized water, but the permeability itself may be affected by parameters that are not considered when calculating Darcy permeability values. These parameters are the absence of chemical reactions, surface tension and differential wettability. Therefore, the ability to withstand acidic environments provides the device with a significant advantage, allowing permeability values for different liquids to be compared, leading to more accurate results when using Flow Analysis.

Compression of the felt electrodes is desirable in terms of electrochemical properties, but undesirable due to hydrodynamic parameters. The data obtained will allow to find the optimum solution to achieve maximum performance with minimum load on the device. Thus, the experimental determination of the permeability of carbon felt electrodes becomes a key step for the optimization of electrolyte flow in redox batteries. The combination of measurements and computational flow analyses will allow the design of more efficient battery systems, which are essential for reliable and economical energy storage. This knowledge is also needed for further development and commercialization of this technology.

VRFB work on the basis of interactions between negolite and posolite, which have different densities in different oxidation states, hence there is also a change in the flow rate in the felt electrodes. The experiments are to investigate the permeability of the felt electrodes at different values of compression and temperature for several liquid media and for several types of felts from different manufacturers.

The working temperature of the VRFB is in the range of 20°-40°C, the optimum temperature is 35°C. Since there is no need to load the battery in the idle state (no power draw), the operating temperature can be close to ambient temperature. Increasing the temperature under load changes the viscosity of the liquid medium, which affects the flow through the felt.

Based on a study [1] which deals with the reduction of electrical resistance in felt electrodes in VRFB`s when they are compressed, measurements will be made in the compression range of 20-40%. The compression of the felt electrodes reduces the electrical resistance in the battery but deteriorates the permeability of the electrolyte, which is a negative consequence. [3][6] The aim is to find the most appropriate ratio of compression and electrical resistance.

The structure of nonwoven felt electrodes can vary from the technological processes used in their production. Four types of felt electrodes are in preparation from the manufacturers AvCarb and Thinkru.

3. Description of the device

The proposed device (Figure 1) for permeability testing of nonwoven felted fabrics consists of a liquid medium tank, a pump, a flow meter, two pressure sensors, a cuvette, power source and a heat exchanger. The pressure sensors are located in front and behind the cuvette and they scan the pressure differences during the experiment. The heat exchanger stabilizes the required fluid temperatures in the circuit.

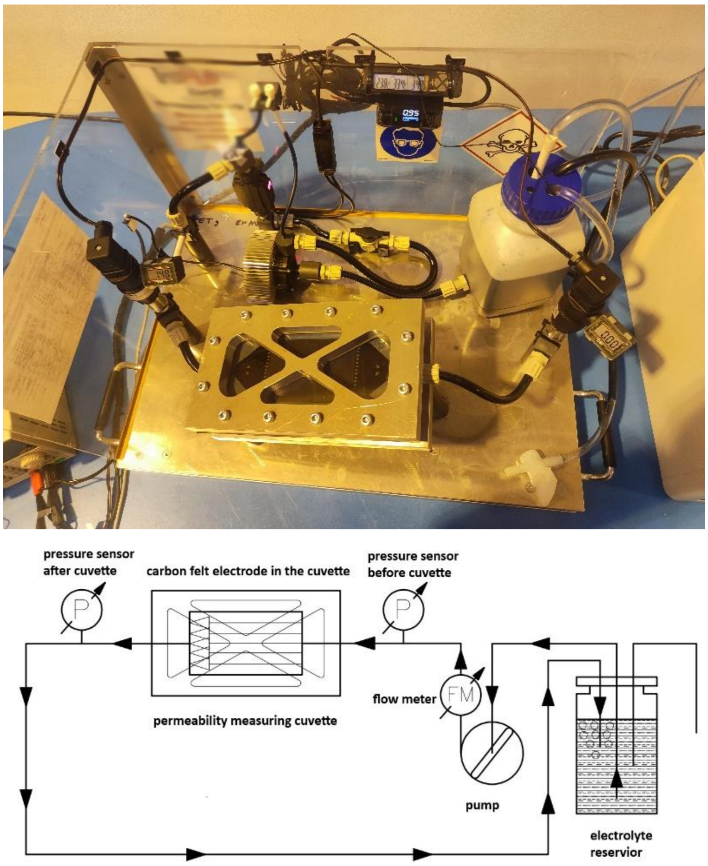

Figure 1. Experimental setup with piping and instrumentation diagram.

The design of the cuvette is shown in Figure 2. The cuvette forms the location in which the felted nonwoven fabric sample is placed and its shape modifies the flow of the liquid medium so that it is evenly distributed over the entire sample volume.

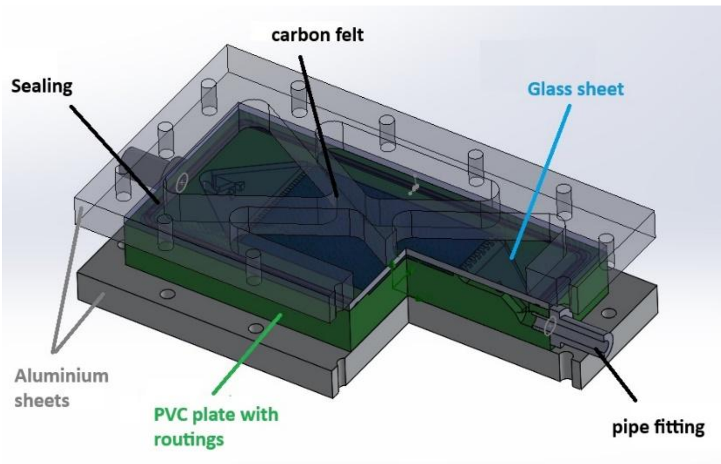

Figure 2. Design of the cuvette.

4. Description of the implementation of the experiments

A felt electrode is inserted into the cuvette, which is compressed to the desired compression value after the cuvette is assembled. A pump is used to inject liquid into the system, the flow rate of which is controlled by the speed of the pump. The flow and pressure values are recorded during the experiment. From the recorded values, a dependency for the given fluid, temperature, compression, felt type, system is obtained. A measurement called experiment zero was performed to calibrate the device. An example of the dependence obtained from experiment zero is shown in Figure 3.

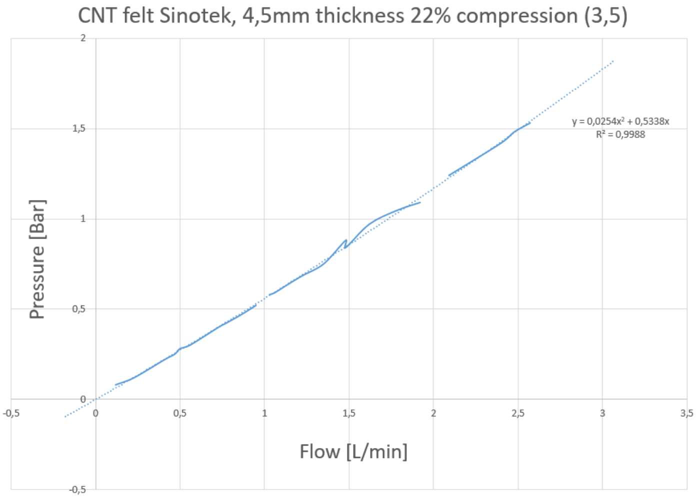

Figure 3. Experiment: zero (Pressure-flow graph at 22.5°C for Thinkru felt and 22% compression, liquid medium: water).

The obtained values are mathematically processed using regression functions to calculate the permeability value for a chosen felt and liquid medium. Figure 4 shows the spreadsheet editor environment implementing the calculation of the necessary values.

flow L/min	Flow m3/s	P before [Bar]	P behind[Bar]	ΔP [Pa]	reg. Poly2	reg.poly2 [Pa]	permeability [m2]
0,12	2,00004E-06	0,08		8000	0,0642864	6428,64	-1,27201E-10
0,23	3,83341E-06	0,12		12000	0,12393665	12393,665	-1,26461E-10
0,41	6,83347E-06	0,22	0	22000	0,22303385	22303,385	-1,25269E-10
0,47	7,83349E-06	0,25	0	25000	0,25647665	25647,665	-1,24876E-10
0,5	8,3335E-06	0,28	0	28000	0,273275	27327,5	-1,24681E-10
0,56	9,33352E-06	0,3	0	30000	0,3070256	30702,56	-1,24292E-10
0,73	1,21669E-05	0,4	0	40000	0,40376665	40376,665	-1,23203E-10
0,77	1,28336E-05	0,42	0	42000	0,42676865	42676,865	-1,2295E-10
0,865	1,4417E-05	0,47	0	47000	0,481763913	48176,39125	-1,22352E-10
0,95	1,58337E-05	0,52	0	52000	0,53140625	53140,625	-1,21822E-10
1	0,000016667			0	0,5608	56080	-1,21513E-10
1,03	1,7167E-05	0,58	0	58000	0,57850465	57850,465	-1,21328E-10
1,06	1,7667E-05	0,59	0	59000	0,5962606	59626,06	-1,21143E-10
1,145	1,90837E-05	0,64	0	64000	0,646847713	64684,77125	-1,20624E-10
1,225	2,04171E-05	0,685	0	68500	0,694835313	69483,53125	-1,20139E-10
1,35	2,25005E-05	0,75	0	75000	0,77054625	77054,625	-1,19389E-10
1,48	2,46672E-05	0,88	0	88000	0,8502304	85023,04	-1,18619E-10
1,48	2,46672E-05	0,84	0	84000	0,8502304	85023,04	-1,18619E-10
1,62	2,70005E-05	0,97	0	97000	0,9371214	93712,14	-1,17801E-10
1,78	2,96673E-05	1,05	0,005	104500	1,0377934	103779,34	-1,16879E-10
1,92	3,20006E-05	1,14	0,05	109000	1,1270784	112707,84	-1,16085E-10
2	0,000033334			0	1,1786	117860	-1,15636E-10
2,09	3,4834E-05	1,25	0,01	124000	1,23699785	123699,785	-1,15135E-10
2,4	4,00008E-05	1,43	0,01	142000	1,44168	144168	-1,13441E-10
2,475	4,12508E-05	1,49	0,01	148000	1,492022813	149202,2813	-1,13039E-10
2,57	4,28342E-05	1,54	0,01	153000	1,55625065	155625,065	-1,12534E-10
						AVERAGE=	-1,20193E-10

Figure 4. Calculation of permeability values of experiment: zero.

The regression functions use the modified Darcy equation to calculate the permeability. [4]

$$k = -\frac{Q\mu L}{A\Delta P} \tag{1}$$

- k: permeability value (m^2)
- Q: volumetric flow rate (m^3/s)
- μ: dynamic viscosity (Pa·s)
- L: flow length (m)
- A: cross-sectional area (m^2)
- ΔP: pressure difference (Pa)

5. Conclusions

Once a sufficient number of experimental values have been obtained, it is possible to establish a dependence of permeability and compression at different temperatures and for specific types of felt electrodes. From these values, the permeability value is calculated using the modified Darcy equation for fluid flow through porous media. These values can be inserted into a database of porous media in CFD (Computational Fluid Dynamics) programs to help analyze and uncover bottlenecks in the so far proposed battery geometry. The proposed process will help to optimize the prototype to the state of well performing product [5].

Acknowledgements: The article was written with the support of the projects APVV SKPL-23-0040 "Research on the possibilities of forming and joining of innovative metal-plastic composites in the manufacture of lightweight thin-walled structures" and VEGA 1/0539/23 "Research on hybrid sandwich structures with customized properties". The authors are also grateful for the support in the experimental work to the project KEGA 050TUKE-4/2023.

References

1. R. Banerjee, N. Bevilacqua, A. Mohseninia, B. Wiedemann, F. Wilhelm, J. Scholta, R. Zeis,Carbon felt electrodes for redox flow battery: Impact of compression on transport properties,Journal of Energy Storage,Volume 26,2019,100997,ISSN 2352-152X, https://doi.org/10.1016/j.est.2019.100997.
2. F.Dominik; J.Slota. Redoxné batérie: pohľad na cenovo dostupnú energiu budúcnosti, Transfer inovácií 2024, 50, Pages 53-56
3. Carbon felt AvCarb. Available online: https://www.avcarb.com/products/carbon-felt/
4. R. Banerjee, N. Bevilacqua, L. Eifert, R. Zeis, Characterization of carbon felt electrodes for vanadium redox flow batteries – A pore network modeling approach, Journal of Energy Storage, Volume 21,2019, Pages 163-171,ISSN 2352-152X, https://doi.org/10.1016/j.est.2018.11.014.
5. S Bortolin, P Toninelli, D Maggiolo, M Guarnieri and D Del Col; CFD study on electrolyte distribution in redox flow batteries; Journal of Physics: Conference Series, Volume 655; S Bortolin et al 2015 J. Phys.: Conf. Ser. 655 012049; DOI 10.1088/1742-6596/655/1/012049
6. Kyeongmin Oh, Seongyeon Won, Hyunchul Ju, Numerical study of the effects of carbon felt electrode compression in all-vanadium redox flow batteries, Electrochimica Acta, Volume 181, 2015, Pages 13-23, ISSN 0013-4686, https://doi.org/10.1016/j.electacta.2015.02.212.

Safety in archives - archival box fire with emphasis on their flammability and smoke density

Adriana Dowbysz [1,*], Bożena Kukfisz [2] and Mariola Samsonowicz [1]

[1] Department of Chemistry, Biology and Biotechnology, Bialystok University of Technology, Wiejska 45A Street, 15-351 Bialystok, Poland; m.samsonowicz@pb.edu.pl
[2] Institute of Safety Engineering, Fire University, Slowackiego Street 52/54, 01-629 Warsaw, Poland; bkukfisz@apoz.edu.pl
* Correspondence: adriana.dowbysz@pb.edu.pl

Abstract: The fire safety of paper archive collections is extremely important in terms of the value they hold. Despite the use of advanced methods to detect and extinguish fires in their early stages, their occurrence still poses a threat to collections. An important element of their storage is the packaging in which they are contained. The aim of this study is to evaluate four types of cardboards in terms of their flammability and smoke emission based on their Limiting Oxygen Index (LOI), total heat of combustion (Q_{PCS}) and smoke density (Ds). Results revealed that LOI values of cardboards are slightly higher than for standard cardboards, which suggests their lower flammability. Similar findings were obtained for the Q_{PCS} values, which were 30 % lower for studied cardboards comparing to traditional cardboard. Smoke density tests revealed that when the ignition of cardboards take place, the maximum values of smoke density ($D_{s\,max}$) are significantly lower comparing to flameless decomposition.

Keywords: fire safety; archives; cardboard; flammability; smoke density

1. Introduction

Ensuring the safety of collections in the event of building disasters is one of the issues facing archives around the world. Although one of the more common problems is dampness and flooding of collections, ensuring fire safety also remains an issue that requires constant monitoring.

One of the greatest fires with enormous losses was a post-fire of the National Personnel Records Center in 1973 in Overland, Missouri. The fire destroyed ca. 16-18 million of military personnel records [1]. Another case of a post-fire whose effects are still being repaired and remedied is the Fire at the Cracow City Archives in 2021 in Poland. The fire destroyed 20 00 running meters of documents [2].

Both paper and cardboard boxes in which important archival documents are stored must meet a number of requirements contained in ISO 9706:1994 Information and documentation - Paper for documents - Requirements for permanence [3] or ISO 16245:2023 Information and documentation - Boxes, file covers and other enclosures, made from cellulosic materials, for storage of paper and parchment documents [4]. These standards describe requirements such as pH, alkaline reserve, oxidation resistance or tear resistance.

The aim of this study is to analyze the flammability and smoke emission of cardboards used for storage of archival documents in terms of their Limiting Oxygen Index (LOI), gross heat of combustion (Q_{PCS}) and smoke density (D_s), in order to assess their fire safety.

2. Materials and Methods

Four cardboards for the storage of archival documents were studied in terms of their flammability and smoke emission.

LOI, defined as a minimum oxygen concentration, in the mixture of oxygen and nitrogen, at which the combustion of material is merely sustained [5], was defined with the use of oxygen index apparatus (Fire Testing Technology, East Grinstead, UK) (Fig. 1).

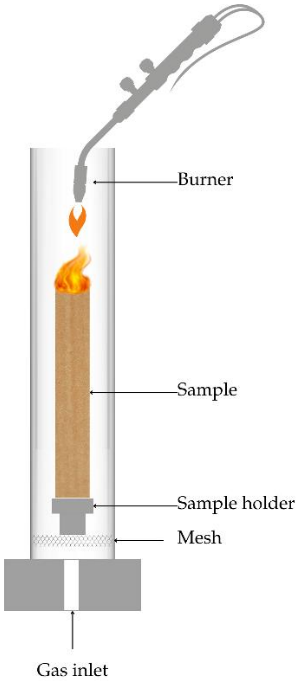

Figure 1. Scheme of a LOI apparatus. Source: own studies based on [6].

A total heat of combustion per unit mass (Q_{PCS}) was measured with the use of oxygen bomb calorimeter (PRECYZJA-BIT, Bydgoszcz, Poland) (Fig. 2). Specimens were combusted in air atmosphere at a pressure of 2 MPa.

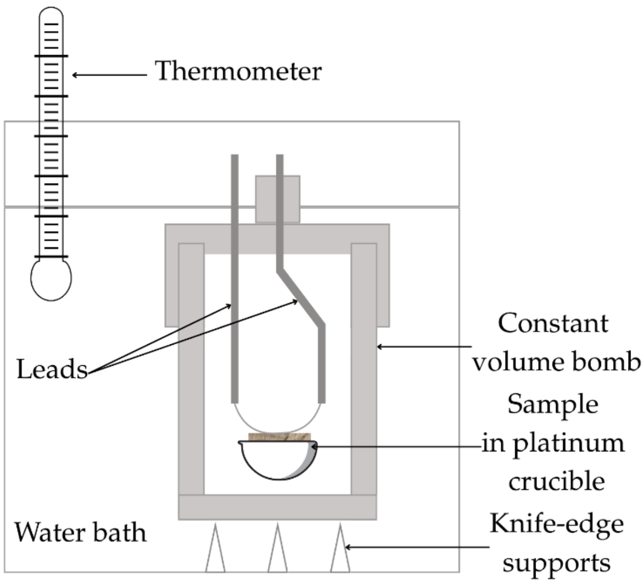

Figure 2. Scheme of an oxygen bomb calorimeter. Source: own studies based on [7].

Smoke density (D_s), measured by the attenuation of the light beam [8], was assessed in the smoke density chamber (Sychta Laboratorium, Police, Poland) (Fig. 3). The measurements were performed under 25 kW/m^2 heat flux with and without a pilot flame.

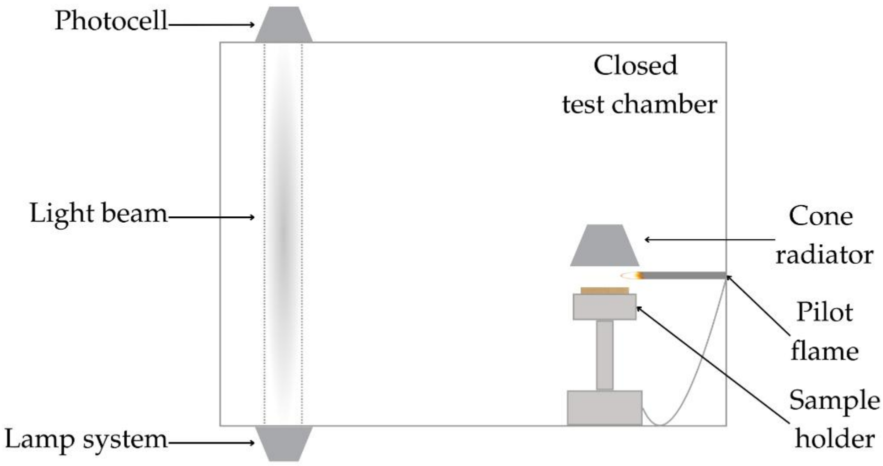

Figure 3. Scheme of a smoke density chamber. Source: own studies based on [9].

3. Results and discussion

3.1. Flammability

The LOI and Q_{PCS} values of cardboards are presented in Table 1.

Table 1. LOI and Q_{PCS} values of studied cardboards.

Cardboard	LOI [V/V %]	Q_{PCS} [J/g]
1	22.4	13.642
2	22.8	13.848
3	23.8	13.238
4	23.6	14.163

All studied cardboards exhibit LOI higher than 21 V/V %, which allows to classify them as self-extinguishing materials. The LOI values are found in the range of 22.4 V/V % - 23.8 V/V %, and the differences between the values for individual cardboards are insignificant. The highest LOI value, and therefore the lowest flammability, provides cardboard 3. The LOI values obtained are a few percent higher than for standard cellulose paper (approx. 19 V/V %) [10,11], indicating the possibility of creating safer conditions in the event of a fire.

As with the LOI results, the cartons differ slightly in their total heat of combustion values. The lowest Q_{PCS} value of 13.238 J/g was obtained for cardboard 3. The Q_{PCS} values obtained for the studied cardboards are approximately 30% lower than for the standard cartons (18.48 J/g) [12], which also indicates their greater fire safety.

3.2. Smoke density

The D_s changes at a heat flux of 25 kW/m^2 for the measurement without and with a pilot flame are presented in Figures 4 and 5, respectively.

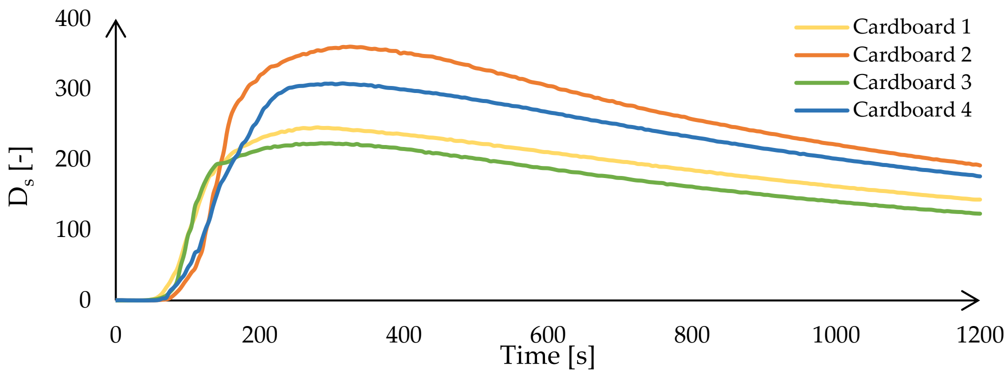

Figure 4. Changes of the specific optical density of smoke D_s in time at the heat flux of 25 kW/m^2 without a pilot flame.

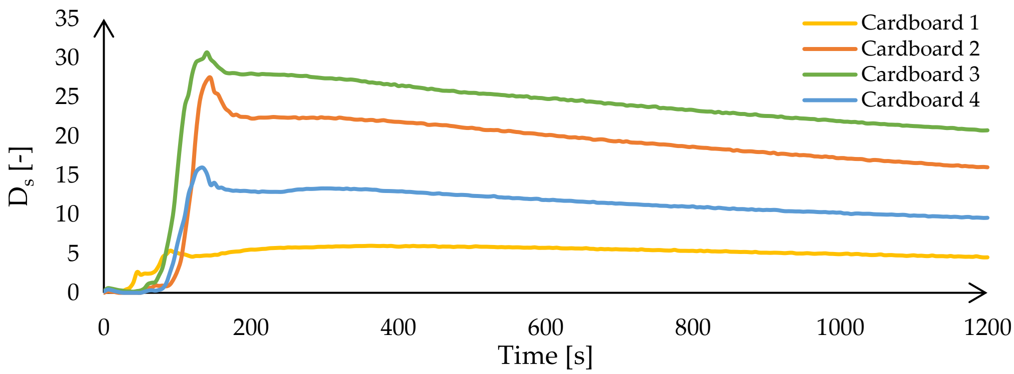

Figure 5. Changes of the specific optical density of smoke D_s in time at the heat flux of 25 kW/m^2 with a pilot flame.

Although the differences between the LOI and Q_{PCS} values for the tested cardboards were not significant, much larger differences were observed for changes in D_s values. The highest smoke emission was observed for cardboard 2 (when measured without pilot flame) (Fig. 4) and for carton 3 (when measured with pilot flame) (Fig. 5).

Table 2. Smoke parameters of studied cardboards.

Pilot flame	**Without**			**With**			
Cardboard	**$D_{s\,(4)}$**	**$D_{s\,max}$**	**VOF4**	**Time to ignition [s]**	**$D_{s\,(4)}$**	**$D_{s\,max}$**	**VOF4**
1	241.57	245.75	495.14	45	5.75	6.00	15.86
2	342.61	360.38	553.54	56	22.39	27.45	49.88
3	220.08	223.26	470.23	53	27.84	30.71	68.32
4	304.62	308.21	473.43	50	12.88	15.95	31.68

The obtained smoke parameters are presented in Table 2. The $D_{s\,(4)}$ values, which stand for the D_s value at the 4th minute of measurement, are very important in terms of evacuation. The lowest values were obtained for cardboards 1 and 3, when measured without pilot flame. The VOF4 is area under D_s curve during the first 4 minutes of measurement was the lowest for cardboard 3. The obtained results suggest that cardboard 3 exhibits the greatest fire safety when flame combustion does not take place.

For the measurement with a pilot flame all materials undergo ignition, which changed the smoke emission process. The ignition occurred the earliest for the cardboard 1. As can be seem from the results, the faster the studied material ignited, the lower the smoke emission and the lower the values of $D_{s\,(4)}$, $D_{s\,max}$ and VOF4 were observed. The safest cardboard when the flaming combustion takes place is the cardboard 1.

4. Conclusions

Results revealed that LOI values of cardboards are slightly higher than for traditional cardboards, which suggests their lower flammability. The highest LOI was obtained for cardboard 3 (23.8 V/V %), which has the lowest flammability among other studied materials.

Similar findings were obtained for the Q_{PCS} values, which were ca. 30 % lower for studied cardboards comparing to traditional ones. Again, cardboard 3 exhibited the highest fire safety level. The Q_{PCS} for that cardboard was 13.238 J/g.

Smoke density tests revealed that when the ignition of cardboards take place, the smoke density is significantly lower comparing to flameless decomposition. Cardboard 3, which was assessed as exhibiting the greatest fire safety, emitted the lowest amount of smoke. However, when the flaming combustion took place, it obtained the highest smoke density parameters. The obtained results suggest that studied cardboards exhibit greater fire safety level comparing to traditionally used cardboard. Hovewer, other methods for improving fare safety in archives, including fire protection systems, should be still applied.

Acknowledgments: This research was funded by a research subvention provided by the Ministry of Education and Science (Poland), grant number WI/WB-IIŚ/8/2022.

Conflicts of Interest: The authors declare no conflict of interest. The funders had no role in the design of the study; in the collection, analyses, or interpretation of data; in the writing of the manuscript, or in the decision to publish the results.

References

1. Stender, W.; Walker, E. The National Personnel Records Center Fire: A Study in Disaster. *The American Archivist* **1974**, *37*.
2. Ciepły, H. Pożar Archiwum Urzędu Miasta Krakowa 2021.
3. *ISO 9706 Information and Documentation - Paper for Documents - Requirements for Permanence*; **1994**.
4. *ISO 16245 Information and Documentation - Boxes, File Covers and Other Enclo-Sures, Made from Cellulosic Materials, for Storage of Paper and Parchment Documents*; **2023**.
5. Dowbysz, A.; Kukfisz, B.; Siuta, D.; Samsonowicz, M.; Maranda, A.; Kiciński, W.; Wróblewski, W. Analysis of the Flammability and the Mechanical and Electrostatic Discharge Properties of Selected Personal Protective Equipment Used in Oxygen-Enriched Atmosphere in a State of Epidemic Emergency. *International Journal of Environmental Research and Public Health* **2022**, *19*, doi:10.3390/ijerph191811453.
6. Hull, T.R. Challenges in Fire Testing: Reaction to Fire Tests and Assessment of Fire Toxicity. In *Advances in Fire Retardant Materials*; Horrocks, A.R., Price, D., Eds.; Woodhead Publishing, 2008; pp. 255–290 ISBN 978-1-84569-262-9.
7. Thermochemistry. In *Practical Chemical Thermodynamics for Geoscientists*; Fegley, B., Ed.; Academic Press: Boston, 2013; pp. 127–172 ISBN 978-0-12-251100-4.
8. Dowbysz, A.M.; Samsonowicz, M. Smoke Generation Parameters from the Cone Calorimeter Method and Single-Chamber Test. *Environmental Sciences Proceedings* **2021**, *9*, doi:10.3390/environsciproc2021009022.
9. McKenna, S.T.; Hull, T.R. The Fire Toxicity of Polyurethane Foams. *Fire Science Reviews* **2016**, *5*, 3, doi:10.1186/s40038-016-0012-3.
10. Wu, T.; Gu, Y.; Zhao, D.; Jiang, G.; Wang, T.; Shen, Y. A Multifunctional Cellulose Paper with Excellent Flame Retardancy, Hydrophobicity and Oil/Water-Separation Performance via Reaction with Ammonium Phytate and Poly(Methylhydrosiloxane). *Polym Degrad Stab* **2024**, *223*, 110738, doi:10.1016/j.polymdegradstab.2024.110738.
11. Szubert, Z.; Mazela, B.; Tomkowiak, K.; Grześkowiak, W. Fire Properties of Paper Sheets Made of Cellulose Fibers Treated with Various Retardants. *Materials* **2024**, *17*, doi:10.3390/ma17133074.
12. Michael Ioelovich Comparison of Methods for Calculation of Combustion Heat of Biopolymers. *Am Journal Sci Eng Techn* **2017**, *1*, 63–67, doi:10.11648/j.ajset.20160102.18.

TECHNICAL UNIVERSITY OF KOŠICE
Faculty of Mechanical Engineering

3D Printing of Silicate Materials and their Advanced Application: A Review

Erika Dubňanská [1,*], Martina Hančinová [1], Barbara Schürger [1] and Róbert Huňady [2]

[1] Department of Applied Mechanics and Mechanical Engineering, Faculty of Mechanical Engineering, Technical University of Košice, Letná 1/9, 042 00 Košice-Sever, Slovakia; erika.dubnanska@tuke.sk; martina.hancinova@tuke.sk; barbara.schurger@tuke.sk
[2] Department of Robotics, Faculty of Mechanical Engineering, VSB - Technical University of Ostrava, 17. listopadu 2172/15, 708 00 Ostrava - Poruba, Czech Republic; robert.hunady@vsb.cz
* Correspondence: erika.dubnanska@tuke.sk

Abstract: The innovative technology of 3D printing of silicate materials, i.e. ceramic clay, concrete mixtures, etc., has been becoming more significant in recent years due to its application in civil engineering, mechanical engineering and general materials engineering. Therefore, there is considerable development interest in this field of additive technologies. Several different techniques and approaches to 3D printing of silicate materials are currently being developed. This article provides a concise overview of silicate materials suitable for 3D printing, focusing on paste silicate-based materials. The paper also discusses the 3D printing technology for paste materials, highlighting the challenges and opportunities associated with material properties and printability. Furthermore, it introduces the advanced applications of 3D-printed silicate materials in fields such as construction, art and design, with an emphasis on their potential for sustainability and innovative construction practices.

Keywords: 3D printing; silicate materials; ceramic clay; concrete

1. Introduction

Additive manufacturing (AM), also generally known as 3D printing is a technology that enables the realization of products by selectively depositing material in successive layers, applying each layer in predefined coordinates. This technology, which emerged in the 1980s, has been widely adopted by various industries for the production of prototypes and specialised products that cannot be efficiently produced by traditional manufacturing methods or are not economically feasible by conventional processes [1,2].

The layer-by-layer approach in AM offers significant advantages, including design flexibility, material efficiency, and sustainability. Due to these benefits as well as advancements in printing technologies and materials, various techniques and approaches for 3D printing are currently being developed, also in the field of silicates [1].

The study by Chen Z. et al. (2019) summarized the advances in 3D printing of ceramics and provided a historical overview of the related techniques [3]. Ricciotti L. et al, 2023, in their study investigated the 3D printing of geopolymers in terms of manufacturing process, printing needs, mixture formulation and material properties [4]. Witte's book (2022) summarizes the knowledge of 3D clay printing, its applications in construction, and the advantages of this technology in the manufacturing of bricks and other construction products [1]. Wolfs et al. (2018) investigated early age mechanical behavior of 3D printed concrete, comparing numerically obtained results with experiment [5]. Chan S. S. L. et al. (2020) in their research explored the relationships between the volume fraction of solids in clay paste inks, their rheological properties, and appropriate printing parameters [6].

In the processing of silicate materials such as ceramic clay and concrete, additive manufacturing (AM) is employed to achieve the desired shape. The layer-based process significantly influences the material's final properties. Following the printing phase, the material undergoes additional stages, such as drying and firing, as the printed object remains in a green state. These post-processing steps induce shrinkage, which can alter the material's characteristics. Therefore, precise control over these processes is essential to maintain the integrity and performance of the final product [1].

2. Silicate materials used in 3D printing

Silicate materials are substances that contain silicate minerals, which are naturally occurring compounds composed of silicon (Si) and oxygen (O), often with other elements such as aluminum (Al), magnesium (Mg), calcium (Ca), sodium (Na), potassium (K), and iron (Fe). Silicates are the most abundant minerals on Earth and form a significant part of the Earth's crust. These materials can be natural or synthetic and are widely used in various industries, such as construction, ceramics, glass manufacturing, electronics, aerospace and medicine [7,8].

Silicate materials used in 3D printing include:

- **Cementitious materials and concrete**

Concrete, as well as wood and steel, is one of the most widely used construction materials. Reactive powder concrete (RPC) is a kind of high performance and high strength concrete mixture. It is composed of very fine powders, such as cement, quartz powder, fine sand, silica fume and fly ash, along with a high-efficiency superplasticizer, and is devoid of coarse aggregates [2,9].

The application of 3D printing technology in concrete construction significantly improves the architectural design of both the interior and exterior, while reducing the overall cost of construction and improving the process of construction from months to a few days [2,9].

- **Ceramic materials**

In general terms, ceramics encompass a wide range of materials that are classified between polymers and metals. They consist of a combination of metallic and non-metallic elements, primarily oxides, silicates and other mineral compounds. Ceramic materials include clay, which is categorized as a silicate ceramic [1,8].

The specific properties of ceramic materials depend on their chemical composition and microstructure. Therefore, these materials can exhibit high heat resistance, favored long term durability, high mechanical strength, and the ability to fluidize, which makes them adoptable to various desired shapes prior to setting and hardening. Due to its properties, it is also used in the manufacturing of medical implants, artificial bones and teeth, prosthetics, electrical conductors and insulators, and various craft components [2,8].

- **Soil-based materials**

Soil-based materials are among the most sustainable and environmentally friendly construction alternatives. Soil has been used as one of the oldest construction materials for thousands of years, and many buildings made of soil have been preserved. It is most used in the construction of adobe structures, low-cost houses or repair of degraded soil structures [2].

3. 3D printing technology

The additive manufacturing of silicate-based materials has seen substantial progress and increasing utilization over the past decades. Although a wide range of AM technologies are available, following specific methods are particularly suitable for silicate materials:

- Binder Jetting;
- Powder Bed Fusion;
- Material Extrusion (ME) [1,2].

Each of these technologies has the potential to create free-formed objects, but they all have different advantages, disadvantages, and areas of application. In the case of Binder Jetting, this technology uses a powder-based material and a liquid binder, which acts as an adhesive between layers. The Selective Laser Sintering (SLS) technology from the Powder Bed Fusion category uses a laser to sinter powder into a single three-dimensional shape. After each section is fused, the powder bed is lowered by one layer thickness and a new layer is applied on top and the process is repeated until the object is completed [1,10].

For 3D printing of clay-based materials such as ceramic clay and concrete, material extrusion technology is the most suitable. The process of this additive technology works on a similar principle to the known method of Fused Filament Fabrication (FFF), except that the paste material is extruded at room temperature and solidified during printing by evaporation of water or other solvents. In the Figure 1 can be seen a schematic of the material extrusion technology [1,11].

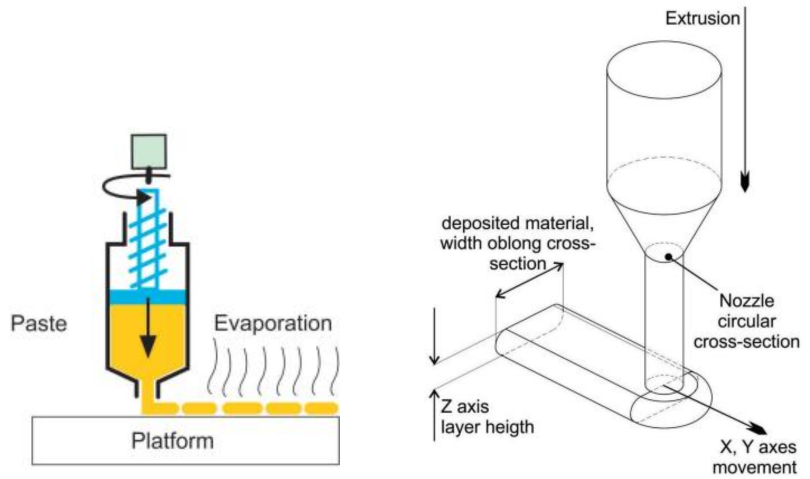

Figure 1. Schematic of material extrusion [11].

The fundamental principle of 3D printing via material extrusion involves the precise deposition of a material in its plastic state through a nozzle onto a platform, whereby the path and extrusion are controlled by an initial G-code. The material is extruded through the die of the nozzle with a circular or rectangular cross-section, and when deposited, it adopts an oblong cross-section. The height of the layer is influenced by several factors such as the viscosity of the material, the extrusion speed, the speed of the nozzle movement and the width of the extruded line. Figure 2 shows schematics of the 3D printing configuration of the paste material [1,2,11,12].

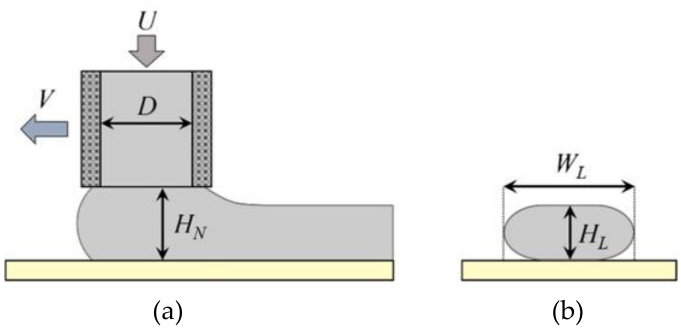

Figure 2. Schematics of the 3D printing configuration of the paste material: (a) Side view: nozzle height H_N, diameter D, extrusion volumetric flux U, and printing speed V; (b) Front view: middle layer height H_L and layer width W_L [12].

The main requirements for 3D printing of clay-based materials include accuracy, speed, the ability to print free-form designs, and the capability to produce dense structures with high surface quality. Additionally, factors such as rheological properties, layer stability, interlayer adhesion, and controlled drying behavior are crucial for ensuring printability. The material must retain its shape after extrusion while allowing for precise deposition of complex geometries [1,13].

Even application of the material is key to achieving the desired strength and consistency of the printed object. In the case of 3D printing with materials such as concrete or ceramic clay, it is also important to control the properties of the material itself, such as its rheological behaviour, to ensure good adhesion between layers. Figure 3 is a close-up of the concrete filament during printing [1,2,7,11].

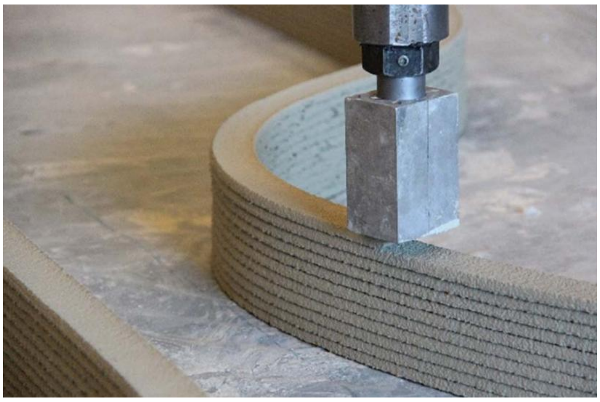

Figure 3. Close-up of concrete filament during printing [5].

Providing a well-optimised material mixture is essential to the success of the printing process. This means ensuring appropriate rheological properties as well as green and hardened strength. A determining role in the rheology and properties of the suspension is also determined by the amount of water. The suspension should solidify and be prevented from flowing smoothly after passing through the nozzle of the 3D printer. Therefore, water should be added so that the slurry is neither too fluid nor too thick. The clay-based material for 3D printing should exhibit easy extrudability, smooth flow, good buildability, mechanical strength, and appropriate setting time to ensure continuous paste flow from the nozzle and facilitate rapid freeform construction [2,7,9,13].

This technology allows the creation of complex geometric shapes without the necessity of moulds, and therefore the process requires precise control of extrusion speed, layer adhesion and geometric accuracy to ensure the structural integrity and dimensional stability of the printed object [1,5,7].

Despite significant advancements in this field, the technology still faces numerous technical challenges, including printing process defects and improper material mixture. These issues can lead to problems such as excessive pressure in the print head, nozzle clogging, or filament tearing. Additionally, factors such as air inclusions in the material, asymmetric drying, loss of stability (elastic buckling, plastic collapse), and poor interlayer adhesion can affect the quality of the printed object. Some printing defects are shown in the Figure 4 [1,5,7].

(a) (b) (c)

Figure 4. Visible 3D printing defects: (a) filament tearing; (b) elastic buckling; (c) plastic collapse [1,14].

4. Advanced applications of 3D printed structures

Since 1986, when C. Hull developed the first 3D printer using stereolithography (SLA), 3D printing technology has rapidly expanded into many industries including manufacturing, bioengineering, aerospace, automotive, art, food and confectionery design, fashion, architecture and construction [2].

3D printing of silicate materials, ceramic clay, and concrete is also utilised in these industries and adapted to their specific needs:

- **Civil Engineering and Architecture**

Research into 3D printing of concrete has advanced significantly in recent years, opening new possibilities for the construction industry. Given that the construction sector is responsible for approximately 40% of global natural resource consumption, innovations in material efficiency and sustainability are crucial. 3D concrete printing offers a promising solution by reducing material waste, lowering labor costs, and enabling the rapid construction of complex and customized structures. Figure 5 shows the first 3D-printed house in basic components and the assembled on the site and the first structure printed in-situ [1,12].

(a) (b)

Figure 5. 3D printed buildings: (a) The first 3D-printed house in basic components and the assembled on the site by WinSun Co. (Shanghai, China, 2014); (b) First structure printed in-situ and printing progress [15,16].

- **Art and Design**

3D printing is used to create unique artistic sculptures, design elements, and architectural features with complex geometries that would be challenging to achieve using traditional methods. Designers utilize this technology for decorative panels, interior components, lighting fixtures, furniture, vases, flowerpots and tiles (Figure 6). This technology opens new possibilities for personalization, sustainable design, and the fusion of traditional craftsmanship with advanced manufacturing techniques [6,13].

Figure 6. 3D-printed decorative features: (a) gargoyle, a common feature in medieval architecture; (b) modern brick featuring waves on exterior side; (c) flowerpot [6,13].

- **Other fields**

3D printing of silicate materials has wide applications in various other fields. In electrical engineering, ceramic materials are applied in the production of insulators, sensors and electronic components. It is also used in the manufacture of refractory and chemical resistant components for industry. It is also possible to produce components such as bench, acoustic damping wall element and other construction structures (Figure 7) [9].

(a) (b) (c)

Figure 7. Concrete components manufactured by 3D printing: (a) Wonder bench; (b) acoustic damping wall element; (c) curved-layered construction component [9].

5. Conclusions

3D printing of silicate materials, particularly cementitious materials and clay-based ceramics, shows tremendous potential in revolutionizing the construction, design, and manufacturing sectors. Despite significant advancements, challenges persist, such as the impact of moisture, material density, curing dynamics, crack formation, adhesion issues, and loss of shape stability in printed layers. These problems highlight the need for continued research and optimization in material properties to ensure successful implementation in real-world applications. As Ma et al. [9] have noted, achieving the ideal balance of extrusion ability, setting time, fluidity, and mechanical strength in cementitious materials remains a complex challenge that requires a deep understanding of material science and engineering.

While there are several additive manufacturing technologies available, only specific methods are suitable for clay-based ceramics and concrete, and a comprehensive understanding of the relationship between the printing process and the final properties of the printed product is still under development.

On the other hand, the use of cement-based mixtures for 3D printing has gained more attention, likely due to their extensive application in modern architecture. Additionally, clay-based materials provide significant environmental benefits, and their increased use could promote more sustainable construction practices.

As research progresses, 3D printing with silicate materials has great potential for further development and overcoming existing challenges, with associated advances in material properties and printing techniques.

Acknowledgments: This work was supported by the Slovak Research and Development Agency under the grant project VEGA No. 1/0516/22.

Conflicts of Interest: The authors declare no conflict of interest.

References

1. de Witte, D. *Clay Printing: The Fourth Generation Brickwork*; Springer: Wiesbaden, Germany, 2022; 1–230.
2. Ahmed, G.H. A review of "3D concrete printing": Materials and process characterization, economic considerations and environmental sustainability. *Journal of Building Engineering* **2023**, *66*, 1–32.
3. Chen, Z.; et al. 3D Printing of Ceramics: A Review. *Journal of the European Ceramic Society* **2019**, *39*, 661–687.
4. Ricciotti, L.; et al. Geopolymer Materials for Extrusion-Based 3D-Printing: A Review. *Polymers* **2023**, *15(24)*, 4688.
5. Wolfs, R.J.M.; Bos, F.P.; Salet, T.A.M. Early age mechanical behaviour of 3D printed concrete: Numerical modelling and experimental testing. *Cement and Concrete Research* **2018**, 106, 103–116.
6. Chan, S.S.L.; et al. 3D printing of clay for decorative architectural applications: Effect of solids volume fraction on rheology and printability. *Additive Manufacturing* **2020**, *35*, 101335.
7. Zhao, Q.; et al. Advances and application potential in the research of silicate mineral-based 3D printing materials. *Progress in Materials Science* **2025**.
8. Carter, C.B; Norton, M.G. *Ceramic Materials Science and Engineering*, 2nd ed.; Springer: New York, USA, 2013; 1–766.
9. Ma, G.W.; Wang, L.; Ju Y. State-of-the-art of 3D printing technology of cementitious material—An emerging technique for construction. *Science China Technological Sciences* **2018**, *61*, 475–495.
10. HP. Available online: https://www.hp.com/us-en/printers/3d-printers/learning-center/3d-printing-process.html?utm_source=chatgpt.com#section=binder-jetting (accessed on 05.12.2024).
11. Ruscitti, A.; Tapia, C.; Rendtorff, N. M. A review on additive manufacturing of ceramic materials based on extrusion processes of clay pastes. *Cerâmica* **2021**, *66*, 354–366.
12. Comminal, R.; et al. Modelling of 3D concrete printing based on computational fluid dynamics. *Cement and Concrete Research* **2020**, *138*, 106256.
13. Gyawali, B.; et al. A review on 3D printing with clay and sawdust/natural fibers: Printability, rheology, properties, and applications. *Results in Engineering* **2024**, *24*, 103024.
14. Vantyghem, G.; Ooms, T.; de Corte, W. VoxelPrint: A Grasshopper plug-in for voxel-based numerical simulation of concrete printing. *Automation in Construction*, **2021**, *122*, 103469.
15. Hager, I.; Golonka, A.; Putanowicz, R. 3D printing of buildings and building components as the future of sustainable construction?. *Procedia Engineering* **2016**, *151*, 292–299.
16. Total Kustom – 3D Concrete Printers. Available online: https://www.totalkustom.com/ (accessed on 06.12.2024).

TECHNICAL UNIVERSITY OF KOŠICE
Faculty of Mechanical Engineering

Evaluation of 3D Scans Generated by Artec Eva and Revopoint Miraco Scanners for Healthcare Applications

Katarína Dudová [1,*], Lucia Bednarčíková[1] and Jozef Živčák [1]

[1] Technical University of Košice, Faculty of Mechanical Engineering, Department of Biomedical Engineering and Measurement, Letná 1/9, 04200, Košice, Slovakia
* Correspondence: katarina.dudova@tuke.sk

Abstract: Burn injuries represent a significant medical challenge due to their severe physical and psychological consequences. Accurate assessment and monitoring of burn wounds are crucial for effective treatment and rehabilitation. This study evaluates the potential of 3D scanning technology in burn injury management by comparing two devices: the high-end Artec Eva and the more affordable Revopoint Miraco 5. The study assessed key parameters, including accuracy, resolution, ease of use, and cost-effectiveness. Results indicate that while Artec Eva provides higher precision, Revopoint Miraco 5 offers a practical, budget-friendly alternative with sufficient accuracy for clinical applications. These findings highlight the potential of 3D scanning to improve wound evaluation, enhance treatment planning, and facilitate patient care.

Keywords: Artec Eva 1; Revopoint Miraco 5 2; burn injuries 3; 3D scanners 4

1. Introduction

Burn injuries represent a critical area of medical research due to their high incidence, complexity, and potential for long-term disability. Each year, millions of people worldwide suffer from burn-related trauma, with severe cases requiring extensive medical intervention, including surgery, rehabilitation, and psychological support. The accurate evaluation of burn severity and healing progress is essential for optimizing patient outcomes, yet traditional assessment methods—such as ruler-based measurements and 2D photography—often lack precision and consistency, leading to variability in clinical decision-making. [1-3]

Recent technological advancements have introduced 3D scanning as a promising tool for medical imaging, allowing for more accurate and reproducible measurements of wound surface area, volume, and topography. Studies have demonstrated the potential of 3D imaging in various medical applications, including burn depth assessment, customized medical device production, and surgical planning. For example, 3D scanning has been employed to improve the accuracy of scar evaluation and assist in the development of patient-specific compression garments for burn rehabilitation. Furthermore, previous research highlights the importance of objective, quantitative methods in burn assessment to reduce inter-observer variability and enhance treatment planning.

Despite the benefits, the adoption of 3D scanning in clinical practice is often limited by cost and accessibility. High-end scanners, such as the Artec Eva, provide superior accuracy but may not be feasible for smaller clinics or resource-limited settings. More affordable alternatives, such as the Revopoint Miraco 5, offer potential solutions but require further evaluation to determine their effectiveness in burn wound analysis.

The objective of this study is to compare the performance of two 3D scanning devices—the high-end Artec Eva and the budget-friendly Revopoint Miraco 5—specifically for burn injury assessment. The research aims to evaluate the accuracy, usability, and cost-effectiveness of these devices to determine whether affordable 3D scanning solutions can meet the needs of clinical and therapeutic applications. [4-6]

2. Materials and Methods

Through 3D scanning, it is possible to create precise digital models of burned areas and monitor the dynamics of their healing over time. This technology enables objective evaluation of the effectiveness of various therapeutic methods and contributes to optimizing the care of patients with severe burn injuries.

This article focuses on comparing two 3D scanners from different price categories: the Artec Eva and the Revopoint Miraco 5. The Artec Eva is a high-end scanner used in a wide range of fields, from medical applications to design and industrial manufacturing. It operates on the principle of structured light and requires connection to a laptop or computer for operation. Its main advantage is the ability to scan detailed objects, including their surface textures. However, its primary drawback is its high cost. [7,8]

The Revopoint Miraco 5 belongs to the category of low-cost scanners. It uses blue light technology, which is non-flickering and therefore suitable for use with patients who have conditions such as epilepsy. Unlike the Artec Eva, this scanner does not require any additional devices during scanning, as it is equipped with a touch screen. The scanned model can be edited immediately after scanning. Similar to the Artec Eva, the Revopoint Miraco 5 is capable of distinguishing colors and surface reliefs. [9]

The aim of this article is to compare the quality of surface structures in scans of burned tissue, emphasizing the potential for using more affordable devices in medical applications. This comparison seeks to evaluate whether accessible technologies can meet the requirements of clinical and therapeutic practices.

2.2 Study Design

The study focused on comparing scans of a patient with grade IIa-b burns covering 17% of the total body surface area (TBSA). The burns were caused by the patient being scalded with boiling water in the areas of the face, neck, torso, and upper limbs. The scanning process took place over 6 weeks from November 5th to December 12th. Both scanners were employed to capture the wound surface, and the acquired 3D models were processed in their respective software platforms (Artec Studio and Revopoint's Revo Scan). The wound's surface area was computed and compared to the ground truth measured.

Scans performed on the same patients and at the same time will be compared to evaluate the performance of the two scanners. The scanning process with both devices was performed on the same day and under the same conditions, including the patient's position, the burned area being scanned, and the intensity of the room lighting.

2.3 Evaluation Criteria

- Accuracy: Comparison of scanned surface area.
- Resolution: Assessment of fine details captured by each scanner.
- Ease of Use: Evaluation based on time required for scanning, software processing, and operator feedback.
- Cost-effectiveness: Comparison of device cost relative to performance.

3. Results

3.1 Accuracy and Resolution

The Artec Eva tends to produce scans with distorted or less accurate colors, which can make precise color-based analysis challenging (Figure 1). In contrast, the Revopoint Miraco generates scans with colors that closely match the real-world appearance of the object (Figure 2). This makes it particularly advantageous when comparing scans based on color differences, such as distinguishing the boundaries between burned and healthy tissue. The more accurate color representation provided by Revopoint Miraco ensures that such contrasts are clearer and more visible, enhancing the precision of evaluations.

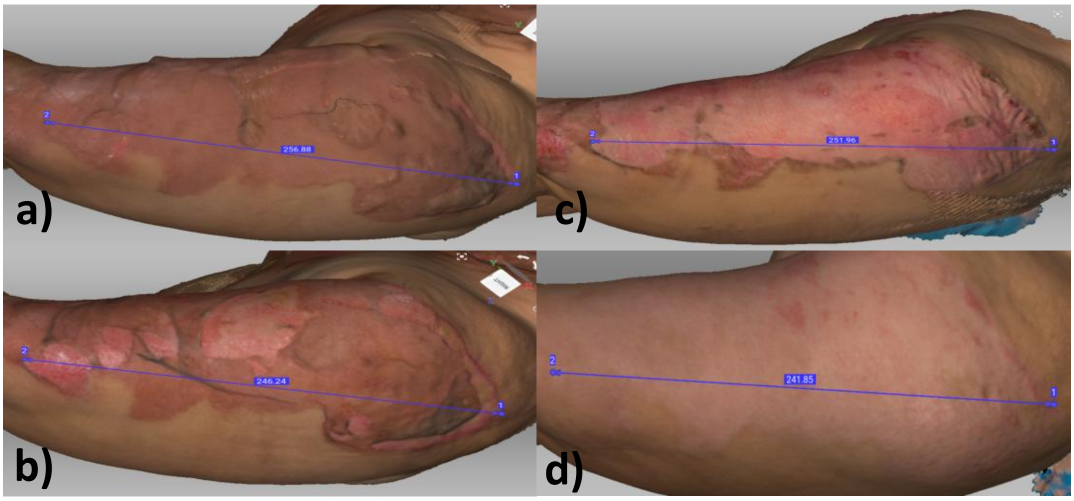

Figure 1. Scans produced by Artec Eva, a) first day of monitoring the burned area (5.11.2024), b) follow-up monitoring three days after the first scan (8.11.2024), c) scan of the burned area after one week (15.11.2024), d) scan form last checkup, one month after injury (12.12.2024).

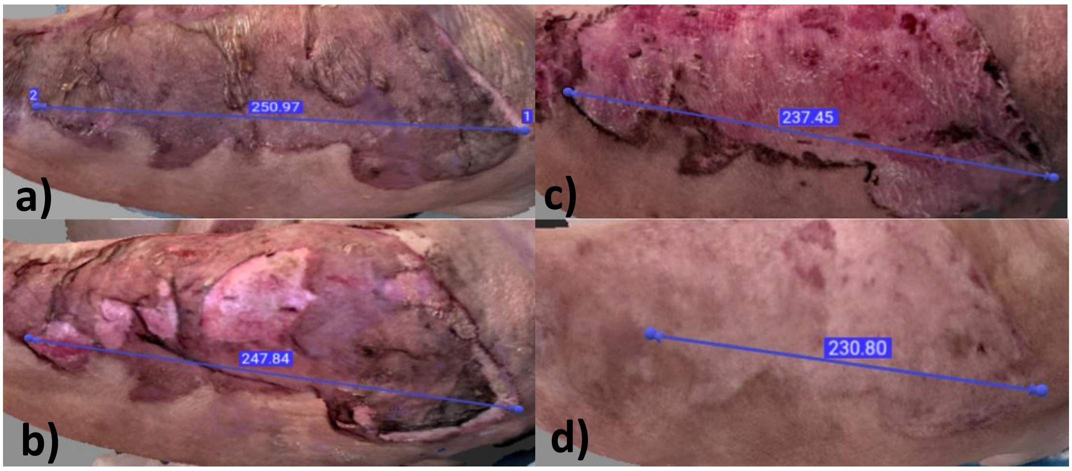

Figure 2. Scans produced by Revopoint Miraco 5, a) first day of monitoring the burned area (5.11.2024), b) follow-up monitoring three days after first scan (8.11.2024), c) scan of the burned are after one week (15.11.2024), d) scan form last checkup, one month after injury (12.12.2024).

To address the question of monitoring the healing process, we decided to measure the distance between two selected points on the edges of the burn area on the arm. The distance of these points was determined for each scan, depending on the visibility of the burn boundary (see Table 1). However, these values are only approximate, as it was not possible to ensure the same positioning during each scan due to the patient's discomfort. The average size change on the scans for the Revopoint Miraco was 6.73 mm, and for the Artec Eva, it was 5.01 mm.

Table 1. Measured distance between two selected points on the edges of the burn area.

Day	Scanner	Distance
5.11.2024	Artec Eva	256,88 mm
	Revopoint Miraco	250,99 mm
8.11.2024	Artec Eva	246,24 mm
	Revopoint Miraco	247,84 mm
15.11.2024	Artec Eva	251,96 mm
	Revopoint Miraco	237,45 mm
12.12.2024	Artec Eva	241,85 mm
	Revopoint Miraco	230,80 mm

3.2 Ease of Use

The Revopoint Miraco provides a more user-friendly scanning experience due to its all-in-one design, which eliminates the need for external devices. It includes a built-in touchscreen, enabling users to directly view the scanned object in real-time. In contrast, the Artec Eva requires monitoring the scan on a separate computer or laptop, which can complicate the process, especially for larger surfaces. Scanning with the Artec Eva often necessitates a second person to adjust or reposition the table with the laptop, and its cable-dependent setup restricts movement, making it less practical.

Additionally, the Artec Eva operates using a flashing light system, which is not suitable for scanning patients with epilepsy. On the other hand, the Revopoint Miraco uses infrared structured light technology, which is less intrusive and safer for sensitive applications, including scanning individuals.

In summary, the Revopoint Miraco is designed for simplicity and portability, offering a seamless scanning experience with fewer dependencies. In contrast, the Artec Eva, while powerful, involves a more complex setup that may hinder its ease of use in certain scenarios.

3.3 Cost-effectiveness

The Artec Eva is significantly more expensive, with a price exceeding 10 000 €, while the Revopoint Miraco is available for under 1 500 €. The performance gap, while noticeable, may not justify the higher cost for some applications, especially in budget-constrained settings. [4–6]

4. Discussion

The results highlight the trade-offs between the two devices. The Artec Eva's precision and advanced software capabilities make it ideal for applications requiring high accuracy, such as surgical planning or complex wound assessments. Conversely, the Revopoint Miraco offers an accessible option for scenarios prioritizing portability and affordability, albeit with a compromise in resolution and accuracy. When selecting a scanner for burn wound assessment, clinicians should consider the specific requirements of their practice. For high-volume clinical settings or research institutions, the investment in Artec Eva may be justified. For fieldwork or smaller clinics, the Revopoint Miraco provides a practical alternative.

Dimensional differences between individual scans can be significantly influenced by the positioning of the scanned body part. In the present study, the focus was on the left shoulder, however, it was not possible to ensure identical arm height or the angle between the arm and the examination table during each scan, as the patient experienced discomfort and pain in certain positions. While discomfort and pain tend to decrease during the healing process, future studies should aim to examine and compare multiple scans of different burn severity levels and various body parts. For more precise comparisons, it would be beneficial to focus on areas such as the torso or lower limbs, where consistent positioning can be maintained during each follow-up scan.

5. Conclusions

The integration of 3D scanning in burn wound assessment offers significant advantages, including enhanced accuracy in wound measurement, improved tracking of healing progress, and better patient care. The study confirms that while high-end scanners like Artec Eva provide superior precision, more affordable devices such as Revopoint Miraco 5 can deliver clinically relevant results at a fraction of the cost. Future research should further explore these technologies in diverse clinical settings to optimize their application in burn treatment and rehabilitation.

Acknowledgments: This research was supported by national project APVV-22-0340- Development and testing of orthoses to support burn treatment using 3D scanning and additive manufacturing, granted by the Cultural and Education Grant Agency of the Slovak Ministry of Education

References

1. Furferi Rocco, et al. A computational method for the investigation of burn scars topology based on 3D optical scan. *Computers in Biology and Medicine*; 2022; pp 149.
2. Edgar Dale, et al. Volume measurement using the Polhemus FastSCAN 3D laser scanning: a novel application for burns clinical research. *Journal of burn care & research*; 2008; vol. 29.6; pp 994-1000.
3. Ahmad Fozi, et al. Development of 3D-printed customized facial padding for burn patients. *Rapid Prototyping Journal*; 2019; vol. 25.1; pp 55-61.
4. Sheng WB, Dong G, Wan Y, et al. Application of three-dimensional technology in assessment of burn area and treatment strategy of burns. *Zhonghua Shao Shang za zhi = Zhonghua Shaoshang Zazhi = Chinese Journal of Burns;* 2014 Aug; pp 350-355.
5. Farrar E, Pujji O, Jeffery S. Three-dimensional wound mapping software compared to expert opinion in determining wound area. *Burns: Journal of the International Society for Burn Injuries*; 2017 Dec; 43(8)pp 1736-1741. DOI: 10.1016/j.burns.2017.05.015.
6. Parvizi D, Giretzlehner M, Wurzer P, et al. BurnCase 3D software validation study: Burn size measurement accuracy and inter-rater reliability. *Burns: Journal of the International Society for Burn Injuries;* 2016 Mar; 42(2) pp 329-335. DOI: 10.1016/j.burns.2016.01.008.
7. Sivanandan J, Liscio E. Assessing Structured Light 3D Scanning using Artec Eva for Injury Documentation during Autopsy. *J Assoc Crime Scene Reconstr; 2016*; vol. 21; pp 5-13.
8. Kisch Tobias, et al. Smart scar care—Industry 4.0 in individualized compression garments: A randomized controlled crossover feasibility study. *Plastic and Reconstructive Surgery–Global Open;* 2021, pp 9-7.
9. Rufino, Sabrina Santos. *A digitalização corporal integrada no design de ortóteses*. 2024. PhD Thesis.

TECHNICAL UNIVERSITY OF KOŠICE
Faculty of Mechanical Engineering

Increasing of data processing security of container terminal model

Pavol Dzurňák [1,*], Martin Mantič [2] and Lukáš Berko [3]

[1] Faculty of Mechanical Engineering, Technical university of Košice, Slovakia; dzurnak@tuke.sk
[2] Faculty of Mechanical Engineering, Technical university of Košice, Slovakia; martin.mantic@tuke.sk
[3] Faculty of Electrical Engineering and Informatics, Technical University of Košice, Slovakia; lukas.berko@student.tuke.sk
* Correspondence: dzurnak@tuke.sk; Tel.: +421 55 602 7654

Abstract: This paper discusses monitoring Azure cloud infrastructure using an ELK stack (Elasticsearch, Logstash, and Kibana). It describes the steps from setting up each component, creating a pipeline, modifying the index template and its lifecycle, creating visualization elements for individual logs and metrics, along with the problems we encountered and the process for solving them. All processed data are statistical data from a control system of container terminal model. To optimize overhead crane operations, data will be stored and analyzed on the Microsoft Azure cloud platform. This data will enable the evaluation of crane control efficiency. To ensure the reliability of the derived insights, robust data security measures must be implemented. The output of the work is a comprehensive system for monitoring Azure infrastructure.

Keywords: Azure, ELK Stack, monitoring, overhead crane, metrics

1. Introduction

The container terminal model is used for verification of different types of bridge crane control, data collection from sensors, detection of container distribution and methods of automated container loading and unloading system. The model of container terminal is shown in figure 1. Statistical data such as the loading and unloading equipment speed, the number of container transshipments, the detection of the number of containers of the given carrier, etc. are sent to the database in the Azure cloud for processing. Similarly, cloud services are already a common part of the operation of IT systems today, mainly due to economic efficiency. In order to be able to use the benefits of operating a database in the cloud, it is necessary to solve the issue of data processing security, which in our case includes quick detection of network intrusions, infrastructure monitoring is very important, regardless of whether it is an on-premises or cloud solution. In today's fast-evolving world, systems and services are complex, which increases their vulnerabilities. Continuous monitoring is essential to identify and mitigate these vulnerabilities. Furthermore, the use of monitoring systems leads to greater security and stability.

Azure cloud services natively generate a wide range of metrics and logs, including those related to authorization, authentication, archiving, and diagnostics [1]. These metrics and logs are a valuable source of information that give the administrator visibility into the infrastructure and services. Due to the sheer number of logs generated, analyzing them in their original form is opaque and tedious. It is therefore necessary to further process, filter and visualise the logs using appropriate types of graphs or tables.

Figure 1. The model of container terminal.

2. Available Monitoring Tools

2.1. Azure Monitor

Azure itself offers the Azure Monitor tool to monitor its services. It's a comprehensive solution that consists of various tools, thanks to which, one can maximize the performance and availability of operated services and also identify issues related to them [2]. This tool aggregates logs and metrics using other tools, which are Log Analytics and Application Insight. User can then use a further range of different tools to gain insight into operated services, visualise the data, analyse it, or respond directly to it with automated elasticity or admin alerts.

2.2. ELK Stack

In addition to the built-in tool, external tools can be used to monitor the Azure platform, with Elasticsearch being one of the most popular part of the ELK stack, what is an open-source platform that combines Elasticsearch (for search and analytics), Logstash (for data collection and processing), and Kibana (for visualization). It is commonly used to centralize, search, and analyze large volumes of log data, making it easier to monitor systems and troubleshoot issues in real time. Despite the built-in Azure tool called Azure Monitor, having its own uses and functionalities, there are several advantages to using Elasticsearch over Azure Monitor. Some of the biggest advantages include the need for a central system to aggregate multiple data from multiple cloud platforms and systems, a preference for on premise solutions, or better administrator expertise in Elasticsearch, which ultimately will make the work faster and efficient. Additionally, Elasticsearch's open architecture and multitude of features allows for extensible integration with other systems. This extensibility allows organizations to meet specific needs, improve adaptability and scalability in complex environments.

When using the ELK stack to monitor Azure, the ELK stack provides all the necessary tools for sending, storing, processing, and displaying data. There are two types of data shippers that can be used to send/ingest data. The first type is the lightweight data shippers, which are also referred in the Elasticsearch's world as Beats [3]. Examples of these Beats tools include Filebeat, Metricbeat, Packetbeat and so on. The second type of data shippers includes Logstash, which can additionally persize, transform, or filter data. When ingressing data from Azure, Filebeat and Logstash can be used. Both of these tools have a module for Azure [4], in which user just need to define an Event Hub and an API key (Application Programming Interface). The Event Hub serves as a central point to receive events from Azure services. The main difference between the two is that Logstash is more advanced and can transform and enrich data in real-time before sending. Filebeat, on the other hand, is more efficient and faster and sends high-throughput data to Elasticsearch.

Lastly, Kibana is a key component of the ELK stack, serving as an front-end of Elasticsearch. With its intuitive and nice interface it allows to easily create dashboards, different types of charts, tables and other visualizations. Besides, Kibana has various powerful analytical tools to analyze [5] data. And it also allows to create alerts or lets run machine learning algorithm over the data.

3. Monitoring Ecosystem deployment

Because of the many outweighing benefits, we decided to use an ELK stack to monitor Azure. The following subsections will cover the individual installation and configuration steps of the entire monitoring process. In this ecosystem, we will use Event Hub as the log ingestion service, which will act as the entry point for logs and metrics collected from various services and sources. Diagram in figure 2 depicts components that make up the Azure monitoring ecosystem.

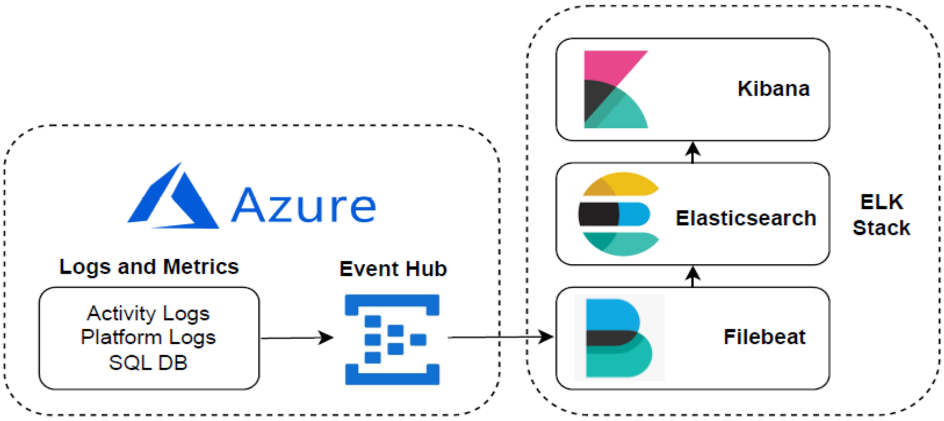

Figure 2. The Azure monitoring ecosystem.

Filebeat will function as the data shipper, forwarding data from Event Hub to Elasticsearch in real time. Elasticsearch will serve as the storage layer, indexing the incoming data from Filebeat. Kibana will be used as the graphical user interface, allowing users to interact with the data. Within Kibana, we will create customized dashboards with various visualizations to provide detailed insights.

3.1. Elasticsearch and Kibana

In our case, we deployed Elasticsearch and Kibana in premise environment instead of in the Azure cloud. The whole installation and configuration process was straightforward, consisting of adding the Elastic repository to the APT packaging system (Advanced Package Tool), along with the GPG key (GNU Privacy Guard), which is essential, for authentication and package integrity. We used Advanced Package Tool (APT) package system to install both Elasticsearch and Kibana. After the installation we set up the username and password for authentication Kibana to Elasticsearch in the configuration file kibana.yaml. Next important step was to secure communication between Kibana and user by configuring Transport Layer Security (TLS) certificate for Kibana. This step was essential to ensure confidentiality of the logs.

Based on our requirements, we deployed a single-node Elasticsearch cluster, which provides sufficient scalability and performance to meet our operational needs.

An alternative way would be to run Elasticsearch directly in Azure. Azure in it's marketplace offers to create an Elasticsearch cluster as a new resource with just a few clicks. Onecan just fill in the required parameters and Azure will create the entire cluster for use. In this case, there is also an option to set up automatic sending of Azure activity and resource logs to Elasticsearch.

3.2. Log shipping

First of all, we needed to create a Namespace in Azure Even Hub that acts as a management container for Event Hubs [6]. In this Even Hub Namespace we created 2 Event Hubs, insightsmetrics-pt1m for collecting metrics and insights-logs-sqlsecurityauditevents for receiving security logs from SQL databases. This was followed by setting access rights using Shared Access Signature, creating an access policy to ingest logs.

As a log shipper, Filebeat was sufficient for our purposes, since we don't need to enrich and transform the logs. In the filebeat.yaml we defined Elasticsearch output with IP of our Elasticsearch node and credentials. Then we enabled Azure module and insude it's configuration file azure.yml, which is in folder modules.d, we set variables for each log section.

3.3. Elasticsearch pipeline

After configuring and running Filebeat, it automatically created a Data Stream named 'filebeat-8.12.0', which included filebeat version in naming convention. This is the default behavior. However, One such configuration that required adjustment was the Index Lifecycle Management (ILM) policy also named 'filebeat' which applies to all indices created by tool Filebeat. Because filebeat created the ILM policy with the default settings, which rotates indices after 30 days or when the index exceeds size 50 GB. And this policy does not include deletion of old indices. This can cause problems later, which can lead to storage filling up over time and degraded system performance. To avoid these problems, we modified ILM policy to automatically delete indices which are older than 60 days.

For easier access, visualization, and querying of the data, we created a Data View called 'azure' for the 'filebeat-*' data stream. The field '@timestamp' was used as the timestamp. This Data View will be utilized for filtering documents and creating visualizations within dashboards.

3.4. Kibana Dashboards

We created 3 dashboards. One for showing authentications via Entra ID, one for SQL audit logs and one for logs and metrics from FileShare. For the authentication-focused dashboard, we created several analytical views of authentication within our Azure infrastructure. The first view is a geographic map that shows successful and failed login attempts based on geolocation. With this map, unusual logins from unusual locations can be quickly identified. Another component is histograms that summarize user logins and also what applications they logged in through, this histogram is shown in figure. 3.

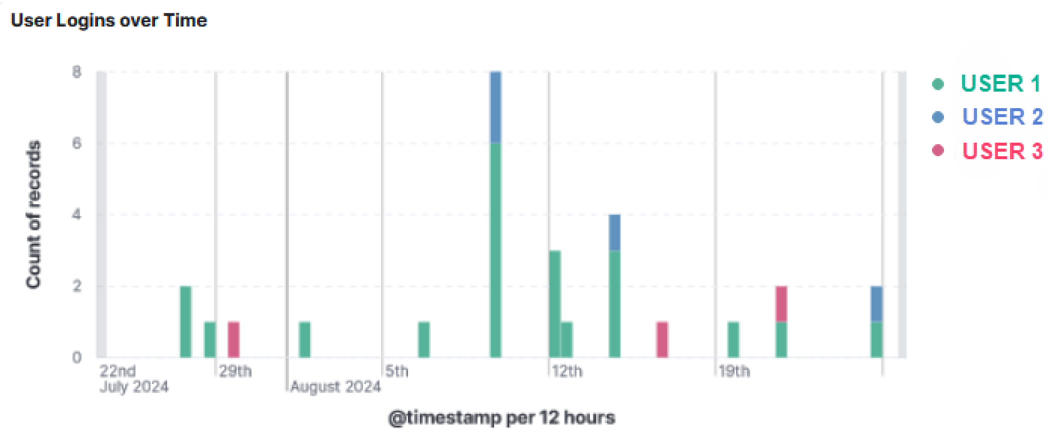

Figure 3. Histogram of users logins.

Azure surprised us with the amount of logged information. It logs for example the name and version of the operating system, user agent, a description of the authentication result, not just that it was successful or unsuccessful. We included all this infromation in the graphs. The types of operating systems used by users to log in and their user agents are shown in figure 4.

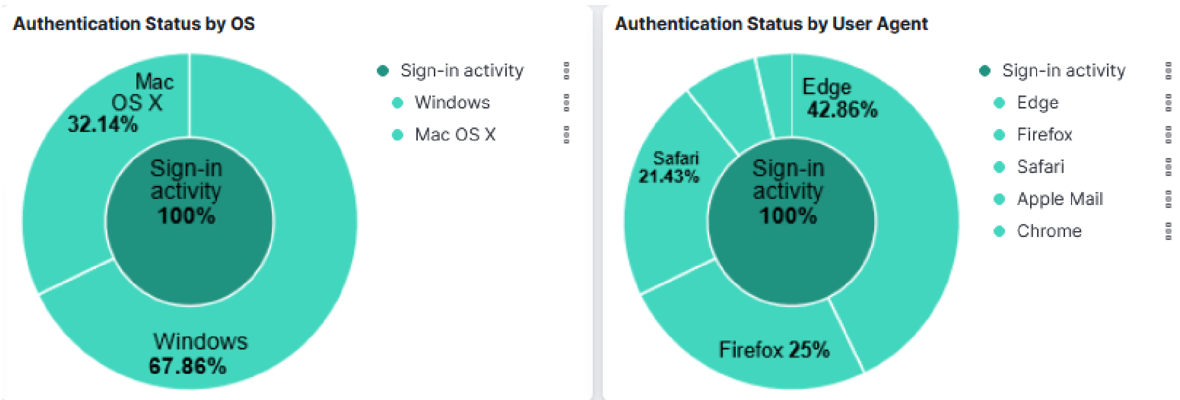

Figure 4. Operating system and browser used by users.

The next dashboard was created to monitor SQL logs from azure databases. During the creating of this dashboard we encountered a significant challenges, which are described below.

Azure stores a lot of important logging information related to SQL in a JSON format, which is processed by Filebeat into a single property field named 'azure.activitylogs.properties', with a flattened data type according to its standard template, as confirmed by the official [8] documentation. The problem is that we can't search within this field, so we needed to break this field into other subfields. One option is to create a runtime array for this field. While this approach is sufficient and functional, on the other hand it is computationally intensive as evidenced by performance analyses [9] [10]. Therefore, we decided to modify the mapping in the template.

In the field mapping for the Filebeat-8.12.0 index template, we changed the data type of 'azure.activitylogs.properties' to 'Object'. The subfields within this object were dynamically mapped to their correct data types. However, this introduced another issue with the mapping of the 'azure.activitylogs.properties.location' field, despite it having been manually mapped correctly in the index template. But still, this field doesn't have much meaning for us since it is the location where the private IP is located, so we decided to delete it. We achieved this by creating a remove location fields pipeline, which we set as the default pipeline for the filebeat-8.12.0 index template.

By doing this, we have achieved that the JSON in the flattened array is dynamically mapped to the individual subarrays that we can further work with. With this method we can view sql queries with the number of rows affected, the applications used within the sql queries, the actions performed and their status, whether they were performed successfully or not, also the username and IP address of the user, who executed the SQL query, name of SQL server and database.

4. Future Work

As part of future research, machine learning could be implemented, which is a already built-in into Elasticsearch [11]. By using machine learning classifiers, it is possible to detect anomalies in logs and metrics or detect unusual activity.

For early detection of threats it is possible to use the function Alert & Action [12], where rules are defined in which it is possible to set a treshold and when it is exceeded, the administrator receives a notification through a different type of communication channel or a ticket is created in the SOAR system. It is also possible to extend the collection to other types of data from other azure services, and even though in our case we only collected data from the services we use, it is possible to collect data from basically all services.

5. Conclusion

Data security is a frequently discussed topic in today's electronic age full of cyber attacks associated with their potential misuse [13]. In general, data security is an important element both for the protection of intellectual property and for strengthening the market position towards customers in terms of their trust in providing their data to cloud platforms. The possibilities of monitoring, collecting and processing data for these purposes were implemented as part of the management of a container terminal model in laboratory conditions. In the future, it is expected that the control of the bridge crane will be expanded to include spreader navigation using image processing from the crane camera. For this, artificial intelligence methods will be used for object recognition or container edge segmentation. Subsequently, commands will be generated for controlling the crane drives so that container manipulation is efficient. Implementing this process using cloud services means using different communication protocols, different data sources, different data types and different methods of data transfer, storage and processing. It is therefore necessary to have some concept for implementing cybersecurity ready. One way to secure data is to use the ELK stack tools mentioned in this article. By implementing the ELK stack components, we streamlined working with logs and metrics from the Azure platform through various visualization elements. The use of Kibana enables analysts to use various advanced analytics tools to analyze and correlate data in more detail. The entire process consisted of creating eventhubs to receive logs, setting up to send logs and metrics via Filebeat to Elasticsearch, modifying the index lifecycle, creating a pipeline, and modifying the index template. Furthermore, we created a dashboard with a variety of visualizations that allow for an easy overview of a large number of logs and metrics and basically the entire infrastructure.

Acknowledgments: This article was elaborated in the framework of the Grant Projects KEGA 044TUKE-4/2024.

References

1. A. Sharif. Azure logging guide: The basics. [Online]. Available: https://www.crowdstrike.com/guides/azure-logging/
2. Azure monitor overview. [Online]. Available: https://learn.microsoft.com/en-us/azure/azure-monitor/overview
3. Beats: Data shippers for elasticsearch. [Online]. Available: https://www.elastic.co/beats
4. Azure module. [Online]. Available: https://www.elastic.co/guide/en/beats/filebeat/current/filebeat-module-azure.html

5. K. Shah, Kibana 8.x - A Quick Start Guide to Data Analysis: Learn about data exploration, visualization, and dashboard building with Kibana. Packt Publishing, Feb. 2024.
6. Features and terminology in azure event hubs. [Online]. Available: https://learn.microsoft.com/en-us/azure/ event-hubs/event-hubs-features
7. T. Engin. Combatting risky sign-ins in azure active directory. [Online]. Available: https://techcommunity.microsoft. com/t5/microsoft-entra-blog/combatting-risky-sign-ins-in-azure-active-directory/ba-p/3724786
8. Azure activity logs. [Online]. Available: https://www.elastic.co/docs/current/en/integrations/azure/activitylogs
9. BenB196. Support flattened field type from elasticsearch. [Online]. Available: https://github.com/elastic/kibana/ issues/25820#issuecomment-1588266181
10. Nicholas-r king. Support flattened field type from elasticsearch. [Online]. Available: https://github.com/elastic/ kibana/issues/25820#issuecomment-1803131428
11. R. Collier, C. Montonen, and B. Azarmi, Machine Learning with the Elastic Stack: Gain valuable insights from your data with Elastic Stack's machine learning features. Packt Publishing, 2021.
12. Alerting. [Online]. Available: https://www.elastic.co/guide/en/kibana/current/alerting-getting-started.html
13. Pekar, Adrian and Jozsa, Richard, Evaluating ML-based anomaly detection across datasets of varied integrity: A case study, volume=251, ISSN=1389-1286, url=http://dx.doi.org/10.1016/j.comnet.2024.110617, DOI=10.1016/j.comnet.2024.110617, journal=Computer Networks, publisher=Elsevier BV, 09/2024, pages=110617

TECHNICAL UNIVERSITY OF KOŠICE
Faculty of Mechanical Engineering

Thermal imaging systems: new possibilities for detection and analysis of thermal radiation

Valéria Eiben [1,*], Ružena Králiková [2], Ervin Lumnitzer [3]

[1] Technical University of Kosice; valeria.eiben@student.tuke.sk
[2,3] Technical University of Kosice; ruzena.kralikova@tuke.sk, ervin.lumnitzer@tuke.sk
* Correspondence: Ing. Valeria Eiben, Lomonosovova 36, 040 01 Kosice, valeria.eiben@student.tuke.sk; Tel.: +421 905 357 097

Abstract: Thermal cameras are passive sensors that capture infrared radiation emitted by all objects with a temperature above absolute zero. This type of camera was originally developed as a surveillance and night vision tool for the military, but recently their price has dropped, which has greatly opened up a wider field of use. The deployment of this type of sensor in vision systems eliminates the illumination problems of conventional grayscale and RGB cameras. This research paper discusses the use of thermal vision systems and their applications. Last but not least, the paper deals with the analysis of the use of thermal imaging cameras, their technical parameters and a more detailed specification of computational methods and mathematical models.

Keywords: thermal imaging systems; thermal radiation; thermodynamics

1. Introduction

Thermography, or thermal imaging, is a widely used technology that allows for the visualization and analysis of infrared radiation emitted from objects, producing thermal images known as thermograms. These systems are instrumental in a wide range of fields, including medical diagnostics, industrial inspections, building energy assessments, and environmental monitoring. The effectiveness of thermographic systems depends heavily on computational methods and mathematical models, which allow for accurate interpretation of thermal data. This article explores the computational techniques and mathematical models crucial for the operation and improvement of thermographic systems [1].

2. Principles of Thermography

Thermography is based on detecting infrared radiation emitted by objects due to their temperature. The radiation is detected by infrared sensors and converted into an image or video. The temperature differences between various regions of an object are represented visually, making thermography an invaluable tool for non-invasive temperature measurement and analysis. For thermographic systems to produce reliable and meaningful data, several computational techniques are employed to enhance the image quality, correct distortions, and interpret the thermal data accurately [2].

2.1. Infrared Radiation and Heat Emission

Every object with a temperature above absolute zero emits infrared radiation. The intensity of this radiation increases with the temperature of the object. For instance, warm objects emit more infrared radiation than cooler ones, and the radiation emitted has different wavelengths, depending on the object's temperature. The human eye can only see a narrow range of light wavelengths, known as the visible spectrum. However, thermal cameras detect infrared radiation, which exists just outside the visible spectrum. This makes them ideal for viewing heat emitted by objects in dark or obscured conditions.

Electromagnetic radiation is the transmission of energy in the form of electromagnetic waves. Electromagnetic waves represent a local modification of the electromagnetic field, a periodic process involving spatial and temporal changes in the electric field strength and, simultaneously, in the magnetic induction vector. Electromagnetic radiation encompasses the entire electromagnetic spectrum, from gamma rays to radio waves. The speed of propagation in a vacuum, i.e. the speed of light, is 299 792.458 km/s, which is the maximum possible speed in the universe according to relativity. Human vision can only perceive a region of the electromagnetic spectrum called visible light, while with frequencies of approximately 380 to 780 nm. In the electromagnetic spectrum, illustrated in Figure 1, there are several ways of imaging, which are defined by the range of frequencies of electromagnetic radiation. These methods provide different information based on their physical principles. Characteristics of infrared radiation emitted by an object is described by Planck's law in terms of the spectral emission of radiation [2].

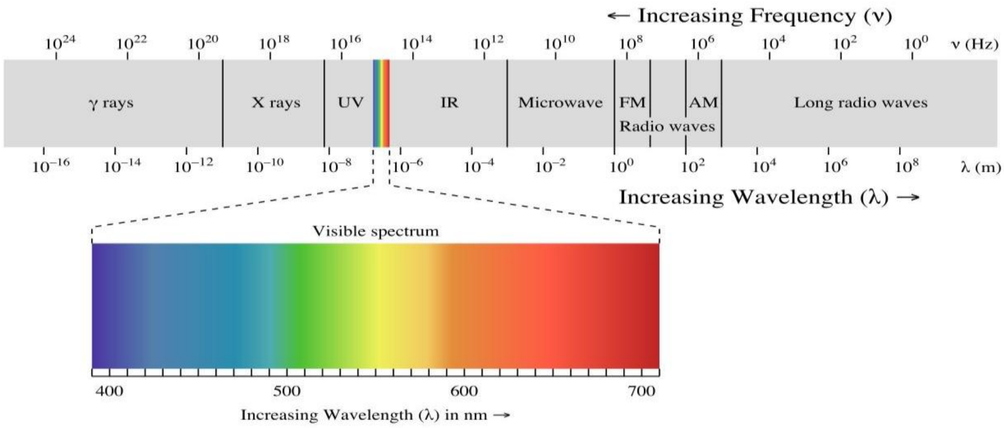

Figure 1. The Electromagnetic Spectrum.

2.2. Detection of Infrared Radiation

Thermal cameras use special sensors called thermopiles, pyroelectric detectors, or microbolometers to detect infrared radiation. These sensors are designed to be sensitive to the infrared light that is emitted by objects based on their temperature.

- Microbolometers are the most commonly used sensors in modern thermal cameras. They consist of an array of tiny, thermally sensitive detectors that can detect minute changes in temperature. These detectors are usually made of materials like vanadium oxide or amorphous silicon, which change their resistance when they absorb infrared radiation.
- Thermopiles detect infrared radiation through the heating effect it causes on a sensor. This temperature change is measured and converted into a voltage that can be interpreted [2].

2.3. Focusing and Capturing the Infrared Radiation

Just like a regular camera, a thermal imaging camera has a lens that focuses incoming infrared radiation onto the sensor. These lenses are typically made from materials like germanium or chalcogenide glass, which are transparent to infrared light but opaque to visible light.

The camera's lens focuses the infrared light onto the sensor, creating a thermal image. Since infrared radiation behaves differently than visible light, this sensor captures temperature differences across a scene, with hotter areas appearing brighter or more vivid and cooler areas darker [2].

2.4. Processing and Conversion to an Image

Once the infrared radiation is captured by the sensor, it is processed by the camera's onboard electronics. The sensor's temperature data is converted into a digital image, where different temperatures are mapped to various colors on a color scale.

The thermal image is then displayed on the camera's screen as a thermogram. In most thermal cameras, the color scheme is chosen so that warmer areas are shown in shades like red, orange, or yellow, and cooler areas appear blue or purple. This color palette makes it easier to identify temperature variations and thermal anomalies in a scene [2].

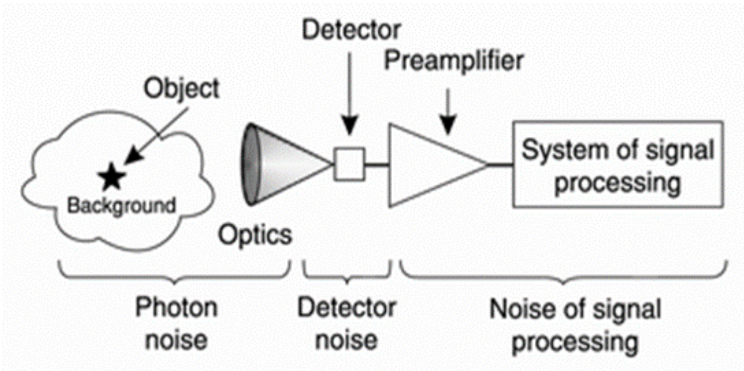

Figure 2. Anatomy of a Thermal Imaging Camera.

3. Computational Methods in Thermographic Systems

3.1. Image Processing and Enhancement Techniques

Thermal images often suffer from noise, low resolution, or artifacts that may compromise their quality. To address these challenges, various computational methods are applied:

- **Noise Reduction:** Thermal images are often noisy due to sensor limitations or external environmental factors. Techniques like Gaussian filtering, wavelet denoising, and median filtering are employed to smooth out noise while preserving the edges of thermal features;
- **Contrast Enhancement:** In some cases, subtle temperature variations need to be amplified to make them more visible. Histogram equalization, contrast-limited adaptive histogram equalization (CLAHE), and other enhancement techniques are used to improve visibility and emphasize significant thermal differences;
- **Edge Detection and Segmentation:** Identifying and isolating regions of interest in thermal images is crucial for analysis. Edge detection algorithms like the Sobel operator, Canny edge detector, and Laplacian of Gaussian (LoG) filter are employed to detect boundaries and structures within the thermographic data;
- **Image Registration:** When comparing thermal images taken at different times or from different viewpoints, it is necessary to align them accurately. Image registration techniques, such as mutual information and feature-based matching, help to align images before they are analyzed for differences in temperature or structural changes [3,6].

3.2. 3D Reconstruction and Modeling

In some applications, like building inspections or medical imaging, it is beneficial to convert 2D thermal images into 3D models to better understand temperature distribution in a three-dimensional context. Computational methods such as photogrammetry, structure-from-motion (SfM), and stereovision are used to generate 3D reconstructions from multiple thermal images. These models allow for more precise analysis, heat flows, and spatial anomalies [3].

3.3. *Artificial Intelligence*

Artificial intelligence (AI) are increasingly being integrated into thermographic systems to automate and improve data interpretation. Algorithms are used for automated object detection, anomaly detection, and classification of thermal patterns. By training models on large datasets, AI can identify complex thermal patterns that might be invisible to the human eye, enhancing the predictive capabilities of thermographic systems. For instance, in industrial applications, AI models can be used to predict equipment failure by analyzing thermal signatures of machines over time [3].

4. Mathematical Models in Thermography

Mathematical models are integral to the interpretation of thermographic data, particularly when translating thermal images into quantitative insights. These models are used to simulate heat transfer, predict temperature distributions, and interpret the physical phenomena [4].

4.1. *Heat Transfer Models*

Thermal behavior in materials is governed by the laws of heat transfer. Key mathematical models used in thermographic systems include:

- **Fourier's Law of Heat Conduction:** This fundamental law describes how heat flows through materials. In thermographic applications, it is used to model the heat distribution across an object. The mathematical form is (1):

$$q = -k\nabla T \tag{1}$$

Where:
q [W/m^2] - the heat flux
k [W/(m·K)] - the thermal conductivity
∇T [K/m] - the temperature gradient.

- **Newton's Law of Cooling:** This model is often used to predict the rate of heat transfer between a hot object and its surrounding environment. The rate of cooling is expressed as (2):

$$dT / dt = -h\,(T - T_\infty) \tag{2}$$

Where:
T [K] - the object temperature
h [W/(m^{2}K)] - the heat transfer coefficient
T_∞ [K] - the ambient temperature.

- **Steady-State and Transient Heat Conduction:** These models help analyze temperature distributions under different boundary conditions. In the case of transient heat conduction, the temperature at a point changes with time, which can be modeled by the heat equation (3):

$$\partial T / \partial t = \alpha \nabla^2 T \tag{3}$$

Where:
α [m^2 s^{-1}] - the thermal diffusivity.

4.2. *Thermal image analysis*

This method involves the analysis of thermal images obtained thermal imaging cameras to identify thermal anomalies, thermal leaks and other thermal characteristics of objects and environments. Thermal images can be analyzed using a variety of algorithms and image processing techniques to obtain detailed information on thermal distributions [4].

4.3. Emissivity Models

The accuracy of thermal measurements depends on the emissivity of the material being imaged. Emissivity refers to the efficiency with which a material emits infrared radiation, and it varies based on material composition and surface properties. Mathematical models are used to account for emissivity variations, ensuring accurate temperature measurements. The Stefan-Boltzmann law, expressed as (4):

$$E=\epsilon\sigma T4 \tag{4}$$

Where:
E - emitted radiation
ϵ - the emissivity
σ- the Stefan-Boltzmann constant
T - the temperature.

4.4. Calibration and accuracy verification

Calibration and verification of thermal imaging cameras accuracy are important steps in the interpretation of thermographic data. Calibration procedures and methods Accuracy verification procedures allow to guarantee reliable temperature measurements and accurate interpretations of thermal images [4].

5. Applications of Thermography

The integration of computational methods and mathematical models significantly enhances the range and accuracy of thermographic systems across various fields, as seen in Figure 3:

- **Medical Imaging:** Thermal cameras are used to detect abnormal temperature patterns in tissues, helping diagnose conditions like inflammation, tumors, or circulatory problems. The algorithms aids in distinguishing between healthy and pathological thermal patterns [5];
- **Industrial Inspections:** Thermography is used to detect hot spots in machinery, electrical components, and mechanical systems. By predicting overheating or malfunctioning components, thermography can help prevent costly failures and improve safety;
- **Building Inspections:** In building diagnostics, thermographic systems are used to identify insulation defects, moisture ingress, and structural issues. The application of heat transfer models helps assess the energy efficiency of buildings;
- **Environmental Monitoring:** Thermography is used to monitor environmental temperature distributions, such as in wildfire detection or monitoring the health of aquatic ecosystems [5,7].

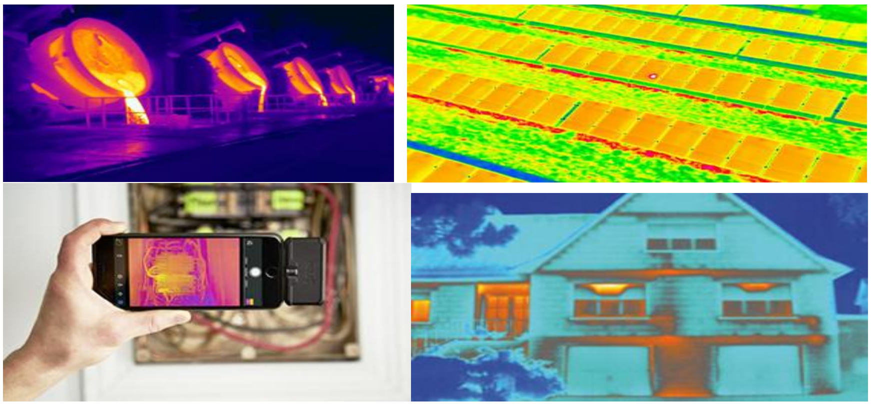

Figure 3. Applications of Thermal Imaging Cameras.

6. Discussion

Despite the promising advancements, thermal imaging systems still face certain challenges. One limitation is the cost, with high-performance systems remaining expensive for many potential users. Additionally, while thermal imaging can identify temperature variations, it cannot directly identify the cause of those variations, which means additional analysis or complementary technologies are often required for a complete diagnosis. As the technology continues to evolve, future developments are likely to focus on improving resolution, reducing costs, and integrating artificial intelligence (AI) for automatic analysis of thermal data. These innovations will allow for more advanced predictive capabilities, greater accuracy, and broader adoption of thermal imaging across various fields.

7. Conclusions

Thermal imaging systems have unlocked a world of possibilities in the detection and analysis of thermal radiation. From industrial inspections and medical diagnostics to security and environmental monitoring, the applications of thermal imaging are vast and growing. With ongoing advancements in resolution, sensitivity, and portability, the future of thermal imaging promises even more powerful and accessible tools for professionals across industries. Computational methods and mathematical models are essential for enhancing the functionality and accuracy of thermographic systems. From image enhancement techniques to complex heat transfer simulations, these approaches enable the accurate analysis and interpretation of thermal data. As technology continues to advance, the integration of AI will further revolutionize the applications of thermography, making it an indispensable tool across a wide range of industries.

Acknowledgments: This work was supported by the Cultural and Educational Grant Agency of the Ministry of Education, Science, Research, and Sport of the Slovak Republic under project KEGA No. 038TUKE-4/2024 titled "Zvyšovanie uplatniteľnosti absolventov na trhu práce implementáciou požiadaviek praxe do výučbového procesu študijného programu inžinierstvo prostredia".

Conflicts of Interest: The authors declare no conflict of interest.

References

1. Niranjan, S.K. Proceedings of the International Conference on Smart Technologies in Computing Electrical and Electronics (ICSTCEE 2020), October 9-10, 2020.
2. Manullang, M.C.T.; Lin, Y.-H.; Lai, S.-J.; Chou, N.-K. Implementation of Thermal Camera for Non-Contact Physiological Measurement: A Systematic Review, Sensors, 2021, pp. 21.
3. Silva, G. P.; Batista, P. I. B.; Póvoas, Y. V. The usage of infrared thermography to study thermal performance of walls: a bibliographic review, In Revista ALCONPAT 2019, pp. 117 - 129.
4. Brynda, P. Úvod do teorie termovizního měření, Praha: České vysoké učení technické, pp. 1-7, 2010.
5. Proszak-Miąsik, D. Use of thermal imaging in construction, In IAPGOS, 2019, pp. 12–15.
6. Liu, L.; Ouyang, W.; Wang, X.; Fieguth, P.; Chen, J. Deep learning for generic object detection: a survey. International Journal of Computer Vision, 2023, pp. 261–318.
7. Nguyen, T. X. B. K.; Chahl, J. A review of modern thermal imaging sensor technology and applications for autonomous aerial navigation, J. Imag., 2021, Volume 7, pp. 217.

TECHNICAL UNIVERSITY OF KOŠICE
Faculty of Mechanical Engineering

Locating the failure of forged bearing rings

Marek Grega [1,*], Janette Brezinová [1]

[1] Technical university in Kosice, Faculty of mechanical engineering, Department of Technology and Materials engineering, Slovakia; marek.grega@student.tuke.sk; janette.brezinova@tuke.sk
* Correspondence: marek.grega@student.tuke.sk

Abstract: The article investigates the formation of surface cracks in steel forgings used for bearing rings in transmission components. The forging and heat treatment processes, conducted under consistent technological conditions, revealed the occurrence of high-temperature annealing cracks caused by plasticity depletion during stress relaxation. Additionally, cold cracks were analyzed, with chemical compositions and hardness measurements indicating susceptibility due to elevated carbon and chromium content, as well as a high cracking parameter. Die-tool wear and damage during forging were identified as key contributors to crack formation, transferring surface defects and creating microcracks that propagate during subsequent processing. The findings underscore the influence of tooling conditions, material properties, and process parameters on the quality and reliability of steel forgings.

Keywords: cracks; forging; bearing ring

1. Introduction

The manufacturing of metal bearing rings for gearbox components is highly demanding in terms of adhering to technological processes to achieve the desired product quality. The final product is influenced by specific technological procedures and the composition of the input material. In standard production, it is challenging to detect latent defects in products during processing. In most cases, defects are identified only during final quality control, requiring subsequent analysis to determine their root causes.

Defect identification in forgings is feasible only through thorough categorization of the defects. Crack-type defects are particularly challenging to identify due to the wide range of factors contributing to their formation. George E. Dieter, in his works published in the ASM Metals Handbook [1, 2], categorized cracks based on their temperature of origin during forging and their type—taking into account orientation relative to the forging axis, location on the forged part, and the forging method used.

A fundamental classification of surface crack types is described in the EN 1011-2 standard [3]. While this standard primarily addresses cracks arising during welding, it is not limited to those occurring in welds but also includes cracks in the heat-affected zones of parent metal. According to this standard, base materials include not only sheets but also pipes and forgings.

Researchers Viňáš, Brezinová, Maňková, and Brezina [4] adopted the basic classification of cracks from EN 1011-2 standard and further refined it into four primary groups, each with subcategories. These groups include: Hot cracks, such as crystallization, liquation, and polygonization cracks. Cold cracks, a broad category without subdivisions. Lamellar cracks, divided into exogenous and endogenous types and annealing cracks.

Cold cracking has been a subject of study for many researchers. Ito and Bessyo [5] proposed a formula and established limits for structural low-alloy steels with higher manganese content (0.8–2.5%). They introduced an equation for calculating the crackcing parameter of the parent metal, denoted as P_c. Also identified a critical threshold of P_c >0.30% for material thicknesses of 25 and 30 mm, indicating a high probability of cracking. Furthermore, they defined permissible content levels for individual alloying elements to minimize crack formation. Their studies showed that cracks were absent in samples with maximum hardness up to 271 HV = 264 HB.

Surface cracking during forging presents a significant challenge in the production of steel forgings, as surface defects can drastically affect the quality and mechanical properties of the forged components. Such cracks may lead to product failure in applications subjected to high mechanical or thermal loads.

The aim of this study is to localize cracks occurring in the forged bearing rings and determine the underlying causes of their formation.

2. Materials and Methods

Empirical observations of defect occurrences were conducted on the product "Bearing ring," designed for gearbox applications as a combined component of a bearing housing and a force transmission converter. The product features a simple geometric shape — a rotational cylinder with a central hole and a non-uniform cross-section.

The product dimensions are as follows: outer diameter - Ø 155 mm, inner diameter of the central hole - Ø 98 mm, height - 63 mm, weight of the forging is approximately 4 kg

The forging is manufactured from 42CrMo4 steel, classified according to EN 10083-3:2007. The material is normalized, annealed, and hardened to achieve the prescribed mechanical properties.

After machining operations, specific areas of the product undergo surface hardening to increase hardness, followed by grinding to reduce surface roughness.

Figure 1. Final product – bearing ring.

The technological and production operations for the forging of the bearing ring are summarized in Table 1. The heating of the billet is performed in a continuous induction furnace at a temperature range of 1160 to 1220°C.

The forging of the "bearing ring" is carried out on a mechanical forging press with a maximum working force of 25 000 kN. The forging tools for this operation are designed to combine two phases: Pre-forging (open die): This phase involves reducing the billet to the desired height of the preform and shaping it to prepare for the next phase.

Final forging (closed die): This phase involves filling the forging cavity to achieve the desired shape of the forging. The result includes a slug for the central hole and flash along the edges of the forging.

Table 1. Technology operations overview.

Tech. operation	Heating	Forging			Cooling	Heat-treatment		
		Open-die	Closed-die	Shearing and punching		Normalizing annealing	Quenching	Tempering
Machine	induction furnace	Mechanical Press 25000kN		Mechanical Press 5000kN	belt conveyor	continuous gas furnace	continuous gas furnace	continuous electric furnace
Material	Ø=90 mm, h=132 mm	Ø=102 mm, h=80 mm	Forging with flash and slug	Final forging; 42CrMo4		42CrMo4+N	42CrMo4 +N+Q	42CrMo4 +N+QT
Working temperature	1160-1220°C	1100-1160°C	1100-1160°C	950 – 1160 °C	20 – 25°C	870 ± 10°C; air cooling	870 ± 10°C; polymer cooling on 25 °C	660 ±10°C

Subsequently, on a separate machine— mechanical press with a maximum working force of 5000 kN—the forging undergoes flash (3) and slug (2) removal. In the first phase, a punching pin removes the slug - membrane from the inner hole of the forging. In the second phase, a cutting plate is used to trim the flash, achieving the final shape and dimensions of the forging.

(**a**) (**b**)

Figure 2. Forging bearing ring (**1**): (**a**) Forging with inner slug (**2**) and outside flash (**3**); (**b**) Forging after cutting slug and flash.

After forging, the product undergoes a heat treatment process consisting of normalization annealing, quenching and tempering. Normalization annealing is carried out in continuous gas furnaces with electronically controlled temperature systems that comply with the DIN 17052-1 standard (Requirements for temperature uniformity). The process is conducted at a temperature of 870°C with a holding time of 30 minutes.

Quenching is performed in a continuous gas furnace, also at a temperature of 870°C, followed by immersion into a synthetic polymer quenching medium at 25°C for a soaking time of 30 seconds. Subsequently, the products pass through a continuous electric tempering furnace at a temperature of 660°C with a holding time of 2.5 hours.

Once cooled, the forgings are shot-blasted in a shot blasting machine to remove surface impurities and prepare them for final quality control.

The forgings were subjected to non-destructive testing. The first phase involved visual inspection according to EN 13018, followed by magnetic particle inspection in the second phase, performed in accordance with EN 10228-1.

To assess mechanical properties, conduct chemical analyses, and perform metallographic observations, a cross-section of the test sample was prepared.

For chemical composition analysis, the method of optical-emission spectroscopy was employed. The chemical composition of individual batches is presented in Table 2. The results of the elemental analyses fall within the specified limits for 42CrMo4 steel.

Table 2. Chemical analysis of individual batches (wt.% , Fe balance).

Chemical element	Batch: 63813 (wt.%)	Batch: T21297 (%)
C	0.38	0.43
Si	0.22	0.29
Mn	0.80	0.75
P	0.013	0.011
S	0.010	0.003
Cr	1.10	1.14
Mo	0.214	0.203
Al	0.023	0.022
Cu	0.17	0.02
V	0.0044	0.004
Ni	0.17	0.03

The method according to Ito and Bessyo was used to determine the cracking parameter P_C.

$$P_c = C + \frac{Si}{30} + \frac{Mn}{20} + \frac{Cu}{20} + \frac{Ni}{60} + \frac{Cr}{20} + \frac{Mo}{15} + \frac{V}{10} + 5B + \frac{t}{600} + H/600 \quad (1)$$

The Charpy impact test was used to evaluate impact toughness, in accordance with EN ISO 148-1. The results of the impact toughness tests are presented in Table 3, meeting the required limit (KV+20°C, minimum 35 J) for 42CrMo4 steel in the N+QT condition.

Table 3. Impact test results.

Batch	KV + 20°C (J)		
	Probe 1	Probe 2	Probe 3
63813	118	108,9	109,5
T21297	111,2	110,67	105,0

The Brinell hardness test was conducted in accordance with EN ISO 6506-1. The measured surface hardness for batch 63813 is 278 HB, and for batch T21297, it is 272 HB. The specified hardness for the tested forging (bearing ring) is in the range of 240–270 HB.

3. Results

Two types of Non-Destructive Testing (NDT) were performed during the final quality control: Visual Testing (VT) and Magnetic Particle Testing (MT). An analysis was conducted on batch number 63813, consisting of 534 pieces, and batch number T21297, consisting of 625 pieces. The number of defective forgings after each inspection phase is presented in Table 4. Cracks were observed on both the outer and inner sides of the forgings.

Table 4. Number of forgings from individual batches by type of non-destructive testing.

Batch	Number of forgings (pc)	Pieces with a crack (pc)	
		VT method	MT method
63813	534	212	381
T21297	625	23	164

The occurrence of cracks in forgings in individual batches is in different volumes: 71.34% in batch 63813 and 26.24% in batch T21297. Only forgings after MT are included in the error rate calculation.

(**a**)

(**b**)

Figure 3. Inspected forging in magnetic testing(MT): (a) Location of cracks on the outside (4) of the forging; (b) Location of cracks on the inside of the forging (5) and on the outside wall of the forging.

Cracks were localized on both the outer side of the forging (Figures 3, position 4) and the inner surface of the hole (Figure 3, position 5). The length of the cracks ranged from 60 to 150 mm. These cracks were observed along the entire profile, most commonly starting and ending at the area where the flash is located. Their progression extended toward the radii at the outer side of the forging, where the edge of the forging thins.

Two zones of crack occurrence were identified, as described in Table 5 and marked in Figure 4. The orange marks of indicate cracks are in: I. the outer flash area, while the blue marks indicate cracks are in: II. the inner slug area.

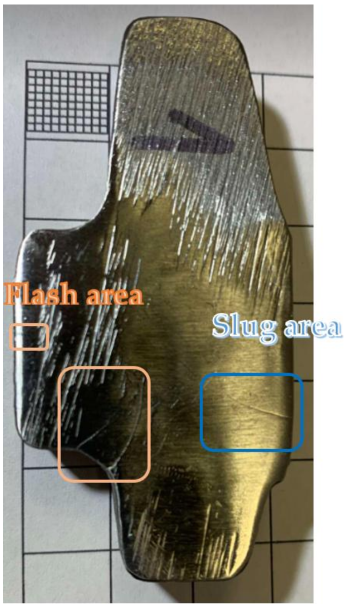

(**a**)

(**b**)

Figure 4. Inspected forging in section: a) Location of cracks on forging from batch 63813; b) Location of cracks on forging from batch T21297.

Table 5. Crack parameters and direction in forging zones.

Cracks zones	Crack parameter (mm)		Direction of cracks
	Depth	Length	
I Flash area	0-33	15-320	centric
II Slug area	0-22	15-145	centric

The direction of the cracks is centric, from the edge and directed to the center of the forging cross-section. On macroscopic observation of the crack – Fig. no. 5, an oxide layer is clearly visible along its entire length.

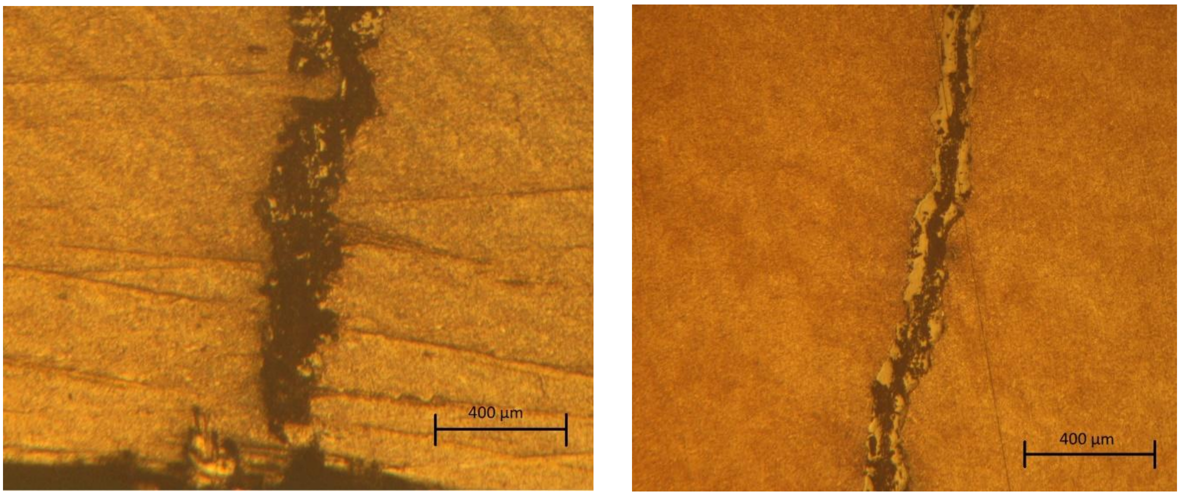

(**a**) (**b**)

Figure 5. Macroscopic photograph of a crack (100x zoom): (a) Beginning of crack propagation at the edge of the forging; (b) Crack with a pronounced oxide layer.

Table 6 shows the calculated cracking parameter P_c for individual batches based on the chemical composition and thickness of the parent metal, according to the method (1) to Ito and Bessyo. Cracks do not occur at values of the cracking parameter P_c below 0.30% for material thicknesses of 25 and 30 mm.

Table 6. Calculating the cracking parameter P_c .

Chemical composition	Batch 63813	Batch T21297
t	30 mm	30 mm
H	1 ppm	1 ppm
P_c	0.57 %	0.61 %

To evaluate the heat treatment process, a hardness test was performed on a cross-section of the forging. The individual measurement values are presented in Table 7. A network of measurement points was established, as shown in Figure 6. The surface hardness of the forging was similar for both batches, exceeding 270 HB. The lowest hardness was observed at the center of the forging cross-section. The difference between the surface hardness and the hardness at the center of the cross-section was 22 HB

Table 7. Measured hardness values in the cross-section of the forging.

Line	1	2	3	4	5	6	7	8	9	10
A	272	272	266	272	266	266	266	272	272	278
B	272	272	266	266	255	266	266	272	272	278
C	-	-	-	272	272	272	-	-	-	-

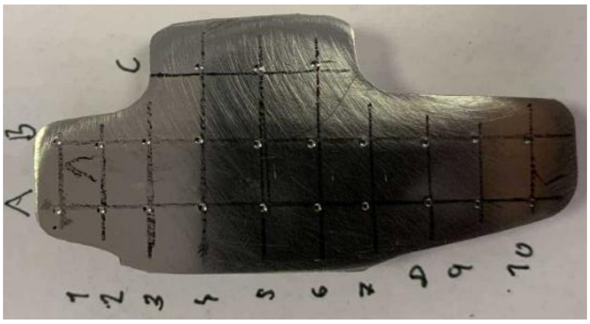

Figure 6. Hardness measurement points in the forging cross-section.

Tool wear was not monitored during forging. After forging the entire batches, the forging tools — specifically the die and trimming tools — were subjected to visual inspection and repaired of dies by milling. Both types of tools exhibited clear signs of erosive wear. A significant crack was observed on the upper die, spanning approximately three-quarters of the die's circumference, as illustrated in Figure 7b (marked in the red zone). Dimensionally, the tools remained within the tolerance limits. On the punch, piercing tool, and trimming plate, substantial wear on the cutting edges and radial cracks in hard metal welds were identified, marked in orange in Figure 7a.

(**a**) (**b**)

Figure 7. Visual inspection of forging tools: (a) trimming plate and prominent radial crack; (b) die with crack and erosion.

4. Discussion

Based on the evaluation of test results and laboratory analyses, it can be conclud-ed that the localization, direction and size of the cracks were identical in both batches. These are high-temperature annealing cracks with brittle fracture, that formed during the quenching pro-cess of the forgings. The root cause of these cracks is the depletion of plasticity in the critical zone of the heat-affected area during heat treatment, specifically during the relaxation of residual stresses [4].

It is important to note that these high-temperature annealing cracks are merely a consequence of intergranular discontinuities transferred from the forging process in the austenitic phase. As illustrated in Figure 8, defects in the forging tools — such as cracks and surface irregularities — can be transferred to the forging itself (indicated by the orange zones), leading to the formation of hot liquation microcracks. The liquating phase typically consists of sulfides, oxysulfides, or carbosulfides.[6]

During the trimming and piercing operations, mechanical removal of a portion of the metal from the wall surface occurs via shearing. This process subtly disrupts the structure of surface bonds, resulting in fractures during the austenite formation phase. This can cause structural disharmony, leading to the development of microcracks, which act as precursors to crack formation (indicated by the blue zones in Figure 8) during subsequent heat treatment processes, such as quenching.

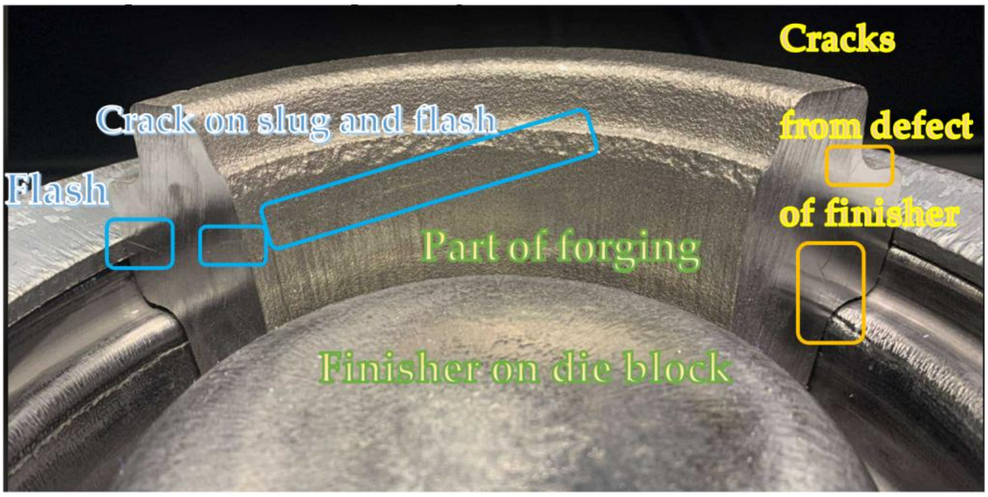

Figure 8. Part of the cross- section of the forging set in the die with the attached location of the flash.

Both batches were forged using the same technological procedure, on the same dies, and underwent identical heat treatment processes. The chemical composition of the melts is comparable, except for the copper (Cu) content, which is 0.17% in batch 63813 and 0.02% in batch T21297. The carbon (C) content exceeds 0.25%, and the chromium (Cr) content in both batches is above 0.9%, exceeding the recommended limit for the occurrence of cold cracks [7], [8].

The cracking parameter (Pc) was 0.57% and 0.61% for the two batches, both significantly above the threshold of 0.30%. The surface hardness exceeded 271 HB, and the hardness difference across the sample cross-section was greater than 22 HB, which are critical parameters that indicate a high likelihood of cold crack formation.

5. Conclusions

Deformations in the shape of forging tools, such as wear or damage, have a significant impact on the formation of surface cracks in forgings. During the forging process, tools experience continuous wear and shape changes, which can influence how forces are applied to the material and its deformation. If the tooling is worn or damaged, it may result in uneven stress distribution within the forgings or the transfer of surface defects, leading to the development of microcracks on the forging surface.

This issue can subsequently cause crack propagation or enlargement during subsequent technological processes or during product use. Such defects reduce the quality of the forgings and compromise their reliability in final applications.

Acknowledgments: This article was prepared with support from the project titled: VEGA: 1/0597/23 "Possibilities of applying laser additive technologies in the restoration of functional surfaces" and APVV-20-0303 – "Innovative approaches to restoring functional surfaces by laser welding"

References

1. George E. Dieter, Material Factors Affecting Workability. ASM Handbook Forming and Forging, **1993**, *Volume 14*, pp. 782-794.
2. George E. Dieter, Forging Defects. ASM Handbook Forming and Forging, **1993**, *Volume 14*, pp. 834-841.
3. EN 1011-2 +A1:2023, Welding - Recommendations for welding of metallic materials - Part 2: Arc welding of ferritic steels,
4. Viňáš, J.; Brezinová, J.; Maňková, I.; Brezina, J. In *Book Technológie a defektoskopické skúšky materiálov.*; Publisher: Edícia študijnej literatúry Košice, Slovakia, 2021; pp. 6–55.

5. Ito, Y.; Bessyo, K., Cracking parameter of high strength steels related to heat affected zone cracking, 1968, Available online: doi.org/10.2207/qjjws1943.37.983
6. Brezinová, J.; Viňáš, J.; Draganovská, D.; Guzanová, A. In *Book Základy materiálového inžinierstva*.; Publisher: Edícia študijnej literatúry Košice, Slovakia, 2020; ISBN: 978-80-553-3745-6; pp. 256–273.
7. Brziak, P.; kol.;. In *Book Materiály a ich správanie sa pri zváraní*.; Publisher: Výskumný ústav zváračský - priemyselný inštitút SR, Bratislava Slovakia, 2014; ISBN: 978-80-96933-09-9; pp. 117.
8. Saha DC, Chang I, Park Y-D. Heat-affected zone liquation crack on resistance spot welded TWIP steels. Mater Charact. 2014; Available online: doi.org/10.1016/j.matchar.2014.03.016

Numerical analysis of the influence of scaffold implantation on load distribution in long bones

Anita Gryko [1,*], Piotr Prochor [1]

[1] Institute of Biomedical Engineering, Faculty of Mechanical Engineering, Bialystok University of Technology, Bialystok, Poland; anita.gryko@sd.pb.edu.pl; p.prochor@pb.edu.pl
* Correspondence: anita.gryko@sd.pb.edu.pl

Abstract: When bone fragment removal is necessary, restoring bone continuity typically involves using bone grafts or plates. However, these approaches come with drawbacks. Recently, scaffolds have emerged as a potentially more effective alternative for restoring bone continuity. This study aimed to evaluate the validity of this claim. The analysis focused on bone defects of three lengths—35 mm, 45 mm, and 55 mm—located in the lower, middle, and upper sections of the femoral diaphysis. The following four methods for restoring bone continuity were assessed: single plate with and without scaffold, two parallel plates with and without scaffold. Simulations modeled forces generated during the human gait cycle, measuring parameters such as maximum and average stresses, strain energy density, and percentage changes in these values relative to those observed in intact bone zones. The findings indicated that the most effective method for restoring bone continuity was the use of a single plate combined with a scaffold. This approach produced stress distributions most similar to those observed in an intact bone model, particularly in terms of load transfer and maximum stress values. The study confirmed that incorporating a scaffold in bone continuity restoration is a potentially more effective approach compared to traditional methods.

Keywords: scaffold, bone, continuity, HMH stress, strain energy density, finite element analysis,

1. Introduction

The human skeleton is a complex system that can be disrupted by diseases, injuries, or genetic disorders, often necessitating the removal of bone fragments and causing complications such as limb length discrepancies and increased energy consumption during movement [1]. Current methods for restoring bone continuity include plates and bone grafts, each with limitations like stress shielding, periosteum damage, or risks associated with transplantation [2].

An emerging alternative involves scaffolds, porous structures designed to support bone regeneration by mimicking natural tissue properties and providing mechanical integration during healing [2]. Scaffolds have gained interest due to their potential to overcome the drawbacks of traditional methods. Research, including numerical and experimental studies [3-5], has focused on understanding the effectiveness of scaffolds and their ability to handle biomechanical loads during locomotion.

Current literature offers limited analyses of bone defects varying in length, location, or osteosynthesis methods, lacking a comprehensive comparison of these parameters. To address these gaps, this study focuses on numerical testing to simulate various approach and predict the behavior of structures under mechanical loads from locomotion. The analysis emphasizes HMH stress and strain energy density to evaluate whether scaffolds provide a superior alternative to conventional treatments and to assess their effectiveness in load transfer, crucial for stimulating bone tissue remodeling.

2. Materials and Methods

2.1. CAD models

The study utilized 442 CT images of a 44-year-old male's left femur to generate a bone model using Mimics Research 23.0 software, with manual post-processing to refine the model. The model was smoothed, exported to SolidWorks, and prepared for finite element analysis. Three variables were analyzed: defect location (100, 160, or 225 mm from the femur head), defect length (35, 45, or 55 mm), and osteosynthesis method [4,5]. To ensure analysis quality, the bone was divided into zones around the defect for detailed stress and strain assessments.

Four osteosynthesis methods were evaluated: one or two plates (current standard) and similar configurations with a scaffold filling the defect. Scaffolds, modeled after the bone gap and fabricated via additive manufacturing, had their Young's modulus calibrated based on prior studies [6]. DePuy Synthes Trauma Locking Compression Plate systems and screws were used for all cases. A total of 36 models were analyzed, along with an intact bone model for reference. Plates were fixed within 2 mm of the bone to allow fluid flow and provide a stable healing environment, a practice validated by previous research on mechanical stability [7].

2.2. FE models

ANSYS Workbench 2020 R1 software was used to conduct numerical studies. Isotropic and homogenous mechanical properties of femur were considered (Table 1). For titanium scaffold, the effective Young's modulus was adopted, which was described in the previous section. A value of 30 GPa was set, which was the value obtained for a scaffold with a porosity of 40% and pore geometry of a sphere. This scaffold structure was considered as the most efficient in the previously conducted and published study [8].

Table 1. Material properties used in analyses.

Property	Mass density [g/cm^3]	Young's Modulus [GPa]	Poisson's Ratio	Effective Young's Modulus [GPa]
Cortical bone	1.74 [9]	20.00 [9]	0.30 [9]	-
Cancellous bone	0.64 [10]	0.40 [11]	0.30 [11]	-
Bone plate and locking screw (SS 316L)	7.85 [12]	190.00 [12]	0.30 [12]	-
Scaffold (Ti6Al4V)	4.50 [13]	-	0.33 [13]	30.00 [8]

The discretization utilized 10-node Solid187 finite elements with a maximum edge length of 4 mm for the general mesh and 1 mm in analyzed zones [14]. Mesh quality was ensured using the Jacobian ratio method, with all models achieving a ratio above 0.4 [15]. A 5% convergence test for maximum HMH stress validated the mesh refinement. Frictional contact (coefficient 0.3) was applied for screws-bone interactions, while frictionless contact was used for plate-bone and plate-screw to simplify modeling [4,16].

Loads were assigned using a local coordinate system at the greater trochanter, simulating gait forces, including joint reaction forces and muscle-generated forces [17]. These forces represented conditions at 25% of the gait cycle, with the distal bone fixed by constraining all degrees of freedom in that region.

3. Results

To evaluate load transfer efficiency, results obtained for each of analysed cases of bone osteosynthesis method were compared to results obtained for intact femur.

Figure 1 present stress distribution maps respectively for intact femur and each of analysed osteosynthesis method in the case of 45 mm long defect in lower, middle and upper sections.

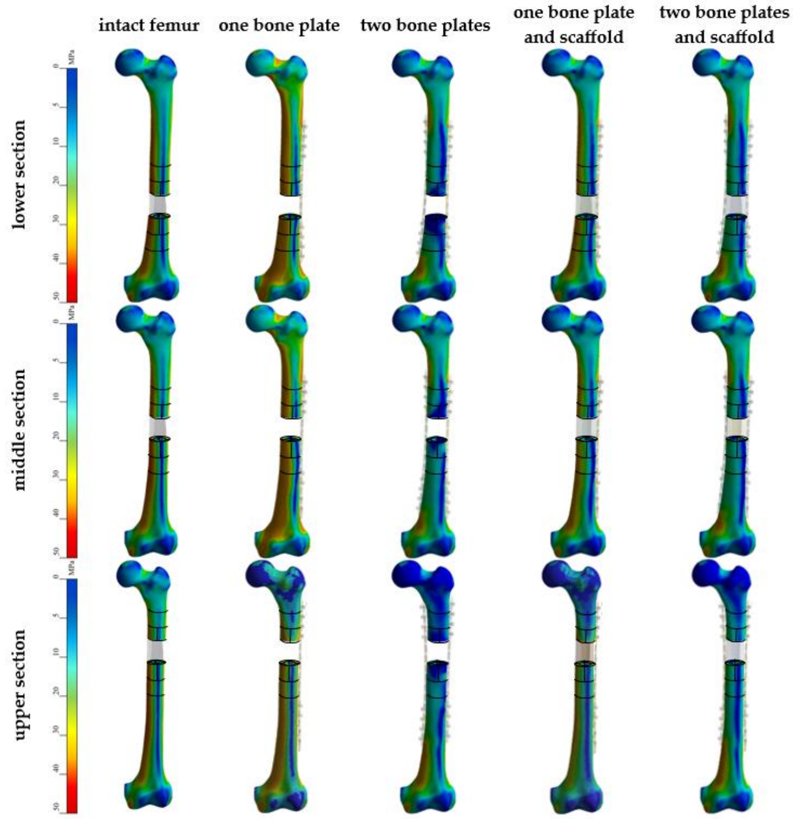

Figure 1. HMH stress distribution.

Figure 2 includes the obtained differences for a 45 mm bone defect located in all considered sections (lower, middle, and upper), for each bone zone (1, 2, 3, 4, 6, 7, 8, 9) directly connected to the bone fragment or scaffold, as well as for bone zones (1–4, 5, 6–9, 10) grouped according to their distance from the bone defect, in terms of strain energy density.

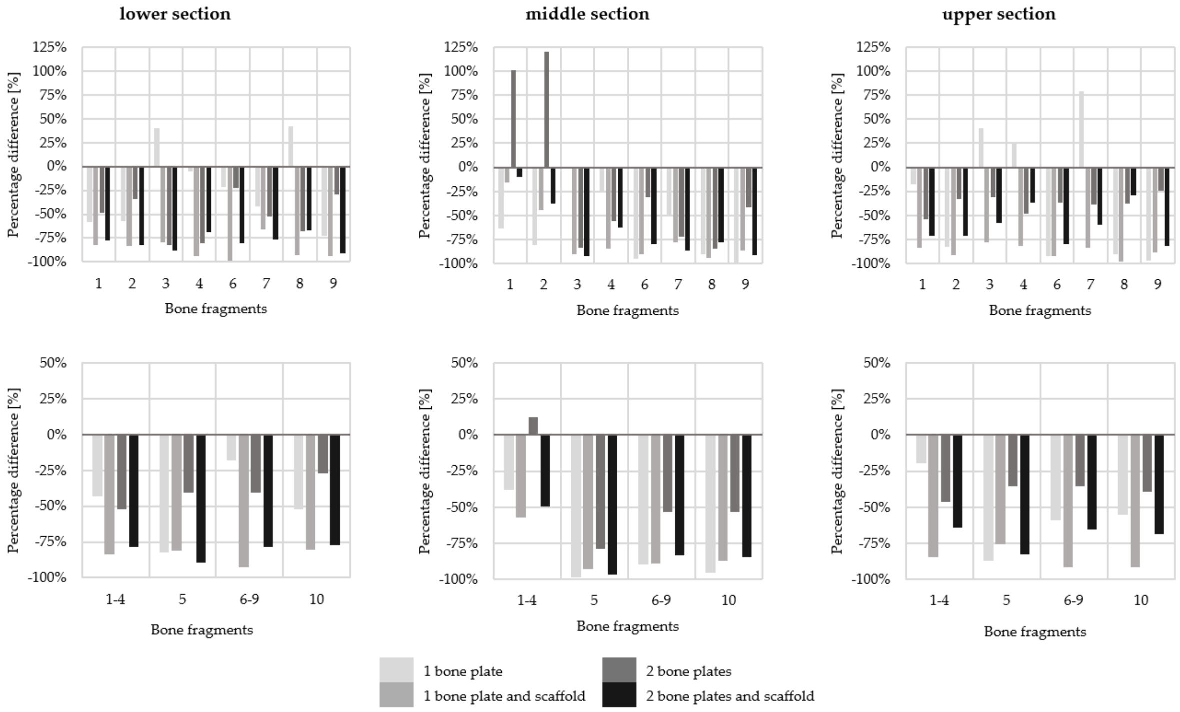

Figure 2. Differences in average strain energy density generated in analysed zones in the case of 45 mm bone defect.

4. Discussion

The study focused on numerical analyses of an intact femur and a femur with a diaphyseal defect, employing various osteosynthesis methods. Key parameters analyzed were percentage changes in average and maximal HMH stress and strain energy density, which are mechanobiological indicators for bone remodeling [15].

Stress maps revealed the highest stresses (~50 MPa) in the intact femur in medial and lateral diaphysis, medial condyle, and femoral neck, while the lowest stresses (1–5 MPa) occurred in anterior/posterior diaphysis, distal epiphysis, greater trochanter, and femoral head. Stress distribution disturbances and stress-shielding were noted with bone defects [18]. Using one bone plate with a scaffold yielded smoother stress distribution (~45 MPa), closely resembling intact femur load transfer and providing a scaffold for tissue differentiation. Double plates showed higher stiffness, increasing stress-shielding [3].

Percentage differences in stress and strain energy density highlighted zones transferring excessive or insufficient loads, with the single plate and scaffold method showing the closest results to intact bone. For intact bone, maximal strain energy density ranged from 0.2e4 to 1.2e4 J/m^3, consistent with the literature [15,19]. Defect length had minimal impact, while defect location significantly influenced results due to differences in plate fixation and thread location.

Numerical methods were justified for simulating stable anatomical conditions, as experimental studies would pose challenges. Plate dimensions also affected outcomes; smaller plates reduced stability, while longer plates increased stress-shielding but risked structural misalignment [20]. Medium-sized plates minimized these issues. Stress values corresponded to bone remodeling stimuli, suggesting zones of insufficient or excessive stress could lead to local resorption or remodeling [21].

Simplifications included modeling bone tissue as isotropic and homogeneous and approximating scaffold properties using effective Young's modulus. These approaches, while not anatomically precise, are standard in numerical studies to reduce complexity [22]. Results provided insight into long-term functionality and remodeling potential of stabilization methods.

5. Conclusions

The study demonstrated that using a scaffold to address a bone fragment defect is a more effective solution compared to conventional treatment methods involving bone plates. The findings also provide a foundation for future research aimed at optimizing scaffold designs and enhancing the overall effectiveness of regenerative medicine.

Acknowledgments: The research was funded by Ministry of Education and Science, Poland as a part of projects WI/WM-IB/6/2023 and WI/WM-IB/5/2023.

Conflicts of Interest: The authors declare no conflict of interest.

References

1. Zhu, L.; Luo, D.; Liu, Y. Effect of the nano/microscale structure of biomaterial scaffolds on bone regeneration. *Int. J. Oral Sci.* **2020**, *12*(6), 1–15.
2. Polo-Corrales, L.; Latorre-Esteves, M.; Ramirez-Vick, J.E. Scaffold Design for Bone Regeneration. *J. Nanosci. Nanotechnol.* **2014**, *14*(1), 15–56.
3. Coquim, J.; Clemenzi, J.; Salahi, M.; Sherif, A.; Tavakkoli Avval, P.; Shah, S.; Schemitsch, E.H.; Bagheri, Z.S.; Bougherara, H.; Zdero, R. Biomechanical Analysis Using FEA and Experiments of Metal Plate and Bone Strut Repair of a Femur Midshaft Segmental Defect. *BioMed Res. Int.* **2018**, *2018*, 1–11.
4. Lu, J.; Wang, G.-Y.; Sheng, J.-G.; Guo, S.-C.; Tao, S.-C. A 3D-printed, personalized, biomechanics-specific beta-tricalcium phosphate bioceramic rod system: Personalized treatment strategy for patients with femoral shaft non-union based on finite element analysis. *BMC Musculoskelet. Disord.* **2020**, *21*, 421.
5. Anitha, D.; Das De, S.; Sun, K.K.; Doshi, H.K.; Lee, T. Improving stability of locking compression plates through a design modification: A computational investigation. *Comput. Methods Biomech. Biomed. Engin.* **2013**, *18*(2), 153–161.
6. Chiu, Y.-C.; Hsu, C.-E.; Ho, T.-Y.; Ting, Y.-N.; Tsai, M.-T.; Hsu, J.-T. Bone plate fixation ability on the dorsal and lateral sides of a metacarpal shaft transverse fracture. *J. Orthop. Surg.* **2021**, *16*, 441.

7. Ahmad, M.; Nanda, R.; Bajwa, A.S.; Candal-Couto, J.; Green, S.; Hui, A.C. Biomechanical testing of the locking compression plate: When does the distance between bone and implant significantly reduce construct stability? *Injury* **2007**, *38*, 358–364.
8. Gryko, A.; Prochor, P.; Sajewicz, E. Finite element analysis of the influence of porosity and pore geometry on mechanical properties of orthopaedic scaffolds. *J. Mech. Behav. Biomed. Mater.* **2022**, *132*, 105275.
9. Herrera, A.; Panisello, J.J.; Ibarz, E.; Cegoñino, J.; Puértolas, J.A.; Gracia, L. Long-term study of bone remodelling after femoral stem: A comparison between DEXA and finite element simulation. *J. Biomech.* **2007**, *40*, 3615–3625.
10. Pan, C.-Y.; Liu, P.-H.; Tseng, Y.-C.; Chou, S.-T.; Wu, C.-Y.; Chang, H.-P. Effects of cortical bone thickness and trabecular bone density on primary stability of orthodontic mini-implants. *J. Dent. Sci.* **2019**, *14*, 383–388.
11. Alkhatib, S.E.; Mehboob, H.; Tarlochan, F. Finite Element Analysis of Porous Titanium Alloy Hip Stem to Evaluate the Biomechanical Performance During Walking and Stair Climbing. *J. Bionic Eng.* **2019**, *16*, 1103–1115.
12. Kuffner, B.H.B.; Capellato, P.; Ribeiro, L.M.S.; Sachs, D.; Silva, G. Production and Characterization of a 316L Stainless Steel/β-TCP Biocomposite Using the Functionally Graded Materials (FGMs) Technique for Dental and Orthopedic Applications. *Metals* **2021**, *11*(12), 1923.
13. Capitanu, L.; Florescu, V. New concept in durability improvement of hip total joint endoprostheses. *Acta Biomed. Bioeng.* **2014**, *16*, 75–82.
14. Andreaus, U.; Colloca, M. Mechanical behaviour of a prosthesized human femur: A comparative analysis between walking and stair climbing by using the finite element method. *Biophys. and Bioengin. Lett.* **2008**, *1*(3), 1–16.
15. Mukherjee, N.; Makem, J.E.; Fogg, H.J. A 3D Constrained Optimization Smoother to Post-process Quadrilateral Meshes for Body-in-white. *Procedia Eng.* **2016**, *163*, 262–275.
16. Nashrullah, M.; Clara Shinta, B.; Hidayat, M.I.P.; Purniawan, A.; Setiyorini, Y. Effect of Screw Diameter in Femoral Fracture Fixation Modeled by Finite Element Method. *IPTEK J. Proc. Ser.* **2016**, *0*, 173.
17. Behrens, B.-A.; Nolte, I.; Wefstaedt, P.; Stukenborg-Colsman, C.; Bouguecha, A. Numerical investigations on the strain-adaptive bone remodelling in the periprosthetic femur: Influence of the boundary conditions. *Biomed. Eng. Online* **2009**, *8*, 7.
18. Fox, M.J.; Scarvell, J.M.; Smith, P.N.; Kalyanasundaram, S.; Stachurski, Z.H. Lateral drill holes decrease strength of the femur: An observational study using finite element and experimental analyses. *J. Orthop. Surg.* **2013**, *8*, 29.
19. Zhang, Y.; Luo, Y. Femoral bone mineral density distribution is dominantly regulated by strain energy density in remodeling. *Biomed. Mater. Eng.* **2020**, *31*, 179–190.
20. Wang, L.; Guo, K.; He, K.; Zhu, H. Bone morphological feature extraction for customized bone plate design. *Sci. Rep.* **2021**, *11*, 15617.
21. Giorgio, I.; dell'Isola, F.; Andreaus, U.; Misra, A. An orthotropic continuum model with substructure evolution for describing bone remodeling: An interpretation of the primary mechanism behind Wolff's law. *Biomech. Model. Mechan.* **2023**, *22*, 2135–2152.
22. Geraldes, D.M.; Phillips, A.T. A comparative study of orthotropic and isotropic bone adaptation in the femur. *Int. J. Numer. Method Biomed. Eng.* **2014**, *30*(9), 873–889.

TECHNICAL UNIVERSITY OF KOŠICE
Faculty of Mechanical Engineering

Trends in the Development of Non-Pneumatic Tyres: A Review

Martina Hančinová [1,*], Erika Dubňanská [1], Barbara Schürger [1] and Róbert Huňady [2]

[1] Department of Applied Mechanics and Mechanical Engineering, Faculty of Mechanical Engineering, Technical University of Košice, Letná 9/B, 042 00 Košice, Slovakia; martina.hancinova@tuke.sk; erika.dubnanska@tuke.sk; barbara.schurger@tuke.sk.
[2] Department of Robotics, Faculty of Mechanical Engineering, Technical University of Ostrava, 17. listopadu 2172/15, 708 00 Ostrava – Poruba, Czechia; robert.hunady@vsb.cz
* Correspondence: martina.hancinova@tuke.sk

Abstract: Non-pneumatic tyres (NPTs), also known as airless tyres, represent an innovative advancement in tyre design by eliminating the need for air pressure for support. This unique structure offers several advantages over traditional pneumatic tyres, including a reduced risk of punctures, lower maintenance costs, and enhanced durability. These benefits make NPTs particularly attractive for applications where reliability and low upkeep are crucial. NPTs are designed to maintain performance and stability while also providing potential environmental benefits due to their longer lifespan and the possibility of using more sustainable materials. As manufacturers continue to explore and develop non-pneumatic solutions for a wide range of vehicles, these tyres are becoming increasingly popular, driven by the growing demand for durability, reduced maintenance, and the focus on enhancing overall vehicle performance. This review article delves into the various design innovations, and applications of NPTs across different industries, such as automotive, military, agriculture, and space exploration, highlighting the potential challenges and future directions in their development.

Keywords: non-pneumatic tyres; airless wheels; non-pneumatic wheel structures

1. Introduction

Current research in tyre safety focuses on two main areas: improving the properties of conventional tyres and developing non-pneumatic tyres that eliminate the risk of blowouts. This trend has become essential due to the increasing demand for safer and more reliable solutions [1].

Non-pneumatic tyres (NPTs) differ from conventional tyres in that they do not rely on compressed air, which eliminates the need for regular maintenance and air pressure monitoring. This significantly reduces the risk of punctures or blowouts and enhances vehicle safety [2]. NPTs also offer several advantages, such as reduced rolling resistance, enhanced safety, and better recyclability, contributing to their growing popularity. Their ability to withstand harsh conditions without blowing out makes them highly suitable for specialized applications [3, 4].

However, one of the drawbacks of NPTs is their relatively high cost. Additionally, since the pressure cannot be adjusted for different surfaces, their performance may be affected. The challenge of optimizing NPTs for high-speed operation remains a significant obstacle to their widespread application [5].

Despite these limitations, NPTs offer significant safety benefits and require minimal maintenance, simplifying usage and enhancing convenience for users. As a result, they are increasingly being adopted in sectors where high reliability and durability are paramount [6].

The Scopus database was used to search for relevant scientific articles on non-pneumatic tyres, following the methodology of Sardinha et al. [3]. The search included keywords such as "non AND pneumatic," "airless," "tire," and "wheel," with logical operators to ensure broad coverage.
After filtering the results based on specific keywords like "non-pneumatic tire/tyre" and "airless tire/tyre," a graphical representation (Figure 1) of the publication trends was created. The data show a steady increase in interest since 2005, with a significant rise in publications from 2014 onward. Despite fluctuations, the number of publications peaked at 32 in 2024, indicating a growing focus on non-pneumatic tyres in scientific research.

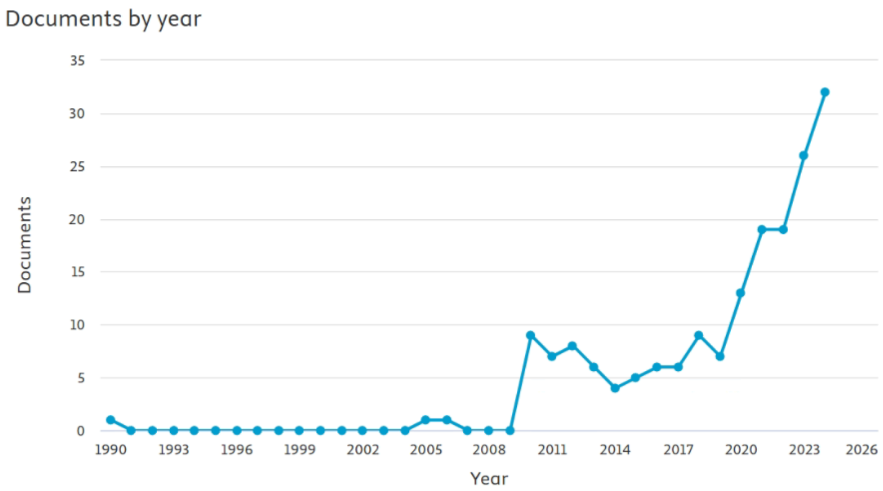

Figure 1. Number of published documents on non-pneumatic tyres over time [7].

2. Structure of non-pneumatic tyres

The non-pneumatic tyres design usually consists of a tread, a flexible supporting structure and a rim. The flexible support structure often includes flexible spokes or a closed structure repeating a honeycomb or other pattern. Figure 2 illustrates a typical construction of a non-pneumatic tyre.

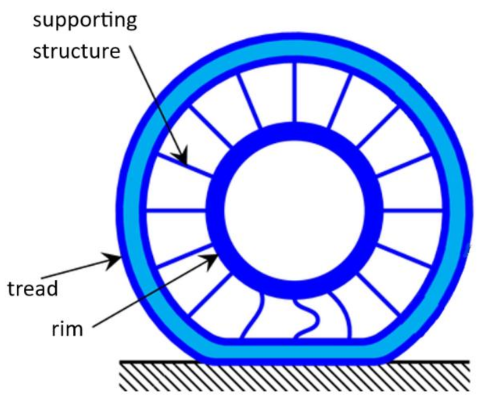

Figure 2. Non-pneumatic tyre construction [8].

Supporting structure distinguishes non-pneumatic tyres from pneumatic tyres (PTs). This component greatly affects the mechanical properties of NPTs. Unlike the uniform tyre pressure providing support in PTs, the elastic support structure in NPTs allows various design options [4]. The study [9] indicates that the structural parameters of the tyre significantly affect the cushioning and performance of the tyre. A well-designed support structure can enhance these performance metrics, making the tyre more effective in handling vibrations and lateral forces. The research shows that the flexible spoke design can lead to improved stability and recovery times when navigating obstacles [9].

Table 1 shows the classification of non-pneumatic tyres according to material composition, structure and possible applications.

Table 1. Classification of Non-Pneumatic Tyres [4,10,11].

Non-pneumatic tyres classification	Material	Rubber Polyurethane Metal fabric or chainmail tyre Alloys Composite
	Structure	Mechanical support Elastomer elastic support Solid type
	Application	Military Engineering Agricultural Other

Mechanical elastic support (Figure 3 a) usually uses support structures or hinge components made from metal [4]. The most frequently researched and widely used type is **elastomeric elastic support** type, which comes in various design variations, including the spoke type (Figure 3 b), honeycomb type, cellular type, and cross-supported type. The most elementary structural variant within the NPT fields is the **solid type** (Figure 3 c). Solid-type tyres are commonly used in construction and industrial applications, especially on forklifts, construction machinery, and material handling equipment.

a) Mechanical support [12] b) Elastomer elastic support [13] c) Solid type [14]

Figure 3. Types of non-pneumatic tyres structures.

3. Applications of non-pneumatic tyres

Non-pneumatic tyres represent a perspective alternative to traditional pneumatic tyres, offering specific advantages such as increased durability and reduced maintenance. As research and development in this area continue, NPTs are becoming increasingly relevant across a range of sectors, including military, engineering, agriculture, and space exploration. While challenges remain, particularly in areas such as high-speed performance and cost, ongoing advancements in materials and design suggest that NPTs will play an important role in the future of tyre technology. These benefits are already being realized in various industries, where NPTs are being applied to meet specific demands for performance and reliability in challenging environments.

a) [15] b) [15] c) [15]

d) [15] e) [16] f) [17]

Figure 4. Practical applications of non-pneumatic tyres.

Military Applications: NPTs enhance stability after obstacles and offer improved resistance to lateral forces compared to pneumatic tyres. They also reduce rolling resistance, leading to better fuel efficiency [9, 3]. These tyres are designed to endure high stresses and deformations, making them ideal for military vehicles operating in tough environments [18]. Michelin manufactures non-pneumatic radial tyres, used in applications such as Side by Sides and Quads (Figure 4 a) [15].

Engineering, Construction, and Agriculture: NPTs are commonly utilized in forklifts (Figure 4 b) and other construction machinery, where they provide durability and performance under heavy loads [3]. In agricultural equipment, their design reduces soil sinkage, making them ideal for environments that prioritize soil health [19]. In addition, they are used on lawn mowers (Figure 4 c).

Sports and Recreational and Autonomous Vehicles:

Non-pneumatic tyres are being explored for use in bicycles, golf carts, and all-terrain vehicles (Figure 4 d) [3]. They are also being tested in autonomous systems, like Goodyear's collaboration with Starship Technologies, which is developing non-pneumatic tyres for autonomous delivery robots (Figure 4 e) [15].

Space Applications: NPTs are considered for lunar and planetary exploration, as evidenced by NASA's development of non-pneumatic tyre technology and the iRings wheel concept for future missions (Figure 4 f) [10, 11].

4. Conclusion

Trends in the development of non-pneumatic tyres highlight their growing importance across various industries, particularly in areas demanding high durability, low maintenance costs, and enhanced performance. Ongoing research continues to refine their structural integrity and expand their range of applications.

Significant innovations have emerged in NPT design, particularly in improving supporting structures. New designs utilizing flexible components, such as mesh or segmented patterns, allow tyres to better conform to different surfaces, improving traction and comfort.

Significant innovations in NPT design, especially in supporting structures, have led to more flexible and adaptive solutions. New configurations, such as mesh or segmented patterns, improve traction and ride comfort by allowing the tyre to conform more effectively to different surfaces.

Another key trend is to improve NPT performance in extreme conditions, including high temperatures and challenging terrain. Possible advances in stability at high speeds could further expand their potential applications.

Lower maintenance costs and the elimination of the need for regular air pressure checks make them an attractive alternative in various applications. While non-pneumatic tyres present numerous advantages, challenges remain in terms of traction and ride comfort. Further research is needed to optimize these tyres for broader applications.

Acknowledgments: This work was supported by the Slovak Research and Development Agency under the grant project VEGA No. 1/0516/22, and by European Union under the REFRESH–Research Excellence for REgion Sustainability and High-tech Industries project number CZ.10.03.01/00/22_003/0000048 via the Operational Programme Just Transition and by the EU NextGenerationEU through the Recovery and Resilience Plan for Slovakia under the project No. 09I03-03-V05-00015.

Conflicts of Interest: The authors declare no conflict of interest.

References

1. Deng, Y. et al. A comprehensive review on non-pneumatic tyre research. *Materials & Design*, **2023,** *Volume 227.* Available online: *https://www.sciencedirect.com/science/article/pii/S0264127523001570* (accessed on 27 November 2024).
2. Hongxun, F et al. Comparative Analysis of Static and Dynamic Performance of Nonpneumatic Tire with Flexible Spoke Structure. *Strojniški vestnik – Journal of Mechanical Engineering*, **2020,** *Volume* 66, **458-466**. Available online: https://www.researchgate.net/publication/343200704_Comparative_Analysis_of_Static_and_Dynamic_Performance_of_Nonpneumatic_Tire_with_Flexible_Spoke_Structure (accessed on 27 November 2024).
3. Sardinha, M. de F. et al. Design, properties, and applications of non-pneumatic tires: A review. *Journal of Materials Design and Applications,* **2023,** *Vol. 237(11),* **2677-2697.** Available online: https://www.researchgate.net/publication/371250020_Design_properties_and_applications_of_non-pneumatic_tires_A_review (accessed on 28 November 2024).
4. Sun, M. et al. The Development of Processing Methods and Materials Used for Non-Pneumatic Tires: A Review. *Materials,* **2024**, *Vol. 17.* Available online: https://www.researchgate.net/publication/385995502_The_Development_of_Processing_Methods_and_Materials_Used_for_Non-Pneumatic_Tyres_A_Review (accessed on 29 November 2024).
5. Żmuda, M.; Jackowski, J.; Hryciow, Z. The Influence of Non-Pneumatic Tyre Structure on its Operational Properties. *International Journal of Automotive and Mechanical Engineering*, **2020**. Available online: https://www.researchgate.net/publication/344543055_The_Influence_of_Non-Pneumatic_Tyre_Structure_on_its_Operational_Properties (accessed on 27 November 2024).
6. Rugsaj, R.; Suvanjumrat, Ch. Dynamic Finite Element Analysis of Rolling Non-Pneumatic Tire. *International Journal of Automotive Technology*, **2021**, *Vol.* 22, 1011-1022. Available online: https://www.researchgate.net/publication/353442947_Dynamic_Finite_Element_Analysis_of_Rolling_Non-Pneumatic_Tire (accessed on 2 December 2024).
7. Scopus. Custom graph generated based on user preferences. Available online: https://www.scopus.com (accessed on 11 December 2024).
8. Maharaj,Y.; James, K. A. Metamaterial topology optimization of non-pneumatic tires with stress and buckling constraints. *International Journal for Numerical Methods in Engineering,* **2019**, *Vol. 121*, 1410-1439. Available online: https://www.researchgate.net/publication/337279820_Metamaterial_topology_optimization_of_non-pneumatic_tires_with_stress_and_buckling_constraints (accessed on 2 December 2024).
9. Chen, K. et al. Key dynamic performance analysis of flexible spoke non-pneumatic tire for matched unmanned ground vehicles. *Proceedings of the Institution of Mechanical Engineers Part D Journal of Automobile Engineering*, **2024**. Available online: https://www.researchgate.net/publication/377494140_Key_dynamic_performance_analysis_of_flexible_spoke_non-pneumatic_tire_for_matched_unmanned_ground_vehicles (accessed on 6 December 2024).

10. Radziszewski, P. et al. iRings Development of a Wheel Prototype Concept for Lunar Mobility. *Can. Aeronaut. Space J.*, **2011**, *Vol. 57*, No. 1, 1-11. Available online: https://www.researchgate.net/publication/235655192_iRings_Development_of_a_Wheel_Prototype_Concept_for_Lunar_Mobility (accessed on 2 December 2024).
11. Asnani, V.; Delap, D.; Creager, C. The Development of Wheels for the Lunar Roving Vehicle. U.S. Patent No. 7,841,383, **2009**. NASA. Available online: https://ntrs.nasa.gov/citations/20100000019 (accessed on 11 December 2024).
12. Donohue, D. Resilient wheel. U.S. Patent No. 9,527,344 B1. **2016** Available online: https://patents.google.com/patent/US9527344B1/en (accessed on 6 December 2024).
13. Deng, Y. et al. Numerical study of steady-state dynamic characteristic of non-pneumatic tire with local structural damage. *European Journal of Mechanics - A/Solids,* **2024,** *Volume 108 < https://www.sciencedirect.com/science/article/pii/S0997753824002080>*
14. Evolution Wheel. What Are the Different Types of Skid Steer Tires. Available online: https://www.evolutionwheel.com/what-are-the-different-types-of-skid-steer-tires (accessed on 5 December 2024).
15. Michelin. Michelin airless tyres. Available online: https://business.michelin.co.uk/tyre/michelin-airless-tyres (accessed on 3 December 2024). Available online: https://business.michelin.co.uk/tyre/michelin-airless-tyres (accessed on 5 December 2024).
16. Goodyear. Goodyear extends airless tire technology to autonomous Starship robots. Available online: https://news.goodyear.eu/goodyear-extends-airless-tire-technology-to-autonomous-starship-robots/ (accessed on 3 December 2024).
17. NASA. NASA readies Perseverance Mars rover's earthly twin. NASA, **2020**. Available online: https://www.nasa.gov/missions/mars-2020-perseverance/nasa-readies-perseverance-mars-rovers-earthly-twin/ (accessed on 3 December 2024).
18. Senanayake, Ch. D. et al. Performance Comparison of Solid Tires and Non-Pneumatic Tires Using Finite Element Method: Application to Military Vehicles. Proceedings of the Holistic Approach to National Growth and Security, 13th International Research Conference, General Sir John Kotelawala Defence University, Sri Lanka, 16.-16.10.2020. General Sir John Kotelawala Defence University: Ratmalana, Sri Lanka. Available online: https://www.researchgate.net/publication/348741223_Performance_Comparison_of_Solid_Tires_and_Non-Pneumatic_Tires_Using_Finite_Element_Method_Application_to_Military_Vehicles (accessed on 3 December 2024).
19. Phromjan, J.; Suvanjumrat, Ch. Non-pneumatic tire with curved isolated spokes for agricultural machinery in agricultural fields: Empirical and numerical study. *Heliyon*, **2023**, *Vol. 9*. Available online: https://www.sciencedirect.com/science/article/pii/S2405844023061923 (accessed on 6 December 2024).

Optimization of a Heat Exchanger for Hydrogen Storage Using AI-Driven Generative Design and Additive Manufacturing

Šimon Hudák [1,*], Marián Lázár [1]

[1] Technical University of Košice, Faculty of Mechanical Engineering, Department of Energy Engineering, Vysokoškolská 4, 042 00 Košice, Slovakia; simon.hudak@student.tuke.sk; marian.lazar@tuke.sk
* Correspondence: simon.hudak@student.tuke.sk

Abstract: Optimizing heat exchangers in metal hydride tanks for hydrogen storage is essential for improving thermal management in metal hydride systems. This study integrates AI-driven generative design and additive manufacturing to enhance heat exchanger performance. Using nTop software, complex geometries like triply periodic minimal surfaces (TPMS) are generated, particularly gyroids. Direct metal laser sintering (DMLS) fabricates high-performance heat exchangers, improving thermal conductivity while minimizing material waste. Simulation-driven validation in ANSYS CFX confirms enhanced heat dissipation and hydrogen absorption. Results indicate AI-driven design, combined with advanced manufacturing, enables efficient, scalable, and sustainable heat exchangers. This approach optimizes metal hydride hydrogen storage, advancing energy-efficient solutions.

Keywords: Generative Design; Additive Manufacturing; Heat Exchangers; Hydrogen Storage; AI Optimization

1. Introduction

Hydrogen is a clean energy carrier with high energy density and minimal environmental impact, making it a key candidate for decarbonizing energy systems. Metal hydride storage tanks play a crucial role due to their ability to safely store hydrogen at moderate temperatures and pressures while offering high volumetric densities. These systems are particularly suitable for portable, stationary, and mobile applications, enabling efficient hydrogen storage and usage [1–4].

Efficient heat dissipation is crucial in hydrogen storage, as poor thermal management slows kinetics Optimized designs like cooling tubes and fins stabilize temperatures and enhance hydrogen uptake. Proper heat control ensures longevity and efficiency [2,5].

Heat exchangers installed in MH tanks for hydrogen storage include cooling tubes and fins, each enhancing heat transfer efficiency. However, limitations such as the low thermal conductivity of metal hydrides, uneven heat distribution, and system complexity hinder performance. Advanced geometries like triply periodic minimal surfaces (TPMS) show promise but require further optimization [2].

Recent advancements in artificial intelligence (AI) have significantly impacted additive manufacturing (AM), particularly through AI-driven generative design and enhanced production processes. Generative design utilizes AI algorithms to explore a vast array of design possibilities, optimizing structures for weight reduction and strength. This approach has been instrumental in industries such as aerospace and automotive, where minimizing weight is crucial for performance [6].

AI-driven generative design tools, such as nTopology, enable the automatic creation and evaluation of various heat exchanger intensifier designs for hydrogen storage systems. These tools optimize structures for thermal performance, material efficiency, and manufacturability, leading to more efficient and compact heat exchangers. By leveraging advanced manufacturing techniques like additive manufacturing, complex geometries optimized through generative design can be realized, enhancing heat transfer efficiency and meeting specific performance requirements [7-8].

The objective of this article is to present a novel methodology for the design and optimization of a heat exchanger. Specifically, it focuses on utilizing AI-driven generative design in nTop software for enhanced modeling, coupled with additive manufacturing techniques for production. By leveraging advanced computational tools and 3D printing technologies, the article aims to demonstrate how innovative processes can lead to more efficient, sustainable, and scalable heat exchangers.

The integration of these methodologies highlights the potential for achieving superior thermal performance, reduced material waste, and faster prototyping cycles compared to traditional manufacturing techniques.

2. Materials and Methods

Traditional CAD software, such as SolidWorks, Autodesk Inventor, and CATIA, is primarily designed for parametric and direct modeling, making it less efficient when handling complex lattice structures and highly optimized geometries required for advanced heat exchangers. Unlike these tools, nTopology utilizes implicit modeling, which allows for real-time modifications without the computational burden of traditional boundary representations. This makes it particularly advantageous for designing triply periodic minimal surface (TPMS) structures, where conventional CAD tools struggle with mesh complexity and processing speed. Additionally, nTopology seamlessly integrates with simulation-driven workflows, enabling **topology optimization and direct export for additive manufacturing (DMLS)** without the need for extensive re-meshing or manual adjustments.

2.1 Generative Design in nTopology

Software Selection: nTopology's generative design capabilities enable the efficient creation and optimization of complex heat exchanger (HE) geometries. Its advanced algorithms allow for iterative design adjustments tailored to user-defined thermal and mechanical constraints.

Design Workflow: The design objective is to maintain the same dimensions as those used in an aluminum heat transfer intensifier, where an asymmetrical star shape, consisting of 10 V-shaped profiles joined longitudinally by welding, was implemented. Additive manufacturing is leveraged to enhance heat transfer efficiency.

Parameterization: Lattice structures are tailored for heat transfer optimization by employing variable densities. Using parametric tools, essential variables—such as lattice structures (e.g., TPMS configurations like gyroid or Schwarz P surfaces), wall thickness, and dimensions—are defined to meet the functional needs of heat exchangers.

Lattice Generation: Generative design facilitates the creation of TPMS structures like gyroids. The porosity and density of these structures are adjusted to achieve an optimal balance between structural strength and thermal performance.

Lattice Configurations as Figure 1:

- Periodic Lattice: Designed with a TPMS unit cell.
- Unit Cell Type: Walled gyroid structure.
- Orientation: UVW axis.
- Cell Mapping: Cylindrical configuration for efficient heat distribution.

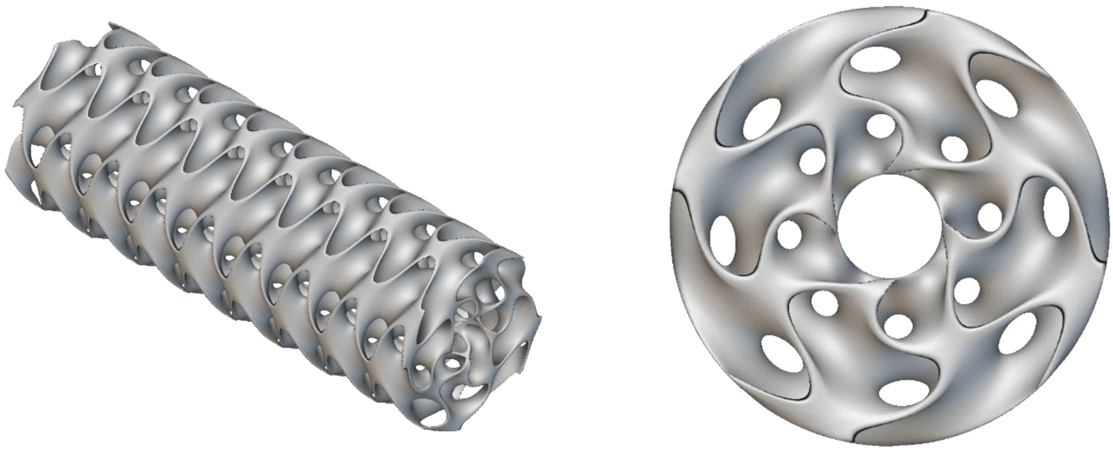

(**a**) (**b**)

Figure 1. TPMS gyroid structures designed with nTop software (**a**) Isometric view of a TPMS gyroid structure; (**b**) Front view of a TPMS gyroid structure.

2.2 Materials: Selection criteria for materials with high thermal conductivity and manufacturability.

- Aluminum (Al): Chosen for high thermal conductivity and lightweight properties.
- It is possible to manufacture it using DMLS (Direct Metal Laser Sintering).

This addition emphasizes the capability of DMLS as a manufacturing method for aluminum structures, aligning with the focus on material selection and advanced manufacturing [8].

2.3 Additive Manufacturing Process

Additive manufacturing, especially Direct Metal Laser Sintering (DMLS), is a technology that fabricates components layer by layer using metal powders. It allows for precise production of complex internal geometries that traditional methods cannot achieve. This makes it particularly suitable for applications requiring intricate designs, offering high accuracy in both internal and external structures [8]. Materials like aluminum are often used in metal hydride hydrogen storage systems because of their excellent thermal conductivity and lightweight properties. These materials are ideal for heat exchangers, as they enhance thermal management and improve overall efficiency [3]. The process can also optimize the direction of printing to reduce deformation and minimize the need for supports. Furthermore, advanced designs, such as gyroid and triply periodic minimal surface (TPMS) structures, maximize surface area and improve heat exchange, which is especially valuable in hydrogen storage systems [3].

Unlike traditional heat exchangers, which involve multiple joints, welds, and connections, components manufactured using DMLS can be built as single, monolithic pieces. This eliminates inefficiencies like pressure loss and increases the durability of the final product [1]. However, additive manufacturing does have its challenges. The primary drawback is the higher production cost compared to traditional techniques. Nonetheless, these costs are often offset by reduced material waste, enhanced design capabilities, and superior performance. Overall, the ability to produce highly intricate and optimized components with reduced waste makes additive manufacturing a promising choice for modern applications.

2.4 Validation and Setup of Simulation for Heat Transfer Efficiency in Intensifiers

The heat transfer generated within the core of the hydrogen storage tank was modeled using finite volume methods in ANSYS CFX. The simulation model includes four primary domains: the metal hydride alloy, the primary storage tank, the cooling fluid, and the heat transfer intensifier, as shown in Figure 2. Each domain is separately defined in the simulation, with an independent mesh created for every component. The overall model comprises approximately one million volumetric elements, optimized to maintain computational efficiency. To reduce computational demand, the model represents a quarter-section of the tank using symmetry functions. The water flow around the storage tank is set to a velocity of 1 cm/s, with an inlet temperature of 20°C, while the simulation operates in a steady-state condition.

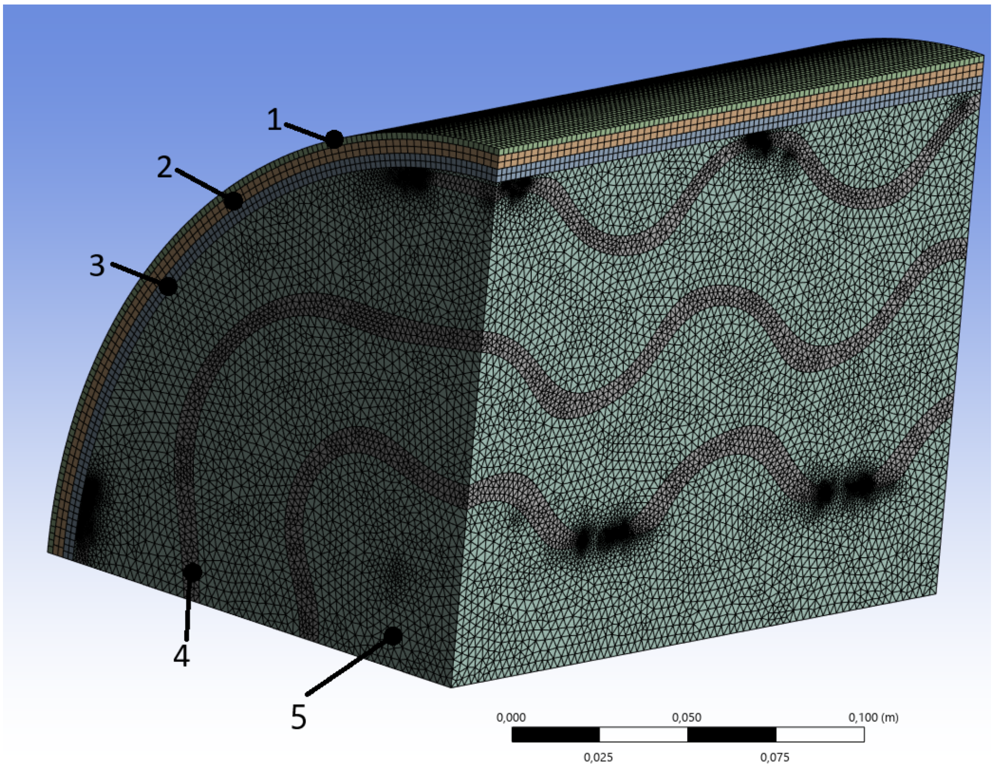

Figure 2. The defined tank domains and material assignments are displayed: 1. External Shell: Constructed from stainless steel 316L, ensuring structural stability. 2. Inner Pressure Vessel: Similarly composed of stainless steel 316L. 3. Cooling Medium: Water flowing between the outer shell and the inner pressure vessel. 4. Heat Transfer Intensifier: Integrated within the tank to stabilize thermal gradients and enhance heat dissipation. 5. Metal Hydride Alloy: A TiZnMnVFe-based composite with specified thermal properties.

Boundary Conditions for the Simulation:
- Heat transfer between primary tank and cooling fluid: 975.572 $W \cdot m^{-2} \cdot K^{-1}$.
- Internal heat generation intensity: 435.16 $kW \cdot m^{-3}$.
- Initial temperature of the metal hydride: 20°C.
- Filling time of the tank: 2400 seconds.

Material Properties of the Metal Hydride Alloy:
- Thermal conductivity: 1 $W \cdot m^{-1} \cdot K^{-1}$.
- Bulk density: 3600 $kg \cdot m^{-3}$.
- Molar mass: 62.55 $kg \cdot kmol^{-1}$.
- Specific heat capacity: 430 $J \cdot kg^{-1} \cdot K^{-1}$.

The heat transfer across these interfaces is managed using the automated "HEAT FLUX" settings in ANSYS CFX. By incorporating these configurations, the simulation accurately captures the dynamic heat exchange processes, enabling precise evaluation of intensifier efficiency.

3. Results and Discussion

The thermal behavior of the hydrogen storage tank in ANSYS simulations reveals critical aspects of heat transfer dynamics during hydrogen absorption. Notably, in the tank core, an increased temperature is observed due to the lack of elements specifically designed for heat dissipation. This highlights the significant thermal load generated by the exothermic reaction of hydrogen absorption, requiring efficient thermal management solutions. If we compare the results of the thermal profile in ANSYS CFX in Figures 3 and 4, we observe a temperature difference of 15 degrees.

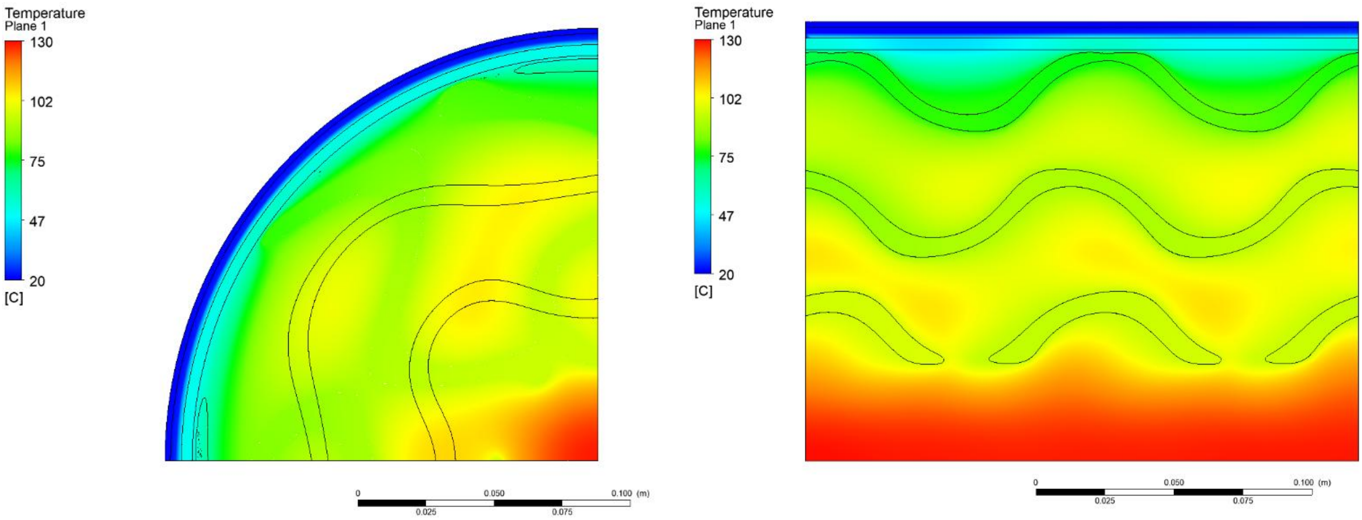

(**a**) (**b**)

Figure 3. Newly designed intensifier thermal profile in ANSYS CFX: (**a**) The model represents a quarter-section radial view from the top; (**b**) The model represents a quarter-section axial view from the right.

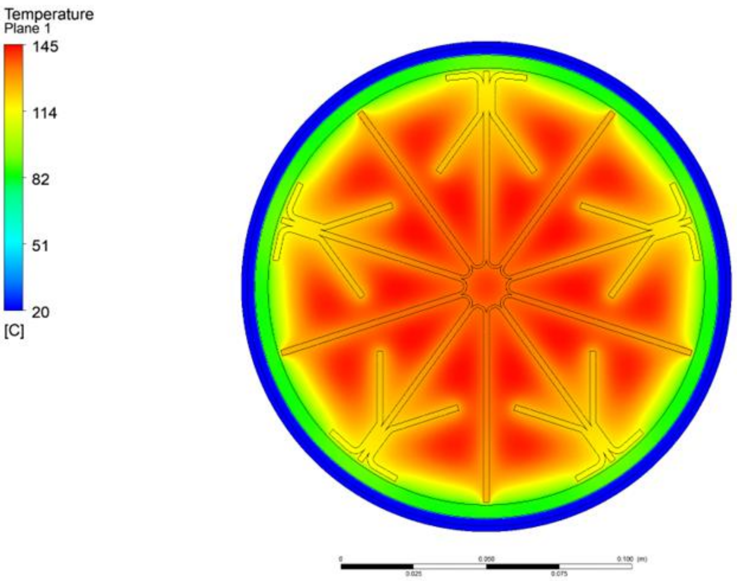

Figure 4. Figure 3 shows the cross-section of the intensifier geometry in the MNTZV-159 hydrogen storage tank with straight blades and secondary blades.

The introduction of a newly designed intensifier significantly impacts the thermal profile. Regions equipped with these elements exhibit a noticeable temperature reduction.

The intensifier's geometry facilitates a more uniform heat distribution across the tank-cross-section, as confirmed by the simulation outcomes. This uniform thermal field minimizes hot spots that could limit the hydrogen absorption process, which is in accordance with the PCI curve for the respective alloy.

Furthermore, the optimized thermal management system achieves a lower overall operating temperature compared to the original lamellar intensifier design. This enhancement not only shortens hydrogen absorption times by maintaining the desired kinetic rates but also improves the reactor's operational stability.

The integration of these intensifiers, crafted from high thermal conductivity materials such as aluminum alloys, ensures effective heat conduction from the core to the periphery, where active cooling elements dissipate the heat. This approach underscores the necessity of combining passive and active cooling strategies for optimal performance in metal hydride hydrogen storage systems..

4. Conclusions

This study demonstrated the potential of integrating AI-driven generative design and additive manufacturing for optimizing heat exchangers used in metal hydride hydrogen storage systems. By leveraging advanced computational tools such as nTopology and manufacturing techniques like Direct Metal Laser Sintering (DMLS), it was possible to design complex geometries, specifically triply periodic minimal surface (TPMS) gyroid structures, which significantly enhance thermal performance while minimizing material consumption.

The numerical simulations conducted in ANSYS CFX validated the improved heat dissipation capabilities of the designed structures, ensuring better thermal management during hydrogen absorption. The optimized geometry not only improves heat transfer efficiency but also reduces refueling time, contributing to the overall scalability and sustainability of metal hydride-based hydrogen storage systems.

Moreover, the integration of AI-driven design workflows opens new avenues for tailoring heat exchanger geometries based on specific operational requirements, further enhancing system performance. The proposed methodology paves the way for developing next-generation hydrogen storage systems that are lightweight, compact, and highly efficient, making them viable for industrial and energy applications aimed at supporting the global transition towards clean energy.

Future research should focus on experimental validation of the proposed structures, exploring alternative high-conductivity materials, and refining manufacturing processes to further improve system durability and economic feasibility.

Acknowledgments: This work was supported by the Slovak Research and Development Agency under the Contract no. APVV-23-0266, by the Slovak Research and Development Agency under the Contract no. APVV-21-0274 and with the financial support from the VEGA granting agency within the Project No. 1/0224/23.

References

1. Cui, Y.; Zeng, X.; Xiao, J.; Kou, H. The comprehensive review for development of heat exchanger configuration design in metal hydride bed. *Int. J. Hydrogen Energy* **2022**, *47*, 2461–2490. https://doi.org/10.1016/j.ijhydene.2021.10.172.
2. Kukkapalli, V.K.; Kim, S.; Thomas, S.A. Thermal Management Techniques in Metal Hydrides for Hydrogen Storage Applications: A Review. *Energies* **2023**, *16*, 3444. https://doi.org/10.3390/en16083444.
3. Lesmana, L.A.; Aziz, M. Triply periodic minimal surface gyroid structure as effective metal hydride hydrogen storage reactor: Experimental study. *Thermal Science and Engineering Progress* **2023**, *42*, 101903. https://doi.org/10.1016/j.tsep.2023.101903.
4. Cui, Y.; Zeng, X.; Xiao, J.; Kou, H. The comprehensive review for development of heat exchanger configuration design in metal hydride bed. *International Journal of Hydrogen Energy* **2022**, *47*, 2461–2490. https://doi.org/10.1016/j.ijhydene.2021.10.172.
5. Dong, Z.; Wang, Y.; Wu, H.; Zhang, X.; Sun, Y.; Li, Y.; Chang, J.; He, Z.; Hong, J. A design methodology of large-scale metal hydride reactor based on schematization for hydrogen storage. *Journal of Energy Storage* **2022**, *49*, 104047. https://doi.org/10.1016/j.est.2022.104047.
6. *How AI is Transforming Additive Manufacturing*. Neural Concept, 2023. Link.

7. Leary, M.; Merli, L.; Torti, F.; Mazur, M.; Brandt, M. Optimal design of heat exchangers: Topology optimization, lattice-based design and MANUFACturability. *Inventions* **2021**, *6*, 60.
8. Anwajler, B. Potential of 3D Printing for Heat Exchanger Heat Transfer Optimization—Sustainability Perspective. *Inventions* **2024**, *9*, 60. https://doi.org/10.3390/inventions9030060.

TECHNICAL UNIVERSITY OF KOŠICE
Faculty of Mechanical Engineering

Influence of microbiological aspects and dust environment on quality in the automotive industry

Róbert Jánošík [1,*] , Tomáš Gazda [1]

[1] Technical University of Košice, Faculty of Mechanical Engineering, Department of Quality, Safety, and Environment, Letná 1/9, 042 00 Košice; robert.janosik@student.tuke.sk; tomas.gazda@student.tuke.sk
* Correspondence: robert.janosik@student.tuke.sk; janosik@cleanlinessaudit.com; Tel.: +421 911 868 200

Abstract: Microbiology and Technical cleanliness in industry is a growing problem due to the growing requirements for safety and reliability of innovative technologies and components associated with the goal of achieving the highest autonomy of machines and devices in new sectors in the electronic, automotive and aerospace industries. Several methods have been defined for the control of contamination as well as microbiology, but none is universal enough to eliminate the risks associated with the danger of failure of finished products. The goal is to eliminate risks that could result in the failure of machines and equipment with fatal consequences for a person or lead to malfunctions and possible safety risks for consumers and users. By using the right combination of methodology to detect unwanted contamination and microbiological factors, the costs of manufacturing errors and defects can be effectively reduced and potential risks of failure can be significantly eliminated. By using the right methodology to detect unwanted contamination, the cost of manufacturing errors and defects can be effectively reduced and potential risks of failure can be significantly eliminated. However, what the correct methodology for contamination detection is questionable and a lot depends on what we want to achieve with proper detection. So what it is the goal of the analysis of clean production and analysis of the impacts of microbiological aspects in industry?

Keywords: Microbiology, Microbiological aspects, Technical cleanliness in processes, Dust particles, Automotive industry, Clean environment, Clean environment verification, Clean room, Clean zone.

1. Introduction

The automotive industry is one of the most technologically advanced industries, which places high demands on the quality and reliability of its products. In addition to the usual technical and material challenges, this industry also has to face environmental factors such as microbiological risks and dustiness of the environment [1, 2]. These factors can affect not only the production quality, but also the long-term functionality of automotive parts. In this article, we look at how the microbiological and dust environment affects the manufacturing process and final products, and what measures can be taken to minimize their impact.

Microbiological aspects and their impact

The following questions should be asked at the beginning:

What are the risks of microbiology in the industry?

How can microbiological aspects negatively affect the reliability and functionality of equipment?

What impacts can microbiology have in the production of components in the automotive industry?

Due to the increasing demands on the autonomy of manufactured machines and equipment, innovative technology, safety, quality and reliability, it is necessary to perceive any potential risks and the possible occurrence of a dangerous event. It is also important to assess the causes of possible failure already at the conception of the development of the final product, as well as the risks of production conditions. In addition to the standard requirements for a clean working environment, the organization of workplaces and the minimization of waste, requirements for technical cleanliness are being pushed to the fore these days. Technical cleanliness includes requirements for minimizing product contamination as well as minimizing contamination in the work environment [3, 4]. In the production and assembly of specific components, rules for the regulation of clean environments and clean zones are defined today. These rules address contamination by solid particles and fibers with the aim of minimizing conductive and hard particles, which pose a major risk mainly to electromobility. Less emphasis is placed on environmental and component contamination through microbiological aspects [5].

2. Materials and Methods

Microbiological contamination in the car industry

Microorganisms such as bacteria, molds and fungi may be present at various stages of the production process. These microorganisms can damage materials used in automobiles, such as polymers, textiles or electronic components. For example, mold can degrade plastic parts, leading to their fragility and loss of functionality. Bacteria, in turn, can cause corrosion of metal parts. A major risk is the formation of biofilm on the surface of the components.

Biofilms on the surfaces

One of the main problems of microbiological contamination is the formation of biofilms. Biofilms are colonies of microorganisms that bind to the surfaces of materials and form a protective layer [6]. This layer not only affects the aesthetic appearance of the parts, but can also prevent proper functionality, for example with sensors or ventilation systems. Among the effective measures for biofilm control is the sampling and inspection of the surface of work surfaces and parts by means of special touch plates. As can be seen in Figure 1, a biofilm sample is taken from the surface using special plates. After cultivation, the colonies of microorganisms are evaluated and the strains found are identified. With the correct identification, it is possible to proceed with effective decontamination in accordance with the applicable hygiene standards. As can be seen in Figure 1, the biofilm is removed from the surface through approved procedures. After cultivation, which is shown in Figure 2, the colonies of microorganisms are evaluated and the strain is identified. With the correct identification, it is possible to proceed with effective decontamination in accordance with the applicable hygiene standards.

Figure 1. Taking a contamination sample from the surface of the components.

Figure 2. Cultivation of samples of microbiological contamination from the surface of components.

Hygiene standards and their significance in industry

Automotive plants must meet strict hygiene standards to prevent microbiological contamination. It is not only a question of microbiological contamination from the point of view of hygiene and their effects on humans, but also of requirements for the prevention of microbiological contamination of processes and products. For example, using disinfectants, regularly cleaning and sterilizing instruments, and controlling humidity in the environment help minimize the growth of microorganisms. At the same time, it is also necessary to monitor dustiness. Solid microparticles are often carriers of bacteria and mold. Figure 3 visualizes the measurement of the air by means of an aeroscope.

Figure 3. Sampling of microbiological contamination using an aeroscope.

Impact of dusty environment - Dust as an invisible enemy

Dustiness is among the factors that significantly affect the quality of production in the automotive industry. Dust can come from the external environment, but also from production processes, such as machining, grinding or pressing. Dust particles can cause contamination of surfaces, mechanical wear of machines and even damage to sensitive electronic components. In order to minimize dust in processes and on products, the Technical Cleanliness system is introduced in the automotive industry with the aim of eliminating the occurrence of harmful dust particles and fibers in the work area [7]. The production of components and assembly must be in controlled conditions with regard to processes, logistics, the surrounding environment and employees who pose the greatest risk due to the introduction of contamination. With a set of measures and controls, we try to bring dust and microbiological contamination below an acceptable level of risk in order to reduce the impact on non-delivery and increase the quality, safety and reliability of finished products. Filtration and dust reduction form a combination of effective prevention against the deterioration of production due to dust particles and microbiological aspects. One of the most effective ways to prevent the negative effects of a dusty environment is the use of modern filter systems. High-efficiency filters can capture dust microparticles and prevent them from spreading in the production area. At the same time, they can also be effective against microbiological threats.

In addition, it is important to ensure regular maintenance of production areas and use antistatic materials to reduce dust adhesion.

So, what is the interaction of microbiology and dust and what is their impact?

Microbiological and dust factors can have a synergistic effect on the degradation of materials. For example, the presence of dust can increase the humidity on surfaces, which promotes the growth of microorganisms. Conversely, microbiological activity can cause dust to break down into chemical compounds that subsequently react with materials and accelerate their wear [8]. At the same time, employees working in a dusty and microbiologically contaminated environment may face health problems, such as respiratory diseases or allergic reactions. This leads to reduced productivity and increased healthcare costs. When predicting risks, it is necessary to set measures to minimize the impact of dust and microbiology. One of the solutions is the introduction of technological innovations. The automotive industry uses advanced technologies to minimize microbiological and dust pollution. These include, for example, robotic systems that work in a controlled environment, or sensors monitoring air quality in real time, see Figure 4. Another effective measure is regular employee training. Proper training of workers in the field of hygiene and maintenance is crucial. Employees should be familiar with contamination prevention procedures and the use of protective equipment. Last but not least, research and development in the field of technical cleanliness and microbiology controls in the industrial area is important.

Figure 4. Robotic systems that work in a controlled environment

Investments in research into new materials resistant to microbiological and dust factors are another important step. For example, antimicrobial coatings or dust-repellent materials can significantly improve the quality and durability of products.

3. Results

The influence of microbiological aspects and the dusty environment on quality in the automotive industry cannot be underestimated. These factors have the potential to affect not only the production process, but also customer satisfaction with the final products. Therefore, it is necessary to pay increased attention to the prevention and control of these risks. The combination of technological innovations, correct work procedures and continuous research enables the automotive industry to maintain high quality standards even in challenging conditions. If we want to prevent disagreements and have the production of products in new, technologically demanding processes under control, it is necessary to introduce effective tools for monitoring the status of processes. Therefore, it is necessary to invest in the development of new technologies and materials that help to eliminate the occurrence of microbiological aspects and dustiness in production processes and in this way to prevent production reliability.

4. Discussion

The issue of technical cleanliness and the effects of microbiology on the quality and reliability of components produced in the automotive industry is a relatively new topic, it is still necessary to leave room for discussion in a wider context. The decisive factor will be the provision of resources and cooperation in the development and research of new materials and technologies, which will contribute to the effective elimination of the undesirable effects of dust and microbiology in clean operations in order to ensure production without losses and complaints. It will also be necessary to provide companies with the necessary information about the possible consequences of not ensuring the specifications related to compliance with the parameters of a clean environment and Technical cleanliness. The risks related to the uncontrolled contamination of the space as well as the components have not only an economic dimension, but also a safety dimension, where the biggest risk is system failure with fatal consequences. It is necessary to give this issue enough space for professional discussion.

Conflicts of Interest: The authors declare no conflict of interest. The funders had no role in the design of the study; in the collection, analyses, or interpretation of data; in the writing of the manuscript, or in the decision to publish the results.

References

1. Szulc, J., et al. Microbiological and toxicological hazard assessment in a waste sorting plant and proper respiratory protection. *Journal of Environmental Management*, **2022**, *303*: 114257.
2. Gutarowska, B., et al. Dust at various workplaces—Microbiological and toxicological threats. *International Journal of Environmental Research and Public Health*, **2018**, *15.5*: 877.
3. Horrevorts, M.; Van Ophem, J.; Terpstra, P. Impact of cleanliness on the productivity of employees. *Facilities*, **2017**, *Vol. 36* No. 9/10, pp. 442-459.
4. Faber, J.; Brodzik, K.; Nycz, M. Understanding technical cleanliness: importance, assessment, maintenance. *Combustion Engines*, **2021**, 60.
5. Weihrich I.; Krickl B. Licensed training on the Specific Requirements of Technical Cleanliness, 2022, Písek (Czech Republic)
6. Weihrich I.; Krickl B. Lecture on the issue of microbiology vs. Technical cleanliness, 2024, Písek (Czech Republic)
7. Weihrich I.; Krickl B. Licensed training Technical cleanliness auditor, 2021, Košice (Slovakia)
8. Weihrich I. Output from the Technical Cleanliness Audit, 2024, Žebrák (Czech Republic)

TECHNICAL UNIVERSITY OF KOŠICE
Faculty of Mechanical Engineering

Design and construction of the pneumatic torsional vibration tuner

Matúš Kačír [1,*], Lucia Žuľová [1], Robert Grega[1], Matej Urbanský[1]

[1] Technical University of Košice, Faculty of Mechanical Engineering, Department of Engineering for Design of Machine and Transport Equipment, matus.kacir@tuke.sk; lucia.zulova@tuke.sk; robert.grega@tuke.sk; matej.urbansky@tuke.sk
* Correspondence: matus.kacir@tuke.sk

Abstract: Our department has been researching pneumatic torsional vibration tuners for a long time. The aim of the research is to minimize torsional vibrations in mechanical systems that can cause failure. We tested the proposed shape of the two-mass flywheel by static load test to determine the degree of linearity of the torsional angle with respect to the torque. An important part of the new prototype is the significant increase in compression volume. The main aim is to achieve the most linear characteristic of the twist angle with respect to the torque.

Keywords: dual mass flywheel, torsional vibration, elimination of torsional vibration

1. Introduction

Torsional vibration tuners are machine components designed for the flexible transmission of load torque in rotating power transmission equipment. Their main task is to eliminate dangerous torsional vibrations and vibrations in systems. It is therefore essential to carefully select a tuner with the specific properties for the specific application, especially with optimum torsional stiffness, to avoid serious failures [1-5].

The flexible elements of these tuners are made of different materials such as rubber, plastic or metal. Rubber and plastic components fatigue and age over long periods of use, while metal components are subject to wear and tear. This gradually changes the properties of the coupling, which adversely affects its functionality in a torsional oscillating mechanical system [6-7].

These disadvantages can be eliminated by using pneumatic spring elements such as air springs. In this case, the elastic torque transmission is provided by a compressed gaseous medium that is not subject to fatigue or ageing. The main advantage of pneumatic tuners is the possibility of controlling the torsional stiffness by adjusting the pressure in the pneumatic elements, which allows the properties to be better adapted to the actual operating conditions of the mechanical system [8-9].

In our department we are devoted to the development, research and implementation of torsional vibration tuners in mechanical systems, where the main aim is to ensure continuous tuning of these systems during their operation, using torsional vibration tuners as active elements for the control of vibrations generated by torsional vibrations. Extensive research in the field of pneumatic torsional vibration tuners contributes to their continuous improvement. In the framework of this work, a new pneumatic dual-mass flywheel (PDMF), which belongs to the torsional vibration tuners, has been designed and manufactured. The aim of this paper is to introduce this innovative PDMF and describe its shape and properties.

2. Pneumatic dual mass flywheel

The pneumatic dual mass flywheel (Fig.1) with an outer diameter of 260 mm and a weight of 20.8 kg consists of a primary clamping plate (1), a secondary clamping plate (2), four pneumatic elastic components (3), four triangular-shaped fasteners (4), eight flanges (5) and a pressure control inlet (6).

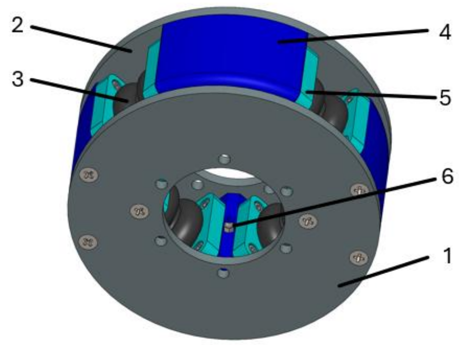

Figure 1. PDMF construction.

The supposed advantage lies in the possible change of stiffness by changing the pressure of the gaseous medium in the pneumatic bags and cavities of the fasteners. Fig. 2 shows the cavities that are formed in the triangular-shaped fasteners (4) in Fig. 1, which are designed to increase the compression volume. The assumed increase of the compression volume of the pneumatic elastic elements is supposed to be manifested by the linearization of the PDMF characteristics. At the same time, these elements serve as the mass generating moment of inertia of the PDMF.

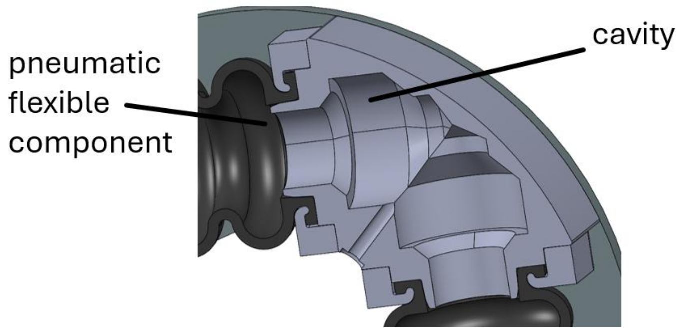

Figure 2. Space for gaseous medium.

The proposed internal arrangement of the PDMF (Fig. 3) shows a simple interconnection of the flexible elements without the use of hoses. From the figure can be seen that the pneumatic elements are arranged tangentially. The elastic elements are connected by means of triangular-shaped fasteners. The connecting elements (1) are attached to the primary clamping plate and the connecting elements (2) are attached to the secondary clamping plate.

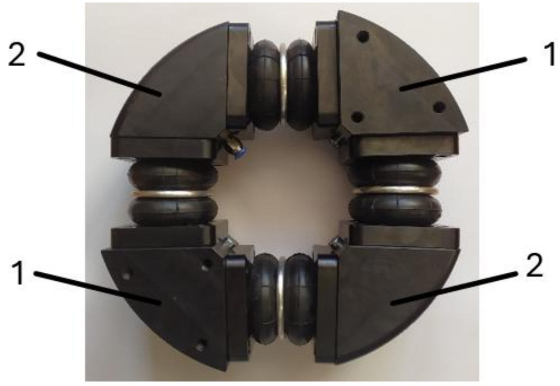

Figure 3. Internal layout of the PDMF.

3. Methodology for measuring the properties of a pneumatic dual-mass flywheel

The measurement of the static loading characteristics of the PDMF was carried out on a measuring bench in the torsional vibration laboratory. The primary part of the PDMF was clamped rigidly, while the secondary part was connected to the protractor via a torque meter. Mutual torsion of the PDMF was provided by a screw jack located under the tilt-arm. The measurement was carried out in the range from 0° to 12°. The torque value was recorded at each stage from 0°to 12° after a period of 30s, due to the relaxation of the elastic elements. The measurement was repeated at initial clutch pressures ranging from 100 kPa to 800 kPa.

The measuring apparatus consisted of a torque sensor MOM Kalibergyár with measuring range 0-2000 N.m, signal processing from the torque sensor is handled by an 8-channel measuring apparatus HBM MX 840 and the resulting values evaluated by the programme Catman Easy.

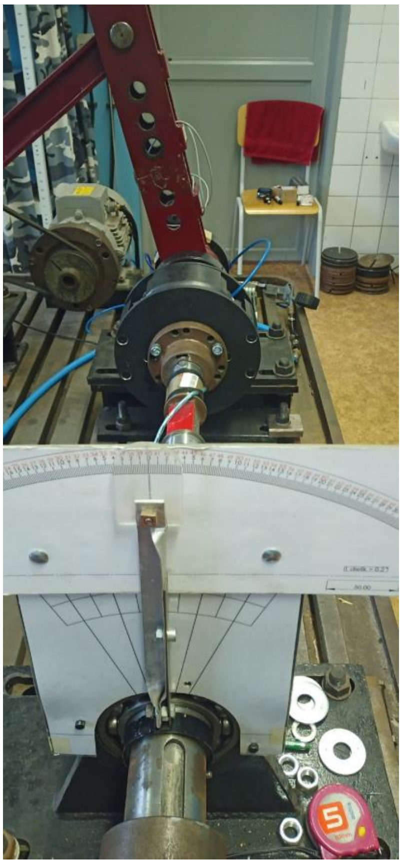

Figure 4. Measuring of PDMF characteristics.

4. Measured PDMF characteristics

The load characteristic is defined as the dependence of the torque M_k and twist angle φ induced by this torque.

In terms of the mechanical properties of the PDMF, loading characteristics (dependence of the loading moment M_k on twist angle φ at different initial values of the overpressure in the compression volume of the PDMF) were expected to be linear. This effect is because of a larger volume of compressed gaseous medium, which leads to a slower increase in overpressure in the compression volume, when the PDMF is twisted relative to each other. Figure 5. shows the average of the results from the three repeated measurements.

From evaluation of measured values, we can conclude the correlation coefficient of the unindividual characteristics R^2 is in range of 0.9996 to 1.00 which represents a high degree of agreement with proposed third-degree polynomials. The increase in torque at a twisting angle of 12° is in the range from 31 Nm to 35 Nm for pressures from 100 kPa to 800 kPa, which means that the change in torque is directly proportional to pressure in PDMF.

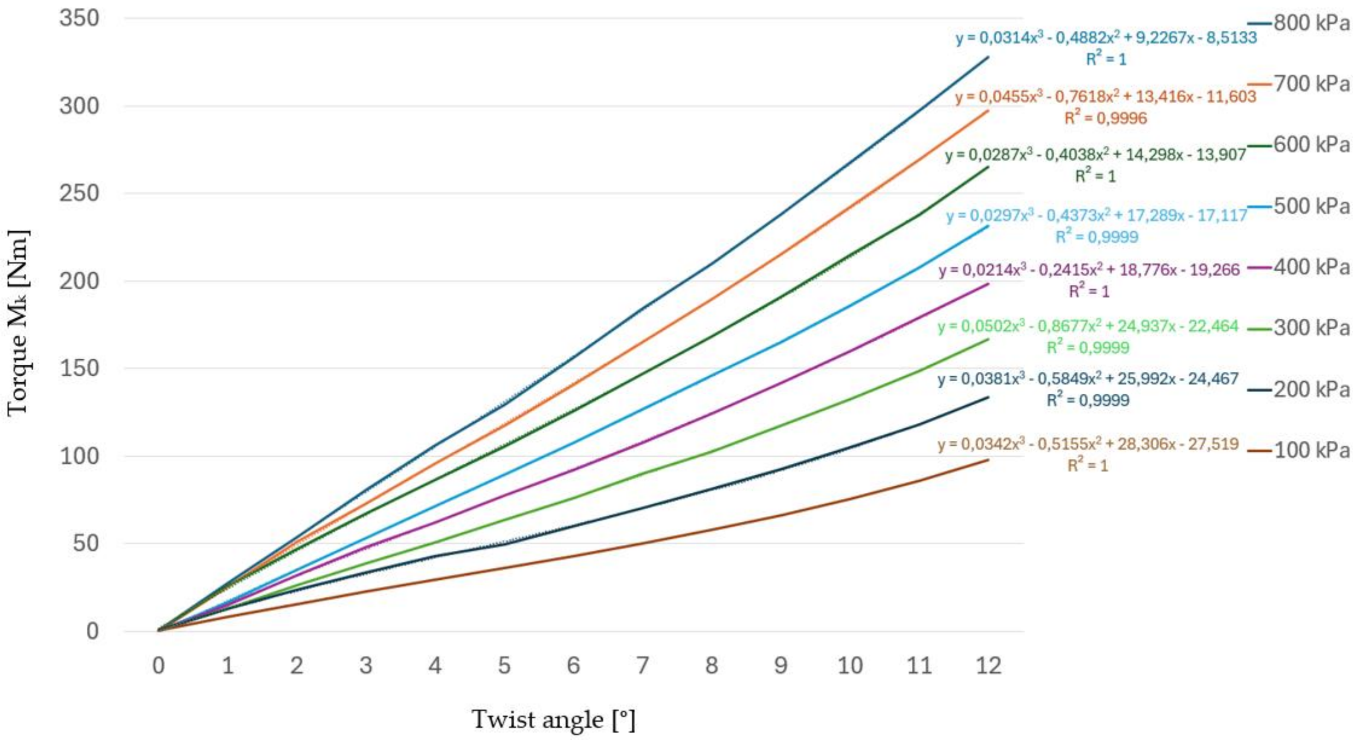

Figure 5. Characteristics of PDMF.

5. Conclusion

The development and technology of internal combustion engines is constantly advancing, so it is advisable to look at technologies that extend component life and reduce adverse vibrations throughout the powertrain. The proposed PDMF has been tested under laboratory conditions by static testing. The test results in load characteristics that start at 0 and increase linearly throughout the twist angle up to a maximum value of 12° with torque 328 Nm at an initial pressure of 800 kPa. The next step of our research will be testing of PDMF with dynamic tests.

Acknowledgments: This paper was written within the framework of the VEGA 1/0573/25 and KEGA: 037 TUKE-04/2024

Conflicts of Interest: The authors declare no conflict of interest.

References

1. Homišin Jaroslav. 2018. Contribution and perspectives of new flexible shaft coupling types – pneumatic couplings. Scientific Journal of Silesian University of Technology. Series Transport. Vol. 99: 65-77, ISSN 0209-3324. DOI: https://doi.org/10.20858/sjsutst.2018.99.6.
2. Homišin Jaroslav. 2002. Nové typy pružných hriadeľových spojok: Vývoj-Výskum-Aplikácia. [In Slovak: New Types of Flexible Shaft Couplings: Development-Research-Application]. Košice: Vienala. ISBN 80-7099-834-2.
3. Kaššay Peter, Grega Robert, Urbanský Matej, Krajňák Jozef, Kačír Matúš, Žuľová Lucia. 2024. Novel Design of Variable Stiffness Pneumatic Flexible Shaft Coupling: Determining the Mathematical-Physical Model and Potential Benefits. Machines. Vol. 12, No. 1: 28, ISSN: 2075-1702. DOI: https://doi.org/10.3390/machines12010028
4. Grega Robert, Krajňák Jozef, Žuľová Lucia, Kačír Matúš, Kaššay Peter, Urbanský Matej. 2023. Innovative solution of torsional vibration reduction by application of pneumatic tuner in shipping piston devices. Journal of Marine Science and Engineering. Vol. 11, No. 2: 261, ISSN: 2077-1312. DOI: https://doi.org/10.3390/jmse11020261
5. Kaššay Peter, Urbanský Matej. 2022. New designs of variable stiffness couplings. Scientific Journal of Silesian University of Technology. Series Transport. Vol. 117: 91-101, ISSN 0209-3324. DOI: http://dx.doi.org/10.20858/sjsutst.2022.117.6.
6. Krajňák Jozef, Homišin Jaroslav, Grega Robert, Kaššay Peter, Urbanský Matej. 2021. The failures of flexible couplings due to self-heating by torsional vibrations – validation on the heat generation in pneumatic flexible tuner of torsional vibrations. Engineering Failure Analysis. Vol. 119: 104977, ISSN: 1350-6307. DOI: https://doi.org/10.1016/j.engfailanal.2020.104977.
7. Radka Jírová, Pešík Lubomír, Žuľová Lucia, Grega Robert. 2023. Method of failure diagnostics to linear rolling guides in handling machines. Sensors. Vol. 23, No. 7: 3770, ISSN: 1424-8220. DOI: ISSN: 1424-8220
8. Gurský Pavol. 2011. Influence of working cycles identification on characteristics of flexible couplings and their comparison. PhD thesis, Košice, Slovakia: Technical University of Košice.
9. Maláková Silvia, Homišin Jaroslav. 2018. Defining of material characteristics for flexible element in pneumatic flexible coupling. In Projektowanie, badania i eksploatacja Tom 1, edited by Jacek Rysiński, 277-282. Poland: Wydawnictwo Naukowe Akademii Techniczno-Humanistycznej w Bielsku-Białej. ISBN 978-83-65182-93-7.

TECHNICAL UNIVERSITY OF KOŠICE
Faculty of Mechanical Engineering

Advanced Designs in Single-Screw Extruders: Enhancing Efficiency and Material Flow Control

Viliam Kapraľ [1,*], Ivan Gajdoš [1], Ján Slota [1]

[1] Department of Technology, Materials and Computer Supported Production, Faculty of Mechanical Engineering, Technical University of Košice, Mäsiarska 74,040 01 Košice, Slovakia; viliam.kapral@tuke.sk; ivan.gajdos@tuke.sk; jan.slota@tuke.sk
* Correspondence: viliam.kapral@tuke.sk

Abstract: The extrusion process involves the plasticization and subsequent extrusion of molten plastic through a mould, necessitating homogeneous mixing and viscosity regulation of the material. The escalating expectations for efficiency and product quality require the development of innovative technical solutions. This paper presents a short review of the new design of the rotational barrel section and active grooved section in the extruder. The proposed design incorporates an innovative geometry of rotating segments that increases the efficiency of plastic mixing and an active grooved section that optimizes material flow control during extrusion.

Keywords: design, single-screw extruder, rotational barrel section, active grooved section, plastics

1. Introduction

Extrusion is a process that integrates multiple activities into one unit. The process entails the continuous plasticization of a polymeric material, which is put in at one end of the extruder and conveyed along the barrel's length by a driving screw. As the material travels the barrel, it undergoes frictional heating, mixing, and intense shearing, especially following the release of pressure at the terminal end. The plasticised material is subsequently extruded via a die with a specific geometry, enabling it to be created into semi-finished or finished products. The configuration of both the screw and the die is essential in influencing the efficiency of the extrusion process and the quality of the end product [1,2].

The main mechanical component of a screw extruder is the plasticizing screw, which facilitates the melting, mixing, measuring, and transportation of plastic material within the barrel. The accurate design of the screw's geometry is essential for the extruder's operation even the most advanced computerised control systems cannot solve issues resulting from improper screw design. The conventional three-zone plasticising screw is commonly used in extrusion processes. The screw design must take into account dispersive mixing, distributive mixing, plasticising capacity, and the constancy of the melting temperature of the plastic material. These parameters directly influence the dimensional consistency and homogeneity of the final goods. The dimensional consistency of the end product is a crucial sign of the extrusion process's overall stability [3,4].

New plasticizing system design constructions are currently available. Contemporary designs provide enhanced regulation of the extrusion process, accommodating the processing of advanced polymer materials, including composites and nanocomposites [5].

The design of the individual concepts is based on patents PL 185728, PL 217558 and PL 221688, taking into account the innovative technologies and solutions contained in these patents.

2. Design of innovative extruder sections

2.1. Rotation barrel section

The recent approach to enhancing the efficiency of the polymer plasticizing process involves the implementation of a rotational barrel segment designed as a sleeve with an inner surface that may or may not include grooves. The rotational segment is constructed with an independent driving system, allowing it to rotate either in alignment with or counter to the direction of screw rotation. It is securely positioned within the melting zone, which is the area exhibiting the highest thermal demand for changing the physical state of the polymer [6].

2.1.1 Design No. 1 of rotational barrel section

The following design introduces the plasticising system shown in figure 1, which comprises four rotational elements. Each element features a cross-section that includes three longitudinal pins, positioned at intervals of 120 degrees. The pins have a width that is half the width of the rotational element and are positioned at its centre. There exists a designated space between the rotational elements for the rotation of specially engineered screw components, which comprise three longitudinal pins arranged at intervals of 120 degrees [7].

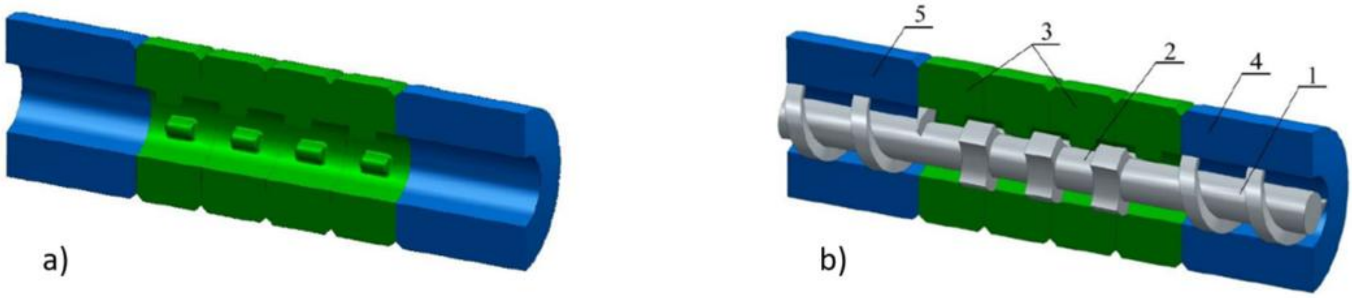

Figure 1. Section of rotational barrel segment Design No. 1, a) without screw, b) with a screw 1 - screw, 2 - modified part of screw, 3 - rotational barrel segment with pins, 4,5 - stationary parts of barrel [7].

2.1.2 Design No. 2 of rotational barrel section

Figure 2 show a constructional solution for the plasticising system, consisting of a rotational segment and a screw section that lacks flights and features an increased root diameter. The size of this section is directly related to the length of the rotational barrel segment. The inner surface of the rotational segment features semi-circular pins with a diameter of 3 mm, arranged alternately in 12 rows. During rotation, these pins facilitate the cutting and mixing of the parallel polymer streams that flow through the screw element, which has an increased root diameter [7].

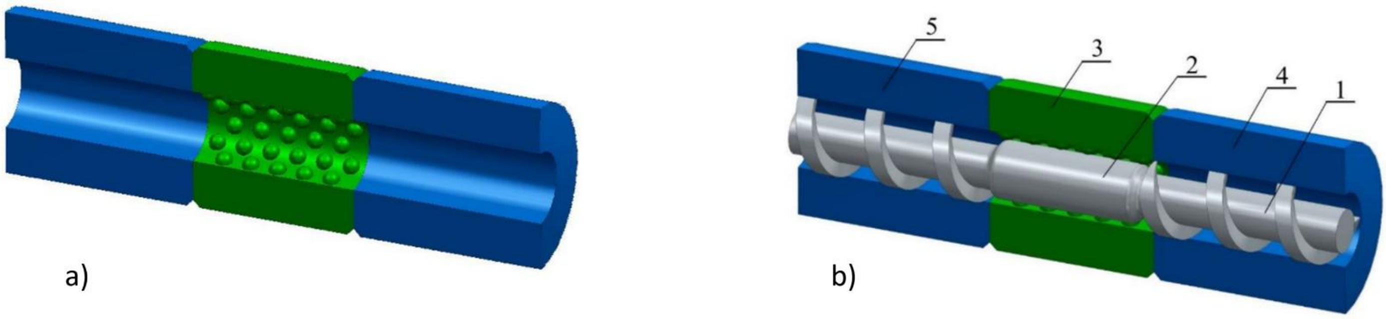

Figure 2. Section of rotational barrel segment Design No. 2, a) without screw, b) with screw 1 - screw, 2 - part of screw with increasing diameter of the root, 3 – modified part of barrel, 4,5 – stationary parts of barrel [7].

2.1.3 Design No. 3 of rotational barrel section

Figure 3 show the last concept of the rotational barrel segment. This concept involves the plasticising system utilising a screw that is without flights along the length of interaction with the rotational barrel segment. The segment features a flight on its inner surface, consistent with the shape of the screw. The plasticising system's efficiency allows the rotational barrel segment to rotate at varying speeds in a direction that is compatible with the screw's rotation direction. The variation in speeds between the barrel segment and the screw affects the extent of polymer mixing and the overall efficiency of the system [7].

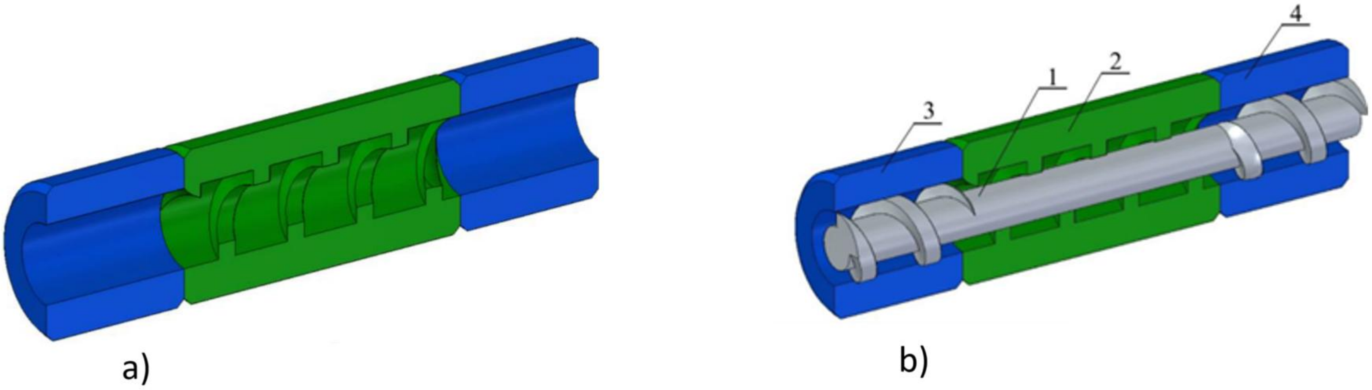

Figure 3. Section of rotational barrel segment Design No. 3, a) without screw, b) with screw 1 - screw, 2 – modified part of barrel 3,4 - stationary parts of barrel [7].

2.2. Active grooved feed section

Another innovative solution is an adjustable, grooved feed section. They enable modifications to design features, including the quantity of grooves and groove depth during extrusion, and adjust these parameters according to the varying granulate size. The primary advantages of implementing an active grooved feed section in extrusion include the ability to modify the extrusion process without stopping the extruder's process or changing the operating parameters. This adaptability allows for adjustments to accommodate the varying dimensions of the granulate, ensuring consistent performance irrespective of the characteristics of the feeding material used in the extruder [8].

2.2.1 Design No. 1 of active grooved section

The operational principle of this adjustable grooved section is to allow for the modification of groove depth throughout the section without stopping the extrusion process or requiring a complicated replacement of the grooved sleeve. Rotating segment 3 around the axis of pivots 7 results in the closing and opening of the grooved section (shown in figure 4). An eighth adjustment screw drives this rotation. This rotation is forced by an adjusting screw 8. The feed section is not subjected to intensive cooling. The heat section of the plasticising system is isolated from the feed section by an innovative component - a separating disc featuring a spiral groove. A spiral groove was created in the front section of the barrel, with a shape that mirrors the one created on the disc. The openings through which the cooling agent goes in and out are made on the side surface of the disc and barrel. Sealing must be provided between the separating cooling disc and the barrel [9].

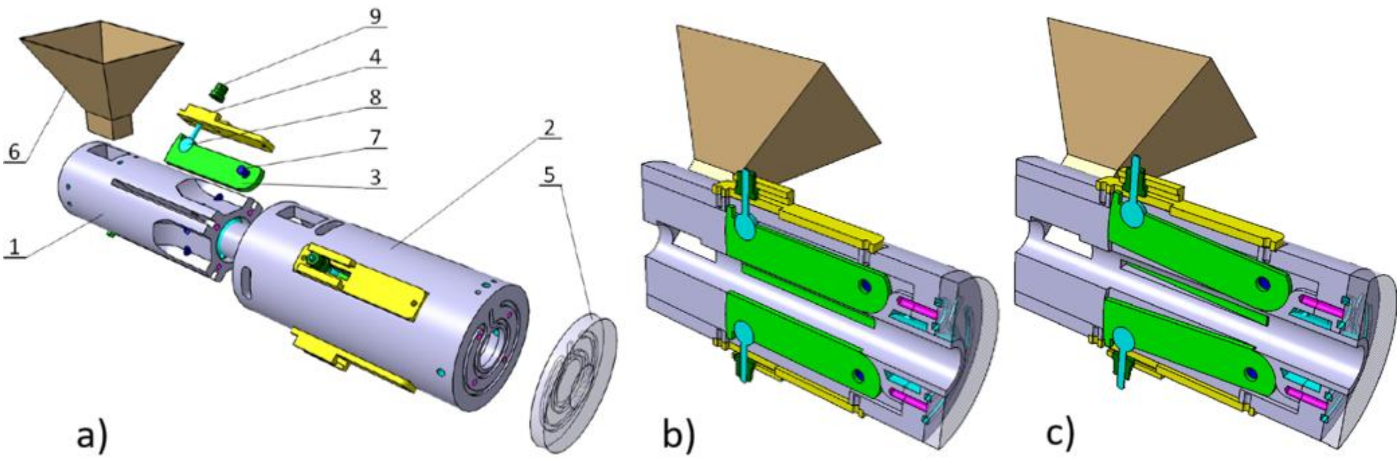

Figure 4. Design No. 1 of active grooved section, a) Exploded view 1 - main sleeve, 2 – barrel, 3 – adjusting element, 4 – fixing element, 5 – separating disk, 6 – hopper, 7 – rotational pivot, 8 – adjusting screw, 9 – special nut, b) Closed position, c) Opened position [9].

2.2.2 Design No. 2 of active grooved section

The sliding motion of the closing element occurs on the sides of the hopper. The primary construction component of this section is the precisely designed sleeve featuring grooves and openings, through which a specially shaped and accurately fitted element with a series of inlets is inserted. The system is actuated by two actuators. Whole design is shown in figure 5 [9].

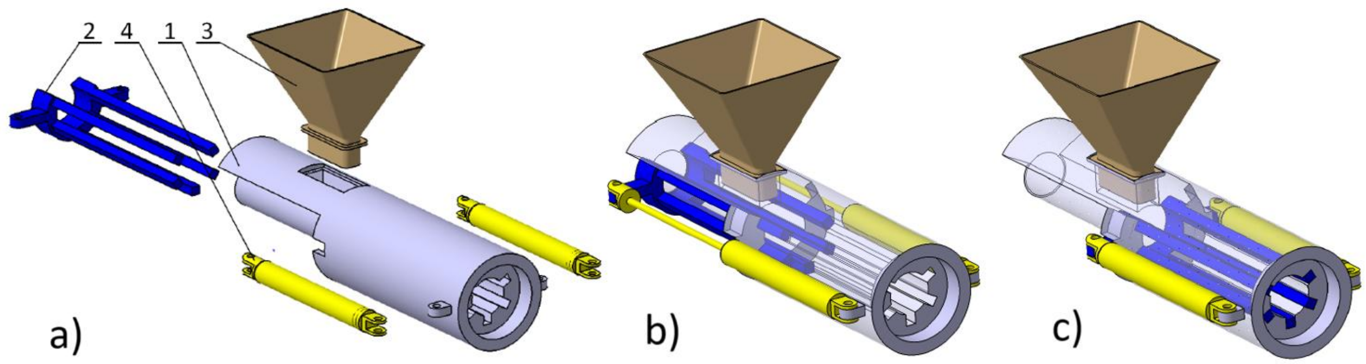

Figure 5. Design No. 2 of active grooved section a) Exploded view 1 - main sleeve, 2 - closing part, 3 - hopper, 4 – actuator, b) Opened position, c) Closed position.

2.2.3 Design No. 3 of active grooved section

The principle of this movable grooved section (shown in figure 6) parallels the solution outlined in design No. 2, with the modification involving the incorporation of an additional component with a set of inlets actuated by supplementary pneumatic or hydraulic cylinders. The sliding return motion of the closing element, equipped with a group of double inlets, occurs on the side of the hopper. Conversely, the sliding return motion of the additional element, which has a group of single inlets, takes place in the opposite direction, on the side of the extruder head. The primary sleeve, featuring precisely designed grooves, constitutes the most important element of this section. The distribution of the grooves is uneven due to the requirement for mounting the polymer hopper. The grooves have a width of 9 mm and a depth of 6 mm. Two thin-walled pipes are securely inserted into the sleeve, serving simultaneously as guideways for the closing elements. The primary closing component comprises a configuration of five double inlets arranged in a circular pattern, aligning with the grooves formed in the main sleeve. A series of individual narrow inlets arranged in a circular configuration compose the auxiliary closing element [9].

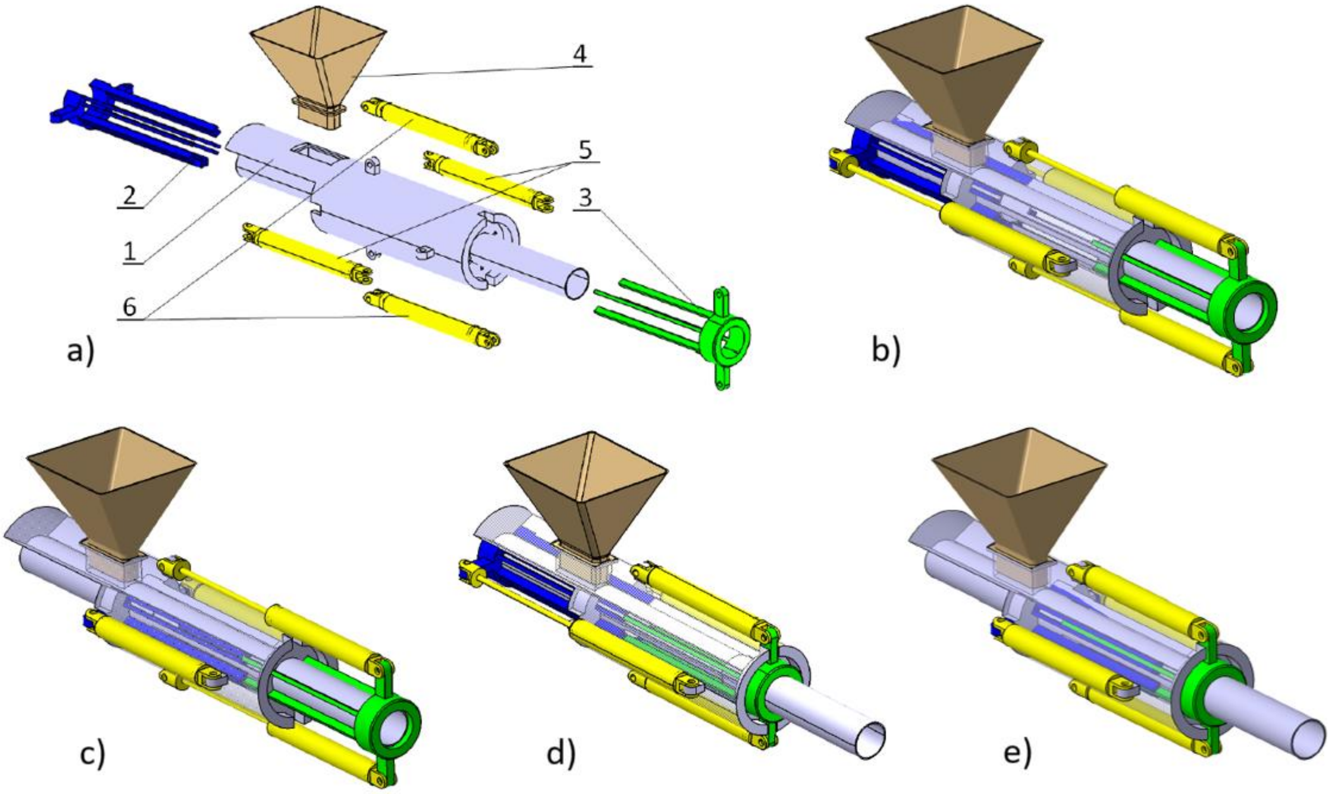

Figure 6. Design No. 3 of active grooved section, a) Exploded view 1 - main sleeve, 2 - rear closing part, 3 - front closing part, 4 - hopper, 5 - actuators for rear closing part, 6 - actuators for front closing part, b) Fully opened position, c) Partly opened position (retracted rear part), d) Partly opened position (retracted front part), e) Fully closed position [9].

3. Strength analysis for the rotational barrel section

The boundary conditions for the numerical model of the rotational barrel segment in the third concept were established by constraining nodes located on the mounting surfaces of the segment, thereby preventing movement along the X, Y, and Z axes at the front borders of the segment. The examined numerical model experienced defined loading conditions, encompassing mechanical loads. These included a rotational speed of 150 rev/min for the segment and an internal pressure of 50 MPa applied to the barrel segment's walls [10].

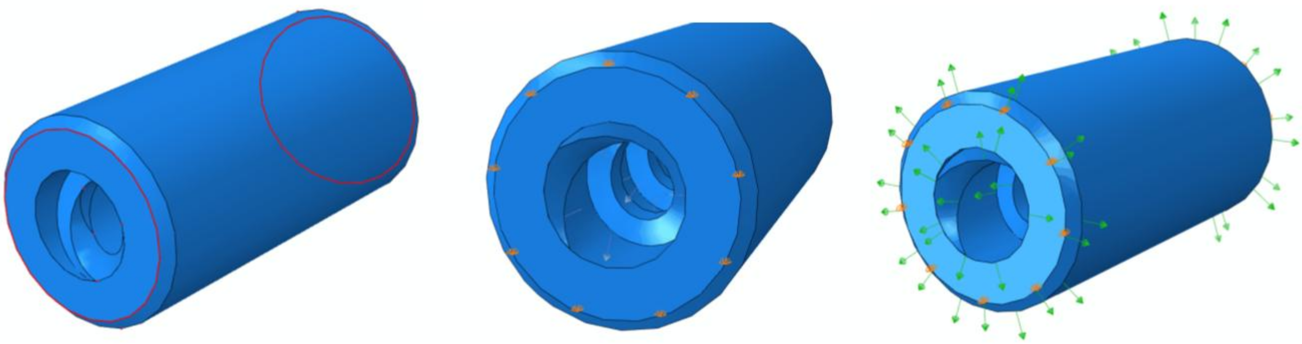

Figure 7. Boundary conditions of the model [10].

The maps of reduced tension for the specific loading states allow estimation of the loading's effect on material construction tension. Figure 8 a) shows that the segment spinning at n = 150 r/min has a maximum tension of σz ≈ 0.0018 MPa, indicating that it does not tension the segment. With an internal pressure of 50 MPa shown in Figure 8 b) the rotating section experiences a tension of σz ≈ 176 MPa. Operating a section under thermal loading circumstances increases tension significantly, equating to continuous construction activity in the duration t = 18000 s. Maximum reduced tension in the elements of construction reaches the level of σz ≈ 885 MPa shown in Figure 8 c). The received value comes from correcting the model, which increases the lowered tension value significantly. Given this, the construction's lower tension under loading does not compromise its safety [10].

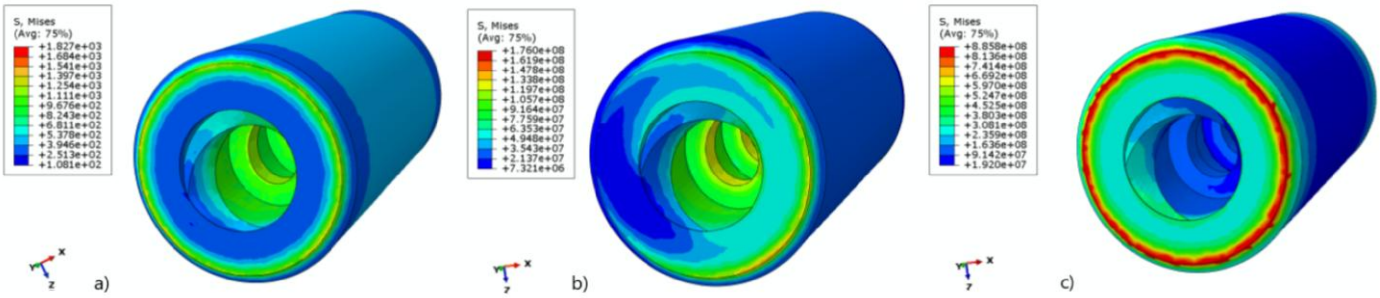

Figure 8. Distribution of total reduced tension H-M-H resulting from loading a) with centrifugal force, b) centrifugal force and internal pressure, c) with centrifugal force, internal pressure and temperature [10].

4. Discussion

Due to the rising demands placed on the plastics industry, it is essential to explore innovative methods aimed at enhancing the efficiency of the extrusion process. The article's initial concept focuses on designing a rotary barrel segment in the melting zone to enhance material mixing. It is important to create a thermal analysis for each concept design, evaluate the results of the individual designs against each other and determine for which type of polymer each concept is suitable. A second concept design for the active grooved section has been presented. The implementation of this concept can be achieved when granulate of varying sizes is delivered to the hopper, thereby ensuring stable process performance. Future efforts should concentrate on developing alternative concepts aimed at enhancing the efficiency of the extrusion process. The design of the individual parts of the innovative extruder will be used in research for the processing of biodegradable composites, with the aim of optimising the production process of these materials and increasing their efficiency and stability during processing while reducing the energy consumption of the entire process. An important aspect of this proposal is also to improve the homogeneity of the compound during extrusion, which will allow an increase in the quality of the resulting products, as well as expand the possibility of using these composites in various industrial applications.

Acknowledgments: This research was funded by the European Union's programme for research and innovation Horizon Europe under the Marie Skłodowska-Curie Action grant agreement No 101129698–PROMATAI– Horizon–MSCA–2022–SE–01. Views and opinions expressed are however those of the author(s) only and do not necessarily reflect those of the European Union or European Research Executive Agency. Neither the European Union nor the granting authority can be held responsible for them. The authors are also grateful for the support in the experimental work to the project KEGA 050TUKE-4/2024. This work was supported by the Slovak Research and Development Agency, project title: Research on the possibilities of forming and joining innovative metal-plastic composites in the production of lightweight thin-walled structures", project numbers: SK-PL-23-0040. The authors are also grateful for the support in the experimental work to the project KEGA 050TUKE-4/2023.

References

1. Sikora, J., Technological and design aspects of extrusion and injection moulding of thermoplastic polymer composites and nanocomposites, Constructional methods of increasing the plasticating efficiency; Sikora, J., Suberlak, O., Lviv Polytechnic Publishing House, Lviv, 2013, pp.16-17, ISBN 978-617-607-372-7.
2. Zheng, Y., Zhao, J., Xu, F., Li, Y., Pretreatment of lignocellulosic biomass for enhanced biogas production, Progress in Energy and Combustion Science, Volume 42, 2014, pp. 35-53, https://doi.org/10.1016/j.pecs.2014.01.001.
3. Wang, M., Arifin, , F., Kuo, J., Dzwo, T., Optimal Design of Plasticizing Screw Using Artificial Intelligent Approach, Journal of Physics: Conference Series, 2019, Volume 1500, https://doi.org/10.1088/1742-6596/1500/1/012022.
4. Rauwendaal, C., Polymer Extrusion, 5th ed.; Extrusion, Hanser Publishers, Munich, Germany, 2014, ISBN 978-1-56990-516-6.
5. Głogowska, K., Spišák, E., Buczaj, M., Technological and design aspects of the processing of composites and nanocomposites, Implementation of the plastication process in an innovative extrusion machine for the processing of composite and nanocomposite materials. Concept and implementation of control system of the extruder. Part 1 – Motors; Dulebová, Ľ., Sikora, J.,Technical University of Kosice, Košice, Volume 4, 2021, pp. 9, ISBN 978-80-553-3817-0.
6. Sikora, J., Technological and design aspects of extrusion and injection moulding of thermoplastic polymer composites and nanocomposites, Constructional methods of increasing the plasticating efficiency; Sikora, J., Suberlak, O., Lviv Polytechnic Publishing House, Lviv, 2013, pp.16-17, ISBN 978-617-607-372-7.
7. Majewski, L., Debski, H., Dulebová, Ľ., Technological and design aspects of the processing of composites and nanocomposites, New concept of rotational barrel segment for a new generation extruder; Sikora, J., Dulebová, Ľ., Lublin University of Technology Publishing House, Lublin, 2019, Volume 2, pp. 34-42, ISBN 978-83-7947-378-6.
8. Ferdynus, M., Chorovsky, P., Debski, H., Gaspar-Cunha, A., Technological and design aspects of the processing of composites and nanocomposites, A concept for a novel polymer extruder part 1: active grooved feed section; Dulebová, Ľ., Sikora, J., Gaspar-Cunha, A., Technical University of Kosice, Faculty of Mechanical Engineering, Košice, 2022, Volume 5, pp. 67-68, ISBN 978-80-553-4073-9.
9. Majewski, L., Debski, H., Dulebová, Ľ., Technological and design aspects of the processing of composites and nanocomposites, New concept of a active grooved feed section for a new generation extruder – CAD models; , New concept of a active grooved feed section for a new generation extruder – CAD models; Gaspar-Cunha, A., Sikora, J., University of Minho, Braga, 2020, Volume 3, pp.12-39, ISBN 978-989-99344-4-3.
10. Majewski Ł., Głogowska K., Review of unconventional barrel designs of plasticizing systems used in single-screw extruders, International scientific journal "INDUSTRY 4.0", 2019, pp. 232-236, ISSN 2534-8582

TECHNICAL UNIVERSITY OF KOŠICE
Faculty of Mechanical Engineering

Quality control of products, manufactured by additive technologies.

Vladimír Kokarda [1,*]

[1] Technical University of Košice, Faculty of Mechanical Engineering; vladimir.kokarda@gmail.com
* Correspondence: vladimir.kokarda@gmail.com

Abstract: Significant new opportunities in rapid prototyping and new ways of manufacturing metal and polymer parts are opening up for the manufacturing industry worldwide. In order to optimise the manufacturing process and maintain or improve the quality of parts produced using 3D printing technology, it is essential to know the properties of the materials used and to continuously monitor the quality of production. Fast and reliable non-destructive testing of composites and polymers is essential to maintain or improve quality, safety, and maintenance costs. In the following study, we will summarise some basic ways of monitoring the quality of polymer products at different stages of their production (from material to final product). We will summarise basic and advanced methods of using industrial microscopy and tomography in quality inspection. The aim is to gain an overview of the material properties at each stage of production and to use this information to produce a product more efficiently, with the desired mechanical properties.

Keywords: quality inspection; 3D printing technology; additive materials

1. Introduction

There are various non-destructive (NDT) and destructive technologies methods based on different principles to ensure quality throughout the life cycle of products and their recyclates. In this article we will review a way of examples, the most commonly used NDT techniques for the detection and evaluation of defect/damage development in the adhesive manufacturing process. For each NDT technique we will give a brief description of the technical principles, equipment and facilities used for research and quality control. Each NDT technique has its own potential and suitability for use in the various stages of product development, production, and post-production. The future of new materials, their efficient production and re-use possibilities depend on materials developed and produced using intelligent and automated inspection systems with high accuracy and efficient data processing capabilities.

The development of 3D printing has great potential in this direction, as it is a low-cost and time-efficient method of production. These quality inspection features are a great advantage in all phases of part production, whether it is the prototype development phase, reverse engineering, mass production, the production of spare parts and components, or even home use. Another advantage is the ability to use recycled blends, where we can use them as much as possible with process control without affecting the future mechanical properties of the product.

2. Materials and Methods

3D printing is the process of creating a physical object by adding layers of material to create a 3D object. The basic principle of additive manufacturing is that instead of starting with a large block of material, we start with a clean area and apply the material gradually. The technology involves three main steps: designing the 3D object digitally, calculating and setting the conditions on the 3D printer, and finally building the object by adding patterned layers of new material. The thickness of each layer affects the final quality of the model. The thinner the layers, the more accurate the print quality. The ability to print as thin a layer as possible is determined by the hardware, which has limits on how thin it can make the layer. Higher quality also affects the software itself, specifically the time it takes to slice the model into many layers. Depending on the application, very different 3D printing technologies can be used with different materials:

FDM

Fused Deposition Modelling is the most widely used method of 3D printing. The principle is similar to using a glue gun. FDM works by. The extruder forces the filament through a hot end that maintains a constant temperature to melt the filament to a viscous temperature. The molten material is applied through a nozzle that performs X and Y axis motion in close proximity to the pad. When a layer is completed, either the nozzle or the pad moves up one level in the Z-axis and continues until the part is complete. (see Figure 1).

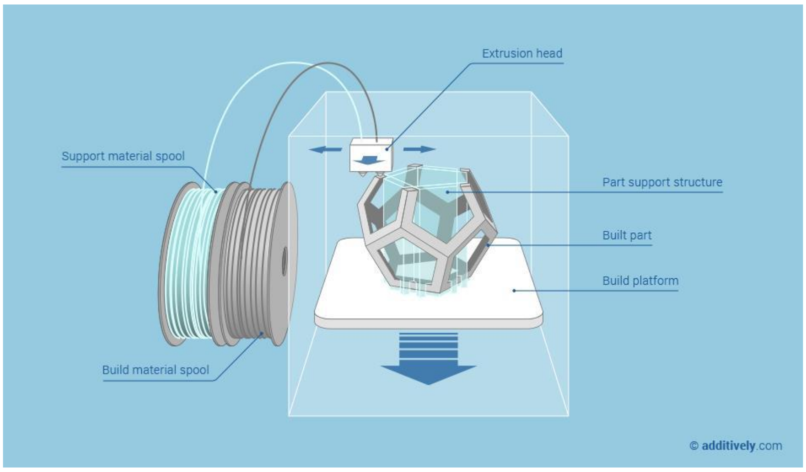

Figure 1. Fused Deposition Modelling: displayed principe is in layering a thermoplastic filament onto a spool attached to an extruder [13].

SLA DLP

Stereolithography uses a photosensitive resin that polymerises under the influence of a UV laser. The UV rays are precisely focused to form a single layer of resin. Once this is complete, the platform on which the product is developed is moved vertically by the size of the next layer. The DLP process can emit UV laser beams in the exact desired distribution of each layer at the same time, creating an entire layer at once, unlike conventional SLA. The surface of the cured model is dipped back into the liquid, which photopolymerises on the next exposure. In this way, the desired object is created layer by layer. Thanks to the precision of the UV laser, SLA printers are able to produce a relatively smooth surface compared to other 3D printing methods, as well as almost imperceptible differences between layers. This is why it is so popular for creating materials with complex shapes. The downside is the higher cost of both the printer itself and the materials [13] (see Figure 2).

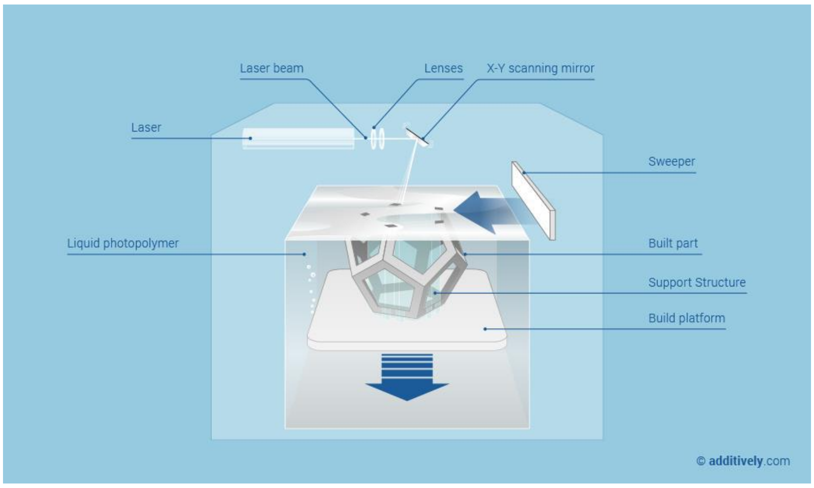

Figure 2. Stereolithography uses a photosensitive resin that polymerises under the influence of a UV laser [13].

3. Results

NON-DESTRUCTIVE TESTING OF MATERIALS FOR THE PRODUCTION OF ADHESIVES

Non-destructive testing /NDT/ plays an important role in the quality management system of the production process (see Figure 4). It allows early detection of internal defects in a product or semi-finished product, which could prevent its effective use or cause construction defects after a certain period of operation. In the field of non-destructive testing, a number of methods based on different physical principles are used for the detection and quantitative evaluation of detected defects.

The advantage of non-destructive methods over destructive methods is that the product remains in an unaltered condition for further use after testing. The NDT methods for testing each type of semi-finished and finished product are specified in the relevant standards and regulations. It is usually the customer's requirement that determines the standard or regulation to which the product is to be evaluated for NDT.

The size and shape distribution is influenced by the material properties and related to these are the defects that occur during the process. The density of defects depends on, among other things, the ageing factor of the powders or the compound used, whether it has been recycled or not. A wide range of equipment is used in industry to determine quality characteristics. Depending on the application and the magnification required, we use optical or electron microscopes for complex analyses, we can use X-ray or CT (see Figure 3).

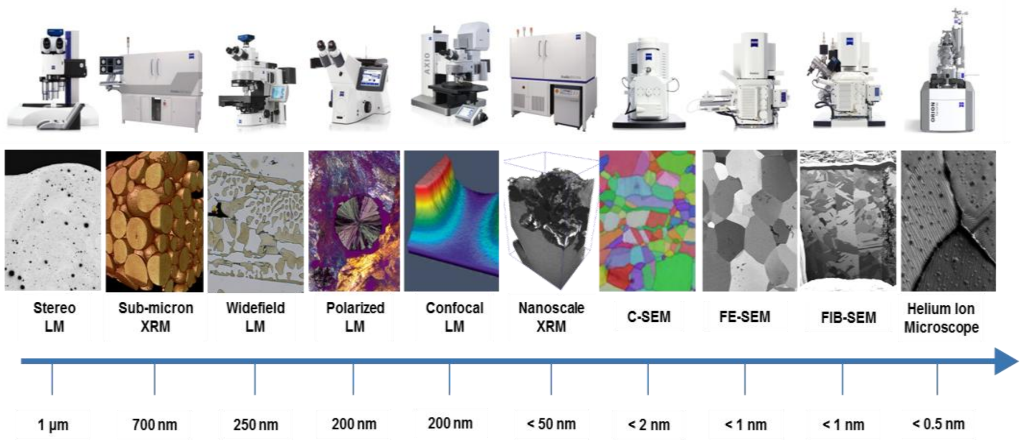

Figure 3. Integrated process of additive manufacturing focused on quality control.

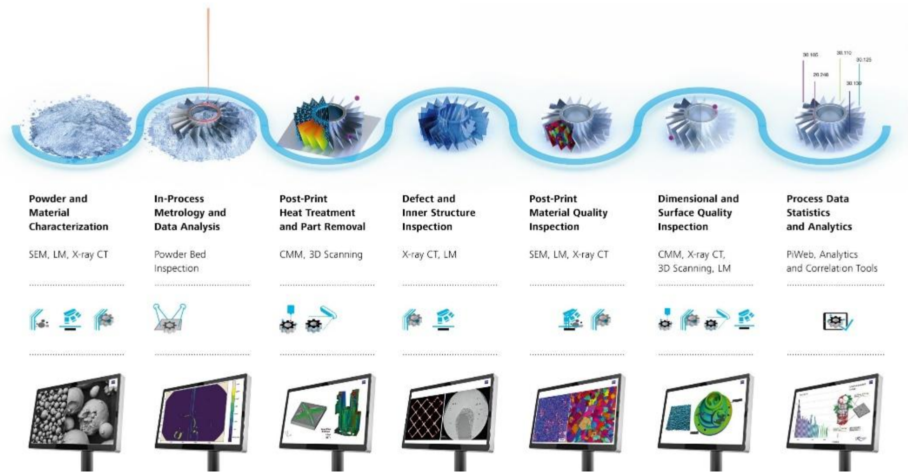

Figure 4. Scheme of integrated process for additive manufacturing -in each step of production phase we can use different quality inspection techniques.

INITIAL STAGE, TESTING POWDER BLENDS

Powder is the building block of additive manufactured parts. The size and shape distribution affects the layout and therefore the potential defects created during the manufacturing process. Defect density is a function of powder recycling and ageing, among other factors. The structure of the powder mix therefore has a major influence on the properties of the future material, which in turn affects the final mechanical properties of the product. Using an electron microscope with high resolution in the nanometre range, we can examine each individual particle to better understand the building blocks of AM materials. Using CT X-rays, we can analyse the volume fraction of pores inside the particles and identify impurities, as well as measuring the density of the particles. Using optical microscopy, we can analyse the particle size distribution. Using artificial intelligence methods, we can train software to define and distribute individual powder particles. In the same way, we can determine the distribution and size distribution of individual particles in relation to the total powder. This data is important for learning the final mechanical properties of the product after curing and for determining the suitability of recycled blends for reuse in the manufacturing process.

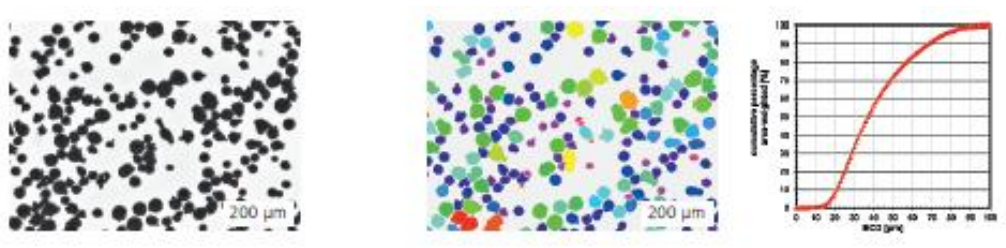

Figure 5. Optical microscopic analysis in a grey value with automatic segmentation of particles (size and type, no Chemical information).

Using of an electron microscope to analyse powder particles that are relatively small in size, typically a few microns to tens of microns in diameter. The scanning electron microscope (SEM) provides nanometre resolution and is able to analyse the chemical composition of each individual particle. This helps to better define the design components for additive manufacturing.

Figure 6. SEM analysis -new powder, and recycled powder.

Industrial tomography allows detailed analysis of particle shape and size. The volume fraction of pores inside the particles and contaminants can be identified non-destructively. The density of the measured particles can also be identified.

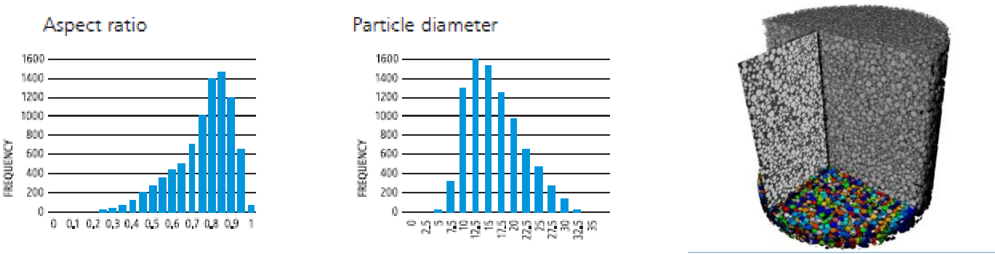

Figure 7. Computer Tomography (CT) analysis 8500+ particles analysed in volume without destruction segmented by shape and size.

ANALYSIS OF STRUCTURE AND INTERNAL DEFECTS AFTER PART MANUFACTURE

Incorrect powder quality and process manufacturing parameters can lead to voids in the structure. Quality control using optical microscopy (OM) or internal structures using high-resolution X-ray CT helps to determine the powder characteristics and process parameters that influence and define the path to optimal process setup. The use of OM to inspect surfaces at high resolution provides insight into part quality. Defects such as pores, microcracks and delamination can be inspected and correlated with process parameters.

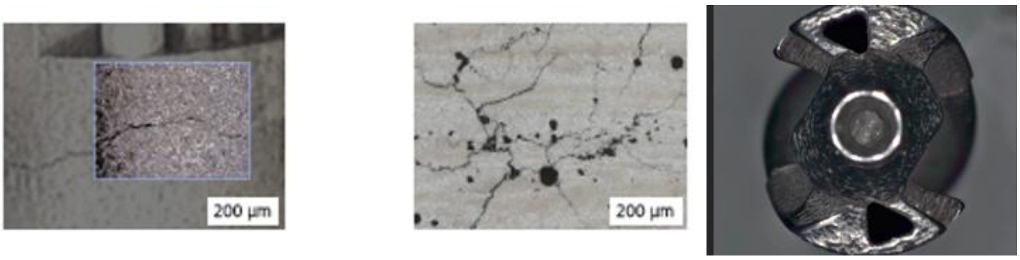

Figure 8. Optical microscopic (OM) analysis -examples of crack surface defects.

We use computed tomography (CT) technology to outline internal defects. With high-resolution CT, we can analyse internal structures at high resolution to identify potential structural defects. This data can help us optimise the 3D printing process. Scanned images of the part can be sectioned in any direction and compared to the nominal CAD view.

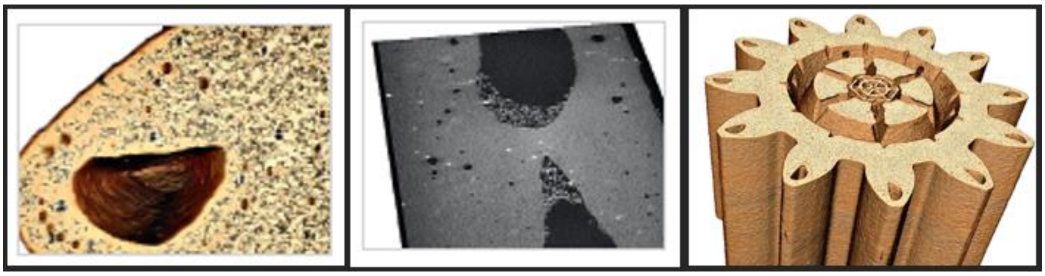

Figure 9. CT analysis -examples of internal porosity defects.

ANALYSIS OF POROSITY AND GRAIN STRUCTURE AFTER PART PRODUCTION

Melt temperatures and process parameters have a significant effect on the crystallography and therefore the properties of the part. Due to the high energy density, additive manufactured parts are typically produced with high temperature gradients and solidification rates. The types of laser firing and weld fields are among the characteristic patterns that can be analysed with optical microscopes and have a direct influence on the mechanical properties. In the next section we will discuss the porosity analysis of AlSi10Mg. Another important property studied is the grain structure. The structure produced by conventional means is very different from a 3D printed part of the same material. This difference will affect the mechanical properties of the finished part Figure 9.

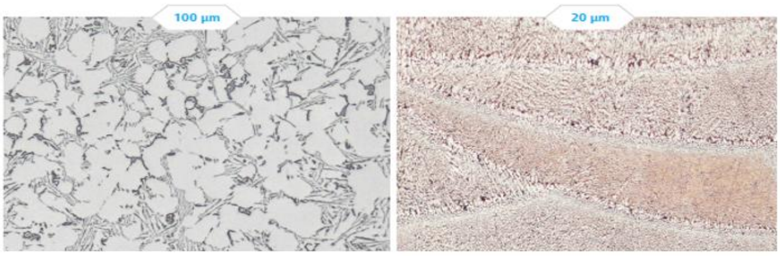

Figure 10. OM analysis -comparison of conventionally and additively manufactured aluminium alloy AlSi10Mg.

ANALYSIS OF POROSITY OF 3D PRINTED PARTS AFTER PART PRODUCTION

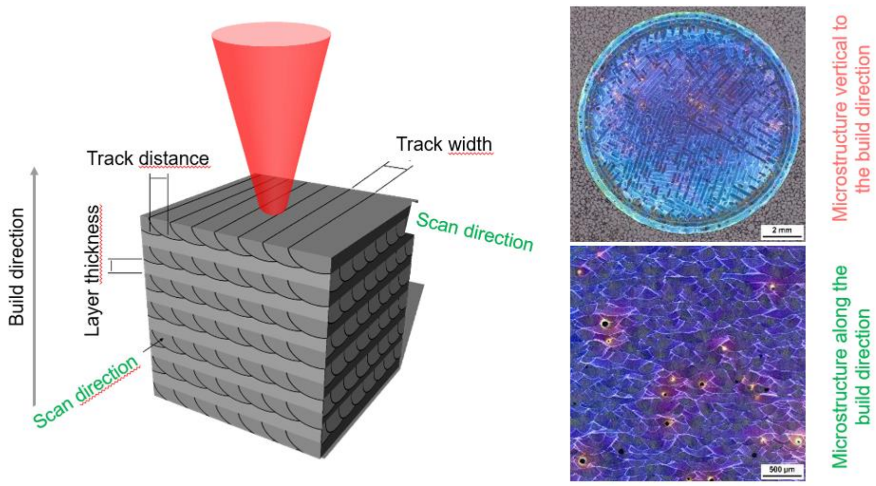

Figure 11. OM analysis -production of microstructure in the additive manufacturing process [12].

Illustration of laser tracks. In the upper right images, you see the laser tracks vertical to the laser direction (see Figure 11).The grey background is unmelted powder. The lower right image shows the layers along the build direction with its laser fronts the sample itself is a cylinder and a test sample, illustating the the printing procedure. It is clearly visible that the outer ring was produced in one step, the next step was a second ring and the third step, the processing of the inner part. This is a common procedure to have three steps and starting from the contour.

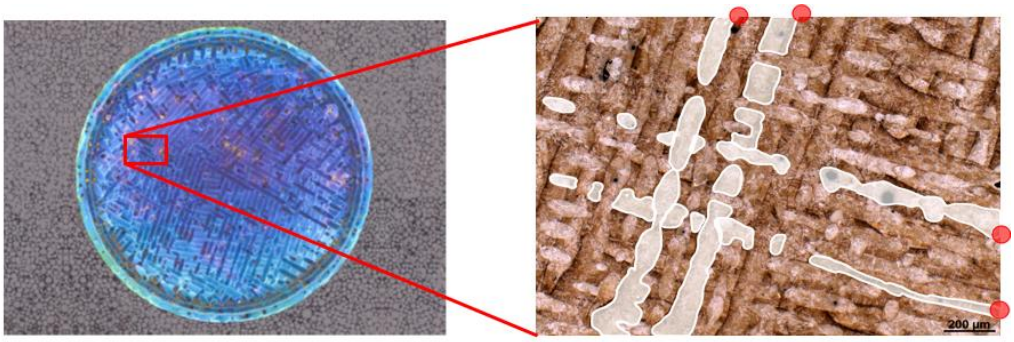

Figure 12. OM analysis -characterisation of the surface of the upper lasered part non destructive method based on AI [12].

When zoomed in, you can see the laser lines along the laser direction (indicated by the light stripes) Laser fronts can affect melting efficiency. They should be at least as deep as the particle size, otherwise possible particle residue may be observed. The parameter of the distance between the laser footprints is crucial, as the overlap affects e.g. the porosity. Different materials have been used, but the top and side views and the laser power dependence are similar.

Figure 13. OM analysis -comparison of porosity for different print energy densities [14].

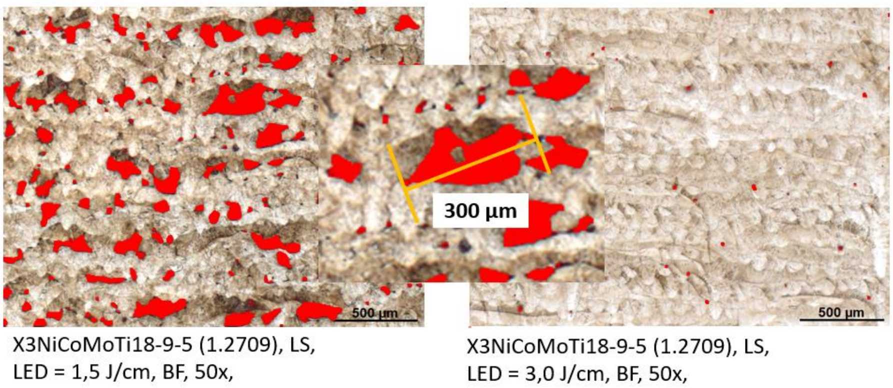

Figure 14. OM analysis -measurement of porosity for different print energy densities [14].

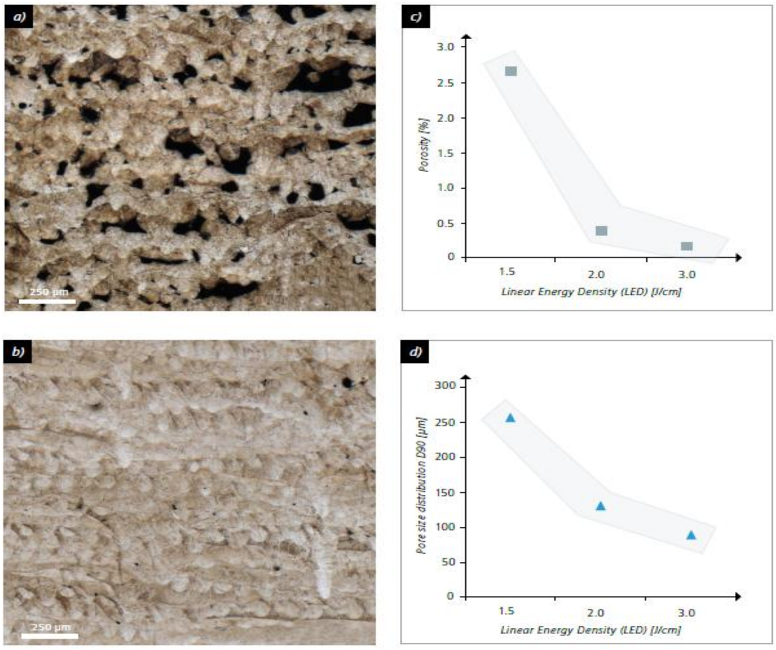

Figure 15. Structure and distribution of pores depending on the density of the linear layer. Microstructural evolution in test cubes made of X3NiCoMoTi18-9-5 in response to the linear energy density (LED) for determination of porosity and defect size; a) SLM, high LED, V2A etchant, cross-section, 50×; b) SLM, low LED, V2A etchant, cross-section, 50×; c) Overall porosity in relation to LED, porosity decreases with higher LED; d) Pore size in relation to LED, pore size decreases with higher LED [14].

Qualitative analysis using industrial microscopes can provide information for process optimisation. In this case, pore analysis can be directly related to the amount of energy to be applied, in this case, higher energy density results in fewer defects.

THE NEAR FUTURE: MICROSCOPY AND CT ANALYSES WITH AI-POWERED SOLUTIONS

Artificial Intelligence (AI) has been a game-changer in many sectors, and microscopy is no exception. AI Microscopy Solutions leverage the power of artificial intelligence to revolutionize the way of acquiring images, analyze and interpret microscopic data and manage the performance of analysis. The main areas of application are the AI module for image segmentation 3D reconstruction or automatic sample detection, to enhance precision, speed, and scalability in research. The future will belong to fully implemented AI modules that fully automate the analysis process and fully replace the operator.

4. Discussion

This has been a brief summary of the most common ways of controlling the quality of 3D printing materials. Looking more closely at the individual production stages, the final mechanical properties of additive manufacturing products can be influenced from the outset by the composition of the structure and the degree of recyclability of the blend. In the future, the aim will be to describe and define the maximum possible amount of recycled additive for different materials and products, while maintaining the mechanical properties of the final product. Also, the use of specialized AI modules aimed at evaluating and analyzing images or data using a microscopy or tomography will improve image analysis and defect detection capabilities in materials at different stages of product manufacturing.

5. Conclusions

The future of new additive manufacturing materials, their efficient production and reusability depends on products designed and manufactured in intelligent facilities, equipped with automated control systems and efficient data processing capabilities, incorporating the latest quality control techniques. These techniques have a major advantage in all phases of additive manufacturing, be it the prototype development phase, reverse engineering, mass production or the production of spare parts and components. They allow early detection of inherent defects in a product or semi-finished product that could prevent its effective use or cause design flaws after a certain period of operation. Each non-destructive testing technique for metal and polymer parts has its own potential and suitability for use in the various development, production, and post-production phases of the product's life. The purpose of the application and the requirements of the final product determine the type of testing required. Qualitative analysis based on light microscopy, electron microscopy, X-ray or CT with the use of automated measurement systems and data processing is commonly used. Measuring instruments with integrated data analysis, image evaluation and learning software are now widely available.

References

1. So-Ree Hwang; Min-Soo Park, Property Analysis of Photo-Polymerization-Type 3D-Printed Structures Based on Multi-Composite Materials. Appl. Sci. 2021, 11, 8545. https://doi.org/10.3390/app11188545
2. Andy Holwell, Solutions in the Steel and Other Metals Industry
3. Tymrak, B.M.; Kreiger, M.; Pearce, J.M. Mechanical properties of components fabricated with open-source 3-D printers under realistic environmental conditions. Mater. Des. 2014, 58, 242–246.
4. Mario Del Rosario,Hannah S. Heil,Afonso Mendes,Vittorio Saggiomo,Ricardo Henriques, The Field Guide to 3D Printing in Optical Microscopy for Life Sciences; https://doi.org/10.1002/adbi.202100994
5. S.Gholizadeh; A review of non-destructive testing methods of composite materials; Conference: XV Portuguese Conference on Fracture, PCF 2016, 10-12 February 2016
6. Bing Wang, Schuncong Zhong, Tung Lik Lee, kevin Fancey; Non-destructive testing and evaluation of composite materials/structures: A state-of-the-art review, February 2020Advances in Mechanical Engineering
7. Michal Gregor, Martin Anetta; Moderná mikroskopia a digitálne spracovanie obrazu
8. Dagmar Jakubéczyová; Experimentálne metódy hodnotenia tenkých vrstiev aplikovaných technológiou ARC a LARC
9. Ultimate 3D Printing Materials Guide. 2018. Dostupné na: https://www.simplify3d.com/support/materials-guide/
10. Bensoussan, H. The History of 3D Printing: 3D Printing Technologies from the 80s to Today. 2016. on: https://www.sculpteo.com/blog/2016/12/14/the-history-of-3d-printing-3d-printing-technologies-from-the-80s-to-today/
11. https://www.additively.com/en/learn-about/fused-deposition-modeling
12. University Aalen source: https://www.hs-aalen.de/de
13. Additively.com: https://www.researchgate.net/
14. Lisa Weissmayer, Tim Schubert; Applications of Microscopy in Additive manufacturing, February 2015

TECHNICAL UNIVERSITY OF KOŠICE
Faculty of Mechanical Engineering

Sustainable Dyeing of Polyamide 12: Research and Prospects

Petra Kolembusová [1,*], Norbert Ferenčík [1], Radovan Hudák [1]

[1] Technical University of Košice, Faculty of Mechanical Engineering, Department of Biomedical Engineering and Measurement, petra.kolembusova@tuke.sk, norbert.ferencik@tuke.sk, radovan.hudak@tuke.sk
* Correspondence: petra.kolembusova@tuke.sk

Abstract: Natural dyes are increasingly being recognized as sustainable alternatives to synthetic dyes, particularly for their environmental benefits and potential compatibility with biocompatible materials. This review focuses on the application of natural dyes for the sustainable coloration of polyamide 12 (PA12), a biocompatible polymer widely used in medical and industrial applications. Following our recent study, which evaluated the performance of a freely available mordant (N-RIT-88150-BUN1), we now explore the potential of natural dye sources such as spinach, red onion, black beans, and others. The review explains key aspects, such as dye extraction, application techniques, and the role of mordants in enhancing adhesion and color stability. Initial findings suggest that natural dyes can provide a viable alternative for coloring PA12 while maintaining its biocompatibility, though challenges remain in achieving consistent results and scalability. This review highlights the need for further experimental work to optimize dyeing protocols. By integrating sustainable practices, this study aims to advance eco-friendly dyeing technologies and support the broader adoption of renewable resources in polymer applications.

Keywords: polyamide 12; 3D printing, mordant, natural dye, compatibility

1. Introduction

Natural dyes, derived from plants, minerals, and other organic sources, offer an eco-friendly alternative to synthetic dyes, particularly in biomedical and polymer applications. Polyamide 12 (PA12), a versatile thermoplastic known for its biocompatibility and robust mechanical properties, is well-suited for these advancements.

In additive manufacturing, powder-bed fusion techniques like Selective Laser Sintering (SLS) and Multi Jet Fusion (MJF) enable the creation of complex geometries with excellent precision. Using the EOS P390 SLS printer, this research explores enhancing PA12 with sustainable dyes for applications in tissue engineering and biomedical devices.

Surface and bulk chemistry significantly influence cell adhesion, proliferation, and differentiation in tissue engineering. Mordant-based dyeing processes improve these attributes by enhancing dye adhesion, color stability, surface smoothness, and resistance to biofouling. This study integrates natural dyes into PA12 components, leveraging the capabilities of the EOS P390 to advance sustainable additive manufacturing.

2. Materials and Methods

A dye is a colored substance with a strong affinity for its substrate. Mordants improve dye fastness when applied in aqueous solutions. Natural dyes, predominantly sourced from plant materials, are used extensively in food, cosmetics, and textiles due to their environmental safety, biocompatibility, and non-toxic properties.

Examples of natural colorants include indigoid, anthraquinone, flavonoid, carotenoid, pyridine, tannin, and quinoid, which contribute to properties such as UV resistance and insect repellence. Vegetable colors, obtained from roots, berries, bark, and organic sources, offer an eco-friendly alternative to synthetic dyes, reducing environmental impact.

Natural dyes are categorized based on chemical structure (e.g., flavonoids, tannins), source (e.g., vegetable, animal, mineral), and application method (e.g., mordant dyes, vat dyes, acid dyes) [3-9].

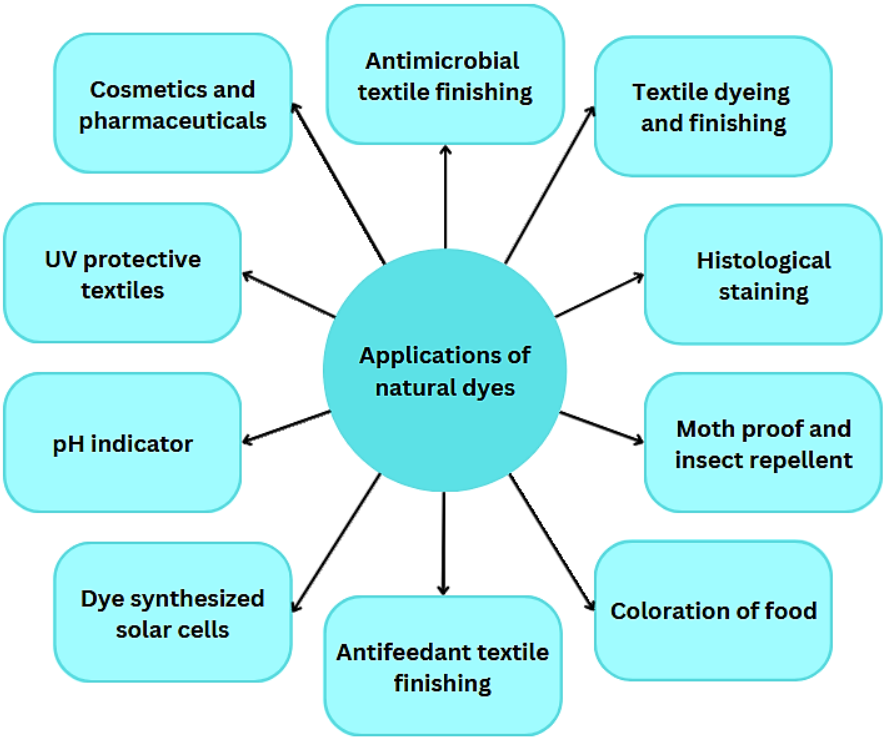

Figure 1. Applications of natural dyes [3-17].

Table 1. Summary of advantages and disadvantages of natural dyes [4].

Advantages	Disadvantages
Most eco-friendly	Most commonly used for natural textiles (cotton, silk, linen wool)
Easier purification and application	Difficult to recreate shades
Biodegradable and renewable	Limited colour fastness properties
More sustainable	Require some extra chemicals like crosslinking chemicals and metallic mordants which create negative effects on the environment
More available in nature	Limited data and statistics are accessible about extraction, purification, chemical structure, and application techniques of natural dyes
No disposal problems	It is tough to create a consistent recipe for using natural dyes
Minimize the consumption of fossil fuel	There is no specific technique for natural dyeing
Mostly anti-bacterial, insect repellent, and anti-allergic	Natural dyes are not accessible in pure or standardized form
Moth proof and repellent	
Anti-ultraviolet	
Intensify dyeing and finishing process efficiency	
Less expensive	
No adverse effects on human health and environment	

Material selection

Polyamide 12 (PA12) will be selected for its mechanical robustness, chemical inertness, and suitability for biomedical applications. We plan to use medical-grade PA12 powder (HP 3D High Reusability PA12) for our experiments. This material, known for its semi-crystalline structure, ensures exceptional quality and reliability. The PA 12 utilized in the EOS P390 system has been rigorously tested and certified for biocompatibility. It meets

USP Class I–VI standards, addressing key safety parameters such as irritation, acute systemic toxicity, implantation, and cytotoxicity (following ISO 10993-5 for in vitro cytotoxicity). It also satisfies ISO 10993-10 requirements for skin irritation and sensitization and aligns with the US FDA's guidelines for Intact Skin Surface Devices [1].

The technical datasheet for this material highlights the following properties: a melting point of approximately 180°C, a powder melting point (DSC) of 187°C (ASTM D3418), part density of 1.01 g/cm³ (ASTM D792), and bulk density of 0.425 g/cm³ (ASTM D1895). The average grain size is 60 µm (ASTM D3451), and it offers excellent mechanical performance, including a tensile strength of 50 MPa at 50 mm/min and an elastic modulus of 1800 MPa in tensile tests (1 mm/min) and 1700 MPa in bending tests (2 mm/min, 10 N) [1, 2].

3D Printing of PA12 samples

The selection of suitable materials and technology, as well as the design of a model for biomedical 3D printing, must be tailored to the specific application. For this purpose, the EOS P390, a Selective Laser Sintering (SLS) 3D printer developed by EOS GmbH (Krailling, Germany), was chosen. This technology utilizes powder-bed fusion to manufacture high-performance polymer components directly from CAD data. The EOS P390 supports Polyamide 12 (PA12), a widely used thermoplastic in biomedical and industrial applications due to its excellent mechanical properties, chemical resistance, and durability. The SLS process involves spreading a thin layer of PA12 powder, selectively fusing it using a laser, and repeating the process layer by layer to build a 3D model. The system achieves precise dimensional accuracy and high-quality surface finishes without the need for support structures, enabling complex geometries to be produced efficiently. [1, 2]

Compared to MJF (Multi Jet Fusion) used in our previous study, SLS with the EOS P390 provides significant benefits for producing PA12 components, particularly in biomedical applications. Its ability to produce complex, high-performance parts with minimal material waste and high dimensional precision makes it an ideal choice for advanced additive manufacturing projects [1].

The EOS P390 offers numerous advantages for additive manufacturing. It provides a large build volume (340 x 340 x 620 mm), enabling the production of sizable parts or multiple components in a single batch. Its Selective Laser Sintering (SLS) process eliminates the need for support structures, allowing greater design flexibility and efficient post-processing. The printer ensures high precision with dimensional accuracy up to ±0.2%, delivering parts with consistent mechanical properties and excellent surface quality. Additionally, it is energy-efficient, minimizes material waste through powder recycling, and does not require chemical post-processing, making it cost-effective and environmentally friendly. These features make it ideal for complex geometries and high-performance applications in industries such as healthcare, automotive, and aerospace [1, 2].

Each sample will be designed with lattice structures to mimic porous scaffolds used in tissue engineering. The scaffold grid will have inner square dimensions of 3 mm and wall thickness of 1 mm.

Dye extraction and mordanting process

Natural dye solutions will be prepared by boiling 100 g of each source material (e.g., black beans) in 500 mL of distilled water for 60 minutes. The extract will be filtered and concentrated. Mordanting will involve immersing PA12 samples in a solution of mordant and natural dye at 88°C for 30 minutes. This step will be followed by stabilization through sequential cold and hot water washes to remove unbound dye particles. Samples will be air-dried at room temperature.

Analytical techniques [1]

- UV-Vis Spectroscopy: Dye absorption and release into culture media will be monitored using a Shimadzu UV-2401PC spectrophotometer.
- Microscopy: Sample surfaces will be imaged using a digital microscope (SONY IMX290) at 200x magnification.

- Cell Culture Assays: Human gingival fibroblasts (hGF06) will be cultured on dyed PA12 samples to assess biocompatibility. The Dulbecco's Modified Eagle Medium (DMEM) supplemented with 10% fetal bovine serum and antibiotics will be used.
- MTT Assay: Metabolic activity and cell viability will be determined by colorimetric analysis of formazan crystals formed by live cells.
- Mechanical Testing: Tensile properties of stained and unstained samples will be assessed using a Universal Testing Machine.

Experimental controls

Clear PA12 samples will be used as controls to evaluate the impact of dyeing on biocompatibility and mechanical properties. Additionally, dye concentrations in culture media will be varied to assess dose-dependent cytotoxicity.

3. Discussion

The adoption of natural dyes promotes renewable resource use and reduces chemical waste. Refining dyeing protocols—including temperature control, mordant concentration, and exposure time—is essential for scalability. Mechanical testing will ensure dyed PA12 meets performance standards for biomedical applications.

Biocompatibility studies should be expanded to evaluate various cell responses to dyed PA12 scaffolds. Understanding cell viability, adhesion, and differentiation will support applications in tissue engineering and regenerative medicine.

Notably, to our knowledge, this is a novel experiment, as we found no prior research applying natural dyes to PA12. This underscores the originality of our study and highlights the potential for new discoveries in sustainable polymer coloration.

By addressing these challenges, this research aims to establish a framework for sustainable dyeing practices in polymer applications, fostering broader industry adoption.

4. Conclusions

This study highlights the potential of natural dyes as sustainable alternatives for coloring PA12 in biomedical and industrial applications. Optimizing dye adhesion, colorfastness, and biocompatibility will be critical to overcoming existing challenges.

Future research will focus on refining dyeing protocols, expanding dye sources, and investigating long-term stability. Additionally, evaluating dyed scaffolds' interactions with diverse cell types will further validate their suitability for tissue engineering.

Acknowledgments: This work was developed with the support of the project VEGA 1/0387/22 - Development and testing of systems for controlled stimulation of cell growth in a bioreactor environment using computer vision.

References

1. FERENCIK, Norbert, DANKO, Maria, NADOVA, Zuzana, KOLEMBUSOVA, Petra and STEINGARTNER, William, 2024. PA12 Surface Treatment and Its Effect on Compatibility with Nutritional Culture Medium to Maintain Cell Vitality and Proliferation. Bioengineering. Online. 30 April 2024. Vol. 11, no. 5, p. 442. DOI 10.3390/bioengineering11050442.
2. Multipurpose PA 12 for industrial 3D Printing | EOS, [no date]. EOS GmbH. Online. Available from: https://www.eos.info/polymer-solutions/polymer-materials/multipurpose#pa-2220-High-Reuse
3. ZANNAT, Akhiri, UDDIN, Mohammad Nasir, MAHMUD, Sharif Tasnim, MIA, Rony and AHMED, Taosif, 2023. Natural dyes and pigments in functional finishing. In: Elsevier eBooks. Online. p. 271–287.
4. REPON, Md.Reazuddin, ISLAM, Tarekul, ISLAM, Tarikul, GHORAB, Ahmed El and RAHMAN, Mohammed M., 2023. Cleaner pathway for developing bioactive textile materials using natural dyes: a review. Environmental Science and Pollution Research. Online. 7 March 2023. Vol. 30, no. 17, p. 48793–48823. DOI 10.1007/s11356-023-26131-0.
5. BHARGAVA, Nitya, SHARANAGAT, Vijay Singh, MOR, Rahul S and KUMAR, Kshitiz, 2020. Active and intelligent biodegradable packaging films using food and food waste-derived bioactive compounds: A review. Trends in Food Science & Technology. Online. 22 September 2020. Vol. 105, p. 385–401. DOI 10.1016/j.tifs.2020.09.015.
6. MARTINS, Natália, RORIZ, Custódio Lobo, MORALES, Patricia, BARROS, Lillian and FERREIRA, Isabel C.F.R., 2016. Food colorants: Challenges, opportunities and current desires of agro-industries to ensure consumer expectations and regulatory practices. Trends in Food Science & Technology. Online. 5 April 2016. Vol. 52, p. 1–15. DOI 10.1016/j.tifs.2016.03.009.

7. POURJAVAHER, Simin, ALMASI, Hadi, MESHKINI, Saeed, PIRSA, Sajad and PARANDI, Ehsan, 2016. Development of a colorimetric pH indicator based on bacterial cellulose nanofibers and red cabbage (Brassica oleraceae) extract. Carbohydrate Polymers. Online. 12 September 2016. Vol. 156, p. 193–201. DOI 10.1016/j.carbpol.2016.09.027.
8. SHAHID, Mohammad, SHAHID-UL-ISLAM, None and MOHAMMAD, Faqeer, 2013. Recent advancements in natural dye applications: a review. Journal of Cleaner Production. Online. 3 April 2013. Vol. 53, p. 310–331. DOI 10.1016/j.jclepro.2013.03.031.
9. PRIYADARSHINI, Balasankar Meera, KOK, Wai Kay, DIKSHIT, Vishwesh, FENG, Shilun, LI, King Ho Holden and ZHANG, Yi, 2022. 3D printing biocompatible materials with Multi Jet Fusion for bioreactor applications. International Journal of Bioprinting. Online. 22 October 2022. Vol. 9, no. 1, p. 623. DOI 10.18063/ijb.v9i1.623.
10. CLEMENTI, Catia, DOMINICI, Franco, LUZI, Francesca, PUGLIA, Debora and LATTERINI, Loredana, 2023. Historically Inspired Strategy to Achieve Sustainable and Effective Coloration of Bioplastics. ACS Sustainable Chemistry & Engineering. Online. 19 June 2023. Vol. 11, no. 26, p. 9643–9653. DOI 10.1021/acssuschemeng.3c01085.
11. ZHAO, Ze, LI, Junchao, YAO, Dingrou and WEI, Yuan, 2022. Mechanical and permeability properties of porous scaffolds developed by a Voronoi tessellation for bone tissue engineering. Journal of Materials Chemistry B. Online. 1 January 2022. Vol. 10, no. 46, p. 9699–9712. DOI 10.1039/d2tb01478e.
12. DIAS, Romim G., MAGALHÃES, Georgia M., DIAS, Luís Gustavo G.G., ROCHA, Jessé R., DIAS, Fernanda G.G., FACIN, Andréia C. and MATTOS, Ewaldo, Junior, 2018. Biocompatibility of polyamide 12 intramedullary rod after humeral consolidation in white Plymouth Rock birds. Pesquisa Veterinária Brasileira. Online. 1 October 2018. Vol. 38, no. 10, p. 1909–1912. DOI 10.1590/1678-5150-pvb-5776.
13. LATKO-DURAŁEK, Paulina, MISIAK, Michał, STANISZEWSKA, Monika, ROSŁONIEC, Karina, GRODZIK, Marta, SOCHA, Robert P., KRZAN, Marcel, BAŻANÓW, Barbara, POGORZELSKA, Aleksandra and BOCZKOWSKA, Anna, 2022. The Composites of Polyamide 12 and Metal Oxides with High Antimicrobial Activity. Polymers. Online. 26 July 2022. Vol. 14, no. 15, p. 3025. DOI 10.3390/polym14153025.
14. EDDOUS, Sayfeddine, LAMÉ, Guillaume, DECANTE, Benoît, YANNOU, Bernard, AGATHON, Antoine, AUBRÈGE, Laure, TALON, Valérie and DACOSTA-NOBLE, Éléonore, 2023. CURRENT AND POTENTIAL APPLICATIONS OF 3D PRINTING IN A GENERAL HOSPITAL. Proceedings of the Design Society. Online. 19 June 2023. Vol. 3, p. 1117–1126. DOI 10.1017/pds.2023.112.
15. VIDAKIS, Nectarios, PETOUSIS, Markos, VELIDAKIS, Emmanuel, KORLOS, Apostolos, KECHAGIAS, John D., TSIKRITZIS, Dimitris and MOUNTAKIS, Nikolaos, 2022. Medical-Grade Polyamide 12 Nanocomposite Materials for Enhanced Mechanical and Antibacterial Performance in 3D Printing Applications. Polymers. Online. 22 January 2022. Vol. 14, no. 3, p. 440. DOI 10.3390/polym14030440.
16. SINGH, Vikram and MISHRA, Ashok K., 2015. White Light Emission from Vegetable Extracts. Scientific Reports. Online. 17 June 2015. Vol. 5, no. 1. DOI 10.1038/srep11118.
17. Kumar, Brajesh, Exploring Colour From Nature to Lab, 2024, 10.5772/intechopen.1001671.

Using IOA and educational robots to create a digital twin

Ján Kopec [1,*], Miriam Pekarčíková [1],

[1] Department of Industrial and Digital Engineering, Faculty of Mechanical Engineering, Technical University of Košice, Slovakia; jan.kopec@tuke.sk; miriam.pekarcikova@tuke.sk
* Correspondence: jan.kopec@tuke.sk; Tel.: +421 55 602 2714

Abstract: Digital Twin technology represents a major advance in industrial automation, education, and research, allowing the creation of a virtual model that is fully synchronized with the physical device. This paper focuses on the implementation of Digital Twin in the environment of the Department of Industrial and Digital Engineering at the Technical University of Košice. Specifically, WLKATA robot technology was used in combination with WLKATA Studio software and Siemens S7-1200 programmable logic controllers (PLCs). The research demonstrated that the digital twin enables accurate simulation and process control, while offering flexibility and efficiency in teaching and practical applications. The WLKATA Studio software provides an intuitive interface that is ideal for educational environments while allowing visual programming of robot movements and simulation of real-world tasks. Integration with PLC devices improves control and communication capabilities between components. The results showed that the digital twin technology brings significant benefits such as minimizing errors, optimizing processes, and improving training and education processes. This project provides the basis for further research and development of smart manufacturing solutions that reflect the requirements of Industry 4.0. The implementation of the digital twin has confirmed its potential in various industries and highlighted its importance for modern industrial and educational applications.

Keywords: IOA, Digital Twin, PLC.

1. Introduction

IOA digital twin is Input-Output-Automatic is the integration of virtual 3D twin technology and intelligent control technology platform, based on digital twin technology, to establish a 1:1 parallel world of virtual digitization and physical signal control, is the first set of AR+ manufacturing simulation system, IOA digital twin adopts the technical concept of "replacing reality with virtuality, controlling virtual with reality", so that the teaching and training of smart factories are truly in line with industry applications, easier to use, more efficient, a more portable new generation of engineering training platform. The virtual digital smart factory adopts a real/virtual robot teaching programming system, industrial robot motion controller, and real numerical control system, through hardware simulation technology to open up the communication between the controller and virtualization, that is, the student operation training adopts PLC programming control, industrial robot teaching programming application, MES scheduling and the practical operation of CNC equipment, through the 3D display of virtual equipment, to achieve the same training effect as the real smart factory. Based on the characteristics of the IOA digital twin and virtual and real interactive simulation, combined with the comprehensive construction of the laboratory, the software system can run through the hardware and industry demonstration of the entire training room and carry out virtual or virtual real simulation of each unit.

Figure 1. IOA digital twin intelligent manufacturing integrated simulation and design platform.

Modern technology has dramatically changed the industrial environment, making it increasingly productive, sustainable, and efficient. DT is a breakthrough technology that, as a concept, brings significant improvements in terms of optimization, prediction, and reliability. Like any technology, the digital twin has evolved incrementally from the stages shown in Figure 2.

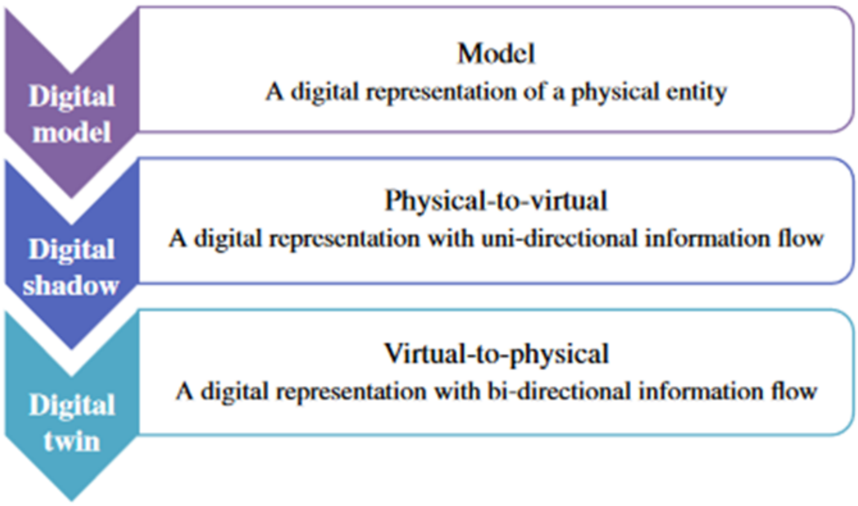

Figure 2. Developmental stages of a digital twin.

2. Materials and Methods

The workplace at the Department of Industrial and Digital Engineering was chosen as a place for practical implementation of the solution. In the laboratory 205 there are 5 educational robots which are shown in Figure 3.

Figure 3. WLKATA educational robots in laboratory conditions.

These robotic devices are controlled via the WLKATA Studio software. WLKATA Studio is a software tool specifically designed to control robotic devices, specifically robotic arms, which are used in a variety of applications such as education, research, simulation, and development. This program allows users to easily adjust the movements of robotic arms in 3D space, in three basic axes (X, Y, Z).

Key features of WLKATA Studio:

- **Intuitive interface:** The software environment is designed to be simple to use, allowing users to quickly become familiar with the control and configuration of robotic movements without the need for advanced technical knowledge.

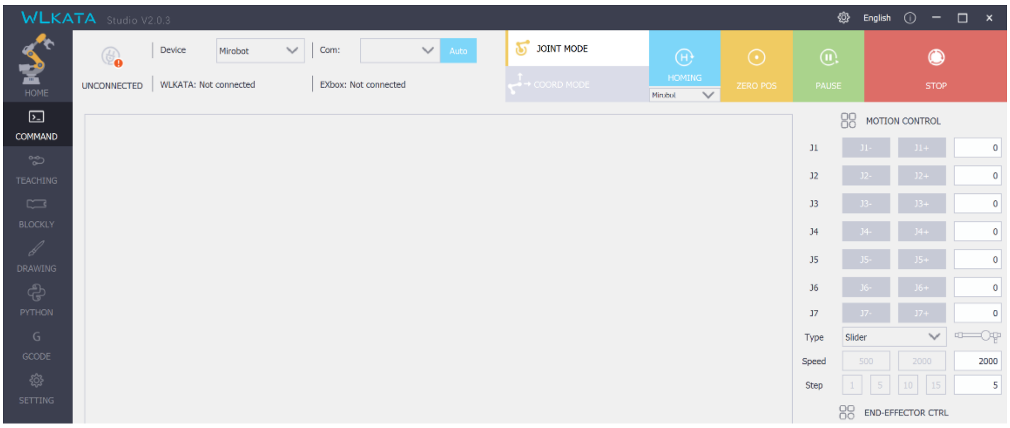

Figure 4. WLKATAStudio environment.

- **Multi-axis support:** The software allows you to control the robotic arms in multiple axes, ensuring precise movements and flexibility when setting up different tasks.
- **Programming with visual tools**: WLKATA Studio offers the ability to program robotic arm movements using visual tools such as drag-and-drop blocks, which are ideal for beginners or educational environments.
- **Support for manual control:** Users can manually control the robotic arm to familiarize themselves with its capabilities or perform simple tasks.

- **Simulation and testing:** Users can simulate and test movements in the software before performing real movements on the physical device, minimising the risk of errors.
- **Integration with other technologies:** The program supports various inputs and outputs, allowing it to integrate with other devices or software such as sensors, cameras or other control units.

As part of the multi-module integration, the IOA program can communicate with PLC devices, e.g. from Siemens, model S7- 1200.

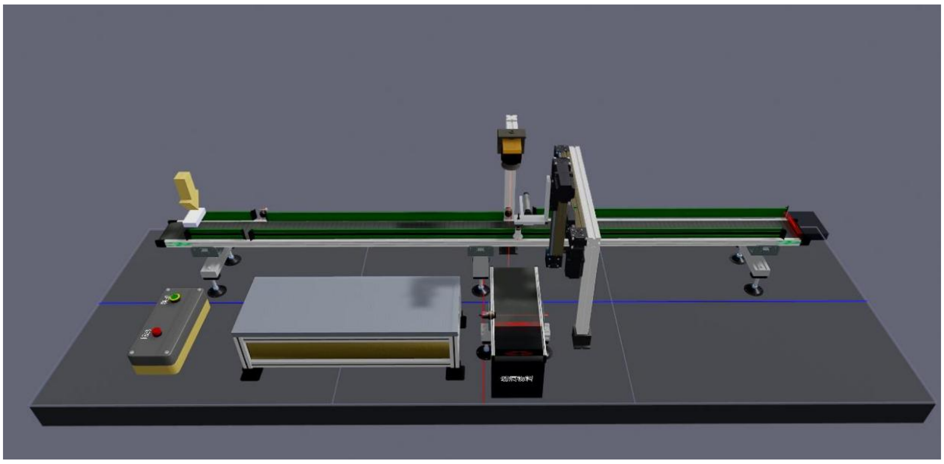

Figure 5.: Digital twin.

Figure 5 shows a digital twin of the real model in a laboratory environment. Any changes made to the digital model are reflected in the physical model and vice versa. This will ensure a smooth flow of information.

3. Results

The Digital Twin technology using WLKATA robots was successfully implemented in the project in Laboratory 205 at the Department of Industrial and Digital Engineering. The main objective was to demonstrate the link between the physical and virtual models and to ensure that any changes made to the digital model are immediately reflected on the physical device, and vice versa. This approach illustrated the capability of seamless data exchange and integration between the virtual and real worlds.
The robotic devices, controlled through the WLKATA Studio software, allowed precise adjustment of movements in three axes (X, Y, Z). Simulations and testing in this software demonstrated the ability to minimize the risk of errors before the real implementation of the tasks on the physical devices. Another important result was the implementation of visual programming, which is suitable for educational environments and allows simple and intuitive control of robotic devices.
The integration of the WLKATA Studio software with PLC devices (e.g. Siemens S7-1200) showed the effectiveness in linking multiple technologies. In addition, the project verified the ability to synchronize between the virtual model and the physical robot, which is crucial for modern solutions in smart manufacturing and industrial automation.
These results confirmed that the digital twin has great potential in education, research, and practical application in industrial processes. The combination of hardware simulations and virtual environments provides an effective tool for training and teaching, thus contributing to the development of professional skills in line with the needs of Industry 4.0.

4. Conclusions

The results of the project demonstrated the successful implementation of Digital Twin technology in conjunction with WLKATA robots, confirming the key benefits of this approach such as accurate synchronisation between physical and digital models. This implementation has shown the potential of Digital Twin in various applications, especially in education and industrial automation, where it plays an important role in process optimization and error reduction.

The use of WLKATA Studio software has contributed to increased efficiency not only through its intuitive interface and visual programming, but also through the simulation capability, which minimizes the risks associated with the practical execution of tasks. These features make WLKATA Studio an ideal tool for educational and research purposes, while also supporting its use in practical industrial applications.

Integration with PLC devices such as the Siemens S7-1200 was a key element of the project, ensuring that the individual modules of the technology could function as a single unit. This compatibility demonstrated the digital twin technology's ability to communicate and adapt effectively to different systems, allowing it to be used flexibly in a variety of industrial environments.

The project has shown that digital twin technology not only improves the efficiency and accuracy of educational and research processes, but also makes a significant contribution to the development of skills needed for modern industrial applications. This opens the way for further research aimed at extending the functionality and portability of the digital twin to other areas such as healthcare, logistics or construction.

In conclusion, this project has laid the foundation for future applications and development of smart manufacturing solutions, confirming the importance of the link between theoretical concepts and practical implementations in the context of Industry 4.0. The above results support further research and innovation in the field of digital twin, which has the potential to transform a wide range of industries.

This section is not mandatory but can be added to the manuscript if the discussion is unusually long or complex.

Acknowledgments: This article was created by the implementation of the grant projects: APVV-17-0258 Digital engineering elements application in innovation and optimization of production flows, APVV19-0418 Intelligent solutions to enhance business innovation capability in the process of transforming them into smart businesses. KEGA 020TUKE-4/2023 Systematic development of the competence profile of students of industrial and digital engineering in the process of higher education. VEGA 1/0508/22 „Innovative and digital technologies in manufacturing and logistics processes and system", KEGA 003TUKE-4/2024 Innovation of the profile of industrial engineering graduates in the context of required knowledge and specific capabilities for research and implementation of intelligent systems of the future.

References

1. Wlkata Robotics,[Online], Available online: https://www.wlkata.com/.
2. TREBUŇA, P., PEKARČÍKOVÁ, M., FIĽO, M. : Digital factory -1.vyd. - Lüdenscheid : RAM-Verlag - 2024. - 355 s. [print]. - ISBN 978-3-96595-043-6.
3. BEE, L. : PLC and HMI Developmnet with Siemens TIA Portal - PACKT PUB - 2022 - 436p.. - EAN: 9781801817226.
4. BERGER, H. : Automating with SIMATIC S7-1200 3e - Configuring, Programming and Testing with STEP 7 - Public MCD Verleg, Germany - 2018 - 745p.. - ISBN: 9783895784705.
5. ATTARAN, M., et.al.; The impact of digital twins on the evolution of intelligent manufacturing and Industry 4.0, 2023, [Online], Available online: < https://link.springer.com/article/10.1007/s43674-023-00058-y >.
6. RATHORE, ULAH, MAZHAR, MUHAMMAD, ET.AL.; The Role of AI, Machine Learning, and Big Data in Digital Twinning: A Systematic Literature Review, Challenges, and Opportunities, February 2021, DOI: 10.1109/ACCESS.2021.3060863, [Online], Available online : < https://www.researchgate.net/publication/349508978_The_Role_of_AI_Machine_Learning_and_Big_Data_in_Digital_Twinning_A_Systematic_Literature_Review_Challenges_and_Opportunities >.
7. MPDI Open Access Journals, Digital Twin Technologies for Turbomachinery in a Life Cycle Perspective. [Online] 25 February 2021 https://www.mdpi.com/2071-1050/13/5/2495.

8. WLKATA ROBOTICS DOKUMENT. OpenMV, LLC. OpenMV IDE v4.1.5, Download Now, 2024 [Online] https://openmv.io/pages/download .
9. ROMAN MALIŠKA: Ponorte sa do tajov robotiky so súpravou WLKATA Mirobot. [Online] TECHPEDIA Sprievodca Svetom Technológií, 29.12.2022 https://techpedia.ta3.com/technologie-pre-ludi/novinky/11184/ponorte-sa-do-tajov-robotiky-so-supravou-wlkata-mirobot .
10. WLKATA ROBOTICS DOCUMENT. Using the TEACHING function [Online] 07. 09. 2023 [date: 07. 09. 2022.] https://document.wlkata.com/?doc=/wlkata-mirobot-user-manual-platinum/13-using-the-teaching-function/.
11. TREBUŇA, Peter - PEKARČÍKOVÁ, Miriam - KLIMENT, Marek - TROJAN, Jozef. Metódy a systémy riadenia výroby v priemyselnom inžinierstve. [et al.] - 1. vyd. - Košice: Technická univerzita v Košiciach - 2019. - 210 s. [print]. - ISBN 978-80-553-3280-2.
12. PEKARČÍKOVÁ, Miriam - TREBUŇA, Peter - KRÁL, Štefan - DUDA, Richard: Logistika pre priemyselné inžinierstvo / Miriam Pekarčíková ... [et al.] - 1. vyd. - Košice : Technická univerzita v Košiciach - 2021. - 333 s. [print]. - ISBN 978-80-553-3988-7.
13. CHRISTOPHER J. TURNER, WINDO HUTABARAT, JOHN OYEKAN, ASHUTOSH TIWARI. Discrete Event Simulation and Virtual Reality Use in Industry: New Opportunities and Future Trends. Innovate UK [Online] June 28, 2016 http://ieeexplore.ieee.org.
14. KOVALČÍK, J., STRAKA, M., TROJANOWSKA, J.; Utilize educational robots to design logistic systems, - 2024. In: Applied sciences. - Bazilej : Multidisciplinary Digital Publishing Institute, 2011 Roč. 14, č. 13 (2024), s. [1-16] [online]. - ISSN 2076-3417 [online], Available online: https://www.mdpi.com/2076-3417/14/13/5664.

TECHNICAL UNIVERSITY OF KOŠICE
Faculty of Mechanical Engineering

EHS Data Digitization and Integration into Production Monitoring Tools to Prevent Occupational Diseases

Peter Krajný [1,*] and Jaroslava Janeková [1]

[1] Institute of Industrial Engineering, Management and Applied Mathematics, Faculty of Mechanical Engineering, Technical University of Košice, Park Komenského 5, 040 02 Košice, Slovakia; peter.krajny@student.tuke.sk (P.K.); jaroslava.janekova@tuke.sk (J.J)
* Correspondence: peter.krajny@student.tuke.sk; (P.K.)

Abstract: In a world that is progressively becoming more digital, the modeling and handling of data have gained high significance. This is especially true as we transition from conventional data management, pass through the era of big data, and enter into the current phase of digitization. This paper describes the study of the digitization of various data types and the interconnections between multiple data sources from a real automotive company. The proposed model focuses on integrating two independent online applications: one designed to connect and process data from the production environment, and the other aimed at evaluating ergonomic scores for individual workstations. The outcome of this study is to assess the feasibility of linking these two systems, which will enable future monitoring of operator workload to help prevent occupational diseases.

Keywords: data digitization; production data; digitization

1. Introduction

Digitization has been recognized as one of the prominent trends reshaping society and business in the immediate and long-term future [1]. The impact of digitization will be substantial; several authors have linked it to the industrial revolution [2-5]. The term "digitization" specifically refers to "the action or process of digitizing; the conversion of analogue data (especially in later use, images, video, and text) into digital form." According to the literature, digitization, or digital transformation, denotes "the changes associated with the application of digital technology in all aspects of human society" [6]. Digitization is also recognized as the "ability to turn existing products or services into digital variants, and thus offers advantages over tangible products" [7,8].

Certainly, numerous challenges are linked to the effective management of various data types. Beyond addressing the substantial volume of big data, there is a necessity to identify and comprehend patterns. Historical data management has consistently prioritized the acquisition of precise depictions of business activities.

The evolution of data management has transitioned from crafting tools and methodologies for conventional, structured data to handling big data, thereby opening avenues for innovative applications of data derived from emerging technologies. Effective data management, along with the archival of data for future utilization [9], is of paramount importance. This paper focuses on digitization of data transformation from the production environment to Cloud Application, using analytical techniques to merge data from multiple sources to obtain one analytical output.

2. Methods and Materials

The case study described in these pages focuses on integrating multiple data sources from production analytical tools, emphasizing Environmental, Health, and Safety (EHS) assessments and their connection with other production indicators.

The study specifically examines how to ingest data from HumanTech software into the Palantir Foundry platform, particularly the Cycle Time Deviation (CTD) application. The primary goal is to transfer ergonomics EHS scores from assessments and generate production reports detailing which operator, at which station, with which EHS score, spent how many minutes. These statistics aim to monitor the duration of working times at the most problematic stations to support the prevention of occupational diseases.

The methodological approach of this research is structured in two main stages. The first stage focuses on understanding current state procedures and analyzing how the process operates. Building on this understanding and identifying the problem, the second stage proposes a solution.

Given the large volume of data processed by the solution, ensuring data quality is critical. To manage this, the Palantir Foundry platform is utilized, with the Pipeline Builder module employed to filter and clean data formats, ensuring accurate calculations. In the logical layer, numerous operations and processes work in the background to prepare high-quality data and maintain proper formatting.

This study is being developed for a major automotive company with a focus on assembly processes.

2.1 Case study description

Currently, two separate systems are in use to manage production and ergonomic data.

The first system, called the Cycle Time Deviation (CTD) application, is built on the Palantir Foundry platform. It collects and processes production data from the corporate Manufacturing Execution System (MES) and other offline sources, integrating this information into a user-friendly front-end interface. The interface is divided into two parts. The first, the CTD Workshop application, is used for live production monitoring. It displays key indicators and color-coded management data, providing line leaders with a concise and clear overview of the health of their processes. The second part, the Shift Report application, is used for reporting, either at the end of work shifts or as needed. This application contains essential indicators relevant to specific plants (see Figure 1).

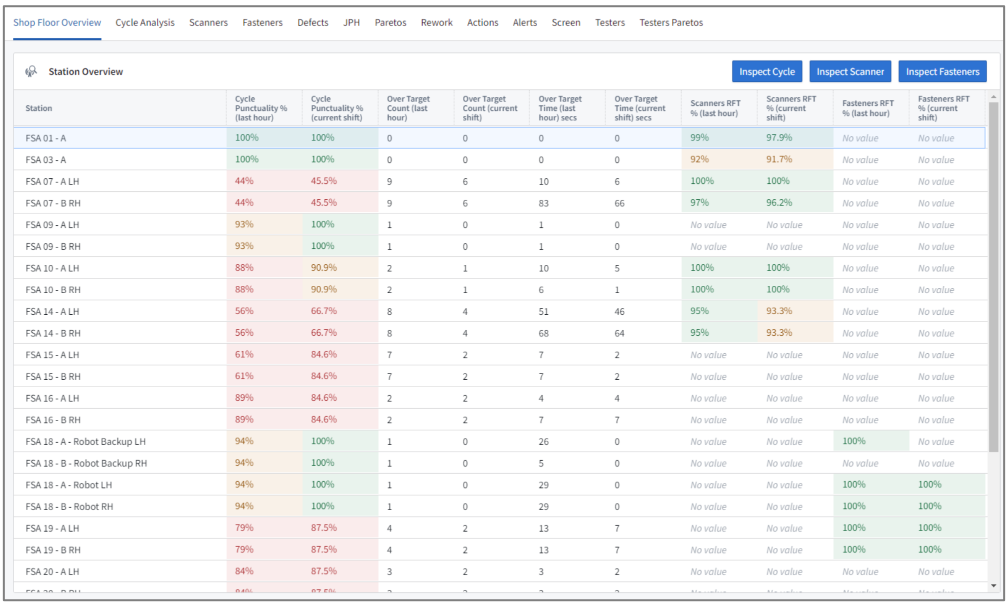

Figure 1. Snapshot from CTD Workshop application with general overview.

The second system, known as HumanTech, is designed for analysis focused on ergonomic studies. These assessments can be conducted in two ways. The first method involves recording a video and analyzing it using the HumanTech front-end application, where an *Artificial Intelligence* (AI) tool evaluates body movements and produces a comprehensive assessment. The second method involves manually entering tasks into the system, which are then evaluated. These analyses generate a difficulty score for each task related to the assembly process at specific workstations. This score helps determine the complexity of assembly operations and evaluates the difficulty of the overall process (see Figure 2).

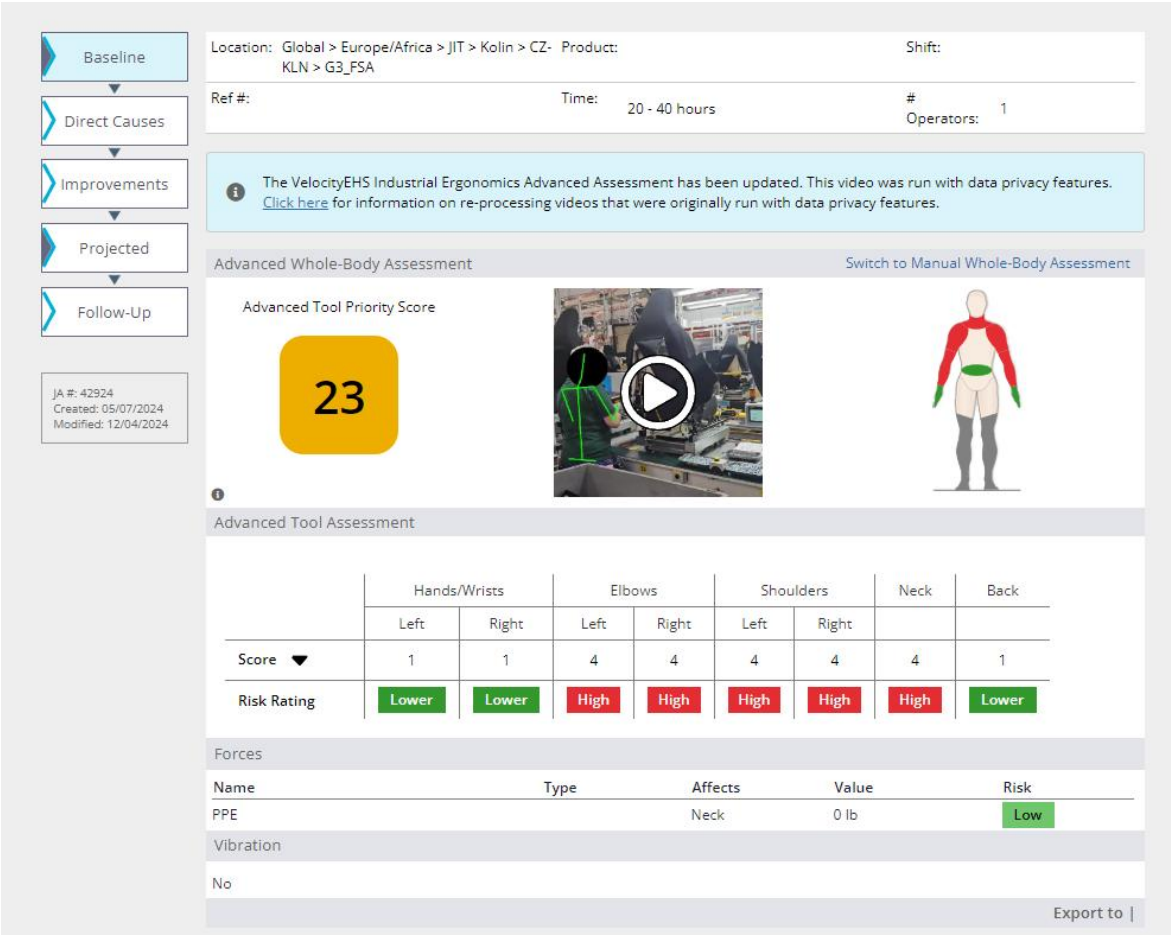

Figure 2. Snapshot from HumanTech software with ergonomics study made on assembly station.

Currently, fixed rules are used for rotating operators between stations without considering ergonomic risk assessments. Given the large scale of production lines, it is difficult to monitor which operator worked at which station and the ergonomic difficulty score assigned to each station.

An automated solution is being sought to address these challenges. The proposed system would enable tracking and reporting of EHS scores for each station, as well as identifying operators who have skipped rotations or spent excessive time at specific stations. Additionally, the system would include active reporting and push notifications for line leaders, ensuring timely alerts to mitigate occupational diseases and improve compliance with ergonomic standards. This approach aims to enhance operator rotation monitoring and promote workplace health and safety.

2.2 Case study solution process

The case study focuses on integrating two independent systems: the HumanTech application, which evaluates ergonomic studies, and the CTD application, which processes and visualizes production data.

As these systems operate on entirely different platforms with distinct data structures, the integration will involve extending the existing CTD application with new modules and analyses. The initial step requires extracting and uploading HumanTech data into the Palantir Foundry environment to examine its format and structure. During this process, relevant datasets for the integration will be identified and filtered to align with the CTD application's current format. The goal of this integration is to display ergonomic EHS data alongside station visualizations within the CTD Workshop and Shift Report front-end applications (see Figure 3).

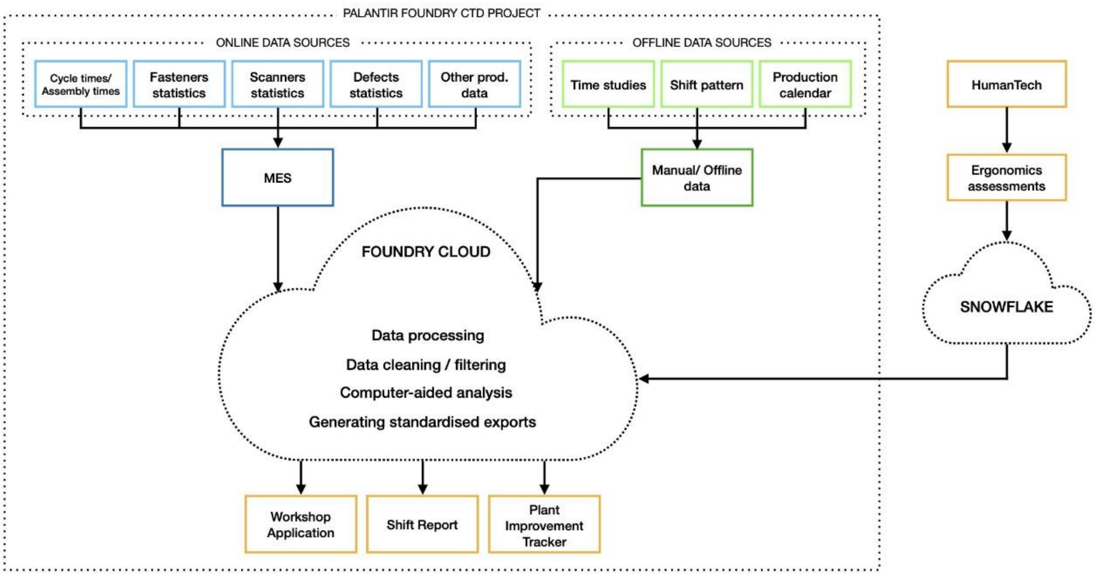

Figure 3. Diagram of the implementation of ergonomics studies into the CTD application.

This study examines the feasibility of integrating these two systems, the adjustments required to map their data effectively, and the development of a unified data structure for processing within the CTD application.

3. Results

During the case study, it was discovered that HumanTech data is stored in Snowflake databases and systematically organized into numerous partial datasets. Since these are external datasets, their integration into Foundry will require setting up periodic updates to ensure automatic data synchronization.

For the study, a dataset named "PUBLIC"."CACHE_JOB_ASSESSMENT_VIEW" was selected. From this dataset, only a limited number of columns will be retained. A key column, "OU_PATH", contains hierarchical information such as:

- Continent
- Division
- Plant name
- Line name
- Process categorization (e.g., logistics, production, maintenance) in certain cases.

Since this information is stored in a single row without the desired structure, the data needs to be cleaned and restructured using the Pipeline Builder tool in Palantir Foundry platform (see Figure 4).

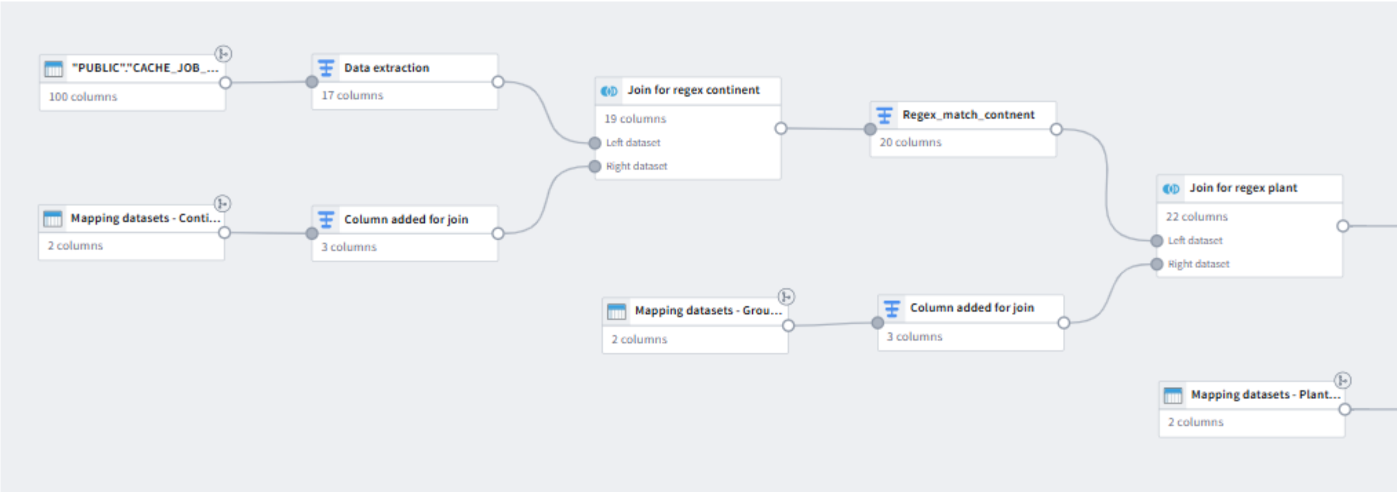

Figure 4. Pipeline Builder – Data processing tool in the Foundry platform.

Data cleaning will involve utilizing a series of synchronized datasets and applying Regular Expressions (RegEx) to split the information into multiple columns. To ensure compatibility between data sources, standard naming conventions must be used. For example, GB-COV represents GB (Great Britain), and COV stands for Coventry (see Figure 5).

plant	regex_plant
FR-FEI	^.{31}(Feignies).*|^.{35}(Feignies).*
CZ-KLN	^.{31}(Kolin).*|^.{35}(Kolin).*
GB-COV	^.{31}(Coventry).*|^.{35}(Coventry).*
GB-RED	^.{31}(Redditch).*|^.{35}(Redditch).*
SK-VOD	^.{31}(Voderady).*|^.{35}(Voderady).*
GB-SUN	^.{31}(Sunderland).*|^.{35}(Sunderland).*
PL-TYC	^.{31}(Tychy).*|^.{35}(Tychy).*|^.{38}(Tychy).*
HU-GYR	^.{31}(Gyor).*
CZ-STR	^.{31}(Stribro).*

Figure 5. Example of regular expressions.

These newly created columns will serve as mapping fields to join Snowflake data with the Foundry CTD application.

The ergonomic EHS scores are stored in two columns within the dataset:

1. MSDAI_SCORE – Represents the baseline analysis.
2. MSDAI_SCORE_FOLLOWUP – Represents the reassessment score after modifications at a station.

By default, the MSDAI_SCORE is used unless a follow-up assessment (MSDAI_SCORE_FOLLOWUP) has been conducted. If the follow-up score is lower, it signifies successful optimization, and this score is retained in the system as the improvement score. In such cases, the value from MSDAI_SCORE_FOLLOWUP should be prioritized over MSDAI_SCORE for subsequent analyses.

The integration of these datasets, combined with the ergonomic scoring system, will establish a seamless connection between HumanTech and CTD, facilitating improved reporting and process optimization in the future.

4. Discussion

Data digitization, as described in these pages, brings us to another level of evaluation and data analysis. Implementing automated data analytical tools using artificial intelligence may help us better understand the processes and save time for additional big data analysis.

We can see similarities with authors Storey and Woo (2018) as they describe in their papers focused on the data challenges in the digitalization era, particularly the issues related to data quality and integration from multiple sources. Our approach of filtering and cleansing data, and the subsequent creation of preprocessed datasets, reflects a similar concern for data quality. Both studies emphasize the critical role of data integrity in achieving accurate and reliable analytical outcomes.

Based on this case study and future research, we aim to define the classification and evaluation of the level of digitalization in industrial enterprises.

5. Conclusion

The digitalization of data and the integration of diverse systems for monitoring the production environment highlight the significance of such solutions. Palantir's cloud-based platform, Foundry, demonstrates substantial potential in this domain. Its high modularity allows for the processing of vast amounts of data, simplifying large-scale data analyses for users.

Additionally, this case study serves as a foundation for future research focused on developing standardized measures to evaluate the level of digitization in industrial enterprises, further advancing the ongoing digital transformation within the manufacturing sector.

Acknowledgments: This paper was developed within the projects implementation: VEGA 1/0219/23 "Empirical research of the relation of implementation of advanced technologies and sustainable behaviour of manufacturing companies in Slovakia" and KEGA 038TUKE-4/2024 "Increasing the applicability of graduates on the labour market by implementing practice requirements into the teaching process of the environmental engineering study program".

Conflicts of Interest: The authors declare no conflict of interest.

References

1. Beck, R.; Avital, M.; Rossi, M.; Thatcher, J.B. Blockchain technology in business and information systems research. Business & Information Systems Engineering. 2017, 59(6), 381–384.
2. Chen, H.; Chiang, R.H.; Storey, V.C. Business intelligence and analytics: from big data to big impact. MIS Q. 2012, 36(4), 1165–1188.
3. Chen, P.P.S. The entity-relationship model—toward a unified view of data. ACM Trans. Database Syst. 1976, 1(1), 9–36.
4. Delcambre, L.M.L.; Liddle, S.W.; Pastor, O.; Storey, V.C. A reference framework for conceptual modeling. In: Conceptual modeling, ER 2018, Trujillo, J.C., et al. (eds.) ER 2018. Springer, LNCS, Cham, 2018; Volume 11157, pp. 27–42.
5. Embley, D.W.; Liddle, S.W. Big data—conceptual modeling to the rescue. In: Conceptual modeling, ER 2013, Ng, W., Storey, V.C., Trujillo, J.C. (eds.) ER 2013. Springer, LNCS, Heidelberg, 2013; Volume 8217, pp. 1–8.
6. Goes, P.B. Editor's comments: big data and IS research. MIS Q. 2014, 38(3), iii–viii.
7. Gupta, M., George, J.F. Toward the development of a big data analytics capability. Information & Manage. 2016, 53(8), 1049–1064.
8. Larsen, H. The crisis of public service broadcasting reconsidered: commercialization and digitalization in Scandinavia. Crisis Journal. 2016. Reconsidered: Democ. Cult. Prof. Codes, Digital Future 43–58.
9. Storey, V.C.; Woo, C. Data challenges in the digitalization era. In: Proceedings of the 28th Workshop on Information Technologies and Systems, Santa Clara, California, 2018.

TECHNICAL UNIVERSITY OF KOŠICE
Faculty of Mechanical Engineering

Prediction of the limit strain curve by numerical simulation and its verification by experiment

Juliy Martyn Kulya [1,*] and Miroslav Tomáš [1]

[1] Department of Automotive Production, Faculty of Mechanical Engineering, Technical University of Kosice; juliy.martyn.kulya@tuke.sk; miroslav.tomas@tuke.sk
* Correspondence: juliy.martyn.kulya@tuke.sk; Tel.: +421 55 602 3528

Abstract: This study explores the effectiveness of the Nakazima test in evaluating the formability of dual-phase high-strength steel DP800. Mechanical testing was conducted to characterize material anisotropy, and Nakazima tests were performed using an Erichsen deep-drawing machine equipped with the Aramis 3D optical system for deformation analysis. The experimental results were compared with numerical simulations based on two material models: Hill 48 anisotropic plasticity with Hollomon hardening and Barlat91 anisotropic plasticity with Krupkowski hardening. The comparison revealed that both models captured the general trend of experimental data, with Simulation Model 1 (Hill 48 + Hollomon) demonstrating better agreement in the plane-strain region, while Simulation Model 2 (Barlat91 + Krupkowski) provided more accurate predictions in the transitional minor strain range. These findings highlight the importance of precise material modeling in numerical simulations and confirm the Nakazima test's role in formability assessment for high-strength steels. The results contribute to improving predictive capabilities in automotive sheet metal forming, aiding in the design of lightweight vehicle structures.

Keywords: Nakazima test, stretching force, punch path, experiment, simulation

1. Introduction

To address the growing need for reducing emissions during vehicle operation, the automotive industry has prioritized the development of lightweight designs without compromising passenger safety. This focus on weight reduction has led to the wide-spread use of advanced high-strength steel (AHSS) grades, particularly dual-phase steels, which offer an excellent balance of strength, ductility, and cost-efficiency [1].

The formability of sheet metal is a crucial factor in manufacturing automotive components, as it directly impacts structural integrity. Formability, defined as the abil-ity of sheet metal to undergo stamping without fracturing, depends on a complex in-teraction of material properties and process parameters [2]. While the material's in-trinsic formability can be evaluated through standard tensile or compression tests, process formability necessitates a detailed assessment of various factors inherent to the manufacturing process [3].

Several experimental methods have been developed to assess formability, includ-ing the Erichsen test, Engelhardt test, Cup test, Limit Dome Height (LDH) test, and Nakazima test [2-4]. Among these, the Nakazima test has gained significant attention for its ability to simulate fracture conditions under controlled deformation scenarios, offering detailed insights into sheet metal behavior under plane-strain deformation [5]. Its relevance has increased over time due to its ability to address a considerable num-ber of stamping-related failures, making it indispensable in the automotive sector.

Since its introduction by Nakazima, the test has undergone various modifications to suit a wide range of materials, sheet thicknesses, and applications, including la-ser-welded dissimilar materials [5,6]. Researchers such as Sahu [7], Xie and Nakamachi [8], Kuramae et al [9], Katragadda et al [10], and Bandyopadhyay et al [11] have extensively applied the Nakazima test to investigate the deformation behavior, formability, and fracture mechanisms of different materials, including high-strength steels and material combinations.

In this study, we focus on comparing the experimental results obtained from Nakazima tests conducted on dual-phase steel DP800 with the outcomes of numerical simulations. Using the Aramis system, major and minor strains are quantified and compared with those predicted by simulation software such as Pam-Stamp, offering valuable insights into the correlation between experimental and simulated data.

2. Materials and Methods

2.1 Material – DP800

The formability assessment of dual-phase high-strength steel DP800 with a thickness of 1.5 mm was conducted using the Nakazima test. To characterize the mechanical properties of the experimental material, standard testing procedures were employed, including ISO 6892-1 for tensile testing, ISO 10113 for plastic strain ratio evaluation, and ISO 10275 for determining the strain hardening exponent. Samples for the mechanical tests were extracted in three directions: 0°, 45°, and 90° relative to the rolling direction, aiming to comprehensively describe material anisotropy. Each direction underwent testing with three specimens, and the resulting average values are presented in Table 1. The experimental tests were performed on a TIRA test 2300 testing machine, equipped with both longitudinal and transversal extensometers with a precision of 0.001 mm.

The plastic strain ratio was assessed at the uniform elongation level, while the strain hardening exponent was determined within the range of 5% to uniform elongation. This comprehensive characterization aims to capture the material behavior under different loading conditions, providing valuable insights into the anisotropic properties of the dual-phase steel under consideration.

Table 1. Mechanical properties of dual-phase steel DP 800, thickness 1.5 mm.

	$R_{p0,2}$ [MPa]	R_m [MPa]	A_{80} [%]	r [-]	r_m [-]	n [-]	n_m [-]
0°	527	828	19.9	0.873		0.126	
45°	508	830	18.2	0.907	0.917	0.125	0.125
90°	496	838	18.4	0.979		0.123	

2.2 Nakazima Test

The Nakazima test, a significant method for evaluating sheet metal forming properties, particularly ductility, was employed in our experiments using the Erichsen 145-60 universal deep-drawn sheet metal testing machine. This machine, with a maximum force capacity of 600 kN, was equipped with Nakajima tooling setup for precise control during the tests. The Nakazima test involves subjecting clamped specimens to strains induced by a hemispherical die until fracture occurs. Various specimen widths, specifically 196, 140, 110, 80, 50, and 30 millimeters, were utilized, as illustrated in Figure 1.

Figure 1. Types of blanks.

To create a deformation mesh on the samples, electrochemical etching was performed using an ÖSTLING EU Classic 300. This process employed a matrix covering the sample, through which electrolyte was fed via a graphite electrode. The electrode moved uniformly over the entire surface, with both the sample and the electrode connected to a DC voltage. The resulting rectangular deformation grid comprised dots with a diameter of 1 mm and a spacing of 2 mm in rows and columns.

For precise measurement of the applied deformation mesh, we utilized the Aramis 3D optical system from GOM, a German company. Renowned for its complexity and reliability, Aramis employs digital image correlation (DIC) to track surface deformation. By applying a speckle pattern to the specimen, Aramis captures images during testing, allowing for detailed analysis of 3D coordinates, strain, and displacement. This comprehensive setup on the Erichsen 145-60 machine with Nakajima tooling provides valuable insights into the formability of dual-phase high-strength steel DP800 under Nakazima test conditions.

2.3 Simulation model of Nakazima test

The simulation model is shown in Fig.2. It consists of three parts – die (green), punch (red), blank holder (turquoise), and blank (purple). These parts were meshed during importing CAD model of the tool and set as rigid surface tools. The picture shows one type of blanks with a width of 196mm. Blanks were meshed by square elements 2x2mm.

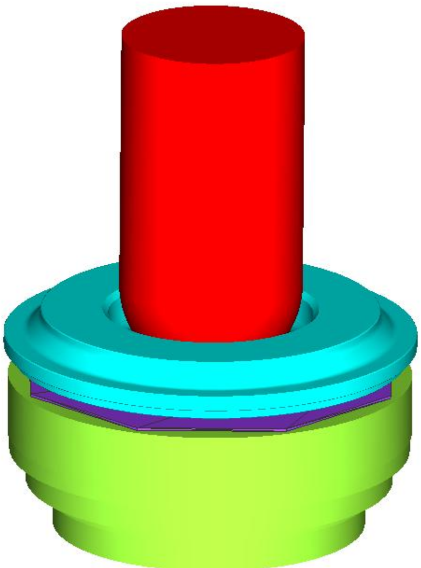

Figure 2. Simulation model.

Yield law and hardening curve describing material behavior were defined as follows:
Hill 48 anisotropic plasticity model:

$$\sigma_1^2 = \frac{r_0(1 + r_{90})}{r_{90}(1 + r_0)}\sigma_2^2 - \frac{2r_0}{1 + r_0}\sigma_1\sigma_2 = \left(\sigma_1^y\right)^2 \tag{1}$$

where: σ_1 and σ_2 are the principal stresses in the material, y - represents the yield stress in uniaxial tension,

Hollomon hardening model:

$$\sigma = K \cdot \varphi^n \tag{2}$$

where K is material constant, n is strain hardening exponent.

In this study, two material models were compared through numerical simulations. The first model utilizes Hill 48 anisotropic plasticity and Hollomon hardening, as described above. The second model combines Barlat91 anisotropic plasticity with the Krupkowski hardening model.

Barlat91 anisotropic plasticity model:

$$f = |S_1 - S_2|^m + |S_2 - S_3|^m + |S_3 - S_1|^m = 2\bar{\sigma}^m \tag{3}$$

S_1 to S_3 are the principal values of the symmetric matrix S with the coefficients C_1 to C_6, m - exponent defining anisotropy and yield shape.

Krupkowski hardening model:

$$\sigma = K \cdot \left(\varepsilon_p + \varepsilon_0\right)^n \tag{4}$$

where: ε_p - plastic strain, ε_0 - offset strain, n - strain hardening exponent, K - material constant.

We chose the combinations of Hill 48 + Hollomon and Barlat91 + Krupkowski models due to the limited availability of material models in Simufact Forming. These were the only suitable anisotropic yield criteria and hardening laws accessible in the software that could adequately represent the material behavior required for our simulations.

The results of these simulations were analyzed to evaluate their accuracy in predicting the material's deformation behavior and fracture limits.

The blank was meshed using quadrilateral shell elements with an element size of 1.1 mm. The mesh was generated automatically based on the software's recommended settings.

3. Results and discussion

The results of the measurement of the maximum tensile forces and the punch path up to the specimen fracture for six different widths of Nakazima blanks (30 mm, 50 mm, 80 mm, 110 mm, 140 mm, and 196 mm) are presented in Table 2. For each blank width, three experimental measurements were carried out, and the average values of the maximum force and the punch path at fracture were calculated.

In the numerical simulations, the same blank widths were modeled to ensure consistency with the experimental setup. The average punch path from the experiments was used as a reference for defining the punch movement in the simulation. Table 2 provides a direct comparison of the maximum tensile forces obtained from the exper-iments and the numerical simulations for each blank width.

Table 2. Measured values of the maximum force and the punch path at fracture.

	Experiment			Simulation	
	Max. Force [kN]	**Average value**	**Stroke [mm]**	**Max. Force [kN]**	**Stroke [mm]**
196	195.9		37.1		
	194.6	201.4	36.9	243.7	34.2
	214.0		41.1		
140	159,2		33.1		
	161,5	160.0	33.5	193.4	29.5
	158,0		33.0		
110	97.7		26.6		
	105.5	101.9	26.9	117.92	23.6
	102.6		26.9		
80	78,4		26.2		
	79,8	79,4	26.6	86.6	22.7
	78,9		26.4		
50	69,4		30.7		
	67,3	68,8	30.4	74,6	29.6
	69,3		31.0		
30	37.2		28.5		
	37.1	37.3	28.4	40.11	24.8
	37.6		28.9		

Figure 3 illustrates the comparison of the Forming Limit Curves (FLCs) obtained from two numerical simulation models (Simulation Model 1 and Simulation Model 2) and the experimental results measured using the Aramis system. The six data points for each method correspond to different strain conditions.

The experimental results from Aramis reveal generally lower major strain values compared to both simulation models. The largest differences are observed in the region of higher minor strain values (above 0.3), where simulation models predict higher deformation limits compared to the experiment.

Simulation Model 1 demonstrates a consistent trend across the strain range, with slightly higher major strain predictions compared to Simulation Model 2. Notably, both models exhibit similar behavior in the region of negative minor strains, closely matching each other up to approximately -0.2. However, discrepancies between the two models become apparent as minor strain values increase.

Table 3. Comparison of Experimental and Simulated Maximum Strain Values.

Experiment		Simulation model 1		Simulation model 2	
Minor	Major	Minor	Major	Minor	Major
-0.133	0.363	-0.254	1.05	-0.255	1.04
-0.0977	0.362	-0.183	0.889	-0.181	0.863
0.00368	0.19	-0.0383	0.434	-0.0341	0.435
0.0351	0.171	0.039	0.392	0.0672	0.26
0.101	0.253	0.35	0.612	0.214	0.404
0.257	0.266	0.526	0.539	0.508	0.53

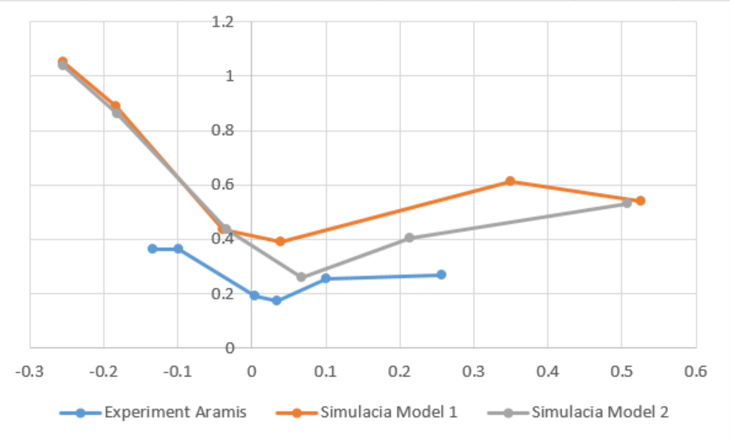

Figure 3. Comparison of FLCs obtained with Aramis and those obtained with numerical simulation.

Simulation Model 2 shows better alignment with the experimental data in the range of minor strains from -0.1 to 0.1, particularly at the transition between negative and positive strains. However, for minor strains above 0.3, the model starts to deviate from the experimental results, predicting significantly higher major strain values.

The experimental FLCs obtained with Aramis serve as a benchmark for the accuracy of the numerical models. While both simulation models capture the general trend of the experimental results, the differences highlight the influence of the selected material models (Hill 48 with Hollomon for Simulation Model 1 and Barlat91 with Krupkowski for Simulation Model 2) on the predicted forming limits. These findings underscore the need for careful selection and calibration of material models to improve the reliability of numerical predictions.

The simulation results overestimate the experimental forming limits due to simplified modeling conditions. Friction is defined as a constant in the simulation, while in the real Nakazima test it can vary with lubrication, temperature, or strain rate. This leads to lower resistance in the model and thus higher predicted strains.

4. Conclusions

This study provides a comprehensive analysis of the formability of dual-phase steel DP800 using the Nakazima test in combination with advanced numerical simulations. The experimental results obtained with the Aramis system demonstrated high precision in capturing strain distributions, allowing for an in-depth assessment of material behavior across six different blank widths. The experimental data revealed clear directional variations in deformation and fracture patterns, emphasizing the material's anisotropic characteristics.

Comparative analysis between experimental and numerical results highlighted the strengths and limitations of the two material models employed in simulations. Simulation Model 1 (Hill 48 with Hollomon hardening) showed strong agreement with experimental data in the plane-strain region, while Simulation Model 2 (Barlat91 with Krupkowski hardening) displayed better accuracy in the transitional range of minor strains. Both models proved capable of predicting general trends but underscored the importance of precise material characterization and calibration to enhance simulation reliability.

The findings of this research reinforce the Nakazima test's critical role in formability assessments for advanced high-strength steels and its integration with numerical simulations for predictive analysis. This work supports the development of lightweight automotive components, offering valuable insights into material behavior under complex deformation conditions. Future studies could expand upon these results by exploring additional material models and incorporating dynamic loading conditions to further improve prediction accuracy.

Acknowledgments: The work was done under the grant project VEGA 2-0080-19 "Prediction of weldability and formability for laser welded tailored blanks made of combined high strength steels with CAE support".

References

1. Oliver S., Jones T.B., Fourlaris G., Dual phase versus TRIP strip steels: Microstructural changes as a consequence of quasi-static and dynamic tensile testing. Materials Characterization, 2007, Volume 58, p. 390-400.
2. Hrivňák A., Evin E. Formability of metal sheets, 1st ed.; Kosice : Technical University, Slovakia, 2004; pp. 223.
3. Mielnik E.M., Metalworking Science and Engineering, McGraw-Hill, 1991, p. 976.
4. Hosford W.F., Caddell R.M., Metal Forming , Mechanics and Metallurgy, 3rd edition, Cambridge University Press, 2012.
5. Narasimhan K., Miles M.P., Wagoner R.H., A better sheet-formability test, Journal of Materials Processing Technology 1995, Volume 50, p. 385-394.
6. ASM Handbook, Forming and Forging, ASM International, 9th Edition Metals Handbook, 1988.
7. Sahu J., Mishra S., Limit dome height test of very thin brass sheet considering the scaling effect. Journal of Physics Conference Series 2016.
8. Xie C.L., Nakamachi E., The effect of crystallographic textures on the formability of high-strength steel sheets. Journal of Materials Processing Technology 2002, p. 104-111.
9. Kuramae H., Ikeya Y., Sakamoto H., Morimoto H., Nakamachi E., Multi-scale parallel finite element analyses of LDH sheet formability tests based on crystallographic homogenization method. International Journal of Mechanical Sciences 2010, p. 183-197.
10. Katragadda S.C., Ramulu P., Investigation of forming behavior prediction of different steel grade materials using numerical simulation, 5 th International & 26th All India Manufacturing Technology, Design and Research Conference, India, 2014.
11. Bandyopadhyay K., Panda S.K., Saha P., Padmanabham G., Limiting drawing ratio and deep drawing behavior of dual phase steel tailor welded blanks: FE simulation and experimental validation. Journal of Materials Processing Technology 2015, p. 48-64.
12. AHSS Guidelines, Available online: https://www.worldautosteel.org/projects/advanced-high-strength-steel-application-guidelines/ .
13. Takahashi M., "Development of High Strength Steels for Automobiles," Nippon Steel Technical Report No. 88 (July 2003).
14. Sun, L.; Cai, Z.; He, D.; Li, L. Aluminum Alloy Sheet-Forming Limit Curve Prediction Based on Original Measured Stress–Strain Data and Its Application in Stretch-Forming Process. Metals 2019, 9, 1129. https://doi.org/10.3390/met9101129

TECHNICAL UNIVERSITY OF KOŠICE
Faculty of Mechanical Engineering

Design of a modular fixture for cyclic testing and climate exposure

Ján Kušnír [1,*], Jozef Brindza [1], Michal Demko [1] and Marek Vrabeľ [1]

[1] Prototyping and Innovation Centre, Faculty of Mechanical Engineering, Technical University of Kosice, Slovak Republic; jan.kusnir@tuke.sk; jozef.brindza@tuke.sk (J.B.); michal.demko@tuke.sk (M.D.); marek.vrabel@tuke.sk (M.V.)
* Correspondence: jan.kusnir@tuke.sk; Tel.: +421 55 602 3371

Abstract: This paper presents the development of a modular fixture device for cyclic testing of components under varying climatic conditions. The device was designed to address key requirements of universality, affordability, and adaptability, ensuring compatibility with different test components and climate chambers. The design process utilized computer-aided design (CAD) tools, incorporating iterative refinements based on dimensional constraints, climatic chamber specifications, and load simulation needs. Aluminum profiles were selected for their cost-effectiveness, flexibility, and ease of assembly. The system uses pneumatic actuators for controlled mechanical loading, force sensors for real-time monitoring, and a PLC-based control unit to automate test cycles while enabling precise data recording. Sensitive electronic and pneumatic elements were positioned outside the climatic chamber to minimize environmental effects. Test parameters, such as force, direction, and cycle duration, are adjustable via control panel. Real operation demonstrated that the device meets all design criteria, offering a versatile, and cost-efficient solution for advanced material and component testing in automotive and other industrial applications.

Keywords: CAD; fixture; automotive; durability;

1. Introduction

The application of computers to support the creation, modification, analysis, or optimization of a design is referred to as computer-aided design (CAD). Design involves creating an original solution to a problem using combination of different methods, resources and products in design. The design process is a series of iterative activities that begin with a preliminary design based on available information, which is refined as more data is collected. It is a progression from identifying the need, defining the problem, finding and developing solutions, to trial production and final use [1].

Vehicle engineering focuses on designing cars with specific physical attributes like durability, NVH (Noise, Vibration, Harshness), handling, and crash safety. These attributes are evaluated through physical tests and simulations using load data, which represent forces, displacements, and accelerations experienced during real-world use or testing. Challenges remain in accurately predicting durability, especially for non-metallic materials and under environmental factors like corrosion or high temperatures. Achieving realistic designs requires understanding load variability, often gathered via customer surveys, load measurements, or onboard monitoring. Despite advancements in numerical simulations, uncertainties in inputs like material properties, geometry, and load conditions highlight the need for comprehensive evaluations in fatigue and load analysis [2].

The armrest is often used to enhance comfort by providing support for the arm, which can help reduce fatigue during long journeys. Frequently, the armrest also includes a storage compartment that may incorporate additional features, such as controls for various car systems. The armrest is among the car interior components that tend to wear out quickly, making it essential to construct it from highly durable materials for prolonged use. At the same time, it must offer comfortable support—being too firm can lead to discomfort, while being overly soft may compromise hand stability [3].

This article focuses on the design of a universal fixture device designed for cyclic testing in armrest with storage in different climatic conditions. The study emphasizes modularity and adaptability and describes an iterative design process using CAD tools to ensure compatibility with different components and environmental constraints. The proposed equipment aims to simulate real-world loading conditions, evaluate the durability of materials, and increase testing efficiency. The findings highlight the importance of cost-effective and flexible solutions to address complex engineering challenges in component testing.

2. Fixture design process

The design process (as shown in Figure 1), which follows iterative computer-aided design (CAD) principles, starts with a preliminary concept based on data provided by the client. The development of a universal fixture for cyclic testing in different climates must be guided by the principles of modularity, simplicity and cost-effectiveness. CAD tools shall be used to refine the design through multiple iterations, integrating knowledge from design requirements, material properties and testing specifications.

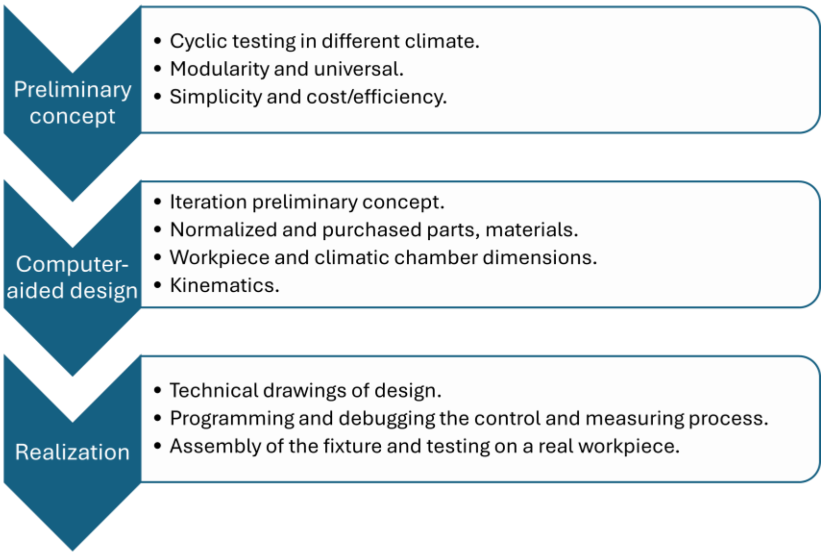

Figure 1. Design process.

Key inputs include the shape of the component under test, the kinematics of the component cover opening, and the application of actuation forces (Table 1and Figure 1), the constraints imposed by the climatic chamber and environment conditions (Table 2). These factors determine the spatial and functional parameters of the device. The structure must be designed to provide robustness under the variable loads presented by forces and movements. Particular attention must be paid to the selection of materials and structural elements to address challenges such as exposure to extreme temperatures and moisture.

Table 1. Requiring activation movements.

Direction	Defined Force	Measuring
F1	-	NO
F2/F3	-	YES
F4	100 N	YES

Figure 26. Armrest with storage compartment accessible by opening the two covers (on the left). Activation directions are shown on the right. F1 shows the direction in which the covers can be automatically opened when pushed. F2 and F3 show the direction and the need to subsequently close the covers. F4 shows the direction of the simulation load.

Table 2. Climate requirements.

Defined climate	Temperature	Relative Humidity
Climate 1	23 °C	-
Climate 2	-20 °C	-
Climate 3	60 °C	-
Climate 4	40 °C	92 %

Actuators should be integrated to simulate mechanical loads to ensure accurate and repeatable test conditions. The equipment should also include provisions for real-time force measurement using load cells, which can allow monitoring of wear trends and performance indicators during test cycles.

The variability associated with realistic conditions, such as fluctuations in environmental factors and potential variability under load, must be considered in the design. Control systems should be using programmable logic controllers (PLCs), while keeping functionality balanced with respect to cost. The system should facilitate automated testing while allowing for manual intervention during setup and troubleshooting.

3. Results

The final fixture was designed to meet versatility, modularity and efficient economic feasibility. Design developed using CAD system. Includes only a few specifically tailored components to ensure easy and quick interchangeability or modification of the components used. Structural elements that are exposed to climatic conditions were designed to be durable, while elements such as control electronics and pneumatic controllers were strategically placed outside the chamber to reduce environmental impact.

The CAD-based design made use of aluminium structural profiles that allow seamless reconfiguration for testing similar components, but also completely different ones. At the same time, the same frame could be adapted to test different components by replacing just a few modular attachments.

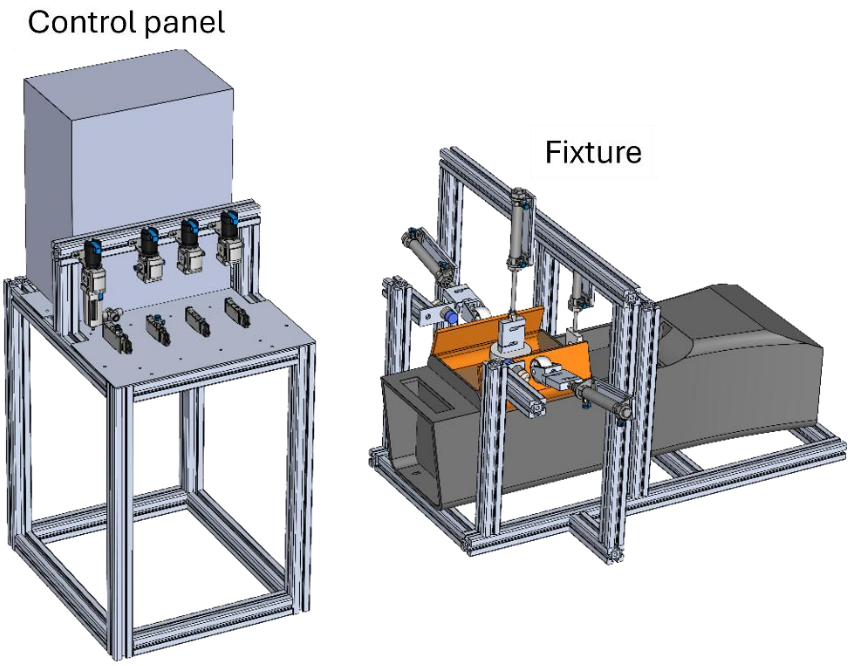

Figure 3. Final 3D design of fixture with controlling panel

Pneumatic cylinders were used to simulate the mechanical loads, replicating the operational stresses of the components under test. The system includes cylinders for opening and closing the cover with integrated sensors monitoring the time or opening of the cover. These sensors provided feedback on deviations such as excessive opening time, which indicated potential failures. Measuring force during the closing phase allowed accurate assessment of operating resistance, a key indicator for determining wear and structural health and integrity.

The system control panel, located outside the climate chamber, provides an intuitive interface for setting predefined cycle counts, starting or pausing tests, and resetting cycles. LED indicators display system status in real time, increasing usability during tests performed in the enclosed climate chamber. Pneumatic adjustments such as pressure and airflow rate control are facilitated by integrated barometers (Figure 4). Manual controls on selected solenoid valves, simplify fine-tuning of test conditions.

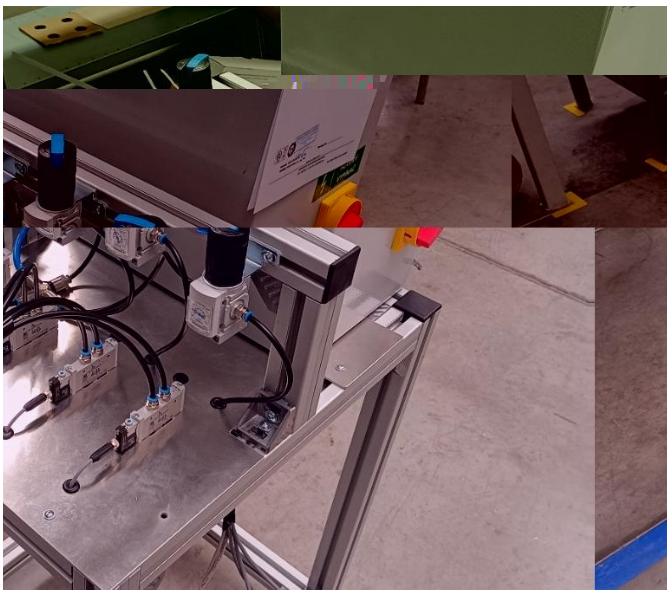

Figure 4. The back of the control panel, which allows pneumatic adjustment and regulation.

Real-time data acquisition was achieved through serial communication with the PLC, allowing detailed analysis of operating parameters such as cycle time and load variation. Using serial communication, large amounts of data can also be easily used and processed in the future. A small sample of the collected data can be seen in Table 3.

Table 3. Recorded data in Excel.

START: Cycle started.			
NUMBER OF CYCLES: 14000			
Cycle	Loadcell1	Loadcell2	Loadcell3
1	7.82 N	6.84 N	109.48 N
2	7.82 N	6.84 N	109.48 N
3	7.82 N	6.84 N	109.97 N
4	7.82 N	6.84 N	109.97 N
PAUSE: Cycle paused.			
STOP: Cycle stopped and reset.			

4. Conclusions and discussion

The proposed fixture successfully met several key objectives and handled operation under difficult conditions. Its elements collectively ensured reliability, adaptability, and compliance with defined testing parameters. The resulting assembly can be seen in Figure 5.

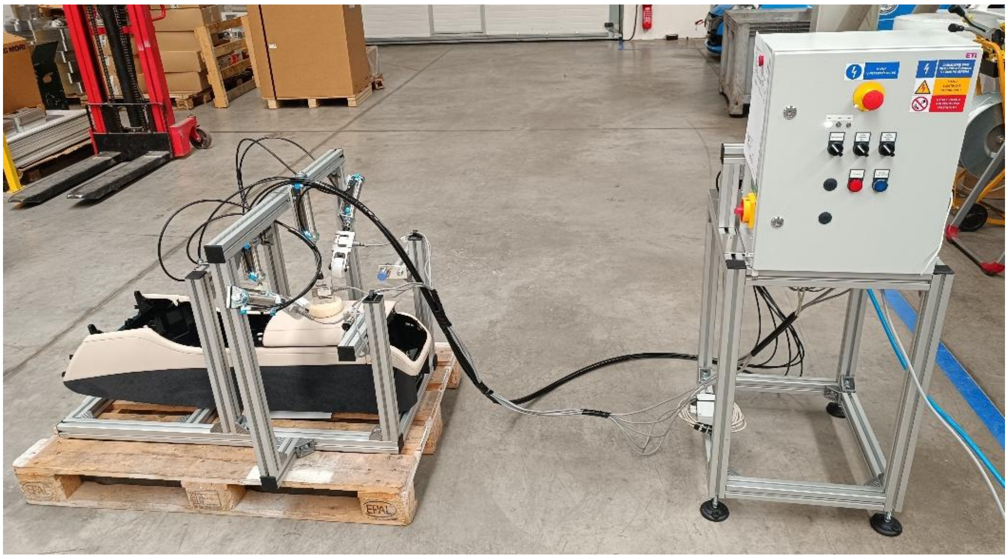

Figure 5. Finished connected and running assembly.

Based on real operation, it has been found that the pneumatic settings in this setup cannot be kept constant at the minimum and maximum temperature but need to be adjusted for the specific operating temperature. The positioning accuracy was sufficient due to the kinematic conditions being met and given that the test procedure only required normal movement during closing and opening (similar to regular use). Changes in the expansion of the structure over the given temperature ranges were within the normal range of functionality of the movements. A disadvantage with some configuration change in this design could be the absence of grounding of the piston rod rotation. Simply checking the opening of the covers using the end sensors may not be sufficient in certain cases, for example if one of the covers fails to close perfectly and thus opens again by itself.

Acknowledgments: This article was created with the support of project: VEGA 1/0457/21. This work was supported by the Slovak Research and Development Agency, project title: Research on the possibilities of forming and joining innovative metal-plastic composites in the production of lightweight thin-walled structures", project numbers: SK-PL-23-0040. The authors are also grateful for the support in the experimental work to the project KEGA 050TUKE-4/2023.

Conflicts of Interest: The authors declare no conflict of interest.

References

1. SARCAR MMM, RAO KM, NARAYAN KL (2008) Computer Aided Design and Manufacturing. PHI Learning Pvt. Ltd., New Delhi.
2. Johannesson Par, Speckert Michael (2014) Guide to load analysis for durability in vehicle engineering. John Wiley & Sons Ltd., Chickester.
3. Knauf Industries (2021) Car armrests - versatile components with many functions. https://knaufautomotive.com/car-armrest-a-versatile-component-with-many-functions/. Accessed 8 Dec 2024.

TECHNICAL UNIVERSITY OF KOŠICE
Faculty of Mechanical Engineering

Node-RED as a tool for industrial data visualization

Ondrej Majerčák [1,*], Marek Vagaš [1]

[1] Technical University of Kosice, Faculty of Mechanical Engineering, Department of Industrial Automation and Mechatronics; ondrej.majercak@tuke.sk; marek.vagas@tuke.sk
* Correspondence: ondrej.majercak@tuke.sk

Abstract: In the Internet of Things, especially in its deployment in the industrial field, data collection, and wireless control play an important role in improving overall production performance by providing feedback and integrating the information with other machines. One of the most widely used control systems in industry is the Siemens PLC. There are many options for data acquisition, visualization, and control, but most of them are expensive and require learning a new complex system. This article deals with data collection, visualization, and control possibilities through the Node-RED platform in an industrial environment. It points out the opportunities and accessibility that this system provides as a cheaper and simpler alternative to the tools already used in industrial automation.

Keywords: Node-RED; visualization; wireless; S7-1200

1. Introduction

Digitalization is changing the world today. This of course also applies to industry. The volume of data collected in modern factories is growing, which brings new challenges for system solutions. In manufacturing processes, data collection from production lines is an ever-present topic. The purpose of this data collection is to improve the overall performance of production processes by monitoring processes, providing feedback, and integrating information with other machines. The ability to control and obtain data through more accessible and less expensive means is increasingly required. The advantage of such solutions is almost continuous operation, which a person can control and, thanks to the Internet of Things, also manage the process [1].

In industrial automation, seamless communication between programmable logic controllers (PLCs) and monitoring systems is paramount to ensure trouble-free operation and optimal performance. The data collection system plays a particularly key role in collecting, processing, and transmitting data from various sources. In industry, communication gateways are also being created for this purpose via the OPC protocol to enable this collection [2].

Many areas need to be addressed just when collecting data from a device – the method of data collection, the communication protocol, the method of visualization, data security, system reliability, etc. With the increase in computing capacity, more information is generated, which also needs to be stored somewhere for further processing [3]. Visualization as a separate area is also important. It serves not only to monitor the device in real-time, or even to control the device remotely but also to create output reports for other components of the company's management and to present data to operators and employees of the company. Some web PLC systems include the possibility of inserting pages for remote visualization of the production system via the Internet [4]. As an example, we can cite the simple Siemens Logo! device, which also provides its own Internet interface. However, in the industry, we have various devices. Therefore, it is important to look for solutions that are universal for various devices in industrial automation. We have various world-class platforms available that offer such solutions as eWON, IXON, etc. The main goal of this article is to deploy and test the possibility of visualizing and controlling an industrial control system via the Node-RED platform, which is a more affordable alternative.

2. Materials and Methods

In this section, we describe the currently available methods for collecting, deploying, and visualizing data from production lines. We describe the equipment used in the experiment and provide basic information about the Node-RED platform.

2.1 Siemens S7-1200

Siemens S7-1200 is a flexible and powerful PLC used for small or medium-sized automation applications. Its application is wide for various industrial areas such as production, logistics, or material processing. It has many inputs and outputs, and there is a possibility of expanding it with other modules as needed. Programming is possible via the TIA Portal software, which also includes diagnostic tools. The system supports a web server for remote monitoring and configuration, making it more flexible. The Human-Machine-Interface (HMI) panel is used for data visualization for operators or directly on the device. Modern versions already support IoT and Industry 4.0 applications. These already provide a web server through which remote monitoring is possible via a web browser without special software. Another option is to use SCADA systems such as WinCC, which allows centralized control and data analysis. Versions with IoT support already provide a connection to Siemens' MindSphere software [5].

In our experiment, we use an older version of S7-1200, which does not yet contain elements for IoT implementation.

2.2 Raspberry Pi

The Raspberry Pi 4 Model B is a powerful single-board computer designed for educational, development, and home applications. It has a quad-core processor with a frequency of 1.5 GHz and offers 8 GB of RAM. It has 2 HDMI ports, Ethernet, USB ports, Wi-Fi, and Bluetooth as we can see in Figure 1. This computer is often used in IoT projects, in which it can also perform the function of a server [6].

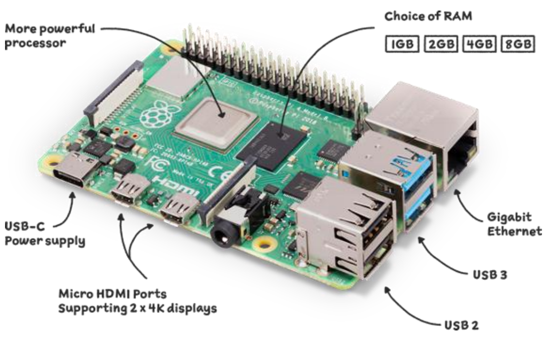

Figure 7. Raspberry Pi 4B model [6].

In our experiment, we use this single-board computer to create a server running Node-RED. At the same time, we can collect and store the acquired data on internal or external storage.

2.3 Node-RED

Node-RED is an open platform for integrating hardware devices of the Internet of Things. It is a free tool based on JavaScript that provides a visual flow editor based on the browser. Its example is also shown in Figure 2. The environment has a menu of tools or nodes on the left side for creating a flow. The flow itself is created by dragging these blocks into the programming environment. In the upper part, there is an option to create or switch between multiple created flows. In the right part of the program, there is a debug window, where we can monitor individual nodes, or data and states. The system has nodes that are represented by the corresponding icons. Node-RED allows you to connect different devices with different protocols to each other. This platform allows you to connect web services, and customize nodes so that they can perform functions such as sending data from sensors or creating simple analyses [7,8].

Another advantage of this platform is that it allows the creation of dashboards, in which it is possible not only to visualize data and the status of devices but also to send messages or manage various devices through the Dashboard.

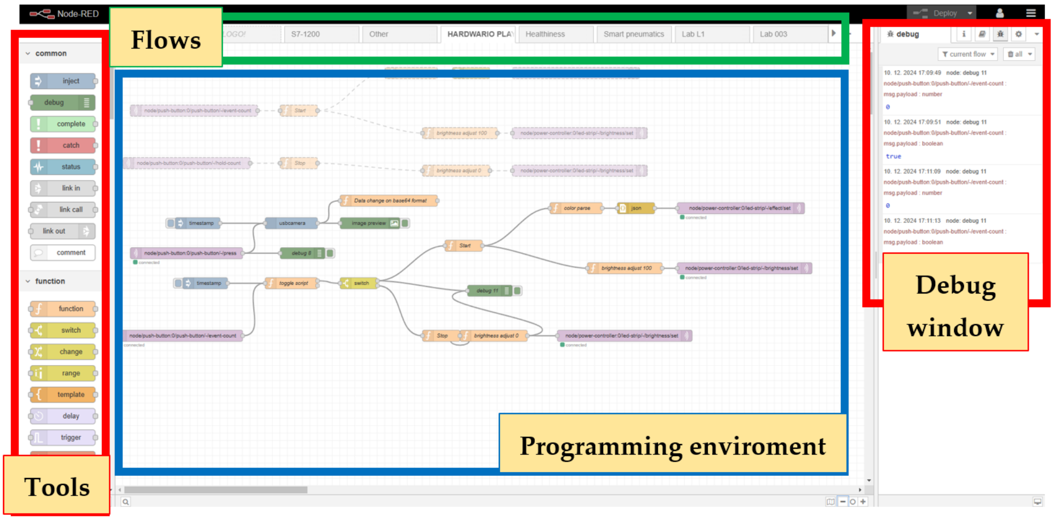

Figure 2. Example of Node-RED platform.

3. Experiment

In our experiment, we use Siemens S7-1200, which is a relatively advanced version. Our used device does not have support for IoT solutions. From our Raspberry Pi, we created a server on our network via Raspbian OS and implemented the Node-RED platform into it. The whole communication idea and visualization of the process is shown in Figure 3.

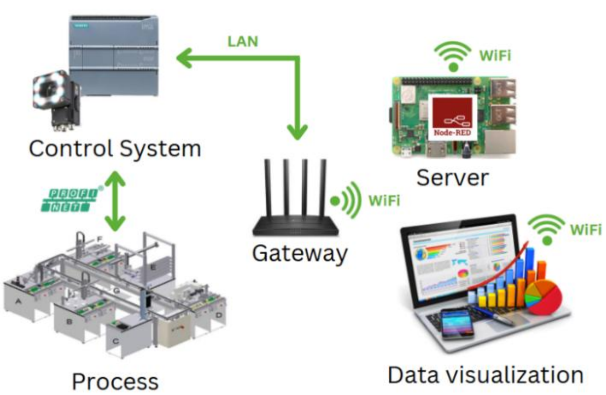

Figure 3. Communication network for data visualization.

We have chosen the industrial application for our PLC as the process of evaluating the correctness of the production of inscriptions on metal packaging. This process is carried out using a camera checker, which, upon receiving an input signal, triggers a camera trigger that creates an image of the object under the camera. This image is then processed in the camera. The output from the camera is information for the PLC whether the given product has a correctly created inscription on the metal packaging or not. The camera sends 2 signals to the PLC.

If we want to share this process status data on Node-RED, we will have to activate full access in the TIA Portal environment in the Protection & Security section, and in the Connection mechanisms subsection, we must enable PUT/GET communication from a remote partner (Figure 4). In this way, we have activated the possibility of accessing data through Node-RED.

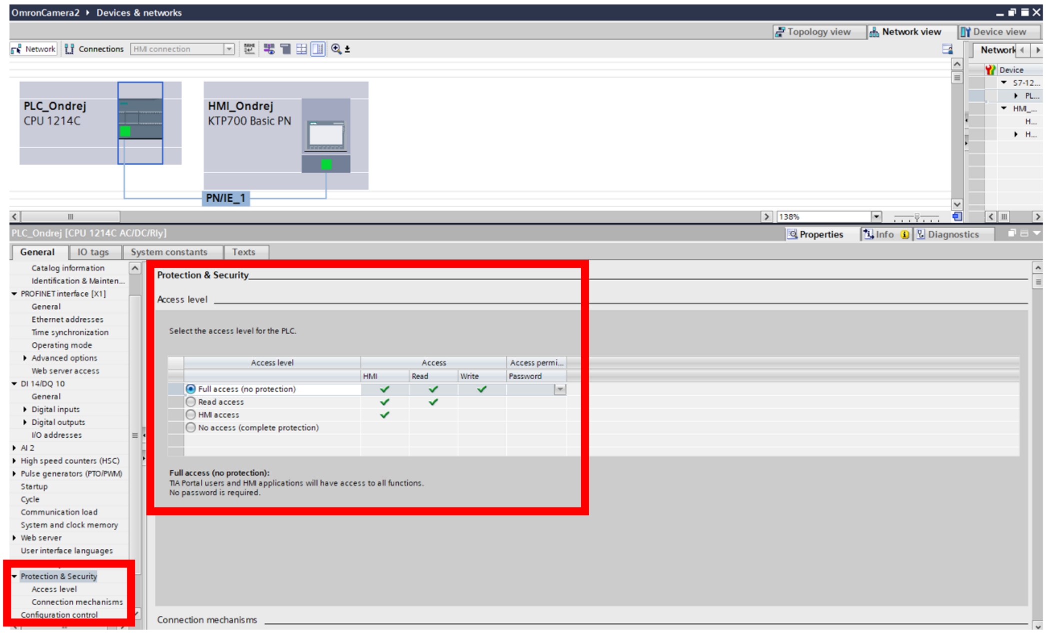

Figure 4. Communication activation for Node-RED.

If we want to communicate and process data from a Siemens PLC in the Node-RED environment, we need to install a pallet called node-red-contrib-s7 into Node-RED. Adding this pallet will add functions for working and communicating with a Siemens PLC (Figure 5).

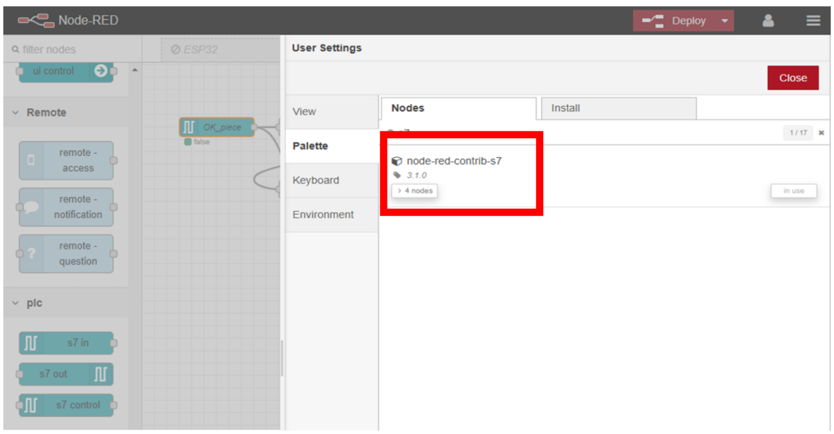

Figure 5. Installing a pallet for communication with Siemens PLC.

When creating a given flow, we still need to set up a node for our PLC. After opening a given node, for example, s7 in, we have a choice in the first PLC section. First, we create our own using the appropriate editing icon. Then, in the Connection window, we set our communication method and our device IP address. In this section, we also have the option to set the communication time and the name of our PLC. In the second window called Variables, we can select the variables we need to use. Then, after saving, we select the variable that we want to use in the first window of our node (Figure 6).

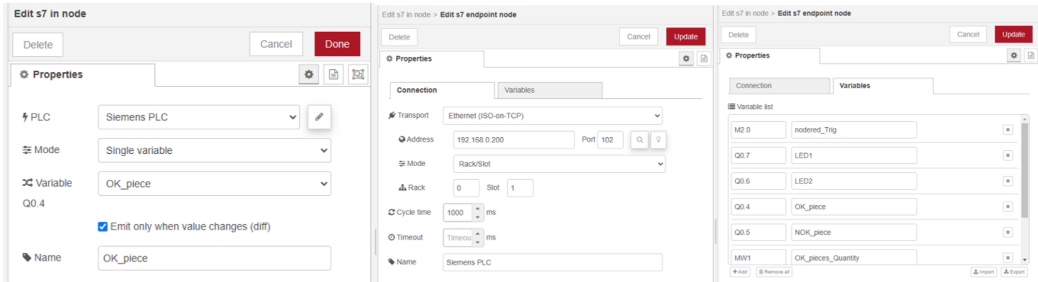

Figure 6. S7 node setup.

In a similar way to the installation of pallet for Siemens PLC, we also install flow-fuse/node-red-dashboard for creating visualization. Subsequently, by connecting individual blocks, we created a functional program with visualization and were able to proceed to test this visualization and its modification. The input is the s7 in the block, in which we select the desired variable and then visualize it. We also converted the input data about good and bad pieces to another format and added the current time to the incoming message via the function block. We used text visualization to visualize the quantity and tried to represent the total number of pieces graphically.

As part of the experiment, we also tried to remotely activate our trigger through visualization for wireless evaluation of the currently stored product. The entire flow for Node-RED is also shown in Figure 7.

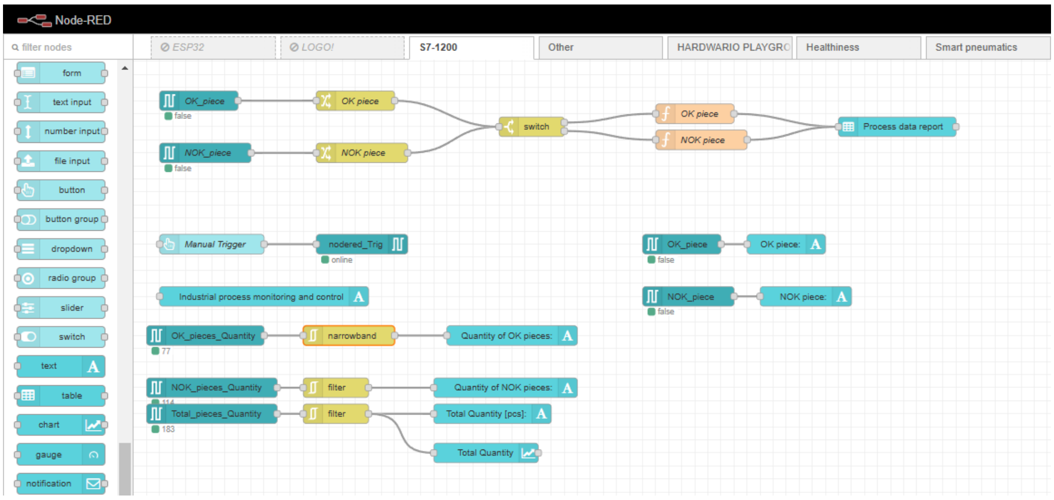

Figure 7. Node-RED flow.

4. Results

The result of our work is a functional visualization (Figure 8) of a simple industrial process in the form of monitoring. As part of the solution, we also implemented the control of the sensing variable and thus achieved wireless control of the evaluation process. We created a functional visualization that is an alternative to many paid platforms and is sufficient for use within a given company. A big advantage is that we can insert devices into this platform without having to significantly modify their software or add hardware. For implementation, we only need one device such as a Raspberry Pi. We tested the reliability and control of devices through this platform and the response was very good.

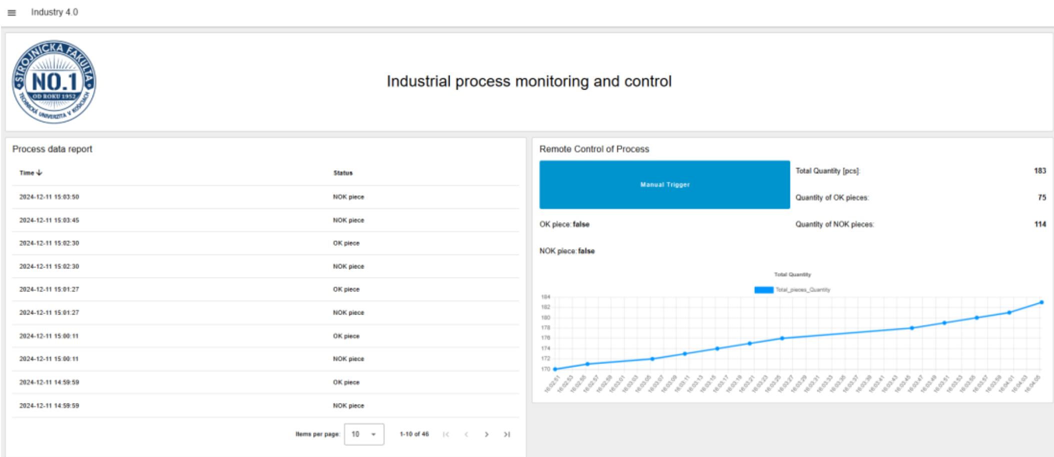

Figure 8. Node-RED dashboard.

5. Discussion

Data visualization is a necessity in today's industrial environment. Most of the available platforms are paid and it is necessary to implement multiple devices, which are also financially demanding. Visualization through the Node-RED platform brought the expected results. We managed to create a suitable and reliable visualization through which the process can also be controlled. We can apply this solution to various industrial control systems from Siemens. Since Node-RED is an open system, we can implement various devices into this system, create reports, or create screens for various production departments. Another advantage is that the server running on Raspberry Pi can be placed anywhere. The only condition for functionality is the connection of devices to the same network. An important aspect that would be good to address is the security of this data and all communication. Within the company's internal network, such visualization can be quite sufficient, but a problem could arise if we did not have a sufficiently secure network for attacks from the outside.

Acknowledgments: This work has been supported by the Slovak grant VEGA 1/0169/22 New methodics approaches to data from automated and robotized workplaces.

Conflicts of Interest: The authors declare no conflict of interest.

References

1. F. Žemla a J. Cigánek, "Remote Data Acquisition Using Cloud Database," *2022 Cybernetics & Informatics (K&I)* , Visegrád, Hungary, 2022, pp. 1-6, doi: 10.1109/KI55792.2022.9925932.
2. N. Wang, X. Fan, F. Feng, Y. Li, H. Ye a Y. Liu, „ An Industrial Communication System for PLC “, *2024 IEEE 4th International Conference on Electronic Technology, Communication and Information (ICETCI)* , Changchun , China, 2024, s. 125 – 129, doi: 10.1109/ICETCI61221.2024.10594451.
3. Rákay, R., Galajdová, A., Šeminský, J., & Cvitić, I. (2019). Selected Wireless Communication Protocols and Their Properties for Use in IoT Systems. *Research Papers Faculty of Materials Science and Technology in Trnava, Slovak University of Technology in Bratislava*, 27(45). DOI: 10.2478/rput-2019-0022.
4. R. P. Moreno, V. L. Egido and J. L. V. Salcedo, "Internet Visualization of PLCs Programs," *2007 5th IEEE International Conference on Industrial Informatics*, Vienna, Austria, 2007, pp. 225-230, doi: 10.1109/INDIN.2007.4384760.
5. SIMATIC S7-1200. Available online: https://www.siemens.com/global/en/products/automation/systems/industrial/plc/s7-1200.html (accessed on 11-th December 2024).
6. Raspberry Pi 4. Available online: https://www.raspberrypi.com/products/raspberry-pi-4-model-b/ (accessed on 11-th December 2024).

7. M. Lekić and G. Gardašević, "IoT sensor integration to Node-RED platform," 2018 *17th International Symposium INFOTEH-JAHORINA (INFOTEH)*, East Sarajevo, Bosnia and Herzegovina, 2018, pp. 1-5, doi: 10.1109/INFOTEH.2018.8345544.
8. Chuquimarca, L., Asencio, A., Torres, W., Bustos, S., Sánchez, J., Saldaña, C. "Evaluation of Data Transfer from PLC to Cloud Platforms-Based Real-Time Monitoring Using the Industrial Internet of Things," 2022 Guarda, T., Anwar, S., Leon, M., Mota Pinto, F.J. (eds) Information and Knowledge in Internet of Things. EAI/Springer Innovations in Communication and Computing. Springer, Cham. https://doi.org/10.1007/978-3-030-75123-4_14

Laser welding using a collaborative robot

Marek Málik [1,*], Rudolf Jánoš [1]

[1] Technical University of Košice, Department of Production Technology and Robotics, Vysokoškolská 4, 042 00 Košice; marek.malik@tuke.sk; rudolf.janos@tuke.sk
* Correspondence: marek.malik@tuke.sk

Abstract: The main objective of this study is to integrate a collaborative robot with laser welding to improve industrial applications. The experimental workstation was equipped with a Fanuc CRX collaborative robot and a Tranyord laser welding tool. The Fanuc robot, known for its safety features and user-friendly programming, was integrated with a fiber laser welding system for precision welding of metals such as stainless steel and aluminum. We performed the workstation simulation using RoboGuide software, which allows us to simulate the workstation and optimize the robot path. The simulations provided important information on the cycle times of the workstation, the smoothness of the robot movement, which allows for the optimization of the manufacturing process. This research work explores the potential of combining collaborative robotics and advanced laser welding technologies to support innovation in industrial automation.

Keywords: collaborative robot; laser welding; simulation

1. Introduction

In this study, an experimental collaborative workplace was created, which serves to investigate the possibilities of combining collaborative robotics and laser welding. The workplace is equipped with a Fanuc CRX-10iA/L collaborative robot, which enables safe co-working with humans. The connection of laser welding technology with a robot was achieved with the help of an external tool that ensures precise integration and control over welding processes. This combination brings new possibilities of automatization in industrial applications, emphasizing safety, efficiency, and flexibility.

Collaborative robots (cobots) are developed to work safely with human operators in a shared workplace. Traditional industrial robots must separate safety barriers from their human operators. Cobots are equipped with sensor systems that enable collision detection and safe stopping of movement. These features make them ideal for applications where flexibility, safety, and the ability to interact with humans are required [1].

Laser welding is performed using conduction or high-power deep penetration techniques. Conduction welding uses a larger, low-power laser beam to transfer heat through thermal conductivity, while deep penetration welding uses a focused, high-energy beam to create a vapor and gas channel (keyhole) for deep, precise welds. Shielding gases ensure weld quality, prevent contamination, and protect optics with the process performed in ambient or controlled atmospheres, with or without filler material. Key laser types include solid-state, gas, semiconductor, liquid, and fiber lasers, selected based on application requirements for efficiency, power, and precision [2].

Robotic laser welding is a trend in automation, an advanced approach that improves efficiency. This has enabled the emergence of a number of robotic workplaces that utilize laser welding technology. One of these workplaces is a workplace for welding pressure vessels using laser welding. The work focuses on creating a workplace with Mitsubishi

PLC and a six-axis industrial robot. The main benefit is the optimization of welding parameters using a uniform design and the implementation of an intelligent control system based on PLC [3].

Robotic laser welding also finds its application in simulations and designs of flexible production structures, which enable efficient and accurate control of welding processes before their implementation in a real environment. One of the advanced tools for this purpose is the FANUC ROBOGUIDE software, which provides the ability to simulate robot movement, optimize their configuration, and design the entire workplace. This technology allows the integration of CAD models of components, fixtures, and end effectors, which is especially important when designing workplaces for complex welding applications, such as pressure vessel welding. The automated generation program in ROBOGUIDE significantly facilitates manual programming, saving time and costs. In addition, the possibility of pre-programming robots and their subsequent visualization and functionality testing reduces the risk of errors during implementation [4].

The article brings benefits in the field of laser welding with a collaborative robot, where the solution of the robot tool is not the classic way directly on the robot flange, but we use the method of an external tool RTCP (remote tool center point), which allows us to insert the tool into the robot workspace. Working with an external tool in laser welding is an innovative way that increases safety and efficiency. The main benefit is the optimization of welding parameters using a uniform design and the implementation of an intelligent control system based on PLC. The article begins with an introduction that introduces laser welding, collaborative robots, and the importance of RTCP (Remote Tool Center Point) in increasing accuracy and efficiency. This is followed by a methodology that describes the design of the workplace, the implementation of RTCP, and simulations in the RoboGuide environment. Simulation results demonstrate the advantages of RTCP and compare it with traditional approaches. The conclusion summarizes the main benefits and recommendations for further research and applications.

2. Materials and Methods

A Fanuc CRX-10ia/L robot was used as a manipulator with the welded part. The Fanuc collaborative robot has a range of 1 418 mm and a maximal weight load of 10 kg. This range allows the robot to work efficiently in various industrial applications such as welding, handling materials, packing and more. One of the most important functions of the Fanuc robot is its ability to protect operating personnel. This ability is characterized by stopping the robot immediately after a collision. The robot is also able to be programmed manually with the manual guide function. This function allows us to guide the robot to our designated spot. Programming of the robot is possible using the i-Pendant tablet, which can be programmed using a simplified HMI, where we use the Drag & Drop function. This is a very quick and easy way to program common things. I-Pendant also allows us to work in a standard mode with the ability to use a standard i-Pendant Fanuc interface [5].

The Tranyond tool was used for laser welding. Tranyond is a professional laser welding tool with multiple functions, designed for efficient welding. It is designed for welding metals, including stainless steel, aluminum, carbon steel, and galvanized sheet metal. However, it is not suitable for working with highly reflective materials such as copper, brass and bronze. [6]Technical parameters:

- Laser beam power: 2000W
- Laser type: Fiber
- Weld width: 0 to 5 mm
- Protective gas: Argon/Nitrogen (Pressure: 5-10 l/min)
- Power requirements: 380±10% V AC, 50/60Hz
- Operating temperature: 10 to 40 °C

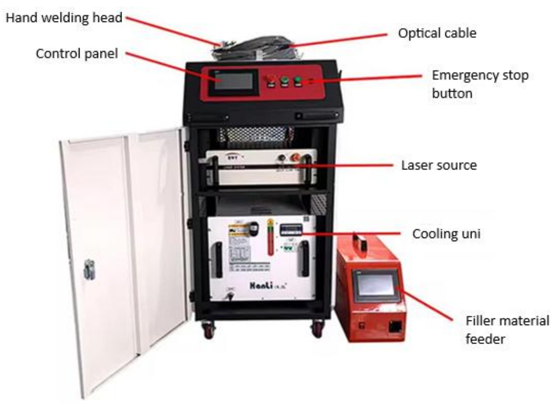

Figure 1.-Tranyond Parts Diagram.

Workplace testing and simulation were performed using ROBOGUIDE software, Fanuc's leading offline programming, and simulation software. ROBOGUIDE allows users to create, program, and simulate robotic workplaces in a 3D environment without the need for a physical prototype. ROBOGUIDE'S key features and benefits include:

- Offline programming: Allowing us to program robots outside of a physical workplace environment, which saves time and installation costs.
- Workplace simulation: Enables the creation and testing of a workplace in a 3D environment, including robot movements and interactions with peripherals.
- Integration of CAD models: Importing CAD models for precise planning and making workplace layouts [6].

An important aspect of the methodology was also the implementation of the RTCP external coordinate system (Remote Tool Center Point). RTCP represents a significant advance in the implementation of various industrial applications, such as the use of spot-welding pliers and similar technologies. The basic principle of RTCP is to move the end-point of the tool to an external object, which enables precise and flexible operations [7][8].

2.1. Subsection

Simulations in an offline environment are a key tool in the design and optimalization of robotic workplaces. Their main benefit is the possibility to verify various processes without the need for physical deployment of equipment, which saves time, money and increases safety. In this article, we describe the creation of a simulation and its optimization for the laser welding process using a collaborative robot in the RoboGuide environment.

Creating simulations in an offline environment

The environment of the RoboGuide program was used to simulate the workplace for the laser welding process. This workplace consists of two welding operations: the welding of the first part and the subsequent exchange and welding of the second part.

A key aspect of the simulation was the use of an external tool defined using the RTCP (Remote Tool Center Point) method. RTCP allows you to create an external tool and define it in robot space. To define the center point of the external tool, we use a user frame. The frame must be set up so that its Cartesian coordinate system has its origin exactly at the center point of the tool, while the orientation of its axes must correspond to the orientation of the tool. In case of a change in the position of the tool, it is possible to simply reorient the user frame without the need for further adjustments. This approach simplifies working with an external tool and increases the accuracy of the operations performed.

The simulation starts with part 1 mounted on the robot flange. The robot approaches the external welding effector, where it performs the two welding paths. After the welding is finished, part 1 is moved to the exchange position, and the operator confirms its replacement with part 2 on the HMI pendant. The robot then performs welding on part 2, while the operator prepares the next part. Parts of the welded component can be seen in Fig. 2.

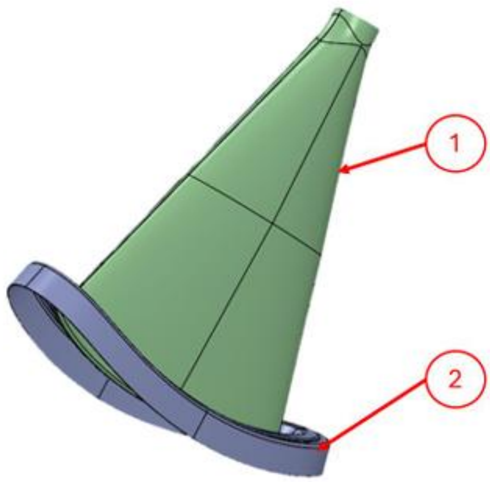

Figure 2. Welding parts.

Overview of the robot path speed

In the simulation, the paths of the robot are visualized by colors, which enables a graphical recognition of their character:

- Dark red: welding paths, low speed.
- Green: zoom movements to the welding effector.
- Orange: movements associated with changing the position of the part.

In the Fig.3 below, we see a visualization of the robot paths around the user frame in RTCP mode. The dark red paths show the low-speed regions that are typical of the welding operations themselves. On the contrary, the green and orange paths show the movements related to the approach and manipulation of the part.

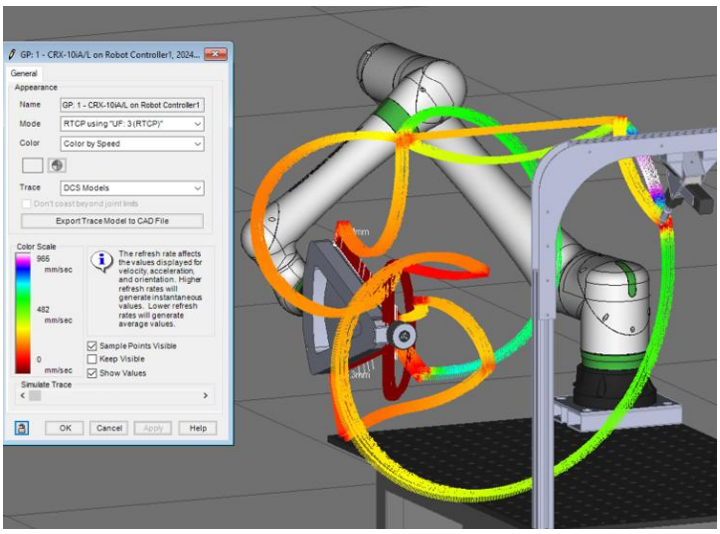

Figure 3. Inspect the robot's path speeds.

The total time of one cycle was calculated by simulation to be 119 seconds, as shown in Fig. 4. This time includes the movement time of the robot, the application time of welding, and the orientation time of changing the parts, which was set to be 10 seconds.

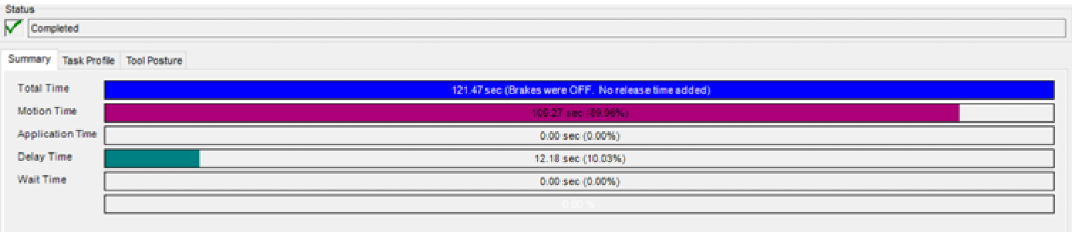

Figure 4. Simulation Time.

Optimalization of the simulation took place in two main areas:

Motion trajectory

Motion trajectories were modified by optimizing points and applying approximation for smoother robot movements. Using a CNT value of 80 guaranteed that the robot would maintain 80% of its speed when approaching the point. This procedure resulted in improved fluidity of movement and reduced cycle time by 1.8 seconds, as shown in Fig. 5.

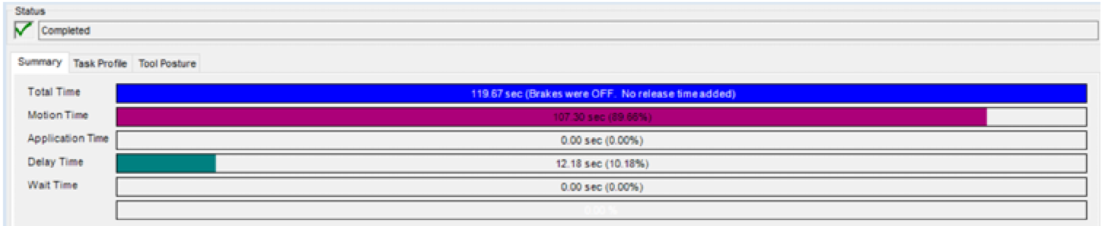

Figure 5. Optimized motion trajectory time.

Welding operation

The welding paths were optimized by adjusting the speed of the robot and adjusting the trajectory on the parts. The approximation was increased to the maximum to avoid stopping at points, which could negatively affect the quality of the weld. The exact CNT values will be fine-tuned and verified on a real robot, because the simulation does not allow us to fully simulate the making of a weld.

Workplace implementation

After optimizing the simulation, we proceeded to upload the program to the robot and create a workplace in a real environment. The workplace layout included a welding unit, a robot and its controller, a protective fence and a glass protecting against laser radiation, which increases safety of workers. An overview of the workplace can be seen on Fig. 6.

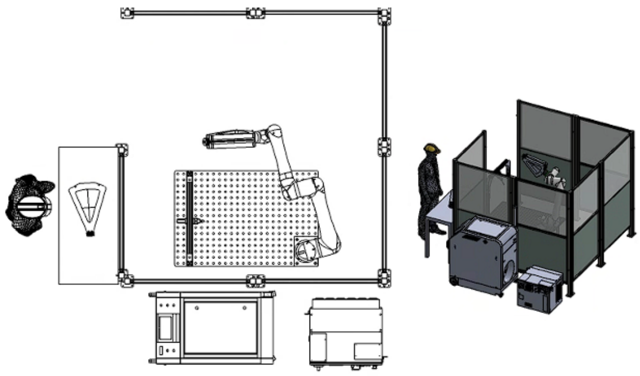

Figure 6. View workplaces in RoboGuide.

3. Conclusions

This research shows that collaborative robotics in conjuction with laser welding can be a key factor for industrial modernization. The Fanuc CRX-10iA/L robot proved itself to be effective in ensuring safety and adaptability, while ROBOGUIDE simulations enabled efficient optimalization of motion trajectories and reduced cycle times by 1.8 seconds. The simulations provided valuable insights, but further verification on a physical robot is needed to improve the welding quality. Successful transition from a virtual implementation to a real workplace demonstrates the practicality of this approach and paves the way for safer, more efficient, and more flexible automation solutions.

References

1. Patil, Swapnil & Vasu, Vishwa & Srinadh, K.. (2023). Advances and perspectives in collaborative robotics: a review of key technologies and emerging trends. Discover Mechanical Engineering. 2. 10.1007/s44245-023-00021-8.
2. Ján Moravec, Radoslav Koňár, Richard Pastirčák, Peter Fabian. Technológia 1, Žilina : Žilinská univerzita, Slovakia 2020;pp. 335-338.
3. W. Gui, L. Zhang, X. Xu, J. Fan and W. Zhong, "Design of robotic workstation for laser welding of pressure vessels," 2023 3rd International Conference on Robotics, Automation and Intelligent Control (ICRAIC), Zhangjiajie, China, 2023
4. Dragos-Lucian Baboi, Julian Andreoiu, Gabriela Bucur. ARC WELDING ROBOTIC FLEXIBLE CELL SIMULATION USING ROBOGUIDE SOFTWARE. Petroleum-Gas University of Ploiesti, Romania. 1.11.2024.
5. M. Málik. Návrh pracoviska s kolaboratívnym robotom Fanuc CRX 10iA/L,level 2 thesis. Technical university in Košice, 2024 Košice
6. Tranyond laser welding machine datasheet, Tranyond, 2024.
7. Fanuc. Available online: https://www.fanuc.eu/eu-en/product/robot/crx-10ia (accessed 5.12.2024)
8. FanucAmerica. Available online https://www.fanucamerica.com/products/robots/robot-simulation-software-FANUC-ROBOGUIDE (accessed 1.12.2024)
9. Using an External TCP. Available online: https://academy.visualcomponents.com/lessons/using-an-external-tcp(accessed 28.11.2024)
10. Inlearc. Available online:https://www.tthk.ee/inlearcs/industrial-robot-functionality-and-coordinate-systems/ (accessed 29.11.2024)

TECHNICAL UNIVERSITY OF KOŠICE
Faculty of Mechanical Engineering

The Potential of 4D Printing in Designing Adaptive Medical Implants

Maksymilian Maślanka [1,*], Jarosław Janusz [1], Anna Kurowska[1], Adam Jabłoński[1] and Izabella Rajzer [1]

[1] Department of Mechanical Engineering Fundamentals, Faculty of Mechanical Engineering and Computer Science, University of Bielsko-Biala, 43-300 Bielsko-Biała, Poland; mmaslanka@ubb.edu.pl (MM); jjanusz@ubb.edu.pl (JJ); akurowska@ubb.edu.pl (AK); ajablonski@ubb.edu.pl (AJ); irajzer@ubb.edu.pl (IR)
* Correspondence: mmaslanka@ubb.edu.pl; Tel.: +48338279248

Abstract: 4D printing holds significant promise in designing adaptive medical implants, offering the ability to create structures that respond to environmental stimuli. This study investigates the printability and shape-memory behavior of terpolymer-based filaments modified with Osteogenon and β-TCP, aiming to optimize their use in medical applications. The methodology involves printing samples under controlled conditions and evaluating their shape-memory properties by observing their recovery to the original shape after deformation. The results show that ambient temperature, airflow, and nozzle size are crucial for successful printing, with a minimum nozzle diameter of 0.8 mm recommended to avoid clogging. Terpolymers modified with Osteogenon exhibited glossy surfaces and stringing, which could impact the final aesthetics and function, while TER_OST filaments were easier to print but required longer printing times. Shape-memory tests demonstrated that the TER_βTCP alloy exhibited the best recovery ability, followed by TER_OST, while the pure TER alloy showed the lowest recovery. The findings underline the importance of material selection and environmental control in 4D printing, suggesting that terpolymer-based materials modified with β-TCP or Osteogenon have strong potential for developing adaptive medical implants that can respond to physiological conditions.

Keywords: 4D printing, shape memory polymers, medical implant, tissue engineering

1. Introduction

The integration of 4D printing technology into biomedical engineering marks a significant advancement in the development of adaptive medical implants. Unlike traditional 3D-printed structures, 4D-printed materials can change their shape, properties, or functionality over time in response to specific stimuli such as temperature, humidity, or pH [1]. This ability makes 4D printing a revolutionary approach for designing implants that can dynamically adjust to the physiological conditions of the human body. Shape-memory polymers (SMPs) are central to 4D printing due to their ability to undergo programmed shape transformations [2]. In biomedical applications, SMPs can be engineered to activate at human body temperature, making them ideal for adaptive implants and minimally invasive medical devices [3]. While SMPs are increasingly valued for their versatility, their high cost remains a challenge. Traditional 3D printing filaments are supplied on spools, leading to material waste when producing small implants for cartilage or bone repair. To address this, the authors propose using small, connectable sticks made from SMPs, which not only reduce material consumption but also enable the customization of implants by combining sticks with different modifications. This approach allows for the production of personalized medical devices using standard 3D printers. Injection molding has been identified as an effective method for producing these SMP-based sticks.

This study explores the application of modified terpolymers enriched with osteogenon and β-TCP for 4D printing of medical implants. Both osteogenon and β-TCP, as bioactive compounds, enhance the material's bioactivity and support bone tissue regeneration [4]. The research explores the design and fabrication of shape-memory polymer-based implants, highlighting their potential for adaptive behavior.

2. Materials and Methods

A terpolymer composed of L-lactide, ε-caprolactone, and glycolide (L-LA/GL/ε-CL 69/16/15) was synthesized via ring-opening polymerization at the Centre for Polymer Materials, Polish Academy of Sciences, using zirconium acetylacetonate as a biocompatible initiator. The terpolymer was mixed with 5 wt.% β-tricalcium phosphate (β-TCP, Merc, Poland) or 5 wt.% osteogenon drug (OST, PIERRE FABRE) and homogenized at 190°C. The blend was processed into granules for injection molding. Injection molding was performed using a Babyplast 6/10P machine (Rambaldi, Molteno, Italy) to produce filament sticks [5, 6]. Pure terpolymer sticks were also prepared for comparison.

The samples were printed using a PRUSA i3 MK3 printer with PRUSASLICER software. After generating the G-code, it was manually edited to adjust the printing parameters according to the specific experimental requirements. Filament in a form of 1.75 mm sticks was extruded at 150 °C. A heatbed temperature was 40°C, and a nozzle diameter 0.8 mm.

Microscopic observations were conducted using stereomicroscope and optical microscope (Kern Optics, Poland) to examine the surface morphology of the printed implants. Samples were analyzed to assess any changes in shape or microstructure after exposure to temperature.

Shape memory behavior was evaluated by subjecting the samples to thermal cycles, where the implants were initially deformed and then heated to body temperature (38°C) to observe their ability to recover to their original shape. The recovery of the shape was monitored and the time required for full shape recovery was recorded.

3. Results

Filaments were successfully produced by injection molding from pure terpolymer and terpolymer modified with β-TCP and Osteogenon drug (Fig. 1a, b). Occasionally, powder agglomerates were observed on the filament sticks (Fig. 1c, 1d).

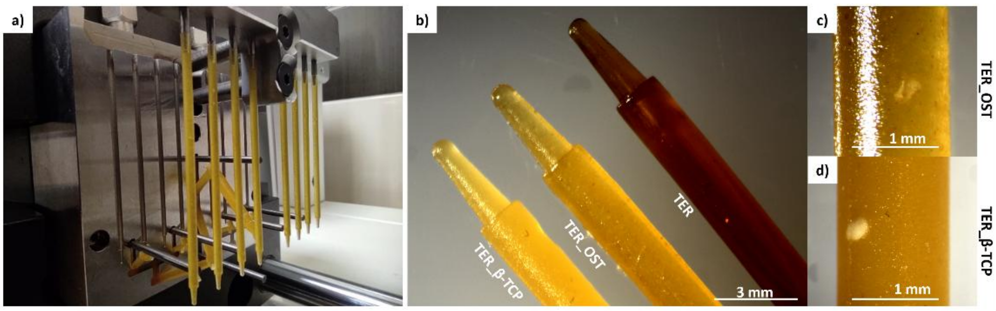

Figure 1. Filament sticks produced by injection molding process.

In Figure 2, the implant model used in the study is presented. The lattice model consisted of three layers of bars with a rectangular cross-section (1 x 0.6 mm), arranged 0.7 mm apart. Adjacent layers were oriented perpendicular to each other, resulting in a lattice structure with cuboid-shaped pores.

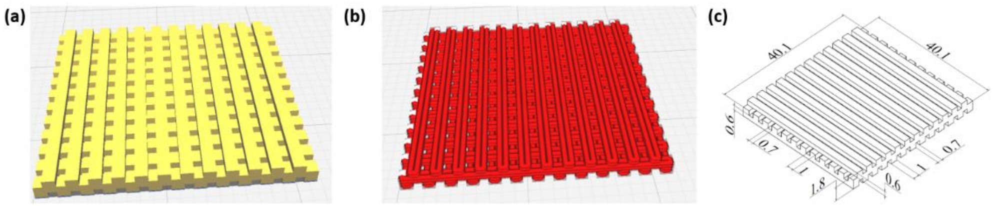

Figure 2. Model of the implant used in the study.

During the printing process, filaments with the most favorable visual distribution of the powders were selected. The microstructure of the samples, obtained by selecting appropriate parameters, is shown in Figure 3. Figure 4 presents optical microscope images that reveal more detailed features of the printed samples. The printed samples were consistent with the designed model. When filaments with well-dispersed fillers (free of visible agglomerates) were used, the printing process proceeded smoothly without any issues. Optical microscope analysis revealed a uniform and well-defined microstructure, indicating good material homogeneity and successful integration of the modifiers.

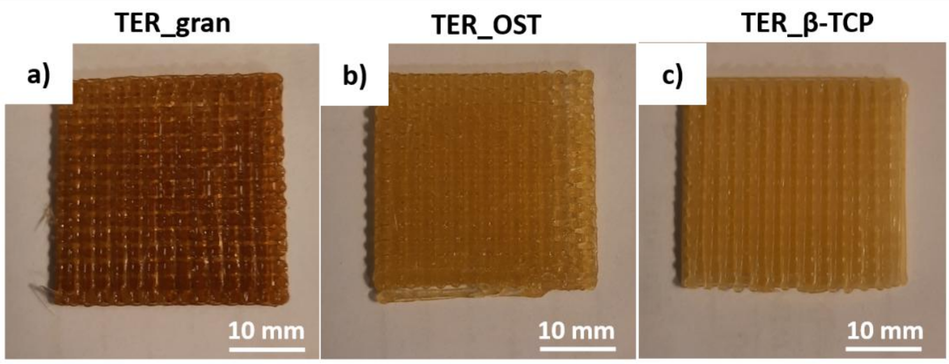

Figure 3. Stereoscopic microscope images of the printed samples: (a) pure terpolymer (L-LA/GL/ε-CL 69/16/15), (b) terpolymer modified with Osteogenon drug, (c) terpolymer modified with β-TCP.

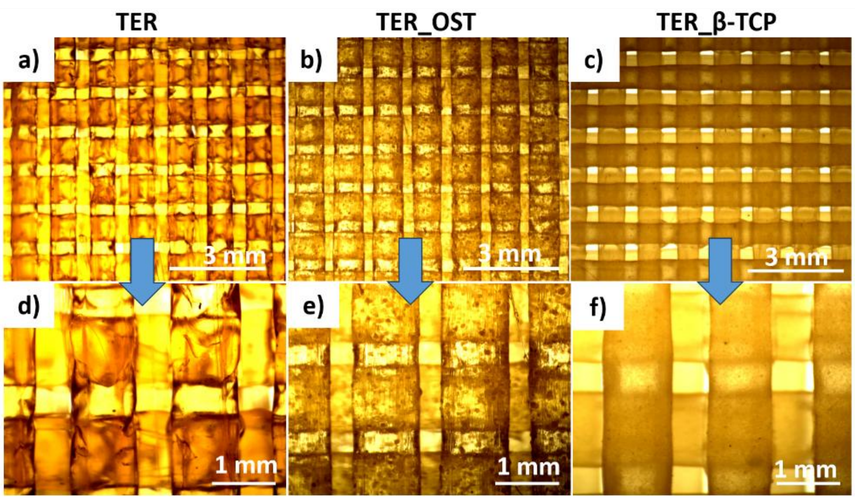

Figure 4. Optical microscope images of the printed samples: (a,d) pure terpolymer (L-LA/GL/ε-CL 69/16/15), (b,e) terpolymer modified with the Osteogenon drug, (c,f) terpolymer modified with β-TCP.

Previous experiments showed that larger agglomerate clusters could lead to nozzle clogging during printing (Fig. 5), highlighting the importance of choosing filaments with a more uniform powder distribution to ensure smooth extrusion and prevent blockages.

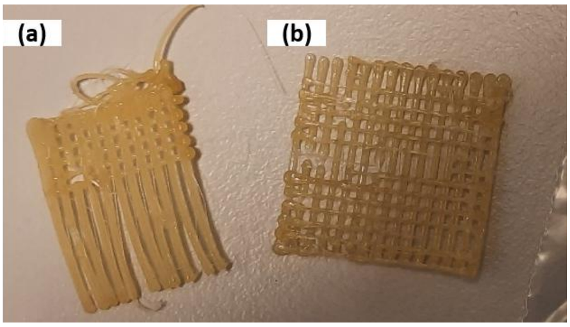

Figure 5. Effect of large agglomerate clusters on nozzle clogging during printing.

Shape memory tests were conducted on a 3D printing filament made from the investigated materials. The secondary (deformed) shape was formed in water at 45°C by winding the filament around a tube with a diameter of 10.5 mm, followed by cooling in distilled water at 10°C. The samples were then immersed in distilled water at 38°C. The process of returning to the original shape was recorded as a video. The Figure 6 shows images of the samples at the moment of immersion in water and after 180 seconds.

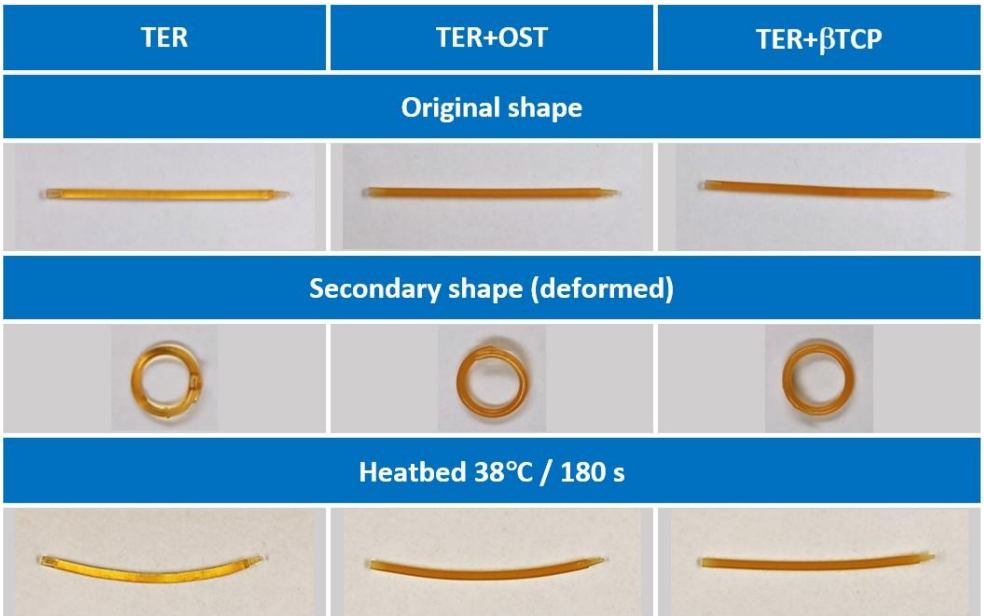

Figure 6. The shape deformation and return to the original form under the influence of temperature, demonstrating the shape-memory behavior.

4. Discussion

The printing process yielded several key observations. Ambient temperature and the absence of airflow significantly influence the printability of the filament. In conditions without airflow and with ambient temperatures exceeding 20°C, print success rates decrease, often resulting in nozzle clogging. It is essential to use a nozzle with a minimum diameter of 0.8 mm, as smaller nozzles are prone to immediate clogging, hindering smooth extrusion. Terpolymer prints modified with osteogenon exhibit a glossy surface and considerable stringing, which may affect the final aesthetics and functional performance of the printed structure. TER_OST filament is slightly easier to print than TER_β-TCP, but it requires a longer printing time, suggesting that while it is less demanding in terms of extrusion, it necessitates more time for layer formation. These findings underscore the critical importance of controlling environmental factors, nozzle specifications, and material handling to achieve optimal results in 4D printing.

Based on the shape-memory behavior experiment, the greatest ability to return to the original shape was observed for the sticks made of the TER_βTCP_5_BL alloy, followed by TER_OST_5_BL. The lowest shape recovery ability was demonstrated by the sample made of the pure TER alloy.

5. Conclusions

The study demonstrates the potential of 4D printing in designing adaptive medical implants by highlighting the critical role of environmental conditions, nozzle specifications, and material preparation in achieving successful printability and functional performance. Shape-memory behavior tests revealed that TER_βTCP_5_BL exhibits the highest recovery ability, underscoring its suitability for applications requiring adaptive, shape-responsive medical structures.

Acknowledgments: This work was funded by the National Science Centre, Poland, in the frame of the project "3D and 4D printing of stimuli-responsive and functionally graded biomaterials for osteochondral defects regeneration," grant number: 2020/39/I/ST5/00569 (OPUS-LAP).

Conflicts of Interest: The authors declare no conflict of interest. The funders had no role in the design of the study; in the collection, analyses, or interpretation of data; in the writing of the manuscript, or in the decision to publish the results.

References

1. Demoly, F.; Dunn, M.L.; Wood, K.L, Qi, H.J.; André, J.C. The status, barriers, challenges, and future in design for 4D printing. Materials & Design 2021, 212, 110193. https://doi.org/10.1016/j.matdes.2021.110193
2. Doostmohammadi, H.; Kashmarizad, K.; Baniassadi, M.; Bodaghi, M.; Mostafa Baghani, M. 4D printing and optimization of biocompatible poly lactic acid/poly methyl methacrylate blends for enhanced shape memory and mechanical properties. Journal of the Mechanical Behavior of Biomedical Materials 2024, 160, 106719. https://doi.org/10.1016/j.jmbbm.2024.106719
3. Smola, A.; Dobrzynski, P.; Cristea, M.; Kasperczyk, J.; Sobota, M.; Gebarowska, K.; Janeczeka, H. Bioresorbable terpolymers based on l-lactide, glycolide and trimethylene carbonate with shape memory behavior. Polym. Chem., 2014, 5, 2442-2452. https://doi.org/10.1039/c3py01557b
4. Rajzer, I.; Kurowska, A.; Frankova, J.; Sklenářová, R.; Nikodem, A.; Dziadek, M.; Jabłoński, A.; Janusz, J.; Szczygieł, P.; Ziąbka, M. 3D-Printed Polycaprolactone Implants Modified with Bioglass and Zn-Doped Bioglass. Materials 2023, 16, 1061. https://doi.org/10.3390/ma16031061
5. Szczygieł, P.; Novotný, R.; Kurowska, A.; Janusz, J.; Jabłoński, A.; Frankova, J.; Rajzer I. Comprehensive Assessment of Materials for 4D printing in Medical Implant Application. Projektowanie, badania i eksploatacja – 2024. https://doi.org/10.53052/9788367652261
6. Rajzer, I.; Kurowska, A.; Janusz, J.; Maślanka, M.; Jabłoński, A.; Szczygieł, P.; Fabia, J.; Novotný, R.; Piekarczyk, W.; Ziąbka, M.; Frankova, J. 4D Printing of βTCP-Modified Shape Memory Polymers for Bone Scaffolds in Osteochondral Regeneration. 10.20944/preprints202412.0137.v1

TECHNICAL UNIVERSITY OF KOŠICE
Faculty of Mechanical Engineering

Impact of Lighting Conditions on Vision Inspection Systems: Analysis, Cost Estimation, and Operational Overview of Cognex Cameras

Maksymilian Maślanka [1,*], Daniel Jancarczyk [1] and Damian Pytka [1]

[1] Faculty of Mechanical Engineering and Computer Science, University of Bielsko-Biala, 43-309 Bielsko-Biala, Poland; mmaslanka@ubb.edu.pl (M.M.); djancarczyk@ubb.edu.pl (D.J.); dpytka@ubb.edu.pl (D.P.)
* Correspondence: mmaslanka@ubb.edu.pl

Abstract: This study investigates the impact of lighting conditions on the accuracy of vision inspection systems. Using Cognex cameras, tests were conducted on colorful gummy bears to evaluate the detection of both shape and color under white, red, green, and blue illumination. Results show that white light yielded the most accurate and unbiased detection, while colored lighting caused variations in detection quality, with some objects being misclassified. The study highlights the importance of lighting choice in industrial applications and suggests avenues for algorithmic improvements to enhance system performance under diverse lighting conditions. These findings contribute to optimizing vision system design and operation in automated inspection environments.

Keywords: Cognex; Machine Vision; Lighting; Automated Inspection.

1. Introduction

In modern industry, vision systems are increasingly and dynamically implemented to accelerate inspection processes and quality control [1]. For instance, in the manufacturing sector, vision systems are used for inspecting shoes [2, 3]. These systems are also applied in robotic operations such as pick-and-place and bin-picking tasks [4]. The latest vision systems can effectively distinguish the color of components as well as their shapes (patterns) [5]. This paper focuses on analyzing the integration of shape and color detection by vision systems under varying illumination colors and comparing the capabilities of color and white illuminated monochromatic systems. The research object, chosen for its wide availability and affordable pricing, consists of colorful gummy bears. Tests will be conducted to evaluate the detectability of both color and shape under white, red, green, and blue lighting.

2. Materials and Methods

The system prepared for vision inspection is presented in the diagram below. It consists of a Cognex D902M camera, a computer equipped with InSight 23.3.0 software, and an electrical box with 24VDC power supply. The camera connects to the software on the computer via an Ethernet cable.

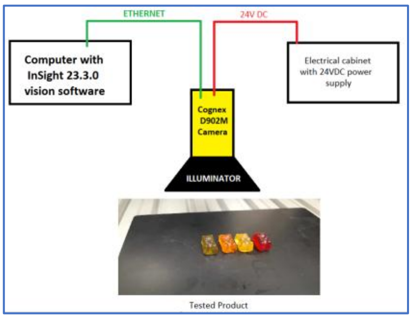

Figure 1. Block diagram of vision system.

The system shown in the diagram above is not the only one used in this article for the comparison of vision systems. The second system is nearly identical but differs in the camera model, utilizing the Cognex In-Sight 2800. The connection scheme remains the same as described above. Initially, four colors of the tested objects were selected—green, orange, yellow, and red. These objects were placed on a black background (a plywood pad), and photographs were taken using various illuminator color settings. Below are the key acquisition settings of the vision system in the InSight Vision Suite software. The camera focus was set automatically using the autofocus function, which adjusted image sharpness when the object distance changed. However, in this study, the focal distance was fixed after initial setup and not modified during the tests. The exposure value was initially set to 4 milliseconds, and the gain was set to 1.0x. These settings are illustrated in the figure below.

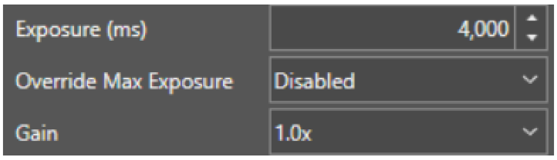

Figure 2. Exposure and gain settings for vision system.

The next step in configuring the system involved adjusting the white balance to ensure that the camera accurately reproduced colors as perceived by the human eye under white lighting. The automatic white balance function was selected, followed by manual correction of individual colors. The final settings are presented in thefigure below.

Figure 3. White balance of system.

To systematize the process, it was established that the objects would not be significantly moved to ensure that changes in their position, and consequently the angle of light incidence from the illuminator, would not affect the final inspection results. Changes in illumination color were made using the dedicated menu in the software, as shown in the figure below.

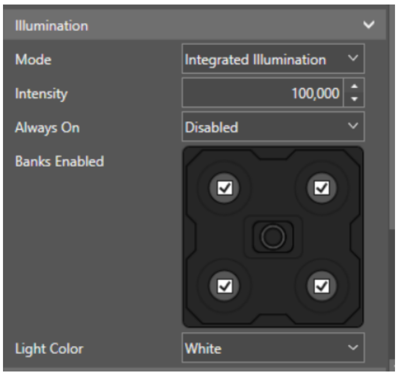

Figure 4. Illumination settings.

After configuring the vision system, the following visual effect was achieved. The colors of the individual gummy bears were visible and not oversaturated. The white balance was maintained, ensuring that under white lighting, the colors were clearly visible and distinguishable.

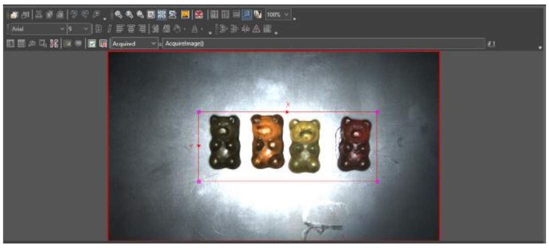

Figure 5. Acquired image.

After setting up and preparing the system for operation, a series of images of the same objects was captured under different lighting conditions—white, red, green, and blue. Additionally, a simple program was developed to detect the bear shape and then determine its color. Representative results obtained during the tests are presented in the figures in the subsequent section below.

3. Results and Discussion

A program for vision inspection was developed, as illustrated in the diagram below. The set of functions labeled as PATTERN MATCHING detects the shapes of the gummy bears and maps their coordinates onto the image, enabling reference to these coordinates through the COLOR MATCHING function. This function evaluates the color of each detected object and overlays the corresponding information onto the image using the Plot function.

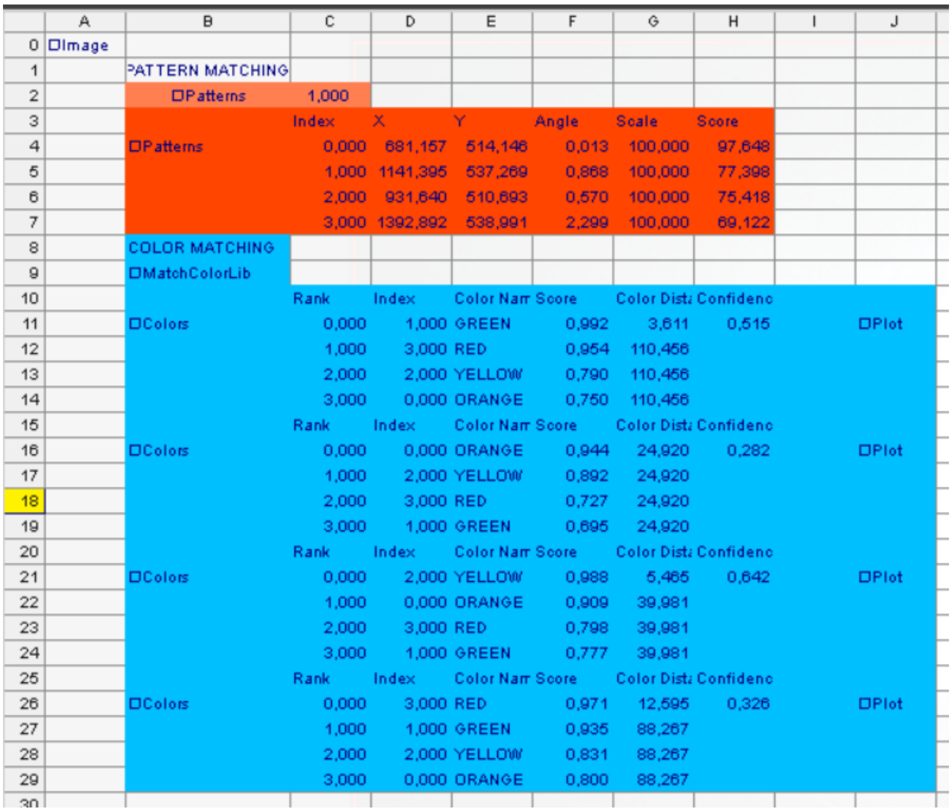

	A	B	C	D	E	F	G	H	I	J
0	□Image									
1		PATTERN MATCHING								
2		□Patterns	1,000							
3			Index	X	Y	Angle	Scale	Score		
4		□Patterns	0,000	681,157	514,146	0,013	100,000	97,648		
5			1,000	1141,395	537,269	0,868	100,000	77,398		
6			2,000	931,640	510,693	0,570	100,000	75,418		
7			3,000	1392,892	538,991	2,299	100,000	69,122		
8		COLOR MATCHING								
9		□MatchColorLib								
10			Rank	Index	Color Narr	Score	Color Dist	Confidenc		
11		□Colors	0,000	1,000	GREEN	0,992	3,611	0,515		□Plot
12			1,000	3,000	RED	0,954	110,456			
13			2,000	2,000	YELLOW	0,790	110,456			
14			3,000	0,000	ORANGE	0,750	110,456			
15			Rank	Index	Color Narr	Score	Color Dist	Confidenc		
16		□Colors	0,000	0,000	ORANGE	0,944	24,920	0,282		□Plot
17			1,000	2,000	YELLOW	0,892	24,920			
18			2,000	3,000	RED	0,727	24,920			
19			3,000	1,000	GREEN	0,695	24,920			
20			Rank	Index	Color Narr	Score	Color Dist	Confidenc		
21		□Colors	0,000	2,000	YELLOW	0,988	5,465	0,642		□Plot
22			1,000	0,000	ORANGE	0,909	39,981			
23			2,000	3,000	RED	0,798	39,981			
24			3,000	1,000	GREEN	0,777	39,981			
25			Rank	Index	Color Narr	Score	Color Dist	Confidenc		
26		□Colors	0,000	3,000	RED	0,971	12,595	0,326		□Plot
27			1,000	1,000	GREEN	0,935	88,267			
28			2,000	2,000	YELLOW	0,831	88,267			
29			3,000	0,000	ORANGE	0,800	88,267			
30										

Figure 6. Simple In-Sight Vision Suite program for pattern and color matching.

The Colors function selects the averaged color of the examined object within the area bounded by the outline of each gummy bear individually. It then compares the obtained data with its color database (MatchColorLib). The color closest to the database entry (with the smallest color distance) is subsequently assigned to each detected object individually. The program's output is presented in the subsections below, for each lighting color separately. The tested objects were arranged in two different configurations to minimize the likelihood of the algorithm "learning" specific positions and colors.

3.1. White light

Under white light, the vision inspection was performed flawlessly. The position and color of the detected objects corresponded accurately to reality. None of the colors stood out significantly from the others – Figure 7.

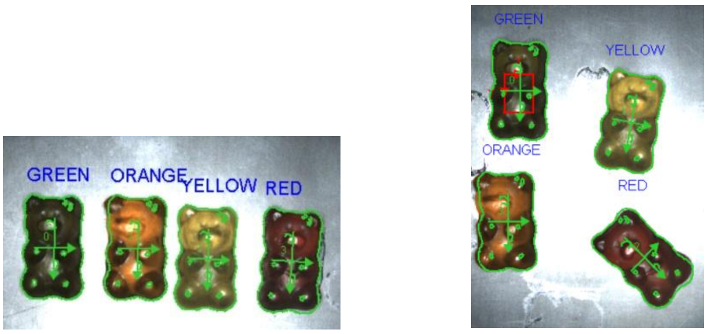

(a) (b)

Figure 7. Gummies properly described by algorithm: (a) positioned in a line; (b) positioned randomly.

3.2. Red light

Under red light, the color detection spectrum shifted towards orange and red hues. The shapes of the objects were detected correctly. The green object had a distinctly different color compared to the others, but it was detected as red. The results are presented in Figure 8.

(a) (b)

Figure 8. Gummies improperly described by algorithm under red light: (a) positioned in a line; (b) positioned randomly.

3.3. Green light

Under green lighting, only green and occasionally yellow colors were detected. The shape of the orange object was not always detected correctly. Among the other objects, the yellow one stood out the most.

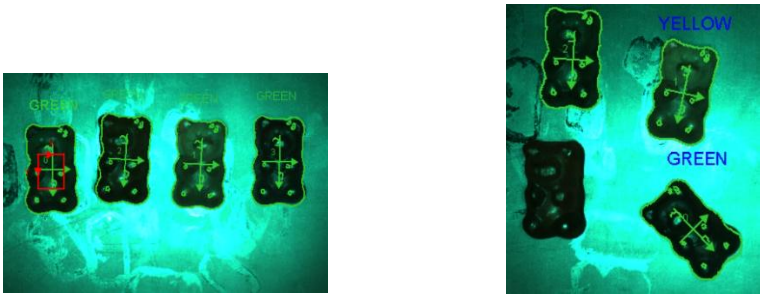

(a) (b)

Figure 9. Gummies improperly described by algorithm under green light: (a) positioned in a line; (b) positioned randomly.

3.4. Blue light

Under blue light, all objects were detected as green, while the orange object was not detected at all. The yellow object was the most distinguishable in this scenario – Figure 10.

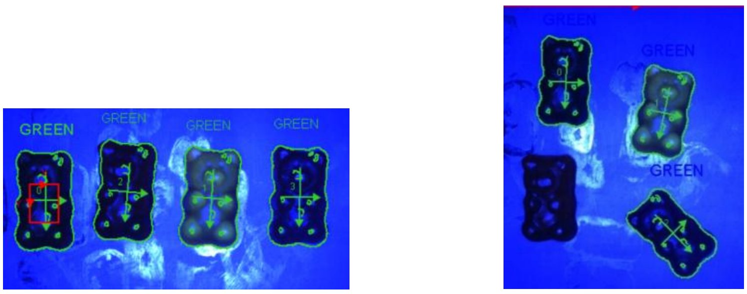

(a) (b)

Figure 10. Gummies improperly described by algorithm under blue light: (a) positioned in a line; (b) positioned randomly.

3.5. Monochromatic camera – white light

In the case of the system with a monochromatic camera and white lighting, the only distinguishable color would be yellow, as it appears as a gray color while the other colors are much darker. The shape was distinguishable every time.

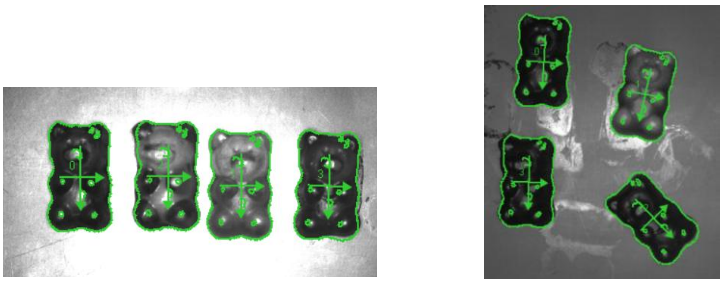

(a) (b)

Figure 11. Gummies improperly described by monochromatic camera: (a) positioned in a line; (b) positioned randomly.

Table 1. Cost estimation of vision systems.

Vision camera model	Type of vision	Resolution	Estimated cost
IS2802C (with wiring)	Color vision	Up to 1440x1080	8 745 EUR
ISD905M (with wiring)	Monochromatic	Up to 2448 x 2048	15 112 EUR

4. Conclusions

The conducted research demonstrates the significant influence of lighting conditions on the performance of vision inspection systems. White light provided the most consistent and accurate detection of both shapes and colors. In contrast, under red, green, and blue lighting, the systems showed varied effectiveness, with specific colors being either emphasized or misinterpreted. For instance, green objects were incorrectly identified as red under red lighting, and yellow objects appeared most distinct under green and blue lighting. The IS2808C system with color vision is cheaper than the monochromatic ISD905M but has lower image resolution.

These findings underscore the importance of selecting appropriate lighting conditions when designing and implementing vision inspection systems. White light is recommended for applications requiring high accuracy and minimal bias. Additionally, the results suggest the potential for further optimization of vision algorithms to enhance robustness under varied lighting environments, especially when dealing with monochromatic or colored illuminators.

Future work could explore advanced image processing techniques or machine learning models to improve accuracy in non-optimal lighting conditions, expanding the versatility and application range of vision inspection systems.

Conflicts of Interest: The authors declare no conflict of interest.

References

1. Jancarczyk, D.; Rysiński, J.; Worek, J. Comparative Analysis of Measurement Tools in the Cognex D900 Vision System. Appl. Sci. 2024, 14, 8296.
2. Klarák, J.; Kuric, I.; Zajačko, I.; Bulej, V.; Tlach, V.; Józwik, J. Analysis of Laser Sensors and Camera Vision in the Shoe Position Inspection System. Sensors 2021, 21, 7531.
3. Giesel, M.; Gegenfurtner, K.R. Color appearance of real objects varying in material, hue, and shape. J. Vis. 2010, 10, 1–21.
4. Giannoccaro, N.I.; Rausa, G.; Rizzi, R.; Visconti, P.; De Fazio, R. An Innovative Vision-Guided Feeding System for Robotic Picking of Different-Shaped Industrial Components Randomly Arranged. Technologies 2024, 12, 153.
5. Yoo, W.S.; Kang, K.; Kim, J.G.; Yoo, Y. Image-Based Quantification of Color and Its Machine Vision and Offline Applications. Technologies 2023, 11, 49.

TECHNICAL UNIVERSITY OF KOŠICE
Faculty of Mechanical Engineering

Exploring Operational Space Controllers for Robotic Manipulators

Tomáš Merva[1,*] and Ivan Virgala[1]

[1] Department of Industrial Automation and Mechatronics, Technical University of Kosice; tomas.merva@tuke.sk; ivan.virgala@tuke.sk
* Correspondence: tomas.merva@tuke.sk

Abstract: For complex tasks in the manipulation domain, it is easier to specify controllers in the operational space of the manipulator rather than in the joint space. This paper explores the use of Operational Space Controllers (OSC) for controlling redundant manipulators. We were specifically interested in how each controller influences the overall performance of the robot. Furthermore, we investigate the integration of nullspace controllers to achieve secondary objectives, such as maintaining joint configurations or avoiding singularities, without compromising primary task performance. We demonstrate the validity of OSC in simulated environments using the Mujoco physics engine. These results underscore the practicality of OSC for a wide range of robotic applications, including industrial automation, human-robot interaction, and adaptive task execution.

Keywords: manipulation, control, motion generation, robotics

1. Introduction

To extend the use of robotics for various complex tasks that consist of multiple steps or specific motions, the control of the manipulator must be fast and intuitive. Operational Space Controllers (OSCs) [2,3,4] provide an alternative approach to control robots through the operational space, without requiring direct control of the robot's joints. Moreover, they can be effectively extended to resolve redundancy, ensuring that both the end-effector and the degrees of freedom (DoF) achieve the desired behavior. A notable property of OSC is its fast control latency, which can reach up to 500 Hz; however, this performance comes at the cost of not accounting for collision avoidance. This limitation can be addressed by using OSC as a low-level controller, complemented by local motion planning methods or learning-based strategies to guide OSC in achieving tasks while avoiding collisions [1].

There are several types of OSCs depending on the specific approach to controlling the end-effector, such as velocity-based, acceleration-based, or force-based controllers. Velocity-based OSC computes the desired joint torques based on a target end-effector velocity, while force-based OSC directly computes the desired joint torques from the reference force applied by the end-effector [3]. In this paper, we implement a position-based OSC with a velocity controller to enhance stabilization and limit end-effector overshooting.

This paper is organized as follows: The first section introduces the general concept of operational space controllers and the design choices for control signals. The second section focuses on the experimental analysis of the designed operational space controllers and nullspace controller in the Mujoco physics engine. The contributions of this paper are twofold:

1. Introduction to operational space controllers
2. Implementation and simulation experiments of OSC

2. Methodology

The robot is controlled via joint torques inputs that can be divided into two terms: A) the controller, B) the gravity compensation.

2.1. Gravity compensation

In this section, we discuss how to cancel the gravitational forces acting on the robot. The robot consists of L links and has N degrees of freedom (DoF). The work done by gravity can be expressed as the summation of the distances $\dot{x}_i$, traveled by each link's center of mass, multiplied by the gravitational forces:

$$W_g = \sum_{i=0}^{\mathrm{L}} \left(\mathbf{F}_{\mathbf{g}_i}^T \dot{\mathbf{x}}_i\right). \tag{1}$$

Gravitational force F_{g_i} is computed as the mass of the i link multiplied by the gravitational acceleration acting on that link:

$$F_{g_i} = m_i g. \tag{2}$$

Building on the concept of conservation of energy, the work done by gravity on the end-effector of the robot is equivalent to the work done by gravity expressed in the joint space. Therefore, we can modify Eq. (1) as follows:

$$\boldsymbol{F}_q^T \dot{\boldsymbol{q}} = \sum_{i=0}^{\mathrm{L}} \left(\mathbf{F}_{\mathbf{g}_i}^T \dot{\mathbf{x}}_i\right). \tag{3}$$

We can substitute the task space velocities by $\dot{\boldsymbol{x}} = \boldsymbol{J}_{CoM_i}(\boldsymbol{q})\dot{\boldsymbol{q}}$, where $\boldsymbol{J}_{CoM_i}$ is the Jacobian of the center of mass (CoM) of link i. By canceling out the joint velocities on both sides, we obtain:

$$\boldsymbol{\tau}_g = -\sum_{i=0}^{\mathrm{L}} \left(\boldsymbol{J}_{CoM_i}^T m_i \boldsymbol{g}\right). \tag{4}$$

resulting in joint torques that counteract the effect of the gravity on the robotic arm.

2.2. Operational Space Controller

The control input representing the joint torque looks as follows:

$$\boldsymbol{\tau}_{des} = \boldsymbol{J}^T(\boldsymbol{q})\boldsymbol{M}_x(\boldsymbol{q})\ddot{\boldsymbol{x}}_{des} + \boldsymbol{\tau}_g(\boldsymbol{q}), \tag{5}$$

where $\ddot{\boldsymbol{x}}_{des}$ denotes the desired acceleration of the robot's end-effector, which, when multiplied by the Jacobian $\boldsymbol{J}(\boldsymbol{q})$ and the task space mass matrix $\boldsymbol{M}_x(\boldsymbol{q})$, transforms the desired acceleration into the configuration space. Eq. (5) allows us to design an arbitrary controller that operates in the operational space and outputs the desired acceleration. In our experiments, we used a PD controller of the following form:

$$\ddot{\boldsymbol{x}}_{des} = K_p(\boldsymbol{x}_{des} - \boldsymbol{x}) + K_V(\dot{\boldsymbol{x}}_{des} - \dot{\boldsymbol{x}}), \tag{6}$$

The desired task space velocity is set to zero to ensure the system reaches zero velocity at the desired pose, thereby avoiding oscillatory behavior.

2.3. Nullspace Controller

Since we want our controller to work for high-dimensional redundant systems, we can create secondary controllers that operate within the nullspace of the main controller. By leveraging the nullspace of the main controller, the secondary controllers do not interfere with its behavior [6]. For instance, a practical example of a nullspace controller is one that biases the system to minimize the difference between a predefined home joint configuration and the current joint configuration. Intuitively, this means that the manipulator's nullspace represents motions of the arm that do not affect the motion of the end-effector. Mathematically, we can project the output of the secondary controller, $\boldsymbol{u}_{sec}$, onto the nullspace of the primary controller as follows:

$$\boldsymbol{u} = \boldsymbol{u}_{prim} + (\boldsymbol{I} - \boldsymbol{J}^T(\boldsymbol{q})\boldsymbol{J}^{T+}(\boldsymbol{q}))\boldsymbol{u}_{sec}, \tag{7}$$

where $\boldsymbol{u}_{prim}$ is the primary controller, $\boldsymbol{I}$ is the identity matrix and $\boldsymbol{J}^{T+}(\boldsymbol{q})$ is the pseudo-inverse of $\boldsymbol{J}^T(\boldsymbol{q})$ that is responsible for filtering out any undesired effect inherited by the secondary controller [5]. The total control signal that consists of OSC and nullspace controller is as follows [6]:

$$\boldsymbol{\tau}_{des} = \boldsymbol{J}^T(\boldsymbol{q})\boldsymbol{M}_x(\boldsymbol{q})\ddot{\boldsymbol{x}}_{des} + \boldsymbol{\tau}_g(\boldsymbol{q}) - \boldsymbol{J}^T(\boldsymbol{q})\boldsymbol{J}^{T+}(\boldsymbol{q})\boldsymbol{u}_{sec}, \tag{8}$$

where the controller that minimizes the deviation from the home configuration has the following form:

$$\boldsymbol{u}_{\mathrm{sec}} = (\boldsymbol{q}_{\mathrm{home}} - \boldsymbol{q})^{\mathrm{T}}\mathrm{K}_{\mathrm{null}}(\boldsymbol{q}_{\mathrm{home}} - \boldsymbol{q}). \tag{9}$$

3. Results

The presented algorithm was evaluated in the Mujoco simulator for various target poses (Fig. 1). In each experiment, we used a 7-DoF Franka Emika Panda manipulator. The operational space controller operated at a frequency of 500 Hz. The simulation and controller were run on a laptop with an Intel Core i7 processor and 16 GB of RAM. In the simulation experiments, we tested (A) position reaching, (B) position and orientation reaching, and (C) the nullspace controller, to evaluate performance and assess the contribution of each term to the general problem.

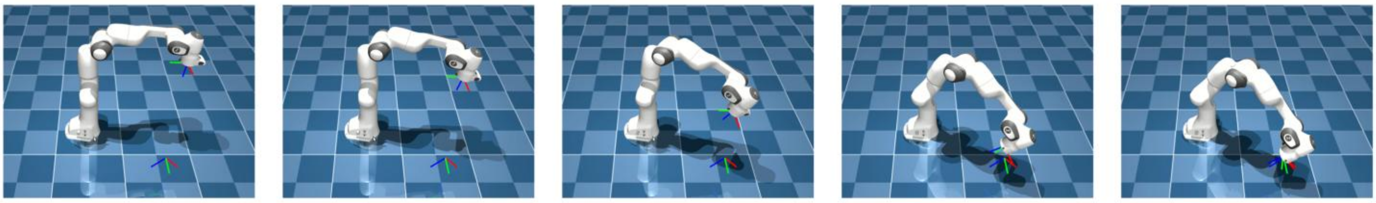

Figure 1. Selected time frames for the PD Operational Space Controller and the nullspace controller of a 7-degree-of-freedom manipulator.

In Fig. 2, the actual task linear position and velocity profiles are compared with the reference task space pose provided to the PD operational space controller. The torque outputs of the OSC are clipped to satisfy joint limits. The constant steady-state error could be reduced by incorporating an integral controller or by better tuning the PD gains. The overall controller used consisted of the main PD operational space controller and the nullspace controller. Potential singularities are handled by singular value decomposition of Jacobians and modifying the small values of the rectangular diagonal matrix Σ.

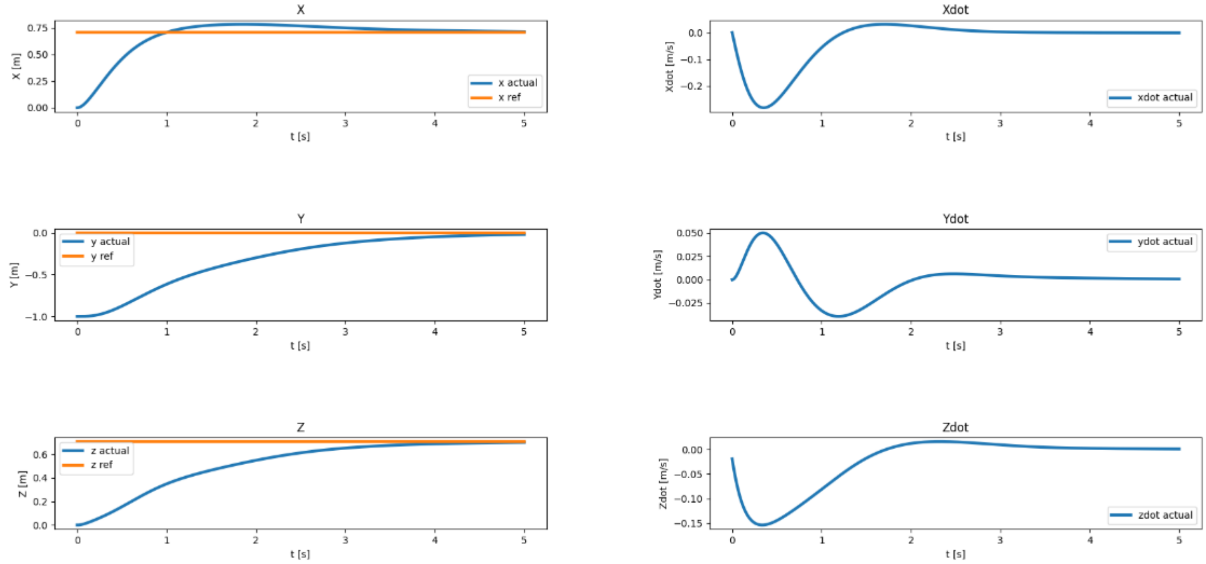

Figure 2. Comparison of the reference and actual task positions, as well as the actual linear task velocity.

In Fig. 3, we demonstrate the influence of the nullspace controller on the overall behavior of the robot. The secondary controller is designed to operate within the nullspace of the main controller to minimize deviations from a predefined joint home configuration.

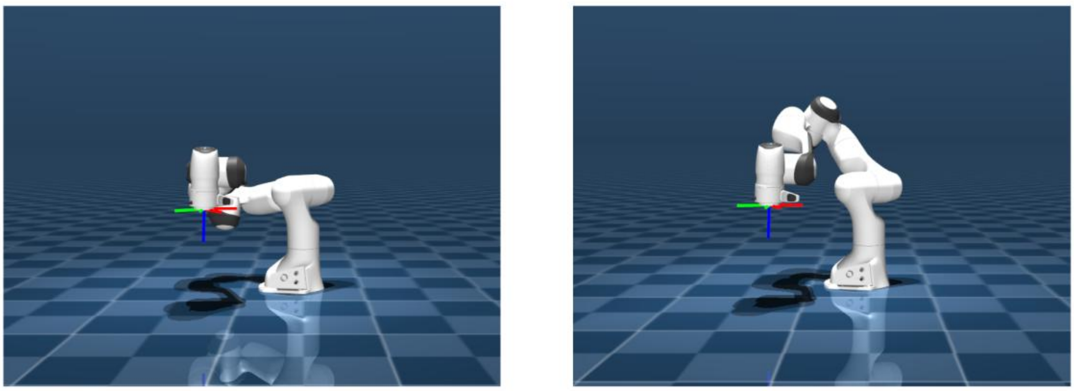

(**a**) OSC without nullspace controller (**b**) OSC with nullspace controller

Figure 3. Comparison of the effect of the nullspace controller that tries to minimize the difference between home joint configuration and the current joint configuration of the robot.

4. Conclusions

In this paper, we explored and demonstrated the implementation of Operational Space Controllers in combination with nullspace controllers for controlling redundant robotic manipulators. Both controllers were successfully implemented in the physics simulator Mujoco, allowing us to validate their effectiveness in handling complex tasks in high-dimensional systems. The Operational Space Controller enabled precise control of the end-effector in task space, while the nullspace controller effectively managed redundancy, facilitating secondary objectives such as maintaining a predefined joint configuration. Our results highlight the versatility and robustness of these controllers when applied to redundant robotic systems. By leveraging the nullspace, we ensured that secondary behaviors did not interfere with the primary task, demonstrating a practical approach to multi-task control in robotics. For future work, we could implement different operational space controllers and compare their accuracy across various tasks. Additionally, integrating path planners to enable features such as collision avoidance would further enhance performance in real-world applications.

Acknowledgments: The authors would like to thank to the Slovak Grant Agency VEGA 1/0201/21, VEGA 1/0436/22 and KEGA 030TUKE-4/2020. This research was also funded by Research grant for young researchers at TUKE Control of kinematically redundant robots for minimally invasive surgeries.

Conflicts of Interest: The authors declare no conflict of interest. The funders had no role in the design of the study; in the collection, analysis, or interpretation of data; in the writing of the manuscript; or in the decision to publish the results.

References

1. Peters, Jan, and Stefan Schaal. “Learning to Control in Operational Space.” The International Journal of Robotics Research 27, no. 2 (February 1, 2008): 197–212. https://doi.org/10.1177/0278364907087548.
2. Nicolis, Davide, Fabio Allevi, and Paolo Rocco. “Operational Space Model Predictive Sliding Mode Control for Redundant Manipulators.” IEEE Transactions on Robotics 36, no. 4 (August 2020): 1348–55. https://doi.org/10.1109/TRO.2020.2974092.
3. Nakanishi, Jun, Rick Cory, Michael Mistry, Jan Peters, and Stefan Schaal. “Operational Space Control: A Theoretical and Empirical Comparison.” The International Journal of Robotics Research 27, no. 6 (June 1, 2008): 737–57. https://doi.org/10.1177/0278364908091463.
4. Caccavale, F., S. Chiaverini, and B. Siciliano. “Second-Order Kinematic Control of Robot Manipulators with Jacobian Damped Least-Squares Inverse: Theory and Experiments.” IEEE/ASME Transactions on Mechatronics 2, no. 3 (September 1997): 188–94. https://doi.org/10.1109/3516.622971.
5. Mistry, Michael, and Ludovic Righetti. "Operational space control of constrained and underactuated systems." (2012).
6. DeWolf, T. (2013, September 17). Robot control 4: Operation space control. Retrieved from https://studywolf.wordpress.com/2013/09/17/robot-control-4-operation-space-control/

TECHNICAL UNIVERSITY OF KOŠICE
Faculty of Mechanical Engineering

Analysis of heat transfer in a delivery bag to assess the possibility of drug transportation

Ivan Mihálik [1,*], Lukáš Tóth [1] and Marián Lázár [1]

[1] Technical University of Košice, Faculty of Mechanical Engineering, Department of Energy Engineering; ivan.mihalik@tuke.sk; lukas.toth@tuke.sk; marian.lazar@tuke.sk
* Correspondence: ivan.mihalik@tuke.sk; Tel.: +421 55 602 2451

Abstract: Using numerical methods, the paper solves heat transfer in a simplified model of a delivery bag with the aim of determining the approximate time during which the temperature of the drug will drop below 0 °C at an ambient temperature of -5 °C. It then compares the obtained data with the values obtained by experimental measurement in the environmental chamber. From the experimental measurement, it is clear that with the given configuration, even after an hour the temperature of the drug will not drop below the permissible value.

Keywords: heat transfer, heat resistance, insulation, CFD simulation

1. Introduction

Delivery services focused on the delivery of meals from restaurants or groceries operating in Slovakia have seen a significant increase in sales and interest from consumers, especially during the Covid-19 pandemic. However, a similar trend could be observed at the global level [1]. The boom in online shopping and the use of delivery services in recent years has caused a greater interest among customers not only in the delivery of food and common goods, but also in the possibility of purchasing and delivering over-the-counter medicines.

The implementation of this type of goods in the portfolio of delivery companies focused primarily on food delivery requires the fulfillment of certain conditions, as pharmaceuticals can be sensitive to exposure to various effects of high or low temperatures [2,3]. The task of ordinary delivery bags is to keep food hot enough or cold enough, depending on its type. When delivering food, the initial temperature difference between the food and the air in the bag is relatively significant, but when delivering medicines, it is assumed that the temperature of the goods and the air in the bag are balanced. Several available studies deal with the insulation of delivery bags for food delivery purposes, but the issue of drug transport by these bags is currently little explored [4-6]. However, the general issue of transporting medications, especially those sensitive to temperature, is described in several articles [7-9].

2. Numerical simulation of heat transfer

Before performing the experimental measurement, a simplified 3D model corresponding to the dimensions and properties of a real delivery bag was created for the purpose of initial assessment of heat transfer and obtaining an approximate time frame during which the temperature of the drug will drop below the permissible level of 0 °C. It was considered storing the cardboard box of the drug in a paper bag, which was subsequently placed in a delivery bag. This simple and economical solution creates an additional insulating layer inside the system, which results in slowing down the cooling of the drug. To reduce the computational complexity, symmetry in the YZ and YX planes was considered.

A model representing a ¼ delivery bag containing a paper bag and a box is shown in Figure 1.

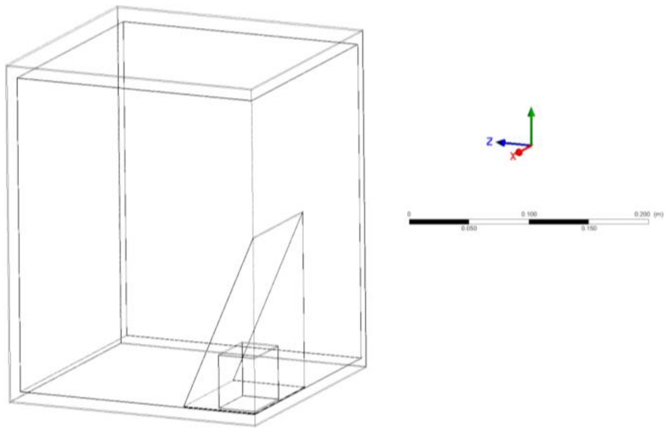

Figure 1. 3D model of a delivery bag.

The properties of the individual layers together with the thickness of the material are defined in Table 1:

Table 1. Properties of insulating layers.

Material	Thickness (mm)	Thermal conductivity coefficient ($W \cdot m^{-1} \cdot K^{-1}$)	Specific heat capacity ($J \cdot kg^{-1} \cdot K^{-1}$)	Density ($kg \cdot m^{-3}$)
Polyester	1	0.38	1,100	1,300
PE foam	9	0.038	2,282	33
Aluminum foil	0.2	237	903	2,702
Paper (bag)	0.3	0.07	1,400	818
Paper (box)	0.7			

During the heat transfer simulation, the initial temperature of all material layers, including the air inside the bag, was defined as 20 °C, which corresponds to the average steady room temperature. The temperature around the bag was -5 °C, while the heat transfer coefficient α was determined for the given conditions using the SPT-VK software [10]. During the calculation, buoyancy was considered. The simulation results are shown in Figures 2 and 3.

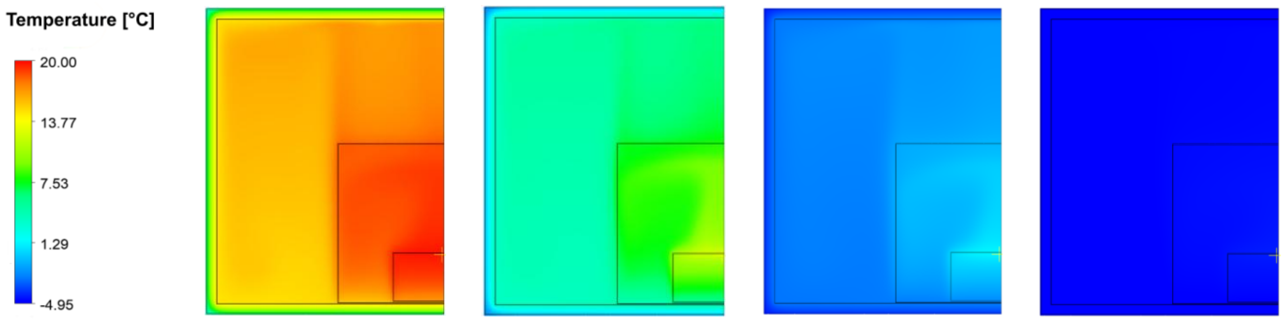

(**a**) (**b**) (**c**) (**d**)

Figure 2. Temperature field in the YX plane after: (**a**) 300 s; (**b**) 900 s; (**c**) 1,800 s; (**d**) 3,600 s.

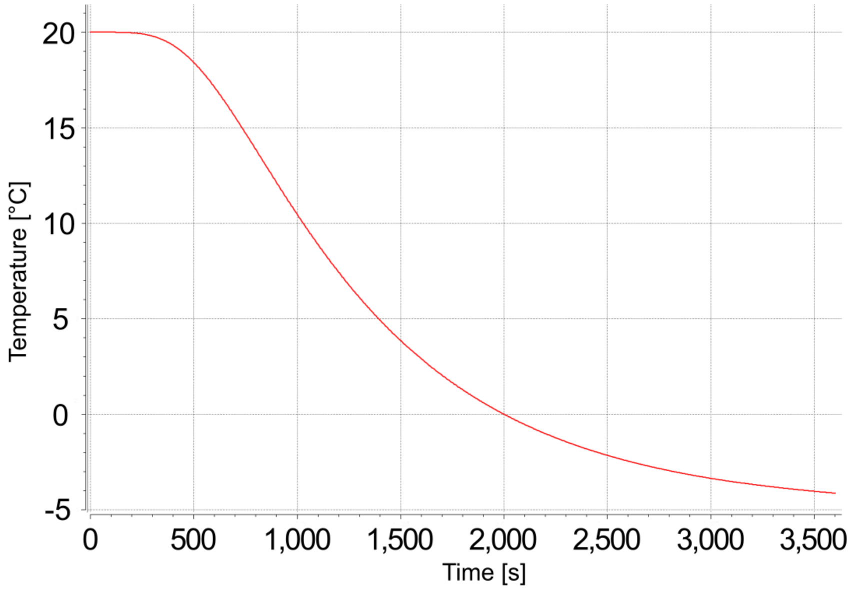

Figure 3. Graph of the temperature inside the paper box.

3. Setup and procedure of experimental temperature measurement

The experimental measurement was carried out in a Thermotron "walk-in" thermal chamber (Figure 4), which allows temperatures in the range of -34 to 120 °C. Thanks to the insulated partition, this chamber enables the creation of two temperature-independent spaces, which are necessary from the point of view of the possibility of immediate transfer of the tested objects after stabilization of temperatures according to the requirements of the experiment.

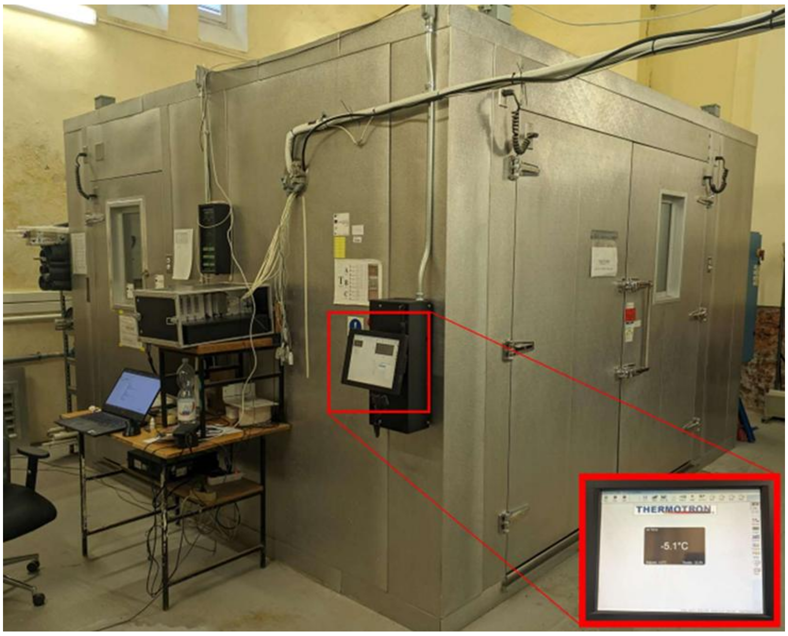

Figure 4. “Walk-in” thermal chamber.

Before the measurement, the temperature of the delivery bag, paper bag and paper box was stabilized at 20 ± 0.5 °C. After stabilizing the temperatures of the individual objects, the paper box with the drug was placed in a paper bag, which was then placed in a delivery bag. The entire process took place in a part of the thermal chamber with an ambient temperature of 20 °C. After closing the delivery bag, the measurement was started and the bag was immediately moved to a part of the thermal chamber with an ambient temperature of -5 ± 0.1 °C. After 60 minutes, the thermal chamber was opened and the measurement was finished.

Resistance temperature sensors Thermistor NTC 10k were used for temperature measurement. NTC 10k thermistors are temperature-dependent resistors with a negative coefficient, i.e. their resistance decreases when heated. They are used as sensitive temperature sensors. The measuring range of these temperature sensors is -20 to +80 °C with a deviation of ± 0.5 °C. A total of 8 temperature sensors were used. The position of the sensor placed inside the paper box is shown in Figure 5.

Figure 5. Position of the NTC 10k temperature sensor inside the paper box.

The obtaining of measured data was ensured by Arduino MEGA microcomputer, and the transfer and storage of data was carried out by Putty software into the evaluation device. The recording of temperatures during the measurement was performed at an interval of approximately 0.75 seconds through all placed temperature sensors.

4. Evaluation of experimental measurement

The graphic evaluation of the measured data (Figure 6) shows a gradual decrease of all the temperatures of the measured areas.

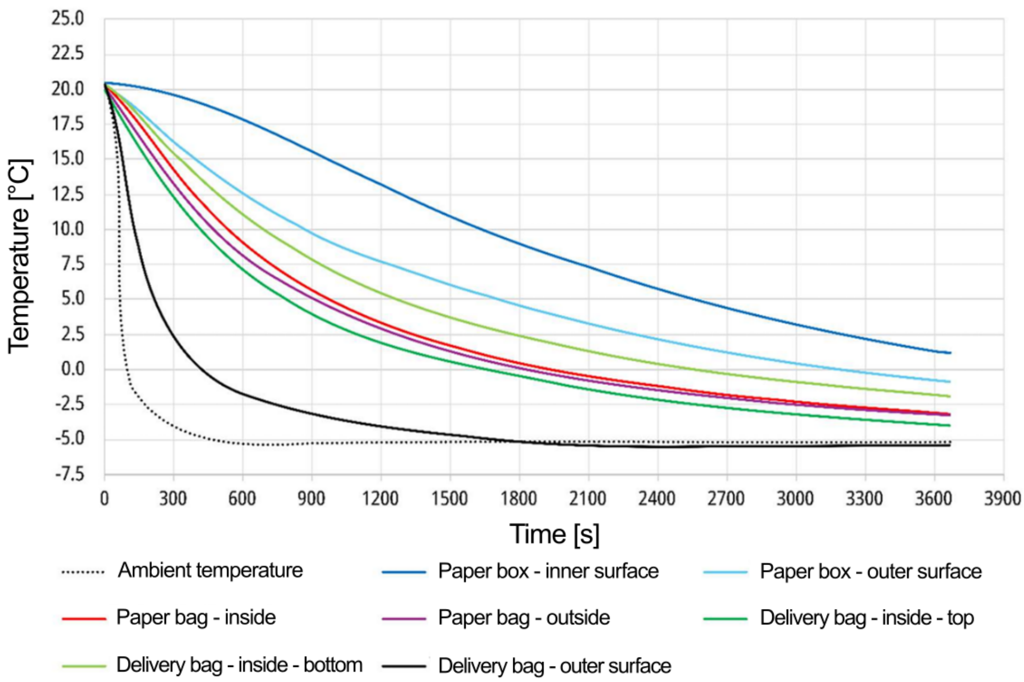

Figure 6. The course of the measured temperatures during the experimental measurement.

The ambient temperature quickly reached approximately -2 °C and then gradually further decreased until it reached -5 °C. The gradual decrease of the ambient temperature between the values of -2 and -5 °C is caused by the proximity of the delivery bag, which releases heat into the environment. It slows down the equalization of the sensor temperature with the temperature in the thermal chamber, of which value is fixed at -5 °C.

The temperature on the surface of the delivery bag decreased more slowly compared to the surrounding air due to the heat capacity of the bag. Due to the larger temperature differential at the beginning of the measurement (+20 and -5 °C), a faster temperature drop occurred initially, while during the reduction of the temperature difference, the heat transfer coefficient also decreased, which also slowed down the rate of temperature drop. With the increase of the layers that separate the individual temperature sensors from the surroundings, the cooling rate of the space decreased.

It is clear from the measurement results that although the temperature on the surface of the paper box dropped below 0 °C after 60 minutes, the temperature inside the paper box with the drug maintained positive values throughout.

5. Discussion

A considerable deviation can be observed between the results obtained through numerical simulation and the experimental measurement, where the temperature drop inside the medicine box is milder in the experimental measurement. This variation is caused by several factors.

In the 3D model, the ideal shapes of the individual layers are considered, but in practice various folds of paper occur, resulting in locally more insulation layers, between which there is also a thin layer of static air. Compared to the real paper box of the drug, the 3D model did not contain the package leaflet and several blister packs, which served as non-negligible insulating layers during the real measurement.

Last but not least, when defining the material properties of individual layers in the Ansys CFX program, generally available average values of certain intervals were used. However, these intervals are quite wide in some cases, and since the exact values of the materials used are not known, defining only approximate values can cause a significantly higher deviation than expected.

6. Conclusion

Due to the global trend of online shopping and delivery of various goods, including over-the-counter medicines, there is an increased demand for these services. However, similar to food delivery, it is inevitable to ensure suitable conditions for transport when delivering drugs. The results described in this work provide a basic overview of heat transfer in a delivery bag during short-term exposure to an ambient temperature of -5 °C. From the results, it is clear that exposure of the delivery bag to this temperature during the average delivery time of 30 minutes will not cause the temperature of the drug to drop below the critical limit of 0 °C and can be considered safe.

The paper also serves as a basis for future research in the area, as it is possible to more accurately define the material properties of individual insulation layers with an iterative method due to the verification experimental measurement and numerical simulation. In further simulations, it will thus be possible to work with a sufficiently accurate model, while it would be appropriate to focus mainly on forced convection caused, for example, by the movement of a bag during delivery on bicycle, and subsequent optimization of the insulation layers.

Acknowledgments: This paper was written with financial support from the VEGA granting agency within the projects no. 1/0224/23 and no. 1/0532/22 and from the KEGA granting agency within the project no. 012TUKE-4/2022.

References

1. Statista.com, *Online Food Delivery – Slovakia*, Available online: https://www.statista.com/outlook/emo/online-food-delivery/slovakia (cit. 10-12-2024).
2. Helm, M.; Castner, T.; Lampl, L. Environmental temperature stress on drugs in prehospital emergency medical service. *Acta Anaesthesiologica Scandinavica* **2003**, *47*, 425-429. DOI: https://doi.org/10.1034/j.1399-6576.2003.00062.x
3. Brown, L.H.; Krumperman, K.; Fullagar, Ch.J. Out-of-hospital medication storage temperatures: a review of the literature and directions for the future. *Prehospital Emergency Care* **2004**, *8(2)*, 200-206. DOI: 10.1016/j.prehos.2003.12.017
4. Hasan, A.; Dincer, I. Experimental evaluation of thermal management options for bags. *Applied Thermal Engineering* **2019**, *148*, 1202-1209. DOI: https://doi.org/10.1016/j.applthermaleng.2018.10.082
5. Ovca, A. et al. The efficiency of thermal insulating bags during domestic transport of chilled food items. *International Journal of Sanitary Engineering Research* **2013**, *7*, 21-30.
6. Hasan, A.; Dincer, I. Investigation of New Insulation Materials for Environmentally-Benign Food Delivery Bags. *Environmentally-Benign Energy Solutions* **2019**, 751-777. DOI: https://doi.org/10.1007/978-3-030-20637-6_37
7. Wallace, T. Transportation of Temperature-sensitive Medications in an Air Medical Setting. *Air Medical Journal* **2019**, *38 (3)*, 165-167. DOI: https://doi.org/10.1016/j.amj.2019.01.005
8. Clancy, J. et al. Temperature-sensitive Medications in Interfacility Transport: The Ice Pack Myth. *Air Medical Journal* **2017**, *36 (6)*, 302-306. DOI: https://doi.org/10.1016/j.amj.2017.05.002
9. O'Donnell, M.A.; Whitfield, J. Analysis of Temperature Variability in Medication Storage Compartments in Emergency Transport Helicopters. *Air Medical Journal* **2016**, *35 (6)*, 360-364. DOI: https://doi.org/10.1016/j.amj.2016.08.002
10. Brestovič T.; Jasminská N.; *Numerické Metódy a Modelovanie v Energetike*, 1st ed.; Publisher: Faculty of Mechanical Engineering, Technical University of Košice, Slovakia, 2015; 113 p. ISBN 978–80–553-2067-0.

TECHNICAL UNIVERSITY OF KOŠICE
Faculty of Mechanical Engineering

Overview of the situation and trends of additive manufacturing using a laser beam

Samuel Mikita [1,*], Ján Viňáš [1]

[1] Department of Technology, Materials and Computer Aided Production, Faculty of Mechanical Engineering, Technical University of Košice, Mäsiarska 74, 040 01 Košice; samuel.mikita@student.tuke.sk; jan.vinas@tuke.sk
* Correspondence: samuel.mikita@student.tuke.sk, Tel.: (+421950546057)

Abstract: In contrast to the conventional method of removing materials, additive manufacturing is built on a new philosophy using the incremental production of materials. Additive manufacturing involves creating shapes layer by layer and consolidating raw materials into arbitrary configurations using a computer-controlled power source. One of the current research focuses of additive manufacturing is the production of functional metal components of complex shape, including metals, alloys and metal matrix composites, to meet the demanding requirements of various industries, be it engineering, biomedical, aerospace or aerospace manufacturing.

Keywords: laser cladding, laser metal deposition, progressive materials, beam, additive manufacturing.

1. Introduction

With the gradual accessibility of these technologies for creating or renovating parts, these methods are moving from prototype to serial production, where they have been referred to as Rapid Prototyping. From the point of view of the advantages of the implementation of these technologies, we count on, for example, fast and efficient production, a high degree of quality of the created parts, flexibility in the use of different types of materials, automation of processes or environmental friendliness. Nowadays, the production of concept prototypes made of polymers is no longer the current main focus of additive manufacturing research. In fact, components produced by additive methods are no longer used only for visualization, but they are also used as real production parts (i.e. final products) with basic mechanical properties meeting industrial requirements.

We still present this technology as a new technique for building metal components by laying layer by layer while simultaneously feeding additional material in the form of various powders or solid wires that come into contact with a heat source, such as a laser beam, electron beam or electric arc. The presented literature review will point to the current situation of layer formation using laser cladding technology. The main focus will be describing the main techniques and selected metal materials associated with this method.

2. Additive manufacturing using a laser beam

The laser beam can be defined as a narrowly directed flow of light, which is created with the help of light amplification through stimulated emission of radiation (Light Amplification by Stimulated Emission of Radiation). Among its key features that describe it are [9]:

- Coherence (synchronized waves resulting in the same phase)

- Monochromaticity (single color based on the same wavelength)
- Divergence (parallel propagation)
- Intensity (high energy density)

Most commercial machines built on the philosophy of additive manufacturing, which are based on the principle of high-power CO_2, Nd:YAG or fiber lasers working in continuous mode. Three typical processes have been developed to meet the requirements of additive manufacturing with a laser beam [9]:

- laser sintering (LS),
- laser melting (LM),
- laser metal deposition (LMD)/ Laser cladding,

Around the world, different institutions and companies use different phrases and names to refer to these three most widespread variants of additive manufacturing technology. Among the main differences between these techniques, we recommend: Metallurgical events that take place during the process, the method of supplying additional material, the typology of the equipment, the primary use of technology, whether it is modeling of complex shapes or the creation of casing layers. The distribution is more comprehensively described in Figure 1. [1,8].

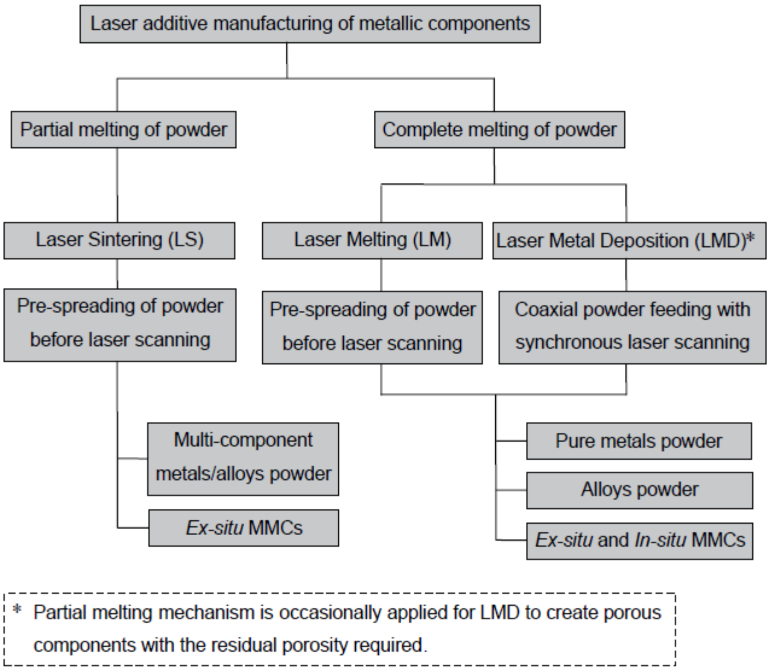

Figure 1. Distribution of laser additive manufacturing techniques for metal materials [1].

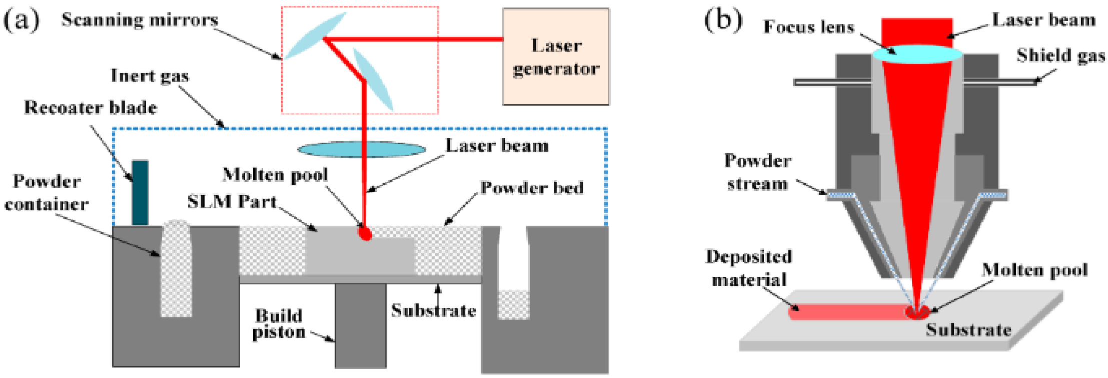

Figure 2. Graphical comparison of additive manufacturing methods using a laser beam. [6] a.) AM using powder coating b.) AM using coaxial head.

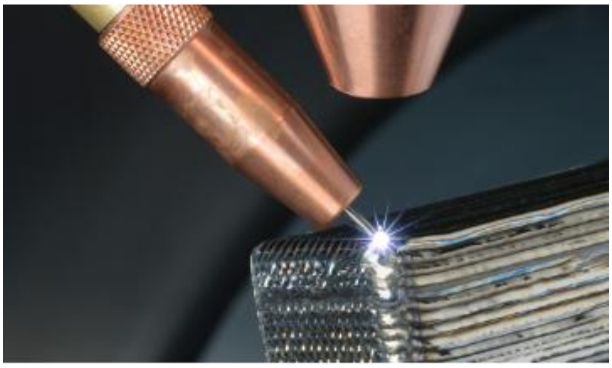

Figure 3. Laser additive manufacturing using filler material in the form of wire [2].

3. Properties and parameters in laser additive manufacturing

Laser cladding technology uses a high-energy laser beam as a heat source that fuses the surface of the substrate and the additive material, either in the form of powder or wire. The additional material is delivered either through a coaxial or an off-axis nozzle, while the protection of the melt pool is ensured by an inert gas atmosphere. After the end of the laser action, the melt solidifies quickly and forms a weld layer on the surface of the material [1,8].

The movement speed of the laser head and the powder flow or wire feed are controlled according to a pre-designed scanning strategy. The laser and powder focus height is regulated by moving the lenses and powder nozzles along the "Z" axis. The workpiece is moved in the "X–Y" direction by means of computer-controlled drive systems, being located under the beam-powder interaction zone to achieve the desired cross-sectional geometry [2].

More detailed input parameters of the laser cladding process using a coaxial head are described in Figure 4.

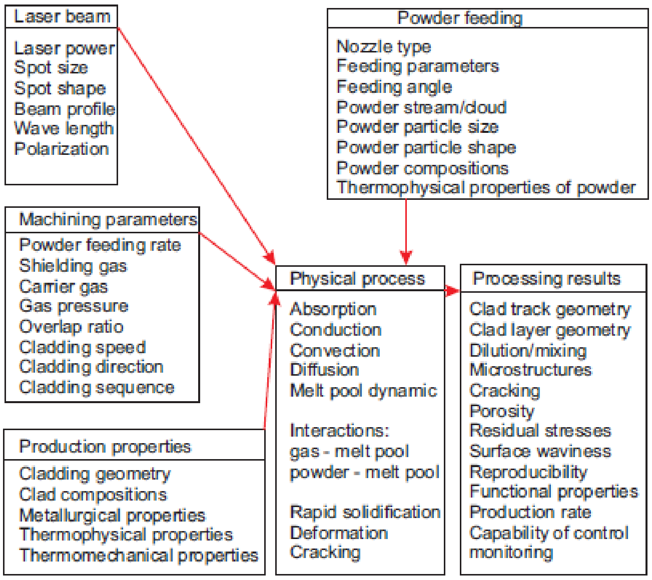

Figure 4. Selected process parameters and properties for the laser cladding method [2].

4. Selected metal materials suitable for laser cladding/ LMD

To support the use of laser cladding, it is necessary to investigate the improvement of the efficiency of the process through various alloy additive materials. It is important to emphasize that the laser welding technology is able to process different powder materials on different metal substrates, which makes it possible to create cladded layers with special functional properties. Nowadays, the main scientific and research efforts are focused on materials with a base: Ni, Ti, Fe, among which some combinations of materials and processes have already entered the phase of practical applications. Laser cladding using Al-based alloys may be another research focus that will face a great challenge in the processing of non-ferrous alloys, mainly due to the high reflection of laser energy [1,8].

Ni-based superalloys, e.g. Inconel 625, 718 and Rene41, 88DT are commonly developed for high performance components in jet engines and gas turbines due to their improved creep balance, wear resistance, adequate tensile properties and corrosion/oxidation resistance. The production and renovation of these parts gradually moved to additive manufacturing using a laser beam, where it achieves the desired results [8].

Typical titanium alloy intended for additive manufacturing using laser technology is Ti–6Al–4 V, it takes its position mainly in the aviation and medical fields. The reason is unique chemical and mechanical properties and well-documented biocompatibility [2].

4.1 Al-based alloys

Louvis et al. [5] and Buchbinder et al. [3] so far, very few research works have been reported on the additive manufacturing of Al-based alloys using LM or LMD. Successful LM/LMD of Al-based powders has a number of difficulties. First, the high reflectivity (>91%) and high thermal conductivity of Al consequently significantly increase the laser power required for melting.

Second, the high susceptibility of Al-based alloys to oxidation acts as a major obstacle to efficient melting. Adherent thin oxide films on molten Al reduce wettability. The oxide also causes problems when it is mixed into the molten pool because the trapped oxide creates weakened areas in the deposit [7].

Thirdly, it is the very properties of the aluminum powder form: they are light with poor fluidity. Consequently, Al-based powders are unsuitable for many existing welding mechanisms [7].

Fraunhofer ILT has successfully qualified laser processing for functional prototypes of the Al–10Si–Mg alloy. Static and dynamic tests demonstrated that the mechanical properties of the laser-treated Al–10Si–Mg samples reached the level of the mechanical properties of series-produced die-cast Al–10Si–Mg components in accordance with EN 1706 specifications. In addition, they noted that preheating significantly improves the dimensional and shape accuracy of thin-walled Al–10Si–Mg parts processed by laser melting. These encouraging results have significant implications for future industrial applications of additive manufacturing technology for aluminum-based alloys [3,4].

5. Results

From the information and data collected so far, it can be concluded that this technology has a significant potential either in the creation of completely new parts or in renovations. The future of this laser beam welding technique is strengthening its position especially due to its high precision and ecological advantage. As an industrial process, this technology will increasingly shape production processes in modern manufacturing. With the help of scientific and research efforts, we are able to constantly improve this additive technique. Examples of current research are special materials such as Al-based alloys, which represent their positions in special operations. Another example is the creation of parts with a porous structure that achieve excellent mechanical and physical properties. Creating precise details of various shapes of parts is a challenge in itself. The goal is to achieve this so that we are not subsequently forced to modify the created surfaces/layers by other special finishing operations.

Acknowledgments: This contribution is the result of the project implementation: Innovative approaches of the restoration of functional surfaces by laser weld overlaying APVV-20-0303 supported by the Slovak Research and Development Agency and supported by the Ministry of Education of Slovakia Foundation under grant projects VEGA No. 1/0597/23, and KEGA No. 046TUKE-4/2022.

References

1. Dondong, D. Laser Additive Manufacturing of High-Performance Materials. Springer Berlin, Heidelberg 2015. 311s. *ISBN 978-3-662-46088-7*
2. Wei Ya. Laser materials interactions during cladding, *PhD Thesis,*University of Twente, Enschede, the Netherlands, (2015) *ISBN: 978-94-91909-31-3*
3. Buchbinder, D.; Wissenbach, K. (2008) Additive manufacturing of aluminum components with minimal distortion. Fraunhofer ILT annual report, Fraunhofer ILT, Aachen, Germany
4. Brandl E, Heckenberger U, Holzinger V et al (2012) Additive manufactured AlSi10Mg samples using selective laser melting (SLM): microstructure, high cycle fatigue, and fracture behavior. Mater Des 34: 159–169
5. Louvis E, Fox P, Sutcliffe CJ (2011) Selective laser melting of aluminium components. J Mater Process Technol 211(2):275–284
6. Liu, Z.; Wang, X.; Kim, H.; Zhou, Y.; Cong, W.; Zhang, H. Investigations of Energy Density Effects on Forming Accuracy and Mechanical Properties of Inconel 718 Fabricated by LENS Process. Procedia Manuf. 2018
7. Chen, M., Yang, X., Zhang, Z. *et al.* (2025) Research status of laser cladding technology on aluminum alloy surface. *Int J Adv Manuf Technol* **137**, 1–21.
8. Mazumder, J., Brandt Milan. (2017) Laser-aided direct metal deposition of metals and alloys, The University of Michigan, Ann Arbor, MI, United States. 978-0-08-100433-3
9. Dawes, Christopher. (1992) Principles of laser welding and its characteristics. Cambridge, England : Abington Publishing. 978-1-85573-034-2

TECHNICAL UNIVERSITY OF KOŠICE
Faculty of Mechanical Engineering

Design of a hydrogen storage system for a four-cylinder internal combustion engine

Peter Milenovský [1,*], Natália Jasminská [1], Marian Lázár [1]

[1] Technical University of Košice, Faculty of Mechanical Engineering, Department of Energy Engineering, Vysokoškolská 4, 042 00 Košice, Slovakia; peter.milenovsky@tuke.sk; natalia.jasminska@tuke.sk; marian.lazar@tuke.sk
* Correspondence: peter.milenovsky@tuke.sk

Abstract: In the current era of increasing demands for reducing emissions and the ecological footprint of newly emerging and existing equipment, there is a need to reduce the carbon footprint of conventional internal combustion engines. Reducing the carbon footprint in internal combustion engines is associated with the gradual replacement of conventional fossil fuels with renewable ones. One of the possible energy carriers for use in conventional internal combustion engines is hydrogen. Its use is associated with the need to solve the problem of a storage and distribution system to ensure a constant supply of fuel to the combustion chamber. The article discusses the design options for a hydrogen storage system, comparing various technologies, their advantages and disadvantages. At the end of the article, a basic storage and distribution system is proposed for the needs of supplying a conventional four-cylinder engine.

Keywords: Hydrogen, Internal Combustion Engine, Mobility, High Pressure Storage

1. Introduction

The gradual development in the field of hydrogen economy allows for an increase in the number of types of devices that are able to use hydrogen as an energy carrier. In addition to the conventional use of hydrogen in fuel cells, the possibilities of direct combustion of this energy carrier as a substitute for natural gas, gasoline and diesel in internal combustion engines are starting to appear again. The combustion of hydrogen in internal combustion engines allows for a significant reduction in the carbon footprint generated by transport. In line with this advantage, however, there are also requirements for changing the infrastructure, storage systems and technical modifications of conventional devices to enable the use of hydrogen as an alternative fuel.

Direct combustion of hydrogen in conventional piston engines is becoming much more interesting over time compared to its use in fuel cells. Its primary advantage is a simpler and, above all, cheaper technology, although at the cost of lower efficiency. Maintenance of conventional combustion engines using hydrogen is simpler and less expensive than maintenance of fuel cells, while it is also possible to assume a longer average lifespan of systems using direct combustion compared to systems using fuel cells, thanks to simpler maintenance and the absence of an intermediate storage system for the generated electrical energy, such as batteries or supercapacitors.

2. Current status of hydrogen compatibility options in vehicles

Hydrogen storage systems for mobile applications have undergone significant development in recent years to meet the requirements for safety, efficiency and adaptability for commercial use. Today, there are three main types of storage: compressed hydrogen, liquefied hydrogen and compound storage.

Compressed hydrogen is today the most common storage method for use in mobile applications, including passenger and commercial vehicles. Hydrogen is stored in specially designed pressure tanks at pressures of 350 to 700 bar. These tanks are made of multiple layers, most often high-strength steel, aluminum or composite materials such as carbon fiber, to withstand extreme conditions. The main goal of this method is to increase the bulk density of hydrogen, which is very low in gaseous form. Despite its simple implementation, this technology has several challenges. The tanks are relatively heavy and take up a lot of space, which limits their use in smaller vehicles. Safety issues are addressed by detection systems that can identify potential hydrogen leaks and by design measures that minimize the risk of explosion in the event of tank damage.

Liquefied hydrogen is an alternative, which is used mainly where it is necessary to store larger quantities of hydrogen at a higher density. The process of liquefying hydrogen consists of lowering its temperature to -253 °C at atmospheric pressure, which causes a phase change, increasing the bulk density by up to eight hundred times compared to its gaseous form. Cryogenic tanks are designed to minimize heat loss through advanced insulation materials such as vacuum layers or foams with low thermal conductivity. The main problem with this method is the "boil-off" phenomenon, in which small amounts of hydrogen constantly evaporate, reducing the efficiency of storage over longer periods of time. The technology is also energy-intensive, as it requires special refrigeration to maintain low temperatures, which increases operating costs. However, liquefied hydrogen is suitable for applications such as trucks or ships, where the space and weight of tanks are more tolerable compared to passenger cars [1,2].

Compound storage uses chemical or physical bonds between hydrogen and materials, allowing for safer and more stable storage at lower pressures or room temperature. An actively researched area of hydrogen absorption storage at KEI, SjF, TUKE is its storage in metal hydrides, where hydrogen is bound to metals such as magnesium, nickel or titanium with which it forms stable hydride compounds. This process is reversible and allows the release of hydrogen when the material is heated or the pressure in the tank is reduced. Although this system offers a higher storage density than in the case of pressure tanks and reduces the risks associated with hydrogen leakage, its disadvantage is the significant weight of the alloy. Another innovative method of hydrogen storage is organic carriers (LOHC), in which hydrogen is chemically bound to liquid compounds such as toluene or ammonia. Hydrogen is released by catalytic processes when heated, which makes this system effective for long-term storage and transportation. LOHC offers the advantage of easy storage at room temperature, but releasing hydrogen requires additional investment in catalysts and the energy required to raise the temperature of the substance to the operating temperature at which hydrogen can be extracted.

Hydrogen storage and its distribution for end use also comes with a certain level of risk. Safety requirements for mobile applications using hydrogen as a fuel are designed to minimize the risks associated with its storage, handling and use, with an emphasis on protecting people, equipment and the environment. These requirements include aspects related to system design, leak detection, risk management and operational standards [6].

Storage tanks for mobile applications such as vehicles, trains or ships must meet strict standards for resistance to high pressure, temperature extremes and mechanical damage. For example, pressure tanks for compressed hydrogen (700 bar) are tested for extreme conditions, including exposure to fire, falling from a height and bursting under overpressure. The tanks must be made of high-strength materials such as carbon composites and must be equipped with pressure control valves and safety fuses to minimise the risk of explosion. Because hydrogen is a colourless, odourless gas, modern systems are equipped with sensor technologies that can detect even small gas leaks. These sensors respond to elevated hydrogen concentrations in real time and immediately activate safety protocols, such as shutting down the system or activating ventilation devices to prevent the build-up of an explosive mixture [2].

One of the most important safety features is the TPRD valve (Thermal Pressure Relief Device). This valve is designed to release pressure if the temperature of the tank reaches a critical level, for example during a fire. If the temperature rises, the pressure in the tank could increase rapidly, which could cause an explosion. The TPRD valve reacts to the increase in temperature by melting the safety element, which allows the hydrogen to be quickly released, reducing the pressure in the tank and eliminating the risk of an explosion. This process is fast and controlled, with the hydrogen being released to safe areas outside the vehicle and quickly dispersing into the atmosphere.

Another key element of the hydrogen circuit are the pressure control safety valves, which are designed to prevent overpressure inside the tank during normal operation. These valves monitor the pressure in real time and are automatically activated if the pressure exceeds a safe limit. Their purpose is to prevent mechanical damage to the tank.

Each pressure tank must be tested according to international standards, such as ISO 19881 and 19882, which define the requirements for the design, manufacture and testing of high-pressure hydrogen storage systems [2,3].

3. Design of a hydrogen storage system for a four-stroke internal combustion engine

The conversion of four-stroke internal combustion engines to use hydrogen or a mixture of hydrogen with traditional fuel involves several technical changes. To begin with, the fuel injection system must be modified to be able to supply hydrogen either as a fuel alone or as a mixture. In the case of hydrogen as the primary fuel, high-pressure tanks for storing hydrogen and special pressure regulators must be installed. The ignition system must be optimized, since hydrogen has a lower ignition energy and a higher burning rate. In the case of an internal combustion engine utilizing hydrogen, it is important to improve the intake system to be able to ensure a sufficient air supply and eliminate the risk of the mixture burning back into the intake manifold. This is often solved by adding check valves and flaps. Hydrogen can be supplied to the combustion chamber either by direct injection or mixed with air in the intake manifold. Due to the high thermal conductivity and low molecular weight of hydrogen, the cooling system needs to be redesigned to prevent the engine from overheating [4,5].

The engine control unit (ECU) needs to be reprogrammed or replaced to correctly handle the hydrogen combustion parameters. Hydrogen has a higher-octane number, which can allow the engine's compression ratio to be increased to improve efficiency [5]. When hydrogen is mixed with another fuel (such as gasoline), the hydrogen dosage can be adjusted to improve performance and reduce emissions. Such a solution reduces overall CO_2 emissions and improves combustion efficiency while reducing fossil fuel consumption [6]. A schematic diagram of the hydrogen-recovery internal combustion engine is shown in Figure 1.

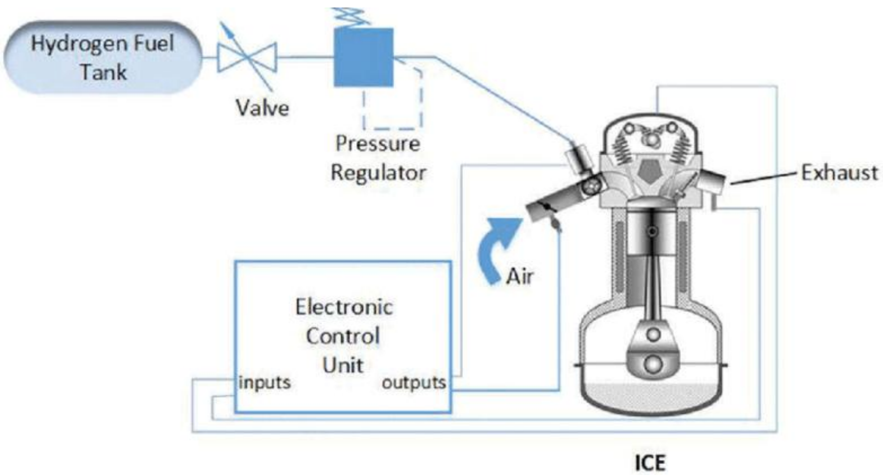

Figure 1. Simplified diagram of direct hydrogen combustion in a piston engine.

The presented work discusses the possibility of supplying a four-stroke internal combustion engine with hydrogen with an output of 110 kW. To ensure maximum engine performance, it is necessary to supply such an amount of fuel to the combustion system that its chemical energy, taking into account all losses, allows for maximum performance. Assuming 25% engine efficiency, the power input on the fuel side is:

$$P_{chem.fuel} = \frac{P_{engine}}{\eta_{engine}} \quad \text{(kW)} \qquad (1)$$

The fuel input, representing the chemical energy of the stored hydrogen to ensure maximum performance of the combustion engine for the exemplary example, represents the value 440 kW.

The fuel mass flow to ensure maximum power, taking into account the calculated power input in the fuel, is determined according to the relationship (1) at the level 0,0031 $kg \cdot s^{-1}$:

$$Q_{m\ fuel} = \frac{P_{chem.fuel}}{q_{fuel}} \quad (kg \cdot s^{-1}) \qquad (2)$$

where q_{fuel} represents the heat of combustion of hydrogen $142 \cdot 10^6$ $J \cdot kg^{-1}$.

Dividing the fuel mass flow by the hydrogen density yields the hydrogen volume flow required to ensure maximum engine power, which is the value 0,0345 $m^3 \cdot s^{-1}$

$$Q_{v\ fuel} = \frac{Q_{m\,fuel}}{\rho_{fuel}} \quad (m^3 \cdot s^{-1}) \qquad (3)$$

Based on the calculated data, carrying out a laboratory experiment while maintaining maximum combustion engine power for 1 minute represents hydrogen consumption at the level of 2070 l.

In accordance with the above calculated hydrogen volumetric flow rate to ensure maximum engine performance, the hydrogen storage system for the selected internal combustion engine was designed. Considering the hydrogen volumetric flow rate, pressure conditions in the storage system, local and length losses of the piping system, individual components of the storage system for a laboratory setup serving for testing a 110 kW internal combustion engine burning hydrogen were specified. A schematic connection of the hydrogen storage and distribution system for the internal combustion engine is shown in Figure 2.

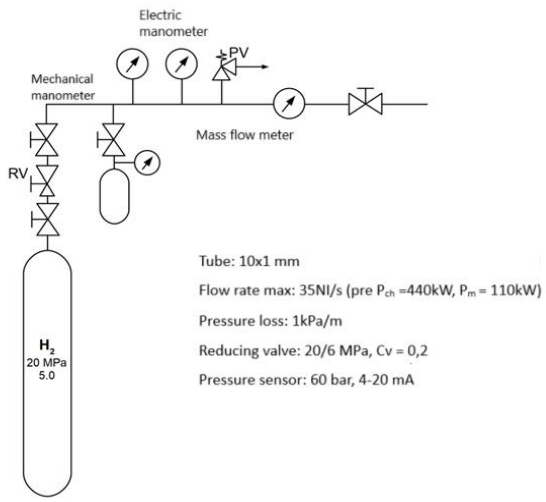

Figure 2. Hydrogen storage and distribution system for internal combustion engines.

The proposed hydrogen storage system consists of a source, which are commonly available pressure cylinders, a pressure reducing valve (RV), ensuring the reduction of the hydrogen inlet pressure from 200 bar to the operating pressure, mechanical valves, a mass flow meter and safety elements (safety valve (PV), pressure sensors).

4. Conclusions

Hydrogen as a fuel represents one of the most promising energy sources for mobile applications, especially due to its ability to minimize greenhouse gas emissions. Systems using direct hydrogen combustion represent one of the alternatives for filling the bridging period between internal combustion engines and other technologies using renewable energy sources. A suitable solution for the storage and distribution system of hydrogen fuel represents one of the main conditions for the simple and safe use of hydrogen in direct combustion processes in mobile applications and therefore its detailed research and development is necessary.

Acknowledgments: This paper was written with the financial support from the VEGA granting agency within the Project No. 1/0224/23 from the KEGA granting agency within the Project No. 012TUKE-4/2022, and with the financial support from the APVV granting agency within the Projects No. APVV-23-0266 and APVV-21-0274.

References

1. Satyapal S.: U.S. DOE Hydrogen Program and National Clean Hydrogen Strategy,2024; Avaiable at: https://www.energy.gov/sites/default/files/2024-02/doe-h2-program-national-strategy-remarks-jan2024.pdf
2. Fletcher N.: FHWA Awards Grants to Develop Charging, Hydrogen Stations,Transport Topic,2024; Avaiable at: https://www.ttnews.com/articles/fhwa-grants-chargers-hydrogen
3. Yaohui,X.,Yang,Z.,Yuting,L.,Zhao,D.: Research Progress and Application Prospects of Solid-State Hydrogen Storage Technology. Molecules 2024, 29(8), 1767; Avaiable at: https://doi.org/10.3390/molecules29081767
4. Efstathios-Al. Tingas.: Hydrogen for Future Thermal Engines,Spingers,2023
5. Enhui S.,Yuhui Y.,Qiukai Z.,Feng C.,Jinliang X.,Yanfeng L: Thermodynamic study of semi-closed rankine cycle based on direct combustion of hydrogen fuel., International Journal of Hydrogen Energy,2024, ; Avaiable at: https://doi.org/10.1016/j.ijhydene.2024.10.371
6. Lázár, M., Mihálik, I., Brestovič, T., etc.: A Newly Proposed Method for Hydrogen Storage in a Metal Hydride Storage Tank Intended for Maritime and Inland Shipping, Journal of Marine Science and Engineering, 2023, Aviable at: https://www.mdpi.com/2077-1312/11/9/1643

TECHNICAL UNIVERSITY OF KOŠICE
Faculty of Mechanical Engineering

Tortuosity Decoder as a Tool for Measuring Parameters of Overhead Contact Lines in Tram Systems

Peter Onderčo [1,*], Jan Rybář [1], Sohaibullah Zarghoon [1] and Jozef Leja [2]

[1] Institute of Automation, Informatization, and Measurement, Faculty of Mechanical Engineering, Slovak University of Technology in Bratislava, Nám. slobody 17, 812 31 Bratislava, Slovakia; peter.onderco@stuba.sk; jan.rybar@stuba.sk; sohaibullah.zarghoon@stuba.sk
[2] Institute of Mathematics and Physics, Faculty of Mechanical Engineering, Slovak University of Technology in Bratislava, Nám. slobody 17, 812 31 Bratislava, Slovakia; jozef.leja@stuba.sk
* Correspondence: peter.onderco@stuba.sk; Tel.: +421 911 291 630

Abstract: This paper describes a tortuosity decoder used to measure the parameters of overhead contact lines for tram systems. The decoder is integrated into the pantograph of the measuring tram operated by Dopravný podnik Bratislava, a. s. (Bratislava Transport Company). Its primary function is to assess the tortuosity of the overhead contact lines, which is linked to the wear of carbon strips on trams. Additionally, it monitors the stable and reliable contact between the pantograph and the overhead contact line. This measurement is crucial for ensuring the smooth operation of urban public transport, directly impacting the quality of services and overall transportation safety. The maintenance of tram infrastructure relies on the regular collection and analysis of these measured data.

Keywords: Tortuosity Decoder, Measurement, Overhead Contact Line, Tram, Tram Systems

1. Introduction

To measure the tortuosity of the overhead contact line for tram operations, a tortuosity decoder is used, which is integrated into the pantograph of the measuring tram. The primary objective is to ensure the proper functioning of trams and the safety of their operation. A key factor in this process is monitoring the geometry of the overhead contact line, ensuring it complies with technical standards and requirements for smooth and efficient tram operation. This also relates to the uniform wear of the carbon strip on the pantographs of the trams. The paper discusses this issue in the context of the tortuosity of the overhead contact line, its security, and the data evaluation necessary for practical application in the operations of Dopravný podnik Bratislava, a. s. (Bratislava Transport Company) [1].

2. Methods for Inspecting and Measuring Tram Lines

When considering methods for inspecting and measuring tram lines, we can use meters tailored to specific quantities or employ more complex measurement techniques, such as those involving a measuring vehicle. This vehicle is typically adapted for the specific measurement tasks and can assess basic parameters. At the same time, it also measures parameters such as temperature, humidity, pressure, and voltage in the network. Additionally, measuring trams are equipped with an observation post, where either a person or a camera system monitors the interaction between the pantograph and the overhead contact line during operation. The contact between the tram pantograph and the overhead contact line is closely observed, and the data collected is crucial for ensuring the safety and reliability of transport services [1-2,8].

After inspection and measurement by the vehicle, repairs are carried out on the identified problem areas. Visual inspection using a camera system offers additional advantages, as the camera captures a large volume of data that can be evaluated retrospectively. For this purpose, a specially modified carbon insert is used in the pantograph, which evaluates the tortuosity (tortuosity decoder). The values are provided in centimeters, and the tortuosity is typically assessed in relation to the rails or pantograph [3].

The tortuosity of the overhead contact line is a crucial parameter for several reasons. The main reasons are: It monitors the interaction between the overhead contact line and the tram pantograph, which is linked to the uniform wear of the carbon strips on trams, ensuring stable and reliable contact [1].

The tortuosity is defined as a perpendicular distance of the rail axis from the overhead contact line (Figure 1). It is more specified in the project (construction) documentation. There is also a standard for projecting of the new tracks, where we can find the tolerance of tortuosity. STN EN ISO 333 516 “Electrotechnical regulations. Regulations for traction line of tram and trolleybus tracks.” and STN EN ISO 376 754 “Designing the traction line of tram and trolleybus tracks.” The exact tolerance that we can find in the standards is permissible tolerance ± 1/3 of the collector length.

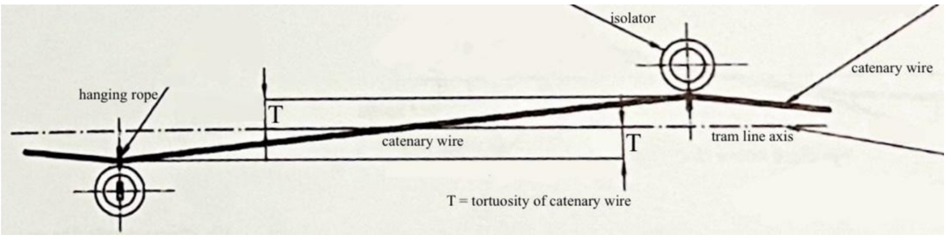

Figure 1. Graphic definition of tortuosity. Source: [4]; modified.

3. Measurement with a Tortuosity Decoder

The tortuosity decoder is used to measure the tortuosity of the overhead contact line and is installed on the tram pantograph. It consists of a specially modified carbon strip on the pantograph, which evaluates the tortuosity of the overhead contact line in comparison with the rails. The pantograph provides electric current to the vehicle from the overhead contact line. For better guidance along the line, the pantograph is equipped with two contact carbon strips. Due to the uniform wear of these carbon strips, the tortuosity of the line along the track is assessed to ensure consistent wear. In practice, however, the middle part of the carbon strip tends to wear the most. Tortuosity is one of the key parameters evaluated during measurements to ensure stable and reliable contact between the pantograph and the line. A higher tortuosity variance typically results in more even wear of the pantographs on the operated vehicles, and is closely linked to the lifespan of the carbon strips [3,8].

However, if the variance is too large, the line may slide along the edge of the pantograph, causing the pantograph’s pressure to push it into an upright position. Therefore, during evaluation, maximum tortuosity values are determined, which are selected by the operator and become the monitored parameter. If the values exceed the tolerance limits, the affected sections must be repaired to restore the system to an operational state and ensure the smooth operation of the trams. In the evaluation software, tortuosity can have two states: a positive state and a negative state. A positive state corresponds to values recorded to the right of the center of the carbon strips, while a negative state refers to values recorded to the left of the center of the carbon strip. More details in the presentation (conference lecture) [1-2].

4. Results of Tortuosity Measurement

Once the carbon strip (Figure 3) is installed on the measuring tram /its collector/ (which is used solely during the measurement due to its durability and sustainability), the data collection process can begin. The strip is connected to the tortuosity decoder via the connector on the bottom of the measuring strip (Figure 2).

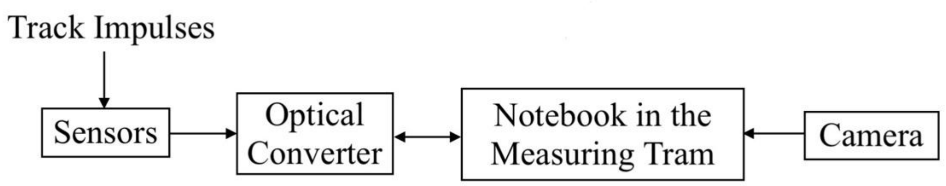

Figure 2. Simplified scheme of the measuring chain in the measuring tram. Source: [7]; modified.

Communication is established only when the entire device is powered on, meaning it is activated only after establishing communication with the evaluation unit, which in our case could be a computer or a mobile phone. All components are connected within the tram. The power supply module is connected to the computer on the measuring tram, and it is remotely powered on only during the measurement. The measured tortuosity data (sample data) are presented in the Figure 4 and Table 1.

Figure 3. Carbon Strip with Tortuosity Decoder, Mounted on the Pantograph of the Measuring Tram. Source: Own.

The measurement takes place while the measuring vehicle is in motion. For this purpose, specialized measuring software is used, which records a file containing the measured parameters of the overhead contact line. Before the actual departure and start of the measurement, it is essential to verify the functionality of the measuring device by switching to simulation mode. In this mode, pulses are generated experimentally without the need for the vehicle to be in motion. This allows all measuring functions to be tested in depot conditions prior to operating on the track. During this phase, we verify that the data is correctly saved, test the video recording functionality, and, if necessary, check the functionality of the GPS system, which provides comprehensive data for collecting overhead contact line information. Once the functionality has been verified, the measuring vehicle sets off to gather data for the city's tram network [2].

The measured values include the impact on the pantograph, driving speed, height of the overhead contact line, and tortuosity. Additionally, temperature, humidity, and pressure are important factors to consider. All of this data is linked to the route traveled and associated with GPS coordinates. From this data, we can determine the absolute value of the tortuosity, the upper and lower limits of the height values, the amplitude of the shock, and the limitations for the selected measured section of the track. All values are presented in centimeters, except for the distance traveled, which is given in kilometers [1-2].

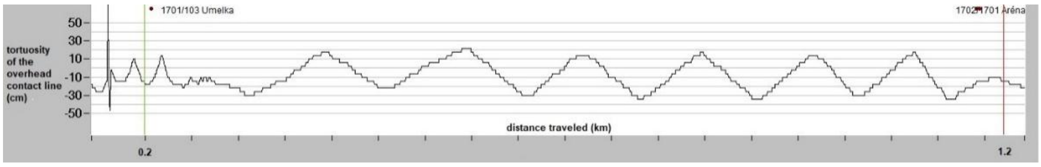

Figure 4. Recording of measured tortuosity data /selected section of track/ [7].

After the measurement, the obtained data is evaluated based on established standards and technical parameters. Any deviations are analyzed and may result in adjustments to the design or maintenance of the overhead contact line, such as tensioning, repairs, replacement of the overhead contact lines, or realignment based on the assessed tortuosity [3].

The aim of these measurements is to ensure the smooth, safe, and efficient operation of tram traffic, while ensuring that the overhead contact line does not negatively impact tram travel.

Table 1. Table of recorded data, including tortuosity values on a selected section of track, data provided by the software for evaluating this data are cited [7].

Measurement of overhead line parameters

position (km)	height (cm)	tortuosity (cm)	speed (km/h)	shocks (-)
1701/103 Umelka				
0.2565	511	-14	20	276
0.2571	512	-14	19	174
0.2576	511	-14	19	154
0.2581	512	-14	19	140
0.2586	512	-10	19	132
0.2592	512	-10	19	126
0.2597	512	-10	18	122
0.2602	512	-10	19	116
0.2608	512	-6	18	162
0.2613	512	-6	19	176
0.2618	512	-6	19	224
0.2624	512	-2	19	188
0.2629	512	-2	18	176
0.2634	512	2	18	144
0.2639	512	2	19	180
0.2645	512	2	19	166
0.2650	512	6	18	160
0.2655	511	6	18	170
0.2661	511	10	18	132
0.2666	511	14	18	128
0.2671	511	14	18	170
0.2676	511	14	18	168
0.2682	511	14	18	130
0.2687	511	14	18	132
0.2692	511	10	18	152
0.2698	511	6	18	136
0.2703	511	6	18	132
0.2708	510	2	18	114
0.2714	510	2	18	118
0.2719	511	-2	18	118

Since tortuosity is one of the most important parameters, which is also mentioned in the standards, we created a mathematical measurement model where we examine tortuosity and its values. We entered all the influencing factors from the measurement model into the Table 2.

Table 2. Influencing factors from the measurement model.

Checked parameter	Type of uncertainty	Definition of checked parameter (unit)
Tor	A	the tortuosity measured by measuring tram (cm)
Influencing parameters	**Type of uncertainty**	**Definition of influencing parameters (unit)**
δSh	B	the influence of shocks of the collector to the overhead contact line (-)
δSp	B	the influence of speed of the ride (km/h)
δHe	B	the influence of height of the overhead contact line (cm)
δGr	B	the influence of the overall grip of the overhead contact line (-)
δMC	B	the influence of meteorological conditions (-)
δTr	B	the influence of the vehicle passing in the section (-)
δGP	B	the influence of the geometrical parameters of the track (-)
δWAT	B	the influence of the wear and tear of carbon strips (-)
δOtF	B	the influence of the other factors (-)

There is mutual influence between the individual influencing factors, while these components contribute to the resulting uncertainty of the measurement. In the further development of this issue, it will be necessary to identify the sources of individual dependence (correlations) and determine a pair of individual estimates for each source. These estimates are determined based on measurements (previous and experimental), and in this way we determine the correlation coefficient, which expresses the degree of dependence between individual estimates. This area requires further mathematical elaboration in the future, it is a question for further research. Most of the influencing parameters don't use the unit, they have specific coefficient resulting from for example the part of the day (δMC). [9]

5. Discussion and Conclusions

When ensuring transport service, it is crucial to maintain the overall infrastructure. To properly care for it, we must first understand its condition. An example of this is the tortuosity of the overhead contact line. Assessing this condition allows us to collect and evaluate data. Measuring the parameters of tram lines is essential for ensuring accurate, efficient, safe, and comfortable transport [4].

On tram lines, the key parameter is the condition of the overhead contact line, which depends on factors such as the distance traveled, travel speed, tortuosity, height, voltage, and others. During measurement or when operating a measuring tram, it is essential to consider ambient temperature, vehicle speed, pantograph pressure, the condition of the tracks, surrounding vehicles, and structural elements of the line. These include the method and distance of suspension. Therefore, the quality of tram lines depends on a comprehensive assessment of several monitored variables [1-2,5].

The tortuosity of the overhead contact line is influenced by factors such as improper tensioning of the wire, poorly positioned supports, insufficient stability of the overhead contact line, wear and fatigue, long-term operation, mechanical wear, and temperature fluctuations. These issues can lead to power supply problems, resulting in power outages and losses, as well as vibrations and noise. Additionally, they can shorten the lifespan of components, increasing repair and replacement costs. Furthermore, if the system is improperly set, safety risks may arise. The measurement and control of tortuosity are performed using various methods that enable the evaluation of geometric accuracy. Techniques such as optical measurement, measuring vehicles, and laser scanning serve as the basis for repairs and preventive measures [1,6].

The measurement and proper maintenance of overhead contact lines are crucial to prevent power supply issues and minimize wear-related problems.

Acknowledgments: The authors would like thank the Slovak University of Technology in Bratislava (Faculty of Mechanical Engineering), Dopravný podnik Bratislava, a. s. (Bratislava Transport Company) and, the grant agency KEGA project number 024STU-4/2023 (Building a laboratory of medical metrology), the grant agency APVV project number APVV-21-0216 (Advanced mathematical and statistical methods for measurement and metrology), the grant agency APVV project number APVV-21-0195 (Research the possibility of digital transformation of continuous transport systems) and the international project number "21NRM05" (Standardization for safe implant scanning in MRI) for their support.

Conflicts of Interest: "The conference paper is not in any conflict of interest. The funders had no role in the design of the study; in the collection, analyses, or interpretation of data; in the writing of the manuscript, or in the decision to publish the results".

References

1. Onderčo, Peter. *Measurement and evalutation of selected parameters of tram lines*. [Diploma thesis]. Slovak University of Technology in Bratislava. Faculty of Mechanical Engineering. Institute of automatization, informatization and measurement. Supervisor: doc. Mgr. Ing. Jan Rybář, PhD. Bratislava: Sjf STU BA, 2024, 79 pages.
2. Rybář, Jan; Onderčo, Peter. Příspěvek k měření parametrů tramvajových tratí /Contribution to the measurement of tram line parameters/. In *Metrologie* /Metrology/. Roč. 32, č. 3 (2023), s. 27 - 30. ISSN 1210-3543.
3. Chudý, Vladimír; Palenčár, Rudolf; Kureková, Eva; Halaj, Martin. *Meranie technických veličín /Measurement of technical quantities/*. Bratislava: STU v Bratislave, 1999. 688 s. ISBN 80-227-1275-2.
4. Kubát, Bohumil. *Městská a příměstská kolejová doprava /Urban and suburban rail transport/*. Praha: Wolters Kluwer Česká republika, 2010. ISBN 978-80-7357-539-7.
5. Rybář, Jan; Onderčo, Peter; Vajgel, Rastislav. Měřicí tramvaj jako pojízdná výzkumná laboratoř /Measuring tram as a mobile research laboratory/. In *Metrológia, skúšobníctvo a technické normy /Metrology, testing and technical standards/*. Roč. 28, č. 1 (2023), s. 5 - 12. ISSN 2989-3178.
6. Dovica, Miroslav; Kelemenová, Tatiana; Palenčár, Jakub. *Bezdotykové metódy merania geometrických veličín /Non-contact methods for measuring geometric quantities/*. 1. vyd. Košice Strojnícka fakulta Technickej univerzity v Košiciach 2020. 171 s. ISBN 978-80-553-3380-9.
7. *Měření parametrů trakčního vedení /Measurement of overhead contact line parameters/*. [document] Softvér pre meranie parametrov trakčného vedenia meracou električkou /Software for measuring traction line parameters with a measuring tram/. Užívateľská príručka /User manual/. 12 strán /12 pages/.
8. *Spolupráce sběrače proudu a trolejového vedení /Cooperation of current collector and overhead contact line/*. Available online: https://docplayer.cz/23310827-Spoluprace-sberace-proudu-a-trolejoveho-vedeni.html (accessed on 25-11-2024).
9. Palenčár, Rudolf; Wimmer, Gejza; Palenčár, Jakub; Witkovský, Viktor. *Navrhovanie a vyhodnocovanie meraní /Designing and evaluating measurements/*. 1. vyd. Bratislava Spektrum STU 2021. 160 s. Edícia vysokoškolských učebníc. ISBN 978-80-227-5080-6.

TECHNICAL UNIVERSITY OF KOŠICE
Faculty of Mechanical Engineering

Innovative Approach to Somatotype Determination

Bibiána Ondrejová [1,*], Lucia Bednarčíková [1], Norbert Ferenčík[1] and Jozef Živčák [1]

[1] Technical University of Košice, Faculty of Mechanical Engineering, Department of Biomedical Engineering and Measurement, Letná 1/9, 04200, Košice, Slovakia; bibiana.ondrejova@tuke.sk; lucia.bednarcikova@tuke.sk; norbert.ferencik@tuke.sk; jozef.zivcak@tuke.sk

* Correspondence: bibiana.ondrejova@tuke.sk

Abstract: Somatotype determination plays a critical role in sports science, biomechanics, and health diagnostics, allowing for a precise assessment of body composition. This paper introduces an innovative system combining advanced 3D body scanning technology and an automated PC application to calculate somatotypes based on the Heath-Carter method. The Heath-Carter system refines William Sheldon's foundational somatotype classification by integrating precise anthropometric measurements for endomorphy, mesomorphy, and ectomorphy components. This study compares the innovative 3D scanning-based method with conventional manual anthropometric measurements. Results demonstrate that the proposed method is more efficient, accurate, and repeatable while significantly reducing human error and measurement time.

Keywords: somatotype; 3D scanning; body composition

1. Introduction

The classification of somatotypes—endomorphy, mesomorphy, and ectomorphy—was originally established by William Sheldon. Sheldon's system was limited to visual assessments and lacked precision in determining body composition. Heath and Carter (1967) modified this approach, incorporating quantitative anthropometric measurements such as skinfold thickness, bone breadths, and limb girths to create a more robust and scientifically valid methodology [1-2].

The Heath-Carter method is widely regarded as the gold standard for somatotype analysis due to its versatility and applicability across different populations, sports disciplines, and clinical diagnostics [1-2]. Despite its accuracy, traditional methods of somatotype determination require manual measurements that are prone to error, time-consuming, and operator-dependent. To address these challenges, advancements in diagnostic and imaging technologies have opened new possibilities for improving somatotype determination. Modern techniques such as dual-energy X-ray absorptiometry (DEXA), bioelectrical impedance analysis (BIA), and air displacement plethysmography allow for precise body composition assessment by measuring fat mass, lean mass, and skeletal components [5]. These methods, however, remain costly, require specialized equipment, and may involve exposure to ionizing radiation in the case of DEXA [4-6].

At the forefront of innovation are 3D body scanning technologies, which offer non-invasive, fast, and highly reproducible methods for capturing detailed anthropometric data. Full-body 3D scanners generate digital models of the body, from which accurate measurements such as limb girths, bone widths, and all body dimensions, except skinfold thickness, can be extracted [6]. These measurements can then be used to calculate somatotype components using validated methods like Heath-Carter, while eliminating the variability inherent in manual techniques [6].

There remains, however, an unmet need for a user-friendly, affordable, and automated method capable of integrating 3D scanning technology with validated somatotype assessment models. Such a system would streamline the process, improve measurement accuracy, and expand the applicability of somatotype analysis to broader fields, including sports training, clinical research, and performance optimization [6-7].

The aim of this study is to present an innovative approach to somatotype determination by integrating full-body 3D scanning technology with an automated PC-based application. The specific goals include designing and implementing an algorithm to process anthropometric data captured via 3D scanning, as well as comparing the results obtained from the proposed system with traditional manual measurements using the Heath-Carter method. By leveraging modern technology, this approach promises to overcome the limitations of traditional manual anthropometry, offering a faster, accurate, and non-invasive alternative for somatotype determination. This work lays the foundation for a new standard in body composition analysis, with significant implications for research, professional sports, and clinical applications [6-7].

2. Materials and Methods

2.1. Equipment and instrumentation

The study utilized a full-body 3D scanner TC^2 NX-16 ($[TC]^2$ Labs, USA), capable of generating anthropometric data, including circumferences, bone breadths, and body dimensions. A prototype PC-based application was developed for the automated computation of somatotype parameters using the Heath-Carter method.

3D Scanner:

- Captured non-invasive, three-dimensional body measurements.
- Extracted key parameters: circumferences (upper arm, calf), bone breadths (humerus, femur).

Manual Anthropometry:

For validation, manual measurements were taken using:

- Skinfold calipers for triceps, subscapular, and suprailiac thickness.
- Measuring tape for limb circumferences (upper arm, calf).
- Caliper for bone breadths (humerus, femur).

2.2. Data acquisition

A total of 77 subjects (36 males, 41 females) aged 17 to 24 years participated, with a mean age of 22.1 ± 4.63 years, height of 173.5 ± 8.96 cm, and weight of 70.2 ± 13.6 kg. The procedure involved each subject undergoing a full-body 3D scan to obtain automated measurements. Simultaneously, manual anthropometric measurements were collected for comparison. These measurements included height (cm), weight (kg), skinfold thickness (mm), bone breadths (cm), and girths (cm).

2.3. Data processing

A custom PC-based application (Fig. 1) was developed to process the 3D scanner outputs and calculate somatotype values based on the Heath-Carter method. The developed PC application for somatotype determination was created using C# programming language. It integrates 3D full-body scanning technology with manual anthropometric input to streamline the calculation of somatotype components. The Heath-Carter method is utilized within the application to categorize body composition into endomorphy, mesomorphy, and ectomorphy based on the extracted data.

The Heath-Carter method was used to calculate somatotype components using the following equations:

1. Endomorphy (fatness):

$$\text{Endomorphy} = -\,0.7182 + 0.1451 \text{ x } (X) - 0.00068 \text{ x } (X)^2 + 0.0000014 \text{ x } (X)^3 \quad (1)$$

where X= sum of the skinfolds (triceps, subscapular, supraspinal) x (170.18: height).

2. Mesomorphy (muscularity):

$$\text{Mesomorphy} = 0.858 \text{ x Humerus Breadth} + 0.601 \text{ x Femur Breadth} + 0.188 \text{ x Biceps Circumference} + 0.161 \text{ x Calf circumference} - \text{Height x } 0.131 + 4.5 \quad (2)$$

3. Ectomorphy (linearity):

$$HWR = \frac{Height}{\text{Weight}^{1/3}} \quad (3)$$

The calculated HWR was then used to classify ectomorphy as follows:

7. If HWR ≥ 40.75 → Ectomorphy = 0.732 × HWR - 28.58
8. If 38.25 ≤ HWR < 40.75 → Ectomorphy = 0.463 × HWR - 17.63
9. If HWR < 38.25 → Ectomorphy = 0.1

The interface consists of input fields for personal information (e.g., name, sex, height, and weight) and anthropometric measurements, including body circumferences (waist, hips, biceps, calf), bone breadths (humerus, femur), and skinfold thicknesses (triceps, subscapular, suprailiac, thigh, and calf), which can be manually entered or automatically extracted from the 3D scanner (Figure 1). The right panel displays the output values, including calculated somatotype components (endomorphy, mesomorphy, and ectomorphy) and additional indices such as BMI (Body Mass Index), WHR (Waist-to-Hip Ratio), HWR (Height-to-Weight Ratio), and Rohrer Index. At the bottom, functional buttons allow users to reset data, perform calculations for somatotype and body composition, and export results for further analysis. The software includes options to export results into formats like MS Excel for further analysis. The system is compatible with Windows-based devices and supports both manual and automated data acquisition workflows.

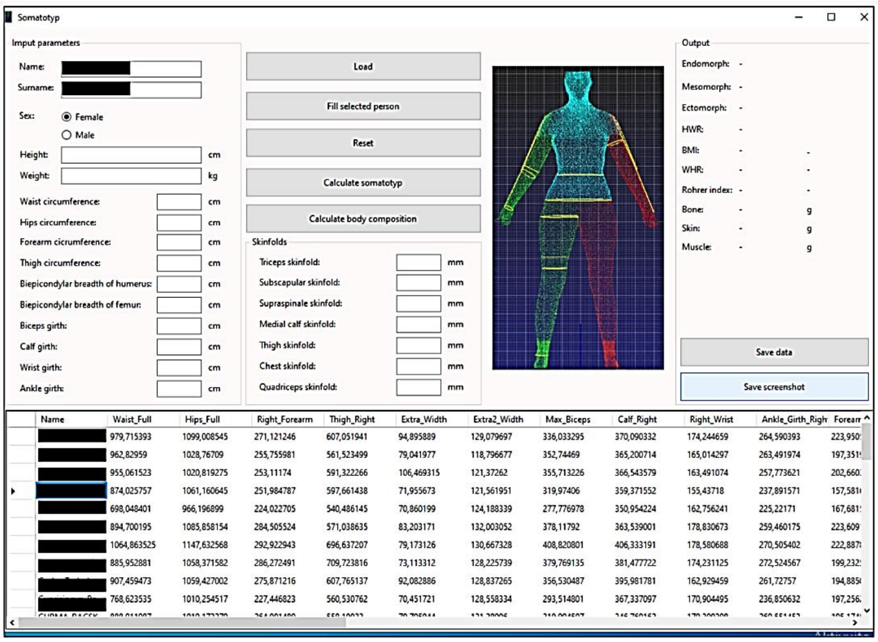

Figure 1. The user interface of the developed PC application for somatotype and body composition determination.

3. Results

3.1. Descriptive statistics

The descriptive statistics for manual and 3D scanner measurements, including mean values, range, standard deviations, and standard errors, are summarized in Table 1.

Table 1. Descriptive Statistics of Manual and 3D Scanner Measurements.

Measurement	Manual Mean ± SD	3D Scanner Mean ± SD	Range (Manual)	Range (3D)
Biceps Circumference (cm)	30.54 ± 3.90	31.46 ± 3.73	24 – 42	24.4 – 40.9
Calf Circumference (cm)	36.66 ± 3.05	36.41 ± 2.81	30 – 46	30 – 44.9
Femur Breadth (cm)	10.22 ± 1.49	12.11 ± 0.95	7.2 – 14.5	9.4 – 15.2
Humerus Breadth (cm)	7.45 ± 1.06	7.50 ± 0.85	5.28 – 9.6	5.2 – 9.9

The results indicate that 3D scanner measurements tend to report slightly larger values for limb circumferences and bone widths compared to manual measurements.

3.2. Correlation analysis

Correlation tests were performed to evaluate the relationship between manual and 3D scanner measurements. Table 2 presents the correlation coefficients and significance levels for the examined parameters.

Table 2. Correlation Between Manual and 3D Scanner Measurements.

Measurement	Correlation Coefficient (R)	P-value	Significance
Biceps Circumference	0.7536	< 0.0001	Significant
Calf Circumference	0.6757	< 0.0001	Significant
Femur Breadth	0.2460	< 0.0001	Significant
Humerus Breadth	0.4561	< 0.0001	Significant

The analysis reveals statistically significant correlations between manual and 3D scanner measurements across all parameters. Strong correlations were observed for arm circumference (R = 0.7536) and calf circumference (R = 0.6757), while moderate correlations were noted for femur and humerus breadth.

3.3. Regression analysis

A linear regression analysis was conducted to evaluate the relationship between manual and 3D scanner measurements. The regression results show (Figure 2) a positive linear relationship, indicating that as manual measurements increase, 3D scanner values increase proportionally.

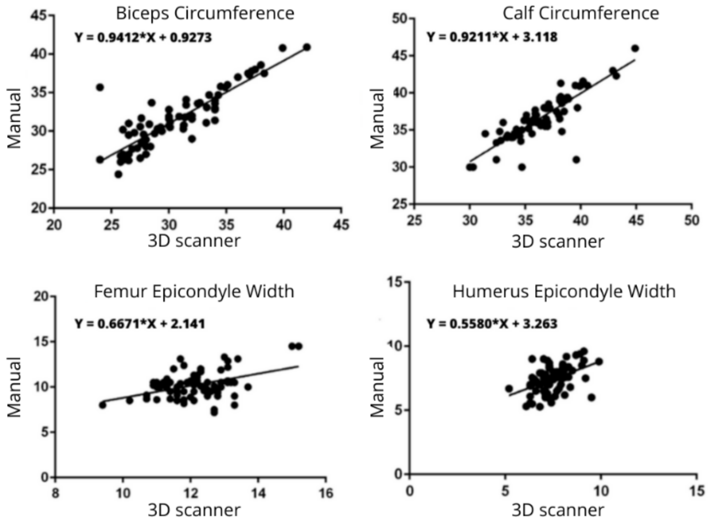

Figure 2. Linear regression of measured data.

3.4. Comparison of somatotype components

The results showed minor discrepancies between manual measurements and 3D scanner outputs (Table 3).

Table 3. Comparison of manual and 3D scanning results.

Parameter	Manual (Mean ± SD)	3D Scanner (Mean ± SD)	Difference
Endomorphy	4.95 ± 0.51	5.02 ± 0.47	0.07
Mesomorphy (Men)	6.11 ± 0.89	7.00 ± 0.85	0.89
Mesomorphy (Women)	6.21 ± 0.92	6.82 ± 0.80	0.61
Ectomorphy	2.45 ± 0.52	2.43 ± 0.50	0.02

Somatotype values were visualized on a Heath-Carter somatochart (Figure 3). The majority of subjects showed higher mesomorphic values, with minor variations between manual and 3D scanning methods.

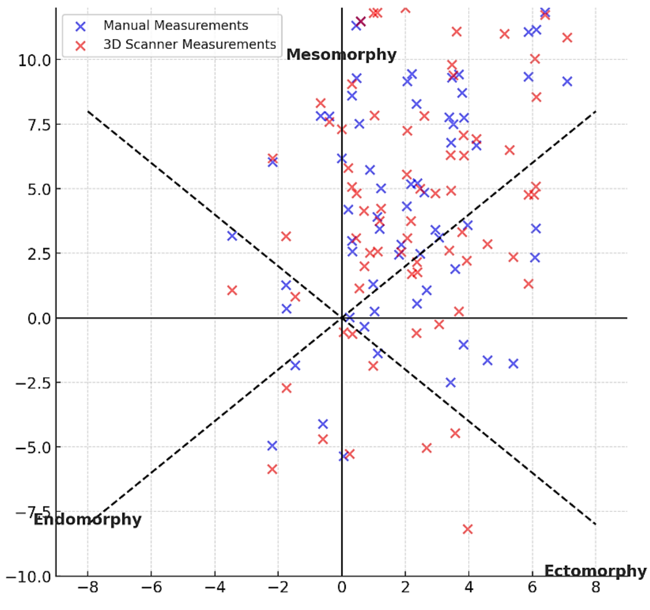

Figure 3. Somatochart: Comparison of manual and 3D measurements.

4. Discussion

The results demonstrate that the automated 3D scanning system can accurately calculate somatotype components using the Heath-Carter method, with minimal deviation from manual measurements. The proposed system significantly reduces measurement time and eliminates operator errors, making it a superior alternative for large-scale studies and clinical applications. The study validated the proposed 3D scanning-based system as an effective alternative to traditional manual anthropometry for somatotype determination using the Heath-Carter method. Additionally, the 3D scanner significantly improved efficiency by substantially reducing the time required for measurements. Furthermore, the method demonstrated reproducibility, delivering consistent results regardless of the operator's level of expertise.

5. Conclusions

This study presents a novel approach to somatotype determination using 3D body scanning technology integrated with the Heath-Carter method. The automated system outperforms traditional manual measurements in terms of efficiency and reproducibility. This advancement has significant potential for use in sports science, health diagnostics, and biomechanics. The results demonstrate that 3D scanning provides reliable anthropometric measurements with moderate to high correlation to manual measurements. Although the scanner produced slightly higher values, significant correlations were observed, allowing for systematic corrections of these discrepancies. Linear regression analysis further confirmed a strong relationship between the two measurement methods, supporting the use of 3D scanning as a viable alternative to manual anthropometry for somatotype determination.

Acknowledgments: This work was supported by the Slovak Research and Development Agency under the contract No. APVV-22-0340. This research was supported by project KEGA 018TUKE-4/2023 Implementation of methods of physicalchemical analyzes in the study program Biomedical Engineering and VEGA 1/0387/22 Development and testing of systems for controlled stimulation of cell growth in a bioreactor environment using computer vision.

Conflicts of Interest: The authors declare no conflict of interest.

References

1. Florescu, O. The Determining Factors in the Formation of Human Body Types (Ectomorph, Mesomorph, and Endomorph). Marathon 2016, 8, 47–49. Available online: http://www.marathon.ase.ro/pdf/vol8/florescu.pdf (accessed on 15 December 2024).
2. Carter, J.E.L. The Heath-Carter Anthropometric Somatotype. Available online: https://www.mdthinducollege.org/ebooks/statistics/Heath-CarterManual.pdf (accessed on 15 December 2024).
3. Chiu, C.; Ciems, R.; Thelwell, M.; Bullas, A.; Choppin, S. Estimating Somatotype from a Single-Camera 3D Body Scanning System. Eur. J. Sport Sci. 2021, 22, 1204–1210. https://doi.org/10.1080/17461391.2021.1921041 (accessed on 15 December 2024).
4. Drywień, M.; Górnicki, K.; Górnicka, M. Application of Artificial Neural Network to Somatotype Determination. Appl. Sci. 2021, 11, 1365. https://doi.org/10.3390/APP11041365 (accessed on 15 December 2024).
5. Bertuccioli, A.; Sisti, D.; Amatori, S.; Perroni, F.; Rocchi, M.; Benelli, P.; Trecroci, A.; Di Pierro, F.; Bongiovanni, T.; Cannataro, R. A New Strategy for Somatotype Assessment Using Bioimpedance Analysis: Stratification According to Sex. J. Funct. Morphol. Kinesiol. 2022, 7, 4086. https://doi.org/10.3390/jfmk7040086 (accessed on 15 December 2024).
6. Wang, M.; Song, Y.; Zhao, X.; Wang, Y.; Zhang, M. Utilizing Anthropometric Measurements and 3D Scanning for Health Assessment in Clinical Practice. Phys. Act. Health 2024, 8, 182–196. https://doi.org/10.5334/paah.379 (accessed on 15 December 2024).
7. Ryan-Stewart, H.; Faulkner, J.; Jobson, S. The Impact of Technical Error of Measurement on Somatotype Categorization. Appl. Sci. 2022, 12, 3056. https://doi.org/10.3390/app12063056 (accessed on 15 December 2024).

TECHNICAL UNIVERSITY OF KOŠICE
Faculty of Mechanical Engineering

Comparison of sensing technologies for mobile robot intended for environments with increased radiation

Patrik Pilát [1,*], Jozef Varga [1], and Ján Semjon [2]

[1] Prototyping and Innovation centre, Faculty of Mechanical Engineering; patrik.pilat@tuke.sk; jozef.varga.2@tuke.sk
[2] Department of Production Technology and Robotics; jan.semjon@tuke.sk
* Correspondence: patrik.pilat@tuke.sk; Tel.: +421908443216

Abstract: Mobile robots are the key to solving the challenges posed by environments with increased radiation exposure, such as nuclear facilities or disaster areas. Their use provides greater safety, efficiency and cost reduction by replacing human labour in hazardous areas. This study examines sensing technologies, in particular a comparison of two depth cameras, the Intel RealSense D435i and the OAK-D Pro, for their use in the hot gas chamber of the decommissioned KS 150 reactor. The analysis highlights the suitability of these cameras for the tasks of localization, mapping and object recognition.

Keywords: mobile robot, decontamination, depth camera

1. Introduction

Mobile robots play a critical role in environments with elevated radiation levels, such as nuclear facilities, space exploration, or disaster zones. The International Atomic Energy Agency (IAEA) recommends the use of mobile robots in nuclear power plants, mainly because of the benefits achieved by this application. The main benefits include the replacement of people performing tasks in a hazardous environment, increased efficiency and overall safety, while reducing costs [1], [2]. The main purpose of using robotics in decommissioning tasks is to minimize the radiation exposure to workers during the decommissioning process. In many cases, due to the high radiation levels and the long half-lives of the radioactive materials, robotics is the only viable solution [3], [4].

With the progress of robotic technologies and artificial intelligence, researchers and engineers have focused on the challenge of enabling mobile robot's operations in increasingly complex environments such as a nuclear power plant environment [5].

The choice of sensing technologies is especially important for these applications, as sensors must provide robust performance. Using the sensing technologies robot can perform localization, mapping, motion task, target reorganization etc.

When choosing the sensing technology, it is necessary to consider the environment in which the robot will work and the type of task it will perform. The environment of nuclear power plants presents many challenges and requirements that are not present in industrial applications [6], [7]. The environment in which the service robot will work is the hot gas chamber of reactor KS 150. This reactor was created in Jaslovské Bohunice represents the beginning of Czechoslovak nuclear energy. Its construction and commissioning represented a significant challenge for the industry at that time. This HWGCR-type reactor, moderated with heavy water and fuelled by natural metallic uranium, was cooled by gaseous carbon dioxide ($CO2$) and had an electrical output of 127 MW. Construction began in 1958, and in October 1972, the first controlled chain reaction occurred in the A1 nuclear power plant's reactor. However, two serious accidents occurred during its operation.

This serious accident rendered the reactor inoperable, and in 1979 the government decided to decommission the A1 plant. The accident was rated as Level 4 on the International Nuclear and Radiological Events Scale (INES). With the approval of the regulatory authorities in 1999 for decommissioning, the actual continuous decommissioning process of NPP A1 started [8]. This process consists of five stages where the reactor is in stage 5 of decommissioning [9].

For this task, a specialized service robot was designed. It consists of a four-wheeled chassis with a robotic arm, allowing access to hard-to-reach spots. The robotic arm has five degrees of freedom, including four rotational and one translational axis. It is equipped with an end effector designed for collecting larger objects. For the proper functioning of this robot in the working environment it was necessary to select suitable sensors, which can be divided into two groups.

Proprioceptive sensors - monitor the robot's internal state by providing data on its position, orientation, and movement, which facilitates self-awareness and internal monitoring. For example, encoders use optical, magnetic, or mechanical methods to measure the rotational position and speed of motors or wheels providing feedback for precise motion control.

Exteroceptive sensors - collect data about the robot's environment by identifying external objects, obstacles, and conditions, enabling interaction with the surroundings. These sensors include RGB, stereo, depth cameras [10], [11].

In this article we will focus on the comparison of depth cameras that could be used for localization, mapping, target reorganization.

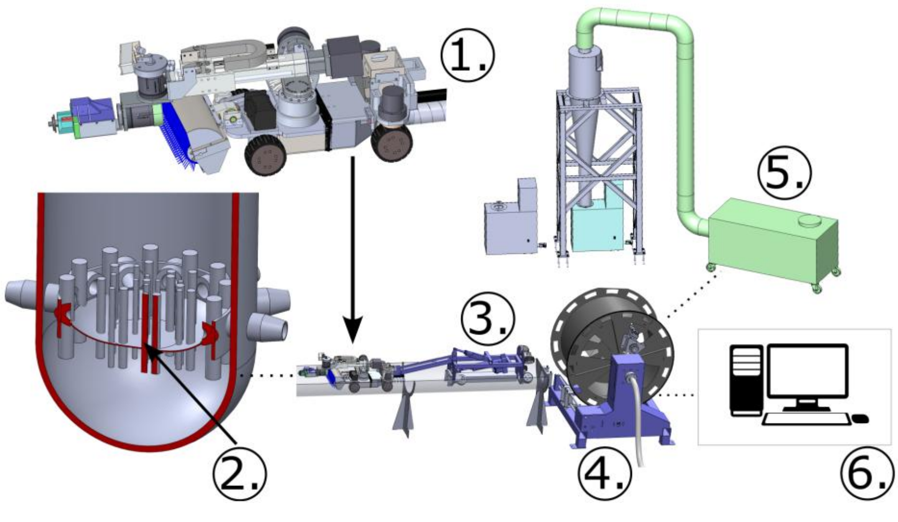

Figure 1. Schematic description of the hot gas chamber decontamination operation.

Description of the application of the hot gas decontamination chamber (Figure 1), 1 – mobile robot, 2- hot gas chamber, 3- second assistant robot, 4- winding device, 5- suction device, 6- remote control workplace.

2. Sensing technologies for mobile robot

A sensor is capable of identifying physical changes in the environment and converting them into electrical signals, which can then be utilized in subsequent processes [12]. Actually, there are many sensors on the market which differ in performance, use and price. In this experiment, we compare two stereo cameras, the AOK-D Pro (Figure 2a) and the Intel RealSense (Figure 2b). These cameras share the same depth-sensing technology, which reconstructs depth by analysing the differences between images captured by the cameras from slightly different perspectives of the same scene [13].

Table 1. Technical specifications of cameras.

Parameter	Intel RealSense D435i	OAK-D Pro
Depth Technology	Stereo depth with global shutter IR sensors	Stereo depth with IR laser dot projector
RGB Camera Resolution	1920 × 1080 @ 30 FPS	12.3 MP (4056 × 3040), 30 FPS
Field of View (FOV)	87° × 58° (depth), 69° × 42° (RGB)	78° × 64° (stereo depth), 81° × 65° (RGB)
Depth Range	0.1 m to 10 m	0.3 m to 35 m
Integrated IMU	Yes	Yes
Illumination	Active IR projector with 850 nm wavelength	Active IR projector with high-power laser illumination
Interface	USB 3.1 Type-C	USB 3.0 Type-C
Power Consumption	~1.5 W	~3.5 W
Operating Temperature	0°C to 35°C	-20°C to 45°C
Dimensions	90 mm × 25 mm × 25 mm	110 mm × 36 mm × 30 mm
Weight	72 g	195 g
AI Processing Capability	None	Built-in AI processing with Intel Movidius VPU

3. Experimental setup

In the picture 2 we can see the placement of cameras 1 – Intel Real Sense and 2 – OAK-D Pro on the mobile robot. We mounted the cameras on the fourth rotary joint of the arm using an aluminum plate. Placing the cameras on the movable arm increases the efficiency of the camera compared to placing the camera on the subsystem of the mobile robot – the chassis. We connected the cameras using a USB connector and used the RTABMap program to transfer the point cloud. The aim of the test was also to evaluate the suitability of placing the camera on the mobile robot.

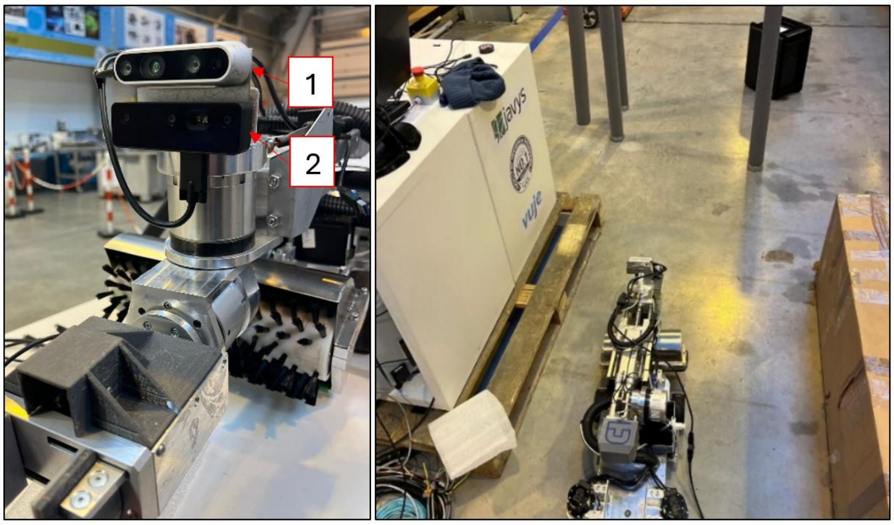

Figure 2. placement of cameras on the robotic arm, initial position of the mobile robot during the experiment.

In the experiment we will simulate the movement of a robot in an indoor environment. There are 4 circular objects in the scanning environment. Scanning of circular objects is based on the shape of a hot gas chamber in which robots will operate (Figure 1).

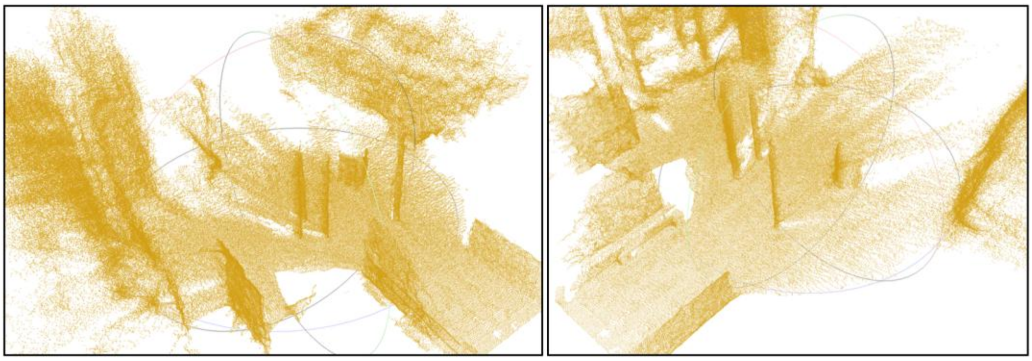

Figure 3. Intel RealSense D435i.

Using the RTAB mapping software based on the SLAM approach, we created a point cloud of the environment.

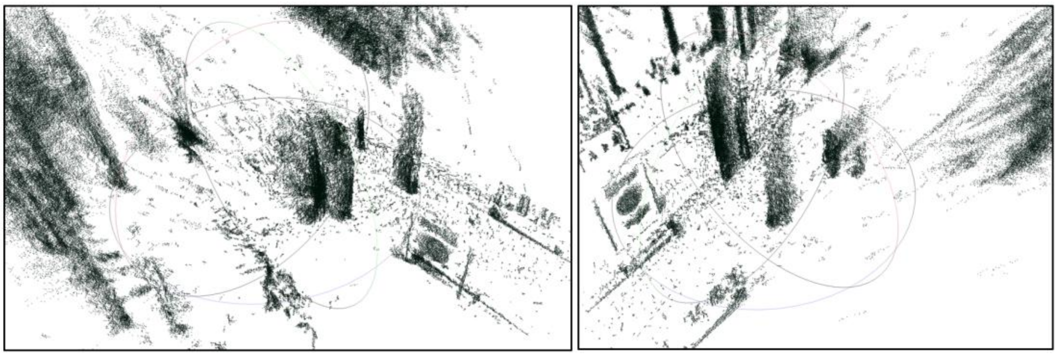

Figure 4. OAK-D Pro.

Using this method, we created a point cloud from both cameras. Which we then overlaid for comparison.

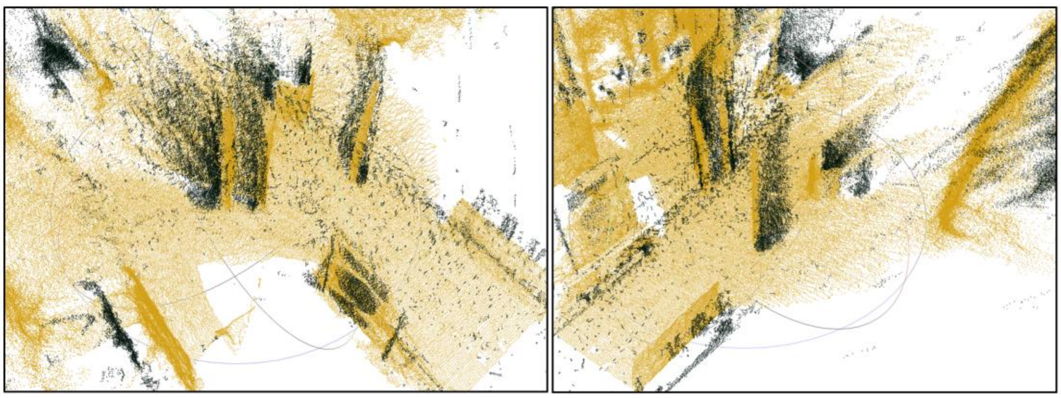

Figure 5. Combined data cloud.

Yellow point cloud is created by the real sense camera and the black point cloud is created by OAK-D Pro. Point cloud created by real sense camera consist of 363.562 vertices and the point cloud created by the OAK-D camera contains 348.257 vertices.

In Figure 3 and Figure 4 we can see the difference in the output data from the cameras. The real sense camera produced a more precise and detailed view. The data processed in this way can then be further used for trajectory planning.

The OAD-D camera produced a less detailed image of the environment. Also, the problem set in the amount of noise points that were created at different distances from the camera. This difference is also due to the characteristics of the cameras.

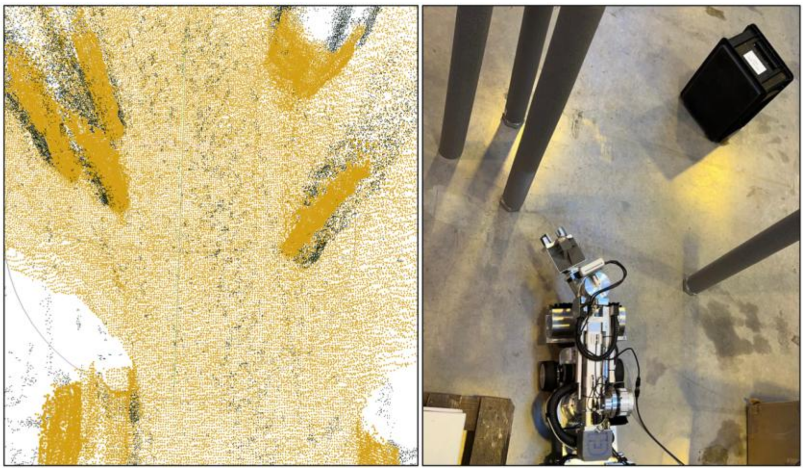

Figure 6. detailed view of the pipes.

The intel real sense camera has a depth range of 0.1 - 10 m and the OAK-D Pro camera has a depth range of 0.3 - 35 m. This caused the creation of a large number of noise points at up to 150 m. In general, we can say that the Intel RealSense camera suits our application better.

5. Conclusions

A comparison of the Intel RealSense D435i and OAK-D Pro depth cameras shows their different capabilities. The Intel RealSense camera outperformed the OAK-D Pro by producing more accurate point clouds with fewer noise artifacts, especially in the closer depth ranges (0.1-10 m). These features make it more suitable on a mobile drone. The OAK-D Pro instrument, despite its greater depth range, generated a higher level of noise, limiting its applicability in this context. This study highlights the importance of selecting appropriate sensing technologies based on specific environmental and task requirements, opening the way to more efficient and reliable robotic operations in hazardous environments.

Conflicts of Interest: The authors do not declare any conflict of interest.

Acknowledgements: This article was created thanks to the VEGA project support: 1/0215/23 Research and development of robotic workplaces equipped with industrial and collaborative robots and REBELION 101104241 - Research and development of a highly automated and safe streamlined process for increased Lithium-ion battery repurposing and recycling-Hop on.

References

1. Smith, R. J.; Cucco, E.; Fairbairn, C. Robotic Development for the Nuclear Environment: Challenges and Strategy, Robotics 2020, 9(4), 94; https://doi.org/10.3390/robotics9040094.
2. Nowakowski M.; Jánoš R.; Semjon J.; Varga J., REMOVAL SYSTEM FOR UNMANNED GROUND VEHICLES USING A MODULAR ROBOTIC ARM. DOI: 10.17973/MMSJ.2024_11_2024057
3. Mohamed J. Bakari, Khaled M. Zied. Development of a Multi-Arm Mobile Robot for Nuclear Decommissioning Tasks. Available online: https://journals.sagepub.com/doi/full/10.5772/5665

4. Semjon J.; Varga J.; Pilát P.; Marcinko P.; Jánoš R., VERIFICATION OF THE PROPERTIES OF AN INDUSTRIAL ROBOT FOR THE NUCLEAR INDUSTRY
5. Ivan Vitanov; Ildar Farkhatdinov, A Suite of Robotic Solutions for Nuclear Waste Decommissioning Available online: https://www.mdpi.com/2218-6581/10/4/112
6. Determine the orientation for randomly distributed objects / Jozef Varga, Michal Šulík - 2016. In: Transfer inovácií. Č. 33 (2016), s. 153-155. - ISSN 1337-7094
7. Kuniaki Kawabata, Toward technological contributions to remote operations in the decommissioning of the Fukushima Daiichi Nuclear Power Station. Available online: https://iopscience.iop.org/article/10.35848/1347-4065/ab82ad/meta
8. Kuruc, J.; Mátel, Ľ. 30. a 29. Výročie nehôd na reaktore jadrovej elektrárne A-1 Jaslovské Bohunice – rádioekologické a rádiobiologické následky, https://inis.iaea.org/collection/NCLCollectionStore/_Public/37/110/37110257.pdf
9. JAVYS, Available online: https://www.javys.sk/sk/cinnosti-spolocnosti/vyradovanie-je-a1
10. Very simple optical sensor to direct and recognition objects for mobile robots / Marek Sukop ... [et al.] - 2016. In: Ukraine - EU. Modern Technology, Business and Law. - Chernihiv : Chernihiv National University of Technology, 2016 S. 330-331. - ISBN 978-966-7496-71-5
11. Ayan Mazhitov; Adilzhan Adilkhanov, Deformable Object Recognition Using Proprioceptive and Exteroceptive Tactile Sensing. Available online: https://ieeexplore.ieee.org/abstract/document/8700392
12. Md. A. K. Niloy; Anika Shama, Critical Design and Control Issues of Indoor Autonomous Mobile Robots: A Review. Available online: https://ieeexplore.ieee.org/abstract/document/9363869
13. Silvio Giancola; Matteo Valenti, A Survey on 3D Cameras: Metrological Comparison of Time-of-Flight, Structured-Light and Active Stereoscopy Technologies. ISBN 978-3-319-91760-3

TECHNICAL UNIVERSITY OF KOŠICE
Faculty of Mechanical Engineering

Risk factors for psychological stress in the workplace

Denisa Porubčanová [1,*], Michaela Balážiková[1]

[1] Technical University of Košice, Faculty of Mechanical Engineering, Department of Quality, Safety and Environment; denisa.porubcanova@tuke.sk; michaela.balazikova@tuke.sk
* Correspondence: denisa.porubcanova@tuke.sk; Tel.: +421 55 602 2501

Abstract: Identifying risk factors in the workplace, whether they are physical or psychological, is an important aspect of protecting the health of workers at work. It also helps to improve working conditions through the identification and subsequent application of preventive measures. The selection of risk factors for psychological stress is quite difficult and therefore often neglected in practice. This article describes the assessment of psychological burden according to the legality in Slovakia and summarizes the results of studies published so far in the field of psychological burden at work and identification of psychosocial risks. It also presents a proposed matrix for the assessment of psychological burden, which can be used to determine the degree of physical and psychological burden and the resulting risk is determined by the product of these two components. Further research will be directed towards the development of a series of coefficients for quantifying the degree of psychological burden for selected risk factors and subsequent modification of the matrix for easy and quick application in practice. This is also expected to increase the rate of its use.

Keywords: psychosocial risks, psychological workload, psychological workload assessment

1. Introduction

Every work environment is burdened to some extent by risk factors for both physical and psychological stress. The identification of risks and the determination of the limit of acceptable levels of risk in the assessment of physical strain is currently at a good level. However, in comparison, the identification of psychosocial risks in the workplace, and in particular the subsequent determination of the limit of acceptable risk, is a complicated process. Therefore, the assessment of psychological stress is carried out using questionnaires based on the subjective perception of the test subject. However, even this subjective method may not give an adequate picture of psychosocial risks and psychological burdens in the workplace. Indeed, the employee's answers may not always be honest, which greatly influences the resulting assessment. Quantifying psychological distress is not easy. It can be done on the basis of salivary biomarker levels, but this can be described as a lengthy method. Another option to quantify psychological burden is to use the measurement of changes in the electrophysiological properties of the skin, which is made possible, for example, by the GSR sensor. Specifically, this involves monitoring changes in the galvanic response of the skin, which is directly related to the level of stress. On the basis of the graph of the measurement course, it is possible to read off the places with the highest value of activation of the organism. This measurement can be described as a suitable basis for the identification of risk factors, the subsequent creation of classes according to the degree of risk and the assignment of the corresponding coefficient for the subsequent calculation of the degree of psychological stress, which also takes into account the time factor of the risk [1, 2, 3].

2. Legislative assessment of psychological burden in Slovakia

The assessment of psychological distress in Slovakia is provided for by the legislative framework. In addition to the laws and regulations of the Government of the Slovak Republic, which lay down the general conditions of occupational safety and health, summarised in Table 1, there is also a decree of the Ministry of Health of the Slovak Republic No. 542/2007 of the Collection of Laws, which provides for the assessment of psychological burden at work. The assessment consists of questionnaires focusing on subjective perception [4, 5]:

- intensity of work and time pressure,
- work pace,
- monotony of work,
- social interactions and relationships,
- levels of responsibility,
- risk to health and life,
- physical discomfort,
- other sources of stress [4].

Furthermore, Decree 542/2007 Coll. prescribes a test of concentration and attention, according to which the psychomotor pace, speed and correctness of the performed activity, the overall concentration of attention are evaluated [4].

Table 1. Legislative framework for occupational health and safety in Slovakia [5].

Law/regulation	Content
Act No. 124/2006 Coll.	Occupational health and safety
Act No. 355/2007 Coll.	Prevention of diseases and other health disorders, healthy living and working conditions.
Slovak Government Regulation No. 395/2006 Coll.	Minimum requirements for the provision and use of personal protective equipment (PPE Requirements Regulation)
Slovak Government Regulation No. 115/2006 Coll.	Basic health and safety requirements for the protection of employees against risks arising from from exposure to noise
Slovak Government Regulation No. 416/2005 Coll.	Basic health and safety standards for the protection of workers against risks arising from exposure to vibration.

3. Psychosocial risk factors in the workplace

For the assessment and subsequent identification of risk factors in the work environment, other methods are used in addition to the legally established methods: self-report questionnaires, which perceive the employee as a subject, the employee answers questions based on subjective perceptions and feelings, e.g. the State-Trait Anxiety In-ventory (STAI) or the Numerical Analogue Scale (NAS). Furthermore, these are questionnaires developed by occupational psychology experts, focusing on the work environment and functioning within it, performance in relation to the environment and environmental influences. The content of the questionnaires may vary depending on the nature of the work [6, 7].

For example, the NAS questionnaire was also used in a study aimed at assessing the workload of workers in the design of industrial products and processes. The study was conducted on 8 employees with an average age of 26 years. RULA, motion tracking sensors, and camera footage were used as additional evaluation elements. During the experiment, the participants were asked to perform their work under normal conditions, under increased physical strain and under increased psychological strain. They then completed the NAS questionnaire after each phase. By evaluating the collected data, it was shown that an increase in psychological strain negatively affects the overall performance and well-being of employees [6, 7].

Physiological measurements of EEG, ECG, blood pressure or skin electrophysiological properties are often used for the assessment of psychological load [7].

In order to identify psychosocial risks in workplaces, many researches and experiments have been carried out in different work areas [8 - 15]. At the same time, the aim of the above publications is to highlight the effects of stress and psychological load on the human body.

According to Michalik, psychosocial risks can be divided into two categories in terms of direct or indirect impact on the performance of work activities. Psycho-logical risks with a direct impact on work performance include, for example, excessive demands on the employee, lack of decision-making capacity, insufficient support from management and the team, inadequate interpersonal relations or undue involvement of the employee in the management of organisational change [16].

Risks that have an indirect impact on job performance include work-life imbalance, challenging life events, personal problems, lack of finances, illness or poor family relationships [16].

EU - OSHA considers the most common emerging psychosocial risks to be :
- New forms of employment contracts and job insecurity,
- an ageing workforce,
- intensification of work,
- high emotional demands at work,
- work-life imbalance [17].

However, following the WHO model, psychosocial risks can be divided into 10 areas:
1. Nature of the work;
2. Workload, work pace;
3. Work scheduling;
4. Decision-making about work;
5. Work environment and equipment;
6. Company culture;
7. Interpersonal relations in the workplace;
8. Role and function in the organisation;
9. Career progression;
10. Work-life balance [15].

Specific examples of psychosocial risks in the workplace include:
- Role ambiguity and conflicting requirements,
- excessive workload/insufficient workload,
- poorly managed organisational change,
- lack of involvement in decision-making that affects the worker,
- ineffective communication,
- lack of support from management and the team,
- job insecurity,
- workplace harassment,

- inadequate working environment conditions - noise, lighting, temperature, ...
- others [18].

The presence of these risk factors for psychological stress in the workplace has a negative impact not only on individuals but also on the organisation as a whole. The most common consequences include high absenteeism, a decrease in employee engagement at work, frequent occurrence of human errors, high employee turnover, reduced performance and productivity, an increase in the number of accidents, an increase in customer complaints, an increase in lawsuits, or an adverse effect on the recruitment of new employees [15].

Preventing not only these impacts on the organization and individual employees is the purpose of assessing and evaluating the risks of psychological distress at work. By correctly assessing and identifying risk factors, it is possible to prevent increased workload through the application of predictive and preventive measures to minimize both physical and psychological strain.

4. Design of a risk matrix for the assessment of psychological distress

Due to the variety of psychological, psychosocial and physical factors affecting the employee at work, it is necessary to take into account all these aspects to assess and determine the resulting risk, Therefore, a new matrix for the assessment of psychological burden has been proposed, which, however, combines the possibility of assessing the psychological risk and the physical risk, with the resulting overall risk being the product of these two components.

Implication (D)				Probability (P)			
Psychical	**D_1**	**Physical**	**D_2**	**Negligible (1)** Minimal occurrence	**Moderate (2)** Occasional exposure - occurrence approximately 2x per week	**High (3)** Regular exposure - daily exposure	**Significant (4)** Permanent exposure - daily exposure throughout the entire work shift
Occasional fatigue	**1**	No changes in physiological functions, sudden increase in blood pressure and heart rate.	**1**	1	2	3	4
Fatigue, decreased ability to concentrate	**2**	Pre-hypertension, headache, digestive disorders, nausea	**2**	2	4	6	8
Psychical fatigue, anxiety, cognitive impairments	**3**	Hypertension 1. grade, cardiovascular diseases, migraine, digestive disorders, muscle pain	**3**	3	6	9	12
Sleep disorders, depression, burnout syndrome, Long-term sick leave	**4**	Hypertenzia 2. – 3. grade, stroke risk, stomach ulcers, muscle spasms and fatigue, Diabetes mellitus, cancerous diseases	**4**	4	8	12	16

Figure 1. Proposed risk matrix for psychological distress assessment.

Figure 1 depicts the proposed risk matrix for psychological burden assessment, which is a combination of two matrices and allows for separate risk assessment of risks

related to psychological consequences and risks related to physical consequences. The resulting risk is then calculated by combining these two components.
The risk related to psychological consequences, denoted R1, is calculated as:

$$\mathbf{R_1 = D_1 \times P} \tag{1}$$

where D1 is the psychological consequence of risk and P is the probability of occurrence.

The risk associated with the physical consequences, R2, is calculated as:

$$\mathbf{R_2 = D_2 \times P} \tag{2}$$

where D2 is the physical consequence of the risk and P is the probability of occurrence.

The resulting risk is calculated according to the formula:

$$\mathbf{R = R_1 \times R_2} \tag{3}$$

where R is the resulting risk, R1 is the risk associated with psychological consequences and R2 is the risk associated with physical consequences.

The resulting risk will have a value between 1 and 256 and the aim of further research is to determine the limit of the acceptable level of risk of psychological distress. Also, the aim is to create risk classes to which coefficients will be assigned depending on the severity of the specific risk factor. The creation of these classes will be possible on the basis of the data measured by the GSR sensor in different plants.

The correct adjustment and assignment of coefficients to individual stress stimuli remains a subject for further research. The result will be the compilation of a comprehensible and easy to apply methodology for the assessment of psychological stress in workplaces.

5. Conclusions

The assessment of psychological distress at work is a complex matter in which a large number of factors enter. Therefore, the process is challenging and is often taken lightly in practice. The matrix proposed in this article could serve as a tool for a more uni-simple risk assessment and evaluation of psychological burden. Further research aims to conduct psychological burden measurements using a GSR sensor to aid quantification. According to the data obtained, psychological burden risk classes will be created based on severity level. A severity coefficient will be assigned to each class, which will be further taken into account in the calculation of the isik and hence the proposed matrix will be adjusted. However, the main objective remains the development of a risk matrix for the assessment of psychological distress that is simple and applicable in practice.

Acknowledgments: This research has been supported by the grant of KEGA Nr. 026TUKE-4/2023 Development Knowledge Support in the field of the quality management system requirements implementation in Aviation, Space and Defense Industry.

Conflicts of Interest: The authors declare no conflict of interest.

References

1. Šušoliaková, O. kol.: Hygiena. 2011. ISSN 1802-6281
2. Vavrinský, E., Tenkovrstvové mikroelektródy pre elektorchemické vodivostné senzory aplikované v biomedicínskom monitorovaní stresu. Dissertation thesis. STU FEI, 2005
3. Morales, Analúcia; Barbosa, Maria; Morás, Laura; Cazella, Silvio César; Sgobbi, Lívia F. et al. Occupational Stress Monitoring Using Biomarkers and Smartwatches: A Systematic Review. Online. Sensors. 2022, Vol. 22, No. 17. ISSN 1424-8220. From: https://doi.org/10.3390/s22176633.

4. Decree No. 542/2007 Coll. of the Ministry of Health of the Slovak Republic of 28.11.2007 on the protection of health against physical stress at work, psychological workload and sensory stress at work.
5. Sventeková, Eva; Makovická Osvaldová, Linda; Dlugoš, Ivan; Malý, Stanislav. Psychická pracovná záťaž ako rizikový faktor pracovného prostredia. Krízový manažment. 2021. ISSN 1336 – 0019. DOI: 10.26552/krm.C.2021.2.25-32
6. BRUNZINI, Agnese; PERUZZINI, Margherita; GRANDI, Fabio; KHAMAISI, Riccardo Karim a PELLICCIARI, Marcello. A Preliminary Experimental Study on the Workers' Workload Assessment to Design Industrial Products and Processes. Online. *Applied Sciences*. 2021, roč. 11, č. 24. ISSN 2076-3417. Dostupné z: https://doi.org/10.3390/app112412066.
7. LONGO, Luca; WICKENS, Christopher D.; HANCOCK, Gabriella a HANCOCK, P. A. Human Mental Workload: A Survey and a Novel Inclusive Definition. Online. *Frontiers in Psychology*. 2022, roč. 13. ISSN 1664-1078. Dostupné z: https://doi.org/10.3389/fpsyg.2022.883321.
8. Kakemam, Edris; Raeissi, Pouran; Raoofi, Samira; Soltani, Ahmad; Sokhanvar, Mobin et al. Occupational stress and associated risk factors among nurses: a cross-sectional study. Online. Contemporary Nurse. 2019, Vol. 55, No. 2-3, pp. 237-249. ISSN 1037-6178. From: https://doi.org/10.1080/10376178.2019.1647791.
9. Rasool, Samma Faiz; Wang, Mansi; Zhang, Yanping a Samma, Madeeha. Sustainable Work Performance: The Roles of Workplace Violence and Occupational Stress. Online. International Journal of Environmental Research and Public Health. 2020, Vol. 17, No. 3. ISSN 1660-4601. From: https://doi.org/10.3390/ijerph17030912.
10. Crump, John H.; Cooper, Cary L.; Smith, Mike. Managerial, Occupational and Organizational Stress. Investigating occupational stress: a methodological approach. 2001. No.1. ISBN 9781315196244. From: https://www.taylorfrancis.com/chapters/edit/10.4324/9781315196244-35/investigating-occupational-stress-methodological-approach-john-crump-cary-cooper-mike-smith
11. Mohajan, H.K.. The Occupational Stress and Risk of it among the Employees. International Journal of Mainstream Social Science. 2012. Vol. 2(2), pp. 17–34. From: https://mpra.ub.uni-muenchen.de/50860/1/MPRA_paper_50860.pdf
12. Ilies, Remus; Dimotakis, Nikolaos a De Pater, Irene E. Psychological and physiological reactions to high workloads: Implications for well-being. Online. Personnel Psychology. 2010, Vol. 63, No. 2, pp. 407-436. ISSN 0031-5826. From: https://doi.org/10.1111/j.1744-6570.2010.01175.x. Cit. [2024-06-27]
13. Ratna, Sari Dewi; Riana, I Gede. The Effect of Workload on Role Stress and Burnout. Journal of Multidisciplinary Academic. Science, Engineering and Social Science Series. 2019, Vol. 3, No. 3. ISSN: 2541-0369/2613-988X
14. Meijman, Theo F.; Mulder, Gijsbertus. Work Psychology – Psychological Aspects of Workload. 2005. ISBN 9780203765425
15. Kordošová, Miroslava: Psychosociálne riziká sú tiež pracovné riziká. Bulletin IVPR, 2023, Vol. 4, Iss. 4. ISSN 2729-9767
16. Michalík, D.: Psychosociální rizika ve firemní praxi., 2015 In: Bezpečnost a hygiena práce, pp.37-38.
17. EU-OSHA: European risk observatory report: Expert forecast on emerging psychosocial risks related to occupational safety and health. Luxembourg, 2007.
18. European Agency for Safety and Health at Work. www.osha.europa.eu. Psychosocial risks and mental health at work. Online. Form: https://osha.europa.eu/en/themes/psychosocial-risks-and-mental-health

TECHNICAL UNIVERSITY OF KOŠICE
Faculty of Mechanical Engineering

A Case Study on Improvements for Sumo Robotics Competitions

Damian Pytka [1,*], Daniel Jancarczyk [1] and Maksymilian Maślanka [1]

[1] Faculty of Mechanical Engineering and Computer Science, University of Bielsko-Biala, 43-309 Bielsko-Biala, Poland; mmaslanka@ubb.edu.pl (M.M.); djancarczyk@ubb.edu.pl (D.J.); dpytka@ubb.edu.pl (D.P.)
* Correspondence: dpytka@ubb.edu.pl

Abstract: This study presents a detailed examination of the iterative design enhancements of a standard sumo robot for competitive applications. The robot underwent significant modifications based on competition insights. Key improvements included reinforcing structural components, increasing weight and improving control algorithms. These enhancements resulted in notable achievements, including medals at national and international sumo robotics competitions between 2021 and 2024. Future development efforts will focus on implementing additional sensors, and real-time operating systems. This case study highlights the importance of iterative design and performance feedback in advancing robotics for competitive environments.

Keywords: Autonomous mobile robots; Robotics competitions; Iterative design

1. Introduction

The sumo robot is modeled after the traditional Japanese sport of sumo wrestling. It is a microcontroller-based mobile robot designed primarily for entertainment and competitive sports applications [1]. During a sumo robot competition, two robots face off in a circular arena, with the goal of forcing the opponent out of the ring, which is delineated by a boundary line. The robot that successfully pushes its opponent out of the arena is declared the winner [2]. Achieving victory in such matches requires addressing a range of design challenges. This paper focuses on analyzing the advancements in standard sumo robot design and performance over years of participation in sumo competitions.

2. Standard sumo dohyo and robot requirements

The dohyo interior refers to the playing surface, which includes the boundary line and the area enclosed within it. Any region beyond this boundary is designated as the dohyo exterior. The ring is circular in shape and adheres to specific dimensional standards, with a diameter of 154 cm for the standard sumo category. The thickness of the boundary line is specified by the regulations of each event and may vary slightly depending on the competition venue [3].

Robots must conform to the size constraints of their respective class, fitting within a square of specified dimensions prior to the start of a match. While robots are permitted to expand in size after the match begins, they must remain a single structure and may not physically separate into multiple parts. Non-compliance with these rules will result in disqualification from the match. However, minor components with a combined mass of less than 5 grams detaching from the robot during the match will not result in disqualification. For the standard sumo category, robots must adhere to strict size and weight limitations, with a maximum length and width of 20.0 cm and a maximum weight of 3.0 kg [3].

3. Initial robot project

The design of an autonomous mobile robot necessitates careful consideration of various components and subsystems. The primary aspects requiring critical project decisions include:

- Selection of materials and manufacturing processes for key robot components, such as the base, wheels, and pusher.
- Choice of motors to drive the robot.
- Determination of the power supply strategy for both the motors and electronic systems.
- Specification of the control architecture to be implemented.

For this robot, a 3 mm steel plate was selected as the material for both the base and the pusher. The base was fabricated with milled cutouts and screw mounting holes, while the pusher was manually sharpened to prevent opposing robots from sliding underneath and gaining an advantage.

The choice of motors was influenced by size constraints; metal gearmotors with dimensions of 37Dx57L mm were selected, as they fit end-to-end within the 20 cm size limit, enabling direct wheel drive without the need for additional gears or belts. A 100:1 gearbox was chosen as an optimal balance between torque and speed. The selection of 12V motors determined the power source, which was a 4S Li-Pol battery.

The control system is based on the ATmega328P microcontroller, selected for its advantageous for this purpose features. The microcontroller's large DIP28 footprint facilitated the design of a single-layer printed circuit board (PCB) for the robot controller, enabling manual fabrication. Additionally, the microcontroller was chosen for its ease of programming, as the Arduino IDE software was utilized for firmware development. Motor control is achieved using a commercial H-Bridge.

For enemy detection, modulated infrared proximity sensors were selected. Although these sensors had the shortest range among the options considered, they demonstrated superior resistance to interference from infrared radiation emitted by various light sources, making them a reliable choice for this application.

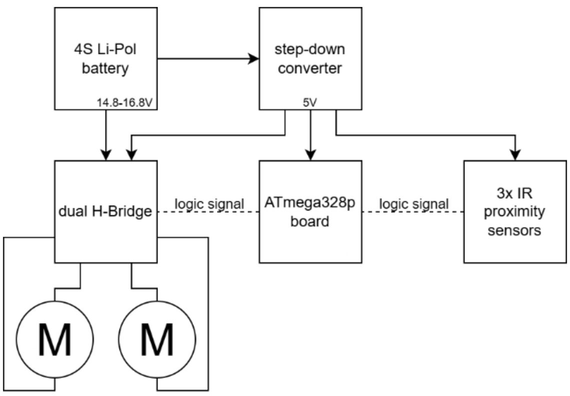

Figure 1. Conceptual diagram of power supply and logic signals.

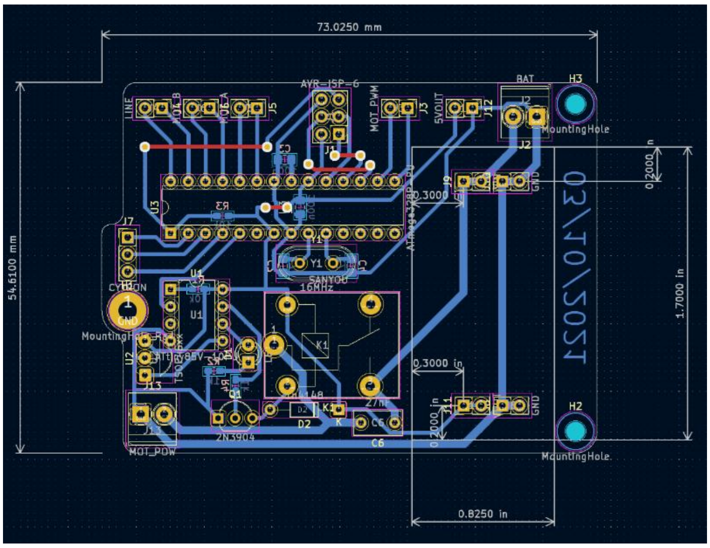

Figure 2. Single layer printed circuit board layout.

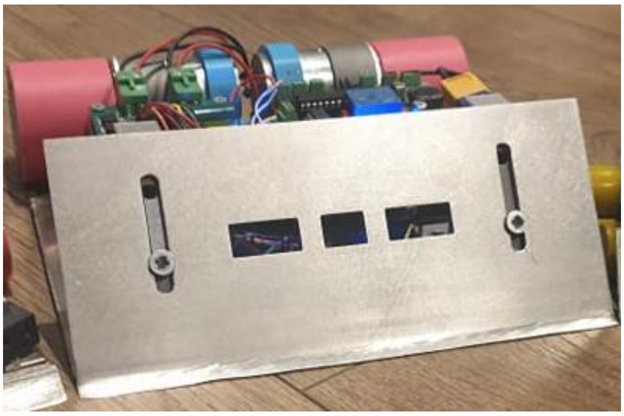

Figure 3. Assembled standard sumo robot from initial project

4. Improvements to the project

The competition with various opponents provided valuable experience and revealed shortcomings in the initial design. The motor mounting components were replaced with more robust elements, and 3D-printed parts substituted the original mounting brackets supplied by the motor manufacturer. Wheel hubs, initially 3D-printed to reduce the moment of inertia, were prone to cracking and were replaced with hubs machined from aluminum.

The robot's original weight of 1.6 kg made it susceptible to being kicked up by heavier opponents; therefore, weights were added to increase its mass to 2.6 kg. Additionally, the robot's open sides were enclosed with 3D-printed elements to prevent opponents from gaining an advantage by hooking onto the rear of the robot's pusher.

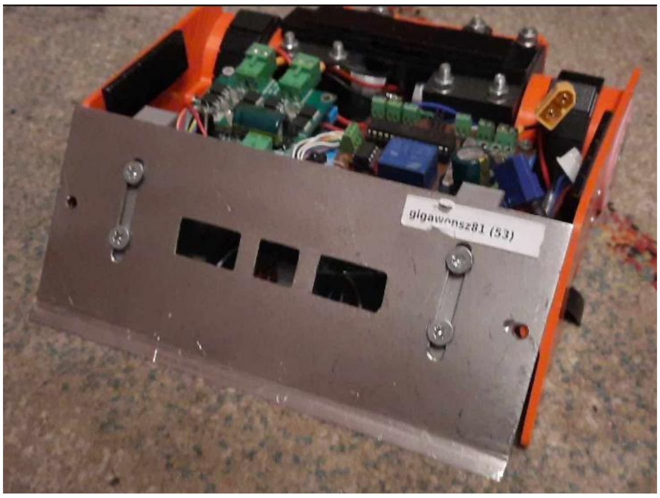

Figure 4. Standard sumo robot after improvements.

Initially, the robot exhibited instability in the operation of the control board. This issue was addressed by adding an electrolytic capacitor after the step-down converter and a ceramic capacitor directly to the power supply pins of the microcontroller.

Additionally, line sensors were integrated into the robot's base to enable the detection of the white boundary line on the edge of the dohyo. Following the integration of these sensors, the robot's control algorithm was updated, ensuring that the robot no longer exited the boundaries of the combat arena by itself.

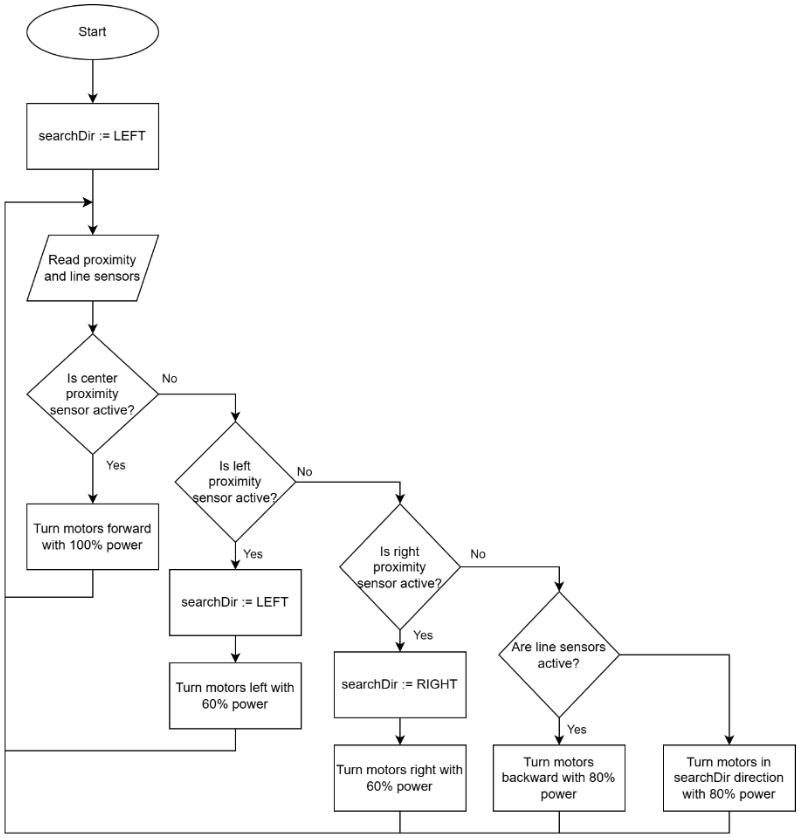

Figure 5. Robot's combat strategy algorithm.

5. Conclusions

The improvements made to the standard sumo robot project, as discussed in this article, have led to significant competitive success at both national and international levels. The achievements include:

- Bronze medal at the XChallenge competition in 2024
- Bronze medal at the Robotic Arena competition in 2024
- Silver medal at the XChallenge competition in 2023
- Silver medal at the Robotic Tournament in 2023
- Gold medal at the EastROBO competition in 2021

Recording matches during these competitions enabled detailed analysis of individual matches, facilitating the identification of potential improvements. High-frame-rate recordings proved particularly valuable, allowing observation of details often overlooked during rapid matches (typically lasting less than 30 seconds).

Future development directions include:

- Incorporating a more advanced microcontroller
- Adding support for additional sensors, such as an accelerometer
- Implementing a real-time operating system to streamline sensor data processing independently of strategic algorithms

To enhance iterative refinement, a new robot is planned, leveraging insights gained from the initial project and current trends in robotics competitions. This new design will aim to minimize the robot's height while utilizing similar motors.

Conflicts of Interest: The authors declare no conflict of interest.

References

1. Aisuwarya, R.; Erlina, T.; Ferdian, R.; Yendri, D.; Darmawan, D. Designing a Microcontroller-Based Sumo Robot with Analysis of Thrust Parameters. In Proceedings of the 2023 2nd International Conference on Computer System, Information Technology, and Electrical Engineering (COSITE); 2023; pp. 49–54.
2. Erdem, H. A Practical Fuzzy Logic Controller for Sumo Robot Competition. In Proceedings of the Pattern Recognition and Machine Intelligence; Ghosh, A., De, R.K., Pal, S.K., Eds.; Springer Berlin Heidelberg: Berlin, Heidelberg, 2007; pp. 217–225.
3. Carbone, G.; Curcio, E.M.; Rodinò, S.; Lago, F. A Robot-Sumo Student Competition at UNICAL as a Learning-by-Doing Strategy for STEM Education. *STEM Educ.* **2022**, *2*, 262–274, doi:10.3934/steme.2022016.

Real-time monitoring of the response of the SMA actuator

Jaroslav Romančík [1,*], Marek Vagaš [1]

[1] Technical University of Kosice, Faculty of Mechanical Engineering, Department of Industrial Automation and Mechatronics; jaroslav.romancik@tuke.sk; marek.vagas@tuke.sk
* Correspondence: jaroslav.romancik@tuke.sk

Abstract: Modern technologies are increasingly focused on reducing the size and weight of devices. The actuator is a critical component of any movable mechanical system, making its miniaturization a key area of emphasis. Intelligent materials with unique properties play a significant role in achieving this goal. This paper explores the design, fabrication, and testing of a NiTinol-based actuator utilizing antagonistically operating springs. These springs are alternately heated to generate the rotational motion of a bearing. One of the primary challenges addressed in this study is the precise position tracking of the system. This article aims to highlight the potential of NiTinol in modern technology and its significant contribution to the development of innovative and efficient actuators.

Keywords: Nitinol spring, Shape Memory Alloy, Linear potentiometer

1. Introduction

The actuation of devices necessitates innovative solutions to enhance their efficiency and functionality. A prevailing trend in contemporary technology is miniaturization—the reduction of devices' size and weight—which expands their applicability across diverse fields, from medicine to industrial automation. A pivotal enabler of these innovations is the development of intelligent materials that exhibit unique properties. Among these materials, NiTinol (nickel-titanium alloy) has garnered significant attention in recent years due to its exceptional shape memory properties [1,2].

NiTinol can revert to its original, pre-defined shape upon heating above a specific activation temperature, a phenomenon known as the shape memory effect (SME). This effect is driven by a phase transformation in the material's internal structure between the austenitic phase (stable, rigid, and high-temperature) and the martensitic phase (flexible, deformable, and low-temperature) [3,4].

This transformation underpins the use of NiTinol as a linear actuator—a device capable of converting thermal energy into mechanical motion and force. Despite its advantages, such as a high force-to-weight and force-to-size ratio, which surpasses conventional pneumatic and hydraulic systems, NiTinol-based actuators face certain challenges. Key issues include relatively slow response times and hysteresis effects. Nevertheless, these actuators present a promising solution in applications where compact size and low weight are paramount [5,6].

This article provides a detailed examination of the properties of NiTinol, its applications in various sectors, and ongoing research aimed at overcoming its current limitations. NiTinol is commonly utilized in the form of wires or springs, each offering distinct characteristics. Wires are ideal for generating high forces but are limited to approximately 4% linear contraction. Springs, on the other hand, provide greater displacement, making them better suited for applications requiring significant linear motion, albeit at the cost of reduced force generation. In our study, we opted for the spring configuration to achieve the desired linear displacement. To accurately measure the actuator's position, we developed an economical and straightforward solution using linear potentiometers. In this setup, one end of the spring is fixed to a stationary structural point, while the other end is connected to the potentiometer's slider. As the spring extends or contracts, its linear displacement translates into a change in the potentiometer's resistance, which can be monitored and processed to determine the actuator's precise position. This approach offers a cost-effective and reliable method for tracking the end-point position of the NiTinol spring.

2. Materials and Methods

The use of a spring as an actuator requires the creation of a mechanical configuration—a setup where the spring is integrated with additional components to generate a force opposing the contraction force. Several approaches can achieve this. In our study, we opted for an antagonistic arrangement of two NiTinol springs (Figure 1.). This configuration is characterized by two NiTinol springs coupled and preloaded at a single point. When the first spring is heated above its activation temperature, it begins to contract and generate force, thereby elongating the second spring. Conversely, heating the second spring initiates a similar process, with the roles of the springs reversed [7].

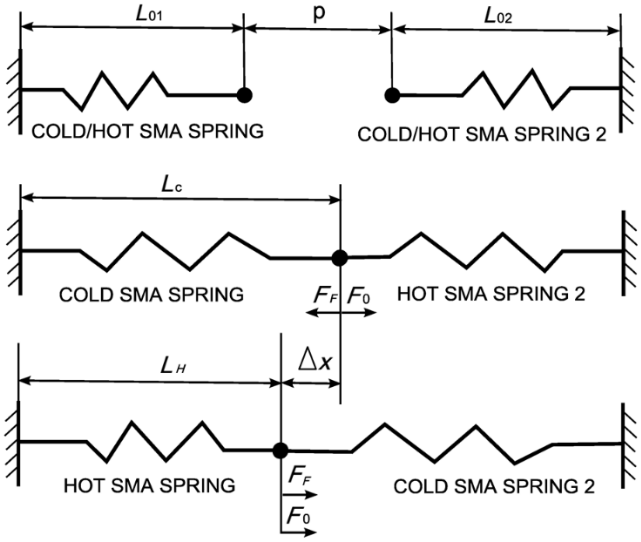

Figure 1. Antagonistically working NiTinol springs [7].

To monitor the contraction and elongation of the springs, we sought a cost-effective and reliable solution. Our approach involved the use of linear potentiometers. Linear potentiometers are three-terminal resistors. Two terminals are connected to the ends of the resistive element, establishing a fixed resistance between them. The third terminal is connected to a slider that moves along the resistive track, altering the resistance between the slider and the other terminals. In our setup, the resistive element is powered by a direct current (DC) voltage. This configuration allows for precise tracking of the spring's movement, enabling real-time monitoring and control of the actuator's operation [8].

3. Actuator design

In the design of the actuator, two aspects are considered: the mechanical and the software aspects. The mechanical aspect is addressed through structural design, while the software aspect is managed using MATLAB as an interface for monitoring and visualizing the acquired data.

3.1. Structural design

The actuator designed in this study consists of the following fundamental components:

- Two RSAON12-10KBX2 linear potentiometers
- Two NiTinol springs
- Arduino UNO
- A 3D-printed bearing made of PETG
- A steel cable
- Sliders

The wire diameter from which the spring is made is 0.75 mm, and the length of the wire is 120 mm. The activation temperature is 40 °C, and their chemical composition is approximately 50% Ni 50%Ti. The linear potentiometers are housed within the PLA body. The sliders of the potentiometers are connected to the ends of the NiTinol springs using brackets, while the opposite ends of the springs are fixed securely within the actuator body. The opposing ends of the brackets are attached to the bearing, establishing a rotational coupling between the springs (Figure 2.).

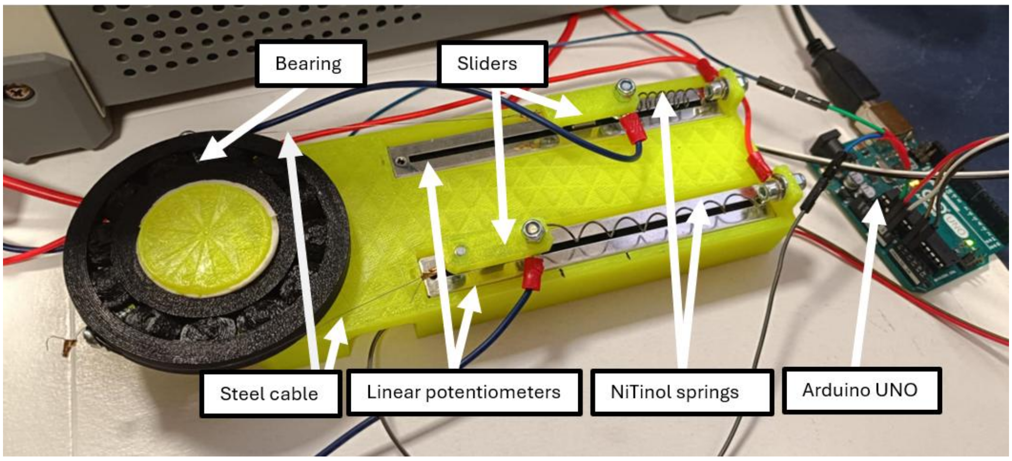

Figure 2. Components of the designed actuator.

During contraction and elongation of the springs, the bearing rotates. The radial rolling bearing was created using 3D printing technology from PET-G material.

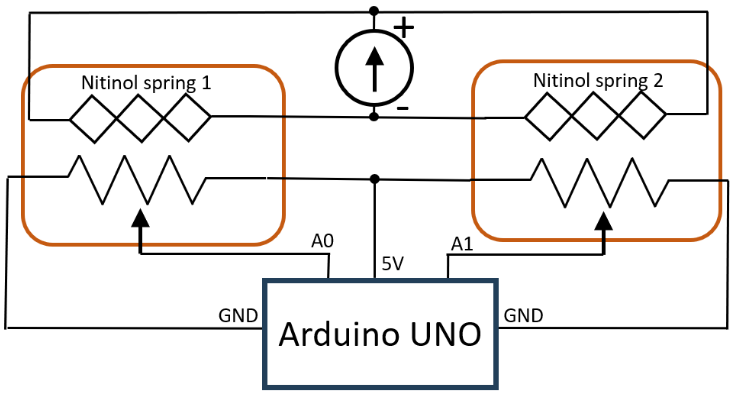

Figure 3. Electrical wiring diagram.

Furthermore, the extension and shortening of the springs are redundantly measured using the potentiometers, ensuring precise monitoring of the actuator's motion. The dimensions of the entire proposed device are 230 x 80 x 35 mm.

3.2. Software

The outputs from the potentiometers are transmitted to a PC via Arduino UNO, functioning as a data bus. The data are captured, processed, and visualized as graphs using the MATLAB platform. Data from both potentiometers are recorded simultaneously (Figure 4.).

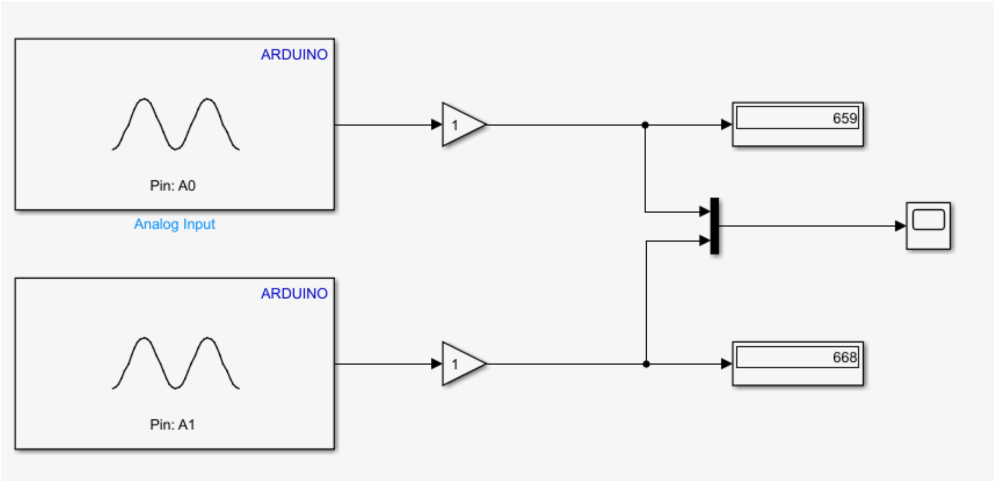

Figure 4. Program in the MATLAB environment – Simulink.

The data evaluation is performed by a custom graphical program developed within MATLAB's Simulink graphical programming environment.

4. Experiment

The objective of our experiment was to acquire and visualize the positional data of the sliders—representing the endpoints of the NiTinol springs—during alternating heating cycles and the resulting rotation of the bearing. Experimental data were collected as resistance values from the potentiometers and plotted over time. The experiment was conducted in two distinct phases. In the first phase, the first spring was heated, resulting in its contraction and the simultaneous elongation (deformation) of the second spring. This antagonistic relationship between the springs was reflected in the data.

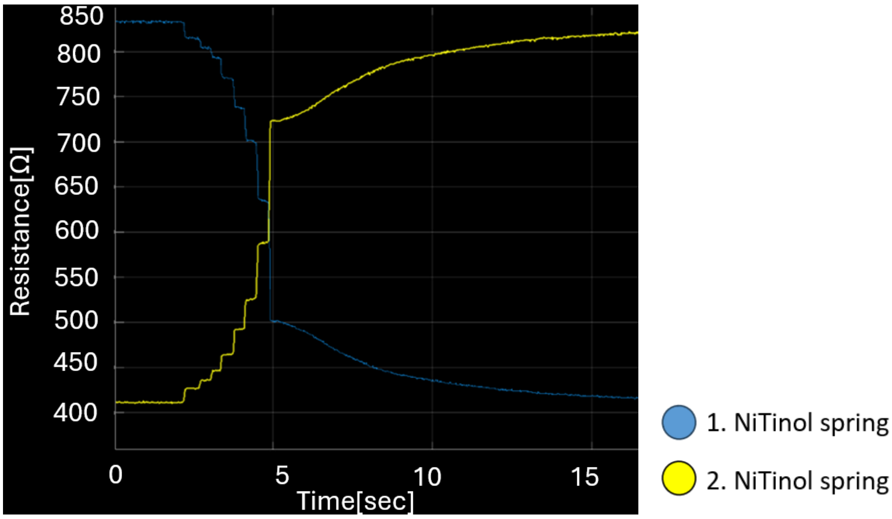

Figure 5. Experimental data obtained from the potentiometers – first phase.

In the corresponding graph, the contraction of the first spring is represented by a blue curve. The graph demonstrates that as the first spring contracts, the second spring undergoes an antagonistic elongation, with the displacement of its endpoint depicted by the yellow curve (Figure 5.).

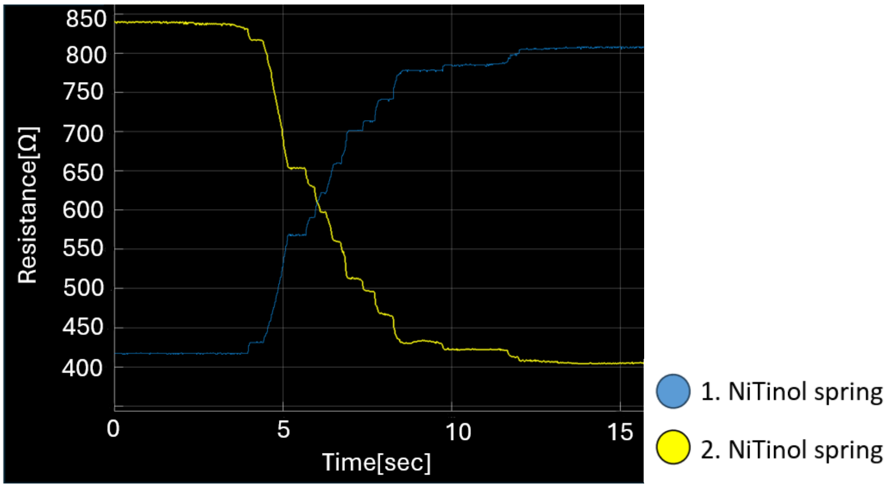

Figure 6. Experimental data obtained from the potentiometers – second phase.

Similar results were observed during the heating of the second spring, where the roles were reversed—the second spring contracted, while the first spring elongated antagonistically. This behavior confirms the expected interplay between the springs, validating the efficacy of the designed actuator system in producing controlled and predictable motion (Figure 6.).

5. Discussion

This article focuses on the design of an actuator driven by two NiTinol springs. The proposed structural solution was verified through data visualization, using graphs to represent the observed results. The response time is conditioned by the write speed and the communication of peripheral devices with the PC for data processing using Matlab-Simulink – internal cycle time, which is not real-time. The acquired data will serve as a foundation for further research in the field of position regulation for NiTinol springs. Additionally, a future direction of this research is the integration of controllable devices with similar actuators, such as fingers of a robotic manipulator, which could be controlled and positioned using such a system. This opens possibilities for advanced applications in robotics and automation, where precise movement and adaptability are essential.

Acknowledgments: This work has been supported by the Slovak grant VEGA 1/0169/22 New methodics approaches to data from automated and robotized workplaces.

Conflicts of Interest: The authors declare no conflict of interest.

References

1. J.M. Jani, M. Leary, A. Subic, M.A. Gibson, A review of shape memory alloy research, applications and opportunities, Materials & Design (1980-2015), vol. 56, 2014, s. 1078-1113,ISSN 0261-3069.
2. K. Susmita, Introduction, Classification and Applications of Smart Materials: An Overview, American Journal of Applied Sciences 10 (8), Jul. 2013, ISSN:1546-9239
3. B. Zohuri, F. Behgounia, F. Behgouni, M. J. Moghaddam, Memory Metals or Shaping Alloys, Modern Approaches on Material Science, Feb. 2021, s. 415-423, ISSN: 2641-6921.
4. M. Kim, J. Heo, H. Rodrigue, H. Lee, S. Pané, M. Han, S. Ahn, Shape Memory Alloy (SMA) Actuators: The Role of Material, Form, and Scaling Effects, Advanced materials, vol. 35 (33), Aug. 2023, doi:10.1002/adma.202208517
5. G. Costanza, M.E. Tata, C. Calisti. Nitinol one-way shape memory springs: Thermomechanical characterization and actuator design, Sensors and Actuators A: Physical, January 2010, Volume 157, Issue 1, pp. 113-117.

6. S. Ba hl, H. Nagar, I.Singh, S. Sehgal, Smart materials types, properties and applications: A review, Materials Today: Proceedings,Vol. 28, Part 3,2020, s.1302-1306, ISSN: 2214-7853.Author 1, A.; Author 2, B. Title of the chapter. In Book Title, 2nd ed.; Editor 1, A., Editor 2, B., Eds.; Publisher: Publisher Location, Country, 2007; Volume 3, pp. 154–196.
7. O. M. A. Taha, M. B. Bahrom, O. Y. Taha, M. S. Aris, Experimental study on two way shape memory effect training procedure for nitinol shape memory alloy, ARPN Journal of Engineering and Applied Science, September 2015, Volume 10, No.17, ISSN 1819-6608A. Spaggiari, I. Spinella, E. Dragoni, Design Equations for Binary Shape Memory Actuators Under Arbitrary External Forces, Journal of Intelligent Material Systems and Structures, Mar. 2012, doi: 10.1177/1045389X12444491.
8. Anonym, Potentiometer: Definition, Types and Working Principle, RoboCraze, quoted: Dec. 2024, available: https://robocraze.com/blogs/post/what-is-potentiometer?srsltid=AfmBOor1A99SgxZSXb7mfQNWV-NY2rOqkcoQKm-nuwITb6kD9m3hWpuRY

TECHNICAL UNIVERSITY OF KOŠICE
Faculty of Mechanical Engineering

The influence of the galvanizing method on the surface properties of thin steel sheets.

František Ruda [1,*], Emil Spišák [1]

[1] Department of Technology, Materials and Computer Aided Technologies, Faculty of Mechanical Engineering, Technical University of Košice, Mäsiarska 74,040 01 Košice, Slovakia; frantisek.ruda@student.tuke.sk; emil.spisak@tuke.sk
* Correspondence: frantisek.ruda@student.tuke.sk; Tel.: +421 910 947 185

Abstract: Galvanized steel is a material widely used in various industries and construction. Its corrosion resistance, durability, and affordability make it a preferred choice for many applications. The galvanization method significantly impacts the surface properties of thin steel sheets. Hot-dip galvanizing creates a thicker, more durable zinc layer, protecting against corrosion and mechanical damage. The surface can be shiny or matte, depending on the steel's chemical composition and the galvanizing process. This paper compares two methods of producing galvanized coatings: GI (Galvanized) and GA (Galvanneal) coatings, focusing on identifying superior properties for steel strip coatings.

Keywords: Sheet metal, zinc, aluminum, coating, slag.

1. Introduction:

Galvanized steel is a steel material protected against corrosion by a zinc layer. Zinc is applied to the steel surface using various methods, most commonly through immersion in molten zinc (hot-dip galvanizing) [1]. The zinc layer forms a barrier that protects the steel from weathering, moisture, and chemicals, significantly extending its lifespan [2-4]. Hot-dip galvanizing is the most common method for galvanizing steel [1]. This material is most often used in transport infrastructure (guardrails, traffic signs), construction (building structures, cladding, roofing, gutters, railings), energy (electricity poles), agriculture (greenhouse structures, fencing, storage silos), and the automotive industry (car bodies, exhausts, doors, etc.) [2-4].

Advantages of galvanized material::

• Corrosion resistance: Effectively protects steel even in high humidity or salty environments.
• Longevity: Durable for several decades due to its corrosion resistance.
• Mechanical resistance: The zinc coating absorbs impacts, protecting the steel substrate.
• Low maintenance: Requires minimal upkeep, often limited to occasional cleaning.
• Aesthetic appearance: A shiny zinc surface provides an attractive look, which can be easily painted.
• Recyclability: Fully recyclable in a closed loop, easily separated from other materials with magnets. Thus, this material will be used for a long time.

2. Development of Continuous Hot-Dip Galvanizing and Current Manufacturing Process.

The difference between immersion galvanizing and continuous galvanizing lies in the coating. Immersion galvanizing offers extended corrosion resistance with thicker coatings and produces materials without trimming [5] Continuous galvanized sheets have thinner, more flexible coatings without intermetallic compounds [5-6].

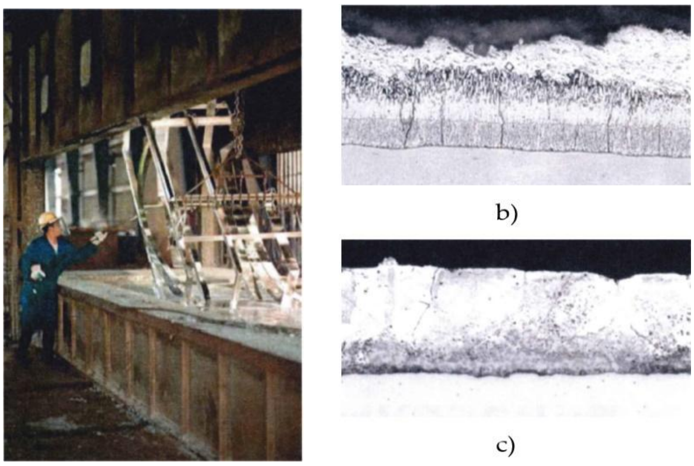

b)

c)

a)

Figure 1. – a) Galvanizing line, b) Dip galvanizing, c) Continuous galvanizing

Before the actual galvanizing process, the sheet must be pre-treated to ensure that the final material meets customer requirements and fulfills all conditions regarding mechanical properties, coating quality, and cleanliness. The material flow is shown in Figure 2.

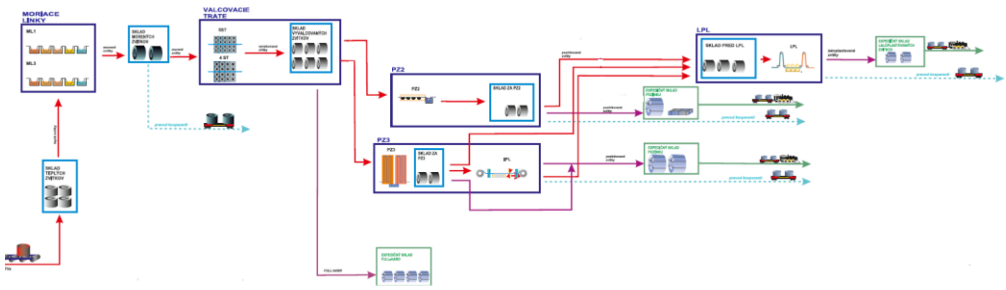

Figure 2. Material flow.

3. Hot- Dip Galvanizing.

Hot-dip galvanizing is a method of applying a zinc layer to a steel strip to achieve the desired surface quality. [7] The formation of a thin intermetallic layer Fe-Al results in a smaller coating thickness, increased adhesion, ductility, glossiness, excellent corrosion resistance, relatively low cost, good formability, paintability, and weldability of galvanized steel sheets [8-10].

Production Method:

The material entering the galvanizing line has a thickness of 0.4 – 2.00 mm and predetermined mechanical properties achieved through previous cold forming on various rolling lines (4 – 5 stands). The coil is delivered to the galvanizing line according to requirements, fed into the uncoiler, welded, and then passed through a storage section to the cleaning area. Here, it is stripped of impurities and scale. It then continues into an annealing furnace where it is annealed to achieve the desired properties before galvanizing. Next, the strip passes through heated rollers (465 - 490 °C) into the zinc bath (458 – 474 °C). It proceeds through air knives, into the GA furnace (during GA coating production), through cooling into a storage section. Subsequently, the strip is rolled, flattened, passivated, and dried. Finally, it is oiled, trimmed, and wound into its final form coil.

3.1. Hot- Dip GI - Galvanized

This is the most widespread method of corrosion protection.

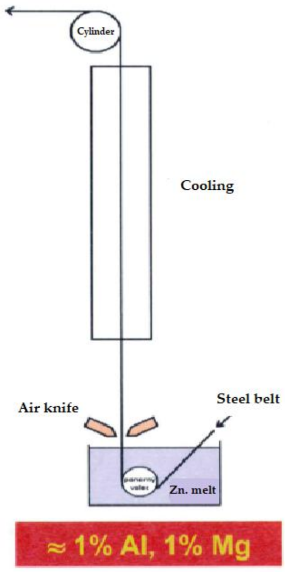

a)

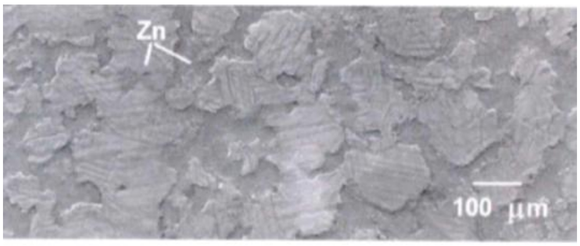

b)

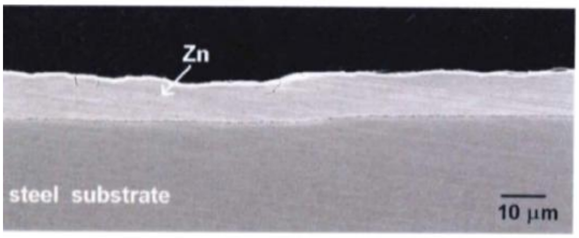

c)

Figure 3. a) method of production and %Al in the malt, b) surface structure of the GI coating, c) cross- section of the GI coating.

One of the most important parts of GI and GA galvanizing is the zinc bath and its composition.

- Aluminum (Al) – Alloying element that improves zinc coating properties – controls reactivity.
- Antimony (Sb) - Previously lead (Pb), these are alloying elements that improve steel wettability during coating, forming zinc flowers.
- Iron (Fe) - Released from the steel strip – creates intermetallic porticles.

Dross form in the Zn melt. Solid particles create upper and dross layers. The formation and placement of dross are shown in Figure 4.

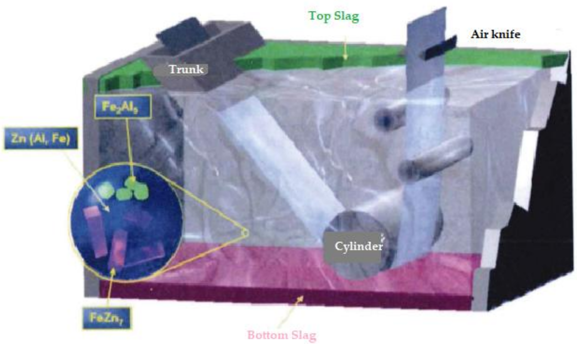

Figure 4. Galvanizing process in Zn bath.

Figure 5 shows the solubility curve of iron and aluminium in zinc. Important components of the molten zinc bath are the upper and lower dross.je uvedená krivka rozpustnosti železa a hlinika v zinku. Dôležite súčast roztaveneho zinkoveho kúpela sú spodná a vrchná trosku

Upper dross: $Fe_2Al_5Zn_x$ – wt% Al – 45, wt. % Fe 35, wt% Zn 20, density 4,5 g/cm^3 – floats.
Lower dross: $FeZn_{7\text{-}10}(\delta)$ – wt% Al – 1,5, wt% Fe 6, wt% Zn 92,5, density 7,2 g/cm^3 – sinks.

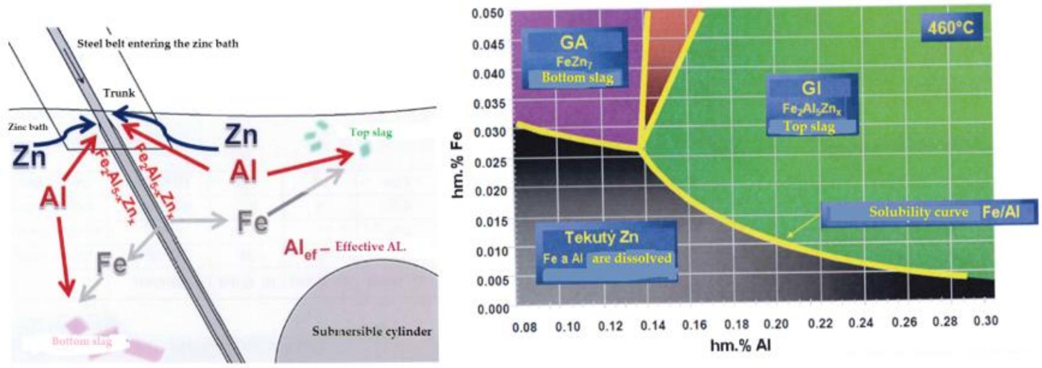

a) b)

Figure 5. a) method of zinc and aluminum deposition on steel sheet from upper dross, b) solubility of iron and aluminum in zinc.

During GI material production, upper dross forms when aluminum is maintained between 0,15% and higher 0,19 – 0,20%.

Effective aluminum (Al ef.) significantly affects surface quality, improving adhesion, weldability, and uniform appearance [11-14].

Too low Al content results in: more difficult removal of the zinc coating, poor coating adhesion, thicker coating. Cross-sections of zinc coatings with low and optimal aluminum percentages are shown in Figures 6 and 7.

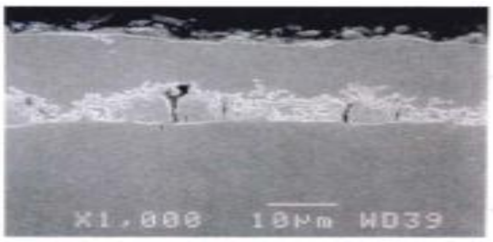

Figure 6. Cross-section of coating with low %Al.

Optimal Al ef.: Good coating adhesion, thinner coating.

Figure 7. Cross-section of coating with optimal %Al.

3.1.1 Role of Al ef in the melt during zinc coating formation

Figure 8 illustrates the effect of aluminum on the galvanized coating.

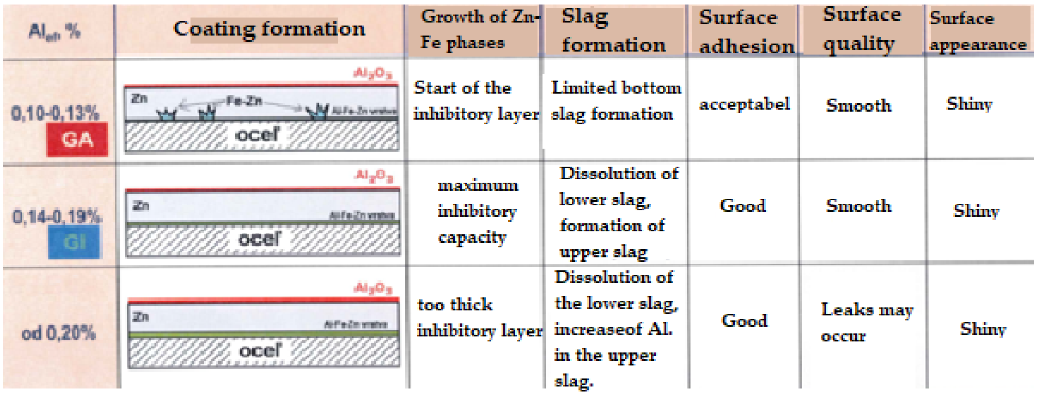

Al_{ef} %	Coating formation	Growth of Zn-Fe phases	Slag formation	Surface adhesion	Surface quality	Surface appearance
0,10-0,13% GA	Al_2O_3 Zn Fe-Zn oceľ	Start of the inhibitory layer	Limited bottom slag formation	acceptabel	Smooth	Shiny
0,14-0,19% GI	Al_2O_3 Zn oceľ	maximum inhibitory capacity	Dissolution of lower slag, formation of upper slag	Good	Smooth	Shiny
od 0,20%	Al_2O_3 Zn oceľ	too thick inhibitory layer	Dissolution of the lower slag, increaseof Al. in the upper slag.	Good	Leaks may occur	Shiny

Figure 8. Effect of aluminum on the coating.

Coating thickness is controlled by two methods: measuring heads – isotope gauge (on-line) and in the laboratory. Coating thickness ranges from 40 to 225 g/m² on one side! Methods for measuring coating thickness are shown in Figure 9.

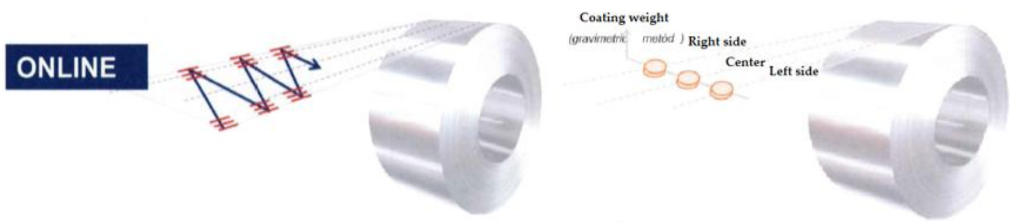

Figure 9. Coating measurement on-line and in the laboratory.

The zinc surface is categorized as follows: - **Surface of usual quality A** allows various scratches, blisters, abrasions, pores, passivation spots, deformation lines, **Improved surface B** allows minor transverse cracks, roller imprints, waviness, fine pores, minor defects caused by passivation, **Best quality surface C** must allow uniform application of quality paint material.

3.2. Galvannealed Coating GA – Overview of Key Technological Parameters

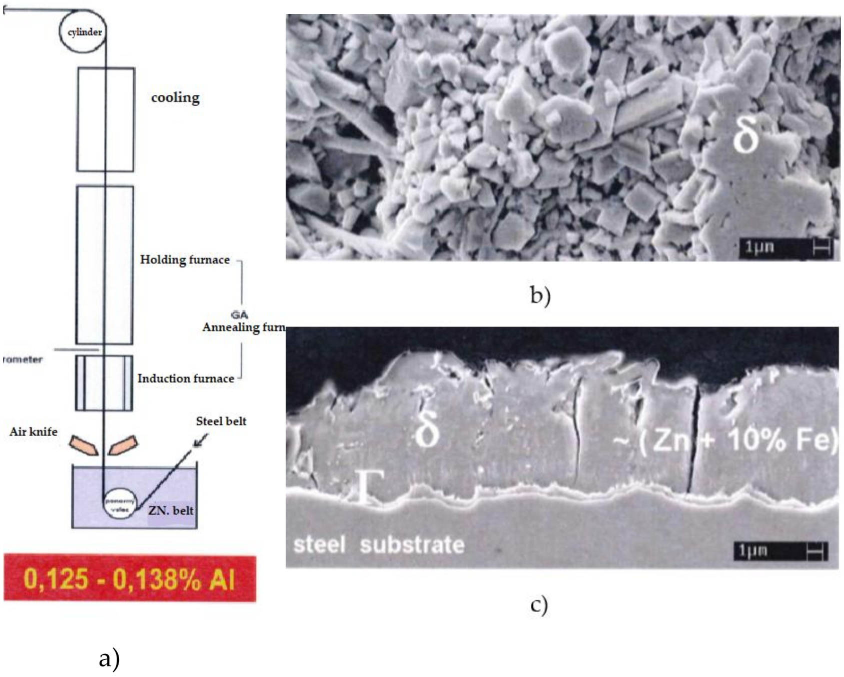

Figure 10. a) illustrates the formation of the GA layer, b) shows the surface structure of the GA layer, and c) depicts a cross-section of the GA coating.

GA Coatings: These are superior to GI coatings and are widely used in the automotive industry for surface parts. They offer better weldability, excellent paintability, increased scratch resistance, and lower zinc consumption compared to GI. The appearance is dark gray and non-flaky. The placement of the GA furnace in the galvanizing process is shown in Figure 11.

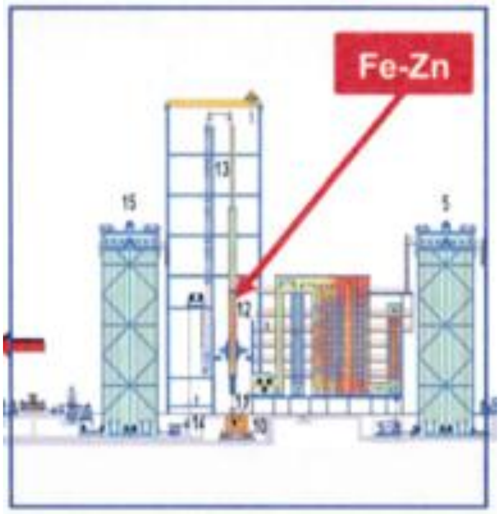

Figure 11. Location of the GA furnace.

In the Ga induction furnace, there are two pyrometers and six thermocouples for temperature control. The GA furnace consists of three parts: induction furnace, movable holding furnace, and fixed holding furnace. Induction heating involves an AC voltage source, an inductor, and heated material placed in the induction coil space (Figure 12).

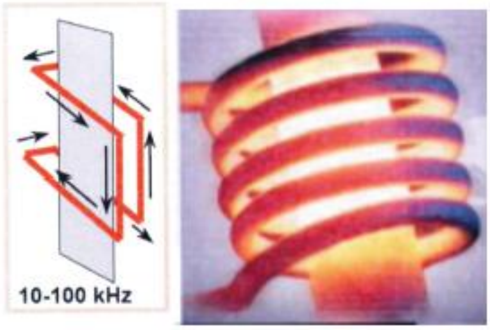

Figure 12: Induction Heating.

Advantages of Induction Heating:
- System reliability (instant on/off, precise temperature control)
- High productivity (heating rate of 1000°C/s)
- Improved quality (no contact with flame, contamination-free)
- Environmental protection (clean process without exhaust)
- Reduced energy consumption (90% process efficiency)

Coating thickness ranges from 30-90 g/m² on one side. Coating measurement is conducted online using two isotopic gauges, with additional adhesion tests performed in the lab. Figure 13 shows methods and sampling locations for coating tests.

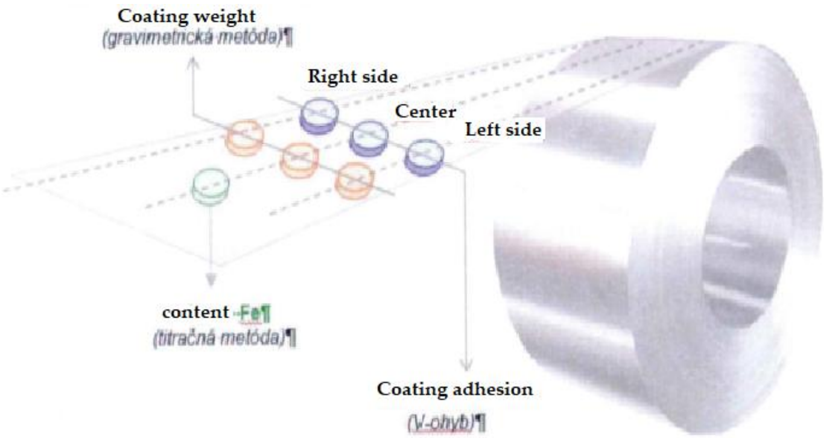

Figure 13. Biting GA material.

4. Conclusion:

Comparing GI (galvanized) and GA (galvannealed) coatings reveals specific advantages based on customer requirements. GI coatings provide better corrosion resistance and a smoother surface, beneficial for aesthetics and oxidation protection. In contrast, GA coatings offer higher hardness and better paint adhesion, making them suitable for the automotive industry while enhancing mechanical resistance. Analysis indicates that GI coatings are generally more advantageous for most production due to lower costs and improved formability and finishing options like painting.

Acknowledgments: This work was supported by the project APVV-21-0418 and project KEGA 018TUKE-4/2024.

Conflicts of Interest: "The authors declare no conflict of interest."

References

1. Billy, J.; Štefan, B.; Slávik, P.; Mikolaj, L.; Gašpar, V.: Oceľové plechy 3-4, 1993, s.21-27.
2. Buršak, M., et al: Proceeding from conf.: Materiál v inžinierskej praxi, 15.- 17.april, 2002, Herl'any s 168.
3. Blaščík, F., Polák, K.: Teória tvárnenia. Alfa Bratislava 1985, s. 374.
4. Blaščík, F. et al.: Technológia tvárnenia, zlievarenstva a zvárania. ALFA Bratislava , 1988.
5. Blaščík, F., Kmec, J. Automatizácia technologických pracovísk v plošnom tvárnení. ALFA Bratislava 1990, s. 393, ISBN 80-05-00055-3
6. Spišák, E., Slota, J., Majerníková, J.: Anisotropy evaluation of tinplates. In. Pro-tech-ma ´07 : Progressive Technologies and Materials: International Scientific Conference: Rzeszów – Bezmiechowa, Poland, 28th June – 30th June 2007. Rzeszów . Politechnika Rzeszowska, 2007. ISBN 978-83-7199-443-2. p. 217-222
7. ANDERSOM, J.C. et al.: Materials Science. Stanley Thornes Cheltenham, 1990, p. 608, ISBN 0-7487-4077-5
8. ASHBY, M.F.: Materials Selection in Mechanical Design. Heinemann, Third edition 2005, ISBN 0-7506-6168-2
9. ŠIMČÁK,D., BILLÝ,J., ŠTEFAN,B., KRAJČÍ,J.: Hodnotenie lisovateľnosti plechov pre automobilový priemysel. Hutnícke listy, 1998, č.6
10. STACHOWICZ,F. - SPIŠÁK,E.: Sposoby oceny zdolności blach cienkich do kształtowania plastycznego na zimno. Rzeszów 1998, s.121, ISBN 83-7199-078-2
11. Evin, E., Spišák, E., Majerníková, J.: Predikcia lisovateľnosti vysokopevných oceľových plechov. In: Materiál v inžinierskej praxí 2008: 7. vedecko-technická konferencia, Herl'any. Košice: TU, 2008, s. 79, ISBN 978-80- 8073-945-4.
12. Čech, J., Grutková, J., Kurian, J., Rodziňáková, O.: Náuka o kovoch, Návody na cvičenia. ALFA Bratislava, 1981
13. ZRŮNEK, Miroslav: Úprava povrchu kovových konstrukcí. Praha: SNTL- Nakladatelství technické literatury, 1981. 120 s. ISBN 04-209-81.
14. ČÍHAL, Vladimír: Kovové povlaky při protikorozní ochraně se zřetelem na jejich fyzikálně – chemické vlastnosti. In: Progresívní a netradiční technologie povrchových úprav: VI. Medzinárodná výstava povrchových úprav Protech ´98, Praha: Fakulta strojní ČVUT, 1998. s. 38 – 44.

TECHNICAL UNIVERSITY OF KOŠICE
Faculty of Mechanical Engineering

Reverse engineering of palate cleft impression trays

Natália Savková [1,*], Branko Štefanovič [1], Marek Schnitzer [1], Juraj Bánovčin [2] and Jozef Živčák [1]

[1] Department of Biomedical Engineering and Measurement, Faculty of Mechanical Engineering, Technical University of Košice, Letná 1/9, 042 00, Košice, Slovakia, dr.nataliasavkova@gmail.com, branko.stefanovic@tuke.sk, marek.schnitzer@tuke.sk, jozef.zivcak@tuke.sk
[2] Clinic of dentistry and maxillofacial surgery, Faculty of Medicine, Pavel Jozef Šafárik University in Košice, Trieda SNP 1, 040 11, Košice, Slovakia, juraj.banovcin@upjs.sk
* Correspondence: dr.nataliasavkova@gmail.com

Abstract: Cleft lip and palate (CLP), affect approximately 1 in 756 births and require comprehensive, individualized treatment strategies. Among the first important interventions is the creation of impression trays for nasoalveolar molding (NAM) plates, which help separate the oral and nasal cavities in newborns. However, traditional tray fabrication methods are labor-intensive, imprecise, and unsuitable for mass production. This study investigates the use of reverse engineering and additive manufacturing (3D printing) to streamline and enhance the production of CLP impression trays. Seventeen tray models were digitally designed using 3D scanning and computer-aided design (CAD) tools and fabricated via stereolithography (SLA) technology using PLA photopolymer resin. The trays demonstrated high precision, with an average consumable usage of 13.09 ml, a weight of 15.04 g, and a production time of approximately 2 hours and 30 minutes per tray. Batch production further reduces manufacturing times, demonstrating scalability. While CAD/CAM workflows significantly improve accuracy, customization, and reproducibility, challenges such as material optimization and cost barriers persist. Innovations like intraoral scanning hold promise for enhancing patient safety and comfort. This study highlights reverse engineering as a precise, efficient, and scalable solution for improving CLP treatment outcomes and clinical practices.

Keywords: impression trays, cleft palate, reverse engineering, CAD/CAM, additive manufacturing

1. Introduction

Orofacial clefts, including cleft lip and palate, occur in approximately 1 in 756 births and result from a disruption in the fusion of facial processes during early gestation. These conditions require long-term interdisciplinary care, and one of the first steps in treatment is creating an accurate impression for customized prosthetics, such as the NAM (nasoalveolar molding) plate, which helps separate the oral and nasal cavities [1–6].

Traditional methods of manufacturing cleft palate impression trays are labor-intensive and lack precision, making it difficult to mass-produce them for widespread clinical use. Advances in reverse engineering, including 3D scanning, computer-aided design (CAD), and additive manufacturing (3D printing), offer a promising solution to these limitations. These technologies enable the creation of accurate, reproducible, and efficient custom trays.

Although research on digital tools for cleft treatment is growing, challenges such as material selection and cost efficiency remain. This study explores the use of reverse engineering in designing cleft palate impression trays to improve production processes and enhance treatment outcomes. The results demonstrate that this approach offers a more precise, reproducible, and less labor-intensive solution for clinical applications.

2. Materials and Methods

2.1. Data Acquisition

A total of 17 palate cleft impression trays were 3D scanned using the optical 3D scanner Revopoint POP 2 (Revopoint 3D technology Inc., Shenzhen, China). Each tray was placed on a compatible turntable with the posterior side facing downward, which resulted in only the anterior surface being captured, as the scanner was unable to detect the posterior side. Scanning parameters were optimized to capture the trays' intricate geometry (Fig. 1). The resulting meshes were exported in STL (Standard Tessellation Language) format for further processing.

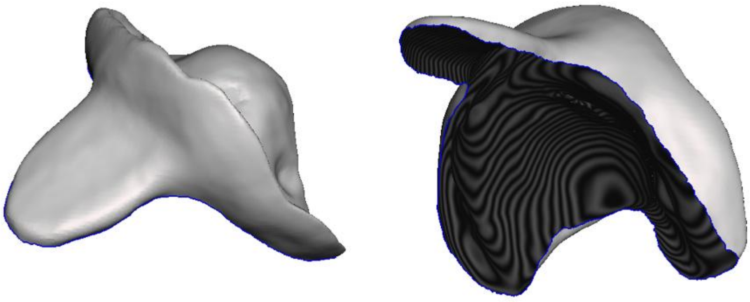

Figure 1. Scanned impression tray for newborns, the model renderings are taken from CAD software, where the models are displayed in a neutral gray color.

2.2. Computer-Aided Design (CAD)

The meshes were edited using Meshmixer CAD software (Autodesk, Inc., San Rafael, CA, U.S.A.). Unnecessary elements were removed, and the tray handle and tray body were segmented. Both segments were extruded inferiorly by 3mm to enhance structural integrity. Subsequently, the models were united, smoothed, and uniquely numbered (Fig. 2). This process was repeated for all 17 trays.

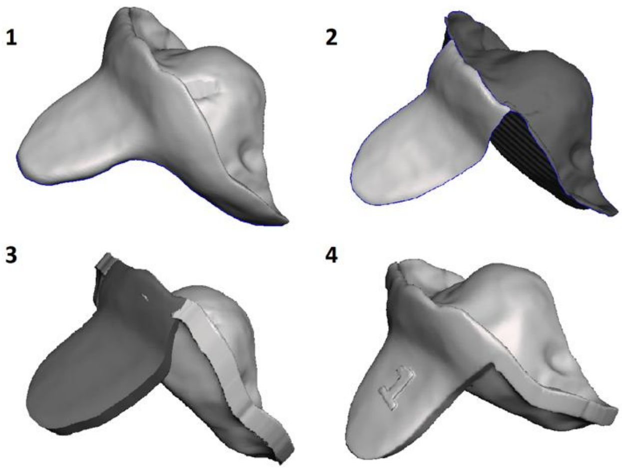

Figure 2. Impression trays from multiple views in the Meshmixer software (1 – unedited 3D scan, 2 – model separation, 3 – extrusion of surfaces, 4 – final 3D model).

2.3. Additive Manufacturing

PLA (polylactic acid) photopolymer resin was used for manufacturing of the individual impression trays via SLA (stereolithography) technology with a Creality Halot

Max 3D printer (Shenzhen Creality 3D Technology Co., Ltd., Shenzhen, China). Each CAD model was prepared in Halot Box software (Shenzhen Creality 3D Technology Co., Ltd., Shenzhen, China), where support structures and printing parameters were defined (see Table 1) [7].

Table 1. Support settings and printing parameters.

Support Settings		Printing Parameters	
Height from platform	6,00 mm	Layer thickness	0,05 mm
Density	50%	Initial exposure	50 s
Tip diameter	0,80 mm	Exposure time	4 s
Support diameter	1,50 mm	Rising height	8 mm
		Motor speed	2 mm/s
		Turn off delay	4 s
		Bottom exposure layers	6

The final designs were sliced into layers and saved in the ".cxdlp" format for printing. (Fig.3).

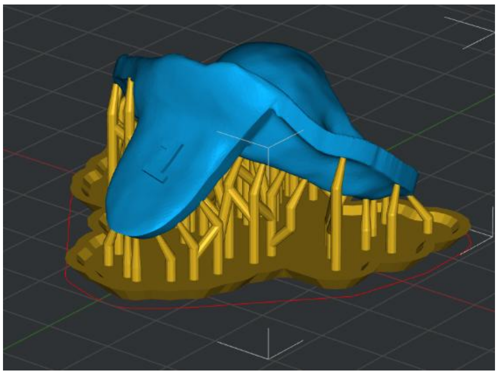

Figure 3. Impression tray prepared to be printed with support structures in the 3D printing software.

3. Results

Each of the 17 trays (Fig. 4) was successfully manufactured. Table 2 summarizes consumable usage, weight, and print times. The data demonstrate that SLA technology produces consistent results with minimal material waste.

The average consumable usage per tray was 13.09 ml, and the average weight was 15.04 g. The average print time per tray was approximately 2 hours and 30 minutes, with variations due to tray geometry. The total cumulative print time for all trays was 40 hours, 58 minutes, and 28 seconds. If all trays fit on the printer's build plate simultaneously, the total printing duration could be reduced to the longest single print time, which was 3 hours, 18 minutes, and 18 seconds.

Table 2. Consumable usage, weight, and print times of the trays.

Model number	Estimated consumable usage [ml]	Model weight [g]	Print time [hh:mm:ss]
1	11,79	13,56	02:55:14
2	10,06	11,57	02:11:03
3	16,29	18,73	03:18:18
4	11,86	13,64	02:51:15
5	11,58	13,32	02:02:05
6	12,25	13,97	02:16:52
7	13,72	15,78	02:15:27
8	14,73	16,94	02:15:39
9	12,26	14,10	02:15:27
10	13,04	15,00	02:03:13
11	12,27	14,11	02:19:08
12	14,58	16,77	02:42:15
13	12,78	14,70	02:09:12
14	13,05	15,01	02:19:08
15	12,55	14,43	02:18:02
16	16,05	18,46	02:26:19
17	13,62	15,66	02:19:51

Figure 4. 3D printed impression trays ready for sterilization process.

4.Discussion

This study demonstrates the feasibility and precision of using reverse engineering for cleft palate impression trays, offering significant improvements over traditional methods. SLA technology proved reliable, with all 17 trays successfully fabricated. The process required an average consumable usage of 13.09 ml and tray weight of 15.04 g, while print times averaged 2 hours and 30 minutes. Notably, batch production could reduce total manufacturing time to 3 hours, 18 minutes, and 18 seconds, highlighting its scalability and efficiency.

Advancements in Nasoalveolar Molding Plate Creation

A different approach involves collecting and scanning plaster casts of newborn patients with CLP to create a stock of prefabricated trays for conventional impressions.[8]

However, the use of intraoral scanners represents an ideal advancement in nasoalveolar molding plate production, eliminating risks associated with traditional impression techniques, such as material aspiration or airway blockage. Despite their potential, intraoral scanners remain underutilized due to their high initial cost, limiting their availability in many hospitals. Wider adoption of this technology could significantly improve patient safety and comfort [9–13].

Benefits and Challenges of CAD/CAM Systems

CAD/CAM systems enhance customization and accuracy, allowing for better tray fit and patient outcomes. Digital workflows also enable rapid prototyping and iteration, particularly beneficial for complex cases. However, challenges such as ensuring uniform extrusion during CAD modeling and optimizing printing parameters persist, requiring careful calibration and expertise [14].

5.Conclusions

Reverse engineering and CAD/CAM systems provide a highly efficient and precise alternative for cleft palate tray manufacturing. Addressing existing challenges and incorporating innovations like intraoral scanning can further enhance this process, improving outcomes for patients and clinicians alike.

References

1. E. Commission, "Prevalence charts and tables," Updated data including birth year 2022. Accessed: Sep. 21, 2024. [Online]. Available: https://eu-rd-platform.jrc.ec.europa.eu/eurocat/eurocat-data/prevalence_en
2. J. Langman and T. W. Sadler, *Langman's Medical Embryology*, 7th ed. 1995.
3. D. Yates, V. Allareddy, J. Caplin, S. Yadav, and M. R. Markiewicz, "An Overview of Timeline of Interventions in the Continuum of Cleft Lip and Palate Care," *Oral Maxillofac Surg Clin North Am*, vol. 32, no. 2, pp. 177–186, May 2020, doi: 10.1016/J.COMS.2020.01.001.
4. X. Gong, R. Dang, T. Xu, Q. Yu, and J. Zheng, "Full Digital Workflow of Nasoalveolar Molding Treatment in Infants With Cleft Lip and Palate," *Journal of Craniofacial Surgery*, vol. 31, no. 2, pp. 367–371, 2020, doi: 10.1097/SCS.0000000000006258.
5. A. M. Kuijpers-Jagtman and B. Prahl-Andersen, "History of neonatal maxillary orthopedics: Past to present," *Cleft Lip and Palate*, pp. 395–407, 2006, doi: 10.1007/3-540-30020-1_25/COVER.
6. P. Nalabothu, B. K. Benitez, M. Dalstra, C. Verna, and A. A. Mueller, "Three-Dimensional Morphological Changes of the True Cleft under Passive Presurgical Orthopaedics in Unilateral Cleft Lip and Palate: A Retrospective Cohort Study," *J Clin Med*, vol. 9, no. 4, Apr. 2020, doi: 10.3390/JCM9040962.
7. J. Zivcak, Material development in personalized implantology, 1st ed. Kosice, 2023.
8. S. Sabir, H. Rokhssi, N. Famma, M. Azhari, and O. Bentahar, "Prefabricated Trays Stock for Impression of Cleft lip and Palate Orthopedic Appliances: A Three-Dimensional Computational Analysis of Maxillary Jaws," *https://doi.org/10.1177/10556656221119075*, vol. 61, no. 1, pp. 119–125, Aug. 2022, doi: 10.1177/10556656221119075.
9. P. Zarean *et al.*, "A Point-of-Care Digital Workflow for 3D Printed Passive Presurgical Orthopedic Plates in Cleft Care," *Children (Basel)*, vol. 9, no. 8, Aug. 2022, doi: 10.3390/CHILDREN9081261.
10. P. Batra, B. F. Gribel, B. A. Abhinav, A. Arora, and S. Raghavan, "OrthoAligner 'NAM': A Case Series of Presurgical Infant Orthopedics (PSIO) Using Clear Aligners," *Cleft Palate-Craniofacial Journal*, vol. 57, no. 5, pp. 646–655, May 2020, doi: 10.1177/1055665619889807/SUPPL_FILE/SUPPLEMENTAL_IMAGE_1.JPG.
11. T. Okazaki, H. Kawanabe, and K. Fukui, "Comparison of conventional impression making and intraoral scanning for the study of unilateral cleft lip and palate," *Congenit Anom (Kyoto)*, vol. 63, no. 1, pp. 16–22, Jan. 2023, doi: 10.1111/CGA.12499.

12. B. K. Benitez *et al.*, “Digital impressions from newborns to preschoolers with cleft lip and palate: A two-centers experience,” *J Plast Reconstr Aesthet Surg*, vol. 75, no. 11, pp. 4233–4242, Nov. 2022, doi: 10.1016/J.BJPS.2022.08.015.
13. C. Shen, C. A. Yao, W. Magee, G. Chai, and Y. Zhang, “Presurgical Nasoalveolar Molding for Cleft Lip and Palate: The Application of Digitally Designed Molds,” *Plast Reconstr Surg*, vol. 135, no. 6, pp. 1007e–1015e, Jun. 2015, doi: 10.1097/PRS.0000000000001286
14. D. M. Kalaskar, *3D printing in Medicine 2nd edition*. Woodhead Publishing, 2022. Accessed: Mar. 15, 2024. [Online]. Available: https://www.elsevier.com/books/3d-printing-in-medicine/kalaskar/978-0-323-89831-7

TECHNICAL UNIVERSITY OF KOŠICE
Faculty of Mechanical Engineering

Overview of the Effects of Light on Mesenchymal Stem Cells

Veronika Sedláková [1,*], Jana Hlubeňová [1], Radovan Hudák[1], Igor Drstvenšek[2], Peter Kneppo[3]

[1] Department of Biomedical engineering and measurement, Faculty of Mechanical Engineering, Technical university of Košice, Letná 9/B, 042 00 Košice, Slovakia; veronika.sedlakova@tuke.sk; jana.hlubenova@tuke.sk; radovan.hudak@tuke.sk
[2] Faculty of Mechanical Engineering, University in Maribor, Smetanova ulica 17, 2000 Maribor, Slovenia; igor.drstvensek@um.si
[3] Department of Biomedical Engineering, Faculty of Mechanical Engineering, Czech Technical University in Prague, nám. Sítná 3105 Kladno 272 01 Czech Republic; kneppo@fbmi.cvut.cz
* Correspondence: veronika.sedlakova@tuke.sk ; Tel.: +421 556 022 745

Abstract: This review explores the effects of light exposure, particularly red light, on mesenchymal stem cells (MSCs). MSCs are multipotent cells capable of self-renewal and differentiation, commonly sourced from adipose tissue and bone marrow. Studies reveal that red light at 630 nm enhances mitochondrial activity, ATP production, and cytokine secretion, with optimal effects observed at 4 J/cm². Lower energy doses show limited impact, and red light does not induce DNA damage or oxidative stress. In contrast, blue light (420-480 nm) inhibits MSC proliferation, induces apoptosis, and increases oxidative stress, limiting its therapeutic utility. Red light emerges as a promising tool for preconditioning MSCs in regenerative medicine. However, the exact mechanisms remain unclear, emphasizing the need for standardized light parameters and optimized dosages. This review consolidates current findings to guide future research in photobiomodulation and MSC applications.

Keywords: stem cells; mesenchymal stem cells; light exposure; cell differentiation; regenerative medicine

1. Introduction

MSCs play a pivotal role in regenerative medicine, thanks to their ability to self-renew, differentiate into various cell types, and produce bioactive molecules that aid tissue repair. To maximize their therapeutic potential, it is essential to optimize both their environment and external factors that influence their viability and function. Among these factors, red light exposure has emerged as a promising non-invasive approach. Photobiomodulation with red light has been shown to enhance mitochondrial activity, boost energy production, and regulate cytokine secretion in MSCs, largely through the interaction with mitochondrial chromophores like cytochrome c oxidase [1,2].

Despite its potential, the use of red light in MSC research is complicated by inconsistencies in experimental conditions, such as variations in wavelength, energy density, and exposure time. Additionally, other wavelengths, like blue light, have been found to inhibit MSC proliferation and increase oxidative stress, further emphasizing the need for standardized protocols. This review explores the use of red light in preconditioning MSCs, highlighting key biological mechanisms and identifying areas for further investigation to support future research and clinical applications [3].

2. Mesenchymal stem cells

MSCs are a type of multipotent stem cell capable of self-renewal and differentiation into various cell types, such as bone, cartilage, and fat cells. They can be isolated from a wide range of tissues, including bone marrow, umbilical cord, adipose tissue, cartilage, and muscle. Over time, the range of sources has expanded to include less conventional tissues, such as menstrual blood, endometrial tissue, breast milk, and even pancreatic tissue. Additionally, fetal tissues, such as the dermis and certain dental tissues, have also been identified as reservoirs of MSCs. Under specific conditions, some differentiated cells can dedifferentiate, contributing further to the MSC population within a tissue. MSCs from different tissue sources often have unique characteristics, including variations in cell surface markers and differentiation potential. Even within a single tissue, MSC populations may be diverse, with some cells exhibiting higher developmental potential than others. This diversity highlights the importance of understanding MSC properties to optimize their application in research and clinical practice [4,5,6].

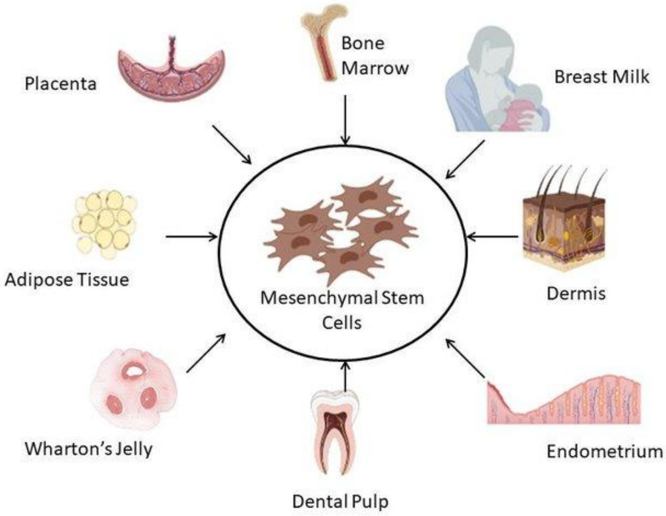

Figure 1. Sources of Mesenchymal Stem Cells [6].

3. Effects of Light on MSCs

The use of light exposure, commonly referred to as photobiomodulation, is applied in therapies to support tissue regeneration, reduce inflammation, and alleviate pain. Studies investigating this phenomenon predominantly focus on red and blue light wavelengths. Light-emitting diodes (LEDs) and lasers are the primary sources of such light. On a cellular level, light is absorbed by mitochondria, leading to changes in cellular metabolism. However, the exact mechanisms underlying these effects are not yet fully understood and may differ depending on the wavelength employed [7].

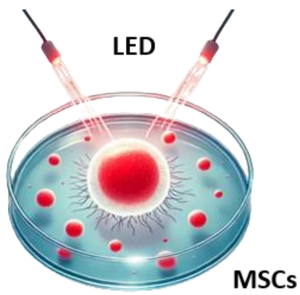

Figure 2. Diagram of Red Light Acting on MSCs.

Red light, typically ranging from 600 to 700 nm, as well as wavelengths in the near-infrared spectrum (NIR, approximately 780–1100 nm), are known to activate cytochrome c oxidase. This enzyme, part of the respiratory chain, also functions as a chromophore a molecule that absorbs photons. When stimulated, this process enhances the production of adenosine triphosphate (ATP) and cyclic adenosine monophosphate (cAMP), initiating a variety of biostimulatory effects. Furthermore, red light influences reactive oxygen species (ROS) levels, which may play a role in cellular signaling. A probable mechanism for cytochrome c oxidase activation involves the dissociation of nitric oxide, which under normal conditions inhibits the enzyme and, as a result, suppresses the entire oxidative chain [8].

Recent findings further highlight how red light affects mitochondria. For instance, adipose-derived mesenchymal stem cells (AdMSCs) exposed to red LED light at 630 nm exhibited altered metabolism and the release of specific factors. Illumination at an energy level of 4 J/cm² significantly improved mitochondrial efficiency and boosted ATP generation. In contrast, lower energy doses, such as 0.5 and 2 J/cm², had minimal impact. Additionally, the light influenced the levels of cytokines, such as IL-6 and IL-10, depending on the energy applied. Despite these observations, the exact mechanisms underlying these effects remain uncertain [9,10].

In research conducted by Ye Yuan, blue light at 470 nm from LEDs was shown to significantly inhibit proliferation in bone marrow-derived mesenchymal stem cells (BMSCs). The study reported increased apoptosis and suppressed osteogenic differentiation under blue light exposure. Furthermore, the irradiated cells displayed a rise in reactive oxygen species (ROS) and DNA damage, indicating that blue light exerts toxic effects on BMSCs and could negatively impact BMSC-based therapeutic applications [11].

In another study, The Selection of Light Emitting Diode Irradiation Parameters for Stimulation of Human Mesenchymal Stem Cells (hMSC) Proliferation by Rafał Lewandowski, the effects of LED irradiation on hMSC proliferation were analyzed. The research utilized red light at 630 nm, with cells positioned 1.3 cm from the light source. The most significant proliferation enhancement occurred with a single dose of 4 J/cm² and a power density of 17 mW/cm² [12].

Maria Surovtseva, in her research, explains that 532 nm laser irradiation influences bone marrow-derived mesenchymal stem cells when applied at various energy densities ranging from 0.5 to 6300 J/cm². Positive effects, such as increased mitochondrial activity, improved cell viability, and enhanced proliferation, were detected only at specific energy densities of 70 and 700 J/cm². While these effects were statistically significant, they were relatively small (around 9%) and consistent with findings from previous studies on other cell types and laser wavelengths. However, the lack of a clear dose-dependent response suggests that these results might be influenced by variability in cell populations or experimental conditions that were not fully controlled [13].

The author Barbara Sampaio Dias Martins Mansano states in her article that three LED irradiations at 630 nm (15 mW/cm²; 4 J/cm²) are safe and enhance the metabolism and secretion of (AdMSCs). The findings suggest that LEDs could serve as a useful tool for preconditioning AdMSCs in vitro before transplantation [14].

4. Results

Studies consistently demonstrate that red light, particularly at 630 nm, enhances MSC proliferation, mitochondrial activity, and cytokine secretion, with optimal effects observed at 4 J/cm². Lower energy doses show minimal effects. In contrast, blue light inhibits MSC proliferation, induces apoptosis, and increases ROS levels, contributing to DNA damage. Green light demonstrates limited and inconsistent positive effects on MSCs.

5. Discussion

The findings confirm that red light significantly boosts mitochondrial efficiency and supports cellular metabolism, making it a promising tool for preconditioning MSCs in regenerative medicine. Blue light exposure, while offering potential for controlled cell suppression, poses risks due to its adverse effects on cell viability. The results emphasize the importance of precise energy dosages and wavelengths for photobiomodulation in MSC applications. Variability in green light outcomes highlights the need for further investigation into its biological impact.

6. Conclusions

Red light at 630 nm has shown great promise as a safe and effective method to enhance the proliferation and energy activity of mesenchymal stem cells, making it a valuable tool for regenerative medicine. However, for these findings to translate successfully into clinical practice, there is a strong need to establish standardized protocols for light exposure such as specific wavelengths, energy levels, and durations. While blue light appears less suitable due to its adverse effects on cell health, green light shows some potential, though its effects remain inconsistent and require further study. Moving forward, research should focus on refining these light-based methods to make MSC preconditioning more reliable and accessible for therapeutic use.

Acknowledgments: The work has been supported by research grants Agency-project VEGA 1/0387/22 – "Development and testing of systems for controlled stimulation of cell growth in a bioreactor environment using computer vision" and KEGA 050TUKE-4/2022 – "Additive manufacturing in medicine - creation of multimedia material and tools to support teaching in biomedical engineering". This publication is the result of the project implementation CEMBAM - Center for Medical Bioadditive Research and Production, ITMS2014+: 313011V358 supported by the Operational Programme Integrated Infrastructure funded by the European Regional Development Fund.

References

1. VASANTHAN, Jayavardini, et al. Role of human mesenchymal stem cells in regenerative therapy. *Cells*, 2020, 10.1: 54.
2. CROUS, Anine; ABRAHAMSE, Heidi. The signalling effects of photobiomodulation on osteoblast proliferation, maturation and differentiation: a review. *Stem Cell Reviews and Reports*, 2021, 1-20.
3. PINTO, Hernán; GOÑI OLIVER, Paloma; SÁNCHEZ-VIZCAÍNO MENGUAL, Elena. The effect of photobiomodulation on human mesenchymal cells: a literature review. *Aesthetic Plastic Surgery*, 2021, 45: 1826-1842.
4. PRIESTER, Caitlin, et al. Examining the characteristics and applications of mesenchymal, induced pluripotent, and embryonic stem cells for tissue engineering approaches across the germ layers. *Pharmaceuticals*, 2020, 13.11: 344.
5. MAHMOUDIAN-SANI, Mohammad-Reza, et al. Comparison of three types of mesenchymal stem cells (bone marrow, adipose tissue, and umbilical cord-derived) as potential sources for inner ear regeneration. *The International Tinnitus Journal*, 2017, 21.2: 122-127.
6. DZOBO, Kevin. Multipotent Human Mesenchymal Stem/Stromal Cells: An Updated Review on Historical Background, Recent Trends and Advances in their Clinical Applications. 2021.
7. KHORSANDI, Khatereh, et al. Biological responses of stem cells to photobiomodulation therapy. *Current Stem Cell Research & Therapy*, 2020, 15.5: 400-413.
8. LI, Hao, et al. The implication of blue light-emitting diode on mesenchymal stem cells: a systematic review. *Lasers in Medical Science*, 2023, 38.1: 267.
9. MOHAMAD, Sherif A., a kol. Fotobiomodulácia mineralizácie v mezenchymálnych kmeňových bunkách. *Photochemical & Photobiological Sciences* , 2021, 20.5: 699-714.
10. MANSANO, Barbara Sampaio Dias Martins, et al. Light-emitting diode can enhance the metabolism and paracrine action of mesenchymal stem cells. *Photochemistry and Photobiology*, 2023, 99.6: 1420-1428.
11. YUAN, Ye, et al. Effects of blue light emitting diode irradiation on the proliferation, apoptosis and differentiation of bone marrow-derived mesenchymal stem cells. *Cellular Physiology and Biochemistry*, 2017, 43.1: 237-246.
12. LEWANDOWSKI, Rafał, et al. The selection of light emitting diode irradiation parameters for stimulation of human mesenchymal stem cells proliferation. In: *Laser Technology 2016: Progress and Applications of Lasers*. SPIE, 2016. p. 117-123.
13. SUROVTSEVA, Maria, et al. Survival and Proliferation of Bone Marrow Derived Mesenchymal Stem Cells Under 532 nm Laser Irradiation. In: *2021 IEEE Ural-Siberian Conference on Computational Technologies in Cognitive Science, Genomics and Biomedicine (CSGB)*. IEEE, 2021. p. 160-163.

14. MANSANO, Barbara Sampaio Dias Martins, et al. Enhancing the therapeutic potential of mesenchymal stem cells with light-emitting diode: implications and molecular mechanisms. *Oxidative Medicine and Cellular Longevity*, 2021, 2021.1: 6663539.

TECHNICAL UNIVERSITY OF KOŠICE
Faculty of Mechanical Engineering

Comparative analysis of honeycomb and re-entrant auxetic structures: Poisson´s ratio and mechanical properties using finite element method

Barbara Schürger [1,*], Peter Frankovský [1], Martina Hančinová [1], Erika Dubňanská [1]

[1] Technical University of Košice, Faculty of Mechanical Engineering, Department of Applied Mechanics and Mechanical Engineering, Letná 9, 042 00 Košice, Slovak Republic; barbara.schurger@tuke.sk; peter.frankovsky@tuke.sk; martina.hancinova@tuke.sk; erika.dubnanska@tuke.sk
* Correspondence: barbara.schurger@tuke.sk; Tel.: +421910116236

Abstract: Auxetic structures with negative Poisson's ratios exhibit unique mechanical properties, including enhanced energy absorption, deformation resistance, and improved impact mitigation. This study presents a comparative analysis of conventional honeycomb and re-entrant auxetic structures, focusing on their Poisson's ratio and mechanical behavior under tensile loading. Finite element analysis (FEA) was conducted in ANSYS Workbench to evaluate the deformation characteristics, stress distribution, and Poisson's ratio of both structures. The obtained results highlight the contrasting mechanical responses of these geometries, with the re-entrant structure displaying a negative Poisson's ratio and enhanced deformation resistance compared to the conventional honeycomb structure. The findings provide valuable insights into the potential applications of auxetic materials in structural engineering, and protective equipment, where tailored mechanical properties are essential.

Keywords: auxetic; honeycomb; re-entrant; metamaterial; FEA; Poisson´s ratio; mechanical properties

1. Introduction

Auxetic materials and structures are characterized by their unique property of a negative Poisson's ratio, meaning they expand laterally when stretched longitudinally. This unique behavior stems from specific geometrical configurations rather than the original properties of the base material. Honeycomb and re-entrant geometries are widely recognized among auxetic structures due to their manufacturability, tunable mechanical properties, and widespread applications [1].

Honeycomb structures, a mainstay in engineering design, are prized for their high stiffness-to-weight ratio and energy-absorbing capabilities, particularly in aerospace and civil engineering [2].

Conversely, re-entrant structures achieve auxeticity through inwardly angled cell walls, providing superior adaptability under mechanical loading. Studies such as [3] underscore how re-entrant geometries enhance deformation resistance.

This research compares the mechanical performance of honeycomb and re-entrant auxetic structures through finite element analysis (FEA). Focused on deformation, stress response, and Poisson's ratio, the study provides a comprehensive evaluation of their strengths. This analysis supports their deployment in domains requiring impact resistance, lightweight design, and energy dissipation.

2. Structural behavior of honeycomb and re-entrant cells

Honeycomb structures can be observed in natural materials, exemplified by the structure of a bee work where individual cells take the form of regular hexagons (see Figure 1a). This natural association has led to the term honeycomb being widely used to describe such cells. However, regular hexagonal cells do not inherently exhibit auxetic behavior. To achieve the deformation characteristics typical of auxetic structures, these cells must be appropriately modified [3].

A common approach involves altering the internal angles of the cells. This modification results in the appearance of so-called concave angles, greater than 180°, within the cell (see Figure 1b). Consequently, the sides that form these angles intrude into the cell's internal space. This phenomenon is described using terms such as inverted or re-entrant in reference to the honeycomb cells. The resulting structure is thus known as the inverted (re-entrant) honeycomb [4].

The precise material characteristics of the structure depend on the relative dimensions of the unit cell, denoted as h (height) and l (length), as well as the angle θ (see Figure 1). By carefully selecting these parameters, it is theoretically possible to design structures with specific desired properties.

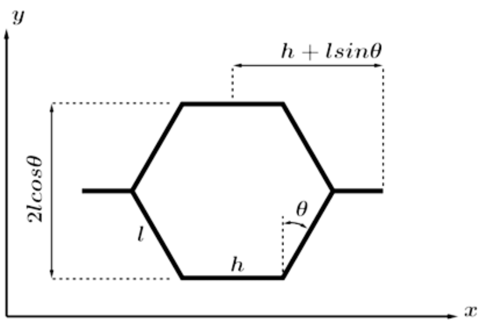

(**a**) (**b**)

Figure 1. Hexagonal structures: (**a**) Non-auxetic honeycomb structure; (**b**) Auxetic re-entrant structure [5].

Analytical models that describe the deformation behavior of structures formed by the periodic arrangement of hexagonal elements consider three primary modes of deformation at the unit cell level [5]:

1. Bending of the cell walls,
2. Elongation of the cell walls, and
3. Rotation of the walls at their connecting points.

The fundamental difference in the deformation behavior of non-auxetic honeycomb and auxetic re-entrant hexagonal cells can be understood through their response to tensile loading. Figure 2 illustrates this behavior under horizontal tensile stress (indicated by red arrows) in non-auxetic honeycomb cells. The vertical direction undergoes deformation in the opposite sense to the applied horizontal stress.

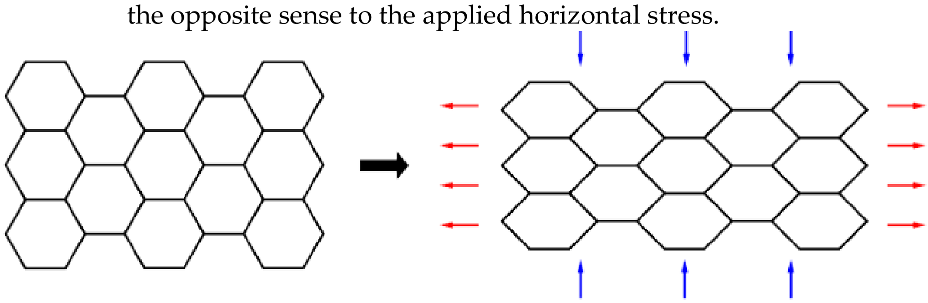

(**a**) (**b**)

Figure 2. Deformation behavior of the honeycomb structure under tensile stress in the horizontal direction: (**a**) Before deformation; (**b**) After deformation.

In contrast, auxetic re-entrant cells exhibit deformation in the vertical direction that is in the same sense as the horizontal tensile stress (Figure 3). This unique behavior results from the re-entrant angles and inverted geometry of the auxetic cells.

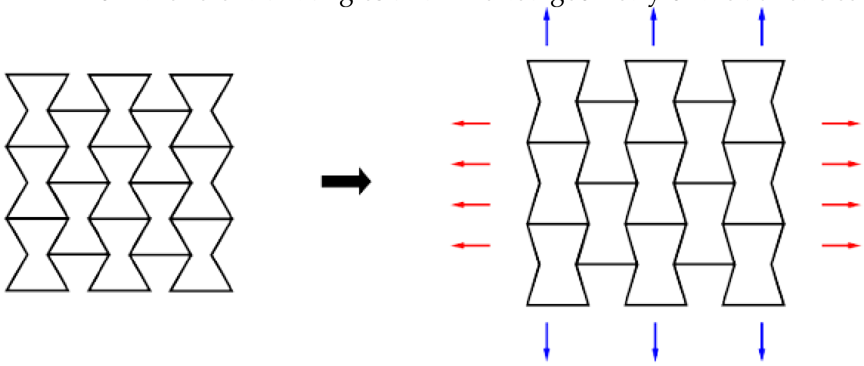

(a) (b)

Figure 3. Deformation behavior of the re-entrant structure under tensile stress in the horizontal direction: (**a**) Before deformation; (**b**) After deformation.

These contrasting deformation responses underscore the ability of re-entrant honeycomb structures to achieve auxetic behavior, making them promising candidates for applications requiring negative Poisson's ratio characteristics.

Poisson’s ratio in general describes how a material or structure deforms in directions perpendicular to an applied load. For honeycomb and re-entrant structures, it depends on the geometry and deformation mechanics of the unit cell [6].

In a honeycomb structure, the unit cell is a regular hexagon, so the Poisson's ratio can be derived using simplified (assuming elastic deformation and negligible shear) analytical models as [6]:

$$\nu = \frac{h}{l} \tag{1}$$

Where h is height and l is length. For regular honeycomb structures, this ratio is typically positive.

In a re-entrant honeycomb structure, the unit cell geometry is modified such that internal angles (θ) become concave (θ>180°). Poisson’s ratio can be approximated as [6]:

$$\nu = -\frac{2(1-cos\theta)}{sin\theta} \tag{2}$$

Where l is length and θ is internal angle. This equation shows that as θ increases (greater re-entrancy), the Poisson’s ratio becomes more negative.

Analytical models provide simplified expressions but may not capture complex behaviors like nonlinear deformation, effects of wall thickness and material anisotropy. That is the reason we are using FEM simulations to measure axial and transverse strains. In this case Poisson’s ratio can be compute numerically [6]:

$$\nu = -\frac{\varepsilon_y}{\varepsilon_x} \tag{3}$$

Where ε_y is transverse strain (perpendicular to the direction of applied force) and ε_x is axial strain (along the direction of applied force).

3. Materials and methods

The geometric configurations for honeycomb and re-entrant auxetic structures were created using Ansys Workbench. Cellular structures were designed to consist of 6 × 4 cells. This specific number of cells was chosen for a reason: to minimize boundary effects in the vertical direction and to maintain symmetry in the horizontal direction. The fixed dimensions in honeycomb structure were as follows: a height of 4 mm, length 4 mm, an inner angle of the cell 120 ° and an inner height of unit cell 6.93 mm (see Figure 4a). The fixed dimensions in re-entrant structure were as follows: a height of 6 mm, length 3 mm, an inner angle of the cell 60 ° and an inner height of unit cell 5.2 mm (see Figure 4b). The thickness of diagonal reinforcement was kept the same as the thickness of the walls same in both model, at 0.42 mm. The dimensions were chosen based on the natural geometry of each structure. The honeycomb follows a regular hexagonal pattern, while the re-entrant structure requires a different aspect ratio to preserve its deformation behavior. This ensures a meaningful comparison of mechanical properties rather than identical cell sizes.

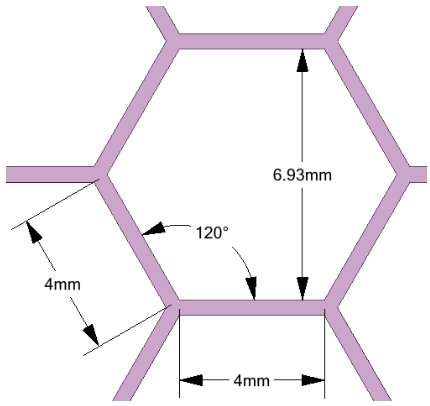

(**a**) (**b**)

Figure 4. Dimensions of unit cells: (**a**) Non-auxetic honeycomb structure; (**b**) Auxetic re-entrant structure.

4. Numerical analysis

The finite element model was then created in software Ansys Workbench. The chosen material of both structures was plastic PVC. For the model, the elements of the maximal dimension 0.25 mm with local concentrations on the edges up to 0.025 mm were applied. The sizing of the mesh was chosen after mesh sensitivity analysis. The principal stresses change was less than 1%. Finite element model of honeycomb structure was made from 498 598 nodes and 247 968 tetrahedral finite elements with quadratic approximation. Finite element model of re-entrant structure was made from 483 908 nodes and 255 106 tetrahedral finite elements with quadratic approximation. Top faces of the model are loaded with total force of 150N (red arrows in Figure 5) and bottom faces are fixed in all directions (blue triangles in Figure 5).

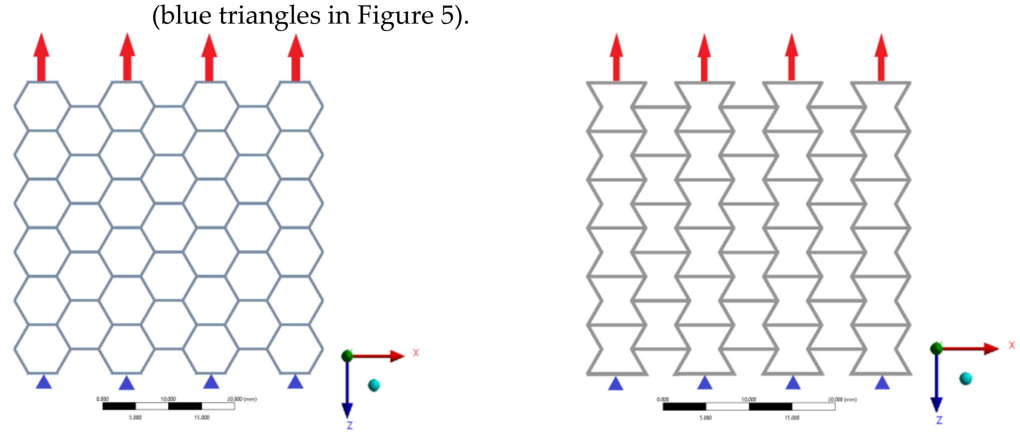

(**a**) (**b**)

Figure 5. Boundary conditions: (**a**) Non-auxetic honeycomb structure; (**b**) Auxetic re-entrant structure.

To determine the Poisson's ratio of the analyzed structures, we conducted a numerical analysis using ANSYS Workbench for both the non-auxetic honeycomb structure and auxetic reentrant structure. A uniaxial tensile load was applied along the Z-axis, and the resulting deformation was evaluated using the **Directional Deformation (Z Axis)** output for both honeycomb structure (Figure 6a) and re-entrant structure (Figure 7a), identifying the maximum and minimum displacement values in this direction. The axial length change ΔL_z was determined as the difference between these values. Similarly, the transverse deformation along the X-axis was analyzed using the **Directional Deformation (X Axis)** output for both honeycomb structure (Figure 6b) and re-entrant structure (Figure 7b), to compute the transverse length change ΔL_x. The Poisson's ratio for both structures was then calculated using the formula [6]:

$$\nu = -\frac{\varepsilon_z}{\varepsilon_x} = -\frac{\frac{\Delta L_z}{L_{0z}}}{\frac{\Delta L_x}{L_{0x}}}, \tag{4}$$

where ΔL is difference between the maximum and minimum deformation in the studied direction, and L_0 is original length of structure in the studied direction.

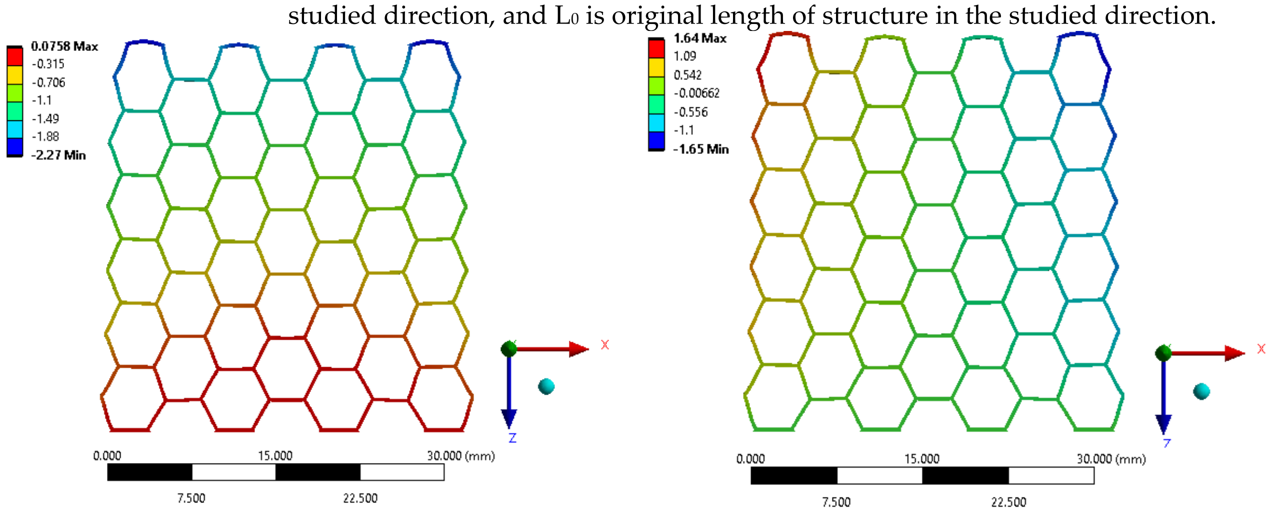

(**a**) (**b**)

Figure 6. Directional deformation of non-auxetic honeycomb structure: (**a**) Z-direction; (**b**) X-direction.

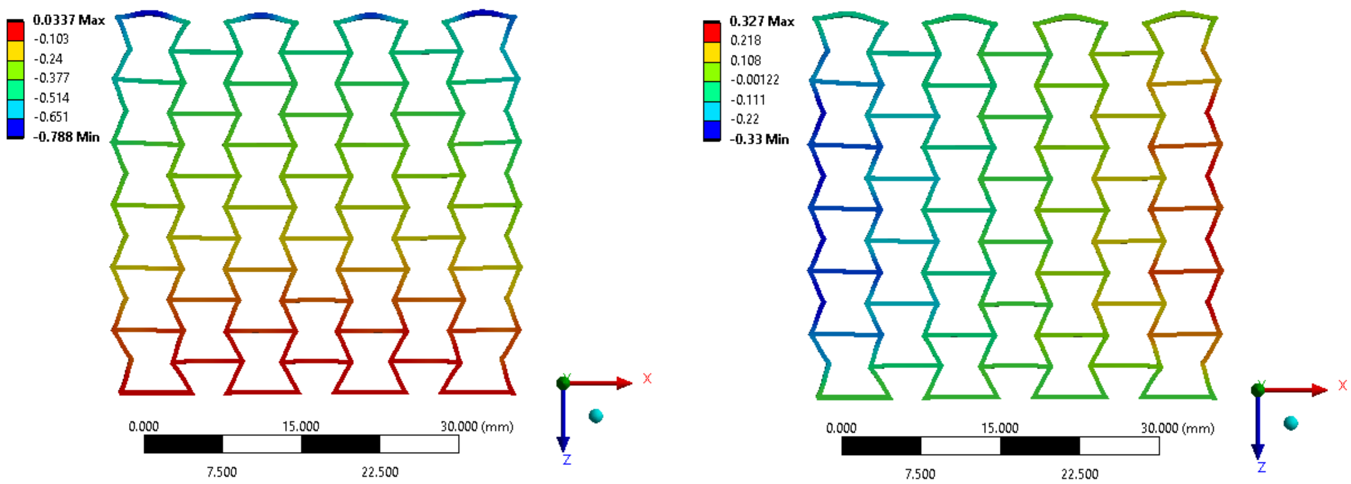

(**a**) (**b**)

Figure 7. Directional deformation of auxetic re-entrant structure: (**a**) Z-direction; (**b**) X-direction.

Obtained values allowed us to compare the mechanical response of the two geometries (see Table 1). The auxetic reentrant structure exhibited a negative Poisson's ratio, confirming its characteristic lateral expansion under tensile loading, whereas the honeycomb structure displayed a positive Poisson's ratio, consistent with conventional materials that contract laterally when stretched.

Table 1. Table of mechanical properties of studied honeycomb and re-entrant structure

Mechanical properties	Honeycomb Structure	Re-entrant structure
Total deformation	2,62 mm	0,79 mm
Equivalent stress (von Mises)	83,17 MPa	67,16 MPa
Poisson´s ratio analytically	1	-1,71
Poisson´s ratio numerically	1,23	-1,72

5. Results

The numerical simulations performed in ANSYS Workbench provided a detailed comparison of the mechanical properties of the honeycomb and re-entrant auxetic structures. The total deformation of the honeycomb structure was recorded as 2.62 mm, while the re-entrant auxetic structure exhibited significantly lower total deformation at 0.79 mm. The von Mises equivalent stress distribution analysis revealed that the honeycomb structure experienced a peak stress of 83.17 MPa, whereas the re-entrant structure showed a lower peak stress of 67.16 MPa, indicating improved load distribution.

The Poisson's ratio was calculated both analytically and numerically. The analytical model predicted a Poisson's ratio of 1 for the honeycomb structure and -1.71 for the re-entrant structure. The numerical simulations resulted in a Poisson's ratio of 1.23 for the honeycomb structure and -1.72 for the re-entrant structure. The significant difference between the analytically and numerically computed Poisson's ratio for the honeycomb structure arises due to the limitations of the theoretical model. The equation 1 is valid only for idealized analytical cases and does not account for elastic behavior of the material, nonlinear deformations and cell interactions and real boundary conditions. For a more accurate result, numerical simulation is preferred as it considers the actual deformations of the structure. These findings confirm the auxetic behavior of the re-entrant structure, characterized by lateral expansion under tensile loading, while the honeycomb structure demonstrated conventional mechanical behavior with lateral contraction.

The comparative analysis underscores the advantages of auxetic structures, particularly in applications requiring superior energy absorption and deformation resistance. The negative Poisson's ratio of the re-entrant structure suggests its suitability for impact-resistant applications, while the honeycomb structure remains optimal for lightweight, high-stiffness applications. These results provide a foundation for further research into optimizing cellular structures for advanced engineering applications.

Acknowledgments: The work was supported by the grant project KEGA 039TUKE-4/2024 and VEGA 1/0152/24.

Conflicts of Interest: The authors declare no conflict of interest.

References

1. Gill, H.S. Mechanical and structure properties of cellular auxetic materials. *Materials Today: Proceedings*. **2021**, 37(2), 3320-3323
2. Nugroho, W.T. et al. Additive manufacturing of re-entrant structures: Well-tailored structures, unique properties, modelling approaches and real applications. *Additive Manufacturing,* **2023**, 78.
3. Wang, Y. et al. Mechanical Properties of Re-Entrant Hybrid Honeycomb Structures for Morphing Wings. *Biomimetics*, **2024**, 9.
4. Zhang, Q.C. et al. Bio-Inspired Engineering of Honeycomb Structure - Using Nature to Inspire Human Innovation. *Progress in Materials Science.* **2015**, 74, 332-400.
5. Yang, L. et al. Mechanical properties of 3D re-entrant honeycomb auxetic structures realized via additive manufacturing. *International Journal of Solids and Structures*, **2015**, 475-490.
6. Wu, Y. et al. Additively manufactured materials and structures: A state-of-the-art review on their mechanical characteristics and energy absorption. *International Journal of Mechanical Sciences*, **2023**, 108102.
7. Yolcu, D.A. et al. Measurement of Poisson's ratio of the auxetic structure. *Measurement*, **2022**, 112040.

TECHNICAL UNIVERSITY OF KOŠICE
Faculty of Mechanical Engineering

Contribution to Blood Pressure Metrology

Andrej Smetánka [1,*], Jan Rybář [1], Stanislav Ďuriš [1], Sohaibullah Zarghoon [1], Jana Gerneschová [2] and Václav Sedlák [3]

[1] Institute of Automation, Informatization, and Measurement, Faculty of Mechanical Engineering, Slovak University of Technology in Bratislava, Nám. slobody 17, 812 31 Bratislava, Slovakia; andrej.smetanka@stuba.sk; jan.rybar@stuba.sk; stanislav.duris@stuba.sk; sohaibullah.zarghoon@stuba.sk
[2] Institute of Automation, Informatization, and Measurement, Faculty of Mechanical Engineering, Slovak University of Technology in Bratislava, Nám. slobody 17, 812 31 Bratislava, Slovakia & Laboratory for Fundamental Metrology, Czech Metrology Institute, V Botanice 1504/4, 150 72 Praha, Czech Republic; jana.gerneschova@stuba.sk & jana.gerneschova@cmi.gov.cz
[3] Unit of Primary Metrology of Pressure, Vacuum and Low Mass Flow, Czech Metrology Institute, Okružní 31, 638 00 Brno, Czech Republic; vaclav.sedlak@cmi.gov.cz
* Correspondence: andrej.smetanka@stuba.sk; Tel.: +421 918 258 757

Abstract: Blood pressure is a critical indicator of cardiovascular health; thus, its accurate measurement and metrological traceability are essential for the proper diagnosis, monitoring, and treatment of various health conditions. Blood pressure metrology focuses on the accuracy, reliability, and standardization of measurements to ensure that results are comparable, objective, and independent of external factors. Accurate blood pressure measurement forms the foundation for precise medical diagnoses as well as for the prevention and effective management of patient health. The objective of this paper is to examine the issue from a metrological perspective, addressing the processes required to ensure accurate measurements and fostering patient trust. Medical metrology plays a pivotal role in establishing a robust relationship among the physician, the measuring device, and the patient.

Keywords: Blood Pressure, Healthcare, Measurement, Medical Metrology, Traceability

1. Introduction

Blood pressure measurement is a fundamental diagnostic tool in medicine, providing critical information about the state of the cardiovascular system and the overall health of the patient. As a physiological parameter, blood pressure is expressed in terms of systolic and diastolic values, which represent the pressure in the blood vessels during heartbeats and between them, respectively. Accurate blood pressure measurement is essential for the early detection and effective management of conditions such as hypertension, a major risk factor for cardiovascular disease [1-2].

Blood pressure metrology encompasses the scientific principles and techniques aimed at ensuring the accuracy, reliability, and consistency of blood pressure measurements. Its primary objectives include establishing standards for measurement devices, verifying their accuracy, performing calibration, and training medical personnel to achieve maximum precision and repeatability of results. Metrological considerations extend beyond the selection of appropriate measurement techniques (e.g., auscultatory or oscillometric methods) to include proper patient preparation, adherence to standardized conditions, and the routine verification and calibration of measurement devices. Oscillometric blood pressure signal simulators represent a valuable tool for ensuring metrological traceability and enhancing the performance of blood pressure meters by enabling measurements under dynamic conditions [1,3].

2. Blood pressure methods and meters

Blood pressure measurement is a commonly performed procedure in medical practice and, aside from certain specialized cases, is considered routine. The determination of optimal blood pressure values has long been a subject of debate [2]. It is well-established that elevated blood pressure is detrimental to health. Optimal blood pressure values are 120 mmHg for systolic pressure and 80 mmHg for diastolic pressure, with acceptable ranges for a healthy individual extending up to 140 mmHg for systolic pressure and 90 mmHg for diastolic pressure [3].

High blood pressure, or hypertension, is recognized as one of the diseases of civilization. Consequently, significant emphasis is placed on accurate blood pressure measurements, as they are a critical component in the prevention and management of hypertension and its associated conditions [3].

Blood pressure meters are typically classified into two categories: mechanical (manual) and electromechanical (automated) devices. Another classification is based on the measurement method employed. From a metrological traceability perspective, these measurements have a direct impact on public health.

3. Results

In practice, the introduction of blood pressure meters presents two primary challenges: ensuring the accuracy of measurements and establishing the metrological traceability of these devices.

The approach to addressing blood pressure measurement accuracy has progressively been standardized through clinical assessments, where the readings of new, tested meters are compared with reference measurements. As noted in [4] and [5], the accuracy testing of oscillometric blood pressure meters was initially guided by various ad hoc test protocols.

Various European hypertension societies have developed test protocols, as referenced in [6-7]. Additionally, harmonized standards, such as those in the EN ISO 81060 series, have been established [8–9]. A common feature of these documents is their provision of standardized procedures for assessing the accuracy of blood pressure meters by comparing the readings of the tested device with those of a reference meter. According to EN ISO 81060-2, testing requires a minimum sample size of 85 subjects, with three measurements per subject. These protocols also define specific criteria, including required blood pressure ranges, age and gender distribution of reference subjects, among others. The parameter of "accuracy" is typically assessed by tolerating an average measurement error of no more than ±5 mmHg, with a maximum standard deviation of 8 mmHg. However, the approaches to accuracy assessment vary significantly among protocols [3].

The accuracy of blood pressure meters is verified through clinical trials prior to their market release. Subsequent metrological traceability, however, remains the responsibility of individual countries, each with its own specific requirements. The metrological traceability of blood pressure meters is ensured in a manner similar to other pressure meters, through an uninterrupted chain of pressure unit transmission. This is achieved by directly comparing static pressure from the primary standard to the blood pressure meter in question [3].

In Slovakia, the primary standard is maintained by the Slovak Metrology Institute in Bratislava. Through direct comparison, secondary standards are linked to this primary standard, and in turn, the main or reference standards of the entities responsible for ensuring the traceability of blood pressure meters are connected via direct comparison. Blood pressure meters are subsequently linked to these standards through direct comparison [10].

With the development and deployment of automatic oscillometric blood pressure meters, blood pressure simulators have been created to enable testing of these devices in dynamic modes that closely resemble real-world use.

The principle of the simulator is straightforward: by using the movement of a piston or membrane, the simulator generates low-amplitude pressure pulses within a pneumatic system. The connected blood pressure meter then interprets these pulses as real oscillometric signals and processes them using an internal algorithm (black box), similar to standard blood pressure measurement procedures. During testing, the blood pressure meter is connected as if a routine measurement were being conducted in medical practice. The cuff is applied either to a) an artificial arm, or b) a rigid cylinder with a softened surface, and a regular measurement is initiated on the meter under test [3,10].

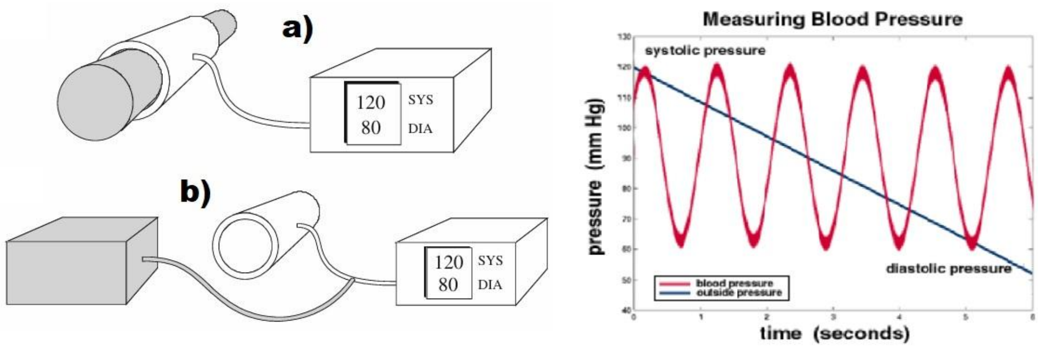

Figure 1. Types for blood pressure simulation, options for ensuring metrological traceability. Source: [12,14], modified.

The artificial arm mimics the physiology of the human arm, featuring a rigid structure that simulates bone running through the center. A hydraulic line, placed beneath the softened surface, simulates an artery, in which the simulator generates pressure pulses.

The metrology of dynamic quantities is an emerging field and remains insufficiently addressed from a metrological perspective. As a result, most measuring instruments used in dynamic conditions are still calibrated statically, often without considering the associated uncertainties. The outcome of dynamic characterization of these instruments typically involves adjustments for correcting dynamic behavior or, in some cases, practical implementation, where the maximum limits of frequencies and amplitudes are not adequately addressed [1,3].

To evaluate blood pressure monitors from a metrological perspective, we propose using a simulator, with the process divided into two parts. The first part involves evaluation under static conditions, which includes static calibration, as well as tests for repeatability and reproducibility of measurements. The second part consists of dynamic testing using the simulator to assess the stability of its performance, along with a qualitative evaluation of the stability of the generated pressure and pulse rate [1,3].

Table 1. Balancing the influencing parameters during the calibration of a blood pressure monitor: A general overview of static and dynamic calibration [3].

static calibration	dynamic calibration
measurement results	measurement results and estimates
standard indication	effect of jitter
reading resolution	random noise effect
hysteresis effect	effect of zero voltage
multimeter measurement effect	effect of fast sampling

power supply effect	effect of linearity change
long-term stability effect	effect of experimental characterization
temperature stability effect	---
linearity effect	---

The table above considers the influencing parameters in general, using both static and dynamic calibration of blood pressure meters.

The use of oscillometric signals will facilitate the full implementation of these meters in ensuring metrological continuity for blood pressure devices. The components are characterized metrologically in static conditions and experimentally in dynamic measurement mode. Further evaluation will, of course, require addressing measurement uncertainties and analyzing individual parameters to achieve more accurate measurements [1,3]. As part of designing and evaluating measurements, this issue is addressed with students and in teaching, in connection with the KEGA project number 024STU-4/2023 (Building a laboratory of medical metrology).

4. Discussion and conclusions

Calibration of blood pressure monitors involves both static and dynamic methods, each with its own specificities, advantages, and disadvantages. The aim of this article is to highlight the issue of metrological traceability of blood pressure monitors in general.

Furthermore, clinical testing of blood pressure monitors is a complex process that involves patient selection, measurement, statistical analysis of the results, and subsequent certification of the monitor. This process ensures that blood pressure measuring devices are sufficiently accurate and reliable for use in healthcare. In medical metrology, traceability is established through a clinically evaluated monitor, which serves as a transfer standard with a classic traceability to SI units.

Approaches to the metrological assurance of blood pressure measurements are diverse. The use of oscillometric blood pressure signal simulators is one option for improving the metrological traceability of most blood pressure meters through dynamic mode measurement. This approach allows for the evaluation of the internal algorithm of the blood pressure meter and the assessment of the stability and accuracy of blood pressure measurements. However, a significant limiting factor is the unresolved issue of ensuring the metrological traceability of the simulators themselves [1,3].

In healthcare, the principles of medical metrology and metrological traceability are applied, based on clinical testing and SI units. Measurements are then considered in practice, accounting for the biological variability of the individual, their medical history, and the potential treatment process. Medical metrology ensures the correct metrological traceability of devices with a measuring function [11]. However, this does not diminish the fact that metrological traceability plays a crucial role in ensuring human health and the accuracy of the pressure gauges used in this context. In the Slovakia, these meters are required to be verified by law (they are designated meters) [13].

Acknowledgments: The authors would like thank the Slovak University of Technology in Bratislava (Faculty of Mechanical Engineering), Czech Metrology Institute and, the grant agency KEGA project number 024STU-4/2023 (Building a laboratory of medical metrology), the grant agency APVV project number APVV-21-0216 (Advanced mathematical and statistical methods for measurement and metrology) and the international project number "21NRM05" (Standardization for safe implant scanning in MRI) for their support.

Conflicts of Interest: “The conference paper is not in any conflict of interest”.

References

1. Sedlák, Václav; Pražák, Dominik; Rybář, Jan. Metrologie tlaku ve zdravotnictví /Pressure metrology in healthcare/. In Metrologie /Metrology/. Roč. 30, č. 3 (2021), s. 22 - 26. ISSN 1210-3543.
2. Musíme mať normálny krvný tlak? A aký je vlastne normálny? /Do we need to have normal blood pressure? And what is normal?/. Available online: https://www.osel.cz/9821-musime-mat-normalny-krvny-tlak-a-aky-je-vlastne-normalny.html#google_vignette (accessed on 11-11-2024).
3. Sedlák, Václav. Novel advanced methods of blood pressure standards traceability. [Dissertation thesis]. Slovak University of Technology in Bratislava. Faculty of Mechanical Engineering. Thesis supervisor: doc. RNDr. Jiří Tesař, PhD. Bratislava: FME STU BA, 2023. 88s.
4. O'brien, Eoin a George S. Stergiou. The pursuit of accurate blood pressure measurement: A 35-year travail. The Journal of Clinical Hypertension. 2017, 19(8), 746-752. DOI: 10.1111/jch.13005. ISSN 15246175.
5. Stergiou, George S., Bruce S. Alpert, Stephan Mieke, Jiguang Wang and Eoin O'brien. Validation protocols for blood pressure measuring devices in the 21st century. The Journal of Clinical Hypertension [online]. 2018, 20(7), 1096-1099. DOI:10.1111/jch.13294 ISSN 15246175.
6. O'BRIEN, Eoin, James PETRIE, William LITTLER, et al. The British Hypertension Society protocol for the evaluation of automated and semi-automated blood pressure measuring devices with special reference to ambulatory systems. Journal of Hypertension. 1990, 8(7), 607-619. DOI:10.1097/00004872-199007000-00004
7. O'BRIEN, Eoin, Neil ATKINS, George STERGIOU, et al. European Society of Hypertension International Protocol revision 2010 for the validation of blood pressure measuring devices in adults. Blood Pressure Monitoring. 2010, 15(1), 23-38. ISSN 1359-5237. Dostupné z: DOI:10.1097/MBP.0b013e3283360e98
8. EN ISO 81060-1. Non-invasive sphygmomanometers – Part 1: Requirements and test methods for non-automated measurement type. 2012.
9. EN ISO 81060-2. Non-invasive sphygmomanometers – Part 2: Clinical investigation of automated measurement type. 2019.
10. Chudý, Vladimír; Palenčár, Rudolf; Kureková, Eva; Halaj, Martin. Meranie technických veličín /Measurement of technical quantities/. Bratislava: STU v Bratislave, 1999. 688 s. ISBN 80-227-1275-2.
11. Rybář, Jan. Selected topics from medical metrology. [Habilitation thesis]. Slovak University of Technology in Bratislava, Faculty of Mechanical Engineering. Institute of automation, measurement and applied informatics. Bratislava: FME STU BA, 2022. 78 p.
12. Gersak, Gregor a Janko Drnovsek. Evaluation of non-invasive blood pressure simulators. 11th Mediterranean Conference on Medical and Biomedical Engineering and Computing 2007 [online]. Berlin, Heidelberg: Springer Berlin Heidelberg, 2007, 342-345. IFMBE Proceedings. ISBN 978-3-540-73043-9. Available online: DOI:10.1007/978-3-540-73044-6_87.
13. Smetánka, Andrej. Analysis of specified measures in health care. [Bachelor's thesis]. Slovak University of Technology in Bratislava, Faculty of Mechanical Engineering. Thesis supervisor: Mgr. Ing. Jan Rybář, PhD. Bratislava: SjF STU BA, 2022. 58 p.
14. Measuring Blood Pressure. Available online: https://math.arizona.edu/~system/archives/maw1999/blood/meas.html (accessed on 19-11-2024).

TECHNICAL UNIVERSITY OF KOŠICE
Faculty of Mechanical Engineering

Advanced Analytics and Digitalization as Tools for Modern Business Management

Dominika Sukopová [1,*], Milan Fiľo [1] and Lenka Vyrostková [1]

[1] Department of Business Management and Economics, Faculty of Mechanical Engineering, Technical University of Kosice, 040 01 Kosice, Slovakia; dominika.sukopova@tuke.sk (D.S.); milan.filo@tuke.sk (M.F.); lenka.vyrostkova@tuke.sk (L.V.)
* Correspondence: dominika.sukopova@tuke.sk

Abstract: This study explores the impact of digital tools and advanced analytics on the competitiveness and market position of Slovak fashion brands. As digital transformation continues to shape industries worldwide, the fashion sector in Slovakia is adopting a variety of digital solutions to enhance business operations, improve customer experience, and drive online sales. The research identifies and categorizes digital tools used by leading Slovak fashion brands, including H&M, Zara, Mohito, and others, focusing on their implementation of e-commerce platforms, customer relationship management (CRM) systems, analytical tools, and mobile applications. Through the analysis of these tools, the study reveals a strong correlation between the number of digital tools adopted and the share of online revenues, indicating that a higher number of digital tools contributes to increased market success. Additionally, a survey of 100 customers provides insights into how these digital tools influence customer satisfaction, showing that a majority of respondents perceive a positive impact on their shopping experience. The findings underscore the importance of digitalization in driving innovation, improving efficiency, and maintaining competitiveness in the fast-evolving fashion industry. The study concludes by highlighting the potential of digital tools to reshape the future of fashion retail in Slovakia and beyond.

Keywords: digital transformation, Slovak fashion brands, digital tools, e-commerce, customer satisfaction, CRM systems, online sales, fashion industry, advanced analytics, market competitiveness

1. Introduction

The fashion industry is one of the most dynamic and competitive sectors worldwide. With increasing customer demands, rising globalization, and rapid technological advancements, it is essential for fashion brands to embrace digital transformation. These changes are not just about enhancing online sales but also optimizing the entire value chain—from product design to inventory management, distribution, and customer service. Advanced analytics, including artificial intelligence (AI) and machine learning, offer fashion brands tools to better understand consumer preferences, predict demand, and improve decision-making processes. In Slovakia, similar to other countries, the number of companies adopting these advanced technologies in their business models is steadily growing. Brands like H&M, Zara, Mohito, and others are starting to use advanced systems for inventory management, demand forecasting, and improving customer experiences through digital channels. Additionally, the use of analytical tools to optimize supply chains and adapt to market changes faster is becoming increasingly important.

The aim of this article is to explore how Slovak fashion brands are utilizing digital tools and advanced analytics and how this impacts their market position. We will also focus on the challenges and opportunities that digital transformation presents in this specific sector.

2. Materials and Methods

After setting the research goal, which is to examine how Slovak fashion brands use digital tools and advanced analytics and how this digitalization impacts their market position, it was necessary to create a detailed sequence of steps to achieve this goal.

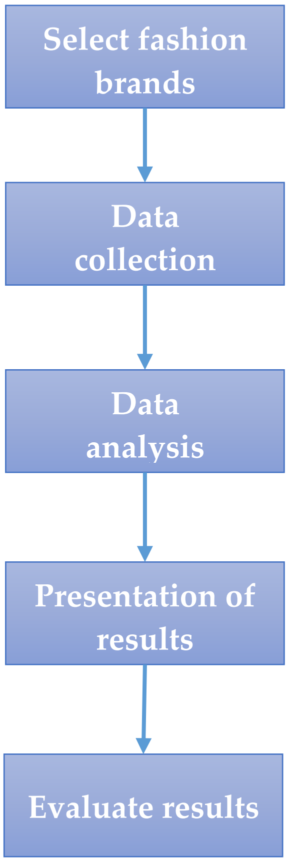

Figure 1. Research Process Flow for Analyzing Digitalization in Slovak Fashion Brands.

As outlined in the process flow diagram (Figure 1), the process began with selecting representative fashion brands that, due to their involvement in digitalization, are relevant for the study in the Slovak context.

After selecting the brands, the next step was data collection, focusing on available secondary sources such as the websites of individual brands, expert articles, press releases, and research studies on digitalization trends in the fashion industry. These data were used to identify the digital tools and analytical techniques employed by various companies.

In the next phase, these data were analyzed to compare the tools and technologies used by the brands and assess their impact on competitiveness and market position. The results were then presented in the form of graphs and tables, showcasing the use of digital tools and their influence on the success of individual brands.

Finally, after analyzing and interpreting the collected data, conclusions were drawn regarding how digitalization contributes to innovation, efficiency, and competitiveness of Slovak fashion brands in the dynamic environment of this sector.

3. Results

The results of this analysis provide valuable insights into the digital transformation within the Slovak fashion industry. Our primary focus was to examine how leading fashion brands are integrating digital tools and advanced analytics to enhance their market position. Based on the data gathered, we identified and categorized the digital tools utilized by brands such as H&M, Zara, Mohito, New Yorker, Bershka, Stradivarius, and Pull&Bear. These tools span across various categories, including e-commerce platforms, CRM systems, analytical tools, marketing platforms, logistics, and mobile applications.

Table 1. Number of Digital Tools Used by Selected Slovak Fashion Brands.

Brand	E-commerce platforms	CRM systems	Analytical tools	Marketing platforms	Logistics	Mobile apps	Other digital tools	Total number of tools
H&M	**1**	**1**	**1**	**1**	**1**	**1**	**0**	**6**
Zara	**1**	**1**	**1**	**1**	**1**	**1**	**0**	**6**
Mohito	**1**	**0**	**1**	**1**	**1**	**0**	**0**	**5**
New Yorker	**1**	**0**	**0**	**1**	**1**	**0**	**0**	**3**
Bershka	**1**	**0**	**1**	**1**	**1**	**1**	**0**	**5**
Stradivarius	**1**	**0**	**1**	**1**	**1**	**1**	**0**	**5**
Pull&Bear	**1**	**0**	**1**	**1**	**1**	**1**	**0**	**5**

All the brands in the table use e-commerce platforms, and most of them include mobile applications and marketing platforms. Brands like H&M and Zara use a wider range of digital tools (6), indicating their comprehensive approach to digital transformation. Brands like Mohito, Bershka, Stradivarius, and Pull&Bear use 5 digital tools, limiting the number of tools in areas such as CRM systems and other digital tools. In contrast, New Yorker uses only 3 tools, showing a lower level of digital integration.

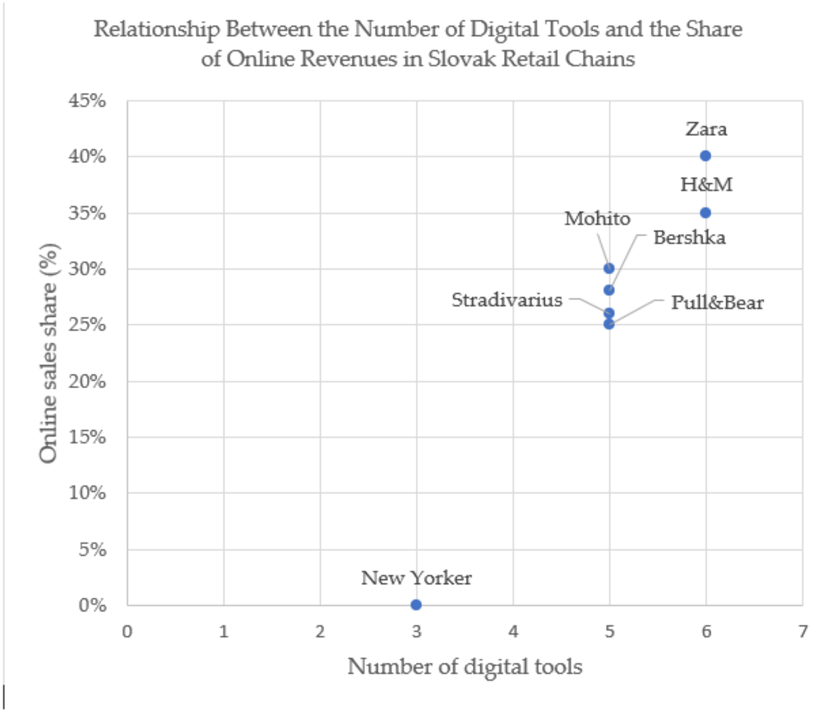

Figure 2. Relationship Between the Number of Digital Tools and the Share of Online Revenues in Slovak Retail Chains.

The chart illustrates the relationship between the number of digital tools and the share of online sales for selected retail chains. The data shows that stores with a higher number of digital tools, such as H&M and Zara, report a higher share of online sales (35% and 40%, respectively). In contrast, New Yorker, which uses only 3 digital tools, has no online sales. This trend suggests that the number of digital tools may positively impact online sales, but other factors, such as the quality of the e-commerce platform and marketing strategy, can also influence these results.

After creating a scatter plot to visualize the relationship between the number of digital tools and the share of online revenues, we proceeded to verify the correlation. The analysis revealed a strong positive correlation, with a value of 0.98, indicating that a higher number of digital tools is associated with a higher share of online sales.

To further validate this finding, we aimed to gather insights from the perspective of customers regarding digital tools. For this purpose, a questionnaire was developed and distributed to 100 customers of the selected fashion brands. The survey focused on customer satisfaction and preferences related to the digital tools used by these retailers. The results of this survey are presented in the following Figure 3, providing additional insights into how digital tools impact the customer experience.

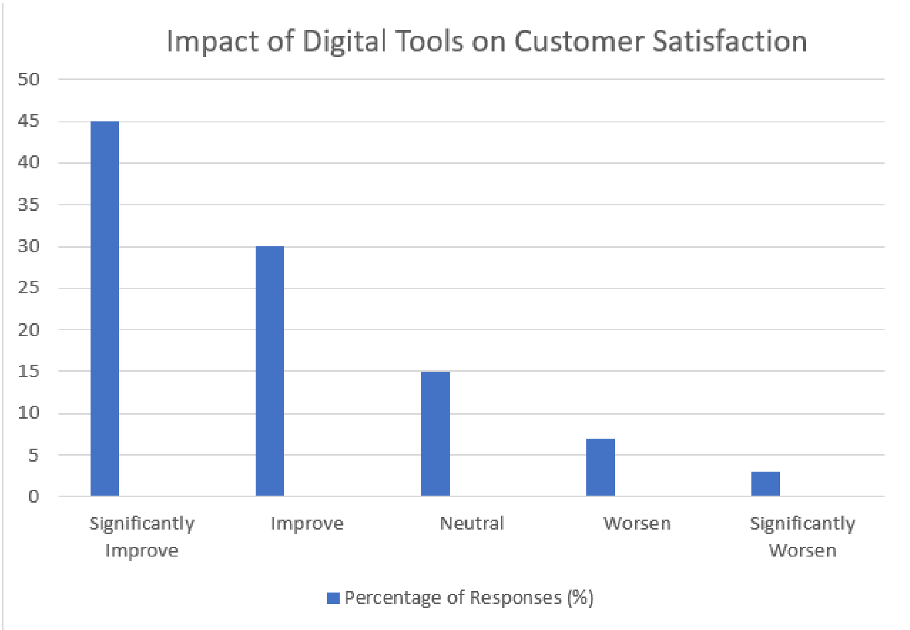

Figure 3. Impact of Digital Tools on Customer Satisfaction.

The results confirm that digital tools have a predominantly positive impact on customer satisfaction. A significant portion of respondents (45%) indicated that digital tools significantly improve their experience, while an additional 30% reported a general improvement. Only a small fraction (10%) perceived a negative effect. These findings suggest that the implementation of digital tools in businesses contributes to enhanced customer perception and satisfaction, aligning with broader trends of digital transformation in improving customer experiences.

Further analysis of the results supports the hypothesis of a strong correlation (r = 0.98) between the adoption of digital tools and improved business outcomes, as measured through customer satisfaction and market performance. This highlights the critical role of digitalization in maintaining competitiveness and meeting modern customer expectations.

4. Discussion

The results of this study provide significant insights into the ongoing digital transformation within the Slovak fashion industry, particularly regarding how leading fashion brands are leveraging digital tools to enhance their market positions. The findings show a clear trend: fashion brands with a higher number of digital tools, such as H&M and Zara, demonstrate stronger online sales performance and higher customer satisfaction. These results confirm the growing importance of digital tools in shaping the future of retail, particularly in an increasingly competitive market where customer experience is crucial.

The correlation between the number of digital tools and the share of online revenues, as depicted in Figure 2, strongly supports the idea that a greater digital presence, especially through e-commerce platforms, CRM systems, and mobile applications, correlates with a higher proportion of online sales. For instance, H&M and Zara, which utilize six digital tools, show a higher share of online sales (35% and 40%, respectively). In contrast, New Yorker, which uses only three digital tools, reports no online sales. This correlation highlights that digital tools are not just a trend but a critical component in driving sales, as they enable brands to engage customers in more efficient and effective ways.

Furthermore, customer satisfaction, as indicated in Figure 3, is positively influenced by the use of digital tools. The survey results show that a significant proportion of customers (45%) report a marked improvement in their overall experience with digital tools, with another 30% noting general improvements. This demonstrates that digitalization contributes to better customer perceptions, which is consistent with existing research suggesting that digital tools, when implemented properly, lead to higher customer satisfaction. It is essential for businesses to understand that customers now expect seamless, convenient, and personalized experiences, and digital tools enable brands to meet these expectations.

The strong positive correlation ($r = 0.98$) between the number of digital tools and both customer satisfaction and online sales provides compelling evidence that the digital transformation is critical for modern businesses. However, it is important to note that while the number of digital tools plays a key role, other factors, such as the quality of the e-commerce platform, marketing strategies, and overall brand positioning, also contribute to the success of digital initiatives. For instance, the quality and user-friendliness of the e-commerce platforms, as well as targeted marketing efforts, can significantly enhance the impact of digital tools.

Despite the overall positive trends, the findings also highlight the need for brands to carefully select and implement digital tools. Brands like Mohito, Stradivarius, and Pull&Bear, while using five tools, lag behind in CRM and other digital tools, which may limit their potential for customer engagement and satisfaction. This suggests that a more comprehensive approach to digitalization, involving a balanced mix of tools across various domains (such as CRM and analytics), could further improve the customer experience and sales outcomes.

Additionally, the case of New Yorker, with its minimal use of digital tools, serves as a reminder of the risks of lagging behind in digital transformation. The absence of online sales for New Yorker underscores the challenges of competing in a digital-first retail environment, where consumer expectations are increasingly shaped by convenience, personalization, and accessibility. Brands that fail to adapt may struggle to remain competitive as digital tools become a fundamental part of the retail landscape.

In conclusion, this study reinforces the critical role of digital tools in shaping the future of the fashion industry. It highlights the importance of adopting a comprehensive and strategic approach to digital transformation, ensuring that brands not only integrate a wide range of digital tools but also focus on the quality of those tools to maximize their impact on both customer satisfaction and business performance. Future research could further explore the role of specific digital tools in driving customer loyalty and long-term business success, as well as investigate the challenges faced by brands in implementing and optimizing these tools.

5. Conclusions

The aim of this study was to explore how Slovak fashion brands implement digital tools and the impact these tools have on their online sales and customer satisfaction. Based on the analysis of selected brands such as H&M, Zara, Mohito, New Yorker, and others, it was found that brands utilizing a broader range of digital tools achieve better results in terms of online sales and customer satisfaction. The results show that a higher number of digital tools correlates with a higher share of online sales, with brands like H&M and Zara, which use 6 tools, achieving 35% to 40% in online sales. In contrast, brands like New Yorker, which only use 3 tools, report no online sales. This trend suggests that digital transformation and the adoption of advanced digital tools are critical for success in digital retail. Customer satisfaction also confirms the positive impact of digital tools, with most respondents indicating an improvement in their customer experience due to the use of modern technologies. These findings highlight the importance of digital transformation, which not only enhances operational efficiency but also positively influences the perception of brands among customers. The research shows that it is essential for fashion brands not only to adopt digital tools but also to implement and optimize them effectively. Based on the results, it is clear that brands focusing on improving the customer experience through e-commerce platforms, CRM systems, and mobile apps have a greater potential to succeed in the digital market.

For future research, it would be interesting to further examine the specific factors influencing the effectiveness of digital tools and their impact on customer loyalty, as well as the challenges that brands face when implementing digital strategies. The results of this study can provide valuable recommendations for Slovak fashion brands looking to enhance their digital capabilities and strengthen their competitiveness in the market.

Acknowledgments: This paper was developed within the implementation of the project VEGA 1-0340-2021 "The impact of a pandemic and the subsequent economic crisis on the development of digitization of enterprises and society in Slovakia".

Conflicts of Interest: The authors declare no conflict of interest.

References

1. Smith, J.; Johnson, P. The Role of Digital Tools in Fashion Industry Transformation. J. Fashion Technol. 2023, 12, 102–115.
2. Brown, T.; Wilson, D. Digital Innovation in Fashion Retail. In Handbook of Digital Transformation, 2nd ed.; Miller, A., Roberts, B., Eds.; Springer: New York, USA, 2021; Volume 3, pp. 154–196.
3. Harrison, L.; Taylor, M. Fashion and Technology: Future Trends, 3rd ed.; Wiley: London, UK, 2022; pp. 54–98.
4. Garcia, M.; Chen, X. Digital Tools and Market Positioning in Fashion Retail. J. Retail Innovation stage of publication (under review).
5. Martinez, R. (University of Barcelona, Barcelona, Spain); Lee, J. (Fashion Institute of Technology, New York, USA). Personal communication, 2023.
6. Thomas, K.; Yang, L.; Hsu, S. The Impact of E-Commerce Tools on Fashion Retail Success. In Proceedings of the Global Fashion Conference, Milan, Italy, May 2023; Garcia, M., Ed.; Springer: Milan, Italy, 2023; Abstract Number 102, pp. 120–130.
7. Davis, P. Digitalization in Retail: A Comprehensive Analysis. Ph.D. Thesis, University of California, Los Angeles, USA, 2021.
8. Digital Trends Report. Available online: www.digitaltrendsfashion.com (accessed on 10 December 2024).

TECHNICAL UNIVERSITY OF KOŠICE
Faculty of Mechanical Engineering

Assessment tools and study design for evaluation of Autonomic Dysfunction in patients with Abdomino-pelvic Vascular Compression Syndromes

Silvia Šišková [1, 2,*], Jozef Živčák[1], Talal Ali[1], Veronika Potočková[3], and Silvia Dobrodenková[4]

[1] Technical University of Košice, Faculty of Mechanical Engineering, Department of Biomedical Engineering, Letná 1/9 | 042 00 Košice-Sever, Slovakia
[2] Asociácia Vaskulárnych Kompresívnych Syndrómov a Ehlers-Danlos, o.z., Balkánska 110/108, 851 10 Bratislava, Slovakia
[3] NeuroMuscular Centre, Department of Neurology, 2nd Faculty of Medicine, Charles University, Motol University Hospital, V Úvalu 84, 150 06 Prague 5, Czech Republic
[4] Travel Health Clinic, Tropical medicine, Tehelná 26, 831 03 Bratislava, Slovakia
* Correspondence: silvia.siskova@student.tuke.sk

Abstract: The objective of this study was to analyze and identify appropriate assessment tools for evaluation of possible autonomic dysfunction, specifically postural orthostatic tachycardia, in the patient population of Abdomino-pelvic vascular compression syndromes (AVCS) in Slovak Republic and Czech Republic. Subsequently, its goal was to formulate a strategy and design a prospective research study, which would use these tools to assess autonomic function in patients with AVCS. After a thorough literature review, knowledge retrieved from conferences focused on Dysautonomia, AVCS, and Ehlers-Danlos Syndromes, and consultations with specialists from relevant fields, the following tests were identified as appropriate assessment tools for the design of this research study: cardiovascular autonomic reflex tests (CARTs) including orthostatic test or NASA Lean Test, Valsalva maneuver, and deep breathing test. Two highly specialized workplaces were identified, one in Slovak Republic and one in Czech Republic. Conditions for cooperation were established and research plan was designed.

Keywords: vascular compression syndromes; autonomic dysfunction; dysautonomia; postural orthostatic tachycardia syndrome; CARTs; orthostatic test; NASA Lean Test, Valsalva maneuver

1. Introduction

Abdomino-pelvic vascular compression syndromes are one of the multiple comorbid conditions associated with Ehlers-Danlos syndrome (EDS), in particular the hypermobile type, and Hypermobility Spectrum Disorders (HSD) [1-6]. They include Median arcuate ligament syndrome (Dunbar syndrome), Left renal vein compression syndrome (Nutcracker syndrome), Superior mesenteric artery syndrome (Wilkie's syndrome), May-Thurner Syndrome and Pelvic Congestion Syndrome [7,8]. These syndromes manifest with a multitude of systemic symptoms, varying considerably among patients. However, there is also a significant overlap of these symptoms with other comorbid conditions commonly associated with EDS and HSD [1-6,9,10].

One of such conditions, frequently also referred to as part of the 'EDS, POTS, MCAS trifecta' is Postural Orthostatic Tachycardia Syndrome (POTS), a subtype of cardiovascular autonomic dysfunction disorders [11,12]. According to the expert consensus, POTS is defined as 1) frequent symptoms which occur with standing, such as lighheadedness, palpitations, tremor, generalized weakness, blurred vision, exercise intolerance, and fatigue; 2) an increase in heart rate of ≥ 30 beats per minute (bpm) within 10 minutes of standing or head-up tilt test (or ≥ 30 bpm in individuals 12-19 years of age) or heart rate exceeding 120 bmp during 10 minutes of upright position; and 3) the absence of orthostatic hypotension (>20 mm Hg drop in systolic blood pressure). In addition, the duration of symptoms should be at least 3 months while at the same time other primary conditions possibly causing sinus tachycardia should be ruled out [13-15].

Other frequent forms of dysautonomia include neurally mediated hypotension (NMH) otherwise known as vaso-vagal syncope or neuro-cardiogenic syncope, orthostatic hypotension (OH) and orthostatic intolerance (OI) [16]. Some patients might even present with a combination of these [17]. The association of POTS and AVCS has already been pointed out by multiple studies and specialists treating these disorders [1-6,18-23]. Figure 1 below is a representation of blood volume redistribution changes in patients with POTS and venous and connective tissue disease [24]. The aim of this paper is to plan and design prospective research study by identifying appropriate assessment tools as well as to establish cooperations with highly specialized workplaces, in order to evaluate the prevalence of POTS or other types of Dysautonomia in patients previously diagnosed with AVCS in Slovak Republic and Czech Republic.

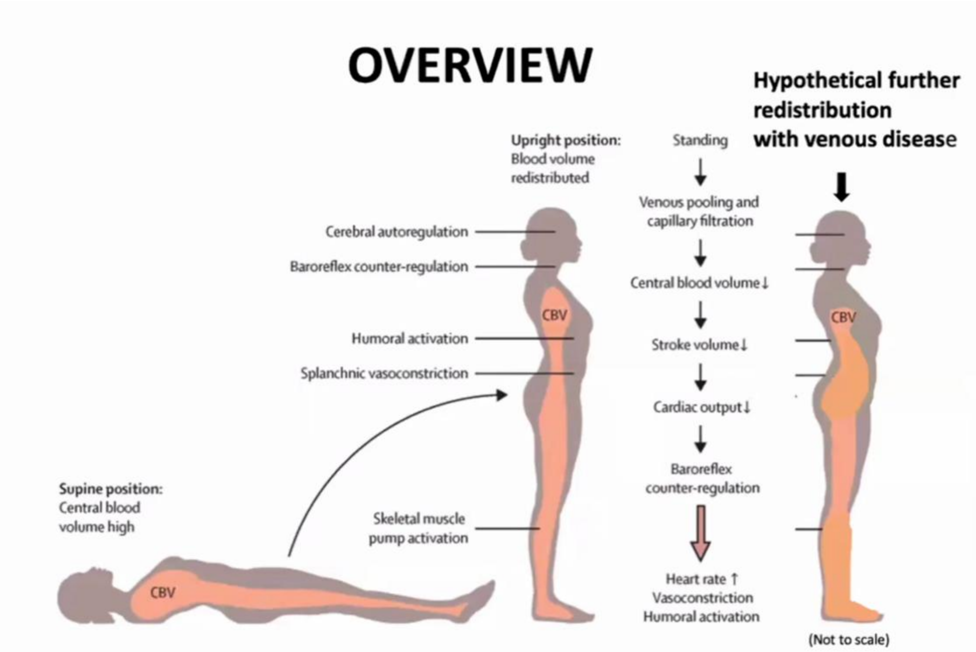

Figure 1. Postural Orthostatic Tachycardia Syndrome in patients with venous and connective tissue disease [24].

2. Materials and Methods

55 patients with previously diagnosed Abdomino-pelvic vascular compression syndromes in Slovak Republic and Czech Republic were enrolled in this study through the patient association Asociácia Vaskulárnych Kompresívnych Syndrómov a Ehlers-Danlos founded in Slovak Republic. It is a non-profit association, dedicated to supporting patients with AVCS and EDS, and advancing awareness, education and research of these conditions. All patients provided written informed consent to participate in this study. Participants younger than 18 years of age signed the informed consent along with their parents or guardians.

In the initial phase of the study, all 55 patients were interviewed to screen for their detailed medical history, including their established or working diagnoses, past surgical interventions and complex symptoms. Patients with symptoms suggestive of possible autonomic dysfunction were identified and selected for this study. Target group of symptoms comprised of the following symptoms listed in Table 1.

Table 1. Symptoms of autonomic dysfunction, used for initial preliminary patient screening.

Orthostatic symptoms *(related to standing or changing body position):*	***Non-orthostatic*** *symptoms (unrelated to body position):*	***Systemic symptoms***
syncope or presyncope, dizziness, light-headedness, palpitations, chest pain or discomfort, shortness of breath, visual and hearing disturbances, exercise intolerance, post exercise malaise, leg swelling and discoloration [13,14,16,25].	gastrointestinal dysfunction, including nausea, early satiety, vomiting, bloating, diarrhea alternating with constipation, abdominal pain; urogenital dysfunction including urinary retention, frequency, urgency, incontinence, erectile dysfunction in men [13,14,25,26].	chronic fatigue, general weakness, tremulousness, temperature dysregulation (cold hands and feet, or excessive sweating), headache, sleep complaints and cognitive impairment, such as brain fog [13,14,25].

Results of this initial screening were summarized, analysed and evaluated in order to be prepared for the second phase of the study.

In the next phase, a thorough literature research was performed in order to identify the most appropriate assessment tools for screening of POTS and Dysautonomia in these patients. Simultaneously, both countries were screened to detect highly specialized workplaces able to accommodate the necessary requirements for POTS and Dysautonomia examination.

3. Results

Out of the 55 interviewed patients with previously diagnosed AVCS, 45 (81.8 %) patients presented with at least one symptom from each category of the above-listed table of symptoms, hence were identified with symptomatology suggestive of possible POTS or other form of cardiovascular autonomic dysfunction disorder. None of these 55 patients have previously been tested and evaluated for POTS or autonomic dysfunction.

After a thorough literature research, cardiovascular autonomic reflex tests (CARTs) including orthostatic test or NASA Lean Test, Valsalva maneuver, and deep breathing test, were identified as appropriate tools for examination and assessment of POTS and other forms of Dysautonomia. Both NASA Lean Test and orthostatic test are described as appropriate methods for POTS testing, both measuring and comparing heart rate and blood pressure values during resting phase and orthostatic challenge phase [13-16, 27-31]. In comparison, NASA Lean Test has the advantage of being very accessible in terms of both cost and required knowledge-to-perform aspects [28-30].

Two workplaces were identified which were able to meet the needed examination requirements, one in Slovak Republic and one in Czech Republic, Travel Health Clinic, Tropical medicine, Tehelná 26, 831 03 Bratislava, Slovakia and NeuroMuscular Centre, Department of Neurology, 2nd Faculty of Medicine, Charles University, Motol University Hospital, Prague, Czech Republic, respectively. Conditions of cooperation were discussed and agreed upon. Figure 2 below shows a patient during NASA Lean Test with the use of a simple pulse oximeter, performed in Slovakia. Figure 3 shows the Fan study device for autonomic nervous system assessment through CARTs used in Czech Republic.

Figure 2. NASA Lean Test, measurement of heart rate and oxygen saturation levels with pulse oximeter.

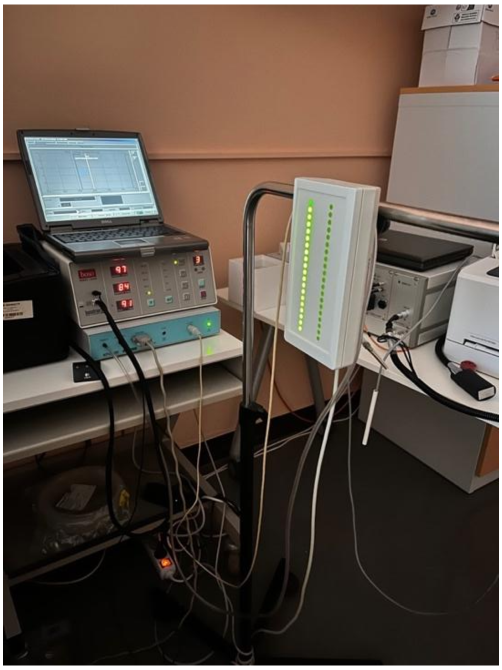

Figure 3. Fan study device (Schwarzer, Germany) used for autonomic nervous system assessment though CARTs used in Prague, Czech Republic [31].

4. Study Limitations

The 2 workplaces identified for research cooperation each utilize slightly different sets of examination techniques as well as equipment used for measurement of vital signs (i.e., blood pressure and heart rate). NASA Lean Test and deep breathing test with the use of a pulse oximeter are utilized at the Travel Health Clinic, Tropical medicine in Bratislava, Slovakia. While orthostatic test, Valsalva maneuver, and deep breathing test with the use of Fan study device for autonomic nervous system assessment, are performed at Neuro-Muscular Centre, Department of Neurology, 2nd Faculty of Medicine, Charles University, Motol University Hospital in Prague, Czech Republic. Moreover, other types of examination tools recommended for further POTS evaluation, such as Head-up Tilt Test, 24-hour Holter, transthoracic echocardiogram, exercise stress test, quantitative sudomotor axon reflex testing (QSART) and autonomic reflex screen (ARS) are not available directly at these two centers [13,27]. Given the slightly different sets of examination techniques as well as equipment used, there might be some differences in the future overall evaluation of patient examination results, thus also the final diagnoses.

Figure 4. Head-Up Tilt Test (prospective option as an additional measurement tool).

4. Discussion

The combined results of literature research on AVCS, EDS and POTS, information and knowledge retrieved from conferences on Ehlers-Danlos Syndrome and Dysautonomia, discussions with specialists from relevant fields with years of expertise, as well as the results of the first phase of this research study, suggest a correlation between Abdomino-pelvic vascular compression syndromes and Postural orthostatic tachycardia syndrome or other forms of cardiovascular autonomic dysfunction disorders. Cardiovascular autonomic reflex tests (CARTs) including orthostatic test or NASA Lean Test, Valsalva maneuver, and deep breathing test are useful and suitable means of assessment tools for evaluation of POTS and Dysautonomia. Proceeding this research will provide further insights into the mechanisms between AVCS and POTS as well as its prevalence.

5. Conclusions

Overall, there seems to be an association between Abdomino-pelvic vascular compression syndromes and cardiovascular autonomic dysfunction. Patients with AVCS should be examined for POTS and Dysautonomia. This proposed prospective study design warrants the necessity of further research in order to allow for a more in-depth understanding of the interconnected relationships.

Disclosures: All data and information were obtained directly from patients, with their approvals to be used in this study.

Acknowledgments: This paper was written with the financial support from the KEGA granting agency within the project solutions No. 050TUKE-4/2022 and No. 021TUKE-4/2022, and with financial support from the APVV granting agency within the project solutions No. APVV-20-0068 and No. SK-CZ-RD-21-0056.

References

1. Kim, K. International Foundation of Abdominal Vascular Compression Syndromes, Baltimore, MD. Abdominal Vascular Compression Syndromes: Current and Future of Management of Abdominal Vascular Compression Syndromes that Includes Median Arcuate Ligament Syndrome, Nutcracker Syndrome, Superior Mesenteric Artery Syndrome, May-Thurner Syndrome, and Associated Pelvic Venous Insufficiency. Journal of Vascular Surgery. April Supplement 2023. PIIS074152142300201X
2. Kim, K. & International Foundation of Abdominal Vascular Compression Syndromes. (2023, April 15). Abdominal Vascular Compression Syndromes: AVCS: Relationship & Interconnectivity of May-Thurner, Nutcracker, Median Arcuate Ligament, Superior Mesenteric Artery Syndromes, & Associated Pelvic Venous Insufficiency [Presentation]. II Venous Summit CCEV 2023 Endovascular Surgery Chapter, Malaga, Spain. https://venous-summit.com/VENOUS-SUMMIT2023
3. Ormiston CK, Padilla E, Van DT, Boone C, You S, Roberts AC, Hsiao A, Taub PR. May-Thurner syndrome in patients with postural orthostatic tachycardia syndrome and Ehlers-Danlos syndrome: a case series. Eur Heart J Case Rep. 2022 Apr 9;6(4):ytac161. doi: 10.1093/ehjcr/ytac161. PMID: 35620060; PMCID: PMC9131024.
4. Rebecca S Steinberg, Weston Dicken, Alexis Cutchins, Narrative Review of Postural Orthostatic Tachycardia Syndrome: Associated Conditions and Management Strategies, US Cardiology Review 2023;17:e13. https://doi.org/10.15420/usc.2022.35
5. Sandmann, W., Scholbach, T., & Verginis, K. (2021). Surgical treatment of abdominal compression syndromes: The significance of hypermobility-related disorders. American Journal of Medical Genetics Part C: Seminars in Medical Genetics, 1–9. https://doi.org/10.1002/ajmg.c.31949
6. Hakim A. Hypermobile Ehlers-Danlos Syndrome. 2004 Oct 22 [Updated 2024 Feb 22]. In: Adam MP, Feldman J, Mirzaa GM, et al., editors. GeneReviews® [Internet]. Seattle (WA): University of Washington, Seattle; 1993-2024.
7. D'Oria M, Zlatanovic P, Anthony A, Dua A, Flores AM, Tanious A, Rodríguez Morata A, Scerrati A, Baccellieri D, Biscetti F, Baldazzi G, Mantovani G, Sen I, Peinado Cebrian J, Rocha-Neves J, Sousa J, Davidovic L, Juszynski M, Markovic M, Oller Grau M, Tessari M, Hynes N, Gloviczki P, Shaw P, Zamboni P, Hinchliffe R, Ricci R, Sultan S, Acharya Y, Troisi N, Antignani PL, Mansilha A, Komlos PP. International Union of Angiology consensus document on vascular compression syndromes. Int Angiol. 2023 Aug;42(4):282-309. doi: 10.23736/S0392-9590.23.05100-3. Epub 2023 Jul 27. PMID: 37498053.
8. Ali T., Tomka J., Bakirli I., Bakirov I. Surgical Treatment of Wilkie's Syndrome by Vascular Transposition. Cureus. 2022 Apr 18;14(4):e24251. doi: 10.7759/cureus.24251. PMID: 35475250; PMCID: PMC9018456.
9. Gensemer C, Burks R, Kautz S, Judge DP, Lavallee M, Norris RA. Hypermobile Ehlers-Danlos syndromes: Complex phenotypes, challenging diagnoses, and poorly understood causes. Developmental Dynamics. 2021; 250:318–344. https://doi.org/10.1002/dvdy.220
10. Daylor, Victoria & Gensemer, Cortney & Norris, Russell & Bluestein, Linda. (2023). Hope for Hypermobility: Part 1—An Integrative Approach to Treating Symptomatic Joint Hypermobility. Topics in Pain Management. 38. 1-9. 10.1097/01.TPM.0000924780.91929.b3.
11. Walker, A. (2021). The trifecta passport: Tools for mast cell activation syndrome, postural orthostatic tachycardia syndrome and Ehlers-Danlos syndrome.
12. Wang, E., Ganti, T., Vaou, E., & Hohler, A. (2021). The relationship between mast cell activation syndrome, postural tachycardia syndrome, and Ehlers-Danlos syndrome. Allergy and Asthma Proceedings: The Official Journal of Regional and State Allergy Societies, 42(3), 243–246. https://doi.org/10.2500/aap.2021.42.210022
13. Sheldon, R. S., Grubb, B. P., 2nd, Olshansky, B., Shen, W.-K., Calkins, H., Brignole, M., Raj, S. R., Krahn, A. D., Morillo, C. A., Stewart, J. M., Sutton, R., Sandroni, P., Friday, K. J., Hachul, D. T., Cohen, M. I., Lau, D. H., Mayuga, K. A., Moak, J. P., Sandhu, R. K., & Kanjwal, K. (2015). 2015 heart rhythm society expert consensus statement on the diagnosis and treatment of postural tachycardia syndrome, inappropriate sinus tachycardia, and vasovagal syncope. Heart Rhythm: The Official Journal of the Heart Rhythm Society, 12(6), e41-63. https://doi.org/10.1016/j.hrthm.2015.03.029
14. Vernino, S., Bourne, K. M., Stiles, L. E., Grubb, B. P., Fedorowski, A., Stewart, J. M., Arnold, A. C., Pace, L. A., Axelsson, J., Boris, J. R., Moak, J. P., Goodman, B. P., Chémali, K. R., Chung, T. H., Goldstein, D. S., Diedrich, A., Miglis, M. G., Cortez, M. M., Miller, A. J., … Raj, S. R. (2021). Postural orthostatic tachycardia syndrome (POTS): State of the science and clinical care from a 2019 National Institutes of Health Expert Consensus Meeting - Part 1. Autonomic Neuroscience: Basic & Clinical, 235(102828), 102828. https://doi.org/10.1016/j.autneu.2021.102828

15. Roma, M., Marden, C. L., De Wandele, I., Francomano, C. A., & Rowe, P. C. (2018). Postural tachycardia syndrome and other forms of orthostatic intolerance in Ehlers-Danlos syndrome. Autonomic Neuroscience: Basic & Clinical, 215, 89–96. https://doi.org/10.1016/j.autneu.2018.02.006
16. Hakim, A., O'Callaghan, C., De Wandele, I., Stiles, L., Pocinki, A., & Rowe, P. (2017). Cardiovascular autonomic dysfunction in Ehlers-Danlos syndrome-Hypermobile type. American Journal of Medical Genetics. Part C, Seminars in Medical Genetics, 175(1), 168–174. https://doi.org/10.1002/ajmg.c.31543
17. Lazúrová Z, Mitro P, Lazúrová I, Lukáčová M, Heidecke H, Lepej J, Marin I, Shoenfeld Y. Postural Orthostatic Tachycardia Syndrome (POTS) of Autoimmune Origin - Case and Review. J Biomed Res Environ Sci. 2024 Jul 24; 5(7): 859-865. doi: 10.37871/jbres1964, Article ID: JBRES1964, Available at: https://www.jelsciences.com/articles/jbres1964
18. Knuttinen, M.-G., Zurcher, K. S., Khurana, N., Patel, I., Foxx-Orenstein, A., Harris, L. A., Lawrence, A., Aguilar, F., Sichlau, M., Smith, B. H., & Smith, S. J. (2021). Imaging findings of pelvic venous insufficiency in patients with postural orthostatic tachycardia syndrome. Phlebology, 36(1), 32–37. https://doi.org/10.1177/0268355520947610
19. Pelling M M, Brown M T, Gilliland C A, et al. (February 10, 2024) Left Common Iliac Vein Stenting in a Case of Postural Orthostatic Tachycardia Syndrome/Pelvic Pain Overlap. Cureus 16(2): e53974. DOI 10.7759/cureus.53974
20. Garcia, M., Almuwaqqat, Z., Steinberg, R., McGeoch, C., Bortfeld, K., Thadani, S., Gilliland, C., & Cutchins, A. (2023). Abstract 15621: Pelvic vein compression in patients diagnosed with postural Orthostatic Tachycardia Syndrome. Circulation, 148(Suppl_1). https://doi.org/10.1161/circ.148.suppl_1.15621
21. Hassan, M, Thadani, S, McGeoch, C. et al. PELVIC VENOUS COMPRESSION IN PATIENTS WITH POSTURAL ORTHOSTATIC TACHYCARDIA SYNDROME. JACC. 2024 Apr, 83 (13_Supplement) 2266.https://doi.org/10.1016/S0735-1097(24)04256-6
22. Thadani, S, McGeoch, C, Steinberg, R. et al. LOWER EXTREMITY VENOUS INSUFFICIENCY IN PATIENTS WITH POSTURAL ORTHOSTATIC TACHYCARDIA SYNDROME. JACC. 2024 Apr, 83 (13_Supplement) 2267.https://doi.org/10.1016/S0735-1097(24)04257-8
23. Gil, R S. (2024, May 11). Dysautonomia, MCAS, gastroparesis, etc… What else should we look for in a patient with a compressive abdominopelvic vascular syndrome? [Presentation]. III Venous Summit CCEV 2024 Endovascular Surgery Chapter, Malaga, Spain. https://venous-summit.com/VENOUS-SUMMIT2024
24. Cutchins, A. (2024, June 29). Exploring a new path in the paradigm of POTS: Venous and connective tissue disease as key contributors [Presentation]. Dysautonomia International 12th Annual Conference. https://www.dysconf.org/
25. Gall, N. (2021). Clinical Presentation. In Postural Tachycardia Syndrome (pp. 11–16). Springer International Publishing.
26. Tailor, V., & Khullar, V. (2021). Gynaecological Considerations in PoTS. In Postural Tachycardia Syndrome (pp. 141–152). Springer International Publishing.
27. De Wandele, I., Rombaut, L., Leybaert, L., Van de Borne, P., De Backer, T., Malfait, F., De Paepe, A., & Calders, P. (2014). Dysautonomia and its underlying mechanisms in the hypermobility type of Ehlers-Danlos syndrome. Seminars in Arthritis and Rheumatism, 44(1), 93–100. https://doi.org/10.1016/j.semarthrit.2013.12.006
28. Harris, B. (n.d.). Home testing for POTS: The poor man's tilt table and NASA lean test. Eds.Clinic. Retrieved November 23, 2024, from https://www.eds.clinic/articles/pots-test-poor-mans-tilt-table-and-nasa-lean-test
29. Bateman Horne Center. "10-Minute NASA Lean Test (a Standardized Passive Stand Test): Clinician Instructions." Bateman Horne Center, 2022.
30. Bateman, Lucinda. "Why the 10-Minute NASA Lean Test?" Bateman Horne Center, 5 July 2022, batemanhornecenter.org/why-the-10-minute-nasa-lean-test/.
31. Potockova, V., Mala, S., Hoskovcova, L., Capek, V., Nedelka, T., Riedlbauchova, L., Baumgartner, D., Mensova, L., & Mazanec, R. (2022). Thermal quantitative sensory testing as a screening tool for cardiac autonomic neuropathy in patients with diabetes mellitus. Brain and behavior, 12(3), e2506. https://doi.org/10.1002/brb3.2506

TECHNICAL UNIVERSITY OF KOŠICE
Faculty of Mechanical Engineering

Bypassing CAD modelling through Parametric G-Code Generation for 3D Printing

Pavol Štefčák [1,*], Ivan Gajdoš [1] and Ján Slota [1]

[1] Slovakia, Technical University of Košice, Department of Technology, Materials and Computer Supported production, Mäsiarska 74,040 01 Košice; pavol.stefcak@tuke.sk; ivan.gajdos@tuke.sk; jan.slota@tuke.sk
* Correspondence: pavol.stefcak@tuke.sk

Abstract: Additive manufacturing is widely used in prototyping and producing functional parts. Industrial robots are increasingly being employed in this process due to their ability to create parts with structures that traditional 3D printers cannot achieve. The robot's degrees of freedom, along with its range of motion and precision, enable the production of larger, stronger parts compared to conventional 3D printing. However, integrating robots into the 3D printing process requires the development of new solutions to improve and simplify prototyping and manufacturing. This work focuses on the need for innovative slicing methods for Robotic Additive Manufacturing. A new approach to generating control codes without relying on external slicers is proposed. The paper introduces a fresh perspective on the slicing process in Robotic Additive Manufacturing.

Keywords: Large Format Additive Manufacturing, Grasshopper, slicing, parametric design, visual scripting

1. Introduction

Currently, 3D printers are widely used for prototyping and creating structures. The appeal of this solution primarily lies in its ability to facilitate Additive Manufacturing (AM) of three-dimensional objects with complex geometries [1]. Researchers in this field have proposed various solutions related to device design, components, and software [2, 3, 4]. Additive Manufacturing (AM) process consists of three phases which are an integral part of the 3D object creation process: preprocessing, processing and postprocessing. Preprocessing phase includes a set of processes that need to be carried out before the actual printing process including the creation of a 3D model and the generation of the G-code for the production machine, while considering the technological possibilities characteristic of the chosen type of AM. Large-format additive manufacturing (LFAM) an increasing trend toward manufacturing of large-scale parts in specified areas of development as a characteristic area of additive manufacturing based on extrusion material is no longer a novelty in research and production industry. However, new possibilities are constantly emerging in the process of G-code generation, a process known as "slicing" is where specialized software is used to convert an STL model into specific instructions for the 3D printer [5]. However, existing slicing solutions are primarily designed for traditional 3D printers [6] which are in most cases not suitable for large-format additive manufacturing, where individual solutions for the specific application are often required. LFAM by Screw-Extrusion Additive Manufacturing (SEAM), in which the material is fed in the form of pellets [7], often require a single path continuous printing and precise tool path planning actions due to retraction of extruded material is impossible or very difficult and mostly continuous path generation is required. That’s why researchers not only analyze the overall processes and various technologies but also direct their attention to pre-processing phase where necessitates the use of a variety of tools, consumes a significant amount of time, and limits the ability to freely modify process parameters [8]. Most solutions proposed in the literature are based on the use of a variety of computer programs such as: Ubuntu OS, Notepad++, Matlab, Microsoft Excel, CAD software, and Slic3r simultaneously trying to find the appropriate tool for the slicing process in the field of LFAM. Therefore there is a need to develop solutions that will enable the reduction in quantity of software utilized in the process of LFAM. A novel approach would certainly reduce model preparation time and facilitate the work of engineers. Currently, time reduction is one group of strategies for improving 3DP highlighted in the research [9]. One such solution could be direct g-code generation without the need of a 3D model. This would help to skip certain steps in the pre-processing process and contribute to saving the overall production time from the idea itself to the final object (Figure 1.).

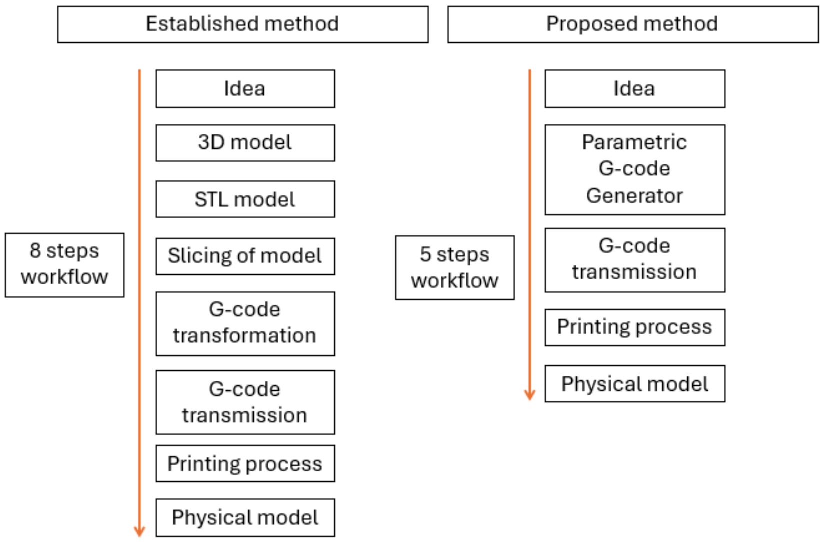

Figure 1. Comparison of the standard and the proposed method in the preprocessing phase.

The potential of such an approach is presented, when the reduction of model preparation time and the reduction of software utilized is achieved. In Figure the difference between the standard solution and the proposed novel approach was presented. As a result of standard solutions, multiple software tools are required, increasing the overall processing time. To address this issue, the article introduces a novel solution that utilizes a parametric model of the component being prototyped and manufactured to directly generate control code for an industrial robot in the LFAM process.

2. Materials and Methods

The suggested approach consists of a multi-modular function system designed in Rhino Grasshopper software (Figure 2.) to be used in robotics LFAM of ribbed components. It is predicated on a novel method of slicing that is carried out using a mathematical model and a predetermined point sequence. An alternative to the popular slicing procedure based on the STL model is this creative solution. The robot's control code and toolpath visualization are the output, whereas the parametric description of the component to be manufactured is the input. The system is made up of well-designed modules that gradually combine and alter the input data to produce the desired output. Figure 3 displayed a system visualization.

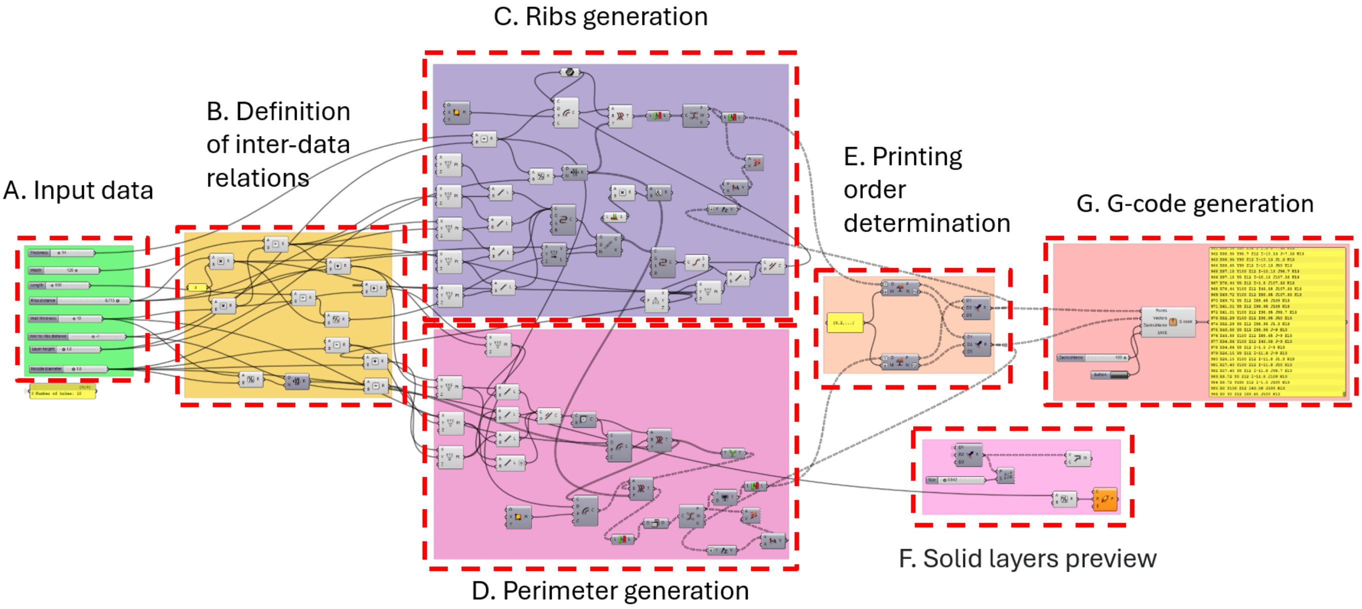

Figure 2. Custom part made Grasshopper direct G-code generator.

The proposed system is possible to divide into 7 sections where a specific process takes place:

A. Input data- Manufacturing process parameters
B. Definition of inter-data relations - The module calculates the basic point coordinates using the input data that characterizes the manufactured component
C. Ribs generation – Section for calculating ribs based on controlled infill principles
D. Perimeter generation - Structure points calculating for the outer perimeter
E. Printing order determination – Section that secures layer and inter-layer point printing order (Figure 3.)
F. Solid layers preview – Inter-data relation representation
G. G-code generation - The Data Combining Module made it possible to combine and present data that came from using the system modules in G-Code format.

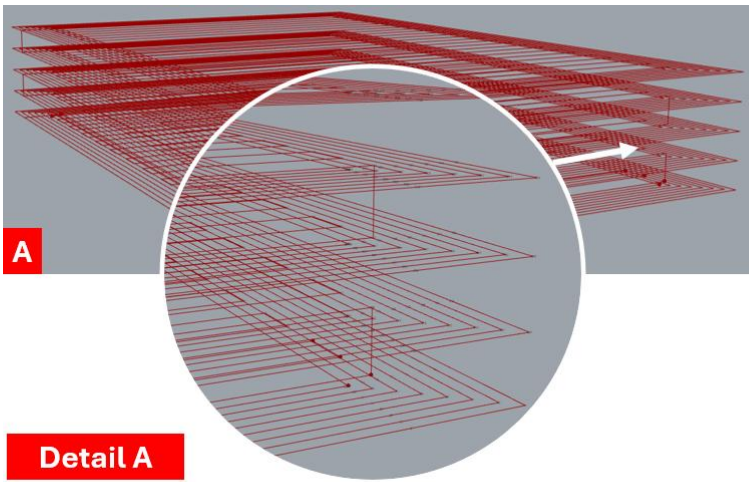

Figure 3. Detailed preview of layer order alternation and tool path movements.

The basis for the proposed system utilization is an adequate parametric description of the ribbed element to be manufactured (Figure 4.).

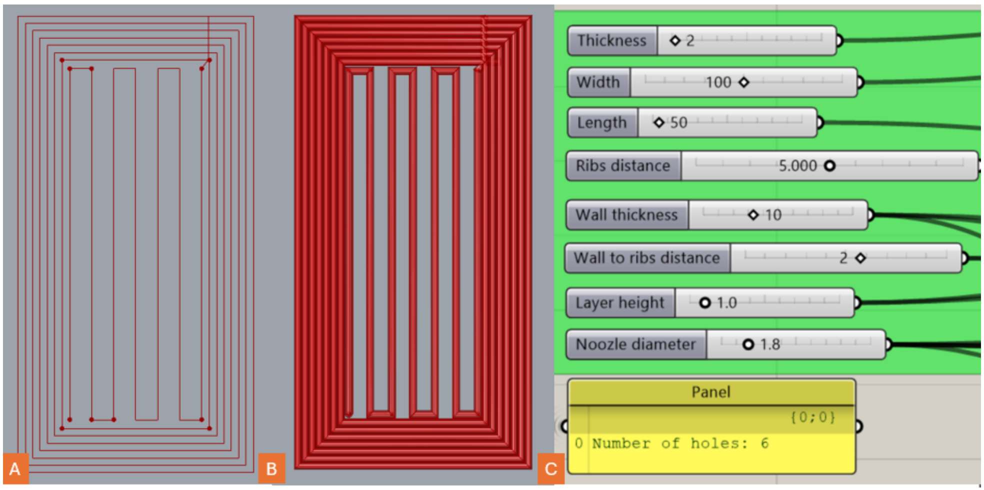

Figure 4. Preview of generated tool paths with referenced parametrically changeable points positioning (A), Preview of material deposition assumption (B), Detailed view of changeable input data (C).

To verify proposed method, several integrated function blocks and special position-obtaining blocks of Rhino Grasshopper software were used. The experiment was conducted on a FANUC M-20iB/25 robot equipped with an MDPH2 pellet extruder (Figure 5).

3. Results

Offline programming and simulation of the robot's movements was done in specialized RoboDK software for industrial robots with 3D printing plugin. Translated robot language was transferred to the control system of the robot and then executed (Figure 5.). The experimental part verified the functionality of the proposed solution. Several samples with different ribs distance were printed for validation of method functionality and used for further analysis.

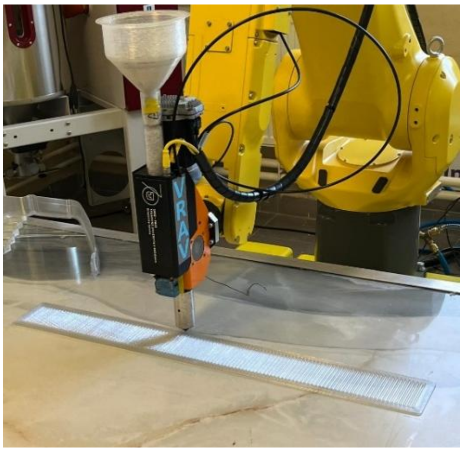

Figure 5. Experimental verification of the proposed solution on LFAM Robotic arm.

In all processes, manufacturing data were settled according to Table 1. and a ribbed structures with custom dimensions was manufactured for textile industry application.

Table 1. Manufacturing parameters used in context of experimental verification.

Manufacturing parameters	Values
Part dimensions	150*950*20 mm
Amount of material used	1,2 kg
Robot accuracy	0,05 mm
Material	PETG
Printing speed	25 mm/s
Layer height	1 mm
Nozzle temperature	220 °C
Cooling	Off

By experimental verification on smaller samples, it was possible to set optimal input data as ribs distance, wall to ribs distance and to ensure overlapping of the material at the frame (perimeter) interface and infill ribs which ensured the interconnection of the material without over extrusion (Figure 6.).

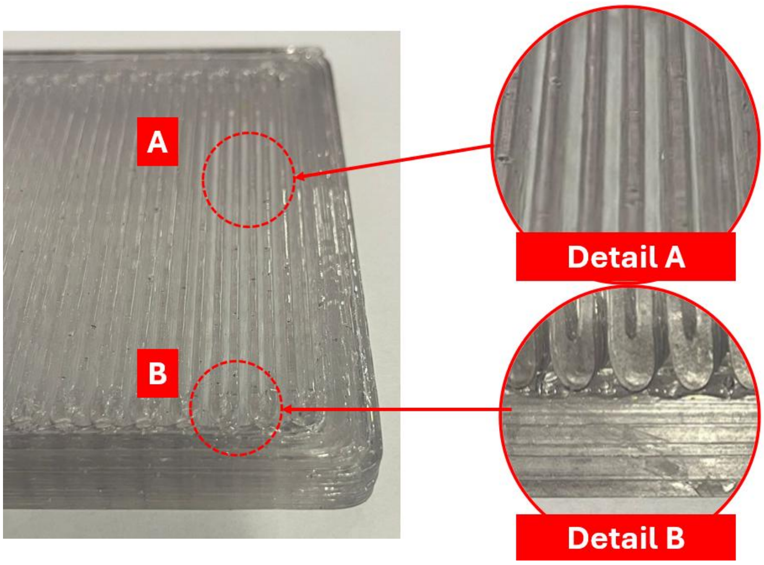

Figure 6. Final ribbed part (A) with overlapped ribs to perimeter connection (B).

4. Conclusion

The verification of the method proposed in this article had a multi-stage character, and the main goal was to evaluate its effectiveness, as well as the possibility of practical application. Each of the stages presented confirmed the validity of the use of the solution in the aspect under consideration. The results of the developed system allowed visualization of the considered elements and generation of the robot code. The obtained G-Code ensured the correct operation of the robot tool, reflecting the key paths of the manufactured model layers. Their implementation into the industrial robot made it possible to actually manufacture the large-size component, as well as other samples. Indeed, the proposed approach allows for the fabrication of alternative ribbed structures - both in terms of the dimensions of the manufactured part and the material. However, despite being dedicated to the manufacture of the aforementioned parts, it is possible to modify the parameters so as to obtain uniform structures (as presented in the case of mats). Wider modification, in turn, allows to implement the method to produce structures of a similar nature. The main benefit of using the developed solution is the reduction in the time required to prepare the model for robotic additive manufacturing. Classically, this process is very time-consuming and requires the design of the part in a CAD environment, the subsequent generation of the STL model, and the implementation of the slicing process using well-known solutions. The proposed solution, on the other hand, makes it possible to manufacture parts in less time than the standard approach. This time will, of course, depend on the designer and operator, but the use of a purely parametric model and the definition of key process parameters will always result in a reduction in the time of pre-process procedures, especially if the final dimensions, geometric characteristics and production parameters are not predetermined or change rapidly depending on the requirements of the final product.

Acknowledgments: This work was supported by the Slovak Research and Development Agency, project title: Research on the possibilities of forming and joining innovative metal-plastic composites in the production of lightweight thin-walled structures", project numbers: APVV SK-PL-23-0040. The authors are also grateful for the support in the experimental work to the project VEGA 1/0539/23: Research on hybrid sandwich structures with customized properties. This work was supported by the Slovak Research and Development Agency, project title: Research on the possibilities of forming and joining innovative metal-plastic composites in the production of lightweight thin-walled structures", project numbers: SK-PL-23-0040. The authors are also grateful for the support in the experimental work to the project KEGA 050TUKE-4/2023.

The authors would also like to express their special thanks to Fanuc Slovakia company for their support in the realization of the research.

FANUC

Conflicts of Interest: The authors declare no conflict of interest.

References

1. Hong, Q., Lin, L., Li, Q., Jiang, Z., Fang, J., Wang, B., Liu, K., Wu, Q., & Huang, C. (2021). A direct slicing technique for the 3D printing of implicitly represented medical models. *Computers in Biology and Medicine*, *135*, 104534. https://doi.org/10.1016/j.compbiomed.2021.104534
2. Barnett, E., & Gosselin, C. (2015). Large-scale 3D printing with a cable-suspended robot. *Additive Manufacturing*, *7*, 27–44. https://doi.org/10.1016/j.addma.2015.05.001
3. Alkhatib, T. (2023). *Robotic 3D Printing of sustainable structures* [Thesis]. Linnaeus University.
4. Werner, J., Aburaia, M., Raschendorfer, A., & Lackner, M. (2021). MeshSlicer: A 3D-Printing software for printing 3D-models with a 6-axis industrial robot. *Procedia CIRP*, *99*, 110–115. https://doi.org/10.1016/j.procir.2021.03.018
5. Piedra-Cascón, W., Krishnamurthy, V. R., Att, W., & Revilla-León, M. (2021). 3D printing parameters, supporting structures, slicing, and post-processing procedures of vat-polymerization additive manufacturing technologies: A narrative review. *Journal of Dentistry*, *109*, 103630. https://doi.org/10.1016/j.jdent.2021.103630
6. Senthil, T. S., Vel, N. R. O., Puviyarasan, M., Babu, S. R., Surakasi, R., & Sampath, B. (2023a). Industrial Robot-Integrated Fused Deposition Modelling for the 3D Printing Process. In *Advances in chemical and materials engineering book series* (pp. 188–210). https://doi.org/10.4018/978-1-6684-6009-2.ch011
7. Li, X., Liu, W., Hu, Z., He, C., Ding, J., Chen, W., Wang, S., & Dong, W. (2024). Supportless 3D-printing of non-planar thin-walled structures with the multi-axis screw-extrusion additive manufacturing system. *Materials & Design*, *240*, 112860. https://doi.org/10.1016/j.matdes.2024.112860
8. Ariffin, M. K. a. M., Sukindar, N. A., Baharudin, B. H. T., Jaafar, C. N. A., & Ismail, M. I. S. (2018). Slicer Method Comparison Using Open-source 3D Printer. *IOP Conference Series Earth and Environmental Science*, *114*, 012018. https://doi.org/10.1088/1755-1315/114/1/012018
9. Rodriguez-Padilla, C., Cuan-Urquizo, E., Roman-Flores, A., Gordillo, J. L., & Vázquez-Hurtado, C. (2021a). Algorithm for the Conformal 3D Printing on Non-Planar Tessellated Surfaces: Applicability in Patterns and Lattices. *Applied Sciences*, *11*(16), 7509. https://doi.org/10.3390/app11167509

TECHNICAL UNIVERSITY OF KOŠICE
Faculty of Mechanical Engineering

Preparation for hydrogen combustion

Pavol Tarbajovský [1,*], Michal Puškár [1] and Matúš Virostko [1]

[1] Faculty of Mechanical Engineering, TU Košice, Letná 9, 040 01 Košice, Slovak Republic; pavol.tarbajovsky@tuke.sk; michal.puskar@tuke.sk; matus.virostko@tuke.sk
* Correspondence: pavol.tarbajovsky@tuke.sk; Tel.: +421 55 602 2355

Abstract: According to the European Union, combustion engines will be prohibited from sale starting in 2035. This is why many car manufacturers are trying to develop new types of fuels for combustion engines since electric vehicles are not suitable for every operating condition. Some countries agreed with the European Commission allowing synthetic fuels, some are trying to enforce alternative fuels. Hydrogen can be considered as one of the alternative fuels. Combustion of hydrogen emits water and no other harmful substances which is very convenient in the current situation when combustion engines are about to be banned. Combustion of hydrogen requires some changes done to the common internal combustion engines and the shape of the combustion chamber is not an exception. That's why new designs are made with different types of combustion.

Keywords: combustion; engine; hydrogen

1. Introduction

By 20235 a new law will prohibit the sale of diesel and gasoline vehicles due to high pollution and environmental damage caused by combustion of internal combustion engines using common fuels. There is no rule without exception for example Germany concluded an agreement with the European Commission allowing sell of internal combustion engines using synthetic fuels as propellant. Many other nations resist this idea trying to find innovative solutions to keep internal combustion engines alive with alternative fuels thus need for new and alternative fuels rises and one such fuel is hydrogen used as an alternative fuel for internal combustion engines. According to research, hydrogen is able to endure combustion while not emitting toxic gas emissions. hydrogen combustion produces water which categorizes Hydrogen as a clean fuel. hydrogen combustion in an internal combustion engine is attractive in sectors where electric propulsion is inconvenient and cost-ineffective.

Internal combustion engines burning hydrogen is a modified alternative to conventional combustion engines combusting gasoline. Based on this statement, new combustion chambers are designed to monitor the combustion of conventional fuel which would be the baseline for further addition of hydrogen into the injected fuel or switching conventional fuel to hydrogen. This article deals with modifications needed for hydrogen combustion, designing and simulation of new combustion chamber as a baseline that can be used for hydrogen combustion.

2. First evolution of hydrogen internal combustion engines

The first hydrogen internal combustion engine was developed by Francois Isaac de Rivaz using a fuel mixture of hydrogen and oxygen. This engine was designed in 1806 followed by Etienne Lenoir (1863) and Paul Dieges (1970) who modified conventional internal combustion engine to combust and run on hydrogen.

The German vehicle manufacturer developed a vehicle with a hydrogen-combusting internal combustion engine reaching a maximum speed of 301 km/h.

There is also a developed rotary engine that can operate with hydrogen and producing such an engine could be cost-effective in way of retooling the production line. Cold-weather applications, where fuel cells or electric vehicles with battery packs are not suitable, demand existing internal combustion technologies [1-2].

3. Conventional internal combustion engine modification requirements

Several modifications need to be done for conventional combustion engines to run on hydrogen. Modifications include higher voltage ignition coil packs, non-platinum spark plugs, injectors designed for gas, heavy-duty crankshaft damper, stronger connecting rods, valves and valve seats that can withstand higher loads, intake manifold designed for turbocharger or positive pressure supercharger, lastly, an oil designed for high operating temperatures. Internal combustion hydrogen engines can burn hydrogen in the same way as gasoline. Hydrogen engines´ power output is approximately 20% higher than gasoline [3].

4. Hydrogen combustion characteristics

The characteristics of hydrogen combustion can be stated in a few points:

4.1. Flammability

In comparison to other conventional fuels, hydrogen has a large scale of flammability which secures that combustion of hydrogen can occur in a wide range of air/fuel mixture. Moreover, the combustion of hydrogen can be in a lean mixture which was also the purpose of the combustion chamber design which will be discussed in the next chapter.

4.2. Ignition energy

To start the combustion of hydrogen, low ignition energy is needed which represents probably one order of magnitude less in comparison to the energy needed for the combustion of conventional gasoline.

4.3. Quenching distance

When gasoline and hydrogen quenching distance is compared, it can be said, that hydrogens´ is smaller. Flames of hydrogen travel much closer to cylinder walls which can represent a problem with its´ extinguishing.

4.4. Auto-Ignition

A characteristic of hydrogen combustion is high auto-ignition temperature which is a very important value because this temperature determines the compression ratio which can be used since the temperature rises during the compression cycle in an internal combustion engine. The higher the compression, the higher the temperature the compressed mixture reaches. The rise of temperature inside the cylinder can be defined by:

$$T_2 = T_1 \left(\frac{V_1}{V_2}\right) \gamma - 1 \tag{1}$$

$\frac{V_1}{V_2}$ = the compression ratio
T_1 = absolute initial temperature
T_2 = absolute final temperature
γ = ratio of specific heats

4.5. Diffusivity

The diffusivity of hydrogen is remarkably high and greater than gasoline which means that it can form a uniform mixture of air and fuel.

4.5. Diffusivity

It is known that hydrogen density is low which can cause problems in terms of combustion. Since the density of hydrogen is low, a large amount is needed to secure the permissible driving range of the vehicle but also, there must be large storage space for hydrogen in the vehicle [4].

5. Baseline combustion chamber design

Since the combustion of hydrogen can occur in lean mixture, which means that we can talk about low-temperature combustion, the design of the combustion chamber was aimed in this way [5-6]. The special shape of the piston was designed with the bowl for better air and fuel mixing. Figure 1 shows the design of the piston.

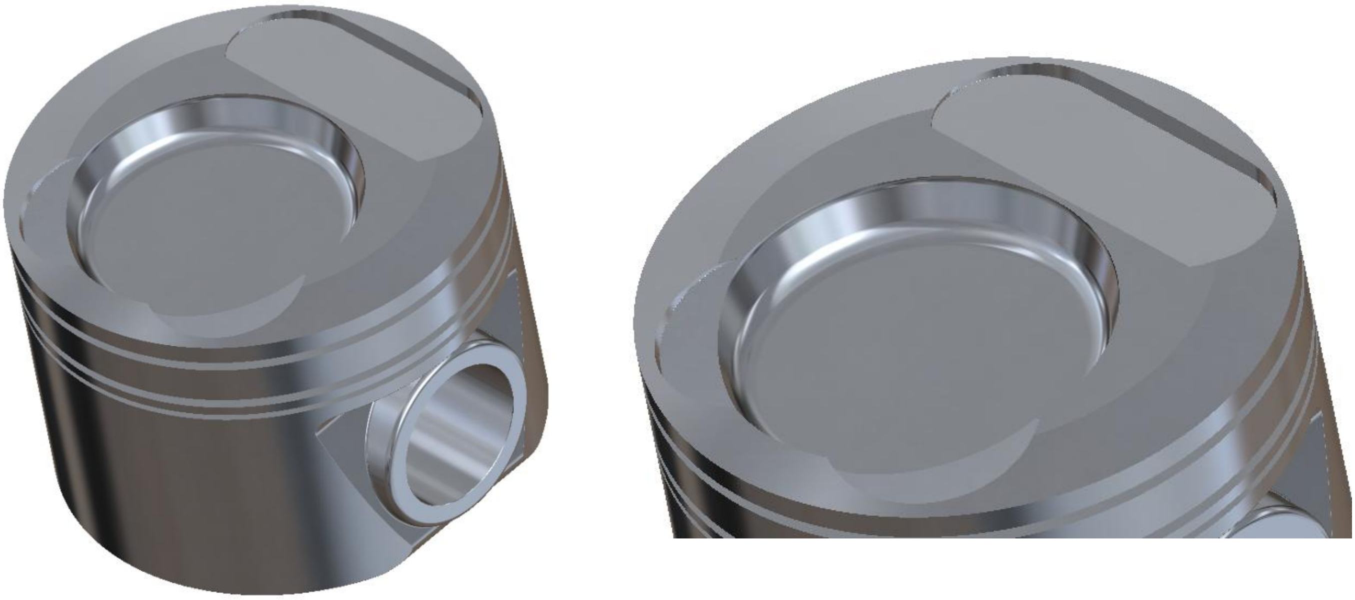

Figure 1. Used piston shape for simulation (bowl-shaped piston).

The combustion chamber with a newly designed piston crown was processed in CAD software which allowed the creation of the volume needed for simulation. Once the volume was created, the meshing process was next. The meshed combustion chamber volume (Figure 2.) was then exported into the Ansys Forte where the simulation was set. Since the simulation was used for shape testing if it was appropriate for combustion and further usage with hydrogen, gasoline was used as fuel.

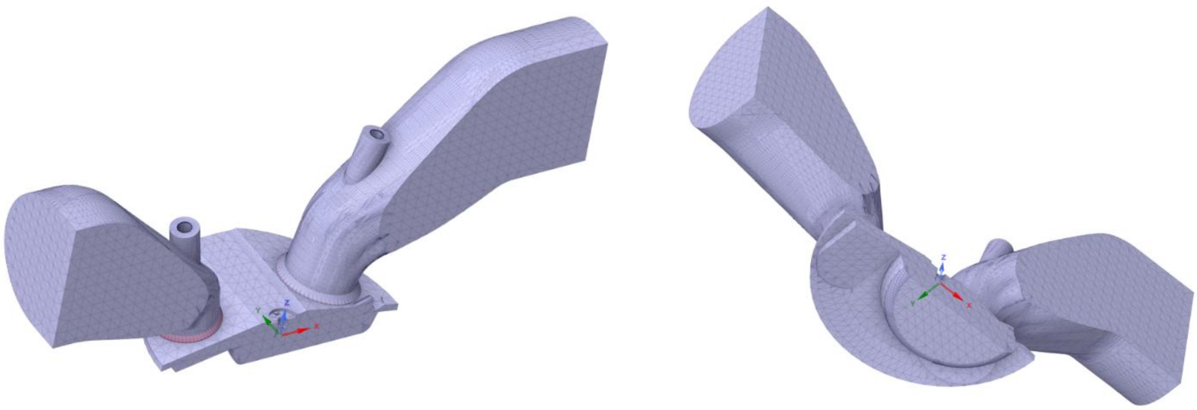

Figure 2. Combustion chamber volume mesh.

Monitored parameters of the simulation where the flow of the mixture inside the combustion chamber since the flow (swirl) inside the combustion chamber is important for the creation of the wanted mixture and the temperature. The design was aimed at achieving low-temperature combustion which was also the reason why the temperature was one of the monitored values.

The bowl-shaped piston crown helped with the mixture swirl (Figure 3) however the bowl must be shallower to increase the compression ratio for future usage of hydrogen potential.

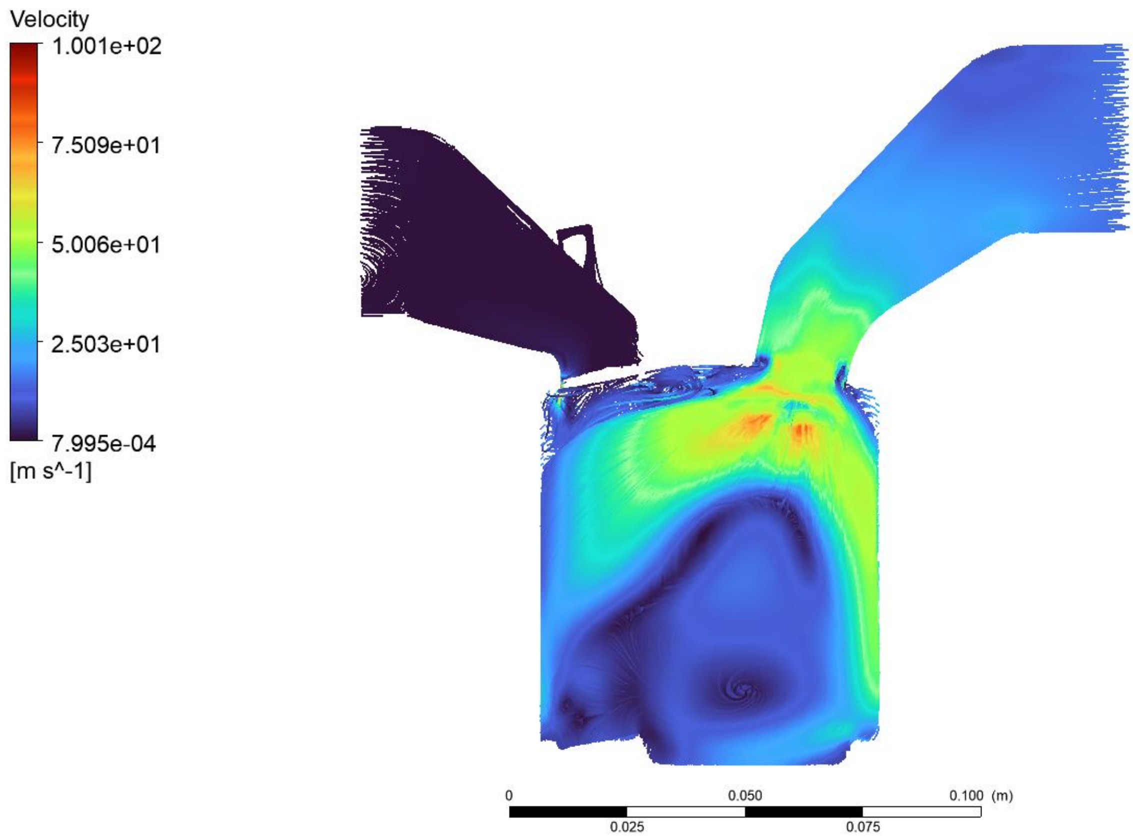

Figure 3. Velocity of air/fuel mixture inside the combustion chamber

The temperature (Figure 4) inside the combustion chamber was lower than in conventional combustion engines but was still able to ignite the mixture and spread the flame. The flame propagation occurs in a small volume which can be changed by increasing the boost pressure which will increase the temperature or by increasing the amount of injected fuel [7].

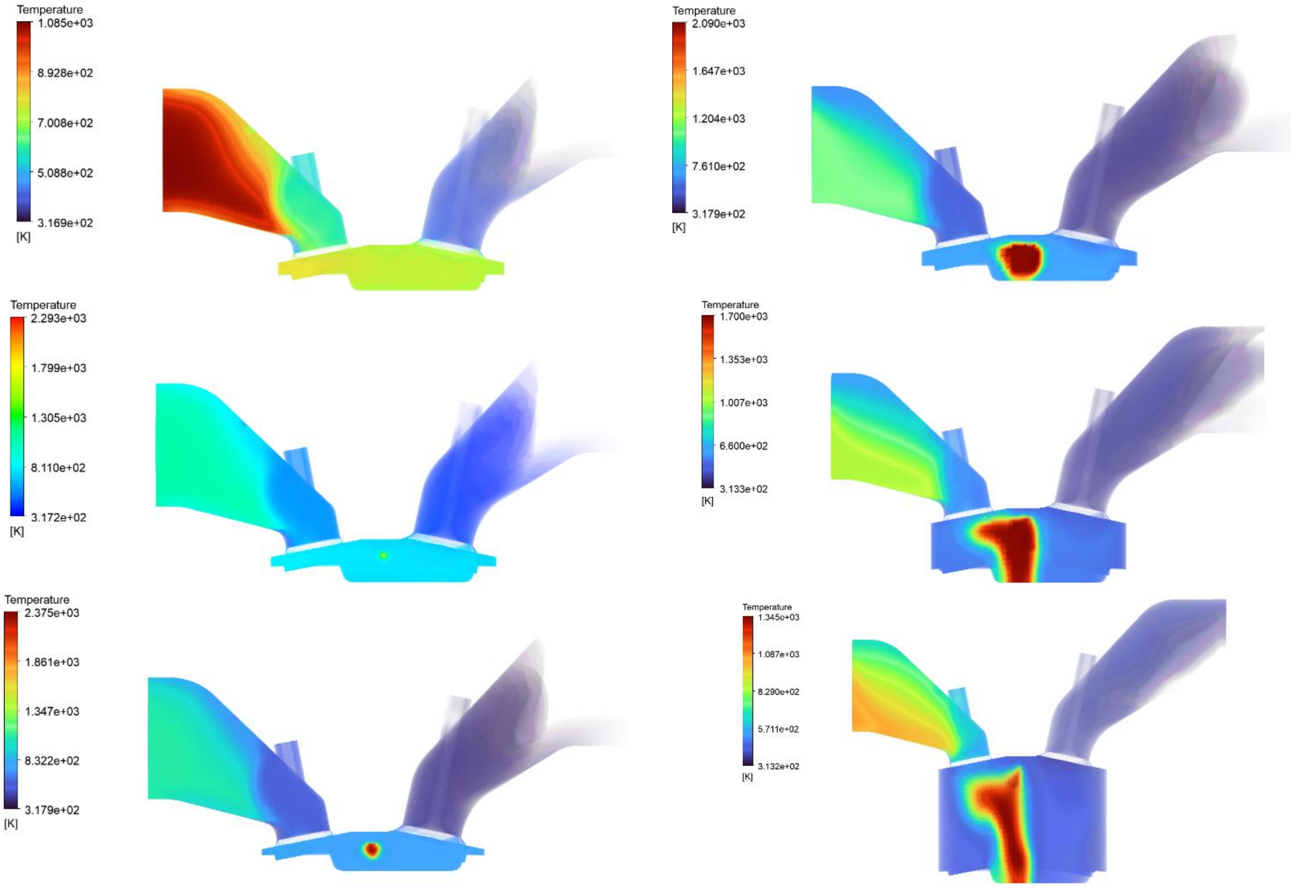

Figure 4. Monitored temperature inside the combustion chamber during combustion.

6. Discussion

2035 should be the year when internal combustion engines will be prohibited, however many nations are against this decision of the European Union, and they are trying to find alternatives in the form of synthetic fuels or alternative fuels that apply to existing combustion engines. Hydrogen can be an alternative fuel which is relatively easy to apply to existing technology of combustion engines. Since there is hope with hydrogen, the creation of a new shape of the combustion chamber was done to see, if it is able to combust, for now gasoline, proved by simulation using simulation software Ansys Forte. The results are promising but a few changes need to be done to switch from gasoline to hydrogen.

Acknowledgments: This work was supported by the Slovak Research and Development Agency under the Contract No. APVV-23-0266.

The article was written in the framework of Grant Projects: VEGA 1/0495/25 "Research and implementation of low-emission technologies for sustainable drive systems in transport" and KEGA 007TUKE-4/2023 "Transfer of innovations and advanced technologies, determined for more ecological and more efficient vehicle drive systems, into the educational process."

Conflicts of Interest: No conflict of interest

References

1. DAS, L. Hydrogen Engine: Research and Development (R&D) programmes in Indian Institute of Technology (IIT), Delhi. In International Journal of Hydrogen Energy . 2002. Vol. 27, no. 9, s. 953–965. .
2. KAHRAMAN, E. - CIHANGIR OZCANLI, S. - OZERDEM, B. An experimental study on performance and emission characteristics of a hydrogen fuelled spark ignition engine. In International Journal of Hydrogen Energy . 2007. Vol. 32, no. 12, s. 2066–2072. .

3. DAS, L. A comparative evaluation of the performance characteristics of a spark ignition engine using hydrogen and compressed natural gas as alternative fuels. In International Journal of Hydrogen Energy . 2000. Vol. 25, no. 8, s. 783–793. .
4. In (PDF) design of hydrogen internal combustion engine with fuel regeneration and Energy Recovery System [online]. [cit. 2024-12-12]. Dostupné na internete: <https://www.researchgate.net/publication/365883230_Design_of_Hydrogen_Internal_Combustion_Engine_with_Fuel_Regeneration_and_Energy_Recovery_System>.
5. TARBAJOVSKY, P. - PUSKAR, M. - FILO, M. Advanced combustion chamber for HCCI technology application. In MM Science Journal . 2024. Vol. 2024, no. 2. .
6. PUŠKÁR, M. - JAHNÁTEK, A. - KÁDÁROVÁ, J. - ŠOLTÉSOVÁ, M. - KOVANIČ, Ľ. - KRIVOSUDSKÁ, J. Environmental study focused on the suitability of vehicle certifications using the new European driving cycle (NEDC) with regard to the affair “Dieselgate” and the risks of nox emissions in urban destinations. In Air Quality, Atmosphere & Health . 2018. Vol. 12, no. 2, s. 251–257. .
7. PUSKAR, M. - KOPAS, M. - SOLTESOVA, M. - TARBAJOVSKY, P. Simulation model of advanced system for application of sustainable fuels. In International Journal of Simulation Modelling . 2022. Vol. 21, no. 2, s. 308–319. .

TECHNICAL UNIVERSITY OF KOŠICE
Faculty of Mechanical Engineering

Current Trends and Future Perspectives in Personalized Anatomical Implants: A Review of Dental Implant Design

Anna Tomaszewska [1,*], Jozef Živčák [2]

[1] Bialystok University of Technology, Faculty of Mechanical Engineering; anna.tomaszewska@sd.pb.edu.pl
[2] Technical University of Kosice, Faculty of Mechanical Engineering 2; jozef.zivcak@tuke.sk
* Correspondence: anna.tomaszewska@sd.pb.edu.pl

Abstract: Dental implants are a widely used solution for replacing missing teeth, with clinical success relying heavily on osseointegration—the biological and mechanical connection between the implant and bone. (1) Background: Implant geometry plays a critical role in achieving initial stability and long-term outcomes. Tapered implants excel in low-density bone due to their ability to evenly distribute forces, while parallel-walled implants maximize bone contact in denser bone but may increase stress in weaker bone. Root-shaped implants offer superior osseointegration, whereas plate-shaped implants are suitable for severe bone loss but demonstrate lower stability under mechanical stress. (2) Methods: This study synthesizes existing literature on the impact of implant geometry and highlights advancements in personalized implant design. It focuses on research findings from orthopedics, craniofacial surgery, and dentistry, emphasizing CAD/CAM and 3D printing technologies for developing anatomical implants. (3) Results: Personalized implants have demonstrated success in orthopedics and craniofacial surgery, showing improved osseointegration, mechanical stability, and reduced complications. However, their application in dentistry remains limited due to insufficient research and lack of standardization. (4) Conclusions: Further clinical trials and computational modeling, such as finite element analysis, are essential to validate the efficacy of anatomical implants in dentistry. Their adoption could transform implantology, offering improved outcomes for complex cases and challenging anatomical conditions..

Keywords: dental implants; anatomical implants; osseointegration

1. Introduction

Dental implants are a commonly used solution to restore missing teeth. Their clinical success depends on the process of osseointegration, which ensures a permanent connection between the implant and the bone. Osseointegration, which is crucial for long-term treatment success, includes the biological connection of the implant to the bone tissue and thus ensures both mechanical and biological stability. The geometric adaptation to the bone structure plays a crucial role in implant design and influences the initial stability and long-term effectiveness [1].

The shape of the implant has a major influence on osseointegration. Due to their narrower shape, tapered implants provide better stability in lower density bones and promote even distribution of forces [2,3]. Parallel-walled implants provide better bone contact along their entire length, which has a positive effect on denser bone tissue, but can place greater stress on weaker bones and potentially hinder stabilization [4]. The type of implant, for example root shape or plate shape, also influences the efficiency of osseointegration. Root-shaped implants, which resemble natural roots, are more suitable for bone structure, while plate-shaped implants with reduced contact area are less effective on low-density bones [5].

Optimal adaptation of the implant geometry to the patient's anatomical conditions is crucial for long-term treatment success. In response to patient needs, there is growing interest in anatomical implants that mimic the natural shape of bone and can improve osseointegration, reduce complications, and improve aesthetics. Technologies such as 3D printing and CAD/CAM enable the customization of implants.

However, their widespread use requires further research. This article examines the current knowledge about the influence of implant geometry on osseointegration and the benefits.

2. Design of dental implants

Tapered implants are characterized by their narrowing shape and were developed to optimize primary stability, particularly in areas with reduced bone density (types III and IV)[6,7]. Their unique geometry promotes the even distribution of forces across the bone structure, minimizing the risk of micro-movements and supporting the early stages of osseointegration [8]. The tapered shape allows the implant to be better anchored in the bone, especially in low-density regions such as the posterior parts of the lower or upper jaw. Studies show that tapered implants generate higher holding forces than parallel-walled implants under these conditions [9,10]. During long-term osseointegration, tapered implants allow for even load distribution, facilitating the efficient formation of new bone tissue around the implant. The tapered geometry also helps reduce apical stresses that can cause biomechanical overload in parallel implants [11,12].

Parallel-walled dental implants are characterized by a uniform diameter over the entire length and are designed to maximize the contact area with the bone. This geometry is mainly used in areas with higher bone density (Types I and II). Compared to tapered implants, parallel-walled designs may have limited anchoring ability in lower density bone due to their lower mechanical efficiency under such conditions [13,14]. Thanks to the larger surface area of parallel-walled implants in contact with the bone, the regeneration process of bone tissue is supported in the later phases of osseointegration.

Root-shaped implants, with their cylindrical or conical shape, are the most commonly used due to their versatility and predictable osseointegration. Studies have shown that root-shaped implants maintain a high level of osseointegration even under biological stress and retention rates of up to 62% are achieved in experimental models despite difficult conditions such as gingivitis [15] Due to their effectiveness, they are ideal for cases with sufficient bone density and volume and provide robust support for single-tooth restorations, overdentures and other prosthetic solutions [16]. However, their success is closely related to bone quality, with higher failure rates reported in severely atrophic bone types or bone types with low density. In such scenarios, advanced imaging and careful surgical planning are essential to avoid complications, especially near vital structures such as the mandibular canal [17].

The alveolar ridge is not sufficient for root-shaped implants. If there is severe bone loss, plate-shaped implants may be the only way to ensure the stabilization of prostheses. Studies by De Moor et al. (2022) show that these implants are effective under extreme clinical conditions, such as: B. in the case of complete edentulism of the upper jaw with a significant reduction in bone mass [18]. Nevertheless, plate-shaped implants have a lower osseointegration efficiency compared to root-shaped implants. Research suggests that their long-term stability may be compromised under conditions of higher mechanical stress [19].

A comparison of various implant types is presented in Table 1, summarizing their key features and clinical indications.

Table 1. Comparison of different dental implant types based on geometry and clinical use.

Implant Type	Characteristics	Clinical Applications
Tapered	Conical shape; enhances primary stability in low-density bone	Used in posterior jaw regions with lower bone density
Parallel-walled	Uniform diameter; maximizes contact in dense bone	Used in anterior jaw or areas with high bone density
Root-shaped	Mimics natural tooth roots; good osseointegration	Suitable for cases with sufficient bone volume and density
Plate-shaped	Flat design; reduced bone contact area	Used in severe bone loss scenarios, especially in edentulous maxilla
Anatomical (customized)	Patient-specific design using CAD/CAM and 3D printing	Ideal for complex anatomical conditions and aesthetic zones

3. Anatomical Implants in Other Medical Fields

Unlike dentistry, where implant selection is primarily based on the biomechanical conditions of the alveolar bone, other medical disciplines have embraced the use of highly personalized anatomical implants tailored to the patient's specific reconstructive and functional needs. In orthopedic and craniofacial surgery, advanced design techniques, including CAD-CAM technology and 3D printing, enable the creation of precise replicas of a patient’s individual anatomy, significantly enhancing therapeutic outcomes.

Applications in Medicine

In orthopedics, anatomical implants are extensively used in hip joint reconstructions to address congenital malformations, bone defects, or revision surgeries. For instance, the Adaptiva® implant, tailored to patients with congenital hip dysplasia, provides a precise fit in the femoral canal, ensuring long-term stability and improved joint function, as evidenced by a 95.4% survival rate over 10 years [20]. Similarly, CAD-CAM models like Zimmer-Biomet minimize loosening by optimizing the fit within the femoral canal, particularly benefiting patients with significant deformities [21].

In knee reconstruction, personalized unicompartmental implant systems allow precise adaptation to bone structure, preserving joint biomechanics and reducing bone tissue loss while ensuring long-term stability[22]. Anatomical implants also play a pivotal role in addressing significant bone deficiencies. In cases involving extensive bone loss, cross-locking screw designs enhance implant stability, even under extreme conditions [23].

In craniofacial surgery, customized implants are indispensable for repairing complex defects, including traumatic injuries, congenital anomalies, and tumor resections. Polyetheretherketone (PEEK) is widely employed for fronto-orbital reconstructions, offering excellent aesthetic outcomes and reduced complication risks [24]. Hydroxyapatite ceramics and CAD-CAM-designed titanium implants are used for reconstructing large cranial defects and eliminating the need for autogenous grafts, significantly reducing associated morbidity [25].

Implications for Dentistry

In dentistry, standard implant designs, such as tapered and parallel-walled implants, are primarily chosen based on bone density but fail to account for individual anatomical variability. This lack of personalization limits their efficacy in complex cases, including severe bone atrophy, narrow alveolar ridges, or the need for aesthetically demanding reconstructions in anterior zones.

Personalized dental implants represent a promising solution for addressing these challenges. For instance, in cases of advanced bone atrophy in the maxilla or mandible, conventional designs often lack sufficient biomechanical stability, increasing the risk of micromovements and treatment failure [15]. Additionally, narrow alveolar ridges could benefit from custom implants that minimize the need for extensive bone grafting [17].

Anatomical implants tailored to the patient's unique bone structure have the potential to improve primary stability, accelerate osseointegration, and reduce biomechanical stress, thereby enhancing implant longevity [20]. Moreover, in aesthetic zones, custom implants could integrate seamlessly with surrounding tissues, delivering superior outcomes and mitigating the risk of soft tissue recession [16].

Despite the clear benefits of personalized approaches observed in orthopedics and craniofacial surgery, their adaptation in dentistry remains limited. Advancements in bioengineering, combined with technologies such as 3D printing, could enable the development of anatomical dental implants that address the unique challenges posed by varying bone density, anatomy, and aesthetic demands [26]. Further research, particularly in silico modeling and clinical trials, is essential to validate their efficacy and promote widespread adoption [21].

This integration of personalized implants into dental practice has the potential to revolutionize the field, offering tailored solutions for complex clinical cases and improving long-term treatment

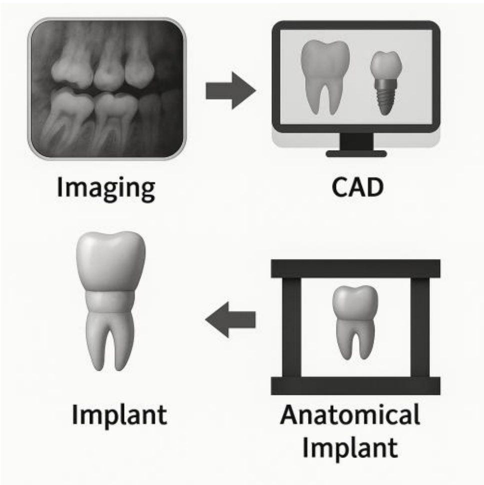

Figure 1. Schematic diagram of the process of designing a personalized anatomical implant using CAD/CAM and 3D printing, including image acquisition (e.g., CT scan), digital modeling, simulation/analysis, and additive manufacturing of the final implant. Insert final anatomical schematic image below this caption.

4. Lack of Comprehensive Research on Anatomically Designed Implant

Current research on dental implants focuses primarily on their biomechanical properties and adaptation to different bone types, such as conical and parallel-walled implants. However, anatomically shaped implants that replicate the natural contours of a patient's bone have not been extensively studied for their use in dentistry.

Findings from other medical areas underline the advantages of personalized implants. Studies by Pellegrini et al. (2018) emphasize that modern surface modifications, including nanotechnology and bioactive molecules, can improve osteogenesis and shorten the time required for osseointegration, which could be particularly beneficial for anatomically designed implants [27]. Similarly, Albrektsson and Wennerberg (2019) emphasize that appropriate surface and topographic properties play a crucial role in the osseointegration process [28].

Recent studies, such as those by Prakash and Narayanan (2021), highlight the importance of optimizing biomechanical interactions between implants and bone, which is critical for designing anatomically shaped implants (Prakash & Narayanan, 2021). Despite promising findings in other areas of implantology, there is a lack of large-scale clinical trials in dental literature assessing the efficacy and long-term stability of anatomically designed implants.

Further research should encompass a wide range of clinical cases, including different regions of the oral cavity, bone densities, and individual patient needs. Particular attention should be paid to understanding the influence of anatomical geometry on biomechanics and the osseointegration process to provide reliable data supporting the development and implementation of these implants in dentistry.

In addressing these research gaps, in silico studies should be the first step in the development of anatomically designed implants. Computational modeling, such as finite element analysis (FEM), can predict dynamic bone remodeling around implants, identify biomechanical risks such as stress concentration, and optimize implant designs before in vivo testing. By simulating patient-specific conditions, these methods could significantly accelerate the design process and enhance the safety and efficacy of anatomically tailored implants in dentistry [29].

5. Conclusions

Different types of implants (tapered, parallel-walled, root-shaped, and plate-shaped) influence biomechanics and osseointegration. Tapered implants are more effective in low-density bone, while parallel-walled implants perform better in denser tissues. Standard dental implants are less effective in cases of advanced bone atrophy and complex aesthetic reconstructions. Personalized implants have the potential to improve biomechanics, stability, and aesthetics, particularly in challenging clinical conditions. In silico studies (e.g., FEM) and clinical trials are required to enhance the design of anatomical dental implants. 3D printing and CAD/CAM technologies are critical for implant personalization; however, uniform standards for production and clinical evaluation are needed. Collaboration with orthopedics and craniofacial surgery could significantly advance the development of dental implants.

Conflicts of Interest: "The authors declare no conflict of interest."

References

1. Pandey, C.; Rokaya, D.; Bhattarai, B. Contemporary Concepts in Osseointegration of Dental Implants: A Review. *BIOMED RESEARCH INTERNATIONAL* **2022**, *2022*, doi:10.1155/2022/6170452.
2. Supachaiyakit, P.; Serichetaphongse, P.; Chengprapakorn, W. The influence of implant design on implant stability in low-density bone under guided surgical template in inexperienced surgeons: A pilot randomized controlled clinical trial using resonance frequency analysis. *CLINICAL IMPLANT DENTISTRY AND RELATED RESEARCH* **2022**, *24*, 444-454, doi:10.1111/cid.13100.
3. Mehboob, H.; Ouldyerou, A.; Ijaz, M. Biomechanical Investigation of Patient-Specific Porous Dental Implants: A Finite Element Study. *APPLIED SCIENCES-BASEL* **2023**, *13*, doi:10.3390/app13127097.
4. Bernabeu-Mira, J.; Peñarrocha-Diago, M.; Viña-Almunia, J.; Romero-Gavilán, F.; Pérez-Sayans, M.; Peñarrocha-Oltra, D. Influence of abutment shape on peri-implant tissue conditions: A randomized clinical trial. *CLINICAL ORAL IMPLANTS RESEARCH* **2023**, *34*, 1015-1024, doi:10.1111/clr.14130.
5. Garcia, D.; Mingrone, L.; De Sa, M. Evaluation of Osseointegration and Bone Healing Using Pure-Phase β - TCP Ceramic Implant in Bone Critical Defects. A Systematic Review. *FRONTIERS IN VETERINARY SCIENCE* **2022**, *9*, doi:10.3389/fvets.2022.859920.
6. Ibrahim, A.; Heitzer, M.; Bock, A.; Peters, F.; Möhlhenrich, S.; Hölzle, F.; Modabber, A.; Kniha, K. Relationship between Implant Geometry and Primary Stability in Different Bony Defects and Variant Bone Densities: An In Vitro Study. *MATERIALS* **2020**, *13*, doi:10.3390/ma13194349.
7. Hadaya, D.; Pi-Anfruns, J.; Bellon, B.; Pippenger, B.; Aghaloo, T. Immediate loading of a fully tapered implant with deep apical threads placed in healed alveolar ridges vs. immediate extraction sockets. *CLINICAL ORAL IMPLANTS RESEARCH* **2022**, *33*, 501-510, doi:10.1111/clr.13910.

8. Tumedei, M.; Petrini, M.; Pietropaoli, D.; Cipollina, A.; La Torre, C.; Di Carmine, M.; Piattelli, A.; Iezzi, G. The Influence of the Implant Macrogeometry on Insertion Torque, Removal Torque, and Periotest Implant Primary Stability: A Mechanical Simulation on High-Density Artificial Bone. *SYMMETRY-BASEL* **2021**, *13*, doi:10.3390/sym13050776.
9. Comuzzi, L.; Tumedei, M.; Pontes, A.; Piattelli, A.; Iezzi, G. Primary Stability of Dental Implants in Low-Density (10 and 20 pcf) Polyurethane Foam Blocks: Conical vs Cylindrical Implants. *INTERNATIONAL JOURNAL OF ENVIRONMENTAL RESEARCH AND PUBLIC HEALTH* **2020**, *17*, doi:10.3390/ijerph17082617.
10. Stacchi, C.; Lamazza, L.; Rapani, A.; Troiano, G.; Messina, M.; Antonelli, A.; Giudice, A.; Lombardi, T. Marginal bone changes around platform-switched conical connection implants placed 1 or 2 mm subcrestally: A multicenter crossover randomized controlled trial. *CLINICAL IMPLANT DENTISTRY AND RELATED RESEARCH* **2023**, *25*, 398-408, doi:10.1111/cid.13186.
11. Chavarri-Prado, D.; Brizuela-Velasco, A.; Alvarez-Arenal, A.; Dieguez-Pereira, M.; Pérez-Pevida, E.; Viteri-Agustín, I.; Estrada-Martínez, A. The Bone Buttress Theory: The Effect of the Mechanical Loading of Bone on the Osseointegration of Dental Implants. *BIOLOGY-BASEL* **2021**, *10*, doi:10.3390/biology10010012.
12. Lovatto, S.; Bassani, R.; Sarkis-Onofre, R.; dos Santos, M. Influence of Different Implant Geometry in Clinical Longevity and Maintenance of Marginal Bone: A Systematic Review. *JOURNAL OF PROSTHODONTICS-IMPLANT ESTHETIC AND RECONSTRUCTIVE DENTISTRY* **2019**, *28*, E713-E721, doi:10.1111/jopr.12790.
13. Kurtulus, I.; Kilic, K.; Bal, B.; Kilavuz, A. Finite Element Analysis of the Stress Distribution Associated With Different Implant Designs for Different Bone Densities. *JOURNAL OF PROSTHODONTICS-IMPLANT ESTHETIC AND RECONSTRUCTIVE DENTISTRY* **2022**, *31*, 614-622, doi:10.1111/jopr.13539.
14. Oliveira, H.; Velasco, A.; Ríos-Santos, J.; Lasheras, F.; Lemos, B.; Gil, F.; Carvalho, A.; Herrero-Climent, M. Effect of Different Implant Designs on Strain and Stress Distribution under Non-Axial Loading: A Three-Dimensional Finite Element Analysis. *INTERNATIONAL JOURNAL OF ENVIRONMENTAL RESEARCH AND PUBLIC HEALTH* **2020**, *17*, doi:10.3390/ijerph17134738.
15. Apablaza, J.; Días, F.; Sánchez, K.; Navarro, P.; Venegas, C.; Fuentes, R. Analysis of the Chemical Composition and Morphological Characterization of Tissue Osseointegrated to a Dental Implant after 5 Years of Function. *INTERNATIONAL JOURNAL OF MOLECULAR SCIENCES* **2022**, *23*, doi:10.3390/ijms23168882.
16. Benalcázar-Jalkh, E.; Nayak, V.; Gory, C.; Marquez-Guzman, A.; Bergamo, E.; Tovar, N.; Coelho, P.; Bonfante, E.; Witek, L. Impact of implant thread design on insertion torque and osseointegration: a preclinical model. *MEDICINA ORAL PATOLOGIA ORAL Y CIRUGIA BUCAL* **2023**, *28*, E48-E55, doi:10.4317/medoral.25576.
17. Freitas, J.; Hernandez, B.; Goncalves, P.; Baptista, E.; Sousa, E. Novel and simplified optimisation pathway using response surface and design of experiments methodologies for dental implants based on the stress of the cortical bone. *PROCEEDINGS OF THE INSTITUTION OF MECHANICAL ENGINEERS PART H-JOURNAL OF ENGINEERING IN MEDICINE* **2021**, *235*, 1297-1309, doi:10.1177/09544119211025375.
18. De Moor, E.; Huys, S.; van Lenthe, G.; Mommaerts, M.; Vander Sloten, J. Mechanical evaluation of a patient-specific additively manufactured subperiosteal jaw implant (AMSJI) using finite-element analysis. *INTERNATIONAL JOURNAL OF ORAL AND MAXILLOFACIAL SURGERY* **2022**, *51*, 405-411, doi:10.1016/j.ijom.2021.05.011.
19. Akkoyun, E.; Demirba, A.; Gümü, H.; Alkan, B.; Alkan, A. Custom-Made Root Analog Immediate Dental Implants: A Prospective Clinical Study with 1-Year Follow-up. *INTERNATIONAL JOURNAL OF ORAL & MAXILLOFACIAL IMPLANTS* **2022**, *37*, 1223-1231, doi:10.11607/jomi.7198.
20. Abrahamsson, I.; Carcuac, O.; Berglundh, T. Influence of implant geometry and osteotomy design on early bone healing: A preclinical in vivo study. *CLINICAL ORAL IMPLANTS RESEARCH* **2021**, *32*, 1190-1199, doi:10.1111/clr.13816.
21. Yin, X.; Li, J.; Hoffmann, W.; Gasser, A.; Brunski, J.; Helms, J. Mechanical and Biological Advantages of a Tri-Oval Implant Design. *JOURNAL OF CLINICAL MEDICINE* **2019**, *8*, doi:10.3390/jcm8040427.
22. San Cheong, V.; Marin, A.C.; Lacroix, D.; Dall'Ara, E. A novel algorithm to predict bone changes in the mouse tibia properties under physiological conditions. *Biomechanics and Modeling in Mechanobiology* **2020**, *19*, 985-1001, doi:10.1007/s10237-019-01266-7.
23. Sotereanos, N.; Senvecke, J.; Raukar, G.; Demeo, P.; Bargiotas, K.; Wohlrab, D. Revision total hip arthroplasty with a custom cementless stem with distal cross-locking screws - Early results in femora with large proximal segmental deficiencies. *JOURNAL OF BONE AND JOINT SURGERY-AMERICAN VOLUME* **2006**, *88A*, 1079-1084, doi:10.2106/JBJS.E.00141.
24. Zhang, J.; Su, Y.; Rao, X.; Pang, H.; Zhu, H.; Liu, L.; Chen, L.; Li, D.; He, J.; Peng, J.; et al. Additively manufactured polyether ether ketone (PEEK) skull implant as an alternative to titanium mesh in cranioplasty. *INTERNATIONAL JOURNAL OF BIOPRINTING* **2023**, *9*, 173-180, doi:10.18063/ijb.v9i1.634.
25. Nguyen, P.; Khechoyan, D.; Phillips, J.; Forrest, C. Custom CAD/CAM implants for complex craniofacial reconstruction in children: Our experience based on 136 cases. *JOURNAL OF PLASTIC RECONSTRUCTIVE AND AESTHETIC SURGERY* **2018**, *71*, 1609-1617, doi:10.1016/j.bjps.2018.07.016.
26. Wang, Z.; Wang, J.; Wu, R.; Wei, J. Construction of functional surfaces for dental implants to enhance osseointegration. *FRONTIERS IN BIOENGINEERING AND BIOTECHNOLOGY* **2023**, *11*, doi:10.3389/fbioe.2023.1320307.
27. Pellegrini, G.; Francetti, L.; Barbaro, B.; del Fabbro, M. Novel surfaces and osseointegration in implant dentistry. *JOURNAL OF INVESTIGATIVE AND CLINICAL DENTISTRY* **2018**, *9*, doi:10.1111/jicd.12349.
28. Albrektsson, T.; Wennerberg, A. On osseointegration in relation to implant surfaces. *CLINICAL IMPLANT DENTISTRY AND RELATED RESEARCH* **2019**, *21*, 4-7, doi:10.1111/cid.12742.

29. Zhao, X.; Zhu, Z.; Cong, Y.; Zhao, Y.; Zhang, Y.; Wang, D. Haptic Rendering of Diverse Tool-Tissue Contact Constraints During Dental Implantation Procedures. *FRONTIERS IN ROBOTICS AND AI* **2020**, *7*, doi:10.3389/frobt.2020.00035.

TECHNICAL UNIVERSITY OF KOŠICE
Faculty of Mechanical Engineering

Development of an AR Training Simulation Using Unity and AR Foundation

Erik Varjú [1,*] and Juraj Kováč [1]

[1] Department of industrial and digital engineering, Technical University of Košice, Park Komenského 9, 04001 Košice; erik.varju@tuke.sk; juraj.kovac@tuke.sk
* Correspondence: erik.varju@tuke.sk

Abstract: This study presents the development of an augmented reality (AR) training simulation designed to enhance the onboarding process for maintenance workers. Utilizing Unity and the AR Foundation framework, the project enables interactive and immersive training experiences by combining real-world environments with virtual objects and instructions. The simulation incorporates advanced AR features such as hand tracking and object manipulation, allowing users to interact with virtual components naturally and intuitively. By leveraging AR technology, this training program offers a cost-effective and scalable solution to address the challenges of traditional methods, such as limited access to physical equipment and safety risks during hands-on practice. The study also explores the capabilities of AR Foundation, including cross-platform support and real-time tracking, which simplify the development of sophisticated AR applications. Initial findings demonstrate the potential of AR-based training to improve skill acquisition and retention. Future work will focus on refining the simulation, integrating feedback from users, and exploring the use of AI to further personalize the training experience.

Keywords: Augmented Reality, Unity 3D, AR training programs, AR Foundation

1. Introduction

Augmented reality (AR) has emerged as a transformative technology in various fields, combining real-world environments with virtual elements to create immersive and interactive experiences. Its applications range from entertainment and healthcare to education and industry, where AR has proven particularly effective in training simulations. By enabling users to engage with digital content in their physical surroundings, AR bridges the gap between theoretical knowledge and practical skills, offering a powerful tool for workforce development.

In industrial settings, effective training is essential to ensure that employees acquire the skills required to handle complex machinery and procedures. Traditional training methods, such as classroom-based lectures and physical demonstrations, often face challenges such as high costs, limited access to resources, and safety risks during hands-on practice. AR-based training simulations address these limitations by providing a safe, scalable, and interactive learning environment where users can practice tasks repeatedly without the constraints of real-world equipment or environments.

This study focuses on the development of an AR training simulation for maintenance workers using Unity and the AR Foundation framework. Unity, a widely used game engine, combined with AR Foundation, a robust development toolkit, enables the creation of cross-platform AR applications that leverage advanced features such as hand tracking, object manipulation, and plane detection. These capabilities make AR Foundation particularly suitable for developing training programs that require precise interactions with virtual objects in real-world settings [1].

The objective of this study is twofold: first, to demonstrate the feasibility and benefits of AR-based training in improving the efficiency and effectiveness of onboarding processes; second, to highlight the technical capabilities of AR Foundation as a tool for creating advanced AR applications. By doing so, this research contributes to the growing body of knowledge on AR in training simulations and explores its potential to revolutionize workforce development in the future [2].

2. Comparison of AR Development Tools

Augmented Reality (AR) involves a new set of design challenges compared to VR or traditional real-time 3D applications. By definition, an augmented reality app overlays its content on the real world around the user. To place an object in the real world, you must first determine where to place for it. For example, you may want to place a virtual painting on a physical wall. If you place a virtual potted plant, you may want it on a physical table or the floor. An AR app receives information about the world from the user's device, such as the locations of planar surfaces, the detection of objects, people, faces, and so on; and must decide how to use this information to create a good experience for the user [2].

To provide a broader perspective on AR training development, Table 1 compares various AR development tools, including Unity with AR Foundation, Unreal Engine, Vuforia, ARKit, ARCore, and PiXYZ Review. Each tool has distinct advantages and limitations, making them suitable for different use cases.

Table 1. Comparison of various development tools.

Feature	Unity + AR Foundation	Unreal Engine	Vuforia	ARKit	ARCore	PiXYZ Review
AR Support	Multi-platform	Multi-platform	Image-based AR	iOS only	Android only	VR/AR model visualization
Interface	Moderate complexity	Advanced (high-end graphics)	Simple (image tracking focus)	Simple	Simple	Designed for CAD users
User Friendly	Beginner to intermediate	Advanced (steeper learning curve)	Beginner-friendly	Beginner-friendly	Beginner-friendly	Intermediate
Best Usage	Interactive training, simulations	High-quality AR visuals, gaming	Marker-based AR, product visualization	iOS AR applications	Android AR applications	Industrial design, CAD model review
Performance	Optimized for real-time AR	High performance but hardware-intensive	Lightweight	Optimized for Apple devices	Optimized for Android devices	Handles large 3D models

As you can see in the table above, Unity appears to be a strong option for starting AR development due to its balance of accessibility, flexibility, and multi-platform support. Its integration with AR Foundation simplifies the development process, making it easier to create interactive AR training simulations without being limited to a single ecosystem. Additionally, Unity's extensive community and documentation provide valuable resources for beginners and experienced developers alike. Given these factors, Unity serves as a practical foundation for the AR training simulation development process that follows in this article.

3. Project Setup and Fundamentals

When you open a typical AR scene in Unity (Fig. 1), you will not find many 3D objects in the scene or the Hierarchy view. Instead, most GameObjects in the scene define the settings and logic of the app. 3D content is typically created as prefabs that are added to the scene at runtime in response to AR-related events [3].

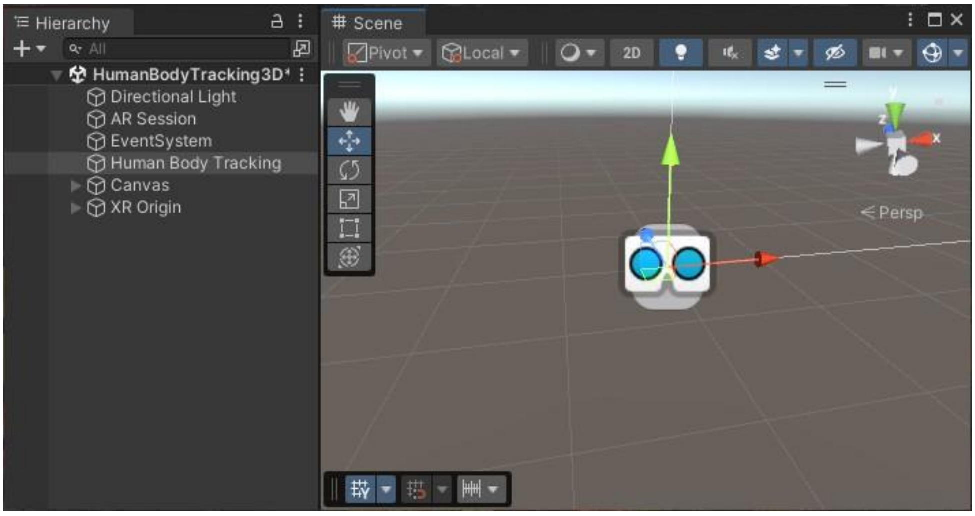

Figure 1. A typical AR scene in the Unity Editor [3].

The AR Session component (Fig. 2) controls the lifecycle of an AR experience by enabling or disabling AR on the target platform. A session refers to an instance of AR. While other features like plane detection can be independently enabled or disabled, the session controls the lifecycle of all AR features. When you disable the AR Session component, the system no longer tracks features in its environment. Then if you enable it at a later time, the system attempts to recover and maintain previously-detected features.

Multiple AR Session components in the same scene can conflict with each other, therefore Unity recommends that you add at most one AR Session component to a scene. [3].

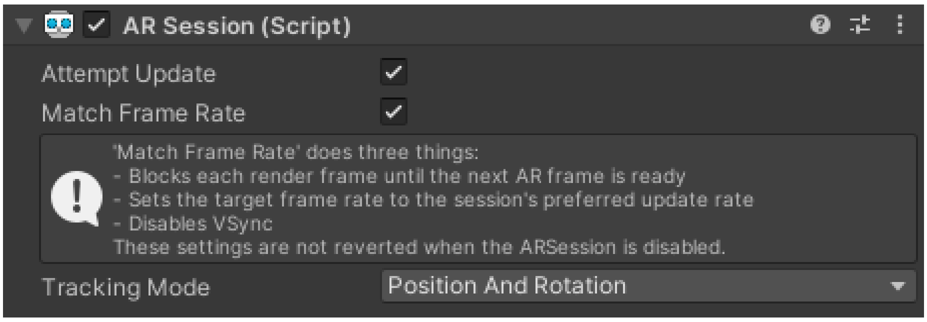

Figure 2. AR Session component [3].

3.1. AR Foundation Capabilities

AR Foundation is a development framework that facilitates the creation of multi-platform augmented reality (AR) applications within the Unity engine. This tool allows developers to integrate various AR features by adding specific manager components to their project scenes. Upon deployment to an AR-compatible device, AR Foundation utilizes the native AR software development kit (SDK) of the respective platform to activate the selected features. This approach enables the development of AR applications that are both efficient and scalable, allowing a single implementation to be deployed across multiple leading AR platforms [6].

3.2. Required packages

The AR Foundation package serves as an interface layer for integrating augmented reality (AR) features but does not independently implement these features. To utilize AR Foundation on a specific platform, developers must incorporate a corresponding provider plug-in package tailored to that platform.

Unity officially supports several provider plug-ins, including:

- **Google ARCore XR Plug-in** for Android
- **Apple ARKit XR Plug-in** for iOS
- **Apple visionOS XR Plug-in** for visionOS
- **OpenXR Plug-in** for Microsoft HoloLens 2
- **Unity OpenXR: Meta** for Meta Quest

These provider plug-ins leverage the native AR implementations of the respective platforms, such as Google's ARCore for Android and Apple's ARKit for iOS. However, the availability of AR features can vary between platforms due to differences in platform-specific capabilities.

Additionally, some AR Foundation features are accessible through XR Simulation, enabling developers to test AR applications directly within the Unity Editor without requiring physical deployment to a device [6].

Table 2. Comparison of AR/VR Headsets.

Headset	Company	Type	Best Use	Advantages	Disadvantages	Price Range
Meta Quest 3	Meta	Standalone VR/AR	Training, gaming, general AR/VR use	Wireless, high-resolution display, hand tracking, supports OpenXR	Limited processing power compared to PC VR	~$500–$650
HoloLens 2	Microsoft	AR	Industrial, enterprise, training	Standalone, high-end mixed reality, great spatial mapping	Expensive, limited field of view	~$3,500
Magic Leap 2	Magic Leap	AR	Enterprise, healthcare, design	Lightweight, improved optics over ML1	High price, limited consumer applications	~$3,000+
Varjo XR-4	Varjo	Mixed Reality	High-end simulation, research	Ultra-high resolution, accurate eye tracking, supports full mixed reality	Very expensive, requires powerful PC	~$3,990+
Apple Vision Pro	Apple	Mixed Reality	Productivity, entertainment, spatial computing	High-end display, intuitive UI, eye and hand tracking	Very expensive, limited software at launch	~$3,499
HTC Vive XR Elite	HTC	Mixed Reality	Gaming, training, enterprise	Compact, modular, supports PC VR & standalone	Battery life concerns, cost	~$1,099
Pico 4 Enterprise	Pico	Mixed Reality	Business, training, productivity	Affordable, standalone, wide FOV	Limited ecosystem outside China	~$900+

The table above (Table 2) presents a comparison of various AR and VR headsets, highlighting their intended use, key advantages, limitations, and pricing. Based on these factors, we evaluated which headset would be the most suitable for developing an AR training application while ensuring compatibility with Unity. Considering the balance between affordability, hardware capabilities, and strong integration with Unity's AR development tools, we selected the Meta Quest 3. It offers standalone functionality with robust AR passthrough features. Additionally, it works well with Unity thanks to its support for OpenXR and Meta SDK, making development smoother and more flexible.

3.3. Object Recognition and Interaction

One of the key features of the training simulation developed in this study is its ability to detect, outline, and interact with real-world objects using AR Foundation. By leveraging plane detection and object tracking, the system creates a virtual overlay on physical objects, enabling users to engage with their environment intuitively.

Figure 3. Simple AR sample scene [6].

Fig. 3 illustrates a real-world scenario where the AR training program identifies and outlines objects such as furniture and plants within the environment. The virtual overlays (highlighted in yellow) demonstrate how the system segments and defines areas for interaction, ensuring precise alignment between physical and virtual elements. This functionality is essential for creating a realistic training experience, as it allows users to interact naturally with virtual objects anchored to their real-world counterparts [7].

4. AR in Simulation Training Programs

Augmented Reality (AR) has revolutionized simulation training by creating immersive, interactive environments that enhance learning experiences across various fields. By overlaying virtual elements onto real-world environments, AR enables trainees to engage with tasks and scenarios in a way that combines theoretical knowledge with practical application. This capability has made AR an invaluable tool in industrial training, medical simulations, and maintenance tasks.

In industrial settings, AR is frequently used to help workers understand complex machinery and processes. For instance, it can project step-by-step instructions directly onto equipment, guiding users through assembly, maintenance, or troubleshooting tasks. In medical training, AR provides a risk-free way for surgeons and healthcare pro- fessionals to practice procedures by projecting virtual organs and tools onto physical models, allowing them to refine their skills without putting patients at risk. Similarly, maintenance training programs leverage AR to create realistic scenarios where users can interact with virtual components, eliminating the need for physical prototypes while still ensuring hands-on experience [4].

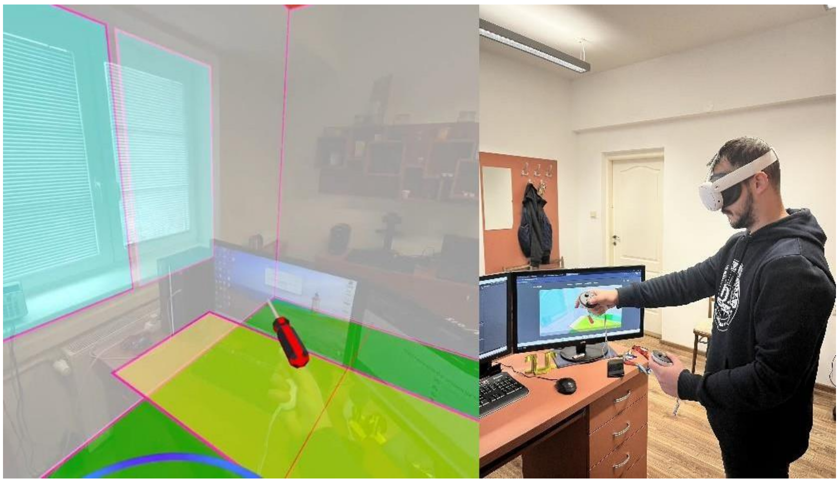

Figure 4 Experimental practice in laboratory conditions.

Fig. 4 demonstrates the practical application of AR in the development of a training simulation using Unity and the AR Foundation framework. On the left, the AR scene identifies and highlights real-world planes, with each plane distinctly color-coded (e.g., green, pink, and yellow). This feature, enabled by AR Foundation, enhances spatial awareness by providing a clear visual distinction between surfaces in the physical environment, ensuring accurate placement and interaction of virtual objects within the AR training simulation.

On the right, I am shown wearing a Meta Quest 3 headset, a device supporting advanced AR capabilities. Using handheld controllers, I interact with a virtual screwdriver in the AR scene. The connected monitor displays the same environment, emphasizing the integration of AR Foundation's plane detection and object manipulation features into the simulation. This setup exemplifies how AR Foundation facilitates the creation of immersive, interactive training programs that blend real-world and virtual elements seamlessly, making it an essential tool for developing AR-based training solutions.

Table 3. Comparison of Traditional Training Methods and AR-Based Training Programs [5].

Criteria	Traditional Training Methods	AR-Based Training Programs
Safety	Risk of injuries when practicing hazardous tasks in real environments.	Eliminates physical risks by simulating dangerous tasks virtually.
Cost	High costs due to equipment, materials, and travel expenses.	Reduced costs by replacing physical equipment with virtual simulations.
Accessibility	Limited to specific locations and equipment availability.	Accessible anywhere with AR-compatible devices.
Repeatability	Limited due to wear and tear on physical resources.	Unlimited repetition without additional resource use.
Feedback	Relies on instructor super- vision for real-time corrections.	Provides instant, auto- mated feedback during the training session.
Scalability	Difficult to scale for large groups or remote locations.	Easily scalable for remote and global training pro- grams.
Engagement	May be less engaging due to static learning materials.	interactive and immersive learning environments.

5. Conclusions

The AR Foundation package is a powerful tool for developing augmented reality (AR) applications, making it easier to create projects that work across multiple platforms. By connecting with native AR systems like ARCore and ARKit, AR Foundation allows developers to design their applications once and deploy them on different devices without

having to redo their work. This saves time, reduces complexity, and helps developers fo- cus on creating innovative features.

For AR-based training programs, AR Foundation provides many useful features, such as object tracking, gesture interaction, and understanding of the environment. These features make it possible to create realistic and interactive training scenarios for various industries, like maintenance, healthcare, or manufacturing. With AR, training can be safer, more cost-effective, and easier to repeat compared to traditional methods.

The potential of AR Foundation goes beyond its current uses. As AR technology improves, AR Foundation will remain an important tool because it supports new platforms like visionOS and OpenXR. This ensures that developers can continue using it for more advanced and scalable AR experiences in the future.

The article was developed with the support of the projects:
APVV-17- 0258,
APVV-19-0418, VEGA 1/0438/20,
KEGA 003TUKE-4/2024, KEGA 019TUKE-4/2022

References

1. Tanyushina, A. A. (2023). Augmenting Our Reality: the Philosophical Foundations of AR-technology. *Voprosy Filosofii*, *8*, 129–139. https://doi.org/10.21146/0042-8744-2023-8-129-139
2. *Unity Real-Time Development Platform | 3D, 2D, VR & AR Engine*. (n.d.). [Online] https://unity.com/
3. *Unity - Manual: AR development in Unity*. (n.d.). [Online] https://docs.unity3d.com/Manual/AROverview.html
4. Lavric, T., Bricard, E., Preda, M., & Zaharia, T. (2021). An Industry-Adapted AR training Method for manual assembly operations. In *Lecture notes in computer science* (pp. 282–304). https://doi.org/10.1007/978-3-030-90963-5_22
5. Lu, G. P., Xue, G. H., & Chen, Z. (2011). Design and implementation of virtual interactive scene based on unity 3D. *Advanced Materials Research*, *317–319*, 2162–2167. https://doi.org/10.4028/www.scientific.net/amr.317-319.2162
6. *AR Foundation | AR Foundation | 6.0.3*. (n.d.) [Online] https://docs.unity3d.com/Packages/com.unity.xr.arfoundation@6.0/manual/index.html
7. Garabet, M. & Neacsu, I. (2010). About virtual interactions with real objects. In *Proceedings of the 5th international conference on virtual learning* (pp. 517-519).

TECHNICAL UNIVERSITY OF KOŠICE
Faculty of Mechanical Engineering

Change in hardness of lightweight alloys when thermal drilling

Nikita Veligotskyi [1,*] and Anna Guzanová [1]

[1] Technical University of Košice, Faculty of Mechanical Engineering, Department of Technology, Materials and Computer Supported Production; nikita.veligotskyi@tuke.sk, anna.guzanova@tuke.sk
* Correspondence: nikita.veligotskyi@tuke.sk

Abstract: This article focuses on the optimization of the thermal drilling parameters of aluminium alloy (EN AW 6082 T6) and magnesium alloy (AZ91) for the production of bushings suitable for joining with thermosoftening matrix composites reinforced with fibres layered in two perpendicular directions. Thermal drilling, a friction-based technique, allows the formation of burr-free bushings in thin-walled materials without cutting.The experiments were carried out using a bench drill and a flowdrill tool at speeds of 2400 and 4800 rpm with slow and fast manual feeds. Metallographic analysis showed that the most suitable bushings, which are characterized by sufficient length and thickness to join with the composites, were produced at 4800 rpm regardless of the feed rate. At 2400 rpm, the quality of the bushing was unsuitable for joining with composites. Hardness testing by Vickers hardness method showed significant softening of aluminum except at 2400 rpm with slow feed rates, while magnesium showed moderate strain hardening under all conditions. The findings suggest that higher speeds are necessary to produce high quality bushings in aluminium and magnesium alloys. These results provide valuable insights for the development of reliable joints of metals and composites in applications that require lightweight and durable joints, such as in the automotive, aerospace and sports industries

Keywords: flowdrill, Vickers hardness test, mechanical joining

1. Introduction

In the automotive, aerospace and sports industries, the challenge is to combine materials of different chemical compositions, structures and thicknesses, especially when joining metals and composites that have completely different properties and can only be joined by adhesive bonding or mechanical joining[1-4].

Thermal drilling is a specialized technique that uses friction-generated heat to create holes with bushings in various materials, such as metals, plastics, and composites, without cutting. This process allows the creation of smooth cylindrical or tapered bushings, where threads and other fasteners can be placed in materials such as sheet metal, tubes or hollow sections. Thermal drilling (flowdrill) technology is a chipless method that, when high axial pressure and rotation are applied, causes frictional heat to soften the material (600-800°C), allowing the tool to penetrate and form it into the desired bushing shape. This process produces a bushing in the direction of drilling and a rim against the direction of tool movement, with the resulting shape depending on the geometry of the tool and selected parameters such as rotational speed, feed rate, length and diameter of the tool, which are adjusted to the thickness of the material being drilled [5-15].

The aim of the experimental work was to determine the optimum parameters for the thermal drilling of selected Al and Mg alloys to be subsequently used for joining with thermoplastic matrix composites reinforced with bidirectional continuous fibers. The optimum thermal drilling parameters will be considered to be those which produce a bushing of maximum length and sufficient thickness.

2. Materials and Methods

2.1 Materials

Precipitation hardened aluminium alloy EN AW 6082 T6 (AlSi1MgMn) with a thickness of 1 mm and magnesium alloy AZ91 with a thickness of 2 mm were used to prepare the holes and monitor the bushing formation under different thermal drilling conditions. In the text they will be referred to as Al and Mg. The chemical composition of the materials is given in Table 1.

Table 1. Chemical composition of Al and Mg alloys in wt.%.

Element	Si	Fe	Cu	Mn	Mg	Zn	Al
Al	1.0	0.4	0.06	0.44	0.7	0.08	balance
Mg	0.09	0.004	0.02	0.14	balance	0.93	8.9

2.2 Machine, tool and parameters of flowdrill

The Al and Mg materials were drilled using a tool flowdrill long with a diameter of 5.3 mm, Figure 1. A simple bench drill was used for joining, as it was not possible to use a CNC machine with precisely defined drilling parameters due to the need to heat the composite. Two different tool rotation speeds were tested: 2400 and 4800 min^{-1} and two different feed rates, which were provided manually. The slow manual feed rate was approximately 60 $mm.min^{-1}$, the fast feed rate was approximately 240 $mm.min^{-1}$.

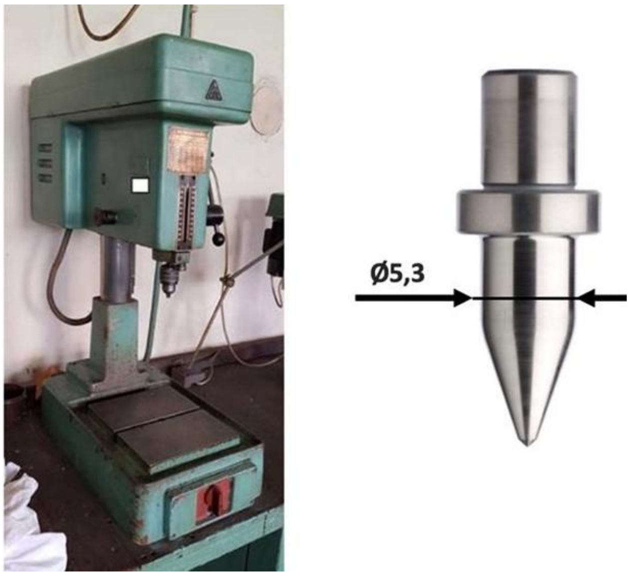

Figure 1. Bench drill machine TOS V 10 A and thermal drilling tool flowdrill long Ø 5.3 mm.

2.3 Clamping fixture

The main final goal of the work is to create a mechanical connection between the metal sheet and the composite material with a thickness of 1.5 mm without damage the continuity of the fibers. This can be achieved by heating the thermo-softening matrix of the composite to a temperature above the Tg of the polymer matrix used, which in the case of the polypropylene matrix is > 165°C. To establish the relative position of the materials to be joined and to ensure heating, it was necessary to design a suitable clamping fixture, Figure 2. The upper part of the clamping fixture is made of steel, the lower part of aluminium with respect to its good thermal conductivity. In addition, the clamping fixture has been designed so that the upper part of the clamping fixture ensures the clamping force of the materials to be joined.

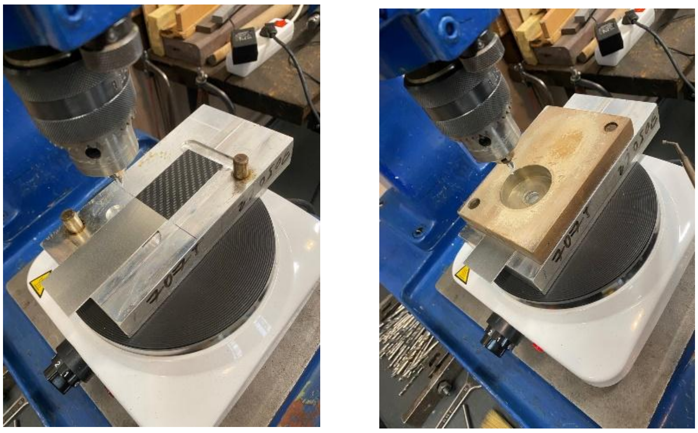

a) b)

Figure 2. Joining clamping fixture (a) bottom part of the fixture with materials set in positions for drilling, (b) assembled fixture ready for drilling.

3. Geometry of bushings prepared by thermal drilling

Table 2 and 3 show the metallographic sections of bushings made in metal sheets by thermal drilling at selected drilling parameters.

Table 2. Metallographic sections through the axis of bushings made at 2400 min-1.

	RPM [min^{-1}] / feed rate [$mm.min^{-1}$]	
	2400/60	2400/240
Al		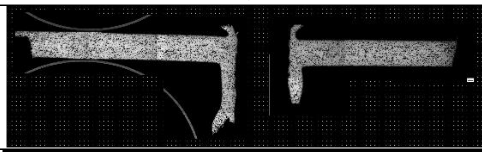
Mg	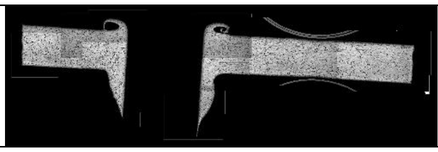	

Table 3. Metallographic sections through the axis of bushings made at 4800 min-1.

	RPM [min^{-1}] / feed rate [$mm.min^{-1}$]	
	4800/60	4800/240
Al	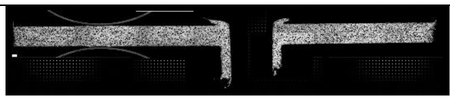	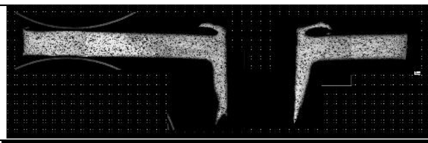
Mg	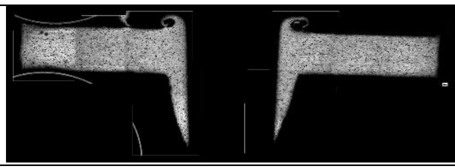	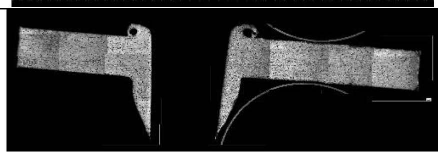

From the above metallographic sections, it can be seen that the shape varies for different materials as well as within a particular material at different thermal drilling parameters. The shape of the resulting Al bushings is cylindrical, with a butt end, and in some cases there is fragmentation of the bushings (petals formation). The Mg sheet bushings are intact, cylindrical inside and conical outside.

The cause of bushing failure in materials with high thermal conductivity is the large heat dissipation to the surrounding material. The forming bushing then does not have sufficient temperature, thus reducing the ductility of the material in the area of the bushing. This causes defects in the shape of the bushing.

For the purpose of future joining with the composite material, it is recommended that the resulting bushing be as long as possible (to penetrate through the composite throughout its entire thickness) at a sufficient bushing thickness, Figure 3. The thermal drilling parameters and the thickness of the base material will affect the proportion of material that is displaced from the plane of the metal sheet into the bushing area and, against the direction of tool movement, into the rim. Based on the metallographic sections, it can be concluded that the longest bushings with sufficient thickness suitable for further use for bonding to the composite material were produced at higher speeds of 4800 min-1 with both slow and fast manual feed. A comparison of the bushing formed when drilling the Al alloy sheet alone and the bushing formed when drilling the Al sheet placed on the carbon fibre reinforced polymer composite is shown in Figure 3.

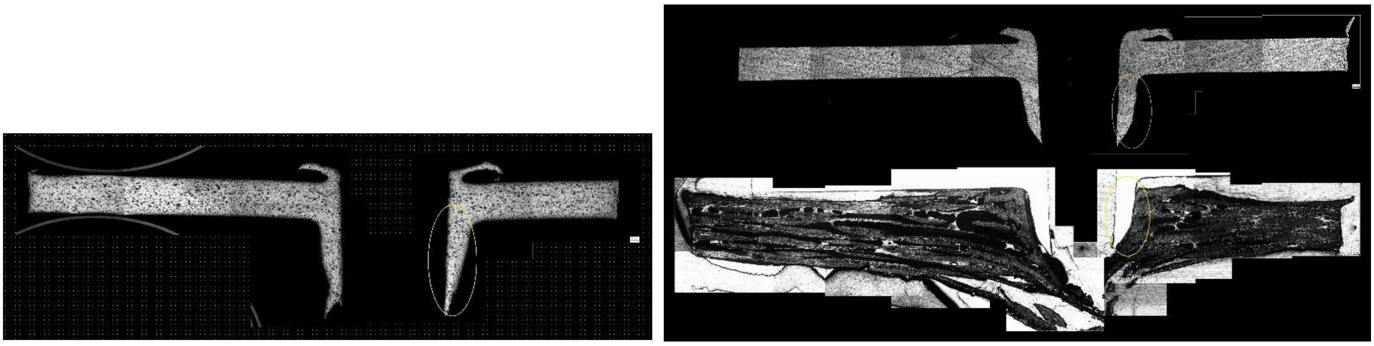

Figure 3. Comparison of the bushing in Al alloy drilled as a single material and the bushing formed when drilling overlapped Al sheet and carbon fibre composite material at 4800 min-1.

Figure 3 shows that the shape of the bushings in the Al sheet, produced by separately drilling the Al sheet and the sheet placed on the composite differs, since the forming bushing is preventing by the resistance to the composite material. In addition to its own forming, the emerging bushing must penetrate the tightly woven carbon mat, which is in seven layers in the composite. This has caused a blunting of the shape of the bushing termination. However, the bushing is still usable for joining with the composite.

4. Monitoring of the strain hardening of the material in the bushing area

Another important material property that is monitored when forming a joint using flowdrill technology is the change in the mechanical properties of the metallic material at the bushing area. The permanentc deformation of the material at that location can lead to strain hardening of the materials. Such a local change in mechanical properties can be monitored by measuring the hardness in the bushing area, which can be compared with the hardness of the unaffected sheet material outside the joint. The hardnesses of the unffected base materials were as follows: Al 115 HV0.1 and Mg 67 HV0.1. The hardness values of the bushings formed by thermal drilling of the sheets alone (without composite) at two rotational speeds and feed rates are given in Table 4 and 5.

Table 4. Hardness numbers of bushings in Al and Mg sheets formed at 2400 min-1.

	RPM [min^{-1}] / feed rate [mm.min^{-1}]	
	2400/60	2400/240
Al	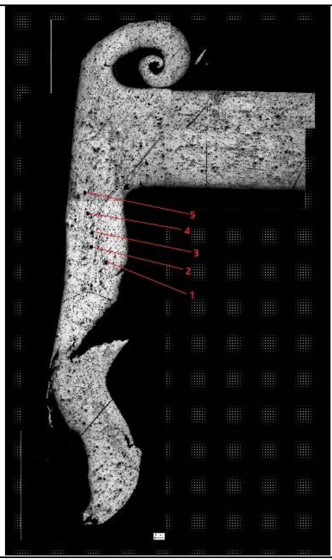	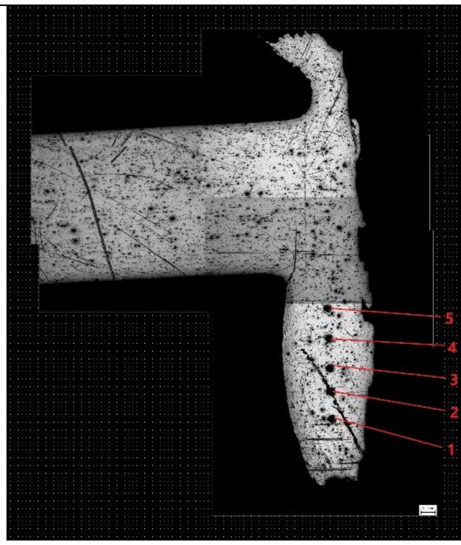
HV numbers	1 – 134 2 – 136 3 – 144 4 – 137 5 – 144 Average: 139 HV0.1	1 – 74.5 2 – 73.4 3 – 77.4 4 – 81.7 5 – 87.8 Average: 78.96 HV0.1
Mg	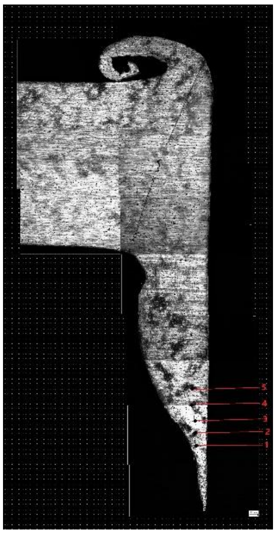	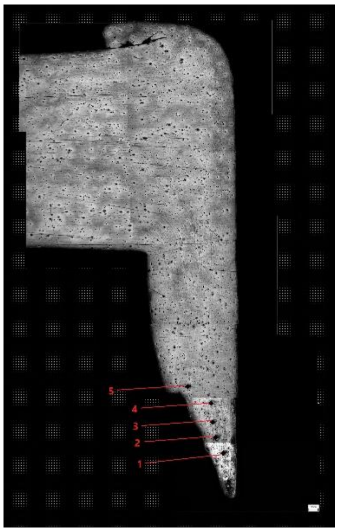
HV numbers	1 – 68.5 2 – 71.8 3 – 77.7 4 – 76.5 5 – 84.3 Average: 75.76 HV0.1	1 – 64.9 2 – 77.4 3 – 80.7 4 – 81.4 5 – 81.4 Average: 77.16 HV0.1

Table 5. Hardness values of bushings in Al and Mg sheets formed at 4800 min-1.

	RPM [min^{-1}] / feed rate [mm.min^{-1}]	
	4800/60	4800/240
Al	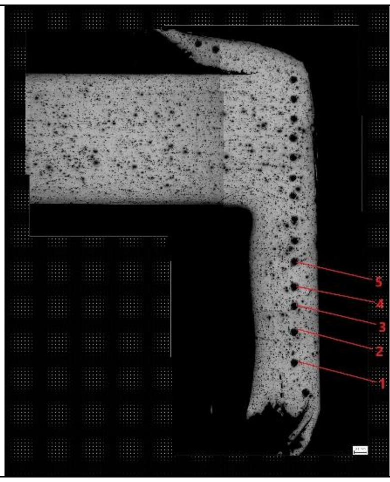	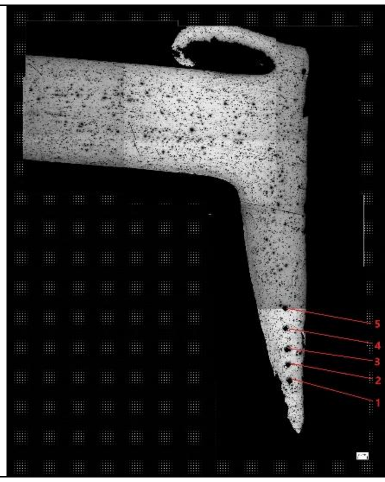
HV numbers	1 – 80.1 2 – 79.2 3 – 75.1 4 – 69.0 5 – 69.7 Average: 74.62 HV0.1	1 – 69.5 2 – 72.3 3 – 75.6 4 – 72.8 5 –75.6 Average: 73.16 HV0.1
Mg	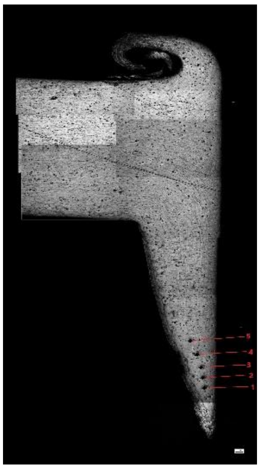	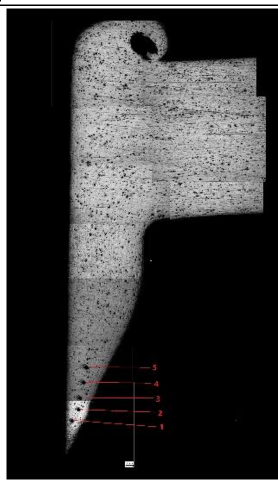
HV numbers	1 – 60.8 2 – 67.5 3 – 71.5 4 – 72.8 5 – 72.8 Average: 69.08 HV0.1	1 – 68.0 2 – 71.0 3 – 73.7 4 – 71.5 5 – 72.0 Average: 71.24 HV0.1

From the measured values of hardness it can be seen that in thermal drilling of Al at different rotational speeds and different manual feed rates, the strain softening of the material was observed, except rotational speed 2400 min-1 and slow feed rate. Al sheet in the initial state is precipitation hardened, there are a large number of small precipitates in its structure which strengthen the material - causing an increase in the stress required to initiate plastic deformation. However, at elevated temperatures, the precipitates can re-dissolve or overaged, resulting in a reduction in their hardening effect. This has occurred in Al alloy in thermal drilling. In the Mg alloy, a slight strain hardening of the material occurred at all thermal drilling parameters.

5. Conclusion

Analysis of metallographic sections of aluminium (Al) and magnesium (Mg) materials perfored by flowdrill technology at different parameters shows that the longest and most suitable bushings were produced for both materials at the higher speed of 4800 min-^{1}, independent of slow or fast manual feed. Conversely, at low speeds of 2400 min-^{1} and both feed rates, it was not possible to form a sufficiently long and high quality bushing for subsequent joining to the composite material.

Hardness measurements showed different behaviour of the Al and Mg materials. For the Al-alloy, the moderate strain softening in all drilling parameters, except at low speeds of 2400 min-^{1} and slow feed, where a slight hardening of the material was observed. For the magnesium alloy, a slight strain hardening of the material was observed in the bushing area and this was observed at all drilling parameters tested.

These findings suggest that for optimum joining results it is important to select higher speeds (4800 min-^{1}) for thermal drilling of the alloys in question to ensure the formation of a sufficiently long and thick bushing suitable for further joining with composite materials.

Funding: This research was supported by project VEGA 1/0229/23: Research on the applicability of thermal drilling technology for the creation of multi-material joints in the automotive industry.

References

1. R. Kumar, N. Rajesh Jesudoss Hynes, Thermal drilling processing on sheet metals: A review, International Journal of Lightweight Materials and Manufacture, Volume 2, Issue 3, 2019, ISSN 2588-8404. https://doi.org/10.1016/j.ijlmm.2019.08.003 2.
2. Sobotová, L. Hodnotenie púzdier vytvorených metódou flowdrill, Transfer inovácií 10/2007, 144-148 [online]. Avaliable: https://www.sjf.tuke.sk/transferinovacii/pages/archiv/transfer/10 2007/pdf/144-148.pdf
3. Composite Pultrusions Manufacturer, Provide Innovative Material Solutions, 21.03.2024 [online], Avaliable on internet: http://m.sk.gfrp-china-es.com/composite-rebar/fiberglass rebar/glass-fiber-reinforced-polymer-rebar.html
4. for Aluminum Extruders Council. Aluminium Joining Manual Automotive, available on the internet: https://www.aec.org/page/extrusion-aluminum- (visited. 2.12.2023) 5. joining-manual Messler, W.S. Joining of Advanced Materials, 1st ed.; Butterworth-Heinemann: Oxford, UK, 1993; 560p.
5. European Aluminium Association (2015): Hybrid joining techniques. Available on the internet: https://www.aec.org/page/extrusion-aluminum joining-manual.
6. Messler, W. S. (1993): Joining of advanced materials. USA: Butterworth-Heinemann, 560 p., ISBN 0-7506-9008-9.
7. Sirisalee, P. a kol. (2006): Multi-criteria material selection of monolithic and multi – materials in engineering design. In: Advanced Engineering Materials, Vol. 8, No. 1-2, pp. 48-56.
8. Mori, K. a kol. (2013): Joining by plastic deformation. In: CIRP Annals - Manufacturing Technology, Vol. 62, No. 2, pp. 673-694.
9. Martinsen, K. a kol. (2015): Joining of dissimilar materials. In: CIRP Annals - Manufacturing Technology, Vol. 64, No. 2, pp. 679 699.
10. Kleiner, M. a kol. (2003): Manufacturing of lightweight components by metal forming. In: CIRP Annals - Manufacturing Technology, Vol. 5, No. 2(2), pp. 521-542.
11. Graf, M. a kol. (2018): Macroscopic modeling of thin-walled aluminium-steel connections by flow drill screws. In: Thin-Walled Structures, Vol. 130, pp. 286-296.
12. Streppel, A. H. - Kals, H. J. J. (1983): Flowdrilling: a preliminary analysis of a new bush making operation. In: CIRP annals: manufacturing technology, Vol. 32, No. 1, pp. 167-171.
13. Guzanová, A.; Draganovská, D.; Veligotskyi, N. Possibilities of joining metals and CFRP/GFRP composites. Innovations: international scientific journal, 2024, s.47-50, 3.
14. Veligotskyi, N.; Guzanová, A.; Ižaríková, G. Behavior of steel, Al and Mg alloys when thermal drilling. Machines, Technologies, Materials, s.118-121, 3.
15. Guzanová, A.; Veligotskyi, N.; Garbacz, T.; Ižaríková, G. Study of the use of thermal drilling in machinical joining of mg sheet and gfrp/cfrp composites with thermosoftening matrix. Acta Metallurgica Slovaca, s. 142-147, 5.

Planning the reconstruction of mandible with patient specific implant.

Jakub Viľcha [1,*], Jozef Živčák [2]

[1] Department of Head and Neck Surgery, maxillofacial surgery, FNsP J.A.Reimana Prešov, Jána Hollého 14, 08001, Prešov, Slovakia, mddr.vilcha@gmail.com (J.V)
[2] Department of Biomedical Engineering and Measurement, Faculty of Mechanical Engineering, Technical University of Košice, 042 00 Košice, Slovakia; jozef.zivcak@tuke.sk (J.Ž.)
* Correspondence: mddr.vilcha@gmail.com

Abstract: Facial bones like the mandible and maxilla are crucial for appearance and function, with deformities or trauma causing asymmetry and mastication issues. Treatments include autologous bone grafts, which offer biocompatibility but risk complications, and custom implants, which avoid donor site issues but are costly and material-dependent. Advances in digital technologies, including CBCT, CAD, and 3D printing, have transformed maxillofacial surgery. These enable precise planning, guided osteotomy, and accurate implant placement, improving outcomes and reducing complications. Despite benefits like shorter recovery times, challenges include high costs, limited access, and training needs. Emerging technologies promise further improvements, making planned surgeries more effective and predictable.

Keywords: facial reconstruction planning, guided surgery, digital technologies

1. Introduction

Among the many bones of the skull, facial bones such as the mandible, maxilla, and zygomatic complex determine overall appearance of the face and also play a role in mastication. In cases of congenital craniofacial deformities or acquired defects due to trauma or tumors, aesthetic and functional problems may arise, associated with facial disharmony, asymmetry, and difficulties in mastication [1].

The primary method of treating such defects is autologous bone transplantation or the placement of individually made maxillofacial implants. Autologous bone grafts offer higher biocompatibility, but problems such as donor site morbidity, graft failure, and difficulties during reoperations may occur. In maxillofacial implant placement, donor site-related complications do not arise, but problems with biocompatibility, depending on the material used, as well as increased surgical costs related to material costs and processing, are much more frequent [2,3].

The continuous advancement in digital technologies has caused a paradigm shift in maxillofacial surgery. For instance, the development of cone-beam computed tomography (CBCT), computer-aided design (CAD), computer-aided manufacturing, and three-dimensional (3D) printers have enabled precise and rapid execution of planned surgical procedures [4,5].

This article aims to provide an insight into the current possibilities and benefits of planning individualized maxillofacial implants.

2. Materials and Methods

Electronic databases including PubMed, MEDLINE, and Web of Science were used to search for current articles using the following keywords: "mandibular reconstrucion"

OR "patient specific implants" AND "biocompatibility" OR "biomaterials" AND "planning" OR "printing" AND "guided surgery". The images were obtained with the consent of the company Materialise, as well as with the consent of the maxillofacial surgeon who performed the surgical procedure.

3. Results

Virtual treatment planning holds tremendous potential for the future of maxillofacial surgery, with vast opportunities for its application. Its integration into practice promises to revolutionize the field, enhancing precision, efficiency, and overall patient care [6].

3.1. Surgical planning

3.1.1. Preoperative imaging

A spiral computed tomography (CT) scanner is used to obtain the data, which are exported as Digital Imaging and Communication in Medicine (DICOM) datasets and then transferred into Proplan CMF (Materialise. Oberdorf, Switzerland), a surgical planning software. The threshold segmentation is adjusted to reconstruct a three-dimensional model of the patient's skull [7,8].

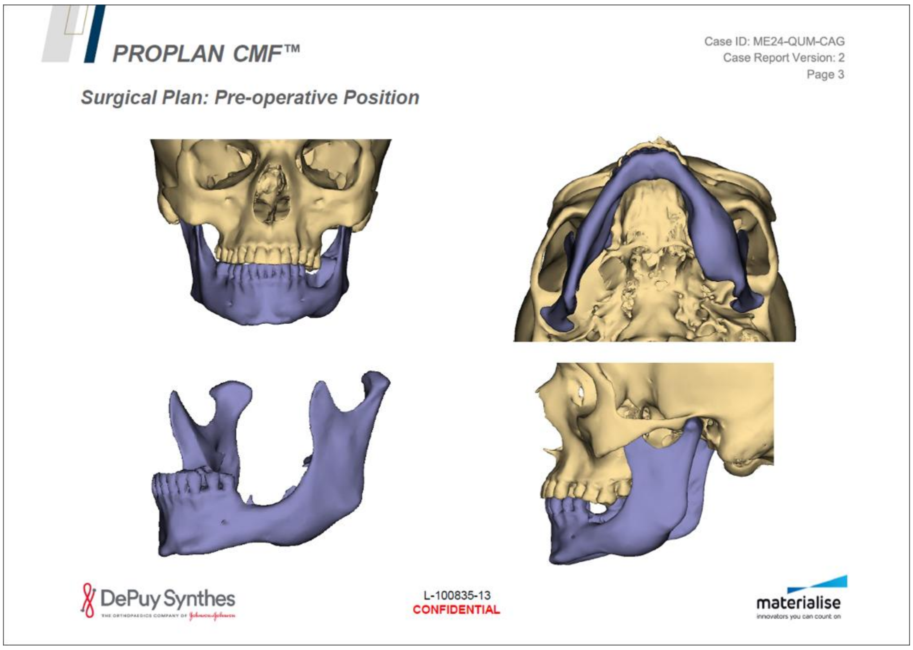

Figure 1. 3D model of skull and the visualization of the affected mandible (marked in blue).

3.1.2. Resection planning

A web-based teleconference involving the surgical team and a biomedical engineer is held to allow remote participation. During this session, the resection, reconstruction, and other crucial factors such as osteotomies, resection margins, and the placement of implants is determined. In cases of traumatic injuries, the virtual planning focuses on reducing fractured bony segments, while in orthognathic surgery, it addresses staged jaw movements [7,8].

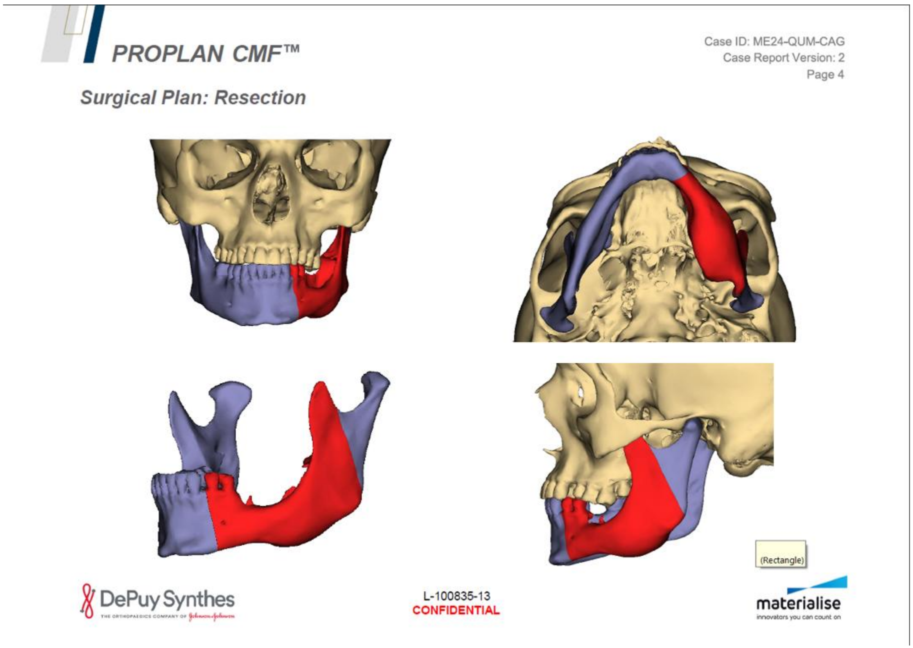

Figure 2. Planning the resection – visualization of the part that is going to be resected (marked as red).

3.1.3. Mandible resection guides

To plan the most optimal implant position, stability, and accuracy, it is important to use so-called cutting guides. The guides are planned and adjusted to the the wish of the surgeon. Modelling follows the virtual surgical plan, where stereolithographic models of the craniomaxillofacial area are created along with cutting guides for resection and implant placemement. These models also include templates for reconstruction plates and plate bending, customized to the surgeon's preferences [7,8].

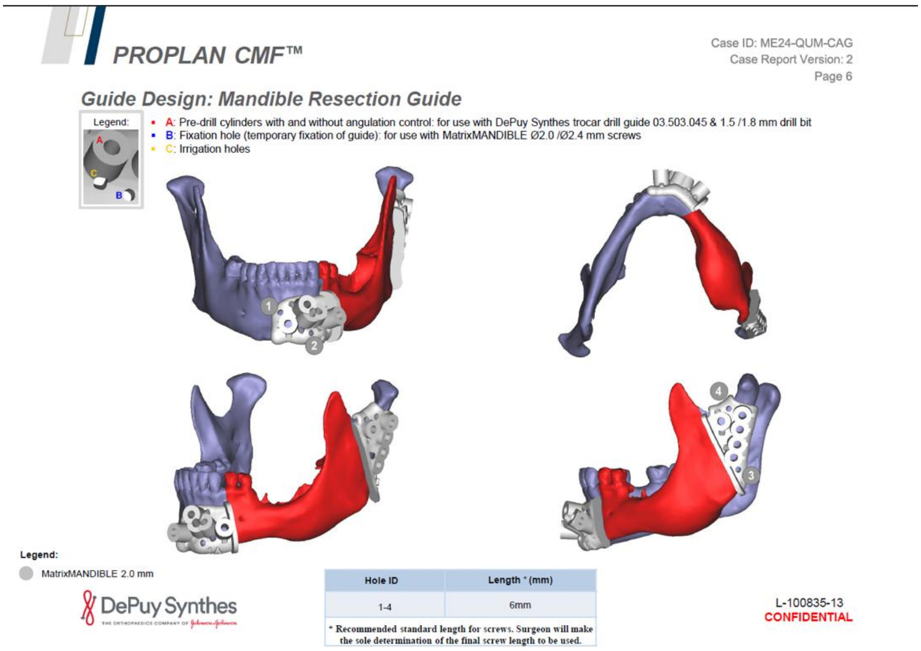

Figure 3. Surgical guides – The image depicts the precise adaptation of surgical guides to the bone, marked in white. These guides serve as a reference for accurate resection and reconstruction, ensuring optimal alignment and stability of the future implant.

3.1.4. Implant design

Finally an individual implant is designed to match the defect created by the guided osteotomy and it should be also designed to not cause any further damage to surrounding tissues, which posses a great challenge for the engineers. Studies show that when a titanium implant is entirely porous, friction with the soft tissue during insertion can cause damage and increase resistance. Therefore, it is crucial for the surface in contact with soft tissue to be solid and smooth. On the other hand, the surface of the implant in contact with the bone can be either solid or porous, each having its own set of advantages and drawbacks [9].

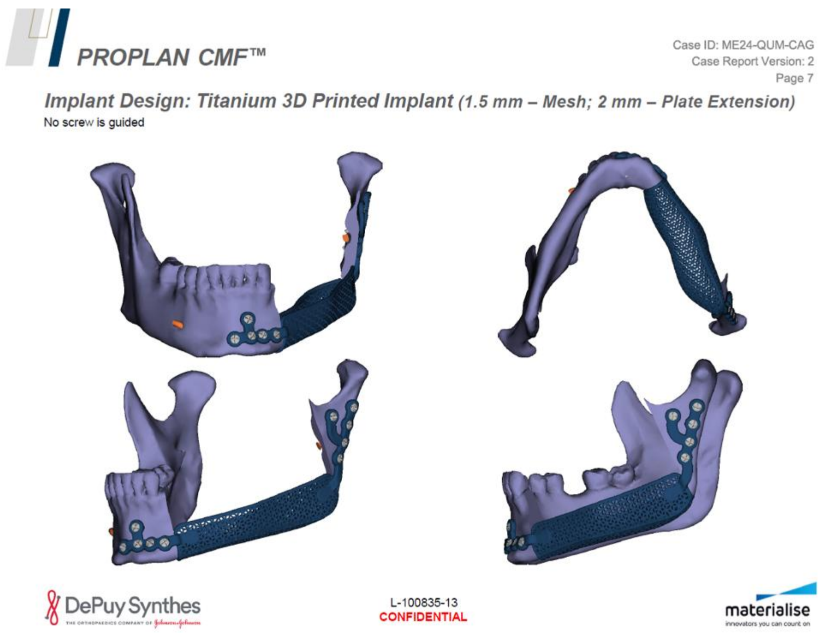

Figure 4. Implant design - The image illustrates the final design of the implant (marked in blue), showing the exact placement of screws (gray). The design ensures proper biomechanical stability and integration with the surrounding bone structure.

3.2. Surgical procedure

Under general anesthesia surgical guides are applied to the bone and osteotomy is performed removing the affected region. In the next step the patient specific implant is placed in the defect, reconstructing the missing bony part [10].

4. Discussion

Planned bone surgery represents a significant advancement in maxillofacial procedures due to technologies like CBCT, CAD, and 3D printing. Compared to traditional methods such as free-hand autologous bone grafting, digital techniques offer improved precision, reduced surgical time, and lower complication rates. Traditional methods often lead to donor site morbidity, increased risk of graft failure, and longer recovery periods. By contrast, patient-specific implants minimize surgical complexity and optimize functional and aesthetic outcomes.

Another crucial factor is cost-effectiveness. While initial expenses for digital planning and custom implant manufacturing may be high, the reduced need for revision surgeries and shorter hospital stays ultimately lead to lower long-term costs. However, these benefits remain limited by the availability of necessary technology and trained personnel, particularly in less developed regions.

References

1. Olate S, Huetequeo-Molina C, Requena R, Uribe F. Patient Specific Implants to Solve Structural Facial Asymmetry After Orthognathic Surgery. J Craniofac Surg. 2021 May 1;32(3):e269-e271. doi: 10.1097/SCS.0000000000007113. PMID: 33027171.
2. Agarwal R, García AJ. Biomaterial strategies for engineering implants for enhanced osseointegration and bone repair. Adv Drug Deliv Rev. 2015 Nov 1;94:53-62. doi: 10.1016/j.addr.2015.03.013. Epub 2015 Apr 8. PMID: 25861724; PMCID: PMC4598264.
3. Schmidt AH. Autologous bone graft: Is it still the gold standard? Injury. 2021 Jun;52 Suppl 2:S18-S22. doi: 10.1016/j.injury.2021.01.043. Epub 2021 Feb 3. PMID: 33563416.
4. Mangano FG, Admakin O, Lerner H, Mangano C. Artificial intelligence and augmented reality for guided implant surgery planning: A proof of concept. J Dent. 2023 Jun;133:104485. doi: 10.1016/j.jdent.2023.104485. Epub 2023 Mar 23. PMID: 36965859.
5. Jacobs R, Salmon B, Codari M, Hassan B, Bornstein MM. Cone beam computed tomography in implant dentistry: recommendations for clinical use. BMC Oral Health. 2018 May 15;18(1):88. doi: 10.1186/s12903-018-0523-5. PMID: 29764458; PMCID: PMC5952365.
6. Saxena V, Krishnan VG, Rangarajan H. Virtual 3D planning in Maxillofacial surgery : The journey so far and the way ahead. Med J Armed Forces India. 2024 Jul-Aug;80(4):392-398. doi: 10.1016/j.mjafi.2024.05.008. Epub 2024 Jun 21. PMID: 39071751; PMCID: PMC11279760.
7. Liu X, Gui L, Mao C, Peng X, Yu G. Applying computer techniques in maxillofacial reconstruction using a fibula flap: a messenger and an evaluation method. J Craniofac Surg 2009; 20(2):372e7
8. Leiggener C, Messo E, Thor A, Zeilhofer H-, Hirsch J-. A selective laser sintering guide for transferring a virtual plan to real time surgery in composite mandibular reconstruction with free fibula osseous flaps. Int J Oral Maxillofac Surg 2009;38: 187e92.
9. Lim, HK., Choi, YJ., Choi, WC. et al. Reconstruction of maxillofacial bone defects using patient-specific long-lasting titanium implants. Sci Rep 12, 7538 (2022). https://doi.org/10.1038/s41598-022-11200-0

TECHNICAL UNIVERSITY OF KOŠICE
Faculty of Mechanical Engineering

Genetic algorithms in Generative design

Matúš Virostko [1,*], Martin Mantič [1] and Pavol Tarbajovský [1]

[1] Faculty of Mechanical Engineering, Technical university of Košice, Slovakia; matus.virostko@tuke.sk; martin.mantic@tuke.sk; pavol.tarbajovsky@tuke.sk
* Correspondence: matus.virostko@tuke.sk; Tel.: +421 55 602 2354

Abstract: One of the approaches to designing structural solutions is the problem-solving process, which focuses on iterative procedures. The resulting design is developed through gradual analysis and simulation testing until it meets the established criteria and requirements. Designers often rely on their own experience and knowledge when creating designs. An alternative approach is generative design, where the user focuses on precisely defining the problem, including its constraints and criteria. The process of finding the optimal solution is then left to algorithms, which can quickly generate and test many alternatives. The output of this process is a set of designs that differ in form, but all meet the specified input parameters and conditions. The main idea of this design method is to streamline the work of designers and achieve optimal solutions through algorithms. The designer primarily focuses on accurately defining input data, creating an ideal foundation for algorithms to generate various variants based on it. Generative design, in its current form, does not replace designers but serves as a powerful application tool to expand their implementation possibilities [11,12].

Keywords: genetic algorithms, evolution algorithms, generative design

1. Introduction

A common challenge for designers, beyond meeting the required functional properties of a component, is achieving an attractive design. Modifying an object requires navigating through various parameters, considering possibilities, accounting for multiple factors, and deciding on preferences. This process can be demanding not only for customers but also for development teams working on new product designs. Designing often relies on a trial-and-error approach, where achieving the "optimal" design requires numerous repeated iterations.

The solution to this problem lies in the use of generative design (Figure 1). This form of CAD design, in collaboration with artificial intelligence leveraging the power of cloud computing, machine learning, and algorithms, enables the automatic creation of designs in a unique way. The algorithm can automatically modify the basic shape, pattern, or object, resulting in infinite variations of the original design within the user-defined parameters.

Two groups of algorithms play a significant role in this process: evolutionary and, most notably, genetic algorithms. These algorithms make generative design an automated process, significantly speeding up the design workflow and allowing the creation of thousands of different designs, from which the most suitable ones can be selected. Moreover, this technology surpasses the limitations of human imagination, opening new possibilities in the field of design. [1,2,10].

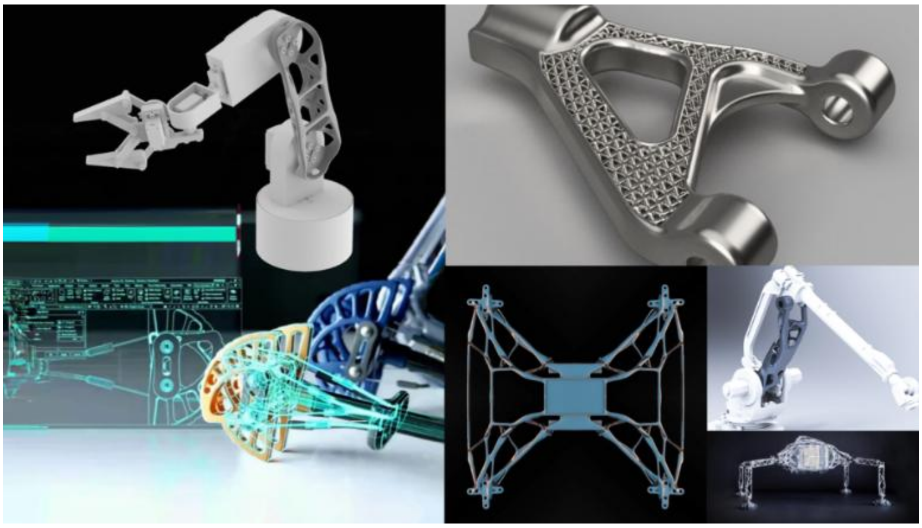

Figure 1. Generative design in practice [3].

2. Generative design

Generative design, with its ability to generate shape elements through input and output data while evaluating correctness and providing immediate feedback, is an ideal choice for finding specific engineering solutions and meeting user requirements. This process facilitates the implementation of a dynamic solution capable of absorbing and transmitting information back into the process, enabling further optimization.

The added value of this design approach lies in algorithms operating in the background to create specific shapes. These algorithms continuously refine and adapt the designs, ensuring they meet both technical criteria and user preferences while maintaining flexibility for ongoing improvements [4,10].

3. Evolution algorithms

Evolutionary algorithms (EA) belong to optimization methods inspired by biological evolution and animal behavior. They mimic genetic improvements in humans and the behavior of animals. These algorithms fall into the category of so-called search algorithms, which represent the principle of solving a problem by exploring possible solutions. The essence of this category lies in navigating the search space. Exploring the given space involves a combination of generating and selecting indicators, followed by their evaluation and testing (Figure 2). This process examines many indicators until an optimal solution is found. Evolutionary algorithms have relatively few requirements, making them versatile and capable of solving a wide range of problems [6,7].

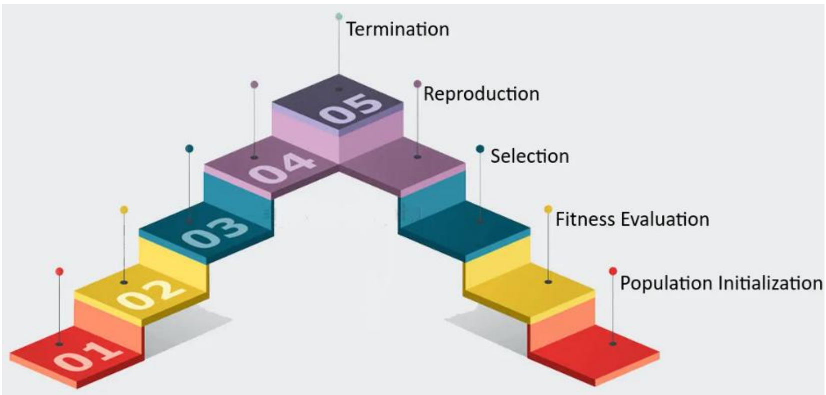

Figure 2. The Hierarchy of Evolutionary Algorithm Workflow [5].

EAs are used in a wide range of fields. They can be divided into several categories based on the principles they use and their application focus. Their fundamental classification falls into three main points based on these criteria:

- **Inspirations:** biology, social behavior, physical processes
- **Mechanisms:** crossover, mutation, selection, cooperation
- **Applications:** discrete problems (e.g. combinatorics), parameter optimization

3.1. Selection of Evolutionary Algorithms Based on Application Focus

- **Genetic Algorithms (GA) -** the most well-known subtype, which focuses on the inspiration from genetic mechanisms.

- **Evolutionary Strategies (ES) -** focus more on mutations than on crossover. They are often used for optimizing real numbers.

- **Evolutionary Programming -** focuses on the development of programs (e.g., genetic programming).

- **Differential Evolution (DE) -** uses differences between candidates to create new solutions [8].

These subgroups of evolutionary algorithms represent different application directions. Given the focus on the connection between algorithms and generative design, the following section will focus on the subgroup of genetic algorithms.

4. Genetic algorithms

Genetic algorithms (GA) play a key role in generative design because they enable an efficient search for optimal designs within vast design spaces. Their connection to generative design lies in their ability to automate the creation and optimization of designs using evolutionary principles [10].

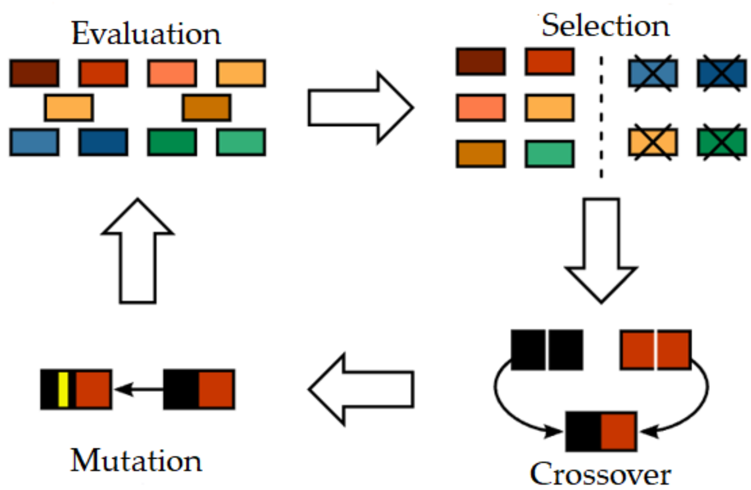

Figure 3. The Operation of Genetic Algorithms [9].

4.1. Genetic Algorithms in Generative Design

The process of applying genetic algorithms in generative design can be divided into the following steps:

1. **Population Initialization –** represents the parameters and constraints of the design (dimensions, materials, physical properties).

2. **Generation of Initial Population –** randomly creates the first set of designs that meet the basic parameters.

3. **Evaluation –** involves a process where each design is tested (e.g., through simulation) based on pre-defined criteria**.**

4. **Selection and Evolution –** creates a selection of the best designs to generate a new generation using:
   - crossover (combination of elements from two successful designs),
   - mutation (random changes in the design to explore new possibilities).

5. **Iterations –** creates a process of repetition until the desired result is achieved (e.g., minimum weight, maximum strength).

6. **Output –** provides several optimized designs, from which the user selects the optimal solution.

4.2. Optimization in Generative Design

Generative design involves finding the best possible solution based on a variety of parameters, such as:

- strength and weight of materials,
- energy consumption,
- production costs,
- ergonomic requirements.

Genetic algorithms, in solving these tasks, can explore vast combinations of parameters and finding not only local but also global optimal solutions.

4.3. Application of Genetic Algorithms in Generative Design

- **Automated design of structures,** where they are used to optimize load-bearing constructions with respect to strength and weight.
- **Product development,** where they are used in industrial sectors to create components with better functionality and lower production costs
- **Optimization of the manufacturing process,** where designs created by genetic algorithms are primarily suitable for additive manufacturing.

4.4. Advantages of using GA in Generative Design

- **Efficient exploration of a large solution space –** GAs can find optimal solutions in complex systems with many interconnected parameters.
- **Automation of design creation –** saving designers' time by autonomously generating designs.
- **Innovation –** generated designs often contain non-intuitive and creative solutions that a human may not have thought of.

4.5. Challenges of Implementing GA in Generative Design

- **Computational complexity –** the process can be very time- and computationally intensive. Simulations and evaluation of thousands of iterations can be demanding on hardware and software resources.

- **Dependency on correctly specified input parameters –** if the input data is not properly set, the results may be unsatisfactory.
- **Limited interpretability –** solutions may be non-intuitive and geometrically complex.
- **Feasibility of implementation –** some generated designs may be financially challenging in terms of their specific manufacturing [10,11,12].

5. Practical example of Genetic algorithms and Generative design in practice

As part of testing generative design and shape creation using genetic algorithms, the following bodies were created, which represent previous studies of the algorithms' performance in optimization processes. In the first case, the task was to create fill structures for rotating components using generative design and genetic algorithms. Three different input constraints for the study were implemented. The results of the study are shown in Figure 4. Fig. 4a represents the output where radial forces are considered as the load, 4b shows the case with torque, and 4c is a combination of the previous cases with the addition of a fully symmetric shape creation.

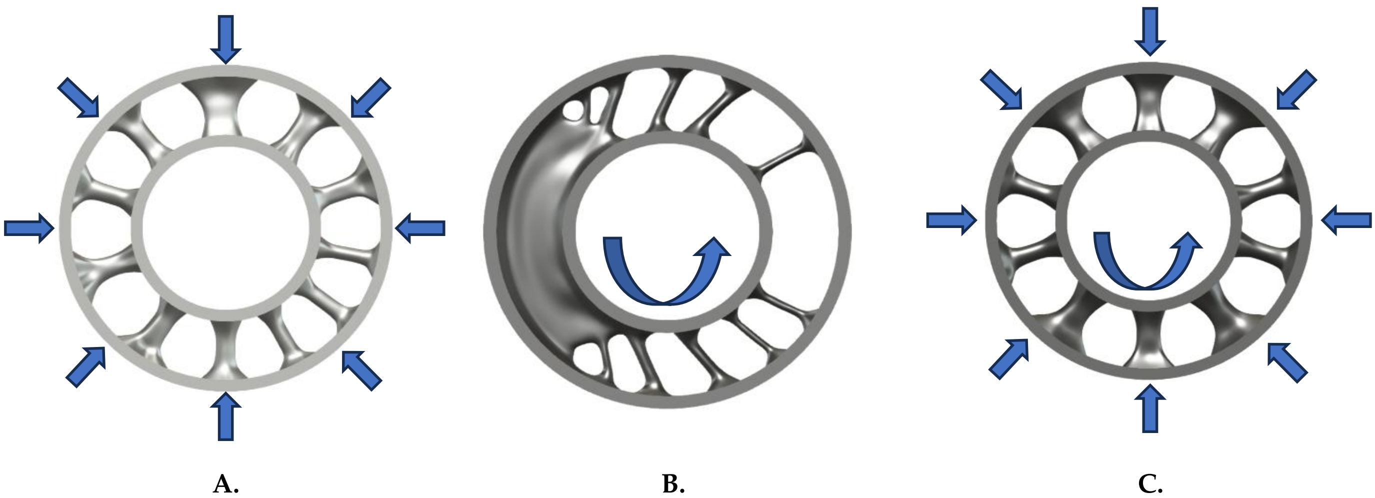

Figure 4. Rotary Components Created through Generative Design

a.) Loading with Radial Forces

b.) Loading with Torque

c.) Combination of Previous Loads and Application of Symmetry.

In the second practical example, the task was to create fill structures for flat components using generative design and genetic algorithms. From the numerous generated variants, two selected outputs were chosen, for example, as shown in Figure 5..

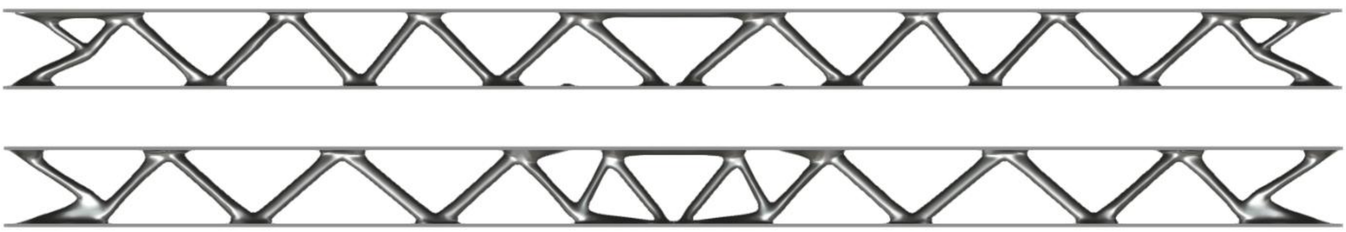

Figure 5. Flat Components Created through Generative Design.

5. Conclusions

Generative design, in combination with genetic algorithms, represents a revolutionary approach to the creation and optimization of designs. These algorithms, inspired by biological evolution, enable the generation of innovative and often counterintuitive solutions that traditional design methods would not uncover. Thanks to the ability of genetic algorithms to explore vast design variants and optimize solutions based on various criteria, they are an ideal tool for applications where the best results must be achieved under multiple constraints. With the increasing power of computers and the development of artificial intelligence, it is expected that generative design combined with genetic algorithms will play an increasingly significant role in the future of design and engineering. This approach is not just a tool for solving problems, but also a new philosophy of creation, bringing construction closer to modeling natural processes and harnessing their inherent perfection [11,12].

Acknowledgment: The contribution was created within the framework of the solution of the project KEGA 044TUKE-4/2024.

References

1. Cad.Map. (2024) Cad - Fusion 360 Generative Design Extension. Available online: https://cad.map.sk/cad/fusion-360-generative-design-extension (accessed on 1.12.2024).
2. Zadania-seminarky. (2012) Generatívne konštruovanie. Available online: https://www.zadania-seminarky.sk/referat/generativne-konstruovanie/41268 (accessed on 1.12.2024).
3. Robotica. (2023) Artificial Intelligence to Expand the Potential of Generative Design of Complex Mechanical Modules. Available online: https://utcn-robotica.ro/generative-design-ai/ (accessed on 30.11.2024).
4. Stavební technika. (2015) Navrhovaniu častí automobilu s využitím princípov generatívneho konštruovania. Available online: https://www.stavebni-technika.cz/clanky/navrhovaniu-casti-automobilu-s-vyuzitim-principov-generativneho-konstruovania (accessed on 2.12.2024).
5. Faster Capital. (2024) Adapting to Change: CSB and Evolutionary Algorithms - Benefits Of Evolutionary Algorithms. Available online: https://fastercapital.com/topics/benefits-of-evolutionary-algorithms.html (accessed on 2.12.2024).
6. doc. Ing. Marián Mach, CSc. (2009 TUKE) Evolučné algoritmy: prvky a princípy, 1st ed, p. 250. ISBN 978-80-8086-123-0.
7. Chamil Abeykoon, Yasith S. Perera, D.A.A.C. Ratnaweera. (2023) Engineering Applications of Artificial Intelligence, The role of artificial intelligence-driven soft sensors in advanced sustainable process industries: A critical review, Volume 121, pp. DOI:doi.org/10.1016/j.engappai.2023.105988.
8. Yue-Jiao Gong, Wei-Neng Chen, Zhi-Hui Zhan, Jun Zhang, Yun Li, Qingfu Zhang, Jing-Jing Li. (2015) Applied Soft Computing, Distributed evolutionary algorithms and their models: A survey of the state-of-the-art, Volume 34, pp 268-300. DOI:doi.org/10.1016/j.asoc.2015.04.061.
9. Paperswithcode. (2019) Genetic Algorithms. Available online: https://paperswithcode.com/method/ga (accessed on 5.12.2024).
10. Sivam Krish. (2011) Computer-Aided Design, A practical generative design method, Volume 43, Issue 1, pp 88-100. DOI:doi.org/10.1016/j.cad.2010.09.009.
11. Luigi Troiano, Cosimo Birtolo. (2014) Information Sciences, Genetic algorithms supporting generative design of user interfaces: Examples, Volume 259, pp 433-451. DOI:doi.org/10.1016/j.ins.2012.01.006.
12. Medium. (2024) Optimizing CAD Designs Using Genetic Algorithms. Available online: https://medium.com/@pepperumo/optimizing-cad-designs-using-genetic-algorithms-e648fed166bd (accessed on 6.12.2024).

Methods of investigating the wear of cylinders intended for the continuous casting of steel into plates and of solving their service life

Jozef Výboch [1,*], Milan Čomaj [2] and Ján Viňáš [1]

[1] Department of Technology, Materials and Computer Aided Production, Faculty of Mechanical Engineering,Technical University of Košice, 040 01 Košice, Slovakia; vyboch.jozef@gmail.com; jan.vinas@tuke.sk
[2] ASKOZVAR s.r.o.. Hraničná 2, 040 01 Košice, Slovakia; askozvar@askozvar.sk
* Correspondence: vyboch.jozef@gmail.com

Abstract: The subject of the investigation was the influence of the wear of the rolls of the continuous steel casting equipment on the technical and economic parameters of the line and the cast plates. Tribological aspects of roller loading - thermal fatigue, adhesion-abrasion effect and high-temperature corrosion were described. Consumables for welding of rolls of the 1st to 3rd generation, tubular core wires of VÚZ - SR (VÚZ - Welding Research Institute) production type RD527 for submerged arc welding with combinations of weld metals with nitrides of CrN and Cr2N type were analyzed. The study enriches the increase of the overall weld quality.

Keywords: tribology; casting; welding; rollers

1. Introduction

The dominant technology for slab production is continuous steel casting. The continuous steel casting equipment is of the curved type (Fig. 1), with the most exposed stressed parts being the rollers, which, in addition to guiding and cooling the slab, also perform the forming work. Their uneven wear causes a change in the axial distance between the respective pairs of feeding rollers and thus a different forming work during the deformation of the solidifying slab. This causes a change in the stress ratios in the solidifying slab, which leads to the formation of cracks in the solidifying slab in some types of steel, or to a casting failure. Therefore, the rollers in the equipment are replaced when wear exceeds the permissible limit (approx. 1 mm) or when corrosion-fatigue cracks develop, which creates a risk of later roller breakage and interruption of the casting machine's operation. The life of the rolls primarily determines the economic aspects of the continuous steel casting plant. Currently, the extension of the life of the rolls is achieved by welding resistant layers onto the working surface of the roll using the SAW METHOD.

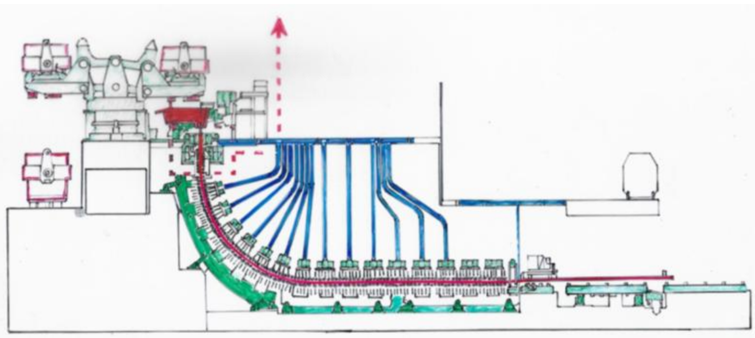

Figure 1. Schematic machine of a continuous steel casting facility.

2. Materials and Methods

From a tribological point of view, rollers are stressed by:

- heat fatigue
- adhesive-abrasive wear
- high temperature corrosion

The cylinders are hollow from the inside and cooled by water. From the outside, they are alternately heated during their rotation at the point of contact with the hot slab and cooled by external water-steam-air cooling. In the upper part of the casting device, the slab has a temperature approx. 1250°C and in the lower part approx. 800°C.

During casting, the rollers are subjected to adhesive-abrasive wear by residues of the casting powder and the plate fasteners. This results in the rollers operating in an extremely aggressive environment. Such an environment is caused by the reaction of free hydrogen ions from the decomposition of water with the slag from the high fluorine casting powder to form aggressive hydrogen fluoride solutions. Corrosion pits form on the surface of the cylinders as potential centers for fatigue cracking. If the cooling water still contains a high content of chloride ions, these become the "driving force" for crack propagation at the crack root.

The basic materials of the rolls are mostly low-alloy heat-resistant steels, see table number 1. The service life of such rolls is very low. The chromium content of the rolls (1 to 2% Cr) does not reach passivation values (12% Cr) and has low wear resistance. Therefore, the rolls are cladded with materials with a chromium content of over 12%, nickel up to 4%, molybdenum 1.5%. The resulting structure of the weld is martensitic, or ferritic-martensitic.

The first generation of these hardfacing systems had a carbon content in the range of 0.15 to 0.20%, a chromium content approx. 13%. With a martensitic structure, the hardfacings had excellent wear resistance, but low resistance to corrosion and fatigue.

In the heat affected zone of the weld bead heated to temperatures of 450°C to 850°C, conditions were created for the formation of intercrystalline corrosion with the formation of precipitates-carbides of the $Cr_{23}C_6$ type . The surrounding area of the precipitates is depleted in chromium, has a significantly lower corrosion potential and preferential development of corrosion-fatigue cracks occurs in it. Furthermore, the matrix is also depleted in carbon, which increases the proportion of the ferritic phase with reduced wear resistance in the HAZ (HAZ - heat-affected area) weld. Fatigue cracks preferentially form in these places, see Fig. 2.

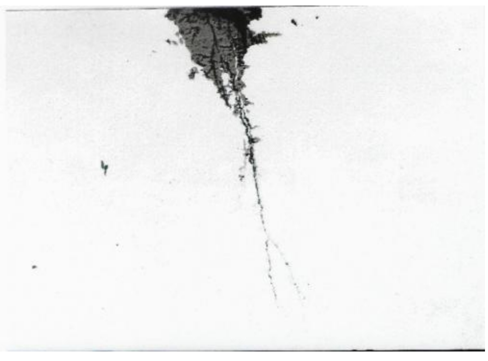

Figure 2. Corrosion-fatigue crack in the cylinder weld.

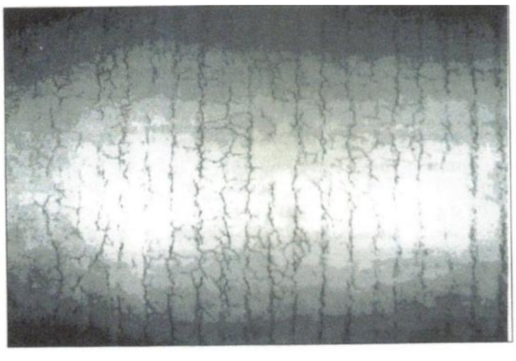

Figure 3. Fatigue cracks in a continuous steel casting roller.

Table 1. Chemical composition.

Steel type	Chemical composition of steel (%)					
	C	Mn	You	Cr	Mo	V
24CrMoV5-5	0.22-0.29	0.40-0.70	0.07-0.37	1.5-1.8	0.25-0.35	0.15-0.30
42CrMo4V	0.38-0.45	0.6-0.9	0.2-0.4	0.9-1.2	0.15-0.30	-

Typical representatives are listed in Table 2. From the production of VÚZ, these were RD531 and RD533 tubular wires welded by the SAW method. The welds had excellent resistance to wear, but lower resistance to corrosion fatigue. The service life of the rolls ranged from 15 -1000 kt of cast steel depending on the place of installation of rolls in the ZKO (ZKO - continuous casting equipment). The modernization of the ZKO equipment has reduced the wear rate, but the dominant problem remained the issue of increasing the service life of the cylinders to reduce the rate of corrosion cracking.

In the heat-affected zone (hereinafter HAZ) of the weld bead heated to temperatures of 450-850°C, conditions were created for the development of intergranular corrosion (hereinafter MKK) with the formation of precipitates - carbides of the $Cr_{23}C_6$ type . The surrounding area of the precipitates was depleted in chromium, had a significantly lower corrosion potential and preferential development of corrosion-fatigue cracks occurred in it. Furthermore, the matrix was also depleted in carbon, which increased the proportion of the ferritic phase with reduced wear resistance in the HAZ weld.

For these reasons, a number of so-called 2nd generation welding materials have been developed to reduce the rate of corrosion-fatigue cracking. They have a significantly lower carbon content in the range of 0.03 - 0.08% and a chromium content of 13-17% and a martensitic-ferritic structure, usually with a delta ferrite content of around 10%. Typical representatives of 2nd generation welding materials are listed in Table 2. Number of such tubular wires have been developed at VÚZ, namely types RD534, RD535 and RD537 [2,3]. This group also includes systems with a so-called stabilized structure, which also contain niobium and vanadium (Weldclad type, Table 2).

This solution to extend the life of the cylinders reduced the rate of corrosion-fatigue crack formation, but the wear resistance of the systems became the limiting factor.

At a steel conference in Baltimore, USA, the idea of replacing reduced carbon in 2nd generation surfacing systems by saturating them with nitrogen was discussed.

VÚZ succeeded in this by developing a nitrogen-saturated flux cored wire labeled VUZ RD527 (with flux 56) for the so-called 3rd generation SAW method, see table number 2, where the flux cored wires and tapes for individual generations of welding materials are listed.

Table 2. Chemical composition.

Weld	Type	Chemical composition (%)	Structure	Hardness HV
1st generation	VÚZ RD531	0.13C; 13Cr; 1.2Mo; 0.3W	Ms.	440
	VÚZ RD533	0.12C; 13Cr, 0.9Mo; 0.1W	Ms.	410
	In Al	0.16C; 14Cr; 0.3Mo	Ms.	420
	Soudometal tape 420	0.2C; 13Cr	Ms.	460

2nd generation	VÚZ RD534	0.07C; 16.5Cr; 0.7Mo; 2.4Ni	Ms+α	300
	VÚZ RD535	0.05C; 16.5Cr	Ms+α	280
	KMS 393, RD537	0.08C; 13Cr; 0.9Mo; 2.5Ni	Ms+α	390
	WLDC 3M2L Weldclad	0.07; 14Cr; 1.5 Mo; 3.5Ni; 0.2V; 0.1 Nb	Ms+α	420
	Oerlikon tape 16-3	0.03C; 15Cr; 1.1Mo; 2.5Ni	Ms+α	350
3rd generation	VÚZ RD527	0.06C; 13Cr; 3.5Ni; 1.0 Mo; 0.1 Nb; 0.14N 2	Ms+Cr 2 N	460

3rd generation VUZ RD527 weld metal system with F56 flux based on Al_2O_3 + CaO + C_2F_2 , after a complete thermal cycle (annealing to remove post-welding stress 500°C/5 hours, cooling 40°C/hour to 220°C then air). It was determined with a Leitz MS dilatometer, start at a temperature of 180 to 220°C, Mf at 85°C.

The weld has a chemical composition in the third layer in Table 3.

Table 3. Chemical composition in the third layer.

Cored wire type	Directional chemical composition in the third layer (%)								Hardness
	C	Mn	Si	Cr	Mo	Nb	No	N	HV
RD 527 + F56	0.07	0.7	0.6	13.0	0.8	0.2	3.8	0.12	420-470

By electron microscopic examination [2], after complete heat treatment, precipitated fine needle-like particles with a high chromium content were found in the weld metal, identified by electron diffraction as βCr 2 N or CrN. The matrix is formed by low-carbon martensite with fine precipitates of Nbc and βCr 2 N, CrN.

Figure 4. βCr 2 N particles.

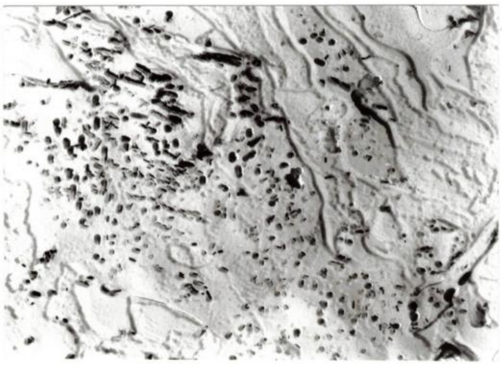

Figure 5. The matrix formed by low-carbon martensite is strengthened by fine niobium carbides.

Nitrides in the design metal block dislocations, grain growth and the formation of carbides of the $Cr_{23}C_6$ type at grain boundaries. This increases the resistance to thermal fatigue, creep, aging of the weld metal and also increases wear resistance. Furthermore, the Ms temperature is reduced to 180 - 220°C, which leads to the formation of low-carbon fine-grained martensite in the weld and in the HAZ of the weld between the beads during solidification, and therefore there is no rapid formation of worn surfaces and pitting in these areas during the operation of the rolls as in the 1st and 2nd generation of weld materials. In this area, there will be no reduction in the chromium content below the passivation limit due to the formation of $Cr_{23}C_6$ carbides , and therefore no MKK. This significantly complicates the conditions for the formation of fatigue cracks in these areas and their propagation, which contributes to a significant extension of the service life of the welded rolls.

With this system, the wear resistance of the welded system also increased, where the matrix formed by low-carbon martensite is strengthened by fine niobium carbides, see Fig. 5, with a microhardness of 538HV $_{0.05}$, hardness of 475 HV10.

Figure 6. View of welded cylinders with 3rd generation materials, preferably with a swing.

3. Results

Preheated roller to an interpass temperature of 250-350°C made of low-alloy steel, the first layer is welded with VÚZ RD 535 as an intermediate layer between the roller and the VUZ RD535 weld, and then preferably with a staggered pattern, two layers of VÚZ RD 527 wire weld, see Fig. 6.

The weld deposit is pore-free, solid, in transition after stress relief heat treatment with a fine bainitic structure in HAZ. The stress relief heat treatment mentioned in the article is important for the formation of the aforementioned CrNiCr 2 N precipitates, and after gradual cooling of the weld deposit, the weld deposit achieves a favorable structure with a matrix formed by low-carbon martensite.

Measurement of hardness in cross-section after heat treatment.

Table 4. Measured hardness values after heat treatment.

Number	**1**	**2**	**3**	**4**	**5**	**6**	**7**	**8**	**9**	**10**	**11**	**12**	**13**	**14**
HV	481	474	465	441	439	457	453	360	441	353	318	334	293	283

Figure 7 shows the measured hardness values after heat treatment.

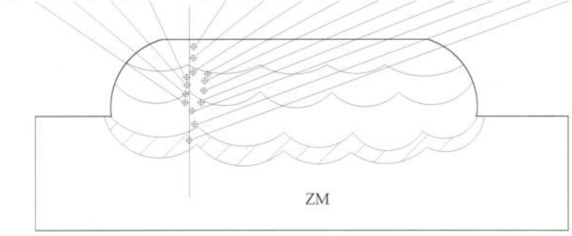

Figure 7. Measured hardness values after heat treatment.

Table 5. Chemical composition of the weld metal from the 3rd layer (RD527) in mass %.

C	Mn	You	Cr	No	Mo	Nb	N_2
0.12	0.71	0.66	14.09	3.81	1.04	0.21	0.08

Legend:
Base material 24CrMo V5-5
1st layer RD 535+F56
2nd layer RD 527+F56
3rd layer RD 527+F56 (planed to a thickness of 5mm)

4. Conclusions

Cylinders with third-generation welds, with the solution of saturating the weld metal with nitrogen using the SAW welding method, have an increased service life compared to first- and second-generation weld systems by approximately 110%.

The necessary properties of the cylinders are provided by the entire cross-section of the weld, which is 3 mm thick. For this reason, the service life of the cylinder can be extended by another approximately 60% by turning the surface of a partially worn cylinder and re-installing the cylinder into the ZKO after lining the section. This way, the cylinders achieve the high service life required by the users.

Acknowledgments: This contribution is the result of the project implementation: Innovative approaches of the restoration of functional surfaces by laser weld overlaying APVV-20-0303 supported by the Slovak Research and Development Agency and supported by the Ministry of Education of Slovakia Foundation under grant projects VEGA No. 1/0597/23, and KEGA No. 046TUKE-4/2022.

References

1. Čomaj, M.: Increasing the service life of cylinders by welding and thermal spraying. [Habilitation thesis] Faculty of Materials Science and Technology, STU Trnava, 1994
2. Mihalkovič, K.: Research on cored electrodes intended for submerged arc welding of cylinders. [Final report] Ev.č.3600/232/8. VÚZ Bratislava, 7/1990
3. Ševčík, D.: Development of flux F25 and F54. [Research report] VÚZ Bratislava, 1991
4. Blaškovič, P., Čomaj, M.: Renovation by welding and heat spraying, STU Bratislava, 2005
5. Welding, welding No. 9/2004 Čomaj, M., Ševčík, D.: Materials for welding working surfaces of rollers of continuous steel casting lines, pp. 233-237
6. Brochures filled with wires and rods, VÚZ Bratislava

A targeted energy transfer in mechanical drive achieved by varying torsional stiffness

Lucia Žuľová [1,*], Robert Grega [1] and Matúš Kačír [1]

[1] Technical University of Košice, Faculty of Mechanical Engineering, Department of Engineering for Design of Machine and Transport Equipment; lucia.zulova@tuke.sk; robert.grega@tuke.sk; matus.kacir@tuke.sk
*Correspondence: lucia.zulova@tuke.sk; Tel.: +421 55 602 2354

Abstract: For the suppression of unwanted vibrations in a variety of mechanical drives, nonlinear energy sinks (NES) have recently attracted significant interest. Generally, this vibration energy is transferred to the NES through the targeted energy transfer (TET). TET is designed to absorb vibrational energy in an irreversible one-way manner with the aim of dissipating it, without returning it back to the system. In this work, a prototype of TET with varying stiffness is designed for use in a wide frequency mechanical drive. Its static characteristics are numerically determined. Considering the advantages of air springs with varying stiffness used in TET, an area of torsional stiffness is determined.

Keywords: targeted energy transfer, air springs, varying torsional stiffness

1. Introduction

The previous conventional vibration absorption devices were linear and required significant mass to be added to the structure and they consist of a damper, a mass block, and a spring. The damping mechanism of the classical tuned mass damper (TMD) was to transfer the vibration energy from the primary structure to the TMD, which dissipates the energy by the damping element but it has a narrow frequency bandwidth and poor robustness. However, the nonlinear system has stronger robustness and their effectiveness is in wider frequency bandwidth, which is conducive to broadband energy absorption. Also, they bring an advantage in irreversible energy transfer [1-3].

In the early stage, nonlinear vibration absorbers mainly used as their stiffness element nonlinear springs. Later, researchers named the vibration absorber with strong nonlinear stiffness and were able to realize the unidirectional transfer of vibration energy from the primary structure to the energy-dissipation element as NES. Therefore, a nonlinear absorber may be used also as a NES and passively absorb energy from a linear system. In addition, when the linear oscillator was weakly coupled to a nonlinear element, it was also called a NES. From the perspective of structure, the NES is mainly composed of three parts, namely, damping element, light additional mass, and strong nonlinear stiffness. The multimode model of the structure with the additional NES is able to capture transient resonances, thus extending its vibration reduction frequency bandwidth.

The mechanism of capturing and dissipating vibration energy through NES is called target energy transfer (TET), which is characterized by irreversible, one-way energy transfer. When resonance capture occurs, the vibration energy of the primary structure is rapidly transferred to the NES and consumed by the damping elements of the NES. Due to the reduction of vibrational energy, the system will escape from the resonant state and be captured by the new state [4].

Many previous researchers have been devoted to different types of NES elements. For example, there are authors dealing with rubber-based NES [5] and multi-stable NES

[6]. Dou et al. proposed a magnet based bi-stable nonlinear energy sink for torsional vibration suppression of rotor system [7] and the authors also focus on the use of air as a vibration absorber- the AirNES [8]. However, many of them have proposed TET systems with efficiency in narrow-frequency bands, or they can perform their function only in a defined frequency band [9].

This paper aims to present a new concept of TET, which varying stiffness allows it to work in a wide frequency band. The concept of TET was designed to provide vibration absorption in mechanical drives of different machines. The model and numerical calculation of the basic operating characteristics of TET are included in this article.

2. TET design

As already mentioned in the introduction, TET systems work in different frequency bands. Taking into account the use only in a narrow spectrum of frequencies, it is inefficient for machines and devices working in dynamically changing operating modes. For this reason, when designing new TET system, we focused on the possibility of using varying stiffness through air springs. These air springs, also used in pneumatic flexible couplings, have been developed for a long time at our workplace [10,11]. Experience and proven use became the impulse for the use of these air springs in our new TET prototype concept.

2.1. Concept

Fig. 1 presents a conceptual 3D view of the pneumatic TET. The main parts of TET are shown in Fig. 1a and represent two discs interconnected with air springs. The use of air springs ensures the elastic parts of the TET. These air springs are attached to connecting elements, which are shown in Fig. 1b, where the driving elements are shown in red, and the driven elements are shown in green. They are placed alternately, which means that two elements facing each other drive two other elements placed opposite each other. The TET is connected to the primary system (pneumatic flexible coupling) via the connection disk (3), where the vibration energy is absorbed by means of air springs (2) and the secondary disk (1) and then dissipated irreversibly to the primary system, as the principle of the TET.

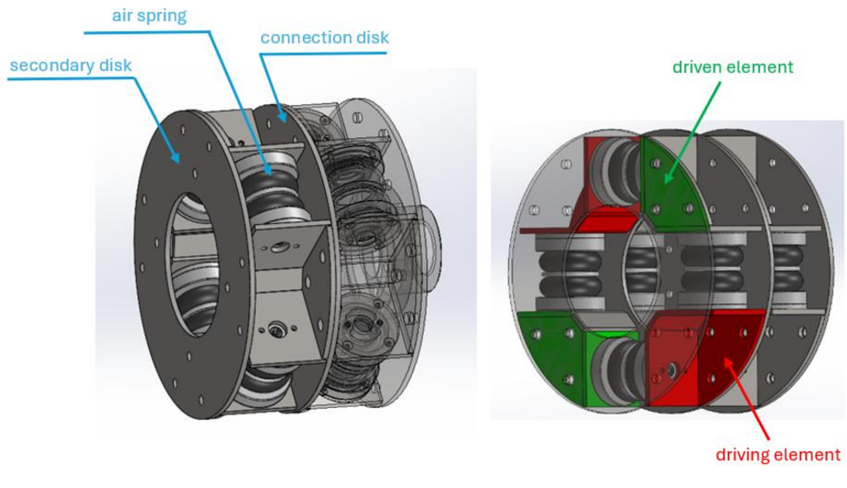

Figure 1. CAD view of pneumatic TET prototype.

The basic parameters of the TET and air springs are shown in Tab. 1.

Table 1. Parameters of TET and Air Springs.

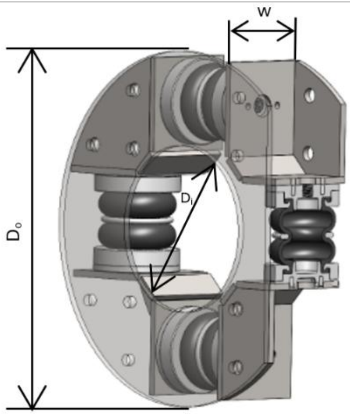

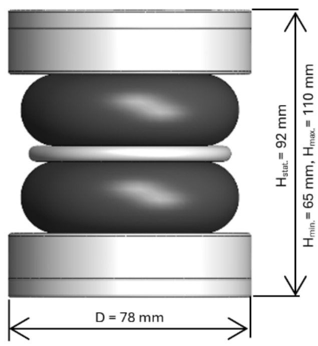

Parameters of TET		
D_o	Outer diameter	320 mm
D_i	Inner diameter	150 mm
w	width	85 mm
Parameters of AIR SPRINGS		
H_{max}	Height max.	110 mm
H_{stat}	Height static	92 mm
H_{min}	Height min.	65 mm
D	Diameter	78 mm

2.2 Air springs

Air springs are designed for many different applications where vibrations should be eliminated. A complete air spring is composed of a rubber-textile bellow, rings among convolutions, two clamping bead rings, a top and a lower cover. Air springs can be inflated either individually or centrally. Air springs bellows are applicable up to maximum operating pressure. This pressure is related to a static height H_{stat} [12].

2.3. Targeted energy transfer

The main principle of TET is the absorption of vibrations from the primary system with the aim of irreversible dispersion of unwanted vibration energy, where this energy is absorbed. The proposed TET prototype is considered to be used in a mechanical drive with a pneumatic flexible coupling (Fig. 2), which represents the primary system. Due to the properties of the pneumatic flexible coupling, which is able to change its torsional stiffness during a dynamic condition of the mechanical drive, it can be tuned to achieve the lowest possible vibration values during its operation. However, these vibrations can be absorbed by other parts of the drive, which is an undesirable phenomenon. Therefore, TET is designed for this coupling, as a secondary system, using air springs, which cause nonlinear dynamics. By changing the stiffness, they can operate in a wide range of frequencies occurring in mechanical drive.

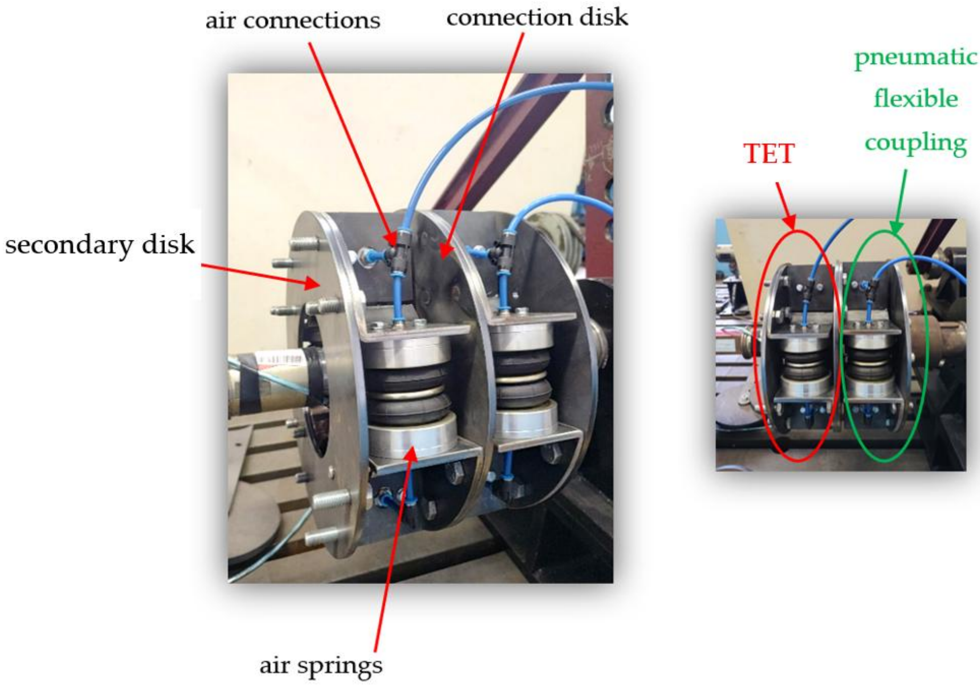

Figure 2. Main parts of TET and connection to pneumatic flexible coupling.

The attachment of TET and pneumatic flexible coupling (as a primary system) is only a connection with screws only. The vibration energy is transferred to the secondary disk via air springs, which can absorb different frequencies from the primary system by varying their stiffness by increasing and decreasing of the air pressure by air connections between each air springs. The air is supplied by the external compressor with a pressure indicator.

3. Results and discussion

Due to the possibility of using the TET system in different types of mechanical drives, with different output loads, the weight of the mass added to the TET system must be taken into account also. Thus, the operating properties of the TET system are directly related to the mass of the primary system itself and its operational properties.

When determining the operating characteristics, the load characteristics (Fig. 3) and the torsional stiffness of TET (Fig. 4) were numerically determined.

The numerical calculation of the static load characteristics was based on the torque load and the twist angle of the coupling, which are detailed described in [13]. For individual air pressures in the air spring from 100 kPa to 700 kPa, the twist angle of the coupling increases linearly with increasing torque. From the graph for torsional stiffness of TET (Fig. 4) we can observe increasing stiffness with increasing load torque. Stiffness of air springs increases in individual pressures and their value rises with a higher torque. This fact became the basis for a new proposed TET.

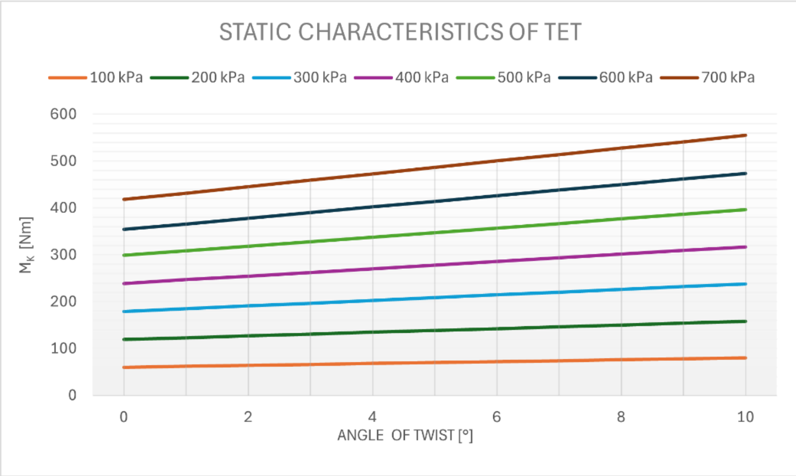

Figure 3. Static characteristic of TET.

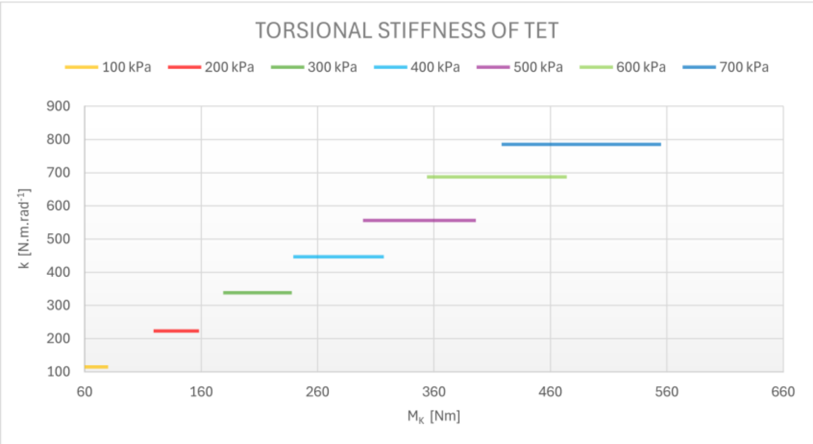

Figure 4. Torsional stiffness of TET.

4. Conclusion

A novel nonlinear energy sink with varying stiffness TET system is proposed to enhance the vibration reduction effects in mechanical drives. Moreover, numerical calculation shows the area of torsional of TET (Fig. 5), where it is demonstrable that with dynamically changing system parameters, TET can improve its performance by adjusting varying stiffness in its air springs.

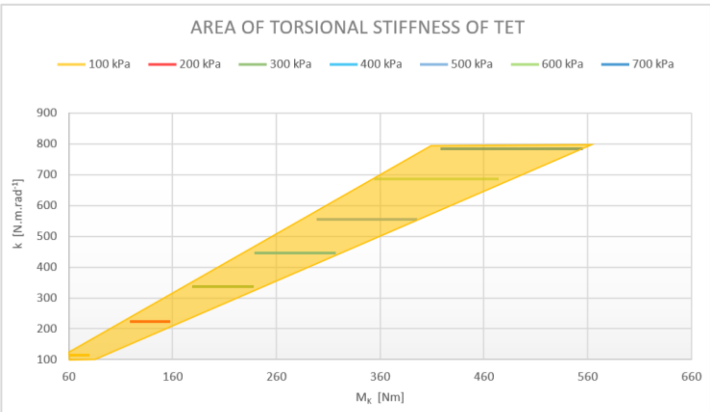

Figure 5. Area of torsional stiffness of TET.

In near future, the authors have an aim to test this new TET prototype in laboratory conditions to obtain knowledge from experimental measurements about:

- the frequency spectrum of use,
- working conditions in resonance,
- amount of absorbed vibrational energy,
- possibilities of use for different types of drives in different types of machines.

Acknowledgments: This paper was written within the framework of the VEGA 1/0573/25 and KEGA: 037 TUKE-04/2024

Conflicts of Interest: The authors declare no conflict of interest.

References

1. Kang, Xiaofang, Tang, Jianjun, Xia, Guanghui, Wei, Jiachen, Zhang, Fuyi, Sheng, Ziyi, Design, Optimization, and Application of Nonlinear Energy Sink in Energy Harvesting Device, International Journal of Energy Research, 2024, 2811428, 33 pages, 2024. https://doi.org/10.1155/2024/2811428.
2. Lee Y. S., Vakakis A. F., Bergman L. A., McFarland D. M., Kerschen G., Nucera F., Tsakirtzis S., and Panagopoulos P. N., Passive non-linear targeted energy transfer and its applications to vibration absorption: a review, Proceedings of the Institution of Mechanical Engineers, Part K: Journal of Multi-body Dynamics. (2008) 222, no. 2, 77–134, https://doi.org/10.1243/14644193JMBD118, 2-s2.0-46749131847.Author 1, A.; Author 2, B. Book Title, 3rd ed.; Publisher: Publisher Location, Country, 2008; pp. 154–196.
3. Wang G., Ding H., and Chen L., Performance evaluation and design criterion of a nonlinear energy sink, Mechanical Systems and Signal Processing. (2022) 169, article 108770, https://doi.org/10.1016/j.ymssp.2021.108770.
4. Ding H. and Chen L., Designs, analysis, and applications of nonlinear energy sinks, Nonlinear Dynamics. (2020) 100, no. 4, 3061–3107, https://doi.org/10.1007/s11071-020-05724-1.
5. Yanbo, Cao & Yao, Hongliang & Dou, Jinxin & Wu, Chao. (2023). Torsional vibration suppression of rotor systems using a rubber-based nonlinear energy sink. Meccanica. 58. 10.1007/s11012-023-01637-6.
6. Hongliang Yao, Yuwei Wang, Yanbo Cao, Bangchun Wen, Multi-stable nonlinear energy sink for rotor system, International Journal of Non-Linear Mechanics, Volume 118, 2020, 103273, ISSN 0020-7462.
7. Jinxin Dou, Zhenping Li, Yanbo Cao, Hongliang Yao, Ruxue Bai Magnet based bi-stable nonlinear energy sink for torsional vibration suppression of rotor system, Mechanical Systems and Signal Processing, Volume 186, 2023, 109859, ISSN 0888-3270, https://doi.org/10.1016/j.ymssp.2022.109859
8. Thomas Roncen, Guilhem Michon, Vincent Manet,Design and experimental analysis of a pneumatic Nonlinear Energy Sink, Mechanical Systems and Signal Processing, Volume 190, 2023,110088,ISSN 0888-3270,https://doi.org/10.1016/j.ymssp.2022.110088.
9. Ke-Fan Xu, Mu-Qing Niu, Ye-Wei Zhang, Cun-Ying Meng, Li-Qun Chen, A nonlinear energy sink enhanced by active varying stiffness for spacecraft structure: theory, simulation, and experiment, Mechanical Systems and Signal Processing, Volume 204, 2023, 110787, ISSN 0888-3270, https://doi.org/10.1016/j.ymssp.2023.110787
10. Grega, R., Krajnak, J., Žuľová, L., Kačír, M., Kaššay, P., & Urbanský, M. (2023). Innovative solution of torsional vibration reduction by application of pneumatic tuner in shipping piston devices. Journal of Marine Science and Engineering, 11(2), 261.
11. Kaššay, P., Grega, R., Urbanský, M., Krajňák, J., Kačír, M., & Žuľová, L.: Novel Design of Variable Stiffness Pneumatic Flexible Shaft Coupling: Determining the Mathematical-Physical Model and Potential Benefits. Machines, 2023, 12(1), 28.
12. https://www.rubena.eu/underwood/download/files/vlnovce_katalog_2023.pdf
13. Kaššay, P.; Grega, R.; Urbanský, M.; Krajňák, J.; Kačír, M.; Žuľová, L. Novel Design of Variable Stiffness Pneumatic Flexible Shaft Coupling: Determining the Mathematical-Physical Model and Potential Benefits. Machines 2024, 12, 28. https://doi.org/10.3390/machines12010028.

Poznámky

Poznámky

Novus **Scientia 2025**

Zborník príspevkov z XXII. Medzinárodnej vedeckej konferencie doktorandov strojníckych fakúlt technických univerzít a vysokých škôl

Názov:	Novus Scientia 2025
Editor:	© prof. Ing. Ján Slota, PhD.
	© Ing. Erika Dubňanská
	© Ing. Martina Hančinová
	© Ing. Barbara Schürger
Vydavateľ:	Technická univerzita v Košiciach,
	Strojnícka fakulta,
	Letná 1/9, 042 00 Košice-Sever
Rok:	2025
Náklad:	75 výtlačkov
Rozsah:	360 strán
Miesto konania:	Strojnícka fakulta, Technická univerzita v Košiciach
Dátum konania:	30.01.2025

ISBN 978-80-553-4828-5